
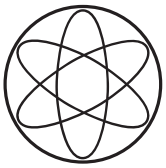

Search for heavy Zh and Wh resonances in 13 TeV proton-proton collisions with the ATLAS detector at the LHC

STEFAN RAIMUND MASCHEK

Dissertation

München 2021

TECHNISCHE UNIVERSITÄT MÜNCHEN
Fakultät für Physik

Max-Planck-Institut für Physik
(Werner-Heisenberg-Institut)

Search for heavy Zh and Wh resonances in 13 TeV proton-proton collisions with the ATLAS detector at the LHC

Stefan Raimund Maschek

Vollständiger Abdruck der von der Fakultät für Physik der Technischen Universität München zur Erlangung des akademischen Grades eines

Doktors der Naturwissenschaften (Dr. rer. nat.)

genehmigten Dissertation.

Vorsitzender:

apl. Prof. Dr. Norbert Kaiser

Prüfer der Dissertation:

1. apl. Prof. Dr. Hubert Kroha
2. Prof. Dr. Lothar Oberauer

Die Dissertation wurde am 17.11.2021 bei der Technischen Universität München eingereicht und durch die Fakultät für Physik am 1.12.2021 angenommen.

Search for heavy Zh and Wh resonances in 13 TeV proton-proton collisions with the ATLAS detector at the LHC

Stefan Raimund Maschek

Abstract

Searches are presented for new heavy resonances decaying into leptonically decaying weak gauge bosons and Higgs bosons decaying into a bottom quark pair using 139 fb^{-1} of proton collision data of the ATLAS detector of the LHC at 13 TeVcenter-of-mass energy. Such diboson resonances are predicted by many extensions of the Standard Model of particle physics. The reconstruction of strongly boosted $h \to b\bar{b}$ decays has been optimized based on b-tagging of track jets and analysis of jet substructure. The searches are is performed in a model-independent way, and the results are interpreted in benchmark models predicting spin-0 or spin-1 resonances. No significant excess has been observed, and improved upper limits have been set on the production cross section times branching ratio. The sensitivity for another fermiophobic spin-1 resonance model has been studied for the first time in the ATLAS experiment.

Acknowledgements
I would like to thank my supervisor Sandra Kortner, who always supported me and gave me advice on physics and often of human nature. She was a helpful and caring supervisor and mentor. With a lot of dedication, she guided me to the completion of this thesis in moments when I had lost the compass and encouraged me in moments when I no longer believed in myself. I would also like to thank Hubert Kroha, my thesis advisor. He introduced me to the world of the ATLAS experiment and gave me the opportunity to write this thesis in his group at the Max Planck Institute for Physics. I am very grateful to him for the many educational opportunities he gave me, such as the autumn school at Maria Laach. I want to thank him for the support for being able to experience shifts in the control room at the world's largest particle detector at CERN.

I would like to thank Norbert Kaiser and Lothar Oberauer for evaluating my thesis and being on my dissertation committee.

I also want to thank Felix Müller, my day-to-day supervisor of my the first year as a Ph.D. student. The foundations for the Higgs-tagger studies were laid with him. These studies eventually resulted in a whole chapter in this thesis and a journal publication. This journal publication would also not have been possible without Tatjana Lenz, Reina Camacho, and Cigdem Issever. I would like to thank them for their patience with me and dedication to the writing of the paper.

For the second half of my time as a Ph.D. student, I was day-to-day supervised by Dominik Duda, whose availability - interrupted only by meetings - seems to have been 24/7. I greatly appreciated his expertise and would like to thank him for all of his advice.

Under his guidance, our analysis group published two conference notes and will soon a journal paper. I would like to thank Tong Qiu, Tong Li, Makayla Vessella, Ulla Blumenschein, and Wade Fisher for their fruitful collaboration in the Vh-resonance group. I would also like to thank Nora Pettersson, whose Skype chats I enjoyed very much and in whom I saw a fellow sufferer in the ever-lasting fight against the software framework's code bugs. I would especially like to thank Andreas Hönle. Besides the fruitful cooperation in the analysis group, I enjoyed the countless table tennis matches and the unforgettable conferences and workshops where Andi turned into a DJ at late hours.

I would like to thank all my fellow students at the Max Planck Institute, especially Verena Valbrecht, Philipp Gadow, Dominik Krauss, and Korbinian Schmitt-Sommerfeld, whom I could always ask questions and count on helpful and competent answers. Thanks to my fellow students Mathias Hüther, Fabian Batsch, and Anna Bachmann, long-time delegated to CERN. It was good to have nice companion there during more extended stays.

Last but not least, I would like to thank my family. My parents always supported me and encouraged me, and showed me that they were proud of me. Mostly, I would like to thank my life companion Csilla, who has always stood by me, in particular through the long process of writing this thesis, and has always encouraged me to finish. Thank you!

Table of contents

INTRODUCTION

The fundamental interactions of the known elementary constituents of matter are described by the Standard Model (SM) of particle physics. In numerous precision experiments, no significant deviations from its predictions have been found so far. With the Higgs boson discovery by ATLAS [1] and CMS [2] in 2012, the last missing particle predicted by the SM was discovered. Since then, measurements of the Higgs boson properties show that the new particle is consistent with the neutral scalar boson as predicted by the Brout-Englert-Higgs mechanism of the SM.

Nevertheless, the SM leaves many questions unanswered, such as the explanation of the low value of the Higgs boson mass despite large radiative corrections, the observed asymmetry between matter and antimatter in the universe, and the existence of Dark Matter.

A large number of theoretical models extending the SM have been introduced to provide answers to the open questions in the SM, including extended Higgs sectors or new strong interactions breaking the weak gauge symmetry dynamically. Many of these theories predict new particles that decay into the discovered Higgs boson h and a weak gauge boson ($V = Z, W$). The postulated particles typically have masses at the TeV scale and could, therefore, be produced in proton-proton collisions at the Large Hadron Collider (LHC). In this thesis, a search for such heavy new resonances decaying into Vh is performed using the LHC Run-II data recorded in the period from 2015 to 2019 by the ATLAS detector. The search is performed in the semi-leptonic final state with leptonic vector boson decays and Higgs boson decay into a $b\bar{b}$-quark pair. The leptons from the vector boson decay allow for an efficient event trigger and the suppression of QCD background contributions. The hadronic Higgs boson decay channel $h \to b\bar{b}$, although challenging to reconstruct, has the highest branching ratio of 60%, much larger than the cleaner di-photon or four-lepton decay channels with branching ratios of 0.23% and 0.01%, respectively.

The b-quarks from the Higgs boson decay undergo a hadronization process, leading to hadronic jets. For low Vh resonance masses, the Higgs boson decay into $b\bar{b}$ results in jets of relatively small radius around the b-quark direction, which are well separated. Each of the two jets can be tagged by the reconstruction algorithms as originating from b-quarks. For higher Vh masses, on the other hand, the Higgs bosons are strongly boosted such that their decay products are strongly collimated, and the two b-jets merge into just one jet with a large radius. In order to tag such large-radius jets originating from boosted $h \to b\bar{b}$ decays, a dedicated Higgs tagger algorithm has been developed. The standard b-tagging algorithm cannot be applied to the merged large-radius jets but only to a jet reconstructed

from tracks of charged particles originating from the hadronization of the two b-quarks. Additional requirements on the jet substructure, such as the jet mass and the number of jet constituents, further improve the Higgs tagger performance. The Higgs tagger is employed for the Vh resonance search in this thesis and in many other ATLAS searches with boosted Higgs bosons.

The Vh resonance search covers a wide range of resonance masses from 300 to 5000 GeV. Thus, both the resolved final state topologies with well-separated b-jets from Higgs decays and the merged topologies with the b-jets from Higgs decays merged into a single large-size jet are taken into account. The signal signature consists of a peak in the invariant mass distribution of the Vh decay products, essentially providing a model-independent search. The measurements are also used to set upper limits on free parameters of several benchmark models beyond the SM (BSM) by comparing Monte Carlo (MC) predictions for signal and background processes with the data. The relevant background processes are additionally constrained, employing dedicated signal-depleted control data.

In addition to the dominant resonance production via quark-antiquark annihilation, the production mode via vector boson fusion (VBF) has been explored in this thesis for the first time in ATLAS. The VBF production process becomes dominant in BSM models in which couplings of the hypothetical new resonance to fermions are forbidden. The vector bosons are irradiated from two quarks in the proton-proton collision, where the emitting quarks leave the characteristic signature of two jets in opposite forward detector regions. This feature of a large rapidity gap between the two jets allows for strong SM background suppression, increasing the signal sensitivity.

The thesis is structured as follows: The SM of particle physics and several extensions which are probed by the Vh resonance search are introduced in Chapter 1. Descriptions of the Large Hadron Collider and the ATLAS detector and the event reconstruction algorithms are given in Chapter 2. In Chapter 3, the studies of the Higgs tagger performance are discussed, including possible improvements using the jet substructure information. The search for the Vh resonances with Run-II ATLAS data is then described in Chapter 4. The extension of the Vh resonance search to the VBF production channel is presented in Chapter 5, followed by conclusions and outlook.

CHAPTER ONE

THEORETICAL FRAMEWORK

In the middle of the last century more and more particles were found which interact via the strong and electroweak nuclear forces, and a fundamental theory describing these particles and interactions was developed, the Standard Model (SM) of particle physics. The SM describes all known elementary particles and their interactions, the electromagnetic, the weak and the strong force in the framework of quantum field theory (QFT) with local gauge symmetries.

A model of a successful QFTs was Quantum Electrodynamics (QED) predicting precisely the hyper-fine structures in atomic energy levels and electron scattering cross sections. The extension of this theory to the weak and strong forces lead to an unified theory of all forces based on local gauge invariance. It has been extensively tested and confirmed by all experiments so far.

The SM is introduced in Section 1.1. Basic concepts of SM predictions for the LHC are discussed in Section 1.2. Finally, Section 1.3 explains the limitations of the SM and introduces the possible extensions investigated in this thesis. The units used in this thesis are the natural units with $\hbar = c = 1$.

1.1 The Standard Model of particle physics

The elementary particles of the SM are consist of the matter particles, fermions, and particles mediating the interactions, vector gauge bosons. All interactions are described by Yang-Mills theories [3] based on local gauge symmetries. To give masses to the elementary particles, the SM also predicts a scalar boson field with the Higgs boson as an excitation which is described in Section 1.1.2. The particle content of the SM is shown in Fig. 1.1.

The fermions in the SM have spin quantum number $1/2$. There are two different kinds of elementary fermion fields, leptons and quarks. Both types of fermions appear in three generations with the same quantum numbers but different masses. The charge quantum numbers of the fermions are related to via the Gell-Mann-Nishijima relation,

$$Q = T_3 + \frac{1}{2}Y, \tag{1.1}$$

with Q the electric charge.

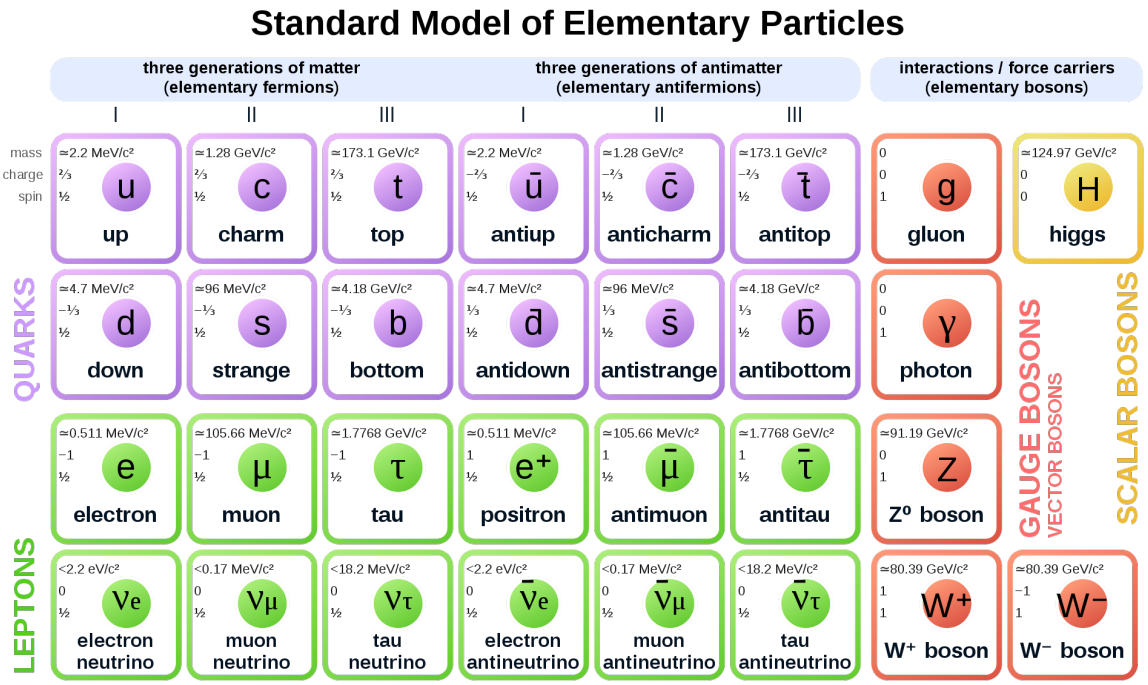

Figure 1.1: The particle content of the SM. Figure from [4].

The earliest known lepton is the electron. The electron and its much more massive partners, the muon and the τ-lepton have one unit of negative elementary electric charge e, the weak isospin T_3 and the hypercharge Y quantum numbers.

The charged leptons have weak isospin quantum numbers $T = 1/2$ and $T_3 = -1/2$ and the hypercharge $Y = -1$. The charged leptons appear in fundamental doublets of the weak isospin gauge symmetry together with their associated neutrinos with $Q = 0$, $T = 1/2$, $T_3 = +1/2$ and $Y = -1$. The anti-particles of the fermions have opposite additive charge quantum numbers T_3, Y and Q. Neutrinos are considered to be massless in SM. Neutrinos only interact weakly and were first observed in 1956 [5].

The three quark generations have hypercharge $Y = +1/3$. The up (u), charm (c) and top (t)[1], have like the neutrinos weak isospin $T_3 = +1/2$ form left-handed $SU(2)_L$ doublets together with down (d), strange (s) and bottom (b) quarks[2], with $T_3 = -1/2$. Quarks have color quantum numbers (r,g,b), the anti-quarks anticolors ($\bar{r}$,$\bar{g}$,$\bar{b}$). Forming fundamental triplets of the $SU(3)_C$ color groups of the strong gauge interaction. The heaviest quark, the top quark was detected in 1995 at the Tevatron and has a mass of $m_t = 172,76$ GeV [6, 7].

Vector bosons with spin 1, photons (γ), the Z and $W^{\pm}$ bosons and the gluon are the mediators of the gauge interactions. Photons are the mediators of the electromagnetic force, the gluons of the strong

[1] collectively referred to as up-type quarks (u^i, with $i = 1, 2, 3$)
[2] collectively referred to as down-type quarks (d^i, with $i = 1, 2, 3$)

force and the $W^{\pm}$ and Z^0 bosons of the weak force. The W and Z bosons were first observed at Super Proton Syncrotron (SPS) at CERN in 1983 and have masses $m_W = 80.38$ GeV and $m_Z = 91.19$ [6, 8].

The gauge symmetries of the interactions in the SM require vanishing masses of the gauge bosons and of the fermions as well in the presence on maximum parity violation by the weak interaction in contradiction to the observations. To solve this problem the electroweak gauge symmetry $SU(2)_L \times U(1)_Y$ is broken spontaneously by a non-vanishing vacuum expectation value (VEV) of an additional scalar field, the Higgs field. With the discovery of the Higgs boson in 2012, a massive excitation of the Higgs field, by the ATLAS and CMS experiments at the LHC the last missing piece of the SM has been found.

1.1.1 Gauge symmetries and interactions

The fundamental interactions of the SM are all described by Yang-Mills theories [3] while introducing local gauge symmetries in the Lagrangian

$$\begin{aligned}\mathcal{L} = &-\frac{1}{4} V^a_{\mu\nu} V^{\mu\nu a} \\ &+ i\bar{\psi}\gamma^\mu D^a_\mu \psi + h.c. \\ &+ \bar{\psi}_i y_{ij} \psi_j \phi + h.c. \\ &+ |D_\mu \phi|^2 - \mathcal{V}(\phi),\end{aligned} \tag{1.2}$$

where a runs over the generators of the SM gauge symmetries and i/j are the fermion generation indices. The different terms are described in the following.

Invariance of the Lagrangian under local gauge transformations requires the introduction of gauge-covariant derivatives,

$$D_\mu = \partial_\mu - igV^a_\mu(x)\hat{\tau}^a\psi(x). \tag{1.3}$$

Insertion of D_μ in Eq. (1.2) results in interaction terms between the fermions ψ and gauge bosons V_μ of the form:

$$\mathcal{L}_{\text{interaction}} = g\bar{\psi}\gamma_\mu V^a_\mu \hat{\tau}^a \psi. \tag{1.4}$$

From the Lagrangian, the general equations of motion are derived according to Hamilton's principle. The wave equation of a massive relativistic free fermion field ψ is given by the Dirac equation derived from the term

$$\mathcal{L} = i\bar{\psi}\gamma^\mu\partial_\mu\psi - m\bar{\psi}\psi \tag{1.5}$$

in the Lagrangian where γ^μ are the Dirac γ-matrices ($\mu = 0, 1, 2, 3$).

The symmetry group of the SM is the direct product of the simplest special unitary:

$$SU(3)_C \times SU(2)_L \times U(1)_Y. \tag{1.6}$$

The elements of the gauge symmetry are local phase transformations of the fermion and the scalar fields depending on the space-time coordinates,

$$\phi(x^\mu) \rightarrow e^{-ig\alpha^a(x^\mu)\tau^a}\phi(x^\mu), \tag{1.7}$$

where $\hat{\tau}^a$ are the generators (charge operators) and α^a the scalar phase parameters of the gauge symmetry group. g is the coupling strength parameter of the respective interaction.

The first term of Eq. (1.2) contains the kinetic terms of the gauge fields with the filed strength tensors

$$V^a_{\mu\nu} = \partial_\mu V^a_\nu - \partial_\nu V^a_\mu + g f^{abc} V^b_\mu V^c_\nu \tag{1.8}$$

where $V^a = G^{1,\ldots,8}$, $W^{1,2,3}$ and B are the vector potentials of the gauge fields of the $SU(3)_C$, $SU(2)_L$ and $U(1)_Y$ groups, respectively. The structure constants f^{abc} are specific for each symmetry group. The generators of the $SU(2)_L$ group are represented by the three Pauli matrices, those of the $SU(3)_C$ group by the eight Gell-Mann matrices and the generator of the Abelian $U(1)$ group by the weak hypercharge. The charges of the $SU(2)_L$ symmetry are the three components of the weak isospin T and the charges associated to the $SU(3)_C$ are eight color charges. There is a gauge field for each operator of the gauge groups.

The fermion fields are spinors, $\psi(x^\mu)$, which are solutions to the Dirac equation. The spinors ψ have right-handed and left-handed chiral components,

$$\psi_L = \frac{1-\gamma^5}{2}\psi \; \psi_R = \frac{1+\gamma^5}{2}\psi, \tag{1.9}$$

with $\gamma^5 = -i\gamma^0\gamma^1\gamma^2\gamma^3$.

The weak interaction only couples to left-handed doublets of the $SU(2)_L$, while the right-handed fermion states are $SU(2)_L$ singlets This is described in gauge theory by the fact that right- and left-handed spinor fields are represented by different multiplets. The left-handed parts transform as doublets, the right-handed ones trivially as singlets,

$$\vec{Q}^i_L = \begin{pmatrix} u^i_L \\ d^i_L \end{pmatrix}, \vec{L}^i_L = \begin{pmatrix} \nu^i_L \\ e^i_L \end{pmatrix}, \vec{e}^i_R, \vec{u}^i_R, \vec{d}^i_R, \tag{1.10}$$

where $i = 1, 2, 3$ denotes the three fermion generations. There are no right-handed neutrinos in the SM.

The quarks transform as triplets under $SU(3)_C$,

$$u^i = \begin{pmatrix} u^i_{\mathrm{r}} \\ u^i_{\mathrm{g}} \\ u^i_{\mathrm{b}} \end{pmatrix}, \; d^i = \begin{pmatrix} d^i_{\mathrm{r}} \\ d^i_{\mathrm{g}} \\ d^i_{\mathrm{b}} \end{pmatrix}, \tag{1.11}$$

while all other fermions form $SU(3)_C$ singlets and do not carry color. The eigenstates of the electroweak and of the strong interaction (mass eigenstates) are not the same but related by unitary transformations combined in the Cabibbo-Kobayashi-Maskawa (CKM) matrix, U_{CKM}, transforming the down-type quark states coupling to the up-type quark mass eigenstates in the charged weak interaction, where the absolute values of the CKM matrix elements have been measured to be [6]:

$$\begin{pmatrix} |U_{ud}| & |U_{us}| & |U_{ub}| \\ |U_{cd}| & |U_{cs}| & |U_{cb}| \\ |U_{td}| & |U_{ts}| & |U_{tb}| \end{pmatrix} = \begin{pmatrix} 0.97 & 0.22 & 0.0038 \\ 0.22 & 0.99 & 0.04 \\ 0.008 & 0.04 & 1.01 \end{pmatrix}. \tag{1.12}$$

The gauge bosons associated to the $SU(3)_C$ group are the eight gluons mediating the strong interaction in QCD. The vector fields W_μ^a and B_μ correspond to the gauge bosons of the electroweak $SU(2)_L \times U(1)_Y$ symmetry.

1.1.2 Electroweak symmetry breaking

The gauge bosons are required to be massless. Gauge invariance together with parity violation in the weak interaction requires also massless fermions. Particle mass are generated in the SM by spontaneous symmetry breaking of the $SU(2)_L \times U(1)_Y$ symmetry. For this purpose, a complex scalar $SU(2)_L$ doublet field ϕ with hypercharge $Y = +1/2$ with the potential

$$\mathcal{V}(\phi) = \mu^2 |\phi^\dagger \phi| + \lambda \left(|\phi^\dagger \phi| \right)^2 \tag{1.13}$$

is introduced. The potential has an infinite set of minima at the so-called VEV $|phi_0| = v$ of the scalar field. While the Lagrangian and the set of minima is invariant under $SU(2)_L \times U(1)_Y$, the choice of one particular vacuum state spontaneously breaks the symmetry. An expansion around the ground state can be expressed as

$$\Phi(x^\mu) = \begin{pmatrix} \xi_1(x^\mu) + i\xi_2(x^\mu) \\ v + h(x^\mu) + i\xi_3(x^\mu) \end{pmatrix}, \tag{1.14}$$

where h is a physical massive scalar field, the Higgs boson and ξ_i are massless excitations of the ground state, referred to as Goldstone bosons. By a choice of the gauge the latter degrees of freedom can be canceled while generating mass terms for the weak gauge bosons $W^\pm$ and Z^0. The $U(1)_Q$ of QED remains unbroken and the photon massless. The Goldstone bosons are absorbed into the longitudinal degrees of freedom of the weak gauge bosons.

The mass matrix of the neutral fields B and W_μ^3 of the electroweak interaction is not diagonal. Diagonalization gives the mass eigenstates,

$$\begin{pmatrix} Z_\mu \\ A_\mu \end{pmatrix} = \begin{pmatrix} \cos\theta_W & \sin\theta_W \\ -\sin\theta_W & \cos\theta_W \end{pmatrix} \begin{pmatrix} W_\mu^3 \\ B_\mu \end{pmatrix}, \tag{1.15}$$

with weak mixing angle (Weinberg angle) θ_W, the massless photon field A_μ and the massive neutral vector boson field Z_μ. The Weinberg angle is related to the coupling constants g_Y and q_W of the $U(1)_Y$

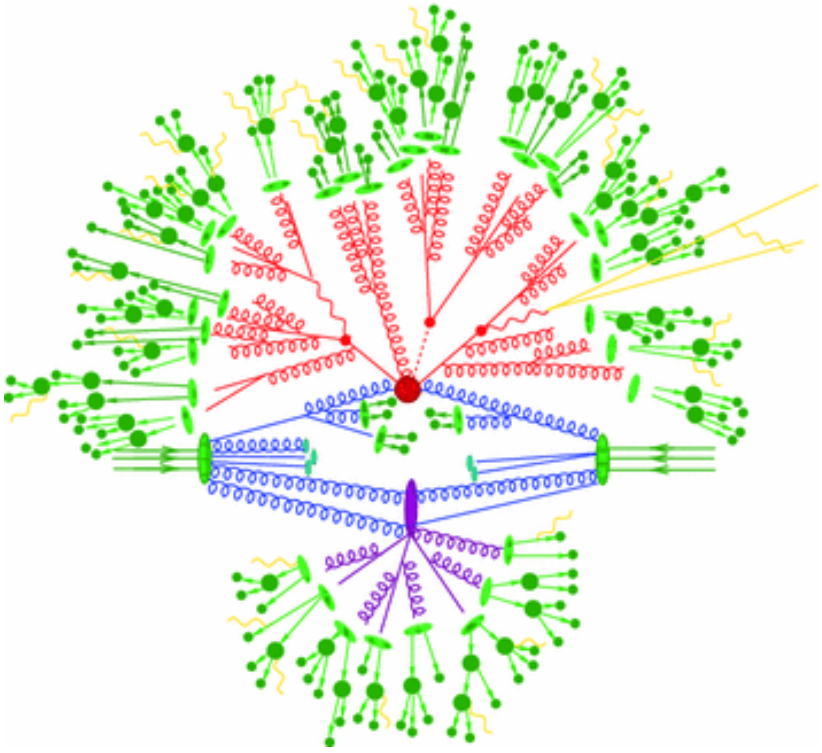

Figure 1.2: Illustration of QCD processes and hadronization in proton-proton collisions: The red point represents the hard interaction, which is characterized by the largest momentum transfer. In red final-state radiation (FSR) of gluons and $q\bar{q}$ production are shown and in green the fragmentation of the final state partons in a parton shower (PS) with subsequent hadronization into mesons and baryons. The underlying event (UE) comprising the interaction of the proton debris is shown in purple. A certain fraction of the initial momenta is also emitted as initial-state radiation (ISR). Figure from [9].

and $SU(2)_L$ via

$$\cos\theta_W = \frac{g_W}{\sqrt{g_W^2 + g_Y^2}} = \frac{m_W}{m_Z}. \tag{1.16}$$

Fermions obtain their masses via Yukawa couplings y_{ij} to the Higgs field (see. Eq. (1.2)).

1.2 Phenomenology in proton-proton collisions

1.2.1 Cross section calculation

The cross section for proton-proton collision processes at the LHC,

$$\sigma_{pp\to X} = \frac{N_{pp\to X}}{\mathcal{L}\cdot t}, \tag{1.17}$$

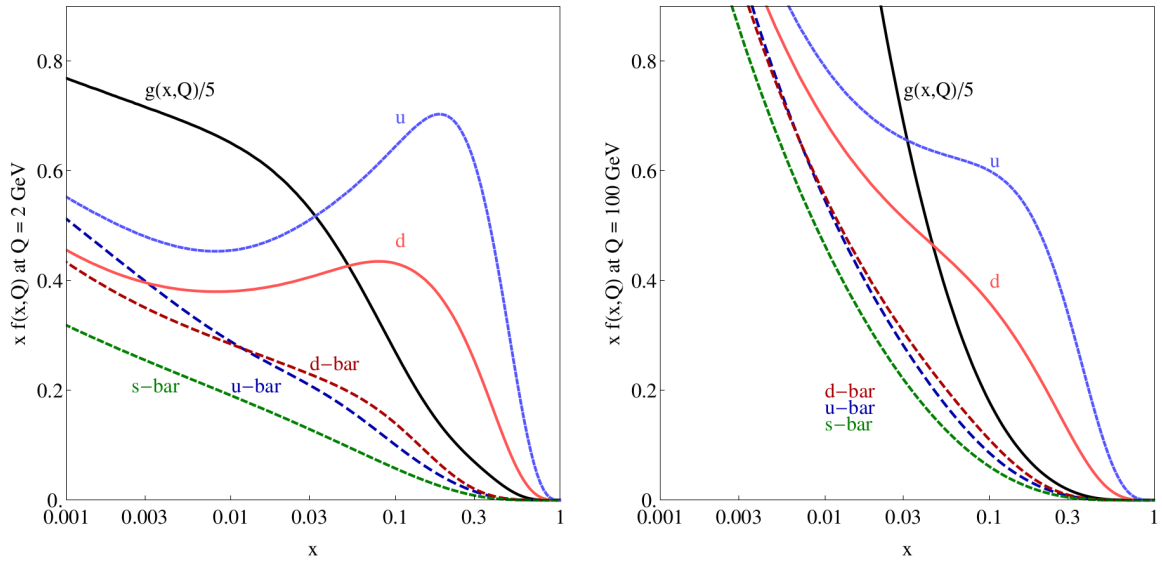

Figure 1.3: Parton density functions (PDFs) in the proton for momentum transfers of $Q = 2$ GeV (left) and of $Q = 100$ GeV (right) in the CT14 PDF set at next-to-next-to leading order (NNLO). Figure from Ref. [11].

gives the number of reactions $pp \to X$ per time interval t for given instantaneous luminosity $\mathcal{L}$.

Since the protons are a bound states of quarks and gluons (partons), the cross section of this process is given by

$$\sigma_{pp\to X} = \sum_i \sum_j \int_0^1 dx_1 \int_0^1 dx_2 f_i(x_1, \mu_F) f_j(x_1, \mu_F) \sigma_{ij\to X'}(x_1, p_1, x_1, p_1, \mu_R, \mu_F) \tag{1.18}$$

using the factorization theorem, where i and j label the incident partons involved in the hard scattering process $ij \to X'$ and f_i is the parton density function (PDF) of the respective parton i. The PDFs depend on the factorization energy scale μ_F. Frequently $\mu_F = |Q|$ is used where Q is the momentum transfer in the hard scattering process.

The PDFs $f_i(x_1, \mu_F)$ have been measured in various experiments [10–12]. The PDFs are p.d.f.s depending on the momentum fraction $x_i = \frac{p_{z,i}}{\sqrt{s}/2}$ of the partons in the protons. The center-of-mass energy of the two scattering partons is given by $\hat{s} = x_i x_j s$. A set of PDFs determined by the CT14 collaboration [11] for instance is shown in Fig. 1.3 for the momentum transfers $Q = 2$ and 100 GeV. The proton valence quarks u and d have their maximum density slightly below $x = 1/3$, the remaining momentum fraction is carried by the sea quarks and gluons. With higher momentum transfer Q, the fraction of gluons and sea quarks increases at small x. The PDFs are available for cross sections calculations in the LHA library [13].

The cross section for the parton-parton hard scattering process $ij \to X'$ is given as a function of the

parton momentum fractions x_i and the energy transfer Q by

$$\sigma_{ij\to X'}(x_i p_1, x_j p_2, \mu_R, \mu_F) = \frac{1}{2\hat{s}} \int d\Phi_n |\mathcal{M}_{ij\to X}(x_i p_1, x_j p_2, p_a, p_b, \mu_R, \mu_F)|^2, \tag{1.19}$$

where $\mathcal{M}_{ij\to X}$ is the scattering matrix element calculated in perturbation theory in the interaction terms in the Lagrangian and

$$d\Phi_n = \prod_{i=1}^{n} \left[\frac{dp_i^4}{(2\pi)^4} (2\pi)\delta(p_i^2 - m_i^2) \right] (2\pi)^4 \delta^{(4)}\left(p_a + p_b - p_{X'}\right), \tag{1.20}$$

the n-body phase space element.

1.2.2 Phenomenology of Quantum Chromodynamics

The strong interaction between quarks and gluons described by Quantum Chromodynamics (QCD) based on the $SU(3)_C$ gauge group, differs from the electroweak interaction. The strong coupling constant diverges below an energy scale of $\Lambda \approx 1$ GeV, where perturbative theory breaks down. Perturbative QCD is valid only at sufficiently large energies. The binding force between color-charged partons in a hadron increases linearly with distance. The potential energy built up by the separation of the partons eventually reaches a level sufficient to generate quark-antiquark pairs from the vacuum which again form color-neutral states, the hadrons. The non-existence of free color-charged particles is called confinement.

The non-perturbative process of hadronization is described by models like the Lund model or the cluster model taking place after the perturbative parton shower (PS) process at a certain low energy cut-off scale. Matching between the PS and the hadronization process is needed to avoid double counting of partons. Fragmentation and hadronization produce by collinear splitting collimated hadron jets, whose total momentum is constrained to the momentum of the (virtual) final state parton.

Jets are formed by certain algorithms in the reconstruction and theoretical predictions. A simple and intuitive jet definition is provided by cones containing hadrons. In the Snowmass accord 1990 [14], the baseline criteria for jet definition were agreed upon taking into account the experimental implementability. On the other hand, the jets must be theoretically well-defined in each order of perturbation theory, i.e. predicting a finite cross section at each order. Furthermore, the obtained cross sections must be relatively insensitive to the hadronization process, including the requirement that collinear and infrared parton splitting does not change the jet multiplicity in the events and the jet four-momenta. This so-called infrared and collinear safety (IRC) requirement is illustrated in Fig. 1.4. Most cone-based jet algorithms do not fulfill this requirement. An exception is the seedless IRC safe cone (SISCone) algorithm [15]. An alternative to the cone-based definitions are so-called sequential jet algorithms. Sequential jet algorithms ensuring IRC safety are provided by the k_t-algorithms [16] which allow for reconstructing jets two orders of magnitude faster than the SISCone algorithm. The k_t algorithms iteratively group four-vectors together in so called called proto-jets. These four-vectors can belong to final state quarks at a certain order of perturbation theory in the PS o hadrons propagating through the detector as used in Section 2.4.5. The algorithm further combines proto-jets which are

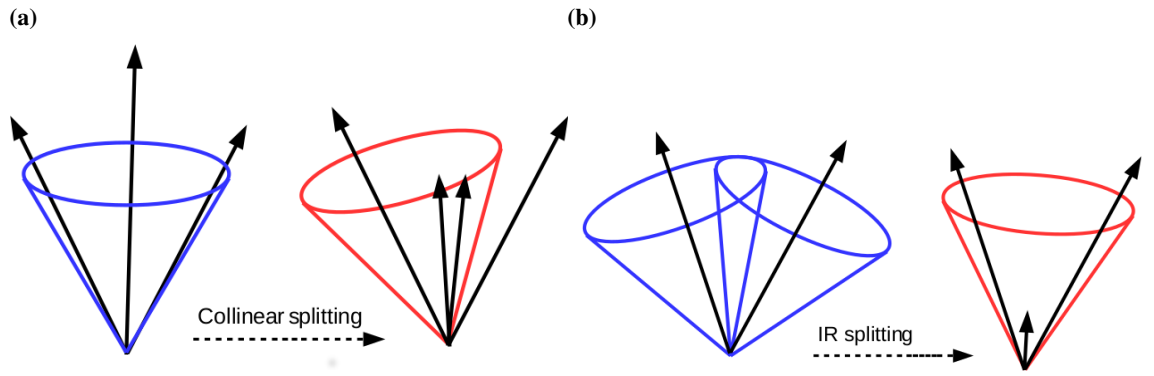

Figure 1.4: Illustration of infrared and collinear safety. The examples illustrate jet definitions not stable against a (a) collinear and (b) infrared splitting of partons.

closest in momentum space. The distance between two proto-jets i and j is defined by

$$d_{ij} = \min\left(p_{\mathrm{T},1}^{2p}, p_{\mathrm{T},1}^{2p}\right)\frac{R_{ij}}{R}, \text{ with } \begin{cases} p = 1 \text{ for } k_t\text{-algorithm [16, 17]} \\ p = 0 \text{ for Cambridge-Aachen (C/A) [18]} \\ p = -1 \text{ for anti-}k_t\text{-algorithm [19]}, \end{cases} \tag{1.21}$$

in different k_t-type algorithms, where R is the jet radius parameter, the maximum angular distance between two proto-jets, and $R_{ij} = \sqrt{\Delta\eta^2 + \Delta\phi^2}$ is the angular distance between the two proto-jets. All combinations of proto-jets are considered. A proto-jet whose smallest distance to all other proto-jets is greater than its p_{T}^{2p} is taken as a jet and removed from the set of proto-jets. The pair of proto-jets with the smallest distance $d_{i,j}$ is replaced by a proto-jet with momentum four-vector equal to the sum of the four-momenta of proto-jets i and j. This procedure is repeated until all proto-jets have been removed.

In the case of k_t-jets ($p = 1$) and, to a lesser extent, for C/A-jets ($p = 0$), the proto-jet distance in momentum space is most similar to the Euclidean distance $\Delta p = |\vec{p}_1 - \vec{p}_2|$. In the PS development this corresponds most closely to parton splitting, and the k_t-algorithm can be interpreted as reversal of the PS development making jet substructures more accessible. On the other hand, in contrast to the anti-k_t-algorithm, the shape of the k_t-algorithm jets is quite irregular making jet energy calibration difficult. The results of the different jet finding algorithms for the same set of input constituents is illustrated in Fig. 1.5. Due to the regular shape of its resulting jets, the anti-k_t algorithm is the most commonly used algorithm in ATLAS.

1.3 Beyond the Standard Model

Although the SM is a consistent theory and very successful describing the measurements so far, there are nevertheless a number of open theoretical questions as well as experimental observations which are not addressed by the SM. Gravitation as described by the General Theory of Relativity cannot

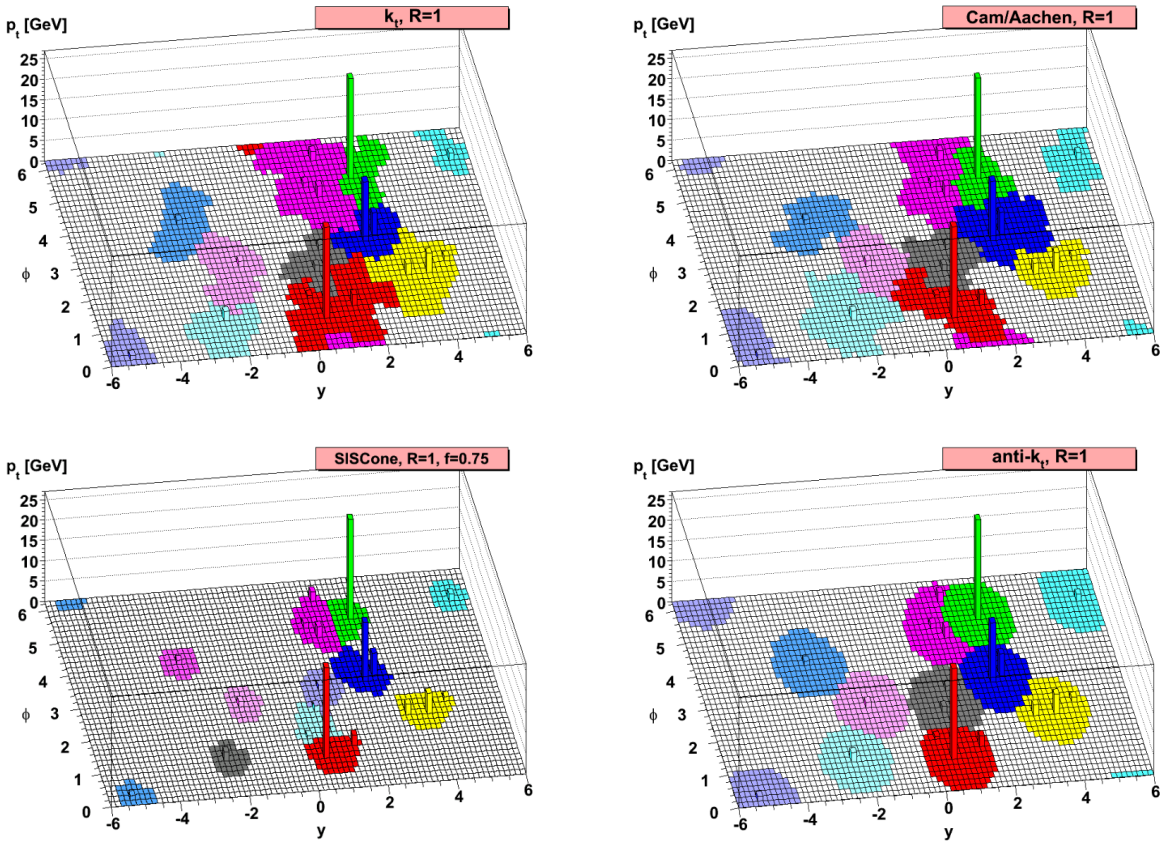

Figure 1.5: Results of the different jet finding algorithms for the same parton-level event. The resulting jets are indicated by different colors. Figure from Ref. [19].

be reconciled with the gauge theories of the SM in a mathematically consistent quantum theory. Measurements of neutrino oscillations show that neutrinos described as massless by the SM must have non-vanishing though small masses ($m_{\nu e} \lesssim 1.12$ eV [6]). Moreover, astrophysical observations suggest that only a small fraction of the energy content of the universe consists of baryonic matter, where the predominant part is at most weakly interacting, massive Dark Matter and so-called Dark Energy responsible for the accelerated the expansion of the universe. Moreover, CP violating effects within the SM are not large enough to explain the observed asymmetry between (baryonic) matter and antimatter in the universe. Baryogenesis models [20] with additional CP violation extending the SM are required.

In the SM, the Higgs boson mass receives quadratic loop corrections from all particles interacting with the Higgs field, with cut-off at the energy scale of the validity of the SM which may be as high as the Planck scale ($m_{\mathrm{Pl}} = 1/\sqrt{8\pi G} \approx O(10^{18}$ GeV) with the gravitational constant G), which are many orders of magnitude larger than the experimentally determined mass of 125 GeV. This problem caused by the large difference between the electroweak and new physics scale is known as the hierarchy problem [21–23]. The large radiative corrections have to be compensated by extreme fine-tuning of the mass parameter in the Lagrangian.

Theories beyond the SM (BSM) have been introduced to tackle the above shortcomings introducing new particles and energy scales below the Planck scale. There is no reason that there has to be only one scalar field breaking the $SU(2)_L \times U(1)_Y$ electroweak gauge symmetry to generate the particle masses as in the SM. Supersymmetric extensions of the SM [24] or theories predicting axions require an extended scalar sector. Theories with two Higgs doublets are introduced in Section 1.3.1. A phenomenological theory introducing new interactions at higher energy scales is introduced in Section 1.3.2.

1.3.1 Two-Higgs doublet models

The SM Higgs sector constitutes the simplest possible implementation of the Higgs mechanism for spontaneous electroweak symmetry breaking necessary for fermions and weak gauge bosons to obtain their masses. However, further $SU(2)_L$ Higgs multiplets are not ruled out. The most straight-forward extension of the scalar sector consists one additional complex Higgs doublet in 2HDMs [25]. 2HDMs can introduce enough CP symmetry violation to explain the large observed asymmetry between baryons and antibaryons in the universe and are included in various baryogenesis models [20]. Furthermore, supersymmetric extensions of the SM [24, 26–29] like the Minimal Supersymmetric Standard Model (MSSM) require a second Higgs doublet. Another motivation comes from the strong CP-problem to explain the smallness of the CP-violating term in QCD by a additional global $U(1)$ symmetry [30]. The spontaneous symmetry breaking of this additional $U(1)$ predicts a pseudo-Goldstone boson, known as Axion. Some of these Axion models [31] require the existence of a second Higgs doublet.

The scalar potential

The 2HDM models considered in this thesis are CP conserving. The most general CP conserving scalar potential for two doublets Φ_1 and Φ_2 with hypercharge $Y = +1$ and imposed $\mathcal{Z}_2$[3] symmetry is given by [25, 32]

$$\begin{aligned} V(\Phi_1, \Phi_2) = {} & m_{11}^2 \Phi_1^\dagger \Phi_1 + m_{22}^2 \Phi_2^\dagger \Phi_2 - m_{12}^2 (\Phi_1^\dagger \Phi_2 + \Phi_2^\dagger \Phi_1) \\ & + \frac{\lambda_1}{2} \left(\Phi_1^\dagger \Phi_1\right)^2 + \frac{\lambda_2}{2} \left(\Phi_2^\dagger \Phi_2\right)^2 \\ & + \lambda_3 \Phi_1^\dagger \Phi_1 \Phi_2^\dagger \Phi_2 + \lambda_4 \Phi_1^\dagger \Phi_2 \Phi_2^\dagger \Phi_1 \\ & + \frac{\lambda_5}{2} \left[\left(\Phi_1^\dagger \Phi_2\right)^2 + \left(\Phi_2^\dagger \Phi_1\right)^2 \right], \end{aligned} \tag{1.22}$$

with eight free real parameters m_{11}, m_{12}, m_{22} and $\lambda_1, ..., \lambda_5$. As for the single doublet in the SM an appropriate choice of the free parameters leads to non-vanishing VEVs

$$\langle \Phi_a \rangle_0 = \begin{pmatrix} 0 \\ \frac{v_a}{\sqrt{2}} \end{pmatrix} \text{ with } a = 1, 2, \tag{1.23}$$

[3] For example the invariance under $\Phi_1 \to -\Phi_1$ as imposed for type I 2HDM.

where v_a are real parameters due to the imposed CP. In order to reproduce the masses of the SM W and Z bosons, the VEVs have to satisfy,

$$v_1^2 + v_2^2 = v^2 \approx (246\ \text{GeV})^2. \tag{1.24}$$

These non vanishing VEVs spontaneously break the the electroweak $SU(2)_L \times U(1)_Y$ symmetry leading to eight real scalar fields as excitations from the symmetry breaking vacuum in the expansion of the two doublets

$$\Phi_a(x) = \begin{pmatrix} \phi_a^+(x) \\ \frac{v_a + \rho_a(x) + i\eta_a(x)}{\sqrt{2}} \end{pmatrix}, \tag{1.25}$$

and their hermitian conjugates. Three of these real fields (one charged and one neutral scalar) are massless Goldstone boson excitations which are eliminated by appropriate choice of gauge providing the longitudinal degrees of freedom of the weak gauge fields $Z, W^\pm$. Due to the imposed CP conservation, the fields η and ρ decouple. The neutral Goldstone boson is given by $G_0 = \eta_1 \cos\beta + \eta_2 \sin\beta$. The massive field orthogonal to G_0 is a real pseudo-scalar field

$$A = \eta_1 \sin\beta - \eta_2 \cos\beta. \tag{1.26}$$

The mixing angle β chosen by convention without loss of generality in the interval $[0, \pi/2]$ is determined by the ratio of the two VEVs,

$$\tan\beta \equiv \frac{v_2}{v_1}. \tag{1.27}$$

while β is chosen by convention and without limiting any physics to be within $[0, \pi/2]$.

The remaining four scalar fields, two real neutral scalar fields ρ_a, a charged scalar field η_a are massive as well. The mass matrices of these fields are non-diagonal. Diagonalization results in a real charged scalar field $H^\pm$ and two neutral scalar fields

$$\begin{aligned} h &= \rho_1 \sin\alpha - \rho_2 \cos\alpha, \\ H &= -\rho_1 \cos\alpha - \rho_2 \sin\alpha, \end{aligned} \tag{1.28}$$

with a mixing angle α. By convention, the lighter CP-even state is called h and the heavier one H. The SM Higgs boson is obtained as superposition of the two neutral scalar fields, as

$$h^{\text{SM}} = \rho_1 \cos\beta - \rho_2 \sin\beta, \tag{1.29}$$

$$= H\cos(\alpha - \beta) - h\sin(\alpha - \beta). \tag{1.30}$$

Hence, in the special case $\alpha = \beta$, the SM Higgs boson corresponds to the heavier scalar, while for $\sin\alpha = \cos\beta$ to the lighter one.

The free parameters of the Higgs potential in Eq. (1.22) can be expressed in terms of seven physical parameters, the four Higgs mass parameters, m_h,m_H,m_A,$m_{H^\pm}$, the two mixing angles α, β and the VEV v.

Table 1.1: The four two-Higgs doublet models (2HDMs) considered in this thesis and their couplings of fermions to the Higgs doublets. The i denotes the fermion generation, with $u_R^i = (u_R, c_R, t_R)$, $d_R^i = (d_R, s_R, b_R)$ and $e_R^i = (l_R, \mu_R, \tau_R)$;

Model	u_R^i	d_R^i	e_R^i
Type I	Φ_2	Φ_2	Φ_2
Type II	Φ_2	Φ_1	Φ_1
Lepton specific	Φ_2	Φ_2	Φ_1
Flipped	Φ_2	Φ_1	Φ_2

Fermion couplings

The most general interaction terms of the Higgs bosons to fermions also contain flavor changing neutral current terms mediated by the Higgs bosons at tree level. To prevent those, each fermion type[4] is restricted to interact only with one of the two Higgs doublets.

Four 2HDMs are usually considered as summarized in Table 1.1. In type I only one of the two doublets, chosen to be Φ_2 by convention, couples to fermions while the other one only interacts with the gauge bosons. The aforementioned $\mathcal{Z}_2$ symmetry is here imposed to be

$$\Phi_1 \rightarrow -\Phi_1, \tag{1.31}$$

preventing a coupling of the fermions to the second Higgs doublet.

In 2HDM type II, the Φ_1 doublet couples only to the right-handed (RH) down-type quarks, while the RH up-type quarks and the RH leptons couple to the Φ_2 doublet[5]. To prevent coupling of fermions to the respective other Higgs doublet, a discrete $\mathcal{Z}_2$ symmetry

$$\Phi_1 \rightarrow -\Phi_1, d_R^i \rightarrow -d_R^i, \tag{1.32}$$

is imposed[6].

In type I and type II models it is assumed, that the right-handed leptons obey the same $\mathcal{Z}_2$ symmetry as the down-type quarks. Two further possibilities exist, the lepton-specific model (also referred to as type X) and the flipped model (also referred to as type Y). In the lepton-specific model all leptons couple to Φ_1 and all quarks to Φ_2. In the flipped model, the leptons couple to the same doublet as the up-type quarks (Φ_2) and the down-type quarks couple to the other doublet (Φ_1).

[4] up-type quarks u_R^i, down-type quarks d_R^i and charged leptons e_R^i with $i = 1, 2, 3$

[5] Note that these fermion coupling terms of the scalar doublets also involves the left-handed fermion doublets $Q_L^i = \begin{pmatrix} u_L^i \\ d_L^i \end{pmatrix}$ and $L_L^i = \begin{pmatrix} \nu_L^i \\ e_L^i \end{pmatrix}$, without an explicit distinction between up- and down-type quarks.

[6] The two-Higgs doublet model (2HDM) incorporated in the MSSM has the same fermion couplings as the type II but instead of a discrete $\mathcal{Z}_2$ symmetry, a continuous symmetry is imposed to prevent the coupling to the second doublet. Furthermore, the Higgs doublet in the MSSM model has only two independent parameters, in contrast to the seven independent parameters in the more general models discussed here.

Table 1.2: Gauge boson and fermion couplings of the pseudo-scalar A relative to corresponding SM Higgs couplings [32]. Couplings (*) do not have corresponding SM couplings and only the dependence on the mixing angles is given [32].

Vertex	Type I	Type II
AVV	0	0
$At\bar{t}$	$i\gamma^5 \cot\beta$	$i\gamma^5 \cot\beta$
$Ab\bar{b}$	$-i\gamma^5 \cot\beta$	$i\gamma^5 \tan\beta$
$A\tau^+\tau^-$	$-i\gamma^5 \cot\beta$	$i\gamma^5 \tan\beta$
AZh (*)	$\propto -\cos(\beta-\alpha)$	
AZH (*)	$\propto \sin(\beta-\alpha)$	

Phenomenology of the pseudo-scalar A

For the phenomenology of the pseudo-scalar A [32], the absence of couplings between the A boson and gauge bosons at tree level is of crucial importance. It prevents the production via vector boson fusion (VBF) as well as the clean decay signature of a gauge boson pair. The dependence of the A couplings to boson and fermion fields on the mixing angles β is shown in Table 1.2.

The dominant production mode of the pseudo-scalar A is via gluon-gluon fusion (ggA mode), where the initial state gluons couple via quark loops to the pseudo-scalar. A further production mechanism is b-associated production ($gg \rightarrow b\bar{b}A$) providing a very clean signature with additional two b-quarks in the final state. The dominant A decay modes are $A \rightarrow b\bar{b}, c\bar{c}, t\bar{t}, \tau^+\tau^-, W^\pm H^\mp, Zh, ZH, gg, \gamma\gamma and Z\gamma$, while the latter three couple via a quark loop, as for the gluon-gluon fusion production. H and h is connected to the SM Higgs boson via Eq. (1.28).

The heavy resonance searches performed in this thesis are sensitive to a pseudo-scalar A decaying into a Z boson and a SM-like Higgs boson. This decay mode is the most relevant one for a pseudo-scalar mass $m_A \lesssim 2m_t$, with the top quark mass m_t. At higher masses, the decay into $t\bar{t}$ pairs is the dominant and the sensitivity for the $A \rightarrow Zh$ decay mode, for $\cos(\alpha-\beta) \rightarrow 0$ is considerably worse.

1.3.2 Heavy vector triplet models

In many BSM theories the hierarchy problem is solved by introducing new physics at energy scales between the electroweak and the Planck scale. The new physics can be for example an extended weak gauge symmetry [33] or the Higgs boson is described as a strong bound state like in the Little Higgs models [34], and in Composite Higgs [35, 36] and certain Technicolor models [37–39].

The models make predictions for physics processes accessible at the LHC. These models, in most cases, have a large number of free parameters and a complete scan of all the parameter space is hardly feasible.

What all models, however, have in common is the prediction of heavy, electroweakly interacting spin-1 resonances with not too large decay widths ($\Gamma/M < 0.1$). For the experimental searches, one simplified model [40] with a phenomenological Lagrangian describing an additional heavy vector

triplet (HVT) are assumed, which includes as free parameters only the masses and coupling strengths of the heavy resonances.

This simplified model serves as a guideline and is not a complete theory. Incorporation into these theories can for instance change the tails of the resonance in the mass distribution.

Effective Lagrangian and model parameters

In addition to the SM fields a real vector field V_μ^a in the adjoint 3-dimensional representation of the weak $SU(2)_L$ gauge group is introduced, representing a charged and a neutral massive spin-1 particle. The dynamics of of this new field is described by the phenomenological Lagrangian

$$\begin{aligned}\mathcal{L}_V = &-\frac{1}{4}D_{[\mu}V_{\nu]a}D^{[\mu}V^{\nu]a} + \frac{m_V^2}{2}V_\mu^a V^{\mu a} \\ &+ ig_V c_H V_\mu^a H^\dagger \tau^a \overleftrightarrow{D}^\mu H + \frac{g^2}{g_V}c_F V_\mu^a J_F^{\mu a} \\ &+ \frac{g_V}{2}C_{VVV}\epsilon_{abc}V_\mu^a V_\nu^b D^{[\mu}V^{\nu]c} + g_V^2 c_{VVHH}V_\mu^a V^{\mu a}H^\dagger H - \frac{g}{2}c_{VVW}\epsilon_{abc}W^{\mu\nu a}V_\mu^b V_\nu^c, \end{aligned} \tag{1.33}$$

with the generators of the $SU(2)$ Lie-algebra $\tau^a = \sigma^a/2$ ($a = 1, 2, 3$) and the totally antisymmetric Levi-Civita tensor ϵ^{abc} and where $W^{\mu\nu a}$ are the SM isospin field tensors. The first line in Eq. (1.33) contains the kinetic term, the mass term and trilinear and quadrilinear interaction terms from the covariant derivative,

$$D_{[\mu}V_{\nu]a} = D_\mu V_\nu^a - D_\nu V_\mu^a,\ D_\mu V_\nu^a = \partial_\mu V_\nu^a + g\epsilon^{abc}W_\mu^b V_\nu^c, \tag{1.34}$$

where g is the usual $SU(2)_L$ gauge coupling constant. Since the V_μ^a fields mix with the gauge boson fields W_μ^a after electroweak symmetry breaking (EWSB), they are not mass eigenstates and the mass parameter m_V does not correspond to the physical mass of the introduced new particles. Diagonalization of the mass matrices of the neutral and the charged vector bosons gives the physical masses and the custodial symmetry relation between the SM gauge boson masses and new heavy boson masses,

$$M_W M_\pm = \cos^2\theta_W m_Z^2 M_0^2, \tag{1.35}$$

with the physical masses $M_\pm$ and M_0 of the charged and neutral heavy vector bosons, respectively. Since lower masses for the new vector bosons are already excluded [41], the measured value of the weak mixing angle $\sin^2\theta_{W,exp} = 0.223$ [6] is only restored for

$$M_\pm^2 = M_0^2(1 + O(1\%)). \tag{1.36}$$

The second line in Eq. (1.33) contains direct interactions of V^a with the unbroken SM Higgs doublet current, which is defined as

$$iH^\dagger\tau^a\overleftrightarrow{D}^\mu H = iH^\dagger\tau^a D^\mu H - iD^\mu H^\dagger\tau^a \tag{1.37}$$

and the fermion currents,

$$J_F^{\mu a} = \sum_f \bar{f}_L \gamma^\mu \tau^a f_L, \tag{1.38}$$

with couplings $g_V c_H$ and $\frac{g^2}{g_V} c_F$, respectively assuming universality of the coupling to the different fermion types in the context of this thesis. The coupling term to the Higgs current includes, in particular, the coupling to the three Goldstone boson resulting from EWSB which represent the longitudinal degrees of freedom of the gauge fields $Z, W^\pm$ after EWSB. The parameters $g_H = g_V c_H$, therefore, describes the couplings of the field V^a to the Higgs boson as well as to the SM gauge bosons determining the decay rates of the heavy vector bosons into final states Zh,Wh as well as the production cross section via VBF. The parameters $g_F = g^2 c_F / g_V$ control the fermionic decay rates and the production cross section via quark-antiquark annihilation, referred to as Drell-Yan-like (DY) production mode. The last line in Eq. (1.33) contains quadratic and cubic V^a couplings which do not contribute directly to V^a decays and for phenomenology at the LHC, where only single-production processes are relevant. Therefore, the last line can be neglected and the only free parameters (see [40]) are

$$g_H = g_V c_H,\ g_F = \frac{g^2 c_F}{g_V} \text{ and } m_V. \tag{1.39}$$

These parameters are useful when connecting the simplified HVT model to explicite models. The parameter g_V represents the typical strength of the V interactions while $c_{H/F}$ describe the difference between couplings to the bosons and to the fermions and are usually assumed in to be on the order of unity. The coupling g_V can vary over one order of magnitude between different scenarios, from $g_V \approx g \approx 1$ for the weakly-coupled case to $g_V \approx 4\pi$ in the strong coupling limit.

Benchmark models

Ref. [40] proposes two simplified benchmark models, model A and model B which are inspired by specific BSM theories describing heavy vector boson production and decay. In these models, the parameters c_H and c_F are fixed to specific values and the coupling strength g_V and the resonance mass remain as the only free parameters. The latter is used as a final discriminating variable in the search.

Model A is inspired by a weakly coupled extension of the SM gauge group introducing a second $SU(2)$ gauge symmetry [33] where g_V has typically small values [40]. The Monte Carlo simulation predictions in this thesis have been generated with $g_V = 1$. In this model, c_H is chosen such that

$$g_V c_H \cong g^2 c_F / g_V, \tag{1.40}$$

resulting in similar decay branching fractions for the dileptonic and the dibosonic decay channel. The coupling to SM particles is thus equally suppressed by the factor $g^2 c_F / g_V$.

Model B, on the other hand, is inspired by strongly coupled extensions of the SM [42], like composite Higgs models with larger typical values of g_V. In this thesis $g_V = 3$ is assumed to study this case.

Although this specific theory has additional freedom in the choice of c_H, it is by definition of model B set equal to -1, leading to unsuppressed bosonic coupling

$$g_V c_H \cong -g_V, \tag{1.41}$$

while the fermionic couplings are still suppressed by the factor $g^2 c_F / g_V \cong g^2 / g_V$[7]. This results in dominant decay of the resonance into SM boson pairs with strongly suppressed fermionic decays on the order of $\lesssim O(1\%)$ branching fraction.

For both model A and model B, the DY production mode is dominant. VBF by more than 4 orders of magnitude compared to the DY production mode.

Apart from the both yet introduced benchmark models, VBF can only become comparable to DY production if the resonance width of $q\bar{q}$ is much narrower than the one of diboson[8]. Large parameter values for g_V lead to a very broad resonance and is therefore not suitable for a diboson resonance search. Therefore, following the classification of the benchmark models A and B proposed in Ref. [40], an additional model C has been defined where the parameter c_F is set to zero, excluding the couplings to fermions and thus not only fermionic decays but also DY production leaving only VBF production and providing a specific benchmark model for the search for diboson resonances produced via VBF.

[7] The change of sign here has no effect on the calculated tree level production cross sections since the matrix element goes in in square, but is necessary to link the results of the model B with the motivating specific theory [42].

[8] Here, the resonance width concerns in particular the production vertex of either $q\bar{q}$ fusion or the VBF.

CHAPTER TWO

THE ATLAS DETECTOR AT THE LHC

THe goals of experiments at high-energy accelerators such as the LHC [43] are to test the Standard Model (SM) and precisely determinate of parameters as well as the search for beyond the prediction of the SM

In this chapter, the LHC and the ATLAS detector are described, whose data have been used analyzed in this thesis. A more detailed description of the LHC can be found in Ref. [43] and a detailed summary of the ATLAS detector in Ref. [44].

2.1 The Large Hadron collider

The Large Hadron Collider (LHC) [43] is a circular particle accelerator designed to accelerate and collide proton or heavy ion pairs from two counter-directed particle beams to up to 14 TeV (5.5 TeV) for proton (lead ion) collisions. The LHC was built in the same tunnel at CERN near Geneva that previously housed the Large Electron-Positron Collider (LEP). It has a circumference of 27 km. The proton-proton collision design luminosity is 10^{34} cm^{-2}s^{-1}. The results discussed in this thesis were obtained from the data of LHC Run where the LHC was operated at a center-of-mass energy of 13 TeV and with peak luminosities of up to 2.1×10^{34} cm^{-2}s^{-1}.

The acceleration of the proton beams to the target energy is performed by several pre-accelerators which are outlined in Fig. 2.1. Taken from hydrogen bottles, the hydrogen atoms are ionized and first accelerated to an energy of 50 MeV by the linear accelerator LINAC2. Subsequently, they are brought to an energy of 25 MeV by means of the Proton Syncrotron Booster (BOOSTER) and the Proton Syncrotron (PS). The BOOSTER consists of four stacked syncrotrons with a radius of 25 m. The PS with a radius of 100 m is successively filled by the four components of the BOOSTER with four bunches of protons each. The beam is bunched using of pulsed dipole magnets. The bunches of protons are then passed to the Super Proton Syncrotron (SPS) where their energy is ramped up to 450 MeV.

The proton bunches of 10^{11} protons each are then successively injected into the LHC ring in opposite directions until it is filled with up to 2808 proton bunches. After complete filling, the beam energy is further increased in radio frequency cavities, which are operated at a frequency of 400 MHz and achieve an energy increase of 485 keV per revolution. The revolution frequency is 40 MHz. The protons are kept in their orbit by 1232 superconducting niobium-titanium magnets operated at 1.9 K,

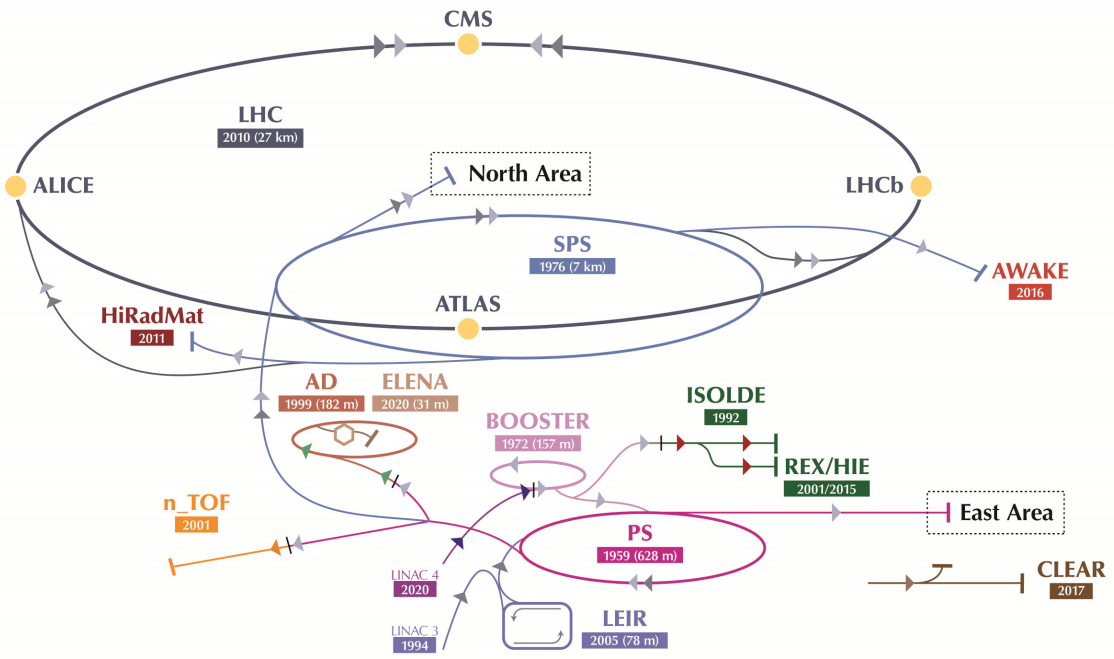

Figure 2.1: The acceleration complex at CERN that are used to ramp up the proton beams energies up to a center-of-mass energy of $\sqrt{s}$ = 13 TeV in the LHC. Figure from [45].

which reach a magnetic field strength of up to 9 T. The strong collimation of the particle beams to 16 μm is achieved by 858 quadrupole and higher multipole magnet systems.

The beams are collided at four interaction points with the four main LHC experiments ALICE[46], LHCb [47], CMS [48] and ATLAS [44] located in underground caverns. The latter two experiments are general purpose detectors for high-p_{T} physics.

The luminosity of the proton-proton collisions is determined using dedicated forward scattering detectors and calibrated using van der Meer scans. The first of the two luminosity detectors used, LUCID (LUminosity measurement using Cerenkov Integrating Detector), is located at a distance of 17 m from the interaction point. LUCID measures the inelastic scattering in the forward region to determine the instantaneous luminosity during operation. The second detector, ALFA (Absolute Luminosity For ATLAS) is located 240 m from the interaction point and can thus be positioned as close as one millimeter to the beam to precisely measure the luminosity in a collision run.

The integrated luminosity in Run 2 is shown in Fig. 2.2(a). It accumulates to a total of 147 fb^{-1}.

The large amount of recorded data obtained by this high luminosity makes it possible to study even physical processes that happen very rarely. The flip side of the high luminosity, however, is a large number of proton-proton pairs colliding simultaneously or in adjacent bunchcrossing. The average number of collisions per bunch crossing within one filling of the LHC depends very much on the set operating conditions of the LHC. These conditions have been varied over the different data taking periods. The global average value is about 33 interactions per bunch crossing and the differences in the individual years are shown in Fig. 2.2(b).

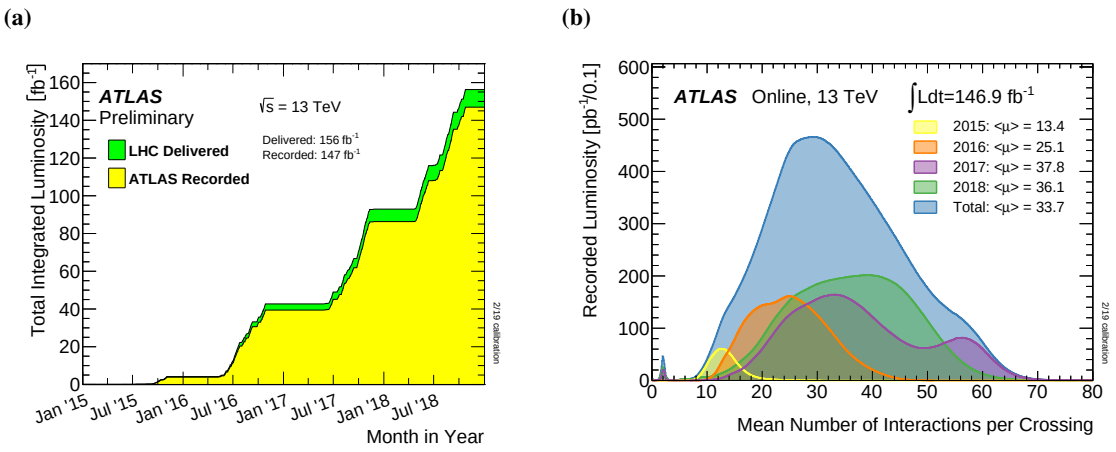

Figure 2.2: (a) Integrated luminosity in Run 2 of the LHC in proton-proton collisions during stable beam operation at $\sqrt{s}$ = 13 TeV. (b) The average number of interactions per bunch crossing in Run 2. Figures from Ref. [49].

2.2 The ATLAS experiment

The ATLAS detector is one of the two general purpose detectors at the LHC. It was built to explore physics at the TeV scale with unprecedentedly high luminosity. With a length of 44 m and a diameter of 25 m, the ATLAS detector is the largest collider detector ever built and weighs about 7 tons.

The high energies, as well as the high luminosity and the associated radiation exposure pose special design challenges for the electronics and detector technology used. The detectors have to provide high granularity up to close to the interaction point to allow for differentiation between the hard scattering event and pile-up events from secondary proton-proton interactions and to reconstruct secondary decay vertices. For the reconstruction of a missing transverse momentum caused by unreconstructed particles such as neutrinos or new stable particles beyond the SM (BSM), as complete as possible coverage of the full solid angle is needed as well as a high energy and momentum resolution. Finally a trigger system capable of detecting events of interest with a high efficiency while rejecting the overwhelming background is required.

A schematic cut-away view of the ATLAS detector showing the different subsystems is shown in Fig. 2.3.

The detector is divided into three main regions: a barrel region enclosing the interaction point and concentric with the beam axis, and two disk-shaped endcap regions at either end of the barrel part. The arrangement is forward-backward symmetric with respect to the beams and has an eightfold azimuthal symmetry in the Muon Spectrometer. For the description of physical processes a right-handed coordinate system with the x-axis pointing to the center of the LHC ring, the y-axis pointing upwards

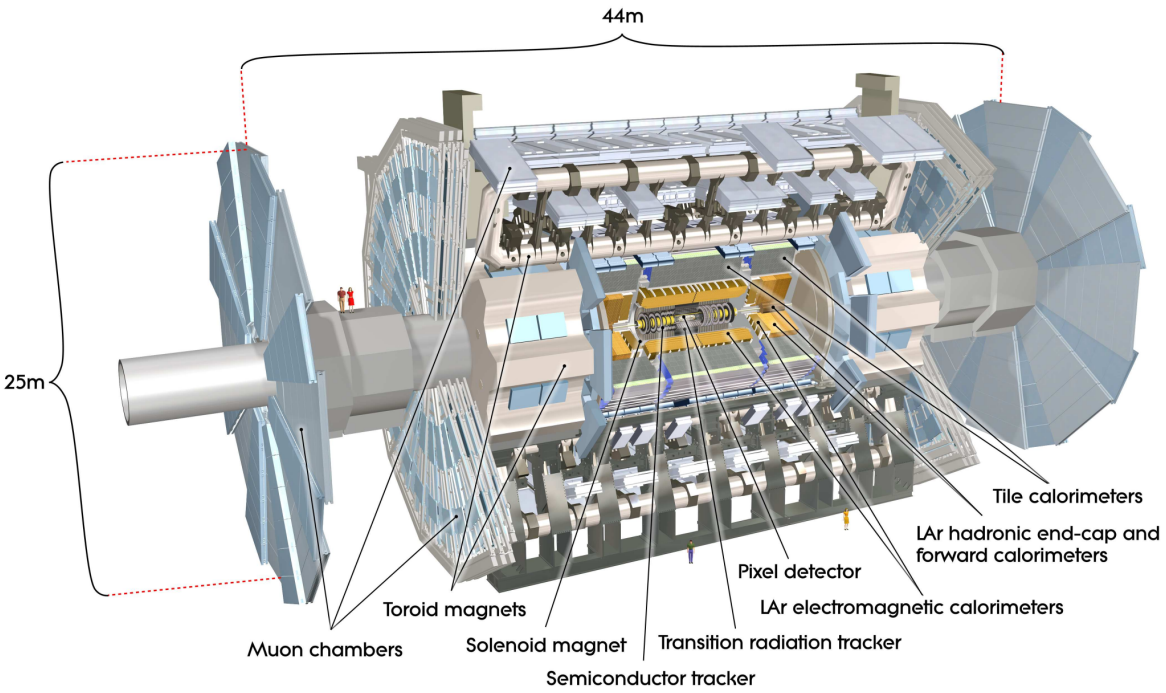

Figure 2.3: Schematic view of the subsystems of the ATLAS detector. Figure from Ref. [44].

and the z-axis along one beam axis. Polar coordinates are defined by

$$r = \sqrt{x^2 + y^2}, \tag{2.1}$$

$$\phi = \arctan \frac{y}{x}, \tag{2.2}$$

$$\theta = \arctan \left(\frac{z}{\sqrt{x^2 + y^2}} \right). \tag{2.3}$$

Due to the composite nature of the colliding protons, the initial momenta of the colliding partons involved in the hard process cannot be determined individually, and large part of the spectator partons leaves the detector unmeasured along the beamline. However, the transverse momentum of the colliding proton-proton system with respect to the beam axis is zero. The precision measurements therefore are performed in the transverse plane and using the transverse momenta $p_{\mathrm{T}} = \sqrt{p_x^2 + p_y^2}$ of the produced particles. The pseudo-rapidity

$$\eta = -\ln \left(\tan \frac{\theta}{2} \right) \tag{2.4}$$

$$\tag{2.5}$$

is mapped isomorphically to the polar coordinate θ and is related to the transverse momentum via,

$$p_{\mathrm{T}} = \sqrt{p_x^2 + p_y^2} = |\vec{p}| \cdot \frac{1}{\cosh \eta,}. \tag{2.6}$$

In the relativistic or massless particle limit, the pseudo-rapidity equals the rapidity, y. The rapidity of initial parton-parton system is unknown. The difference in the rapidity of two outgoing particles is invariant under Lorentz boosts along the beam axis. Thus a Loretz invariant measure of the angle between two objects is given by

$$\Delta R = \sqrt{\Delta\eta^2 + \Delta\phi^2}, \tag{2.7}$$

in the relativistic limit.

The detector is divided into three main subdetector systems. In the innermost subsystem, the Inner Detector (ID) records the tracks of charged particles by means of highly granular silicon sensors and straw drift tubes which curve of a solenoidal superconducting coil surrounding it. Surrounding the ID is the Calorimeter System, which absorbs electrons, photons and hadrons and records the deposited energy. Apart from neutrinos, muons are the only SM particles that traverse the Calorimeter System. Their identification and the measurement of their momenta is performed in the Muon Spectrometer (MS), outside of the Calorimeter System and immersed in a toroidal magnetic field.

In the following sections, the magnet system as well as the three subdetectors and the data acquisition system are described.

2.2.1 The Magnet System

Momentum and charge of charged particles are determined in the ATLAS detector by the curvature of their particle tracks in magnetic fields. Four large magnets generate the required fields, and the lightweight design is always optimized to minimize the interaction of the particles to be measured. All four magnets are superconducting niobium-titanium coils cooled by 4.5 K liquid helium-3.

The ATLAS magnet system consists on the one hand of an axial magnetic field which extends through the region of the inner detector by a solenoidal magnet with a field strength of 2 T and thereby bends charged particles in the azimuthal direction, allowing the transverse component of the momentum to be determined. The solenoid has a length of 5.3 m and a diameter of 2.5 m and is installed between the inner detector and the calorimeter system.

Three additional, large, air-core toroidal magnets generate a magnetic field within the measuring range of the Muon Spectrometer. They extend at a radial distance of 9.4 m to 20.3 m from the beam axis. Each of these magnets consists of eight coils and is arranged radially symmetrically around the beam axis. The toroidal magnet provides a magnetic field in the barrel region with an average strength of about 0.5 T, which depends strongly on the pseudo-rapidity region. At each end is another endcap magnet, embedded in the barrel toroid and aligned with the central solenoid magnet. The 8 coils of the endcap magnets are inserted half-periodically with respect to the 8 coils (22.5 °) of the barrel magnet in order to keep the drop of the field strength in the transition area as low as possible. The field strength in the endcap area is on average about 1 T. The toroidal magnetic field is highly inhomogeneous and is

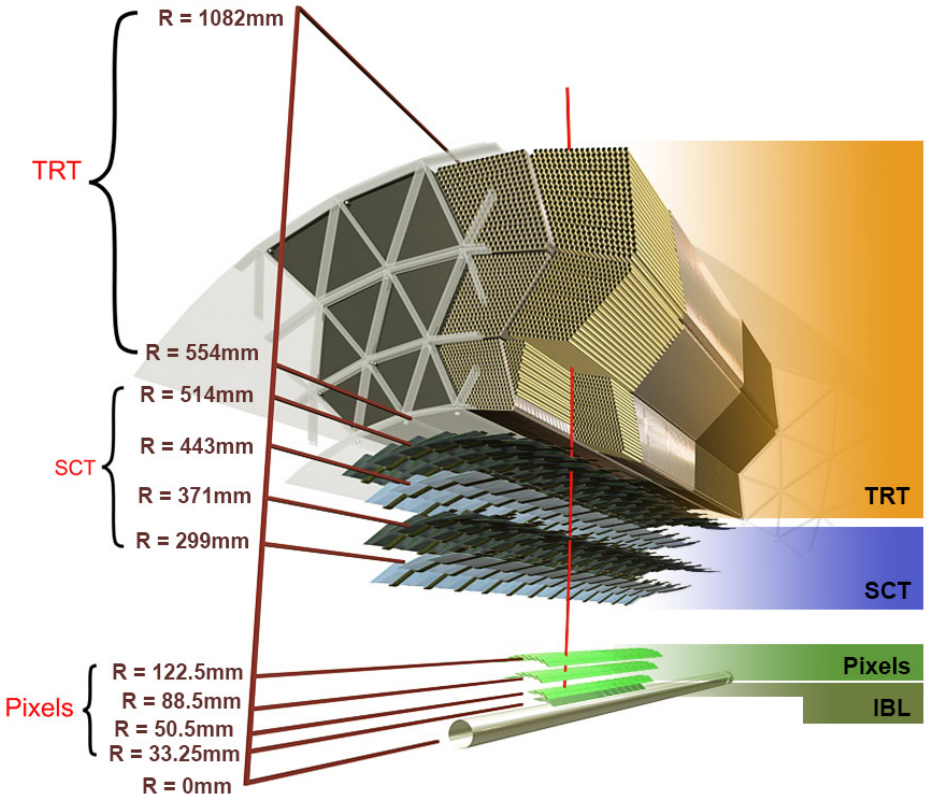

Figure 2.4: A cut-away view of the layers of the ATLAS Inner Detector (ID) with different detector technologies. Figure from Ref. [50].

therefore precisely measured for the determination of the expected track curvatures by about 1800 Hall sensors distributed in the area of the MS.

2.2.2 The Inner Detector

The innermost subsystem of the ATLAS detector, the ID, extends from a distance of 33 mm to 1.08 m in an area directly adjacent to the beam axis. The ID, which is arranged cylindrically around the beam axis, has a total length of 6.2 m and thus covers a range of pseudo-rapidity up to $\eta = 2.5$.

Its purpose is to record the overlapping trajectories of about 10^3 particles, which emanate from the interaction point every 25 ns, which requires a high granularity. On the other hand, a large energy loss within the ID is to be avoided, thus the additional requirement of a lightweight construction is given. This is made possible by an interaction of three systems of different sensor types, which is shown in Fig. 2.4.

Closest to the interaction point is a semiconductor pixel detector (PXD), which is arranged in four layers starting at a distance of 5 cm to a radius of 12 cm from the beam axis. The disk-shaped pixel detectors in the endcaps are placed at a distance of 50 cm to 65 cm from the nominal interaction point.

The identical pixels have a dimension of 50 μm in the transverse direction and 400 μm^2 along the beam axis, providing an intrinsic spatial resolution of 10 μm in the transverse plane and 115 μm in the longitudinal direction along the z-axis. In total, this results in about 84 million readout channels for the pixel detector.

The second system of the inner detector consists of the Semiconductor Tracker (SCT), which is made of silicon microstrip, and starts at a radius of about 30 cm and extends up to 51 cm in the barrel region. The SCT modules in the endcaps are arranged in nine disks per endcap between 85 cm and 2.7 m from the nominal interaction point. The individual strips of the SCT have a pitch of about 80 μm and are glued together in pairs at an angle of 40 mrad on the backside, so that the transitions through typically eight strips result in 4 three-dimensional local points. The strips in the rectangular SCT modules of the barrel are approximately parallel to the beam axis and the strips in the fan-shaped modules of the endcaps are radially oriented. The individual sensors connected in series are 6.4 cm long. The total intrinsic spatial resolution is about 17 μm in transverse plane and 580 μm in longitudinal z-direction. This granularity of the SCT is coarser than that of the PXD, which is, however, sufficient for the given distance to the interaction point and has to be read out only by 6.3×10^6 channels.

In the outermost part of the ID is the Transition Radiation Tube (TRT), which requires only $3.4x10^5$ readout channels. The TRT modules of the endcaps are placed alternately with those of the SCT modules at a distance of 85 cm to 2.72 m. The coverage in the pseudo-rapidity is up to $\eta < 2.0$ for the TRT. The barrel modules extend at a radial distance between 55 cm and 1.08 m from the beam axis. For this purpose, drift tubes running parallel to the beam axis (radial in the case of the endcaps) with a total length of 1.46 m are used in the barrel, which can determine the position of the transition in the transverse plane to within 120 μm. Due to the larger distance from the interaction point, this resolution is sufficient to determine the curvature of the tracks and the TRTs offer a low cost possibility to cover a large spatial range. The TRT in the barrel consists of 73 layers of drift tubes, of which (with $p_{\mathrm{T}} > 0.5GeV$) at least 35 are crossed by a single track. The drift tubes have a diameter of 4mm and are made of polymide with a thin (0.2 μm) aluminum layer applied to the inner wall. Coaxially there is a 30 μm thick gold plated tungsten wire. The drift tube is filled with a gas mixture of 70% xenon, 27% CO_2 and 3% oxygen, and is subjected to a voltage of 1530 V.

2.2.3 The Calorimeter System

The calorimeter system must fully absorb all electrons, hadrons and photons through a series of collisions and determine the energy deposits of the resulting secondary particle showers with sufficient resolution. The calorimeters are finely segmented in three dimensions to measure the angle of the particle showers to match them with the tracks of the ID and to identify electrons, photons and hadron jets. The particles have different requirements for the absorbing material due to the different interaction modes and particle masses. A so-called punch through into the MS further outside is to be prevented as far as possible.

A schematic representation of the complete calorimeter system is shown in Fig. 2.5, consisting of four sub-components, the Electromagnetic Calorimeter (ECal), the hadronic calorimeter, consisting of a tile calorimeter in the barrel and a Hadronic Endcap (HEC) adapted to the endcaps, and finally the Forward Calorimeter (FCal) very close to the beam axis.

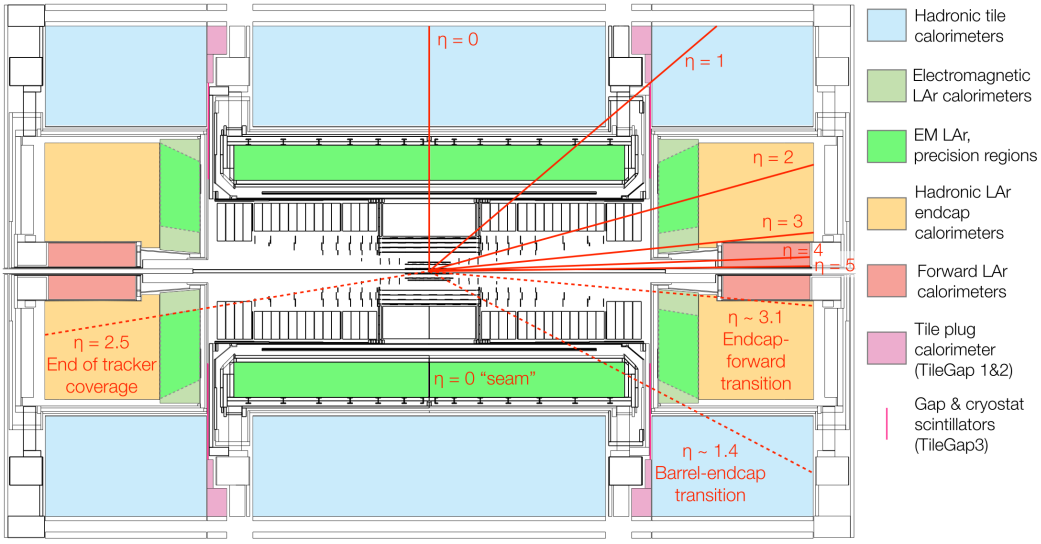

Figure 2.5: A longitudinal cross section of the ATLAS calorimeter system. Figure from Ref.[51].

Closest to the interaction point, located next to the solenoid magnet, is the electromagnetic calorimeter (ECal). The ECal is installed in the same cryostat as the solenoid magnet. The inner and outer radius of the barrel ECal are 1.4 m and 2 m respectively. The endcap modules of the electromagnetic calorimeter (EMEC) each consist of two coaxially arranged wheels covering the range up to a pseudo-rapidity of 3.1. In the ECal, electrons and photons in the range of eta<3.1 are absorbed by finely segmented lead plates, whose total thickness is at least 22 times the radiation length (X_0) and thus fully absorbs electrons and photons.

The ECal consists of lead absorber plates with liquid argon (LAr) between them. The accordion-shaped pleated plates and interposed Kapton electrodes extend over the entire covered area. This accordion geometry provides a complete φ symmetry without azimuthal cracks and can be seen together with the angular resolution of the ECal layers in Fig. 2.6. A combination of several cells of the outermost ECal layer with a coarser resolution of $\Delta\eta \times \Delta\phi = 0.1 \times 0.1$ serve as calorimeter trigger units, the so-called trigger tower.

At the outer edge of the ECal, however, the much more massive hadrons are only partially absorbed, corresponding to about 2-4 interaction lengths (λ). The Hadronic Calorimeter (HCal) is much thicker and extends subsequently from a radius of 2.28 m to an outer radius of 4.25 m. The HCal, including the semi-massive hadrons, is only partially absorbed. The HCal including the support structures absorbs hadrons corresponding to a distance of 11 λ. The barrel part of the HCal consists of the tiles of scintillating plastic. The tile calorimeter is mechanically divided into an inner barrel ranging up to $\eta = 1.0$ and an extended barrel ranging up to $\eta = 1.7$. Steel plates are used as absorber material, while the scintillating tiles are connected to photomultiplyers by wavelength shifting fibers. Steel and scintillator tiles alternate periodically in a volume ratio of 4.7 : 1.

The endcap region of the HEC consists of 2 disk-shaped modules per endcap, each consisting of 32 wedge-shaped modules. The HEC covers an η range of 1.5 to 3.2 and uses layered copper plates as

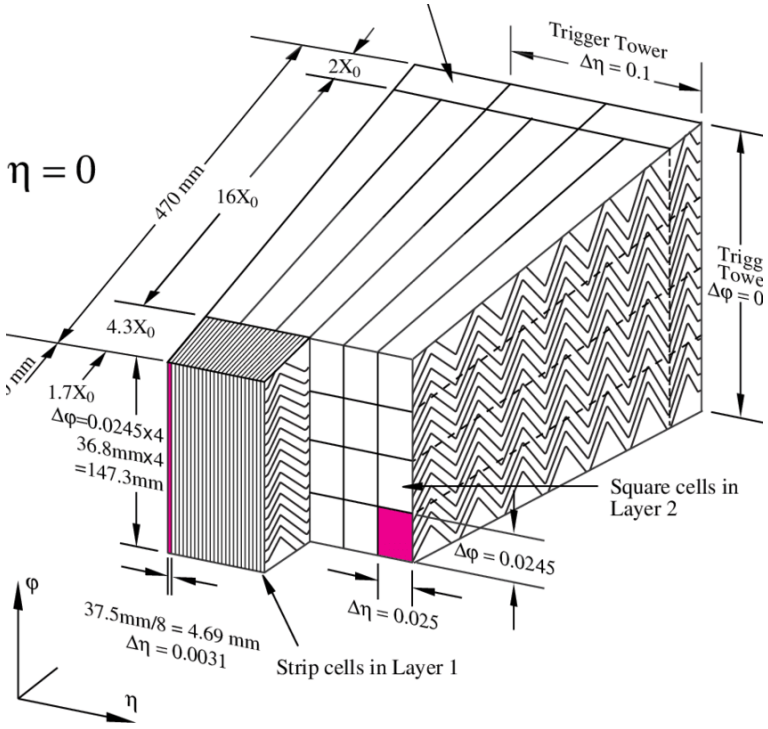

Figure 2.6: Sketch of a electromagnetic calorimeter module. The accordion shaped geometry of the absorber plates and readout panels and the segmentation are shown. The granularity in η and φ of the cells in each of the three layers and of he trigger towers is also shown. Figure taken from Ref. [44].

absorbing material. Liquid argon is used as the active material between the copper plates.

The increased radiation exposure in the forward directions places additional demands on the region close to the beam axis. The forward calorimeter (FCal) is specifically designed for this high rate and has sufficiently good energy resolution also for electrons, up to a pseudo-rapidity of 4.9. This corresponds to a range of only 1.3 degrees uncovered by the calorimeter system and thus allows almost complete detection of the transverse component of all outgoing particle pulses. The FCal consists of one module optimized for electromagnetic calorimetry and two modules designed for hadronic calorimetry.

2.2.4 Muon Spectrometer

Muons are much heavier than electrons and are therefore decelerated considerably less by Bremsstrahlung in the calorimeter. They penetrate the calorimeter almost unhindered. For the measurement of the muon kinematics, a special detector subsystem was installed, the Muon Spectrometer (MS), which covers the pseudo-rapidity range up to eta<2.7.

The MS uses the sagitta of the curvature of the muon trajectory in the toroidal magnetic field measured by chambers with focus on high spatial resolution in the bending direction for the precise measurement

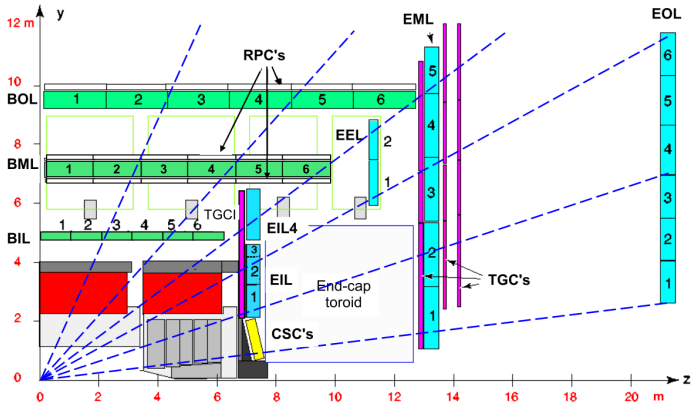

Figure 2.7: A lengthwise cross section of a quadrant of the ATLAS detector, along modules of large size. The modules belonging to the Muon Spectrometer, MDT, RPC, CSC and TGCs are labeled, whereas MDTs are labeled with the following 3-letter coding: First letter (B or E) for the barrel or endcap module, second letter (I, M, O or E) for inner, middle, outer or extra module; the last letter (here always L) denotes the large module. Small modules are shifted in azimuthal direction of $2\pi/16$ and thus not visible in this cross section. Figure from Ref. [44].

of the muon momenta.

Muons are also part of particularly clear signatures and typically feature events of interest, which additionally requires high precision timing. Therefore, special detector modules designed for high time resolution are used as trigger chambers, which allow the assignment to the individual bunch crossings with reduced spatial resolution.

A longitudinal section of the different modules of the Muon Spectrometer is shown in Fig. 2.7. The MS is characterized by an eight-fold symmetry, in which modules of each module type 2pi/8 are periodically repeated, alternating with one large module and one smaller module of the same type.

Monitored drift chambers (MDT) chambers allow precision measurement of muons in a range up to $\eta = 2.4$. The MS consists of three concentric layers of MDT in the barrel region. Each of these layers consists of two chambers with three or four drift tubes, similar in function to those of the TRT. They are oriented perpendicular to the principal bending direction. The MDTs are located at 5 m, 7.5 m and 10 m from the beam axis. The MDT endcap modules, consisting of four wheel-shaped modules, are located at 7.4 m, 10.8 m, 14 m, and 21.5 m from the nominal interaction point. The detector wheel at 10.8 m is located radially outside the endcap toroidal magnet. This additional wheel provides a third spatial measurement point in eta regions not covered by the outer wheel. All drift tubes have a diameter of 3cm, are made of aluminum and contain a tungsten-rhenium wire with a thickness of 50 μm. They can provide spatial resolutions of 35 μm. The drift tubes are filled with an argon-CO2 gas mixture (97:3) at a pressure of 3 bar. A voltage of 3080 V is applied to the tube which causes ionization products generated by muon-transition to drift to the corresponding electrode. The maximum drift time is 700 ns which leads to blind times, at a bunchcrossing interval of 25 ns.

Stable use of the MDTs requires counting rates below 150 Hz/cm2. In the endcaps, in the eta>2 range near the interaction point, the counting rates are increased. Therefore, the innermost module of the

precision chambers is not implemented by MDTs, but uses 16 Cathode Strip Chamber (CSC) per side, which can withstand rates up to 1000 Hz/cm^2. They cover the region of $2.0 < \eta < 2.7$ and are tilted inwards to be parallel to the expected muon flight direction. CSC are multiwire proportional chambers. Each CSC consists of four identical layers. In each of these layers, 30 μm thick gold-coated tungsten-rhenium wires are arranged in parallel as anode wires at 2.5 mm intervals, with the centerwire arranged radially. To each side of the anode wires are 17 μm thick copper coatings, which serve as cathodes. A voltage of 1900 V is applied to the argon/CO^2 gas mixture (80/20) contained in the CSC. The cathodes are separated into strips by lithographic etching so that 192 cathode strips are produced in the muon-bending direction and 48 strips in the non-bending direction. The muon passage can thus be reconstructed with 4 independent local points. In bending direction a spatial resolution of 60 μm is achieved, while the resolution in non–bending direction is 5 mm.

For the precise determination of the time, special additional trigger chambers are used. They have the additional task of determining the azimuthal coordinate, since the MDT tubes are arranged along this and do not provide any information about the azimuthal coordinate. In the barrel region up to $\eta = 1.05$, this is ensured by 606 RPCs, whereas thin gap chamber (TGC) are used in the forward region.

The RPCs are attached to the outside of the MDT chambers in three layers. The action of the RPCs is given by two resistive plates arranged parallel to each other at a distance of 2 mm, which consist of phenolic-melaminic plastic laminate. Between the plates is a gas mixture of $C_2H_2F_4$, Iso-C_4H_10 and SF_6 in a ratio of 94.7:5:0.3. This mixture only requires a relatively low working voltage of 9.8 kV. Muons generate ion pairs during the passage, which trigger an avalanche by the high voltage. The signal of this avalanche can be read out by metal stiffeners by capacitive coupling with a width of only 5 ns.

Also the trigger chambers have to be adapted in the area of high rapidity. The TGC are also multiwire proportional chambers characterized by a smaller wire-to-cathode distance (1.4 mm) than the wire-to-wire (1.8 mm) and a high quencher gas content.

2.2.5 Trigger and data acquisition

With a bunch-crossing period of 25 ns and about 40 interactions per bunchcrossing, the rate of events goes up to an order of magnitude of 1 GHz. With an information content of about 1.3 MB per event, this would require a bandwidth of data transfer in the order of 10 TB per second. There is therefore a need to pre-select events that may be of interest.

The ATLAS trigger and data acquisition system (TDAQ) uses a two-level trigger system consisting of a hardware-based level-1 trigger and a software-based HLT. A schematic representation of the TDAQ system is shown in Fig. 2.8.

The first instance, the L1 trigger systems estimate transverse momenta and energies by highly simplified reconstruction methods, while the event information is still buffered in the front electronics. The L1 trigger system allows a reduction of the event rates to about 75 kHz. In addition to this reduction, the level 1 triggers provide information about features and the geographical position of these features, the so-called regions of interest (RoI).

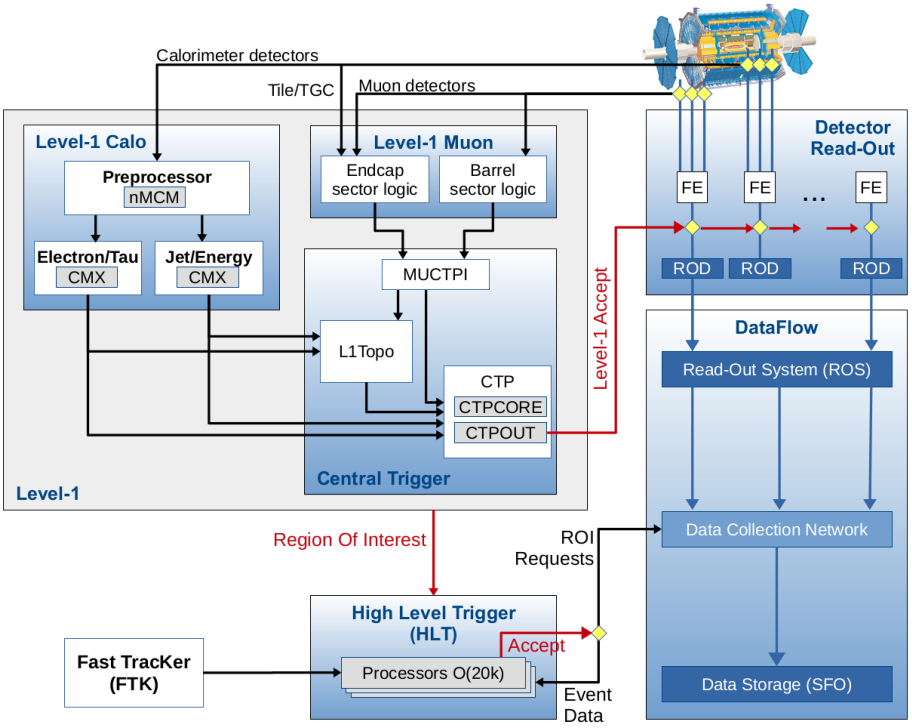

Figure 2.8: A schematic view of the triggering workflow in ATLAS. Figure from Ref. [52].

The trigger decision of the L1 system is performed in the CTP. It combines information from the L1 muon triggers and the L1 calo triggers, with a latency of 2.5 μs.

The L1 muon triggers consist of a coincidence circuit between different layers of RPC in the barrel region or TGC in the endcap region. Muons with infinite momentum would generate hits along a straight line through the three layers of the trigger chambers. A deviation from this straight line generated by the magnetic field can be used as a fast estimate of the muon transverse momenta. Only the discrete L1 trigger decisions with thresholds between 4 GeV and 20 GeV and the geographic (eta-phi) position of the muon path are passed to the CTP.

The L1 calo triggers process the signal from the 7000 calo trigger towers. These towers represent a coarser segmentation (eta x phi = 0.1 x 0.1) of the electromagnetic and hadronic calorimeter and thus a projection of the calorimeter system in eta-phi plane. Signals in the tower cells can be identified by the CTP as electrons, photons, hadronic decaying tau leptons or hadrons and assigned an energy which must meet a case-specific energy threshold. In addition, by combining the signals of the entire solid angle, the CPT can detect events with a particularly high energy sum or a missing transverse momentum and trigger its further processing.

If the kinematics estimated in this way satisfy the thresholds to be met, the readout of the VU is enabled by the readout drivers (ROD). In the ROD, the data streams of the individual detector cells are bundled and their information density is increased by analog-to-digital conversion. This information is buffered in the readout system (ROS) until a decision is made by the HLT.

The ROS are evaluated on the software side by the approximately 28000 processors of the HLT with full detector granularity, which ensures a significantly more precise determination of the energies and moments. A positive decision of the HLT activates the data collection network which writes the event data to disk and makes them available for the offline reconstruction software.

2.3 Monte Carlo event simulation

Events produced by processes of interest are generated by Monte Carlo (MC) event generators. The invariant matrix element is computed in perturbative QCD in fixed order of QCD in conjunction with the associated phase space parametrization. The matrix element generators used in this thesis are MadGraph5_aMC@NLO [53], Sherpa 2.2.1 [54] and PowhegBox [55–58], which both compute with NLO accuracy in QCD. The nominal parton density function (PDF) is given by NNPDF [10] which was determined with NNLO in QCD and taken from the LhaPdf library [13]. The parton shower was described using the dedicated PS algorithms Pythia8 8, which describes the parton shower using the Lund model [59]. Sherpa 2.2.1 provides both the matrix element and the parton shower algorythm. The parton shower in Sherpa is described using the clustermodel [60]. Potential double-countings between soft emmisions of the parton shower generator and higher order terms from the matrix element were resolved by matching and merging prescriptions.

The interactions of the propagating particles with the ATLAS detector are finally simulated with Geant 4 [61] simulation tool-kit.

The collection of simulated hits is then parsed to the same reconstruction algorithms as the recorded data.

2.4 Event reconstruction

To perform a physics analysis with the data, the large amount of readout channels must be processed into a more manageable form that defines individual particle types and distinguishes their signatures. A corse overview of different particle signatures within the ATLAS detector is shown in Fig. 2.9. For electrons and muons, for example, this signature is relatively clean. Other particles such as hadrons or neutrinos, however, can be identified at least by their closest proxy, as is given by jets in the case of collimated hadrons bunches or by a missing transverse momentum in the case of neutrinos. The signatures of both the clear particles and the proxies are collectively called physics objects. The identification of these physics objects is aided by auxiliary objects, tracks and calorimeter clusters, which are derived by preprocessing steps and serve as a common building blocks for physics objects or can be used for background rejection.

2.4.1 Track and vertex reconstruction

The trajectories of charged particles in the inner detector are called tracks. Tracks are reconstructed from a transverse momentum of 0.4 GeV, within a pseudo-apidity of $|\eta| < 2.4$, by connecting hits

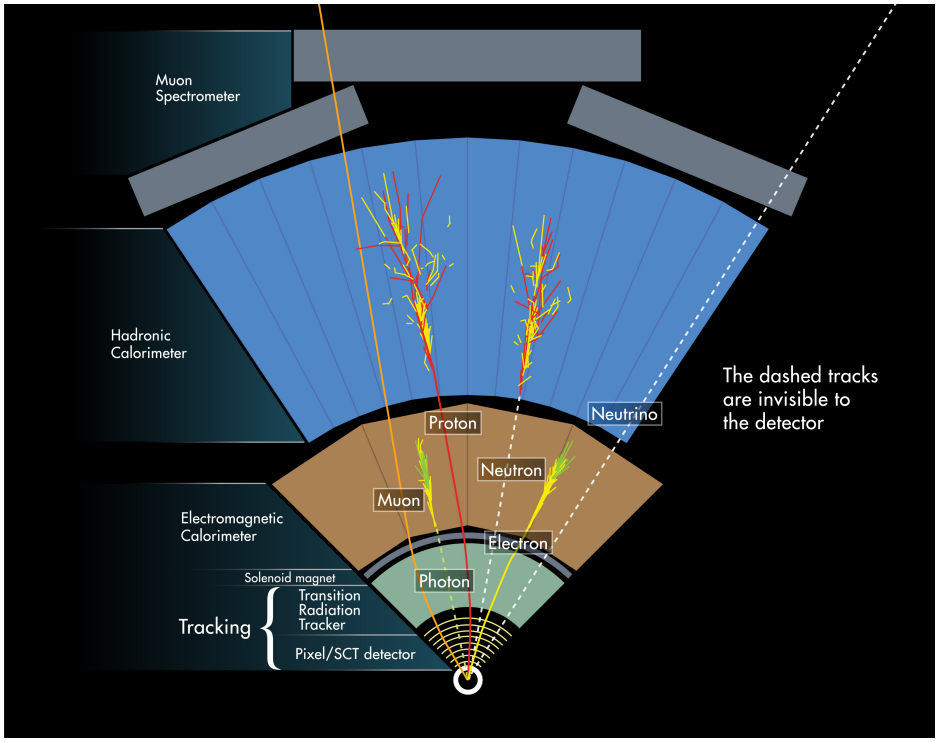

Figure 2.9: Schematic illustration of different physical particles traversing the different subsystems of the ATLAS detector. The dashed lines denote part of the particles trajectory that is invisible to the respective subsystem. The sketch illustrates the basic reconstruction strategies pursued for the particle identification. Hadrons, as protons and neutrons are usually not produced individually in collisions but are produced and reconstructed as jets. Figure from Ref. [62].

of the inner detector. Reconstructed tracks can be extrapolated to common points of origin, called vertices.

A track can be parameterized by a set of five parameters: The angular orientation of the outgoing particle by θ and φ, the ratio of transverse momentum and charge p_{T}/q determining the track bending, and the two so-called impact parameter (IP). A longitudinal IP (z_0) and a transverse IP (d_0) give the minimum distance of the extrapolated track to the vertex of the interaction. The transverse IP d_0 is the distance from the beamline to the point of closest approach, whereas the longitudinal IP z_0 is the z-coordinate of that point relative to the interaction vertex.

Tracks are determined by a series of tracking algorythmen [63]. The reconstruction of tracks and vertices is done in three steps. In a first preprocessing step the hits in the pixel detector and in the SCT are bundled to spatial clusters and the raw drift times of each TRT are converted to calibrated drift circles, i.e. the still ambiguous position around each anode wire of the TRT.

The actual tracking algorithms are basically divided into two different approaches: the default approach and the back-tracking approach.

The default approach is based on a set of at least three clusters in the three layers of the pixel detector

and the first layer of the SCT as seed. To the tracks extrapolated from these clusters further clusters of the SCT or drift circles of the TRT are added, using a combinatorical Kalman filter [64]. The default approach is particularly suitable for identifying particle tracks whose origin is in the vertex of the hard interaction, also called prompt tracks.

Complementary, the so-called back tracking algorithm is used for the reconstruction of particle tracks originating from secondary decay processes, e.g. b-hadron or hadronic tau-lepton decays. Here, starting from unusual, not yet assigned track segments in the TRT, the tracks are extrapolated inwards to the interaction point and are associated to such pixel or SCT hit clusters, which could not be associated to any track before.

The number of clusters along such a proto-track can be used as quality criteria as well as missing expected clusters in active parts of the ID along the proto-track. Such missing clusters are called holes. Using these and other quality criteria, fake tracks can be efficiently identified and rejected. After all clusters and drift circles belonging to a track have been identified, the fit is repeated with all hits of the three sensor types.

In a third step, common origin points, so-called vertices, are identified and assigned to the tracks [65]. For this all tracks are included, which are compatible to originate from the interaction point.

The z-coordinate of the considered tracks is given by the position closest to the collision point. The global maximum of the z-coordinates of all tracks represents the seed for a vertex. This vertex, as well as all surrounding tracks, are then fitted using a χ^2 based technique [66], which downweights incompatible outliers in such a way that an optimal localization of the vertex can be done. All tracks that are more than 7σ incompatible with the vertex are removed from the fit and used as seed for a new vertex in a new iteration. This procedure is repeated until either no more tracks are left or no more vertices can be reconstructed.

The primary vertex of the hard interaction is defined as the vertex whose square sum of the p_{T} of all associated tracks is the highest. after prompt vertices are identified, vertices from secondary decays or photon conversion are identified. After the vertices are identified and their position is determined, tracks are refitted with the additional boundary condition of originating from the vertex associated with them. Tracks from a vertex other than the primary vertex can be identified as originating from pile-up.

The resolution of these tracking algorithms in determining the IP is p_{T}-dependent. The resolution for the transverse (longitudinal) IP for tracks with $p_{\mathrm{T}} \geq 10$GeV is most accurate with 0.2 mm (0.1 mm) and deteriorates with decreasing momentum to a resolution of 0.14 mm (0.4 mm).

2.4.2 Topological calorimeter clusters

As further fundamental objects, three-dimensional collections of energy-deposits are reconstructed in the calorimeter system. These so-called topological calorimeter clusters (TopoClusters) consist of spatially connected calorimeter cells, which presumably and ideally represent the energy of individual shower particles.

The reconstruction of the TopoClusters is done by a seed-and-collect procedure [67]. So-called protoclusters of cells are seeded, which have at least four times the signal value above the average expected background noise. Neighboring cells are iteratively added to the protocluster if the absolute amount of the signal in this cell reaches at least 2 times the average expected value of the noise. If no other neighboring cells with this condition can be found, all other calorimeter cells adjacent to the proto-cluster are added to it. If there are two or more local maxima within a proto-cluster, each with a signal greater than 500 MeV within the electromagnetic calorimeter, the proto-cluster is split in all three dimensions.

The topo custer is considered as a massless pseudo-particle with the momentum four-vector spanned by η_{det}, φ and the cluster energy. The η direction is related to the coordinate origin and not to the actual primary vertex to describe the geographic position within the detector.

The basic method used to assign a corresponding energy to each cluster is the so-called *electromagnetic (EM) calibration* [68]. It takes into account energy losses in the dead material of the detector as well as out-of-cluster effects, but not the different nature of the EM and the nuclear interaction of the traversing particles. For the topocluster clustering process described above, the calorimeter cells are calibrated with EM scale.

In addition to the four-vector of the cluster, different so-called cluster moments are defined. These cluster moments parameterize e.g. geometric shape of the shower, position in the detector and energy distributions. These cluster moments allow conclusions about the particle nature without having to hypothesize the particle nature.

In particular electromagnetic shower production, e.g. by electrons or photons, is characterized by a compact uniform shower shape with begin already in the innermost calorimeter layers. In contrast, hadrons interact in the detector at random intervals and penetrate deeper into the calorimeter system.

Electromagnetic showering can thus be distinguished from hadronic showering. In the so-called *local hadronic cell weighting (LCW) calibration* [69], individual cells are weighted with a different energy scale based on the probability of being assigned to a hadronic or electromagnetic shower.

2.4.3 Electrons

As shown in Fig. 2.9, electrons leave a track in the inner detector and generate an electromagnetic shower in the electromagnetic calorimeter. The reconstruction of prompt electrons [70] is strongly entangled with that of prompt photons. Electrons can emit bremsstrahlung photons by interaction with the material of the inner detector. On the other hand, photons can generate electron-positron pairs by interaction with the inner detector. Prompt photons, unlike electrons, have either no inner detector track or exactly two, which can be assigned to a common secondary vertex. However, photons are not part of this thesis, for more detailed description of identification and calibration please refer to Ref. [70, 71].

Electron candidates A dynamical, topological cell clustering algorithm [72, 73] starts with topo-clusters sorted by p_{T}. Bremsstrahlung can lead to the formation of further smaller clusters in the calorimeter, separated from the seed cluster, which are called satellite clusters. The seed cluster must have at least $p_{\mathrm{T}} = 1$ GeV, calibrated with the EM scale, and be spatially matched with a track with at least 4 hits in the silicon detectors. The algorithm adds the clusters identified as satellites within a range of $\Delta\eta \times \Delta\phi = 0.075\text{x}0.125$ to so-called superclusters and thus collects a large part of the primary electron energy. Subsequently, the ID tracks are refitted with a trajectory corresponding to the electron hypothesis, which takes into account the possibility of Bremsstrahlung. The refitted tracks are matched with the superclusters.

Electron identification As signal electrons are considered only those produced in the final state of the hard interaction vertex, so-called prompt electrons. Electron identification [73, 74] is used for signal purification of the electron candidates against backgrounds, e.g. charged pions or electrons produced by photon conversion.

A data-driven, likelihood-based discriminant is used, incorporating information from associated tracks and cluster moments. The likelihood for signal (background) is defined by,

$$\mathcal{L}_{S(B)}(\vec{x}) = \prod_i P_{S(B),i}(x_i), \tag{2.8}$$

where x_i are the typically 13 input observables distributed in at signal (background) electrons with the probability distribution function (p.d.f.) $P_{S(B),i}$. The p.d.f.s of the signal is obtained by a tag-and-probe method in recorded data of $Z \rightarrow e^+e^-$ events (for E_{T} >15 GeV) and $J/\psi \rightarrow e^+e^-$ events (for E_{T} <15 GeV). The p.d.f.s of background electrons were taken from data events containing at least one electron. These so chosen events consist for the most part of dijet events. The input observables are, for example, the ratio between track momentum and calorimeter energy deposit, angular distance between cluster and extrapolated track, or the number of hits in the tracker. The likelihood discriminante is defined as the natural logarithm of the ratios of the signal and background likelihoods.

Based on this LH discriminant, three different strict working point (WP) are defined, whose larger background reduction comes at the price of reduced signal efficiency. A *loose LH* WP with a signal efficiency of 93% on average and a *medium LH* WP with 88%. In addition, for the *tight LH* WP electron candidates are discarded for which a photon conversion vertex can be reconstructed whose momentum is closer to the cluster energy than that of the electron track. The signal efficiency of the *tight LH* WP results in 80%. The efficiency of all three WPs increases gradually with increasing E_{T}. In an energy range of 20 GeV $< E_{\mathrm{T}} <$ 50GeV, the background rejection of the *tight LH* (*tight LH*) WP with respect to the *loose LH* WP is improved by a factor of 3.5 (2).

To ensure the electron stemming from the primary vertex (PV), spacial requirements are imposed to the IP. The longitudinal IP needs to satisfy $|z_0 \sin(\theta)| < 0.5$ mm and the transverse IP is required to be $|d_0|/\sigma(d_0) < 5.0$.

Electron isolation Hadronic activity in the vicinity of a reconstructed electron can be an indication of the non-prompt nature of the electron, such as occurs in the semi-leptonic *b*-hadron decay. These

Working Point	Calorimeter isolation	Track isolation	Efficiency
Gradient	p_{T}, η dependent	p_{T}, η dependent	$\varepsilon = 0.1143 \times p_{\mathrm{T}} + 92\%$
High-p_{T}	$E_{\mathrm{T}}^{cone,0.2} < \max(0.015 \times p_{\mathrm{T}}, 3.5)$ GeV	—	p_{T}, η dependent ($\approx 97\%$)
Loose	$E_{\mathrm{T}}^{cone,0.2}/p_{\mathrm{T}} < 0.2$	$p_{\mathrm{T}}^{varcone,0.2}/p_{\mathrm{T}} < 0.15$	p_{T}, η dependent ($\approx 99\%$)
Tight	$E_{\mathrm{T}}^{cone,0.2}/p_{\mathrm{T}} < 0.6$	$p_{\mathrm{T}}^{varcone,0.2}/p_{\mathrm{T}} < 0.6$	p_{T}, η dependent ($\approx 90\%$)

Table 2.1: Definition of the electron isolation working points and isolation efficiency ε [73].

hadronic activities in the ID or in the calorimeter in close proximity are identified and quantified by means of an isolation algorithm.

Two classes of isolation observables are introduced [73]:

- $E_{\mathrm{T}}^{\mathrm{cone},r}$: The sum of all positive topo-clusters within a radius r in η-ϕ plane. The energy clusters of the electron as well as pile-up and leakage correction terms are subtracted from this. The radius usually used for electrons is $r = 0.2$.
- $p_{\mathrm{T}}^{\mathrm{varcone},r}$: The sum of the momenta of all tracks not associated with the electron in a radius of $R = \min(r, 10\ \mathrm{GeV}/p_{\mathrm{T}})$. The variable radius takes into account that high energy electrons are created in strongly collimated decays and are therefore naturally accompanied by other particles. The minimum cone radius for muons is typically chosen as $r = 0.2$.

Tighter requirements lead to a more efficient background rejection but to a lower signal efficiency. For the definition of an isolation different WPs are defined. They are defined either by η-uniform signal efficiency or by fixed threshold values of the isolation observables. The different isolation criteria are summarized in Table 2.1.

2.4.4 Muons

Muons are measured in the ATLAS detector with a large range of different transverse momenta, starting at 3 GeV up to muons of about 3 TeV. The reconstruction [75, 76] of the muons is implemented in different algorithms, which involve several detector subsystems if possible. If the muon's transverse momentum is sufficient to escape from the axial magnetic field inside the detector, its signature is characterized by a trajectory crossing the ID as well as the dedicated MS. Muons also leave characteristic energy deposits in the calorimeter system along this trajectory, which are compatible with a minimally ionizing particle.

MS standalone tracks The reconstruction of the so-called MS standalone tracks, which are independent of the other subdetectors, starts with the reconstruction of muon segments. Muon segments are short straight lines of hits in an individual MS station. The information from the MDT precision chambers along the bending plane is combined in a first rough parabolic fit with the information of the second angular coordinate from the trigger chambers (TGC,resistive plate chamber (RPC)). Subsequently, a global χ^2 fit of the muon trajectory through the reconstructed segments is performed, taking into account the exact magnetic field distribution, as well as potential interactions with the detector material.

Muon candidate types Depending on the transverse momentum and the position in $\eta - \phi$ direction, additional detector subsystems besides the MS can be used for the reconstruction of the muon. Reconstructed ID tracks with a minimum p_{T} of 2 GeVare used. Five independent reconstruction algorithms define five muon candidate types:

- **Combined muons (CB):** The MS standalone track is extrapolated in the direction of the interaction point and matched with tracks from the inner detector. Energy losses in the calorimeter system are taken into account. Combined muons are both the most signal-pure and the most frequently reconstructed muon types. A subcategory of this type are the Silicon-associated forward (SiF) muons, which have only short track segments by pixel and SCT detectors due to lack of coverage of the TRT.

- **Inside-out combined muons (IO):** In a complementary approach, the tracks of the inner detector are extrapolated outward and matched with hits from the muons spectrometer. This approach can recover muons that did not produce a full MS standalone track due to low transverse momentum or lack of MS coverage.

- **Muon spectrometer extrapolated muons (ME):** In regions outside the ID coverage (eta>2.5) muons up to eta=2.7 are reconstructed by the Muon spectrometer alone by extrapolating MS standalone tracks in the direction of the beam axis.

- **Segment tagged muons (ST):** An extrapolation of an ID track into the MS is used to match the track with individual muon segments. If at least one segment can be matched, the muon reconstructed as ST is reconstructed with the parameters of the ID track.

- **Calorimeter tagged muons (CT):** ID tracks with a minimum p_{T} of 5 GeV are extrapolated into the calorimeter to search for energy deposits along the extrapolated trajectory that are compatible with a minimally ionizing particle. If such energy deposits are found, the muon reconstructed as ST is reconstructed again with the parameters of the ID track. ST muons recover the signal efficiency in the region lacking of MS coverage by instrumentation at $|\eta| < 0.1$.

The preliminary trajectory generated by the above algorithms allows identification of the relevant hits. To improve the fit quality, outlier hits of the fit are removed and previously unassociated hits are added along the preliminary trajectory. Subsequently, a new global fit is performed.

Muon identification The reconstruction of in-flight-decay of hadrons represents the largest source of background for the reconstruction of prompt muons. An explicit distinction is made between the decays of light-flavor (LF) hadrons (i.e. hadrons containing only u,d and s quarks) and heavy-flavor (HF) hadrons (i.e. hadrons containing c- and b-quarks).

For the identification of prompt muons and the rejection in-flight-decaying LF hadrons four WP, i.e. sets of requirements are defined, matching each the different needs of the large bandwidth of different physics analyses: A medium, a loose, a tight and a special High-p_{T} WP.

In addition to the selection of the muon type and a corresponding requirement on respective hit multiplicities, there are three discriminating upper variables for muon identification:

- q/p-significance: q/p is the ratio of the charge to the momentum. Its significance is defined as the absolute difference of this quantity measured individually in the ID and the MS, in relation to the square sum of their uncertainties.

- ρ' The absolute difference of the track p_{T} measured individually in ID and the MS in relation to the combined track pt.

- normalized χ^2 of the global fit.

The criteria of the four WP mentioned above are the following:

- The **loose WP** maximizes selection efficiency while maintaining good fit quality. For loose muons all muon types mentioned above are used, but CT and ST muons (ME) are restricted to the region of missing MS coverage at eta<0.1 (eta>2.5).

- The **medium WP** minimizes systematic uncertainties associated with reconstruction and calibration and allows only CB, IO, and ME muons, with the latter used only in the range $2.5 < |\eta| < 2.7$. At least three hits in at least 2 MDT chambers are required. and the q/p significance must be less than seven. Muons satisfying the medium WP are a subset of those satisfying the tight WP.

- The **tight WP** maximizes the purity of prompt muons. Muons satisfying the tight WP are a subset of those satisfying the medium WP. CB or IO muons are used that have at least 2 segments in the MDTs, with at most one MDT station having a hole. The normalized chi^2 must be less than 8 and p_{T} and η dependent requirements on the q/p-significance and ρ', which is designed to optimize subsurface suppression.

- The goal of the **high-p_{T} WP** selection is to optimize the momentum resolution in muons with $p_{\mathrm{T}} > 100GeV$. For this purpose, regions in the η-ϕ plane are rejected, which are known to be not optimally aligned, since the momentum reconstruction is very sensitive already to small misalignments. The reconstruction of the muons is limited to CB and stringent requirements on the number of stations in the MS are set. The q/p-significance and ρ requirements are the same as for the medium WP. In addition, an upper limit to the relative uncertainty is set on the q/p ratio of the combined fit. Muons satisfying this WP are a subset of those satisfying the medium WP. The momentum resolution improvement by an average factor of 2 is shown in Fig. 2.10 as a function of the muon-p_{T}.

The listed identification criteria are suitable to efficiently reject LF hadron decays. Cosmic muons and HF hadron decays can be better rejected with requirements to the association of the muon with the primary interaction vertex, quantified by the IP, or isolation criteria. The longitudinal IP must satisfy $|z_0 \sin(\theta)| < 0.5\mathrm{mm}$. The transverse IP d_0 is required to be less than three times its uncertainty.

Furthermore, semi-leptonic HF quark decay can be efficiently rejected by isolation requirements. Analogous to electrons, two isolation parameters $E_{\mathrm{T}}^{\mathrm{cone},r}$ and $p_{\mathrm{T}}^{\mathrm{varcone},r}$ are defined. With the difference that the maximum radius for the cone definition of $p_{\mathrm{T}}^{\mathrm{varcone},r}$ is typically $R = 0.3$ for muons. Different working points with different requirements for the isolation observables are used for the specific needs of different physical analyses.

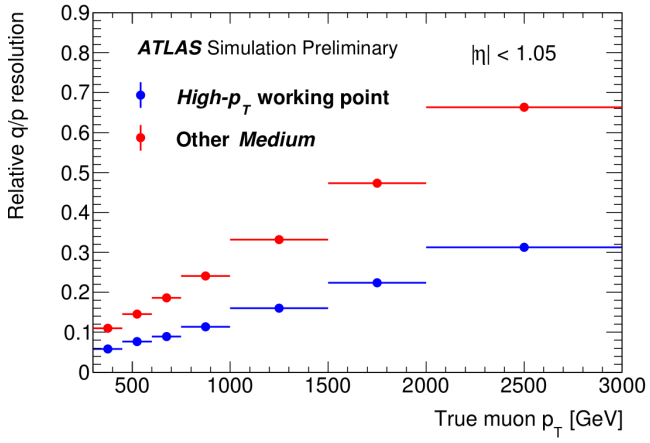

Figure 2.10: The q/p resolution as a function of the transverse momentum for muons, shown separately for muons passing the high-p_{T} working point (WP) requirements and for the complementary selection fulfilling common (medium WP) requirements. Figure from Ref. [75].

2.4.5 Jet reconstruction

Due to the nature of the hadronization process as explained in Section 1.2.2, the reconstruction and simultaneous theoretical prediction of the production of single hadrons is not possible. Hadronic final states must therefore be described as jets, an observable describing the collimated collection of several hadrons. This observable is a pure question of definition and not a quantity given by nature. The most frequently used definition of a jet in ATLAS is given by the anti-k_t algorithm [19], c.f. Section 1.2.2. This sequential jet finding algorithm iteratively combines the four-momenta of its input constituents within a cone of radius R. Its efficient implementation in the FastJet package [77] was used in this thesis.

On the one hand, such input constituents for a jet finding algorithm can be stable particles ($c\tau > 10mm$) on MC generator particle level, which leave significant energy deposits in the calorimeter system, i.e. neutrinos and muons are excluded. Jets formed with such generator level particles are called truth jets and serve as a theoretical reference for the energy calibration of a detector level jet. On the other hand, in the course of event reconstruction, clusters or tracks can also be considered as pseudo-particles and their momentum four-vectors, constrained by defining the constituent to be massless, serve as input. Based on this, three such reconstruction level jets are defined in this thesis. Calorimeter jets are formed from topo-clusters, track jets from ID tracks and a dedicated combination of both, the so-called track-calorimeter cluster (TCC) [78], form the constituents of the so-called TCC-jets.

The TCC are designed to combine the fine granular angular resolution of the inner detector with the precise energy resolution from the calorimeters, by connecting tracks and individual energy deposits in the calorimeter, before running the jet finding algorithm. Thus, TCC improve resolution of the substructures (c.f. Section 3.4) within a jet. The matching between tracks and cluster is done by the requirement of $\Delta R < \sqrt{\sigma^2_{\mathrm{track}} + \sigma^2_{\mathrm{topo}}}$, with σ_{track} the track extrapolation uncertainty and σ_{topo} the topo cluster width. Three types of TCC exist, a track without a topocluster, which is referred to as a charged

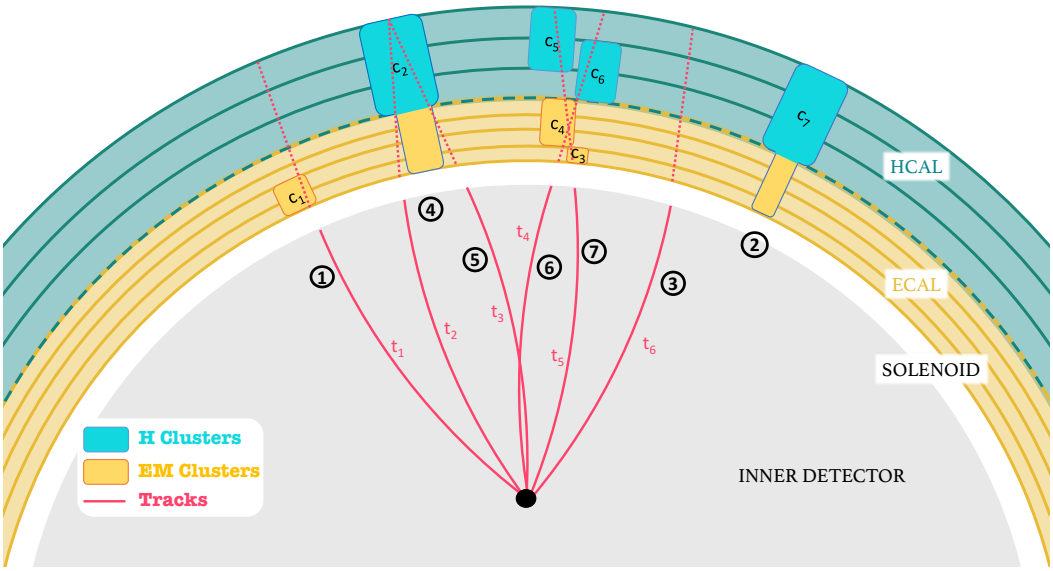

Figure 2.11: Illustration of the different combinations of calorimeter and track based energy measurements leading to the different types of track-calorimeter clusters (TCCs). Figure from [78].

TCC, a topocluster without a track, referred to a neutral TCC and the combined TCC with a match track and a topo cluster. Furthermore, multiple tracks can often be matched to such a topoclusters, as it is illustrated in Fig. 2.11. Tracks can be used to share cluster energy between a hard scatter jet and a pile-up jet. To build the TCC momentum four-vector from the different schemes are applied.

1. For a direct single match as combined TCC, the topo-cluster energy and the track direction are used.

2. In the case of neutral TCC the topo-cluster 4-vector is directly used.

3. The momentum four-vector of the track defining an charged TCC is directly used.

If there is a match between multiple tracks and/or multiple topo clusters (c.f. cases 4-7 in Fig. 2.11) the situation becomes more complex. Still there is one TCC object per track reconstructed with the angular coordinates taken from the track. The scale coordinates are adapted to account for energy sharing between the different matches according to the p_{T} fraction of individual tracks over the sum of all p_{T}. The TCCs are capable of successfully reducing pileup contributions if the track is not associated to the primary vertex.

Despite the by definition massless constituents, the summation of the angularly separated four-vectors allows the jet to acquire a significant mass,

$$m^{\mathrm{jet}} = \sqrt{\left(\sum_i E_i\right)^2 - \left(\sum_i \vec{p}_i\right)^2}, \tag{2.9}$$

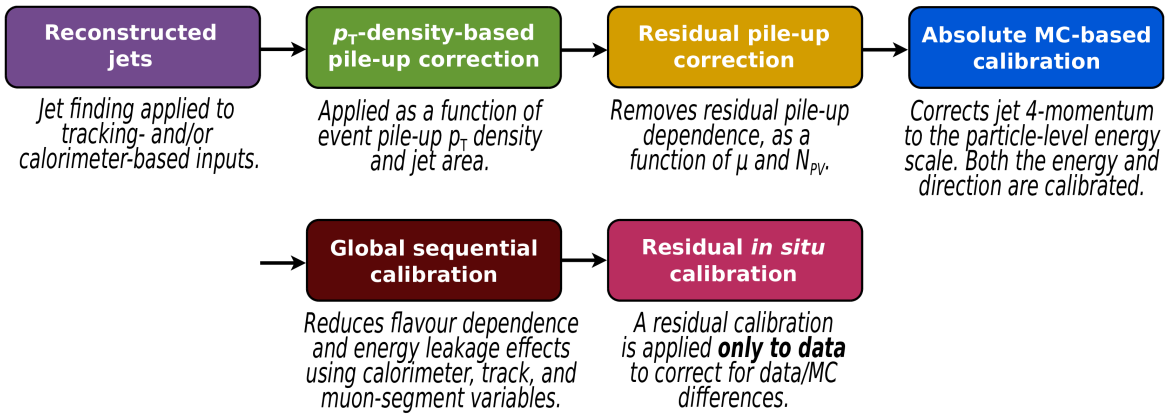

Figure 2.12: The workflow of the calibration of small-R jets. Figure from Ref. [51].

which ideally correspond to that of a massive seed particle, such as an top quark, a Higgs boson, or a gauge boson, that initiates the jet.

Jet calibration

Different sizes of jets are subject to different biases and energy losses. Even if the calibration follows similar strategies, they have to be performed independently for $R = 0.4$ and $R = 1.0$.

Small-R jets (anti-k_t, $R = 0.4$) The steps used for the calibration [51, 69, 79] of calorimeter jets with $R = 0.4$ are shown in Fig. 2.12.

Especially in the reconstruction of jets pile-up plays an important role. Activities from neighboring collisions of the same bunchcrossing (in-time pile-up) or successive bunchcrossings (out-of-time pile-up) inevitably contribute to the energy deposits in the coarser granulated calorimeter cells. This energy contribution must be estimated as best as possible. In a first step, the transverse momentum of the small-R jet is corrected event-wise by the median of the p_T-density ρ of pile-up jets. The calculation of this pile-up jet p_T density is performed using MC event jets formed from positive-energy clusters within $|\eta| < 2$. The p_T density is multiplied by the active area of the reconstructed jet to determine and subtract its pile-up content. The steps used for the calibration of EMTopo calorimeter jets at radii of $R = 0.4$ are shown in Fig. 2.12. A linear dependence of the p_T response on the multiplicity of the primary vertices within the event N_{PV} and on the average number of interactions per bunchcrossing *mu* has been identified. N_{PV} is a measure of the in-time pile-up activity, whereas μ, the $\langle N_{PV} \rangle$, is a good measure of out-of-time pile-up. The two linear coefficients α and β are determined in four coarse bins of different $|\eta|$ ranges. Overall, the pileup-corrected jet p_T is then given by,

$$p_T^{corr} = p_T^{reco} - \rho \times A - \alpha \times (N_{PV} - 1) - \beta \times \mu. \tag{2.10}$$

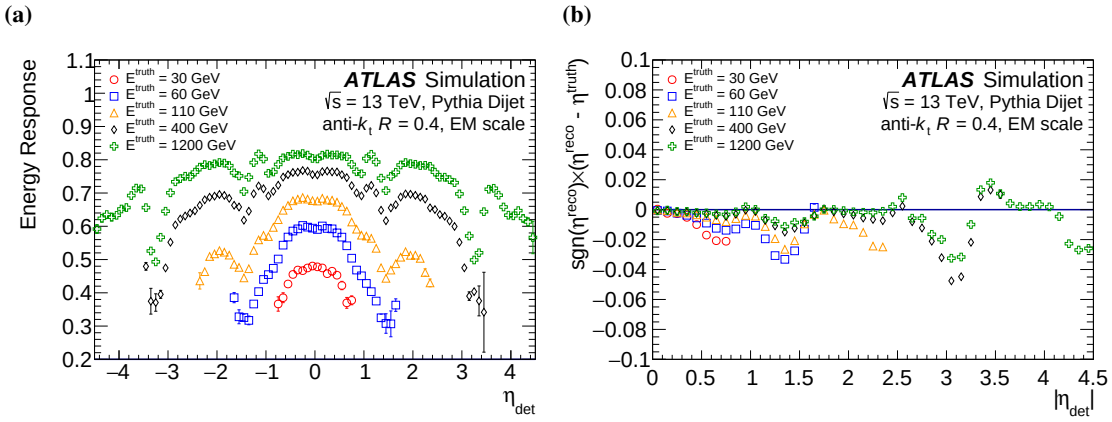

Figure 2.13: (a) The energy response as a function η_{det} and the (b) bias in the η reconstruction as a function of $|\eta_{\mathrm{det}}|$ for jets with different energies. Figure from Ref. [80].

The absolute MC based correction, so called jet energy scale (JES) and the η calibration then corrects the reconstructed calorimeter jet energy and η so that on average they correspond to the truth jet energy and η. For the derivation of this calibration step only isolated jets are considered. The average energy response is defined as $E_{\mathrm{reco}}/E_{\mathrm{truth}}$ and derived as a function of η_{det} and the jet energy by numerical inversion. Thereby η_{det} reveals the causes in the detector geometry and instrumentation. The transitions can be seen in Fig. 2.13(a). These transitions between two different detector technologies also cause a bias in the jets η measurement. One of the two sides has a relatively higher energy response and thus shifts the energy barycentre of the jet and thus the η coordinate. This can be seen in Fig. 2.13(b) at the detector transitions between central-endcap at $\eta = 1.4$ and at the transition between endcap-forward detector at $\eta = 3.1$. This necessitates a correction term of the reconstructed jet η as a function of the jet energy and η, which is determined via numerical inversion. This correction changes the p_{T}, but leaving the total jet energy unchanged. Hereafter the jets are calibrated according to the so called EM+JES scale.

The last step of the calibration addresses the differences in the jet response between data and MC. Differences can occur, for example, due to insufficiently accurate modeling of the response of the active and dead detector material, modeling of the pile-up, and theoretical uncertainties in the description of the hadronization process. For the in-situ measurements, the jets to be investigated are each balanced in transverse planes with well-measured reference objects. The response is then determined as the ratio of the p_{T} to the reference object. The corrections are applied to the jets in the recorded data using correction scale factors and are derived from the statistical combination of the following three measurements. In a first measurement, the so-called η-intercalibration, di-jets events are selected, each balancing a well calibrated jet in the central region ($\eta_{\mathrm{det}} < 0.8$) with jets in the forward region ($0.8 < \eta_{\mathrm{det}} < 4.5$). The second, Z/γ+jet balanced calibration step use a well-calibrated photon or $Z \rightarrow e^+e^-\mu^+\mu^-$ decay to measure the p_{T} response of the recoiling jet. The p_{T} response is evaluated up to a p_{T} of 950 GeV. In the last step, the so-called multijet balance (MJB), central (eta<1.2), high-p_{T} jets (300<p_{T} <2 TeV) are opposed to a collection of several well-calibrated low-p_{T} jets. The calibration steps of the last two steps are performed with central jets only, but are also applicable to forward jets

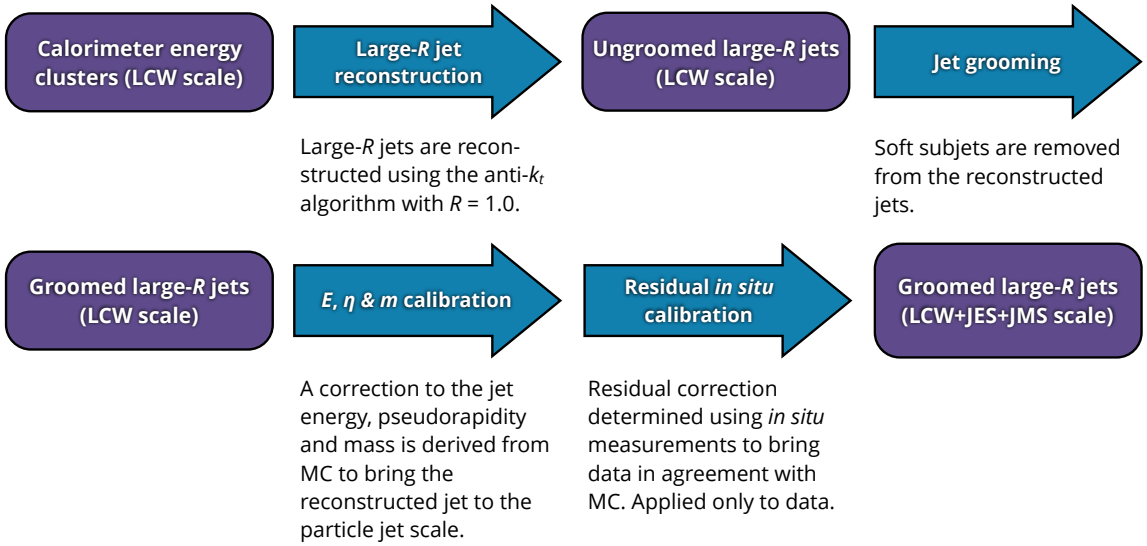

Figure 2.14: The workflow of the calibration of large-R jets. Figure from Ref. [81]. Figure from Ref. [81].

due to the preceding η-intercalibration. Each in-situ calibration step introduces uncertainties due to missmodeling of physics effects, uncertainties in the measurements of the reference re-coil object and the modeling of the p_{T} balance due to the selected event topology.

Large-R jets (anti-k_t, $R = 1.0$)

Large-R-jets in this document use LCW topoclusters or TCC as input constituents. The increased jet area and pre-calibrated constituents need different Calibration and pile-up strategies. The calibration TCC-jets and calorimeter jets follows the same strategy but has to be done individually. The calibration steps of the jets with a radius of $R = 1.0$ adapted to the largeR jet is shown in Fig. 2.14.

The large jet area makes the jets specifically vulnerable to contamination from pile-up, initial-state radiation (ISR) and the underlying event (UE) (c.f. Section 1.2). To reduce this type of background, a number of different so-called grooming procedures have been developed and tested [82–86], which use jet substructures to identify and subtract background contributions. In particular, trimming [82, 87] has proven itself due to its simplicity and effectiveness. In trimming, the constituents forming the large-R jet are reclustered using the anti-k_t algorithm with radius parameter $R_{\mathrm{sub}} < R$. The sub-jets thus generated are subtracted from the large-R jet if their p_{T}^{i} is less than the fraction f_{cut} of the original $p_{\mathrm{T}}^{\mathrm{jet}}$ of the untrimmed jet possess. Fig. 2.15 illustrates the trimming process.

The actual energy and mass calibration [81] of the large-R jets is then performed in two steps. First, the momentum four-vectors of the trimmed jets are calibrated in an MC-based step, in analogy to small-R jets. For this purpose, truth jets with $R = 1.0$ are defined, which undergo the same reconstruction steps (anti-k_t, $R = 1.0$) and trimming algorithm as their reconstructed counterparts. The truth jets are then matched to the reconstructed jets using a procedure that minimizes the distance in ΔR. The jet energy (mass) response is defined as the ratio between energy (mass) of the reconstructed jet divided

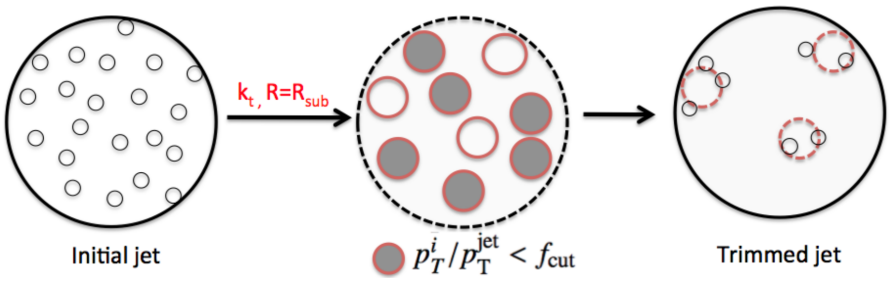

Figure 2.15: Illustration of the jet trimming process used for large-R jets. Figure from Ref. [82].

by that of the matched truth jet, $E_{\text{reco}}/E_{\text{truth}}$ ($m_{\text{reco}}/m_{\text{truth}}$). Like the small-$R$ jets, energy scale and η calibration are performed as functions of η_{det} and E_{reco}.

In an additional step, the mass of the jet is corrected using a further multiplicative scaling factor, which is additionally parameterized in the observable $\log(m_{\text{reco}}/E_{\text{reco}}$. This additional step is important when using the jet mass in a physics analysis, since the jet mass is highly affected due to wide-angle contributions and due to cluster merging and splitting. The corrected four-vector is then given by,

$$E_{\text{reco}} = c_{\text{JES}} E_0 \tag{2.11}$$

$$m_{\text{reco}} = c_{\text{JES}} c_{\text{JMS}} m_0 \tag{2.12}$$

$$\eta_{\text{reco}} = \eta_0 + \Delta\eta \tag{2.13}$$

$$p_{\text{T}}^{\text{reco}} = c_{\text{JES}} \sqrt{E_0^2 - (c_{\text{JMS}} m_0)^2}/\cosh(\eta_0 + \Delta\eta). \tag{2.14}$$

The calibration of the JES and JMS induces a systematic uncertainty in the order of 10%. These relative high uncertainties can be reduced by a factor of 3 by in-situ calibrations. Two steps are followed for this purpose. In a first step, the JES is determined analogously to that of the small-R jets by balancing the transverse pulses using the well-measured reference objects. The absolute calibration is a statistical combination of the three measurements analogous to small-R in events with Z+jets, γ+jets and MJB and the η-intercalibration. This calibration is finally applied to the four-momenta of all jets in recorded data, and thus also affects the measurement of jet mass.

In a dedicated second step, the JMS is corrected. The correction factor is determined by two complementary methods which are statistically combined and applied after the JES described above. One method [88] uses semi-leptonic decaying $t\bar{t}$ events for the determination, in which the leptonic decaying side can mark the event and the hadronic side can be probed. The mass distribution of the jets in these events forms peaks around the mass of the W boson and the top quark which is determined by a fit. A second measurement uses an independent mass determination by the inner detector [82] by measuring the calorimeter-to-tracker response ratios in data and MC.

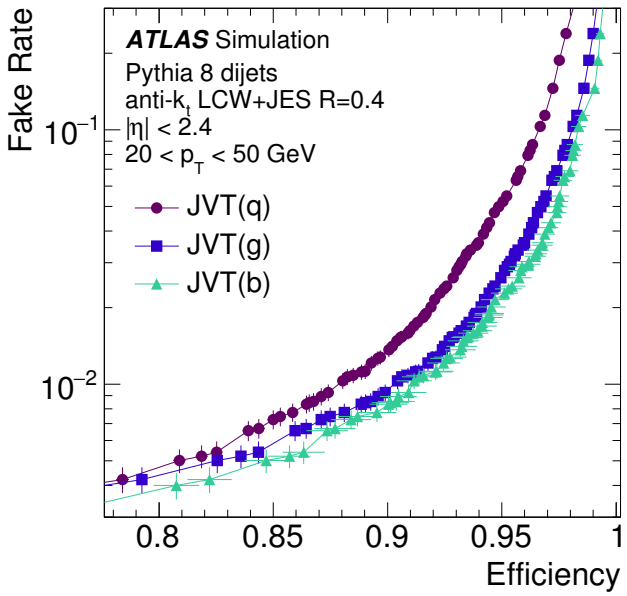

Figure 2.16: The fake rate, aka the rate of jets from pile-up, as a function of the signal (hard scatter) efficiency. Figure from Ref. [89].

Jet vertex tagging

Jets from the hard scattering (HS) process can be distinguished from pile-up jets by requireing a significant fraction of the tracks be associated with the jet originating from the PV. The jet vertex tagger (JVT) [89] is constructed using two low-level input observables as a two-dimensional likelihood derived using simulated dijet events and based on a k nearest neighbours (kNN) algorithm. For each point in the two-dimensional observable plane, the relative probability for a jet at that point to be of signal type is calculated as the ratio of the number of HS jets over the total number of jets found in the vincinity around the point using each a signal and pile-up training sample.

The two variables are calculated for each jet

- The variable R_{pT} is defined as the scalar sum of the p_{T} of the tracks that are ghost-associated [90] with the jet and originate from the hard-scatter vertex divided by the fully calibrated and pile-up subtracted jet p_{T}.
- The corrected jet vertex fraction (corrJVF) is calculated as the ratio of the scalar sum of the p_{T} of ghost-associated tracks that originate from a given PV to the scalar sum of p_{T} of all matched tracks in the jet, while a correction term weights the tracks not associated the hard scatter PV to decorrelate the corrJVT from the multiplicity of primary vertices in the bunch crossing.

The pile-up rate as a function of the signal jet efficiency is shown in Fig. 2.16. Lacking of inner detector coverage, the JVT is only available in the range $|\eta| < 2.4$.

Identification of b-hadron jets

The identification of jets that contain a b-hadron, is referred to as b-tagging. As a consequence of the almost diagonal nature of the CMKS matrix (c.f. Eq. (1.12)), the decay of b-quarks is strongly suppressed and leads to a lifetime of $\tau = 1.5ps$ resulting in an average flight length of half a millimeter, which can be reconstructed as secondary vertex by the high resolution of the inner detector. This unique property of b quarks is particularly interesting for identifying decays of the top quark or the Higgs boson. b tagging allows an extremely pure selection of $t\bar{t}$ pairproduction events and improves immensely the sensitivity to hadronic Higgs decays, which represent the dominant decay channel of the Higgs boson.

The b-tagging [91, 92] is done in two steps, based on the jet associated tracks. First, several low level algorithms are used to check the properties of the input tracks for compatibility with a displaced vertex. The input track set is assigned a LH for signal and for background based on reference likelihoods extracted from MC events. The ratio between signal LH and background LH is then used as a discriminant between b-hadrons and c-and LF hadrons.

Two such algorithms [91] exploit the large expected IP of the individual tracks belonging to a b-hadron decay. The IP2D algorithm uses the signed significance transverse IP for this, whereas the IP3D uses both IP.

Independently, the secondary vertex algorithm (SV1) [93] reconstructs a secondary vertex based on a subset of the original tracks, which additionally fulfill certain quality requirements. Observables such as the invariant mass of the vertex and the number of two-tracks vertices form the basis of the signal and background LH.

In addition, the JetFitter algorithm [94] reconstructs the entire b-hadron decay chain including the consecutive c-hadron decays. The algorithm is based on a modified Kallman filter and searches for a common decay axis of the two secondary vertices. The observables of the two secondary vertices then form the basis for an LH ratio discriminant.

The output discriminants from these low-level algorithms are passed to a multivariate classifier, which combines the individual discriminants together with kinematic observables of the jet p_{T} and η into a single powerful discriminant using machine learning. The multivariate algorithm (MV2 [95, 96]) used in this thesis employs a boosted decision tree (BDT) for this purpose. The BDT was trained on a combination of simulated $t\bar{t}$ pair production events and heavy Z' resonance events. The background sample was artificially composed of 7% c-jets and 93% LF jets. This training allows the BDT to assign a value between -1 – for very background-like jets and 1 – for very signal-like jets to each set of low-level observables, the so-called MV2 score. The MV2 score distribution of b-, c- and light jets is shown in Fig. 2.17. If this score meets a certain threshold value, the jet is called tagged.

***b*-tagging calibration** Both the low-level algorithms and the MV2 algorithm are based on MC. For application in data, the performance of the MV2 classifier was corrected by means of data events [92, 97]. For this purpose, four WPs with a fixed cut on the MV2 score were defined with a b-tagging efficiency of 60,70,77 and 85%. Correction scale factors are applied to the simulated event samples to compensate for differences between data and MC in the b-tagging efficiency. The correction

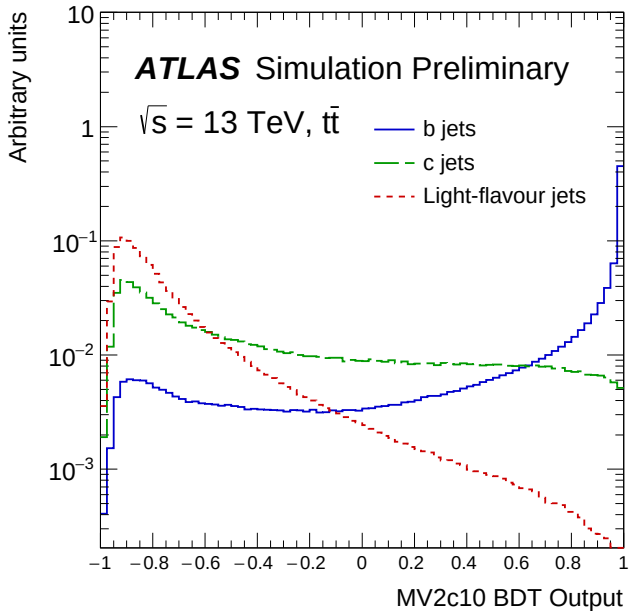

Figure 2.17: The discrimination score of the multivariate b-tagging algorithm MV2 for the signal b-jets and background c and light-flavor (LF) jets. Figure from Ref. [96].

scale factor and its uncertainty for b- and c-jets are estimated in $t\bar{t}$ events, while the light-flavor-jet misidentification rate correction factor and uncertainty are determined using dijet events [98–100].

These scale factors for the tagging efficiency at the 70% WP are given as a function of η and p_{T} and can be seen in Fig. 2.18.

Track jets

track jets were defined to identify the flavor content within large-R jets using b-tagging procedures. The flavor content thus determined can subsequently be used to identify strongly boosted massive bosons such as the Higgs boson. The procedure for identifying Higgs bosons is described in Chapter 3.

Two types of track jets are used in this thesis, fixed radius [101] and variable radius track jets [102–104]. Both types are reconstructed with the anti-k_t algorithm from inner detector tracks coming from the primary vertex. The tracks for the FR (VR) track jets must satisfy $p_{\mathrm{T}} > 0.4$ GeV ($p_{\mathrm{T}} > 0.5$ GeV) and $|\eta| < 2.5$. Each track must have at least seven hits in the pixel and SCT detectors and at most one of the hits in the pixel detector must be shared by multiple tracks. In addition, the longitidinal IP must satisfy $|z_0 \sin\theta| < 3$ to reduce contributions from pileup. The radius parameter of the anti-k_t algorithm for fixed radius track jets is $R = 0.2$.

Strongly boosted bosons result in strongly collimated decay products which can no longer be resolved by two separate fixed radius (FR) track jets with a radius parameter $R = 0.2$. Without the requirement

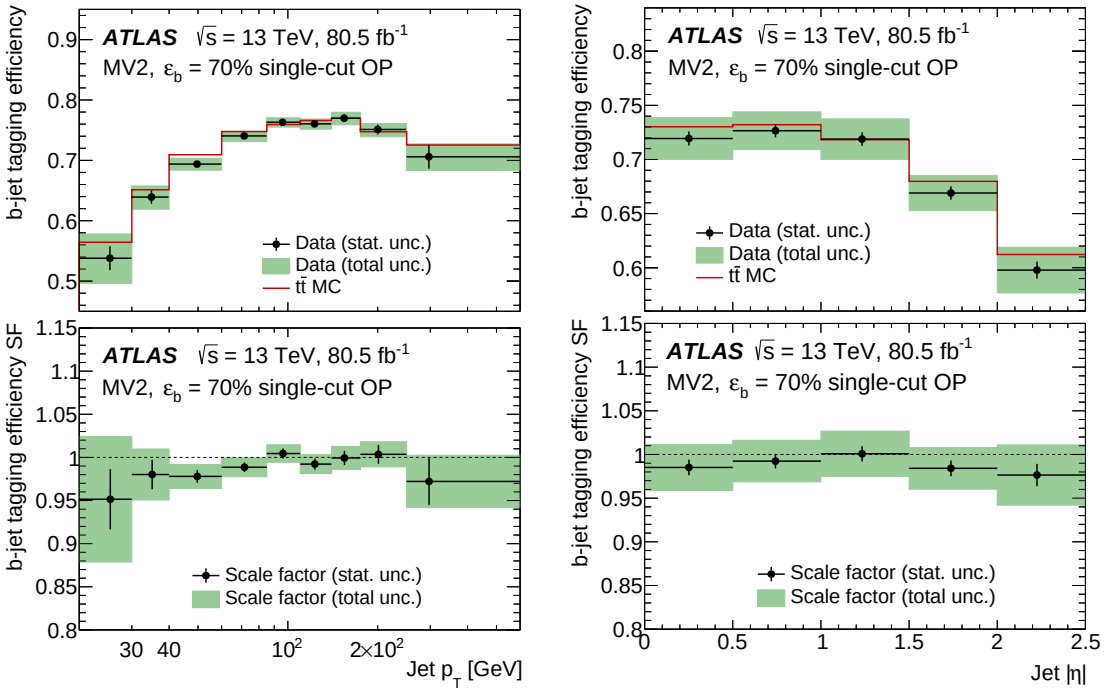

Figure 2.18: The upper panels show the selection efficiency as a function of (left) jet p_{T} and (right) jet η in data and MC. The lower panel shows the ratio of the efficiency in data over that in MC, corresponding to the scale factor applied to correct for missmodeling in MC events. Figure from Ref. [96].

of an energy calibration a track jets with radius parameter can be defined which adapts to the p_{T} of the track jets,

$$R \longrightarrow R_{\mathrm{eff}}(p_{\mathrm{T}}) = \min(R_{\mathrm{min}}, \max(R_{\mathrm{max}}, \frac{\rho}{p_{\mathrm{T}}})), \tag{2.15}$$

where $\rho = 30$ GeV, $R_{\mathrm{min}} = 0.02$, and $R_{\mathrm{max}} = 0.4$.

After the track jet is set, additional tracks that previously missed the IP requirements are matched with the track jet and added to the input set of the MV2 algorithm to improve the necessary track selection efficiency. These tracks must satisfy $p_{\mathrm{T}} > 10$ GeV and $|\eta| < 2.5$ and satisfy a p_{T}-dependent spatial criterion $R(\mathrm{track, track\ jet}) < \Delta R(p_{\mathrm{T}}^{t} rack jet)$ that accounts for the collimation of more heavily boosted decays. [105] The so-selected tracks are given to the MV2 algorithm that is optimized and trained for small-R jets.

The calibration [97] of the b-tagging efficiency and misidentification rate is done with a technique analogous to the small-R jets calibration [106]. The p_{T} dependent scaling factors are shown in Fig. 2.19. The total uncertainties are $1-10\%$, $15-50\%$, and $50-100\%$ for b-jets, c-jets, and LF jets, respectively.

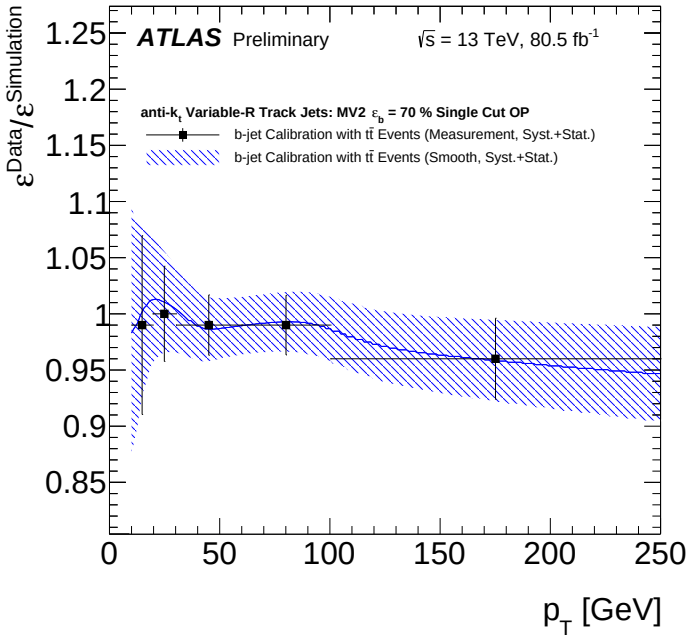

Figure 2.19: The correction scale factor accounting for discrepancies between the reconstruction efficiency in data and simulation of b-tagged track jets as a function of the track jet p_{T}. Figure from Ref. [97].

Hadronically decaying τ-leptons

τ-leptons have a decay length of $c\tau = 87\mu m$ [6] and decay either leptonically or hadronically. When decaying leptonically at a branching fraction of 35%, they are reconstructed by the stable muon or electron, with some momentum loss due to the escaping neutrinos.

When decaying hadronically, τ-leptons are reconstructed as small-R jets and identified using multivariate techniques, similar to that of b-tagging. The τ decay is characterized by an odd number of ID tracks, mostly by one or three, caused by collimated charged hadrons, accompanied by further neutral hadrons. Similar to b-tagging different WP are introduce to match the different needs of physics analyses, with increasing purity and decreasing effiziency. Three working points, referred to as tight, medium and loose are defined by the a nominal signal efficiencies of 75%, 85%, and 95%, respectively.

2.4.6 Missing transverse momentum

Neutrinos do not interact electromagnetically and are thus invisible for ATLAS. Nevertheless, the imbalance in momentum conservation infers the presence of undetected, escaping particles.

Because spectator partons within the collision may escape along the beam line, the longitudinal component of the momentum is not known and difficult to reconstruct. Anyway, because the transverse

momentum of the colliding partons is negligible, the decay product's momenta in the transverse plane must add up to zero.

The so-called missing transverse momentum or energy [107, 108] is defined for each component, x and y, as

$$E_{x/y}^{\text{miss}} = -\sum_{i \in \text{objects}} E_{x/y}^{i} - \sum_{j \in \text{soft terms}} E_{x/y}^{j}, \tag{2.16}$$

where the first term sums over the momenta of a certain selection of objects, defined analysis-specific (e.g. in Section 4.2.1. These momenta are commonly determined over the calibrated energy deposit in the calorimeters, this is why the letter E is used. The second so-called soft term is calculated from ID tracks associated with the primary vertex with $p_{\text{T}} > 400$ MeV and further quality requirements but not associated with any of the selected objects.

A frequently used variable is the magnitude of the transverse momentum, the missing transverse energy,

$$E_{\text{T}}^{\text{miss}} = \sqrt{(E_x^{\text{miss}})^2 + (E_y^{\text{miss}})^2}. \tag{2.17}$$

CHAPTER THREE

IDENTIFICATION OF BOOSTED HADRONIC HIGGS DECAYS

With the LHC commissioning at a center-of-mass energy of 13 TeV, new kinematic regimes have become available and searches for heavy new resonances already probe resonance masses at the TeVscale. The studies within this thesis focus on scenarios in which such heavy particles decay predominantly into highly boosted Higgs bosons which subsequently decay into two strongly collimated b-quarks, resulting i teh correspondingly collimated jet structures. As a direct consequence of the four-momentum conservation in a two-body decay, the angular separation ΔR between the two Higgs boson decay products in the $\eta - \phi$ plane can be approximated by,

$$\Delta R \approx \frac{1}{\sqrt{z(1-z)}} \frac{m_h}{p_{\mathrm{T}}^h}, \tag{3.1}$$

where m_h and p_{T}^h are the mass and the transverse momentum of the Higgs boson and z is the p_{T} fraction of one of the two decay products.

The large branching ratio for the $H \rightarrow b\bar{b}$ decay for the discovered Higgs boson with $m_h = 125$ GeV motivates studies of the reconstruction of hadronic Higgs boson decays. The standard jet reconstruction in ATLAS employs the anti-k_t algorithm with the radius parameter set to $R = 0.4$ (referred to as small-R jets). The small-R jets have been extensively tested and calibrated [51] and are used in many physics analyses. Nevertheless, depending on the choice of the jet radius parameter R, with increasing momentum and thus collimation of the decay products, the reconstructed jets the Higgs boson decays overlap. Using the standard small-R jet reconstruction for decays of Higgs bosons with transverse momentum of about 300 GeV, the two jets from the b-quark hadronization start to merge and compete[1] for jet energy cell clusters in the calorimeters. Above $p_{\mathrm{T}}^h = 600$ GeV, constituents emerging from the sub-leading b-hadron decay fall typically completely into the area of the leading b-jet. This overlap between the Higgs decay products impairs the identification of the b-quarks and therefore the Higgs boson identification.

The machine learning-based identification of b-hadrons is trained on jets containing the hadronization chain of exactly one b-quark. Therefore a second hadronization chain within a single reconstructed jet cannot be identified and also deteriorates tagging of the first decay chain. Furthermore, the missing constituents of the sub-leading jet may lead to an underestimate of the jet p_{T} which can potentially fall below the p_{T} reconstruction threshold. Thus, an overlap of reconstructed decay products also

[1] In a jet overlap, each cluster is associated with exactly one jet. However, the association with the respective jet is not necessarily the one that reflects the real shower.

affects the reconstruction of the energy, momentum, and mass of the Higgs dijet system. Therefore, the radius parameter of $R = 0.4$ is unsuitable for the identification of a boosted Higgs boson decay. A jet reconstruction using smaller radius parameter values only shifts the described problem to higher Higgs boson transverse momenta. These alternative jet collections would also require additional dedicated calibration measurements, and it must be ensured that the definition of these jets is infrared and collinear safe.

The more practicable solution to the described problem is discussed in the following. The new approach relies on the reconstruction of boosted hadronic Higgs boson decays using jets clustered with the anti-k_t algorithm, but using a radius parameter of $R = 1.0$ instead of $R = 0.4$. The jets with this larger radius parameter are referred to as large-R jets in the following. In this way, the whole Higgs boson decay is reconstructed as a single large-R jet. The large-R jet mass can be used to distinguish between Higgs bosons and other hadronically decaying objects. The further identification of the Higgs boson decay is based on flavor-tagging (b-tagging) techniques applied to track-based jets within a given Higgs boson candidate large-R jet. The input constituents of a so-called track jet are four-momenta of tracks from the inner detector which are clustered using the anti-k_t algorithm with $R = 0.2$ [109] (c.f. Section 2.4.5). These track jets are thus independent and complementary to the large-R jet collection. In the following studies, a large-R jet is referred to as a Higgs candidate jet if it has a p_{T} above 250 GeV, a $|\eta| < 2.0$, and at least one track jet associated to it. Additional information on the substructure of a large-R jet can be obtained from dedicated substructure variables, which are based on kinematic properties of the calorimeter constituents.

In this section, various techniques are discussed that aim to separate the actual Higgs boson jets from other large-R jet backgrounds using either flavor-tagging approaches, the large-R jet mass or jet substructure information. These studies are performed in the frame thesis and are published in Ref. [110].

3.1 Simulated jet samples for the Higgs tagging study

Constituent clusters used to reconstruct large-R jets in the context of the present study have been calibrated locally using the hadronic cell weighting scheme, as described in Section 2.4.2. Trimming (c.f. Section 2.4.5) is used to mitigate contamination of pile-up, multi-parton interactions, or initial state radiation by subtracting sub-jets with radius parameter $R_{\mathrm{sub}} = 0.2$ with a p_{T}-fraction smaller than $f_{\mathrm{trim}} = 5\%$ from the raw, so-called ungroomed jet.

track jets are are matched to the large-R calorimeter jet using so-called ghost-association [90, 111, 112]. In this matching method, the track jet four-momentum is first modified such that its angular orientation is preserved while its magnitude is set to an infinitesimal value. Such a ghost track jet is then included in the clustering of calorimeter cells. In this way, the clustering procedure automatically provides the association of the track jet to corresponding large-R jet into which it has been clustered, without changing the kinematic properties of this large-R jet. Compared to the geometrical matching procedure based on the angular separation within a ΔR cone size, the ghost association has more advantages in dense environments where jets may possess a more irregular shape.

In studies of simulated MC samples, the jet's origin is assessed by matching the generated particles to candidate jets. A candidate large-R jet is labeled as a true Higgs jet if exactly one Higgs boson on particle (generator) level and at least two particle-level b-hadrons from its decay chain can be geometrically matched to that large-R jet within $\Delta R < 1.0$. The particle-level Higgs boson is required to have a p_{T}^{h} of at least 250 GeV and be within $|\eta| < 2.0$, while the b-hadrons must have $p_{\mathrm{T}} > 5$ GeV and $|\eta| < 2.5$. The Higgs jet signal acceptance, i.e. the fraction of hadronically decaying Higgs bosons that can be reconstructed as (matched to) a candidate large-R jet, is shown as a function of the particle-level Higgs boson p_{T}^{h} in Fig. 3.1. The acceptance reaches a plateau of fully reconstruction efficiency for Higgs boson p_{T}^{h} values above about 500GeV.

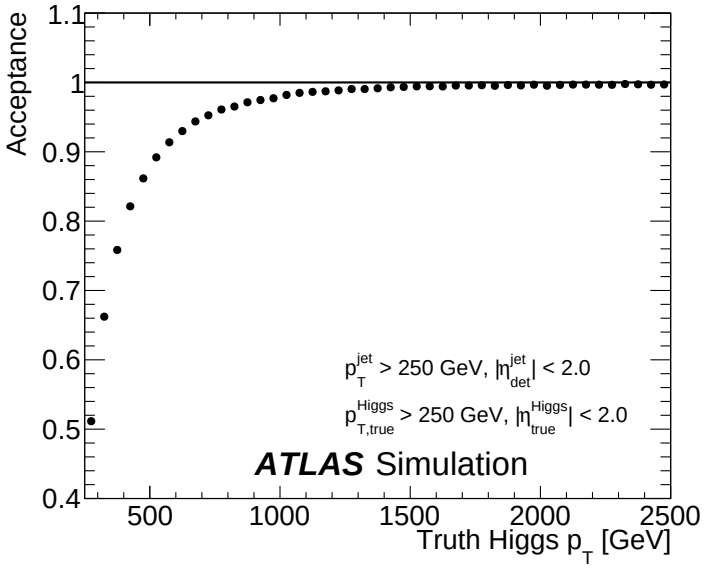

Figure 3.1: The Higgs jet acceptance, i.e. the fraction of (labeled) Higgs jets that are reconstructed as a large-R jet, as a function of the particle-level Higgs boson p_{T}^{h}.

As potential background sources for the Higgs jet identification, the most common processes that appear in different physics analyses are studied in this chapter. They can be mainly grouped into two categories. A hadronic top quark decay ($t \to Wb \to qq'b$) induces one source of background, by capturing the hadron shower either of all or only part of its decay products. Although top quarks can be produced in a single top quark production process, top quark pair production usually represents one of the most dominant physics analyses backgrounds. Large-R jet background induced by top quark decays is referred to as a top jet background. A candidate jet is labeled as a top jet if exactly one particle-level top quark is found in the MC event within the cone size $\Delta R < 1.0$ from the large-R jet axis.

In addition to the top jets, the most frequent processes at LHC are hard interactions described by QCD. Irradiations of hard quarks or gluons in a proton-proton collision also lead to fake Higgs candidates. Events producing such jets are all collectively referred to as multi-jet events. The gluons might split into a pair of quarks, including b-quarks pairs ($g \to q\bar{q}, b\bar{b}$). Every large-R jet not labeled as a Higgs- or a top jet is labeled as QCD jet.

The identification of the jet origin that is based on reconstructed observables, and is therefore also applicable to real data, is referred to as tagging. This tagging identification procedure can also miss-identify jets of non-Higgs origin as Higgs tagged jets, so-called false positive tags or miss-tags. The reciprocal value of the miss-tag efficiency ε_{bkg} is the rejection rate, $R_{\text{rej}}^{\text{bkg}} = \frac{1}{\varepsilon_{\text{bkg}}}$, defined individually for top jet and QCD jet background ($\varepsilon_{\text{bkg}} = \varepsilon_{\text{top}}, \varepsilon_{\text{QCD}}$).

The tagging techniques for Higgs identification studied in this chapter are evaluated in terms of the Higgs tagging efficiency ε_{sig}, i.e. the efficiency of selecting a true Higgs jet via the tagging procedure, and in terms of the background rejection rate of the both above introduced background jets.

Many discriminating observables used for the Higgs tagging have a (pseudo) continuous distribution. To discriminate between signal and background large-R jets, one may choose any particular value as the selection requirement on one of these observables, trading a high signal efficiency against a high background rejection. By a continuous variation of the selection requirement, a direct relation between the signal efficiency and the background rejection can be defined, the so-called receiver operating characteristic (ROC) curve. The discrimination power of two different observables can thus be compared by comparing the two corresponding ROC curves. The observable which gives a higher rejection for the same signal efficiency has a better discrimination power. A scalar measure of a discriminator's quality based on the ROC curve is usually given by the area-under-the-curve (AUC) value of this ROC curve.

However, for a given physics analysis, the full ROC curve is not decisive, but only the working point defined by the actual cut on a corresponding discriminating observable. A good approximation for the signal sensitivity based on a statistical significance σ is given by,

$$\sigma \approx \frac{N_{\text{sig}}}{\sqrt{N_{\text{sig}} + N_{\text{bkg}}}}, \tag{3.2}$$

or in the limit of small signal content,

$$\sigma \approx \frac{N_{\text{sig}}}{\sqrt{N_{\text{bkg}}}}, \tag{3.3}$$

with N_{sig} (N_{bkg}) is the number of large-R jets with are correctly (falsely) tagged as Higgs jets.

In order to obtain a signal sensitivity measure independent of the integrated luminosity, a relative sensitivity improvement $\Delta\sigma = \sigma^{\text{tag}}/\sigma$, with σ^{tag} the sensitivity after the tagging, can be expressed in terms of the signal and background tagging efficiencies,

$$\Delta\sigma = \frac{\varepsilon_{\text{sig}}}{\sqrt{\varepsilon_{\text{bkg}}}}. \tag{3.4}$$

A maximal value $\Delta\sigma^{\text{max}}$is determined for each discriminating observable by varying the selection requirements on this observable. The discriminator with the largest value of $\Delta\sigma^{\text{max}}$is considered to provide the best signal-to-background discrimination. The maximal value $\Delta\sigma^{\text{max}}$is used to assess and compare the different discriminator capabilities.

The signal tagging efficiency and the background rejection rate are dependent on the choice of the physics process, e.g. the full event topology, density of non-Higgs-related activities, or the distributions of kinematic variables. To optimize the Higgs tagging procedure as process independent as possible, three MC samples are defined from the available MC samples containing exclusively Higgs-, top-, or QCD jets, respectively. The simulated samples take into account the detailed GEANT 4-based [61] description of the detector response. The samples are chosen such to reflect critical Higgs tagging features as closely as possible for the application in different analyses. without loss of generality. Since the distributions of discriminating observables often depend on the large-R jet transverse momentum p_{T}^{J}, the samples are chosen such to have the same signal and background p_{T}^{J} spectra.

The sample with true Higgs jets are obtained from simulated decays of Randall-Sundrum gravitons into a pair of Higgs bosons, $G^{*} \rightarrow hh \rightarrow b\bar{b}b\bar{b}$, in a benchmark model with a warped extra dimension [113]. The simulated signal events with graviton masses $m_{G^{*}}$in the range between 300 and 6000 GeV provide a broad spectrum of Higgs boson transverse momenta. These events are simulated using the MADGRAPH5_aMC@NLO [114]. parton shower (PS) and multi-parton interactions are modeled with PYTHIA8 8 [115].

The background sample containing true top jets comprise the decays of a heavy vector boson resonance Z' decaying into $t\bar{t}$ pairs and cover a broad range of top-quark transverse momenta. Z' bosons are simulated with masses $m_{Z'}$between 400 and 5000 GeV using PYTHIA8 8 for the matrix element (ME) and the PS calculation. The sample with QCD jets contain the events from the inclusive multi-jet production generated by PYTHIA8 8.

For all three samples, leading order (LO) NNPDF 2.3 LO PDF set [116] and the A14 set of tuned parameters [117] were used. The PYTHIA8 showering algorithm has been interfaced with EvtGen [118] to model the decay of b- and c-hadrons. All samples include the effect of additional proton-proton interactions in this or an adjacent bunch crossing (pile-up events) by overlaying each simulated event with additional minimum-bias events. The minimum-bias events were simulated by PYTHIA8 8 using the A2 tune [119] and the MSTW2008 LO PDF [120].

Jet reweighting

In contrast to the MC sample with the inclusive multi-jet production, where the predicted spectra of discriminating observables directly correspond to the multi-jet spectra in the recorded data, the Higgs jet and top jet samples are superpositions of several graviton or Z' mass points and thus have an unphysical spectrum. These two samples are reweighted such that the distribution of the large-R jet transverse momenta matches that of the QCD sample that is shown in Fig. 3.2. The p_{T}^{J} spectrum of QCD jet is chosen since it is a monotonous steeply falling distribution similar to the background distributions in many physics analyses.

Since Higgs jets and top jets originate from a graviton or Z resonance generated with zero decay width, the transverse momentum spectra of their initial partons, p_{T}^{h} (p_{T}^{t}), peak sharply at the kinematic limit of approximately half the resonance mass. The peak position of p_{T}^{h} (p_{T}^{t}) is referred to as the *natural* p_{T}^{h} (p_{T}^{t}) of the corresponding graviton (Z') decay in the following. Transverse momenta of reconstructed Higgs jets (top jets) can deviate from the *natural* p_{T}^{h} (p_{T}^{t}) of the generated graviton (Z') decays for two main reasons. The first is that the resonance is not produced at rest, but has a finite

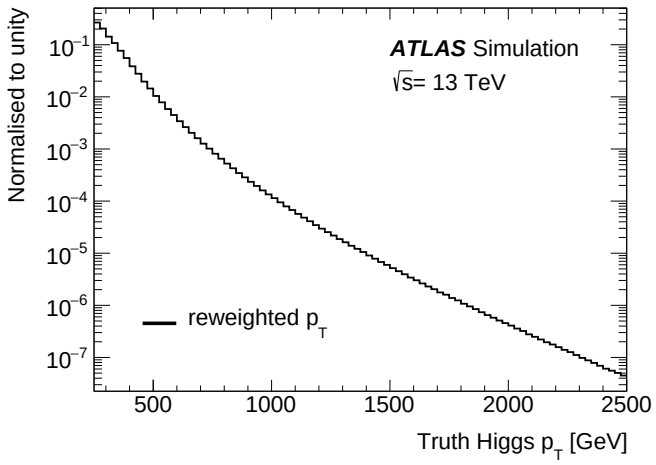

Figure 3.2: p_{T} spectrum of large-R jets resulting from QCD processes. Samples of large-R jets induced by hadronic Higgs and top-quark decays are each reweighted in a two-step process to match this spectrum. [110]

transverse momentum due to the recoil of either initial state radiation or an underlying event in a multi-parton interaction. This first effect is desired since a more continuous Higgs boson spectrum is obtained. In contrast, the second reason for a transverse momentum deviating from the peak position induces difficulties. The reason is the finite resolution of the reconstruction of the Higgs jet and the top jet momenta. This is, on the one hand side, due to the finite detector resolution for the detection of the individual particles.

On the other hand side it is the ensemble of particles itself which does not entirely correspond to the Higgs boson decay products. Jet containing high contributions from initial-state radiation or pile-up may have a p_{T}^{J} significantly higher than the *natural* Higgs boson p_{T}^{h} by a factor of up to 3. For events in which the p_{T}^{h} (p_{T}^{t}) of the two Higgs bosons (top-quarks) is unevenly distributed, there is a possibility that the recoiled ISR products fall into the cone of that Higgs jet (top jet) that is seeded by the Higgs boson (top-quark) with higher transverse momentum[2]. Therefore, on average the contribution from ISR is strongly increased for the large-R jet seeded by the lower-momentum Higgs boson (top quark). To mitigate such contamination the jet-samples are created using only that one of the two jets from the Higgs boson (or top-quark) decays that has the higher transverse momentum.

On the contrary, the reconstructed large-R jet momenta can be significantly lower than those of the seed particles, if the trimming procedure removes too many clusters originated by the seed particle or if the decay products fall partly outside of the reconstructed large-R jet. Furthermore, in semi-leptonic b-hadron decays, the fraction of p_{T} carried away by the neutrino can significantly reduce the energy in the corresponding calorimeter clusters reflecting the b-hadron decay. This can even enhance unwanted trimming effects since the remaining decay products are more likely to fall below the trimming p_{T}-threshold. In extreme cases a branch of b-hadron decay is completely removed. For Higgs jets this

[2] Note, that the jet seeded by the higher-momentum particle is not necessarily the higher-momentum jet due to ISR contributions.

results in a one-prong decay. Such rare Higgs jet candidates are nearly impossible to be correctly identified.

Regions in the p_{T}^{J} spectrum between the *natural* p_{T}^{h} (p_{T}^{t}) values are initially[3] less populated by orders of magnitude and, more importantly, strongly dominated by the rare Higgs jet (top jet) candidates with the above described faulty associations. The direct p_{T}^{J}-reweighting of the Higgs jet (top jet) sample to match the p_{T}^{J}-spectrum of the QCD jets depicted in Fig. 3.2 would strongly pronounce such rare events. Therefore, the reweighting must be done with caution. In contrast, to the steeply falling p_{T}^{J}-spectrum of the QCD jets, with bin content ranging over several orders of magnitude, the p_{T}^{J} values in the Higgs jet (top jet) sample is relatively equally distributed across the whole p_{T}^{J} range. Thus the Higgs jets and top jets receive weights with very diverse magnitude. A direct p_{T}^{J}-reweighting based on the reconstructed large-R jet would introduce a massive bias towards Higgs boson decays in which only a low fraction of the total Higgs boson p_{T}^{h} has been reconstructed, i.e. due to escaped neutrinos or unwanted trimming. E.g., Higgs bosons with p_{T}^{h} = 1000 GeV and a p_{T}-reconstruction fraction of 60% receive, on average, a weight which is 100 times higher than in events with regularly reconstructed p_{T}^{J}. This bias and the resulting differences in the evaluated Higgs tagging efficiencies are sensitive to the initial set of graviton (Z') mass points entering the Higgs jet sample, that cannot longer be considered as topology independent study.

A two-step reweighting procedure was therefore done to avoid this bias. The Higgs jet (top jet) samples are reweighted based on the particle-level Higgs boson p_{T}^{h} (top quark p_{T}^{jj}). The resulting intermediate p_{T}^{J}-spectrum of reconstructed candidate jets is already close to the p_{T}^{J}-spectrum from QCD jets. At the same time events containing Higgs bosons (top quarks) of similar momentum are reweighted by similar weights. In a second step, the residual differences between the intermediate p_{T}^{J}-spectrum of the Higgs jet (top jet) sample and the QCD jet sample is reweighted based on the large-R jet p_{T}^{J}, employing an additional weight in the order of unity.

In the following , three different Higgs tagging approaches will be studied: The Higgs tagging based on the b-tagging of track jets, withing the large-R jets; the Higgs tagging based on the mass of the large-R jet; and the Higgs tagging based on the substructure of the large-R jet.

3.2 Higgs tagging based on the b-tagging of track jets

The main discriminating feature of a boosted $h \to b\bar{b}$ decay to background large-R jets is the presence of displaced vertices within the jet arising from the decay of the two long-lived b-hadrons. The multivariate identification algorithm MV2 (c.f. Section 2.4.5) of b-hadron induced track jets has been trained on simulated Monte Carlo (MC) samples of inclusive $t\bar{t}$ production [95, 96, 121]. The $t\bar{t}$ process grants the advantage that the b-tagging techniques can be validated in data and the observed mismodeling can be corrected by utilizing a tag-and-probe method. In this method, a semi-leptonic top quark decay is used to tag the $t\bar{t}$ event and the efficiency of the b-tagging of the b-quark from the second top quark decay is probed. In this section, the applicability of the MV2 algorithm for the Higgs

[3] The initial unweighted p_{T}^{J} distribution is the superposition of samples with different m_{G^*}($m_{Z'}$) with local extrema at their corresponding *natural* p_{T}^{h} (p_{T}^{t}).

tagging identification of b-hadrons from hadronic Higgs boson decays is studied. Four Higgs tagging options are studied:

- The **double b-tagging** requires that the MV2c10[4] scores of the two leading track jets are above a certain threshold value.
- The **single b-tagging** requires that at least one of the two track jets passes that MV2c10 requirement. This Higgs tagging criterion is considered to be satisfied even if there is only one track jet within the large-R jet.
- The **leading single b-tagging**, i.e. the single b-tagging of leading track jets only is applied as a third Higgs tagging option, disregarding the b-tagging information from a potential second track jet.
- As the last option, an **asymmetric b-tagging** is tested by requiring two different MV2c10 scores on the two track jets. The MV2c10 requirement on one of the two track jets is hereby set to a commonly used working point at a 70% b-tagging efficiency (see below).

In a physics analysis, the there is often no decision between single b-tagging or double b-tagging, but both options are combined to increase the signal sensitivity. A further tagging option is introduced to avoid double-counting of events when using both, single- and double b-tagging:

- The **exclusive single b-tagging** requires that *exactly* one of the two track jets passes that MV2c10 requirement.

The discriminating power of this tagging option alone is much lower than the other options. It will be studied only in the context of the jet substructure-based tagging in Section 3.4.

3.2.1 Calibration of the b-tagging working points uncertainties

Four b-tagging WPs are defined by means of four different requirements on the lower threshold of the MV2c10 output score. Each working point corresponds to a certain b-tagging efficiency, as obtained for the b-jets in the inclusive $t\bar{t}$ MC sample. For example, the requirement of an MV2c10 score of at least 0.85 selects 70% of all b-jets in a $t\bar{t}$ sample and therefore defines the 70% working point (WP). A jet that passes this selection requirement is referred to as a b-tagged jet. At this WP, the rejection rate of light-quark (u,d,s) and gluon seeded track jets is about 120 [100] and for c-jets about 7 [98]. The four WP at 60%, 70%, 77%, and 85% b-tagging efficiency are calibrated with $t\bar{t}$ data, measuring the p_{T} and η dependent correction factors to match the simulation to data using the tag-and-probe procedure [99]. The misidentification rate for light-flavor jets is calibrated using dijet events [100]. The total calibration uncertainties for the b-tagging efficiency and the misidentification rate of c-jets and light-flavor jets are $1-10\%$, $15-50\%$, and $50-100\%$, respectively.

These correction factors are usually applied to the jets in simulated events to compensate for differences between data and simulation. Since the studies in this chapter purely rely on simulation consists of MC-studies, the described b-tagging correction factors are not applied, while the relative uncertainties

[4] The MV2c10 score is obtained by training the MV2 algorithm on a dataset with a 10% contribution to the background training data by jets seeded by a c-quark, c.f.Section 2.4.5

on these b-tagging correction factors are taken into account. The uncertainties derived for the 70% working point are used. This relative uncertainty is applied event-wise on each track jet on which the b-tagging procedure is applied. In this way, the impact of b-tagging uncertainties on the stability of the Higgs tagging performance is taken into account.

3.2.2 Performance of the track jet-based Higgs tagger

The efficiency of the Higgs tagging for the two most relevant Higgs tagging options, the single b-tagging and the symmetric double b-tagging is shown in Fig. 3.3 as a function of the reconstructed large-R jet p_{T}^{J}.

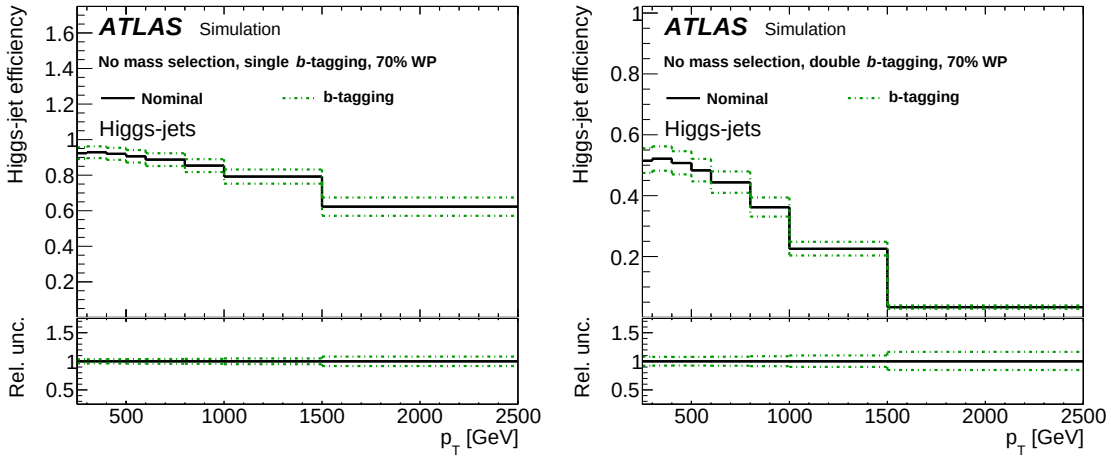

Figure 3.3: Efficiency of the Higgs jet tagging by means of the (left) single b-tagging and (right) the double b-tagging of track jets within the large-R jet using the 70% b-tagging WP, shown as a function of the large-R jet p_{T}^{J}. The dashed lines indicate the uncertainty due to the b-tagging calibration uncertainties. No mass requirement is applied to the large-R jets. The ratio panels show the relative uncertainty with respect to the nominal Higgs tagging efficiency. Plot published in Ref. [110].

The Higgs tagging efficiency for the symmetric double b-tagging at a 70% b-tagging WP varies from 52% ± 3% at low p_{T}^{J} values to about 5% ± 0.7% for p_{T}^{J} = 1500 GeV. For large p_{T}^{J} values, in particular, this tagger starts failing since the two track jets with radius parameter $R = 0.2$ start to merge due to a stronger collimation of b-hadrons when track jets start to merge above about 1-1.2TeV. The Higgs tagging efficiency utilizing the single b-tagging at the 70% b-tagging WP is as high as 92% ± 0.3% for large-R jets with transverse momenta of about 400 GeV. This Higgs tagger can partially recover the efficiency drop due to merged track jets.However, since the second b-quark is merged within one track jet, The Higgs tagger efficiency also deteriorates with increasing p_{T}^{J} values down to less than 60% ± 0.4% for p_{T}^{J} of more than 1.5TeV.

Fig. 3.4 shows the product of the Higgs jet acceptance (c.f. Fig. 3.1) and the Higgs tagging efficiency of these candidates, i.e. the fraction of all particle-level that are reconstructed as a large-R jet and tagged as a reconstructed Higgs jet. This product can be referred to as the boosted $h \to b\bar{b}$ detection

probability. The maximum Higgs jet detection probability by the double (single) b-tagging at a 70% b-tagging WPis 50% (80%) at a Higgs boson p_{T}^{h} of 500 GeV.

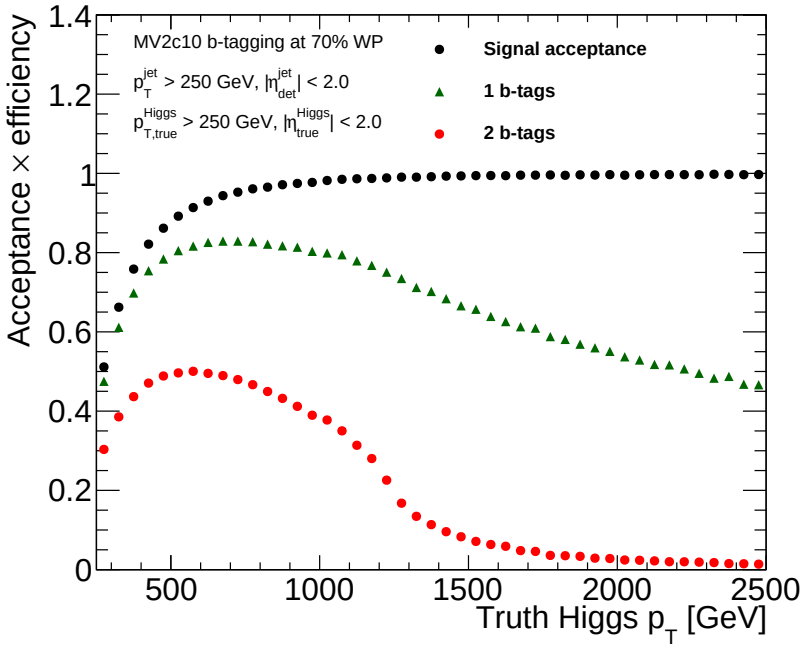

Figure 3.4: Higgs boson acceptance × Higgs tagging efficiency as a function of the particle-level Higgs boson p_{T}^{h}, shown for the two Higgs tagger options single b-tagging and and double b-tagging at a 70% b-tagging WP.

The Higgs tagging rejection rates for top jet and QCD jet backgrounds are shown in Fig. 3.5. The rejection rate stays relatively constant over the entire p_{T}^{h} range. FOr the Higgs tagger with the single b-tagging the rejection factor is close to 2 for top jets and between 15 and 18 for QCD jet backgrounds. The low top jet background rejection rate is due to the presence of one real b-quark within the top jet. The rejection of top jets increases to values of 40 - 70 for low jet p_{T}^{J}, if a second b-tagged track jet is required, within the Higgs candidate large-R jet. The rejection rate of QCD jets is in that case enhanced to a rate of 250 (500) at large-R jet p_{T}^{J} of 500 GeV (1500 GeV).

In order to obtain the Higgs tagger ROC curves the MV2c10 threshold is continuously varied instead of looking only at the four calibrated WP, as the application to recorded data would be restricted to. Fig. 3.6 shows the corresponding top jet and QCD jet background rejection rate as a function of the Higgs tagging efficiency (ROC). The star on the ROC curve correspond to the four calibrated b-tagging WPs at 60%, 70%, 77% and 85% b-tagging efficiency. The Higgs tagging performance is evaluated for all candidate large-R jets with $p_{\mathrm{T}}^{J} > 250$ and separately for the subset of jets with $p_{\mathrm{T}}^{J} > 1000$[5].

For a broad range of Higgs tagging efficiencies, the best tagging option is the double b-tagging with symmetric or asymmetric WPs. A large fraction of QCD jets can already be strongly suppressed by a single b-tagging. Very high QCD jet rejection rates can be achieved for Higgs tagging efficiencies of less than 70% (50%) at large-R jet p_{T}^{J} of 250 GeV (1000 GeV). double b-tagging slightly improves

[5] Note that jets with $p_{\mathrm{T}}^{J} \gtrsim 200$ GeV above these thresholds contribute less than 1% due to the steeply falling spectrum.

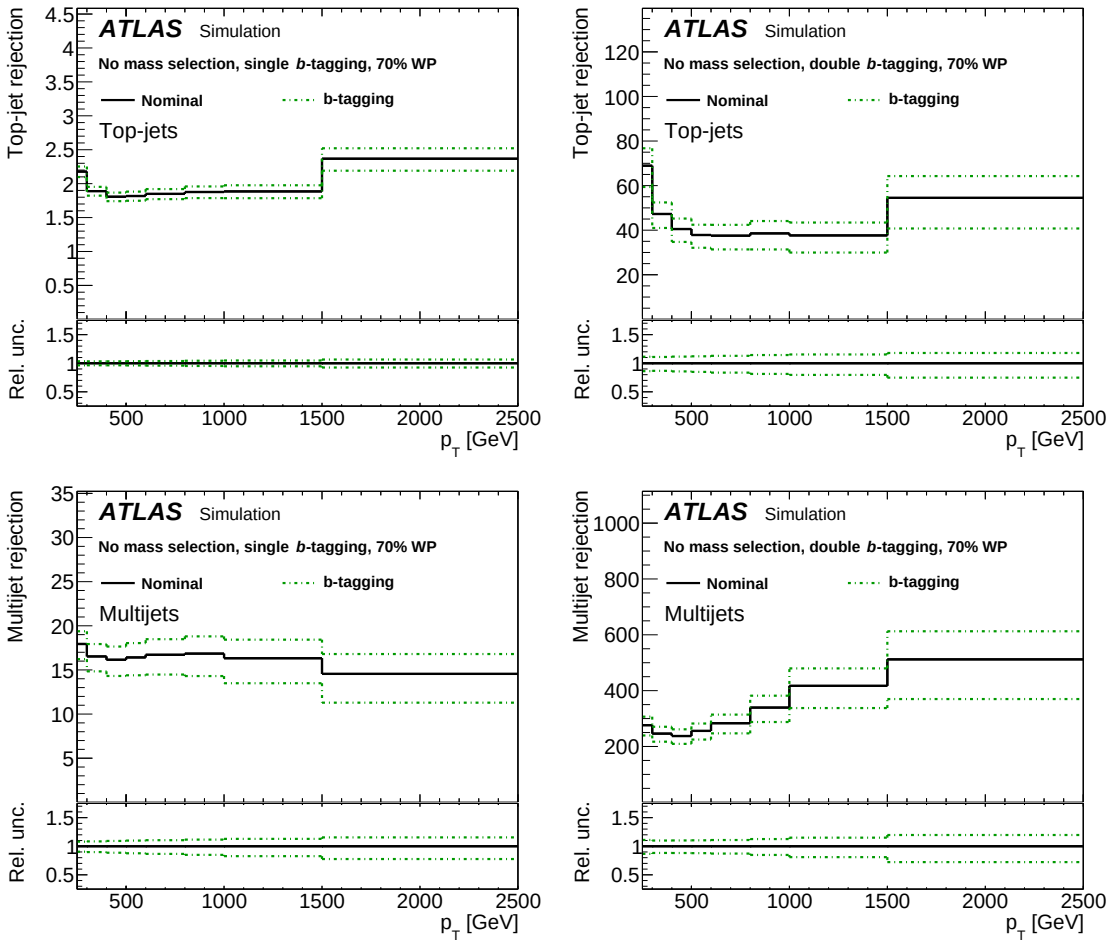

Figure 3.5: The Higgs tagger background rejection rate of (top) top jets and (bottom) QCD jets by (left) single b-tagging and (right) double b-tagging at a 70% b-tagging WP. The dashed lines indicate the uncertainty due to the b-tagging calibration uncertainties. No mass requirement is applied to the large-R jets. The ratio panels show the relative uncertainty with respect to the nominal Higgs tagging efficiency. Plot published in Ref. [110].

these rates, but requirements tighter than the 70% WP do not reject significantly more QCD jets than Higgs jets. This is due to a large fraction of $g \to b\bar{b}$ induced QCD jets that occupy this region of phase-space. Rejection of top jets by means of the single b-tagging in general only gives rejection rates of order 1, as already seen in 3.5. To achieve higher top jet rejection rates calls for the use of the double b-tagging. In contrast to the QCD-rejection rate, the tighter the MV2c10 requirement of the double b-tagging is, the more efficient is the rejection of jets from c-quarks which are the dominant contribution in the sample of top jets, satisfying looser double b-tagging criteria.

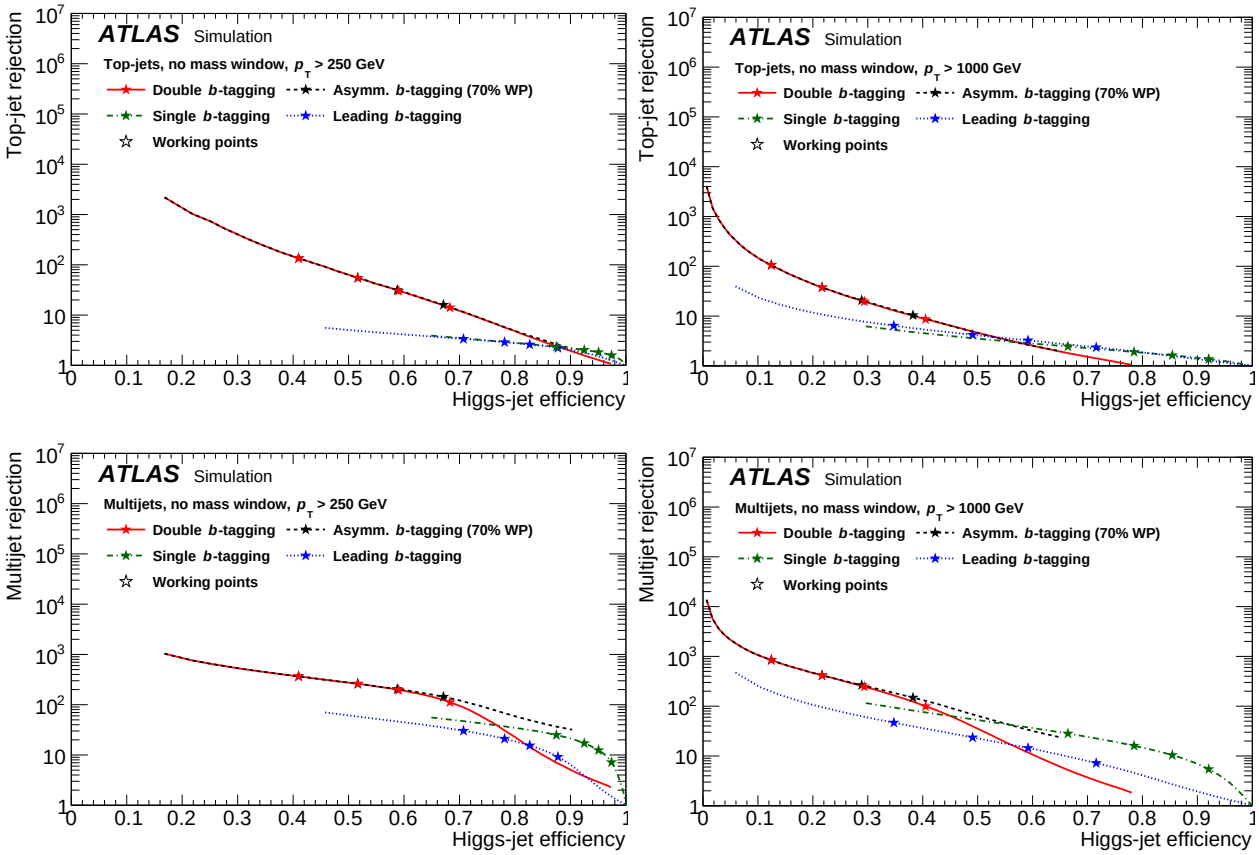

Figure 3.6: Comparison between the ROC curves of the four options for the Higgs tagger based on the b-tagging of the two leading track jets. The (top) top jet and the (bottom) QCD jet rejection as a function of the Higgs tagging efficiency for large-R jet p_{T}^{J} above (left) 250 GeV and above (right) 1000 GeV. The stars denote the 60%, 70%, 77% and 85% b-tagging WPs (from left to right). The curves corresponding to the double b-tagging and the asymmetric-b-tagging working points overlap over a large range of Higgs tagging efficiency values. Plot published in Ref. [110].

3.3 Higgs tagging based on the large-R jet mass

3.3.1 Expected performance improvement

The reconstructed large-R jet is another powerful discriminant that allows for efficient separation between hadronic Higgs boson decays and the background jets. The large-R jet mass is required to be compatible with the SM Higgs boson mass of $p_{\mathrm{T}}^{h} = 125$ GeV. The jet mass resolution (JMR) σ_m varies as a function of the large-R jet transverse momentum. It decreases for low transverse momenta due to out-of-cone effects,

$$\sigma_m \propto \frac{a}{p_{\mathrm{T}}}, \tag{3.5}$$

where a is a constant parameter. This follows from the increasing angle between the Higgs boson decay products at decreasing Higgs boson p_{T}^h values. The calorimeter energy resolution decreases linearly with the cluster energy [122]. Accordingly, the jet mass and energy resolution deteriorates linearly with increasing p_{T}^J values,

$$\sigma_m \propto bp_{\mathrm{T}} + c, \tag{3.6}$$

where b and c are constant parameters. Therefore, optimizing a large-R jet mass window around the Higgs boson mass may improve the separation between the Higgs jets and the background large-R jets. The optimized mass window is defined in dependence on the large-R jet p_{T}^J. Due to the limited angular resolution of the calorimeter system, the resolution of the large-R jet mass m_{calo} measurement in the calorimeter degrades with high jet transverse momentum. This resolution can be improved by employing also the information from the inner detector. An independent estimate of the jet mass is obtained from the inner detector tracks. The invariant mass of the tracks m_{tracks} that can be ghost-associated to the large-R jet is scaled by the ratio of the transverse momentum of the tracks $p_{\mathrm{T,tracks}}$ and the large-R jet p_{T}^J,

$$m_{\mathrm{TA}} = m_{\mathrm{tracks}} \frac{p_{\mathrm{T}}^J}{p_{\mathrm{T,tracks}}}, \tag{3.7}$$

with m_{TA} referred to as the track-assisted mass [123]. For the optimal Higgs jet identification, a weighted combination of the calorimeter and the track-assisted mass measurement is used, the combined mass [123]

$$m^{\mathrm{comb}} = \frac{\sigma(m_{\mathrm{calo}}^{-2})}{m_{\mathrm{calo}}^{-2} + m_{\mathrm{TA}}^{-2}} \cdot m_{\mathrm{calo}} + \frac{\sigma(m_{\mathrm{TA}}^{-2})}{m_{\mathrm{calo}}^{-2} + m_{\mathrm{TA}}^{-2}} \cdot m_{\mathrm{TA}} \tag{3.8}$$

with $\sigma(m_{\mathrm{calo}})$ ($\sigma(m_{\mathrm{TA}})$) the individual resolution of the calorimeter based mass (track-assisted mass). The combined mass resolution starts to become significantly better than the calorimeter-based measurement for the jet transverse momentum above ≈ 700 GeV and improves further with increasing p_{T}^J.

The energy can also be degraded due to muons from semi-leptonic b-decays, since they do only deposit a small fraction of their energy in the calorimeter system. If a reconstructed loose muon (c.f. Section 2.4.4) can be matched by a geometrical criterion of $\Delta R < 0.2$ to one of the both associated track jets, the large-R jet four-momentum is corrected accordingly. The muon energy deposits in the calorimeter are subtracted from the original large-R jet and the muon momentum measured in the muon spectrometer is added instead. In the case of more than one muon in the decay, the correction is

applied only for that muon, that has minimal distance to one of the both track jets. Also the impact of undetected neutrinos due to the semi-leptonic b-decay is not corrected, resulting in an average Higgs jet mass slightly below the Higgs boson mass $m_h = 125$ GeV. This correction is only applied to the m^{calo} component of the combined mass and is referred to as the *muon-in-jet correction*. The resulting distribution after the muon-in-jet correction is shown in Fig. 3.7. The large-R JMR for Higgs jets with transverse momentum between 350 to 500 GeV is improved by about 10%. In contrast, for higher large-R jet p_{T}^J, this improvement is less significant.

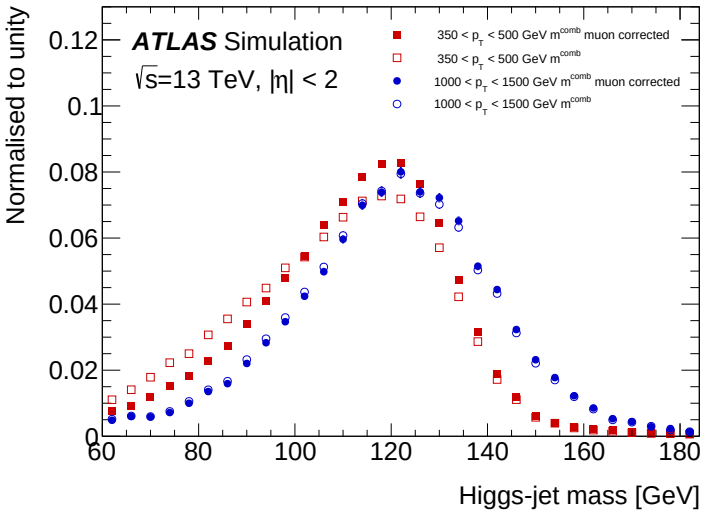

Figure 3.7: Distribution of the reconstructed large-R jet masses in the Higgs jet sample. Plot published in Ref. [110].

High contributions from initial state radiation dominate a mass measurement of values above 150 GeV. In contrast, a measurement of low masses (e.g. about 50 GeV) results from the trimming procedure and out-of-cone effects, which are commonly observed for boosted hadronic decays [112]. In particular for Higgs boson transverse momentum slightly above the threshold of the large-R jet reconstruction (250 GeV), such effects can be enhanced. If the $b\bar{b}$ decay axis in Higgs boson rest frame is closely aligned to the Higgs boost vector, the momentum is distributed very asymmetrical between the two b-hadrons in the laboratory frame. The sub-leading b-hadron decay products are much less collimated. Therefore, it is more likely to be removed by the trimming procedure. The decay products of the leading b-quark constitute the jet clustering seed and the sub-leading b-quark is further separated from the seed axis. Its showering products may therefore fall partially outside of the clustered jet. Consequently, the axis of the Higgs candidate is close to the orientation of the leading b-quark decay. The angular separation of the jet constituents, which is the dominant factor in the jet mass formation is much smaller than the decay would insist. Therefore, the reconstructed large-R jet mass m_J is strongly reduced compared to the original particle-level mass m_h. This feature results in a small bump in the distribution of the Higgs jet mass for low Higgs jet p_{T}^J, as shown in Fig. 3.8. These $h \rightarrow b\bar{b}$ candidates with large angular separations of its decay products may be better reconstructed from standard small-R jets with a radius parameter of $R = 0.4$. To overcome the impact of these non-uniform tail effects on the definition of the Higgs jet mass window, a fit of a superimposed Landau and Gaussian function

to the reconstructed mass distribution is performed. The modeling function is chosen empirically, describing well the peak of the mass distribution while neglecting the tails.

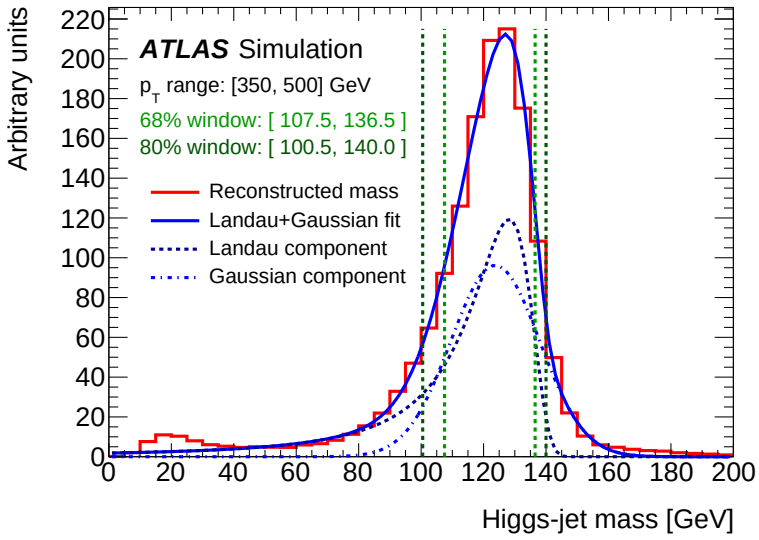

Figure 3.8: Distribution of the reconstructed mass for Higgs jets with $p_{\mathrm{T}}^{J} \in [350, 500]$ GeV. A mass window with 68%/80% efficiency is constructed around the Higgs jet mass peak based on a fitted superposition of a Landau and a Gaussian function. Plot published in Ref. [110].

The fit is performed in slices of Higgs jet p_{T}^{J}. The Higgs jet mass window requirement is optimized using the fitted mass distribution by requiring the smallest possible mass window interval that contains a certain minimal fraction of the fit function integral. In particular these fractions are required to be 80% for a loose mass window and 68% for a tight mass window requirement. Such an optimization is independent of the background jet distributions. The choice of the lower and upper mass threshold is subject to the statistical fluctuations in the mass distribution. The uncertainty on the threshold values is determined by generating a large number of toy jet mass distributions based on the fit function. The distributions are randomly varied around the best-fit function using the full covariance matrix of the fit parameters. Peak mass value (from the fit function) and the lower and upper mass threshold values for the tight and loose mass window requirement are shown in Fig. 3.9 together with the corresponding uncertainties, separately for each slice of Higgs jet p_{T}^{J}. Motivated by the relations in Eqs. (3.5) and (3.6), the p_{T}^{J}-dependence of upper and lower mass thresholds is fitted by

$$\sqrt{\left(\frac{a}{p_{\mathrm{T}}^{J}} - d\right)^{2} + \left(b p_{\mathrm{T}}^{J} + c\right)^{2}}, \tag{3.9}$$

where a, b, c and d are the free parameters of the fit. The resulting fit parameter values are given in Table 3.1.

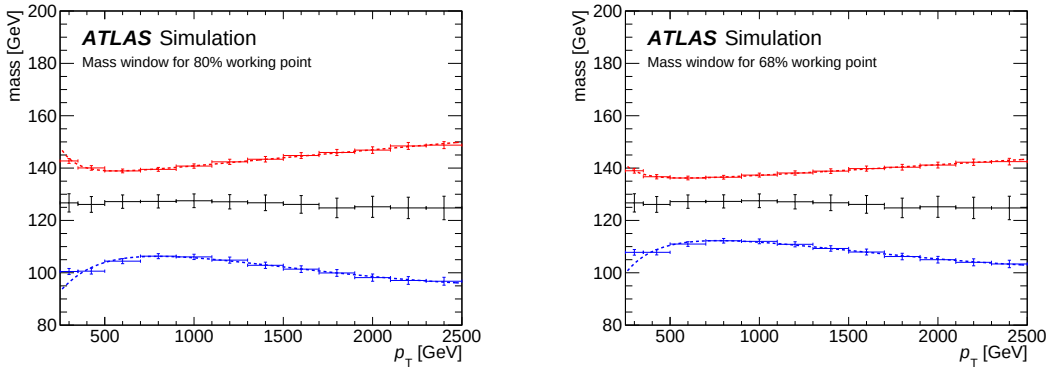

Figure 3.9: The optimized (left) tight and (right) loose Higgs jet mass window requirements as a function of the Higgs jet candidate p_T^J. Plot published in Ref. [110].

Table 3.1: Best-fit parameter values for the parametrization of upper and lower Higgs jet mass window thresholds in dependence on Higgs jet p_T^J, obtained using Eq. (3.9)

		a[GeV^2]	d[GeV]	b	c[GeV]
loose Higgs jet mass window	$m_{\text{cut}}^{\text{up}}$	-13101.2	7.93471	0.00413788	133.015
	$m_{\text{cut}}^{\text{low}}$	-11544.4	105.315	0.0263134	-86.9576
tight Higgs jet mass window	$m_{\text{cut}}^{\text{up}}$	-20096.3	23.5206	0.00555487	135.257
	$m_{\text{cut}}^{\text{low}}$	-16235.0	100.543	0.0294992	-93.2813

3.3.2 Systematic uncertainties on the mass-based Higgs tagging

The performance of the Higgs tagging based on the mass window selection is affected by the JMR and jet energy resolution (JER) uncertainties, as well as the uncertainties on the jet energy scale (JES) which are estimated in dijet data events by comparing the ratio of the calorimeter- to track-based measurements [124]. The various sources for uncertainties on the JES measurement are treated fully correlated in this analysis. The post-fit uncertainties on the free parameters of the fit in Ref. [124] are applied to the MC simulation in this analysis to estimate the impact of JES to the Higgs tagging efficiency.

The large-R JMR uncertainty σ_m is treated separately for the considered signal and background jets. The relative uncertainty is shown in Fig. 3.10 as a function of the large-R jet p_T^J. The impact of the JMR uncertainty on the Higgs tagging efficiency is studied by an additional smearing of the large-R jet mass, degrading the resolution by additional 20% relative to the nominal JMR. Similarly, the impact of the jet energy resolution uncertainty is estimated by degrading the nominal resolution by an absolute value of 2%

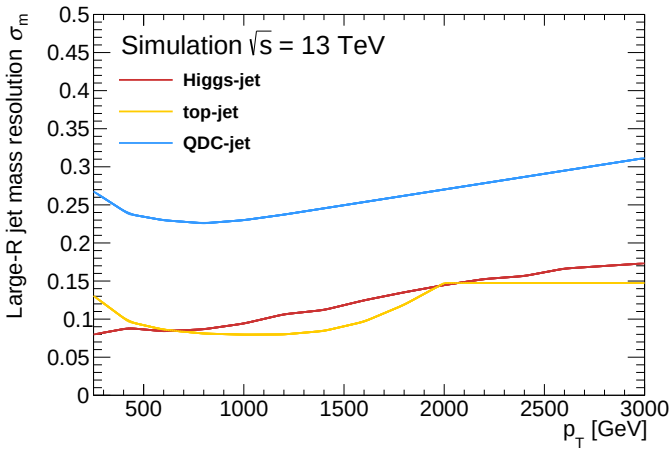

Figure 3.10: Nominal mass resolution of Higgs candidate large-R jet for the Higgs jet signal, top jet and QCD jet background jets, shown as a function of large-R jet p_{T}^{J}. The resolution of top jets is treated constant for $p_{\mathrm{T}}^{J} > 2$ TeV.

3.3.3 Performance improvements with mass-based Higgs tagging

Applying the jet mass window requirement parameterized by Eq. (3.9) and Table 3.1, in addition to the track jet-based Higga-tagging improves the rejection of the top jet and QCD jet background as shown in Fig. 3.11 for the loose mass window selection. Similar efficiency curves for the tight mass window selection can be found in Appendix A.1. Compared to the rejection rates from the track jet-based Higgs tagging (c.f. Fig. 3.5) and after applying the loose (tight) mass window requirement to jets with p_{T}^{J} of about 400 GeV and increases to a factor of 10 (14) for p_{T}^{J} values above 1000 GeV. The rejection rate of double b-tagged QCD jets is improved after the loose (tight) mass window requirement with an additional factor of 6 (9.5). Higgs tagging uncertainties due to the jet (mass and energy) resolution calibration as well as the JES calibration are small compared to the uncertainties induced by the track jet b-tagging. In case of top jets, the mass window selection provides a much more significant improvement in the high-p_{T}^{J} regime than at the low p_{T}^{J} values. In the low-p_{T}^{J} regime, the improvement after applying the loose (tight) mass window requirements is only about 2.3 (2.7) and 1.4 (2.1) for the single- and double b-tagged top jets, respectively. In the high-p_{T}^{J} regime, for $p_{\mathrm{T}}^{J} > 1000$ GeV, the top jet rejection rate improves by a factor of 11 after a loose mass window selection of single b-tagged jets and by up to a factor of 20 after applying the tight mass window requirement of double b-tagged candidates. In the case of top jets, the Higgs tagging from the jet mass scale calibration and resolution measurements become comparable to those induced by the track jet b-tagging.

A comparison of the ROC curves for the Higgs taggers before and after applying the different mass window requirements is shown in Fig. 3.12 for QCD jets. The scan over the Higgs tagging efficiency is obtained via varying the MV2c10 score thresholds for the track jet b-tagging. For a wide range of Higgs tagging efficiencies, the loose mass window selection provides the best performance among the considered mass window selections against QCD jets. Only the regime of high Higgs tagging efficiencies is per design not reachable using a mass window cut.

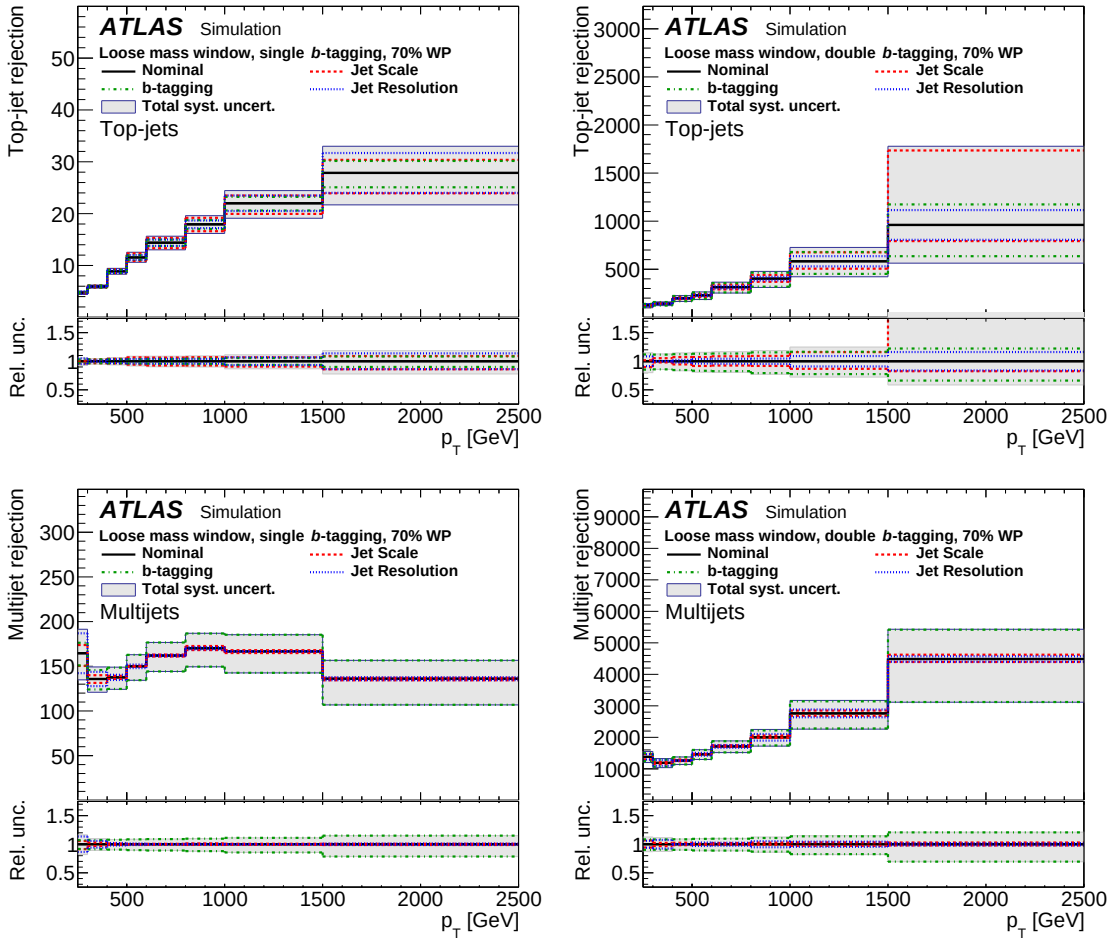

Figure 3.11: The Higgs tagger rejection rate for (top) top jets and (bottom) QCD jet background when using the Higgs tagger with (left) single b-tagging or right double b-tagging in combination with a loose large-R jet mass window requirement as a function of the large-R jet p_{T}^{J}.

In the case of low-p_{T}^{J} top jets, the rejection rates are only marginally improved by the mass window requirements for both single- and double b-tagged jets, as shown in Fig. 3.13 (top). For high-p_{T}^{J} candidate jets (Fig. 3.13, (bottom)), however, the mass window selection leads to a massive improvement by more than one order of magnitude for any given Higgs tagging efficiency. The differing rejection capabilities for low- and high-p_{T}^{J} top jets are explained by a bias in the jet content, that is strongly correlated with the jet momentum in the used sample. Low-p_{T}^{J} top jets are primarily formed by two seed partons, missing the decay products of the third quark in the $t \rightarrow W \rightarrow bqq'$ decay. The mass is therefore distributed around values lower than the top quark mass and falls to a large extent into the mass window selection. top jets with $p_{\mathrm{T}} > 1000$ GeV are merely seeded by all three quarks. The mass distribution peaks therefore at the top quark mass and is therefore efficiently rejected by the upper mass window threshold requirement.

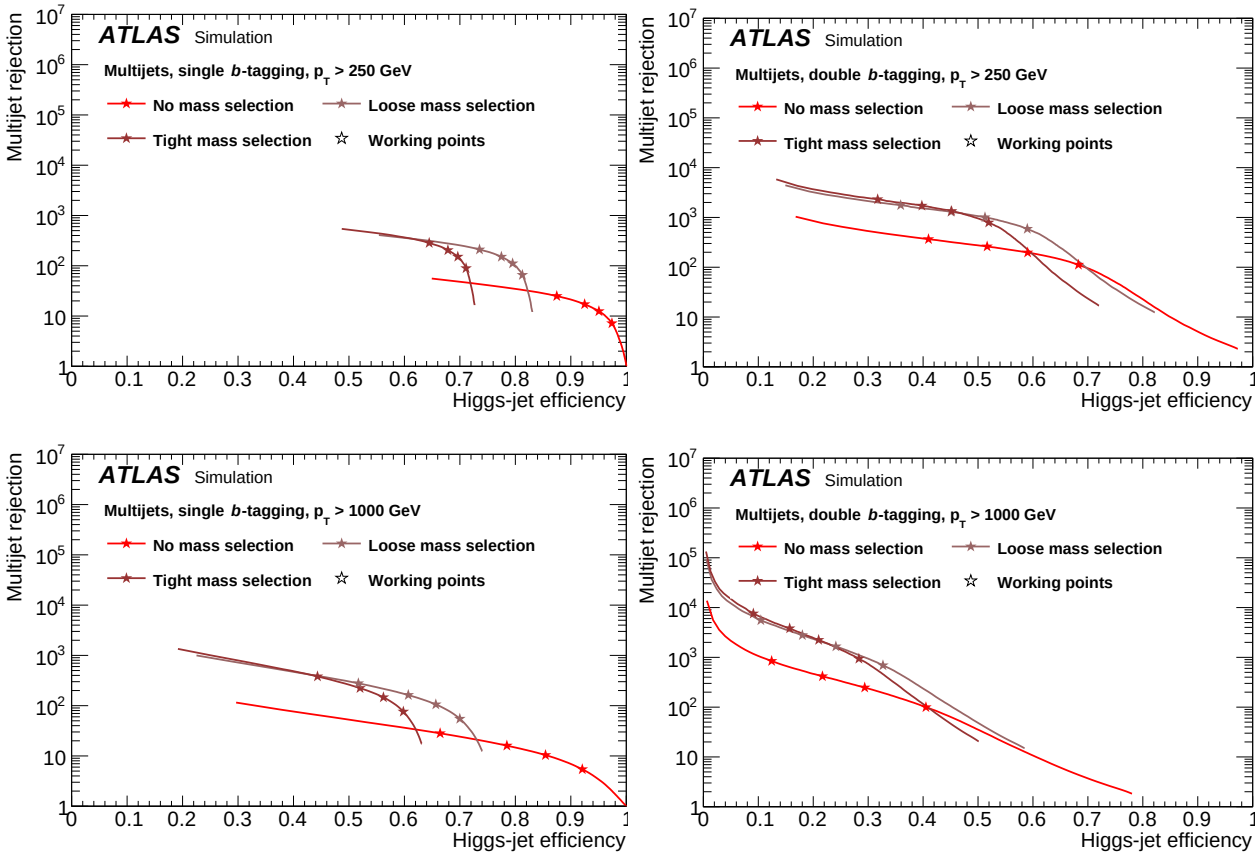

Figure 3.12: Comparison of the Higgs tagger ROC curves with and without the large-R jet mass window selection. The Higgs tagging efficiency is varied by varying the MV2c10 score thresholds for the (left) single b-tagging and (right) double b-tagging The top (bottom) panels are obtained for QCD jets with $p_{\mathrm{T}} > 250$ GeV ($p_{\mathrm{T}} > 1000$ GeV). The stars indicate the 60%, 70%, 77% and 85% b-tagging WPs (from left to right). Plot published in Ref. [110].

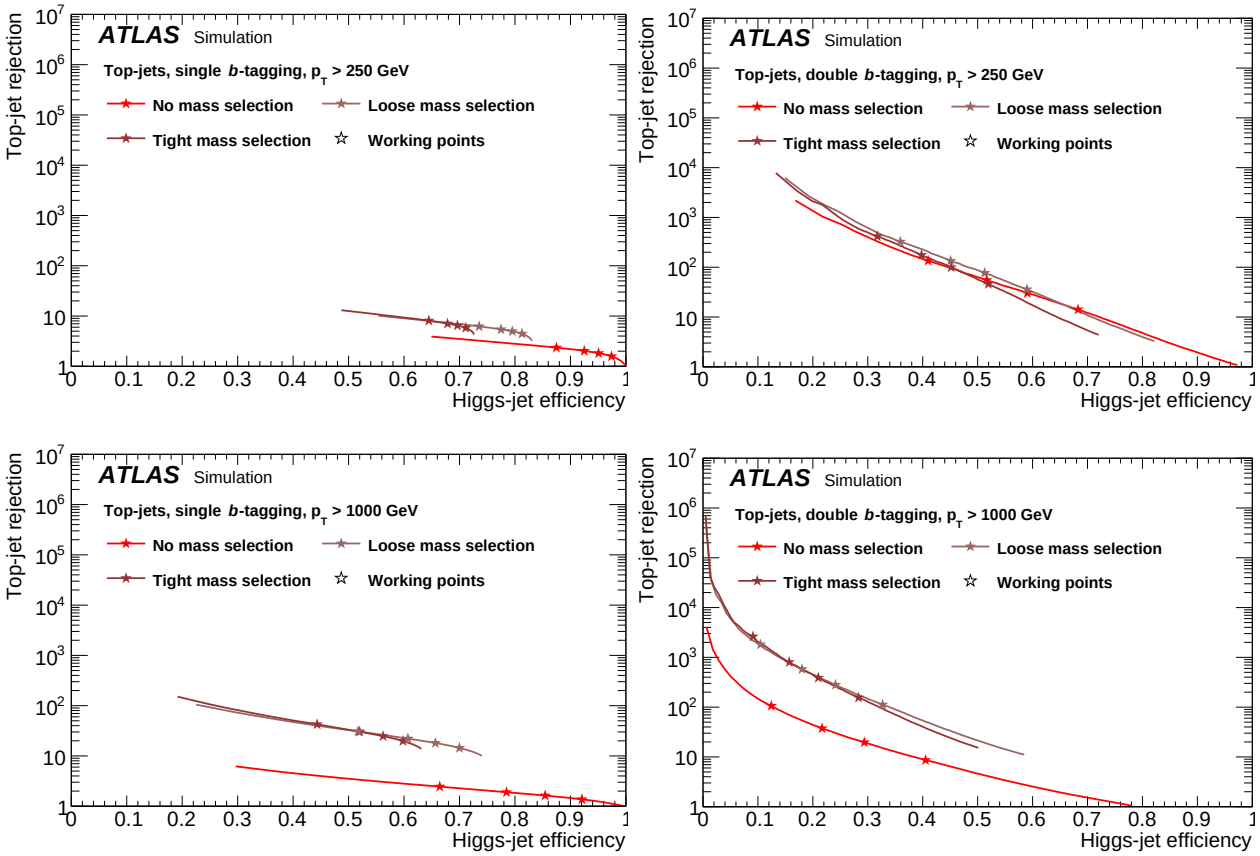

Figure 3.13: Comparison of the Higgs tagger ROC curves with and without the large-R jet mass window selection. The Higgs tagging efficiency is varied by varying the MV2c10 score thresholds for the (left) single b-tagging and (right) double b-tagging The top (bottom) panels are obtained for top jets with $p_{\mathrm{T}} > 250$ GeV ($p_{\mathrm{T}} > 1000$ GeV). The stars indicate the 60%, 70%, 77% and 85% b-tagging WPs (from left to right). Plot published in Ref. [110].

3.4 Higgs tagging based on a large-*R* jet substructure

The properties of calorimeter clusters within a large-*R* jet may give additional information on the origin of large-*R* jet constituents. Such substructure observables may be used to quantify how likely it is that a Higgs candidate jet originates from two distinct sub-jets, how much irradiation is between the dominant clusters of the jet and how symmetric the decay products are distributed. The substructure information can be obtained from the calorimeter systems and is thus complementary to the track jet-based Higgs tagger. In particular, there is the sensitivity to electromagnetic neutral particles, which do not leave any signal in the inner detector.

The large-*R* jet mass can be regarded as a such a substructure variable. Furthermore, many different jet substructure (JSS) observables have been introduced [125–144] to tag the large-*R* jets from $W \to qq'$, $Z \to q\bar{q}$ or $t \to qq'b$ decays, or are designed to distinguish between quark and gluon induced irradiation. The study presented in this section considers a large number of these observables, over 40 in total, to estimate their potential discriminating power for the tagging of Higgs jets and the to improvements of the top jet and QCD jet background rejection.

The discriminating power of each JSS observable is evaluated in terms of the maximization of the relative sensitivity $\Delta\sigma$ (Eq. (3.4)) and by studying the corresponding ROC curves. The ROC curve is defined by all possible combinations of a lower and upper thresholds on a given discriminating JSS observable, including also the complementary selections, i.e. selections in which the signal lies outside a given window.

3.4.1 Large-*R* jet substructure observables

In the following, each substructure observable will be described in more detail.

Energy correlation functions: The N-point energy correlation functions ECF_N [131, 133] are defined as,

$$ECF_1^{(\beta)} = \sum_{i \in J} p_{\mathrm{T}}^{(j)}, \tag{3.10}$$

$$ECF_2^{(\beta)} = \sum_{i<j \in J} p_{\mathrm{T}}^{(i)} p_{\mathrm{T}}^{(j)} \left(R_{ij}\right)^{\beta}, \tag{3.11}$$

$$ECF_3^{(\beta)} = \sum_{i<j<k \in J} p_{\mathrm{T}}^{(i)} p_{\mathrm{T}}^{(j)} p_{\mathrm{T}}^{(k)} \left(R_{ij} R_{ik} R_{jk}\right)^{\beta}, \ldots ECF_N^{(\beta)} \quad = \sum_{i \in J} \left(\prod_i p_{\mathrm{T}}^{(i)} \right) \cdot \left(\prod_{i<i'} R_{ii'} \right)^{\beta}. \tag{3.12}$$

$$\tag{3.13}$$

where β is an free parameter, $p_{\mathrm{T}}^{(i)}$ is the transverse momentum of the i-th subjet and R_{ij} distance between the i-th and the j-th subjet. $ECF_N^{\beta=1}$ tends to small values for all jets induced by a decay with less than N primary decay products. Thus $ECF_2^{(\beta=1)}$ can be used to distinguish between QCD jets with centrally distributed constituents (i.e. 1 primary decay product) and Higgs jets from a 2-body decay.

This can be seen in Fig. 3.14(a). In contrast, the 3-point correlation function $ECF_3^{(\beta=1)}$ (Fig. 3.14(b)) can be used to distinguish between boosted W/Z/Higgs bosons and top jets. It is a good discriminator against the top jets background, if all three top quark decay are fully captured within the large-R jet. The two maxima in the $ECF_3^{(\beta=1)}$ distribution of top jets correspond to large-R jet with 3 or 2 captured top quark decay products, respectively.

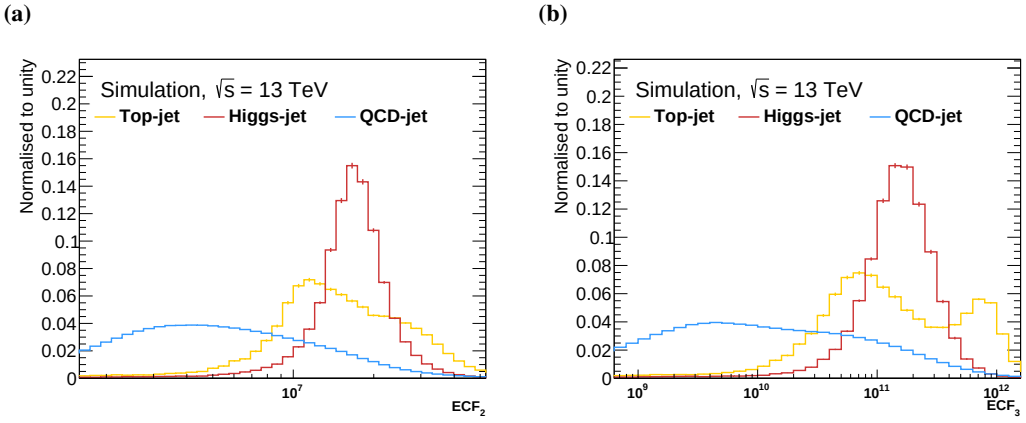

Figure 3.14: Distribution of the (a) 2- and (b) 3-point energy correlation function $ECF_N^{(\beta=1)}$ for the Higgs jet signal and top jet and QCD jet backgrounds.

The introduced energy correlation functions are strongly dependent on the large-R jet transverse momentum scale. The ratios ECF_{N+1}/ECF_N are introduced to reduce this dependence. Variables defined by double ratios of energy correlation functions [131, 133] provide a dimensionless measure for the probability of a two-prong decay structure within a large-R jet. These variables are defined as

$$C_2^{(\beta)} = \frac{ECF_3^{(\beta)} \cdot ECF_1^{(\beta)}}{(ECF_2^{(\beta)})^2}, \tag{3.14}$$

$$D_2^{(\beta)} = \frac{ECF_3^{(\beta)} \cdot (ECF_1^{(\beta)})^3}{(ECF_2^{(\beta)})^3}. \tag{3.15}$$

With the caveat that $C_2^{(\beta)}$ has shown to be pile-up sensitive [130], both variables are well suitable for identifying 2-prong decays. Their distributions for $\beta = 1$ are shown in Fig. 3.15.

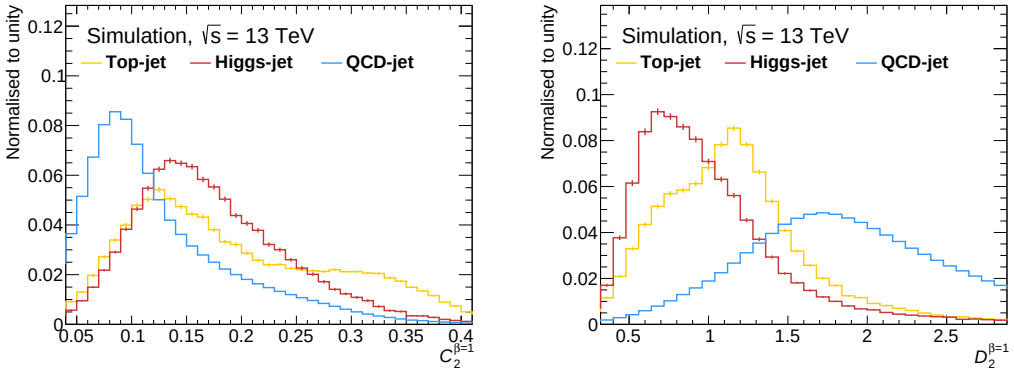

Figure 3.15: Distribution of the energy correlation double ratio variables $C_2^{(\beta=1)}$ and $D_2^{(\beta=1)}$ for the Higgs jet signal and top jet and QCD jet backgrounds.

N-subjettiness: The N-subjettiness variables τ_N relate directly to the probability that the substructure of a given jet J is compatible with a hypothesis that the jet is composed of N or fewer sub-jets [142, 143]. It is a p_{T}-weighted average of the closest distances $\min_{j \in N} R_{j,i}$ of all jet constituents $i \in J$ to the closest candidate subjet.

$$\tau_N = \frac{1}{d_0} \sum_{i \in J} p_{\mathrm{T}}^{(i)} \cdot \min_{j \in N} R_{j,i} \tag{3.16}$$

$$\text{with } d_0 = R \sum_{i \in J} p_{\mathrm{T}}^{(i)}. \tag{3.17}$$

These candidate subjets are ideally determined by minimizing τ_N. Since this is computationally intense, two alternatives are studied in this chapter. The first approach is based on a reclustering the large-R jet constituents by means of the exclusive-k_t algorithm requiring exactly N subjets with their jet axes defining the subjet direction.

The distribution of different subjettiness observables for the Higgs jets, top jets, and QCD jets are shown in Fig. 3.16. Another approach of defining the direction of subjets [142, 143] that has been shown to improve the agreement of the τ_N with the so-defined subjet axes to the optimum[6], is to define the subjet direction by the jet constituent with the highest p_{T} in each of the subjets. The so-defined subjets are referred to as winner takes all (wta) in the following. The corresponding subjettiness distributions τ_N^{wta} are similar to the ones from the first approach and can be found in Appendix A.6.

All τ_i variables tend to have smaller values for QCD jets since these jets are centered around a single subjet axis. In contrast, τ_1 values for Higgs jets are large compared the the corresponding τ_2. This reflects the fact that well-reconstructed Higgs boson decays would result in two primary clusters around the two subjet axes. The top jet distribution also peaks at small values for τ_2 due to only partially collected top decays products resulting in two instead of three axes. However, compared to the Higgs jets, there are also significantly more top jet entries in the tail with high τ_2 high values

[6] i.e. the computational intense definition

which originate from fully collected 3-body top quark decays. The distributions of the τ_3 variable is similar for Higgs jet and top jet, resulting in a small discrimination power.

Highly collimated jets tend to have smaller values of all N-subjettiness variables simultaneously. To remove this momentum dependence, the N-subjettiness variables are often replaced by the ratios,

$$\tau_{21} = \tau_2/\tau_1,$$
$$\tau_{32} = \tau_3/\tau_2.$$

The distributions of N-subjettiness ratios τ_{21} and τ_{32} are shown in Fig. 3.17. While τ_{21} provides good discrimination against one-prong decays such as QCD jets, the τ_{32} variable can provide discrimination against the 3-prong top jets.

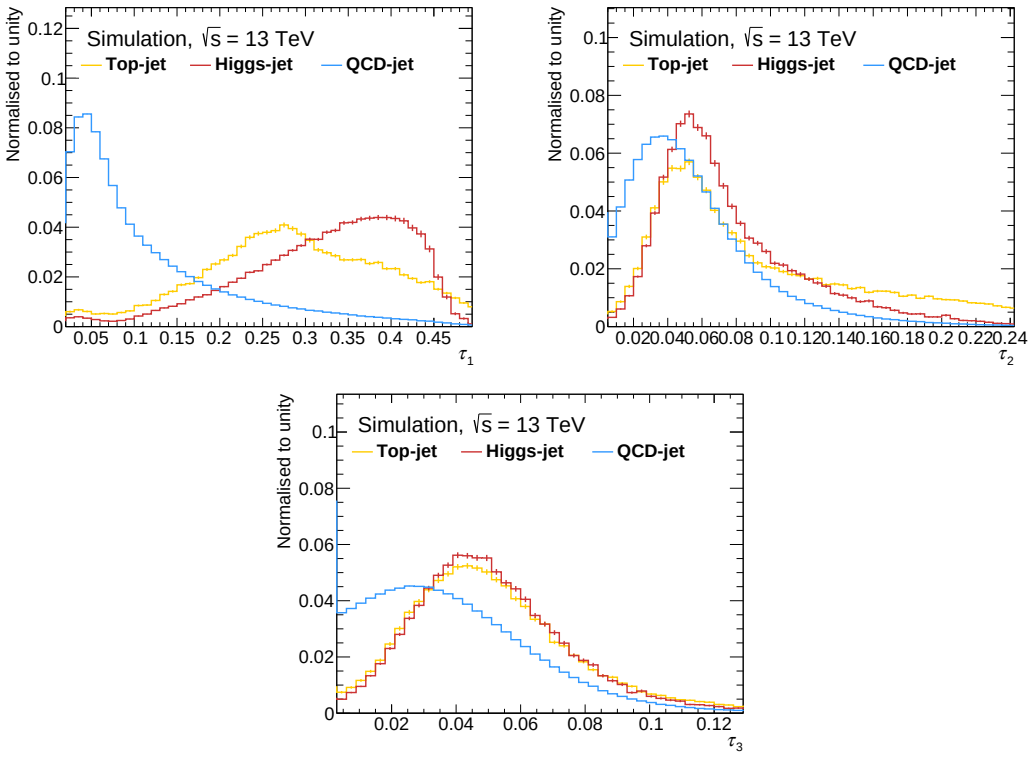

Figure 3.16: Distribution of the subjettiness variables τ_1, τ_2 and τ_3 for the Higgs jet signal and top jet and QCD jet backgrounds.

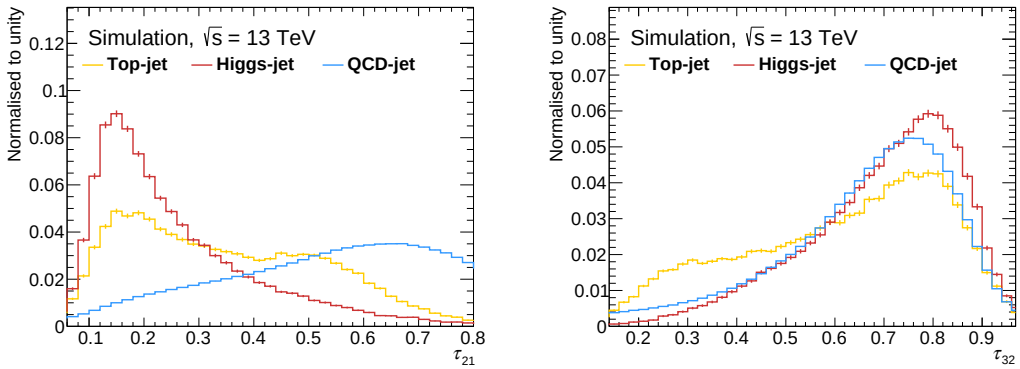

Figure 3.17: Distribution of the subjettiness ratios $\tau_{21} = \tau_2/\tau_1$ and $\tau_{32} = \tau_3/\tau_2$ for the Higgs jet signal and top jet and QCD jet backgrounds.

Dipolarity: The dipolarity variable is introduced to quantify the probability that a pair of two jets j and k is induced by a color singlet [132]. THis variable is shown to discriminate between top jets and QCD jets. It is defined as

$$\mathcal{D}_{jk} = \frac{1}{R_{jk}^2} \sum_{i \in J} \frac{p_{\mathrm{T}}^{(i)}}{p_{\mathrm{T}}^{J}} R_i^2, \tag{3.18}$$

where p_{T}^{J} is the transverse momentum of the large-R jet, R_i is the minimum euclidean distance between the i^{th} calorimeter cell (with transverse momentum $p_{\mathrm{T}}^{(i)}$) and the line segment connecting the two subjets. R_{jk} is the distance between the two subjets. Two definitions of subjets are used for the calculation of the dipolarity: exclusive k_t-algorithm with exactly 2 subjets; or, second, the k_t-algorithm with a jet threshold of 5 GeV. Dipolarity distributions based on the exclusive-k_t algorithm are shown in Fig. 3.18(a) for the studied jet samples, while the corresponding distributions obtained with the second subjet reconstruction approach shown in Figs. 3.18(b) to 3.18(d). The subscript in for the different dipolarity observables $\mathcal{D}_{ni}$ denote the n-th and i-th p_{T}-leading subjet.

The dipolarity $\mathcal{D}_{ni}$ is evaluated only for the case, a n^{th} subjet could be formed by the k_t-algorithm. In case of $n = 3$ there are 25%, 40%, and 10% such jets in the Higgs-, top-, and QCD jets samples, respectively. Otherwise a value of $\mathcal{D}_{ni} = 0$ is assigned to such jets.

Small values of dipolarity are expected, if most of the hadronic activity is recorded in the region between the considered subjets. Contributions with significant distance from from the subjets are seen as a product of semi-soft irradiation and indicate the color configuration of the large-R jet initiator. Color singlets that decay into two jets (such as the Higgs boson) tend to induce small dipolarity values, while irradion emitted by colored objects induce larger values.

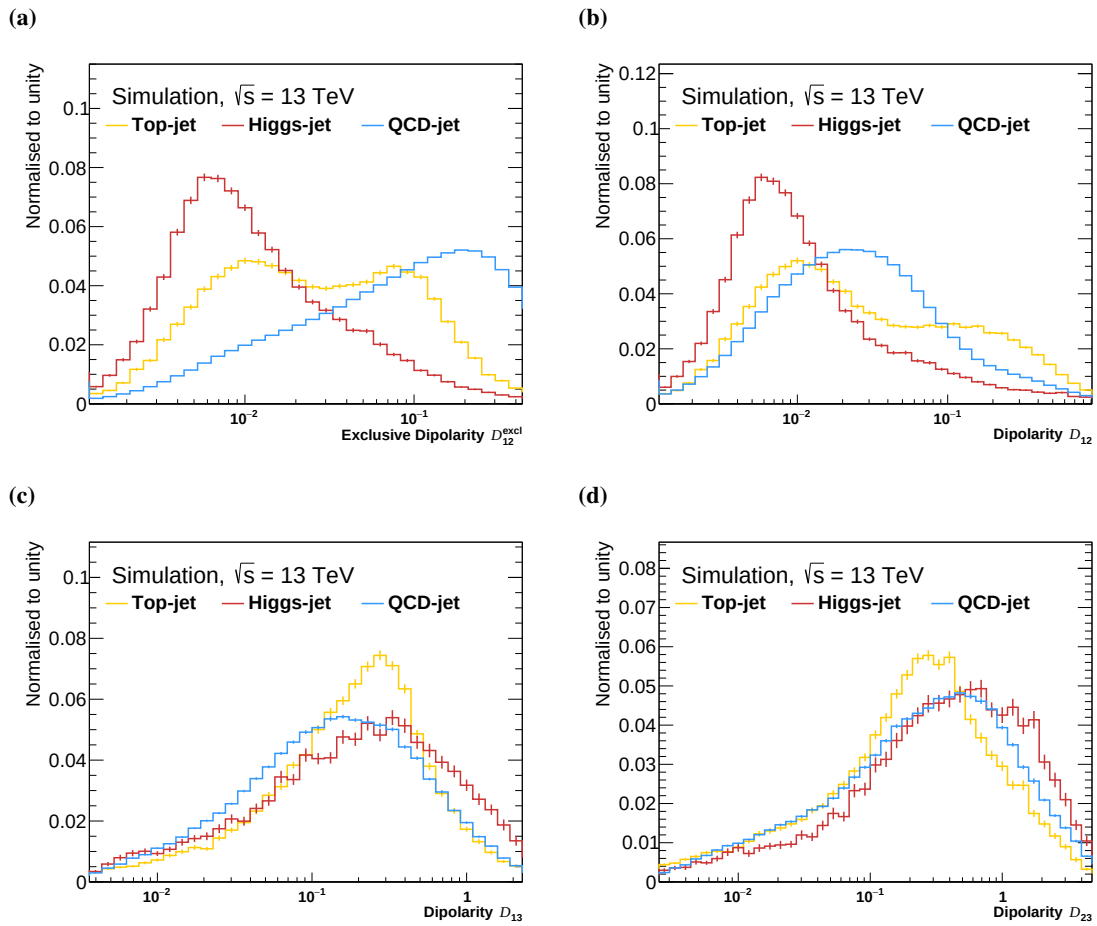

Figure 3.18: Dipolarity distributions of Higgs-, top- and QCD jets using (a) the subjets selected by the exclusive-k_t algorithm or (b-d) the three leading k_t clustered subjets obtained with the k_t-algorithm with $p_{\mathrm{T}}^{\mathrm{subjet}} > 5$ GeV.

Cluster sequence: A set of sub-structure variables is defined based on a reclustering sequence of large-R jets, based on the is k_t-algorithm. The sequenced clustering algorithms, such as the (anti-)k_t-algorithm, start with the jet constituents that are closest in distance (c.f. Section 2.4.5). The distance measure, k_t^{ij} between two constituents i and j, employed in the k_t-algorithm (c.f. Section 1.2.2) is closely related to the actual distance in momentum space within the decay. In perturbative QCD calculation, terms describing such partons that are close in momentum space are divergent, i.e. these partons have a high probability to be both the result from the same quark or gluon splitting. Thus, jet constituents that are close to each other in momentum space are likely to result from partons that have split in a late stage of the showering. For this reason, the k_t-algorithm provides an approximate history of the shower building process.

One substructure variable exploiting this shower building history is the so-called splitting scale $\sqrt{d_{ij}}$ [128, 141]. It is the k_t-algorithm's distance measure in the clustering step from $j \rightarrow i$

constituents (c.f. Section 2.4.5). E.g., $\sqrt{d_{12}}$ is the distance of the 2 subjets that are combined in the final clustering step to 1 jet. This $\sqrt{d_{12}}$ variable is expected to receive larger values for a 2-prong jet than for a QCD jet. This is shown in Fig. 3.19(a).

The top jet distribution of the splitting scale in the second last clustering step ($\sqrt{d_{23}}$) has an even larger tail resulting from fully captured 3-body top quark decays.

These described substructure variables are influenced by the total transverse momentum of the jet. A further less, p_{T}^{J}-dependent variable based on this clustering sequence is,

$$Z_{cut}^{ij} = \frac{\min(p_{\mathrm{T}}^{(1)}, p_{\mathrm{T}}^{(2)})}{p_{\mathrm{T}}^{(1+2)}}, \tag{3.19}$$

where $p_{\mathrm{T}}^{(1)}$ and $p_{\mathrm{T}}^{(2)}$ are the momenta of the both subjets that are combined in the $j \rightarrow i$-th clustering step, resulting in the combined subjet transverse momentum $p_{\mathrm{T}}^{(1+2)}$. Z_{cut}^{ij} measures the asymmetry of the cluster step. The variable tends to have a value of 0.5 for two-body decays with equally massive decay products. The distributions of the Z_{cut}^{12} variable is shown in Fig. 3.19(a) for the last clustering step. The distributions of splitting scales ($\sqrt{d_{ij}}$) and Z_{cut}^{ij} variables from earlier clustering steps can be found in Appendix A.5.

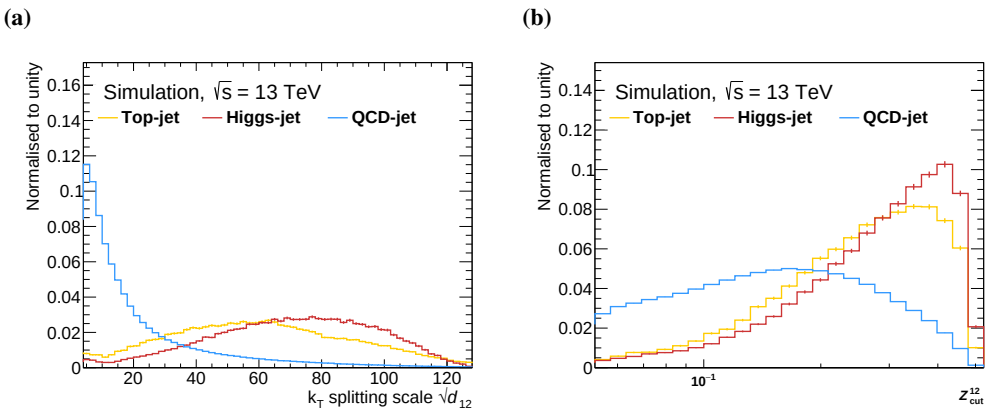

Figure 3.19: Distribution of the (a) splitting scale $\sqrt{d_{12}}$ and (b) the asymmetry Z_{cut}^{12} variables for the Higgs jet signal and top jet and QCD jet backgrounds.

The mass drop variable [127] is defined as

$$\mu_{12} = \frac{m_1 m_2}{m_J}, \tag{3.20}$$

$$\tag{3.21}$$

where m_1 and m_2 are the masses of the parent subjets in the last clustering step and m_J is the large-R jet mass. This variable is expected to have small values for the two-body decay of a Higgs boson into much lighter b-hadrons, as shown in Fig. 3.20(a), since the reconstructed large-R jet mass mainly results from a large angular separation between the low-mass subjets. The angular separation

between these low-mass subjets is described by the $k_t\Delta R$ variable [129], whose distributions are shown in Fig. 3.20(b). $k_t\Delta R$ provides very good discrimination power against QCD jet backgrounds and moderately good discrimination against 3-prong top jets.

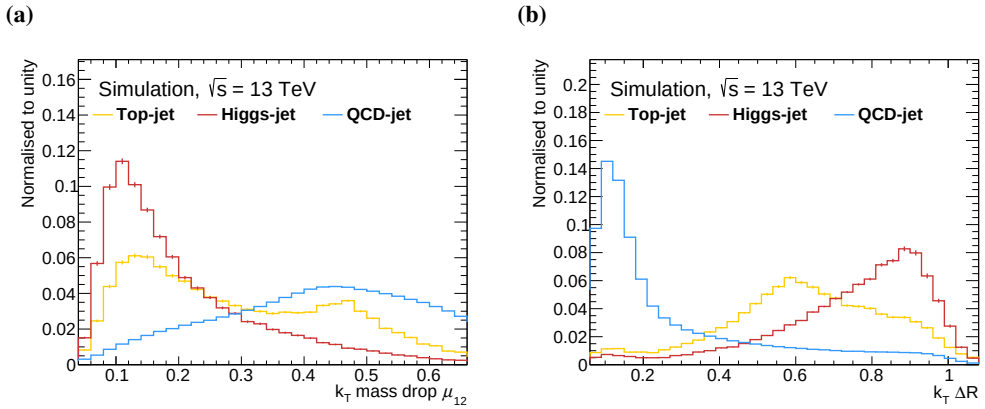

Figure 3.20: Distribution of the (a) mass drop μ_{12} and (b) angular separation $k_t\Delta R$ variables for the Higgs jet signal and top jet and QCD jet backgrounds.

Substructure in the rest frame of the large-R jet: Several variables are defined in the center-of-mass rest frame of the large-R jet, with four-momentum denoted with p^μ. In such a rest frame, Higgs jets have a back-to-back topology formed by two similarly collimated jets. In contrast, top jets containing all top quark decay products are following a three-body decay pattern. QCD jets acquire their masses through off-shell gluon or quark radiation. Their constituents are rather isotropically distributed. The degree of isotropy within a large-R jet can be quantified by observables such as thrust, sphericity, aplanarity, and the so-called Fox-Wolfram moments.

In the center-of-mass frame, the thrust axis, $\hat{T}$, is defined as the direction that maximizes the longitudinal momentum components of the large-R jet constituents [144]. The thrust major and minor moments, T_{maj} and T_{min}, are then defined as,

$$T_{maj} = \frac{\sum_i |\hat{T} \cdot \vec{p}^{(i)}|}{\vec{p}^{(i)}} \text{and}$$
$$T_{min} = \frac{\sum_i |\vec{p}^{(i)} \times \hat{T}|}{\vec{p}^{(i)}},$$

with $\vec{p}^{(i)}$ being the momenta of the large-R jet constituents in the center-of-mass frame. T_{maj} (T_{min}) can adapt values between 0.5 for isotropic distributions and 1 (0) for two-body decays of high resonance masses. Fig. 3.21 shows the corresponding thrust distributions for the three studied large-R jet samples.

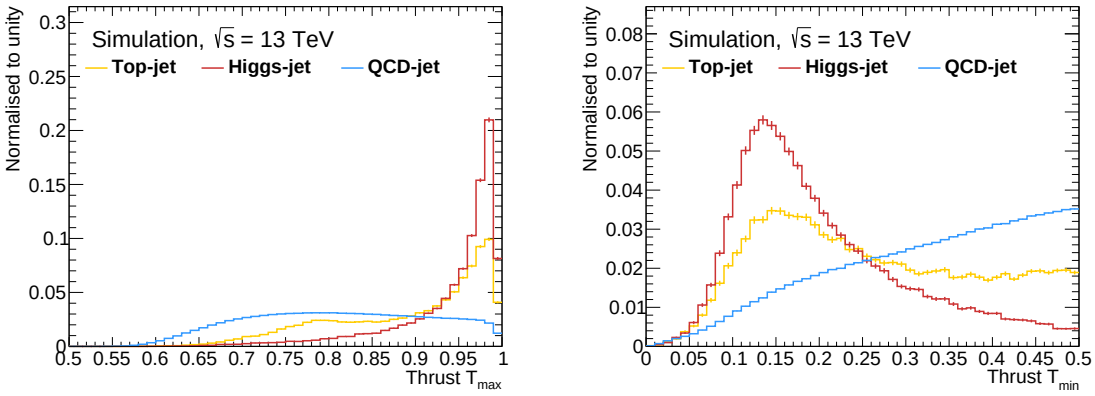

Figure 3.21: Distribution of the thrust moments T_{maj} and T_{min} for the Higgs jet signal and top jet and QCD jet backgrounds.

The sphericity and aplanarity variables [139] are defined via the sphericity tensor,

$$(\overleftrightarrow{\mathcal{S}})^{\alpha,\beta} = \frac{\sum_i p^{\alpha}_{(j)} p^{\beta}_{(i)}}{\sum_i |\vec{p}_{(i)}|^2},$$

where α and β denote the spacial components of momentum $p^{\mu}_{(i)}$ of the i-$^{\text{th}}$ large-R jet constituent, in the large-R jet rest frame. The sphericity is then defined as,

$$\mathcal{S} = \frac{3}{2}(\lambda_2 + \lambda_3),$$

with λ_2 and λ_3 being the two smaller of the three eigenvalues of the tensor $\overleftrightarrow{\mathcal{S}}$. The aplanarity is defined as,

$$A = \frac{2\lambda_3}{2},$$

quantifying the smallest of the three principal axes of the sphericity tensor. Both, the sphericity and the aplanarity tend to have small values $\mathcal{S}, A \to 0$ for two back-to-back subjets within the large-jet, and $\mathcal{S} = 1$ and $A = 0.5$ for fully isotropic distributions. The sphericity and aplanarity distribution for signal and background large-R jets is shown in Fig. 3.22.

The class of the Fox-Wolfram moments [134] is defined by,

$$H_l = \sum_{i,j \in J} \frac{|\vec{p}_i||\vec{p}_j|}{E^2} P_l(\cos\theta_{ij}), \tag{3.22}$$

using the Legendre polynomials, $P_l(\cos(\theta_{ij}))$, where θ_{ij} is the angular distance between two subjets i and j, while E is the total energy of the large-R jet in the center-of-mass frame. The most powerful Fox-Wolfram moments for the discrimination between the Higgs jets and the top jet and QCD jet backgrounds are the even moments $\mathcal{F}_2$ and $\mathcal{F}_4$ whose distributions are shown in Fig. 3.23. The ratios

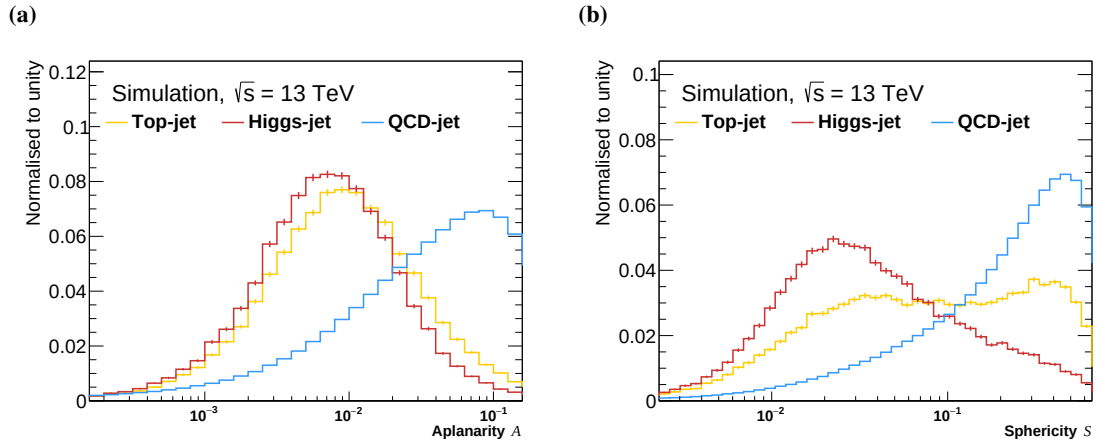

Figure 3.22: Distribution of the sphericity and aplanarity for the Higgs jet signal and top jet and QCD jet backgrounds.

of the Fox-Wolfram moments are also considered, removing the momentum dependence.

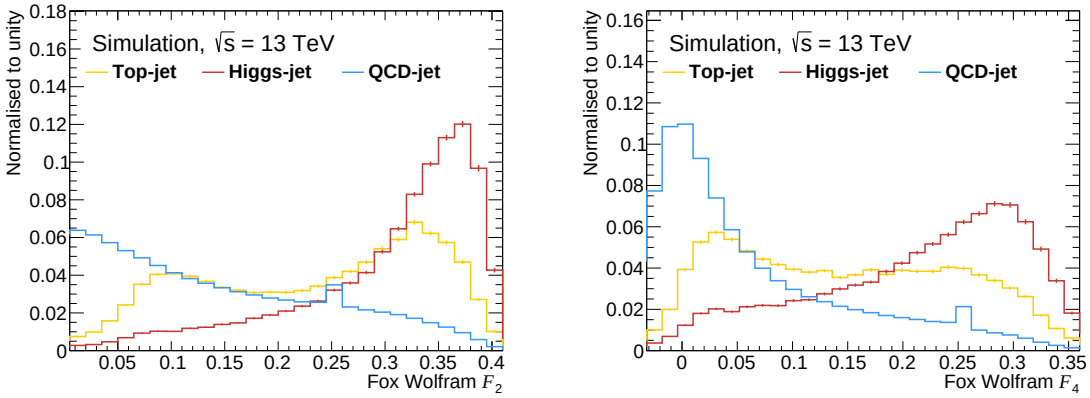

Figure 3.23: Distribution of the Fox-Wolfram moments (left) $\mathcal{F}_2$ and (right) $\mathcal{F}_4$ for the Higgs jet signal and top jet and QCD jet backgrounds.

Planar flow: The planar flow variable $\mathcal{P}$ quantifies to which extent the jet energy is evenly distributed over the entire jet area [126, 138]. This variable is defined via the determinant of a 2×2-matrix $\overleftrightarrow{I}_E$,

$$\mathcal{P} = 4 \cdot \frac{\det(I_E)}{\mathrm{Tr}(I_E)^2}, \tag{3.23}$$

$$\text{where } (\overleftrightarrow{I}_E)kl = \frac{1}{M} \sum_{i \in J} \frac{1}{E^{(i)}} p_k^{(i)} p_l^{(i)}, \tag{3.24}$$

with M being a normalization factor, $E^{(i)}$ and $p_\mu^{(i)}$ are four-momentum and energy of the i-th jet constituent, respectively. Planar flow values close to zero correspond to a linear energy deposition, as expected for the 2-prong decays, while a fully isotropic distribution results in a planar flow value of 1. In accordance with this, Fig. 3.24(a) shows the planar flow distribution for the Higgs jets peaking close to 0 and the distribution of QCD jets peaking at 1.

Angularity: The angularity variable a_3

$$a_3 = \frac{1}{m_J} \sum_{j \in J} E^{(j)} \sin^{-2}(\theta^{(j)}) \cdot (1 - \cos(\theta_i))^3 \,.$$

is sensitive to the symmetry of the energy flow [125, 126, 140]. Here, $\theta^{(j)}$ is the angle between the jet constituent and the jet axis, while $E^{(j)}$ is the energy of that constituent. Angularity distributions for large-R jets with kinematic properties of a two-body decay and a mass M should peak at the minimum,

$$\left(\frac{M}{2p_\mathrm{T}}\right)^{1-a} \approx 10^{-2},$$

for average large-R jet p_T close to 250 GeV, due to the reweighting, as confirmed in Fig. 3.24(b).

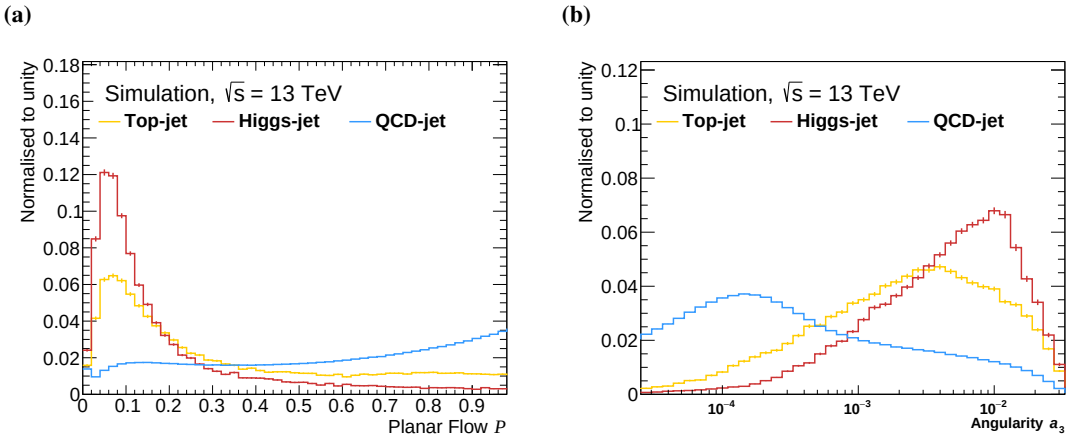

Figure 3.24: Distribution of (a) the planar flow $\mathcal{P}$ and (b) angularity a_3 for the Higgs jet signal and top jet and QCD jet backgrounds.

In the following, the potential improvements of the Higgs tagger performance by means of additional requirements on the introduced variables will be studied.

3.4.2 Performance of the substructure-based Higgs tagger

The Higgs tagging based on the large-R jet substructure is not expected to provide better background discrimination properties than the track jet b-tagging approach using the unique properties of the two b-quarks in the decay. In the first part of this sub-section the discriminating power of substructure variables will compared to the Higgs tagging techniques introduced in Sections 3.2 and 3.3 it will be shown that jet substructure cannot be used instead but only combined with the other two tagging methods. In a second part, a combination of b-tagging-based and substructure-based Higgs tagging approach is studied and the corresponding expected performance is presented.

The comparisons of the b-tagging, mass-, and substructure-based Higgs tagging is given by means of the corresponding ROC curves in Figs. 3.25 and 3.26. The quantity $\sigma \approx s/\sqrt{b}$ (c.f. Eqs. (3.3) and (3.4)) is approximately proportional to the signal search sensitivity, with s the number of signal events and b the number of background events. It provides a scalar measure of the discriminating power. Selection requirements that provide signal efficiency and background rejection that result in an equal σ are may be considered as equally powerful. As a guideline in the plots shown in this chapter, all $\varepsilon_{\text{signal}} - \varepsilon_{\text{bkg}}$ value pairs resulting in an σ equal to the baseline selection, i.e. $\Delta\sigma = 0$ are denoted by a dashed line. A second line denotes $\varepsilon_{\text{signal}} - \varepsilon_{\text{bkg}}$ value pairs resulting in the maximal possible sensitivity by either a b-tagging or a JSS-based tagger, i.e. $s/\sqrt{b} = \Delta\sigma^{\text{max}}$. Figs. 3.25 and 3.26 show that the best $\Delta\sigma$ can be achieved by symmetric double b-tagging.

This can be compared to the rejection power against QCD jets utilizing the most effective substructure variables, the k_t-splitting scale $\sqrt{d_{12}}$ (see Fig. 3.25(a)). For the same Higgs tagging efficiencies double- (single-) b-tagging provides more than a factor 10 (4) better rejection than the substructure discriminant , as can be seen in Fig. 3.25(b).

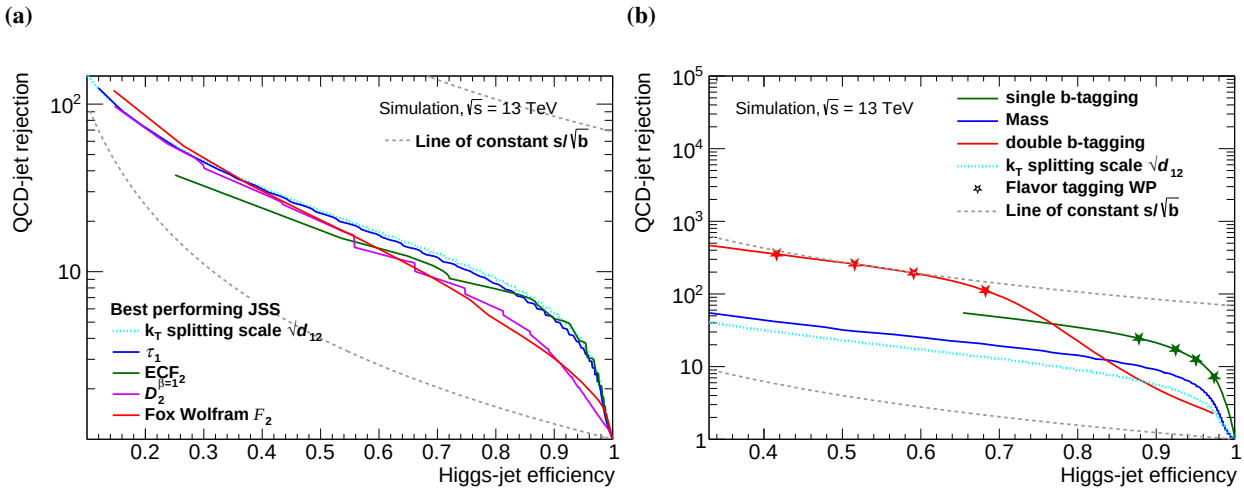

Figure 3.25: ROC curves comparing (a) the performance of different jet substructure (JSS) variables based Higgs tagger against the QCD jet backgrounds and (b) the performance of the best of these JSS-based taggers to the track jet b-tagging and mass-based Higgs tagging.

For the rejection of the top jet backgrounds, ECF_3 is the best discriminating substructure variable (see Fig. 3.26(a)). Still, as seen in Fig. 3.26(b) this variable provides a worse background rejection than the single b-tagging. At efficiencies compatible with double b-tagging, it has down to only 5 percent of its rejection power.

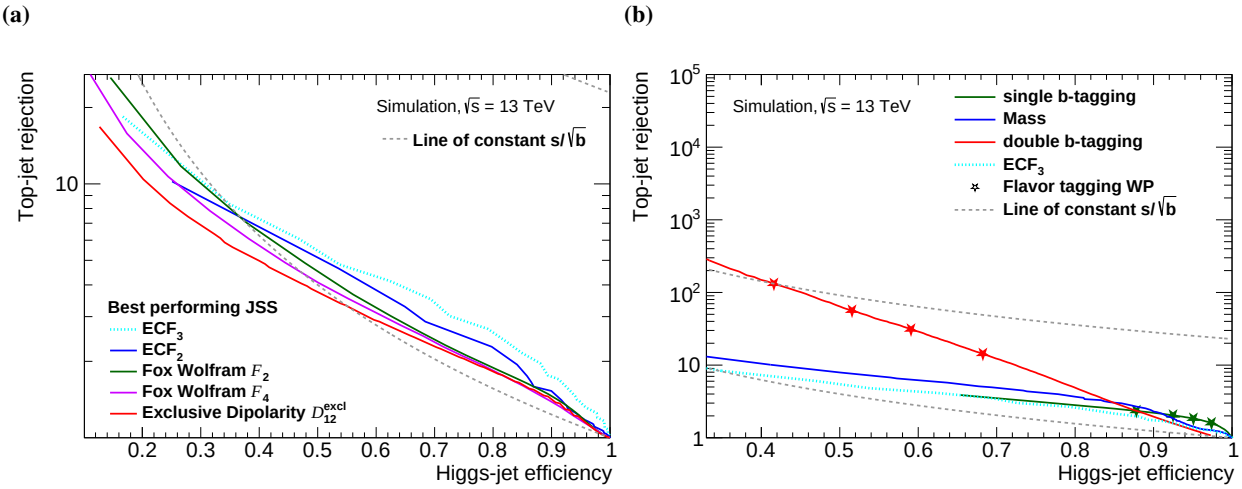

Figure 3.26: ROC curves comparing (a) the performance of different jet substructure (JSS) variables based Higgs tagger against the top jet backgrounds and (b) the performance of the best of these JSS-based taggers to the track jet b-tagging and mass-based Higgs tagging.

As a result of these studies, the substructure-based Higgs tagger can only be applied in combination with the Higgs tagger based on the b-tagging of track jets or track mass. Figs. 3.27 and 3.28 show the ROC curves for the Higgs taggers in which the JSS variables are applied together with the track jet b-tagging requirements. In all cases here, a b-tagging working point with 70% b-tagging efficiency is used for the b-tagging based Higgs tagger shown. Corresponding ROC curves with a looser b-tagging WP with 85% b-tagging efficiency can be found in Appendix A.3.

The performance of the Higgs tagger with single b-tagging (Fig. 3.27) can best be further improved in case of the top jet rejection by applying an additional b-tagging requirement to the yet untagged second track jet (asymmetric b-tagging). This comes, however, at the cost of low Higgs tagger efficiencies. To preserve a high signal efficiency, the optimal mass window requirement which maximizes $\Delta\sigma$ from Eq. (3.4) is a better choice as an additional requirement. The mass variable mass window derived in Section 3.3 is optimized independent on the background but only on a minimal window size to achieve a given signal efficiency. A window with a Higgs jet efficiency of 73% turns out to result in the best sensitivity improvement of $\Delta\sigma^{\text{max}} = 1.85$, in case of a pure top jet background. In case of a pure QCD jet background, the corresponding choice is a window with an Higgs jet tagging efficiency of 64%, that corresponds to a maximal signal sensitivity improvement $\Delta\sigma^{\text{max}} = 10$.

Furthermore, the performance of the Higgs tagger with double b-tagging is shown in Fig. 3.28. In order to reject the top jet background, all JSS variable provide very similar rejection rates. To improve the rejection of QCD jets, the best performing JSS variable at high Higgs tagging efficiencies is the

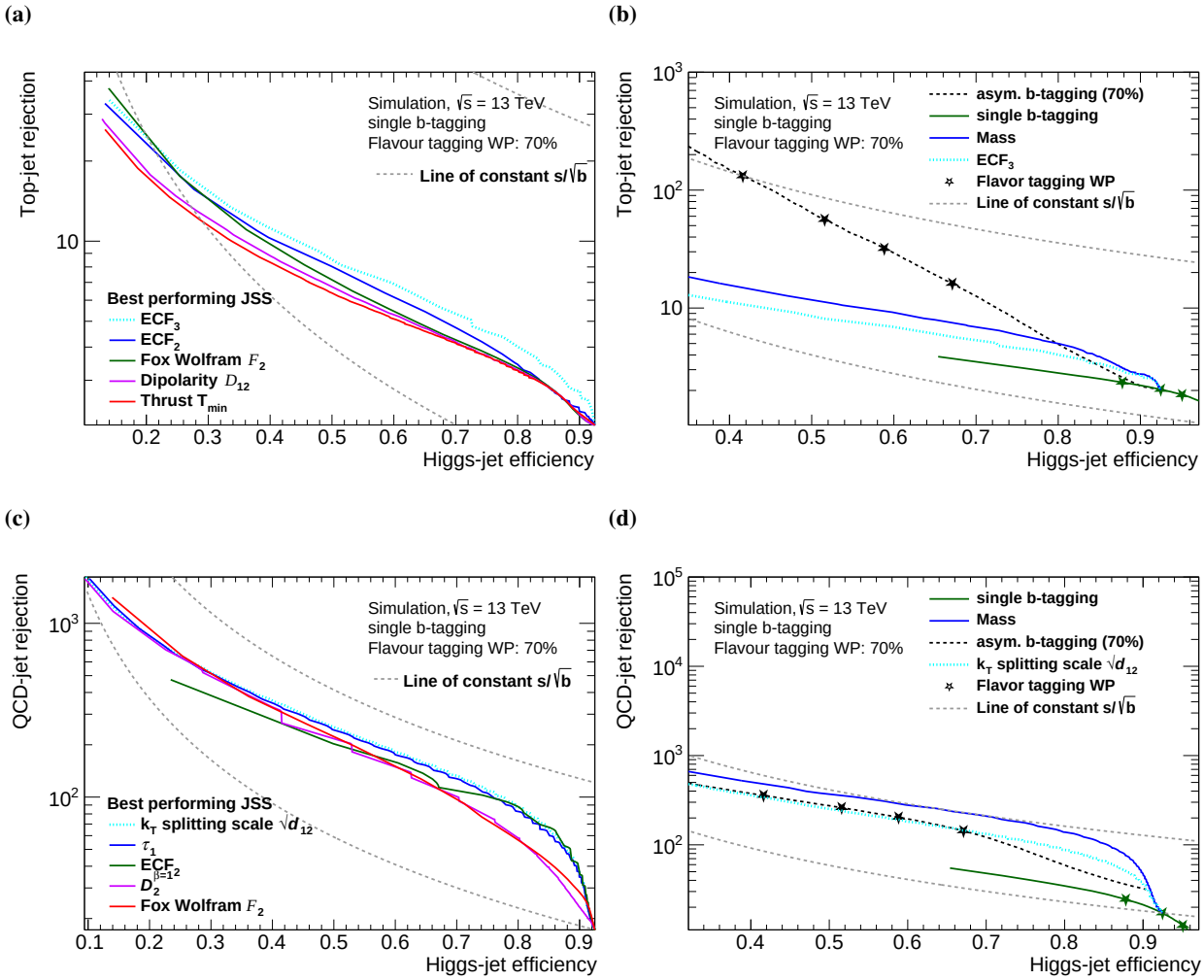

Figure 3.27: ROC curves comparing the performance of different Higgs taggers in which the jet substructure (JSS) variables (including the jet mass) are applied in addition to the single b-tagging requirement with the working point at 70% b-tagging efficiency; (top) against top jets; (bottom) against QCD jets.

angular separation variable $k_t\Delta R$. At low Higgs tagging efficiencies the best discriminating JSS variable is the 1-subjettiness variable τ_1. For both types of background, an optimized mass selection provides the best achievable σ.

Table 3.2 shows the most powerful JSS variables which are applied on top of a given track jet b-tagging option. Their discrimination power is comparable to the mass window selection requirements. The corresponding correlation coefficients between these most powerful observables are shown for top jets in Fig. 3.29(a). The ECF_2 and ECF_3 variables are strongly correlated with the mass distribution and therefore do not provide additional discrimination power. In contrast, the variables τ_1, dipolarity, and the second Fox-Wolfram moment are less correlated to the mass distribution, with linear correlation coefficients between 0.17 and 0.41, and may therefore improve the Higgs tagging performance. These

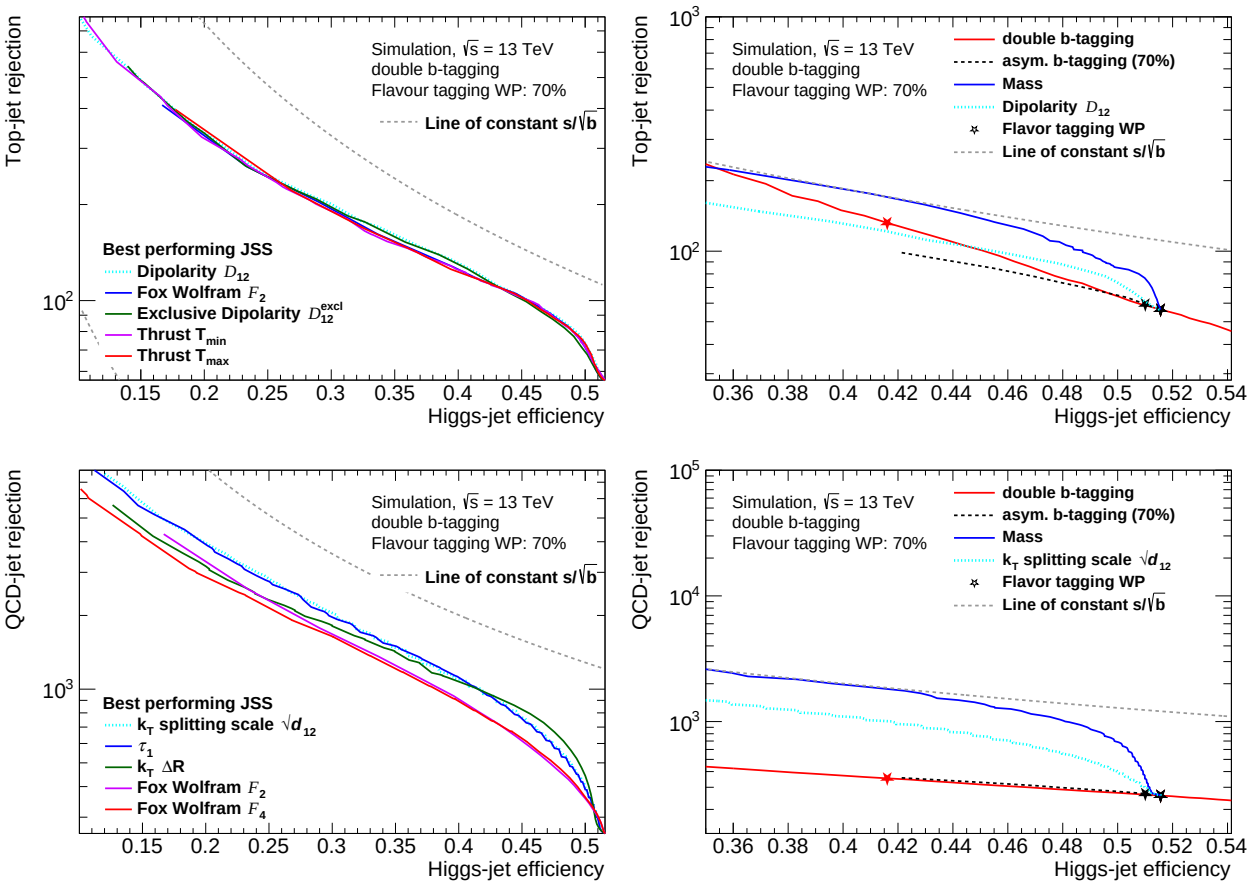

Figure 3.28: ROC curves comparing the performance of different Higgs taggers in which the jet substructure (JSS) variables (including the jet mass) are applied in addition to the double b-tagging requirement with the working point at 70% b-tagging efficiency; (top) against top jets; (bottom) against QCD jets.

additional observables are all closely correlated to each other, such that no major improvement can be expected from using the combination instead of just one of these variables.

Similar correlation study for the QCD jet background is shown in Fig. 3.29(b). To reject QCD jets after an already imposed single b-tagging requirement is best improved by the mass window discriminator, which improves the relative sensitivity by a factor of 10 for a mass window with 64% signal efficiency. Other substructure variables can improve the signal sensitivity σ within a QCD jet background by up to a factor of 8. The corresponding background rejection improvement is comparable to the additional rejection that can be achieved by imposing the b-tagging requirement to the second track jet within the large-R jet (asymmetric b-tagging). In Fig. 3.27(d) it can be seen that the ROC curve of the splitting scale observable $\sqrt{d_{12}}$ is close to the one for the asymmetric b-tagging and significantly performs better at higher signal efficiency. The QCD jet rejection improvement by other substructure variables after b-tagging is summarized in Table 3.2. The variables D_2 and $\mathcal{F}_2$ only provide moderate discrimination power but are less correlated to the large-R jet mass (see Fig. 3.29(b)).

Table 3.2: Ranking of the best-performing discriminating variables. The requirements on the variables are optimized after applying one of the three b-tagging scenarios. The corresponding resulting optimal relative sensitivity $\Delta\sigma^{\max}$and the Higgs tagging scenarios are shown as well. In case of an additional b-tagging, the corresponding improvements is obtained by choosing a tighter b-tagging working point.

single b-tagging (70%)					
top jet			QCD jet		
asym. b-tagging	$\Delta\sigma = 4.78$	$\varepsilon_S = 0.42$	Mass	$\Delta\sigma = 10.18$	$\varepsilon_S = 0.64$
Mass	$\Delta\sigma = 1.85$	$\varepsilon_S = 0.73$	asym b-tagging	$\Delta\sigma = 8.39$	$\varepsilon_S = 0.59$
ECF_3	$\Delta\sigma = 1.63$	$\varepsilon_S = 0.72$	k_T splitting scale $\sqrt{d_{12}}$	$\Delta\sigma = 8.16$	$\varepsilon_S = 0.67$
ECF_2	$\Delta\sigma = 1.52$	$\varepsilon_S = 0.70$	τ_1	$\Delta\sigma = 8.04$	$\varepsilon_S = 0.62$
Fox Wolfram $\mathcal{F}_2$	$\Delta\sigma = 1.46$	$\varepsilon_S = 0.79$	ECF_2	$\Delta\sigma = 7.76$	$\varepsilon_S = 0.72$
Dipolarity $\mathcal{D}_{12}$	$\Delta\sigma = 1.45$	$\varepsilon_S = 0.77$	$D_2^{\beta=1}$	$\Delta\sigma = 7.52$	$\varepsilon_S = 0.53$
Thrust T_{min}	$\Delta\sigma = 1.45$	$\varepsilon_S = 0.77$	Fox Wolfram $\mathcal{F}_2$	$\Delta\sigma = 7.48$	$\varepsilon_S = 0.53$
			ECF_3	$\Delta\sigma = 7.14$	$\varepsilon_S = 0.75$
double b-tagging (70%)					
top jet			QCD jet		
Mass	$\Delta\sigma = 5.44$	$\varepsilon_S = 0.41$	Mass	$\Delta\sigma = 17.92$	$\varepsilon_S = 0.35$
double b-tagging	$\Delta\sigma = 4.78$	$\varepsilon_S = 0.42$	k_T splitting scale $\sqrt{d_{12}}$	$\Delta\sigma = 13.60$	$\varepsilon_S = 0.30$
Dipolarity $\mathcal{D}_{12}$	$\Delta\sigma = 4.59$	$\varepsilon_S = 0.41$	τ_1	$\Delta\sigma = 13.57$	$\varepsilon_S = 0.35$
Fox Wolfram $\mathcal{F}_2$	$\Delta\sigma = 4.57$	$\varepsilon_S = 0.45$	k_T ΔR	$\Delta\sigma = 13.22$	$\varepsilon_S = 0.35$
Exclusive Dipolarity $\mathcal{D}_{12}^{excl}$	$\Delta\sigma = 4.57$	$\varepsilon_S = 0.41$	Fox Wolfram $\mathcal{F}_2$	$\Delta\sigma = 12.41$	$\varepsilon_S = 0.34$
Thrust T_{min}	$\Delta\sigma = 4.57$	$\varepsilon_S = 0.46$	Fox Wolfram $\mathcal{F}_4$	$\Delta\sigma = 12.21$	$\varepsilon_S = 0.33$
Thrust T_{max}	$\Delta\sigma = 4.56$	$\varepsilon_S = 0.44$	τ_1^{wta}	$\Delta\sigma = 12.09$	$\varepsilon_S = 0.33$
Sphericity $\mathcal{S}$	$\Delta\sigma = 4.56$	$\varepsilon_S = 0.45$	$D_2^{\beta=1}$	$\Delta\sigma = 11.88$	$\varepsilon_S = 0.33$
exclusive 1-b-tag (70%)					
top jet			QCD jet		
Mass	$\Delta\sigma = 1.32$	$\varepsilon_S = 0.76$	Mass	$\Delta\sigma = 1.86$	$\varepsilon_S = 0.71$
asym. b-tagging	$\Delta\sigma = 1.28$	$\varepsilon_S = 0.40$	k_T splitting scale $\sqrt{d_{12}}$	$\Delta\sigma = 1.51$	$\varepsilon_S = 0.68$
ECF_3	$\Delta\sigma = 1.20$	$\varepsilon_S = 0.77$	τ_1	$\Delta\sigma = 1.50$	$\varepsilon_S = 0.68$
ECF_2	$\Delta\sigma = 1.12$	$\varepsilon_S = 0.75$	ECF_2	$\Delta\sigma = 1.49$	$\varepsilon_S = 0.76$
k_T splitting scale $\sqrt{d_{23}}$	$\Delta\sigma = 1.07$	$\varepsilon_S = 0.96$	ECF_3	$\Delta\sigma = 1.39$	$\varepsilon_S = 0.81$
Fox Wolfram $\mathcal{F}_3$	$\Delta\sigma = 1.06$	$\varepsilon_S = 0.93$	k_T ΔR	$\Delta\sigma = 1.39$	$\varepsilon_S = 0.77$
τ_3, 2	$\Delta\sigma = 1.06$	$\varepsilon_S = 0.94$	τ_1^{wta}	$\Delta\sigma = 1.34$	$\varepsilon_S = 0.70$
τ_{32}^{wta}	$\Delta\sigma = 1.05$	$\varepsilon_S = 0.93$	Fox Wolfram $\mathcal{F}_2$	$\Delta\sigma = 1.32$	$\varepsilon_S = 0.61$

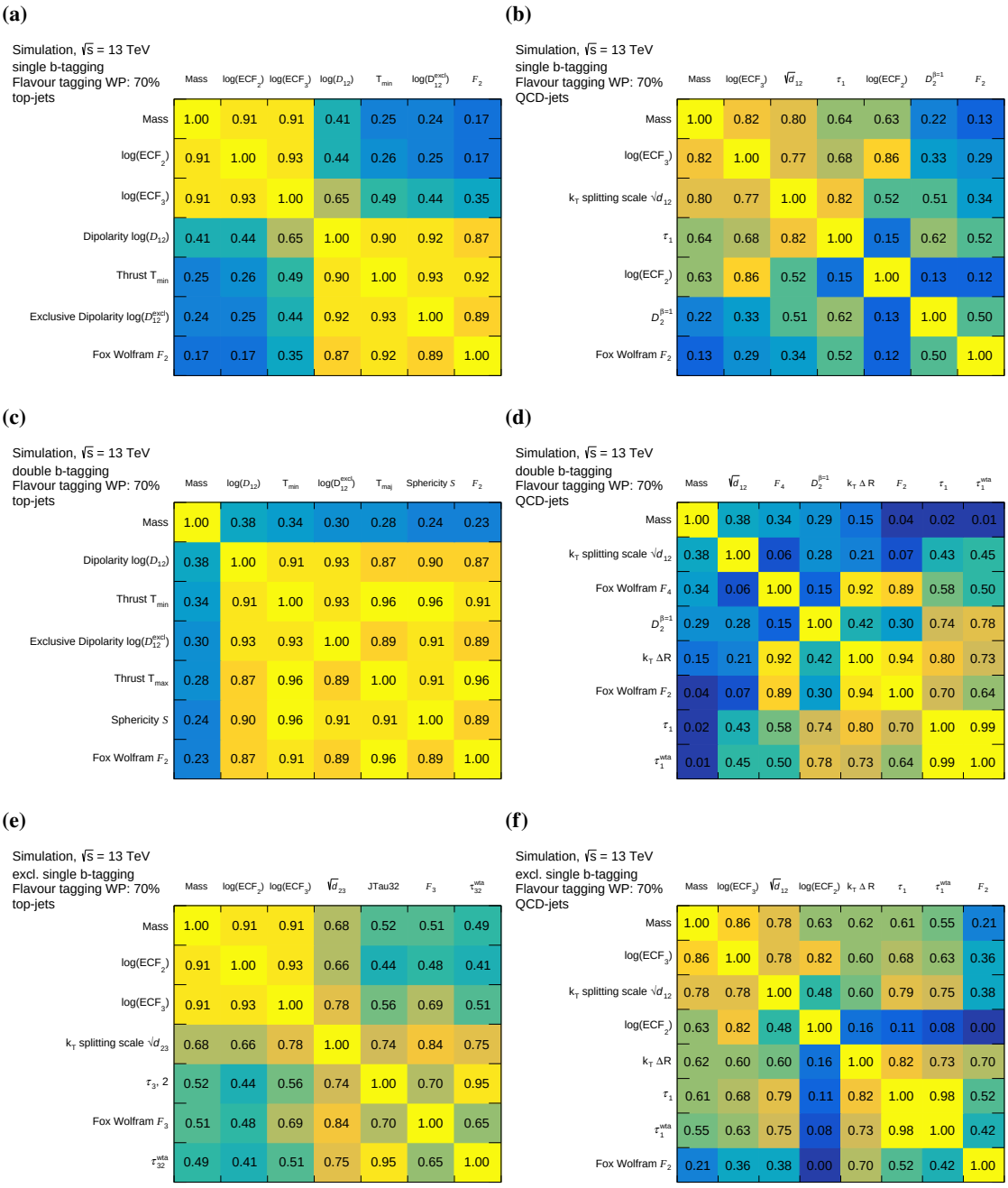

Figure 3.29: Pearson correlation coefficient between the best performing substructure observables in case of the (left) top jets and (right) QCD jets after a applying one of the three *b*-tagging options: (top row) single *b*-tagging, (middle row) double *b*-tagging or (bottom row) the exclusive 1 *b*-tag selection using the *b*-tagging working point with 70% *b*-tagging efficiency.

After applying double b-tagging, the best background rejection improvement is obtained from the mass window selection. By the mass thresholds corresponding to a signal efficiency of 41% (35%) for top jets (QCD jets) rejection, an additional rejection improvement by a factor 176 (2600) can be reached. Following the mass window selection, the second best discriminating variable against the top jets (QCD jets) is dipolarity $\mathcal{D}_{12}$ (splitting scale $\sqrt{d_{12}}$). Both, dipolarity and splitting scale, have a moderate correlation to the large-R jet mass, with a linear correlation coefficient of 0.38 (see Figs. 3.29(c) and 3.29(d)). Other JSS variables have slightly weaker discrimination power, with the strongest ones listed in Table 3.2.

Many physics studies with boosted hadronic Higgs boson decays in the final state do not choose between single- or double b-tagging. Instead, events that fail the double b-tagging requirement enter an exclusive single b-tag region. Such events can only profit from an additional asymmetric double b-tagging, if the required b-tagging working point of for the second track jet is below the original one with 70% b-tagging b-tagging efficiency. The ROC curves for these exclusive set of events with a single b-tag is shown in Fig. 3.30. In these events, the large-R jet mass window requirement shows the best discrimination power against both the top jet and QCD jet background. The relative sensitivity can be improved by 30% for top jets and by 80% for QCD jets.

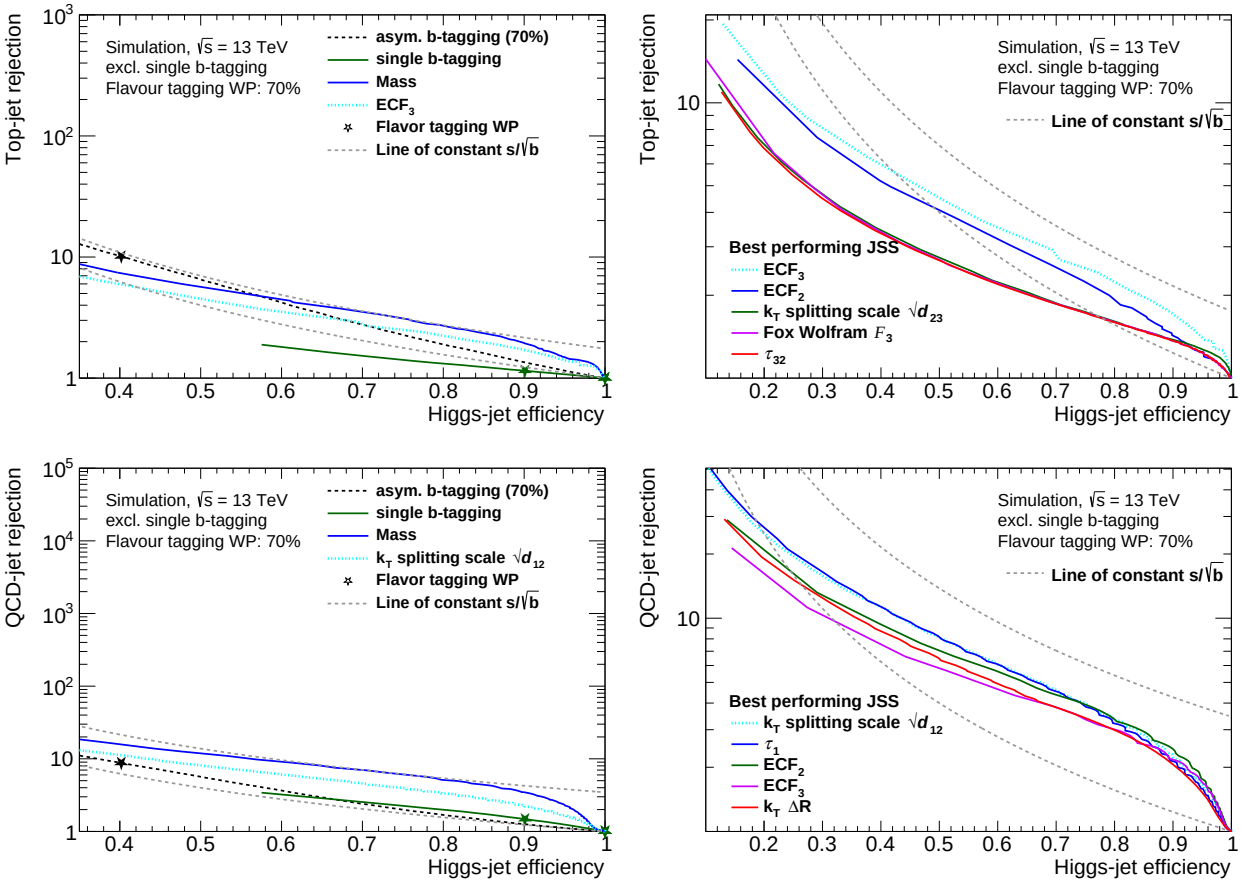

Figure 3.30: ROC curves comparing the performance of different Higgs taggers in which the jet substructure (JSS) variables (including the jet mass) are applied in addition to the exclusive single b-tagging requirement with the working point at 70% b-tagging efficiency; (top) against top jets; (bottom) against QCD jets.

3.4.3 Combined Higgs tagger performance

The Higgs tagging based on the jet mass window requirement and the b-tagging of the track jets is indispensable for an efficient identification of hadronic Higgs boson decays and is therefore applied as a baseline selection. For this selection, a loose mass window criterion as defined in Section 3.3 is applied. The baseline selection with the exclusive single b-tagging and with the of symmetric double b-tagging options are studied separately. The substructure requirements are applied on top of these baseline selections in order to study the corresponding potential Higgs tagger performance improvements.

Fig. 3.31 shows the ROC curves for different substructure requirements after applying a baseline Higgs tagger selection consisting of the mass window and exclusive single b-tagging requirements at a b-tagging working point with 70% efficiency. The best performing substructure variables are τ_{32} against the top jet backgrounds and τ_{21} against the QCD jet backgrounds. The only possibility of

further improving the relative sensitivity against the top jets and QCD jets is by imposing the b-tagging requirement on a second track jet with an b-tagging working point above the 70% signal efficiency, but at the cost of more than halfing the Higgs jet signal efficiency. The ROC curves for other substructure variables (Figs. 3.31(b) and 3.31(d) have a similar form as those for the best performing ones, showing all a deterioration of signal sensitivity for top jet backgrounds and only negligible improvement for QCD jet backgrounds.

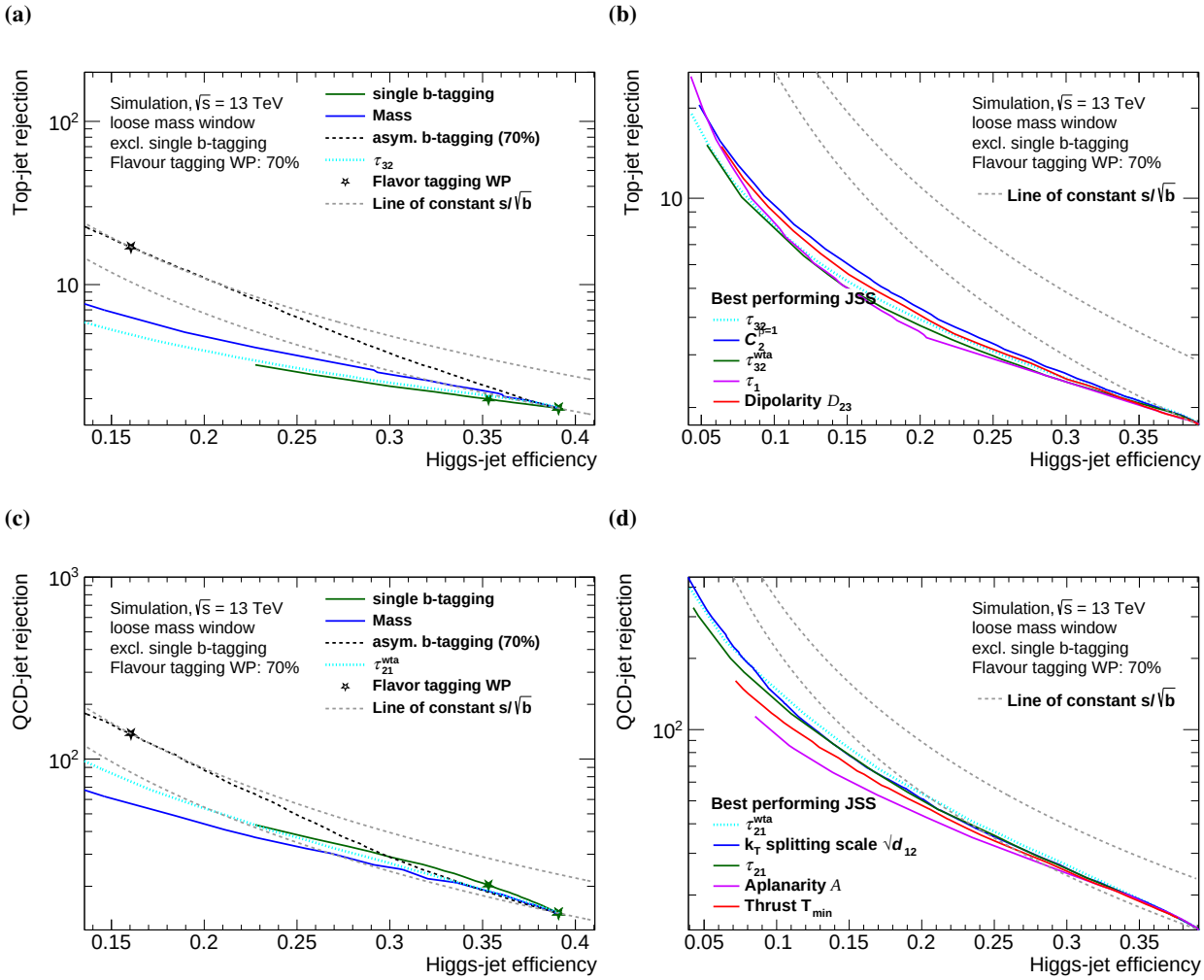

Figure 3.31: ROC curves comparing the performance of different Higgs taggers in which the jet substructure (JSS) variables (including the jet mass) are applied in addition to the exclusive single b-tagging requirement with the working point at 70% b-tagging efficiency and a loose p_{T}^{J}-dependent mass window requirement as defined in Section 3.3; (top) against top jets; (bottom) against QCD jets.

A similar comparison of ROC curves for a baseline Higgs tagging selection with the loose mass window and the double b-tagging at the 70% b-tagging working point is shown in Fig. 3.32. The best rejection performance against the top jet backgrounds is achieved by tightening the double b-tagging

requirement from an efficiency of 70% to 60%, as shown in Fig. 3.32(a). The best substructure variable to reject the top jets is the dipolarity, $\mathcal{D}_{12}$. The corresponding ROC curves for other substructure variables are shown in Fig. 3.32(b). The QCD jet background can be best further suppressed by additional its substructure requirements rather than by tighter b-tagging, as can be seen in Fig. 3.32(c). At high Higgs tagging efficiencies, substructure variables such as the fourth Fox-Wolfram moment $\mathcal{F}_4$ or the subjettiness ratio τ_{21} provide the best QCD jet background rejection improving the relative signal sensitivity σ by 10%.

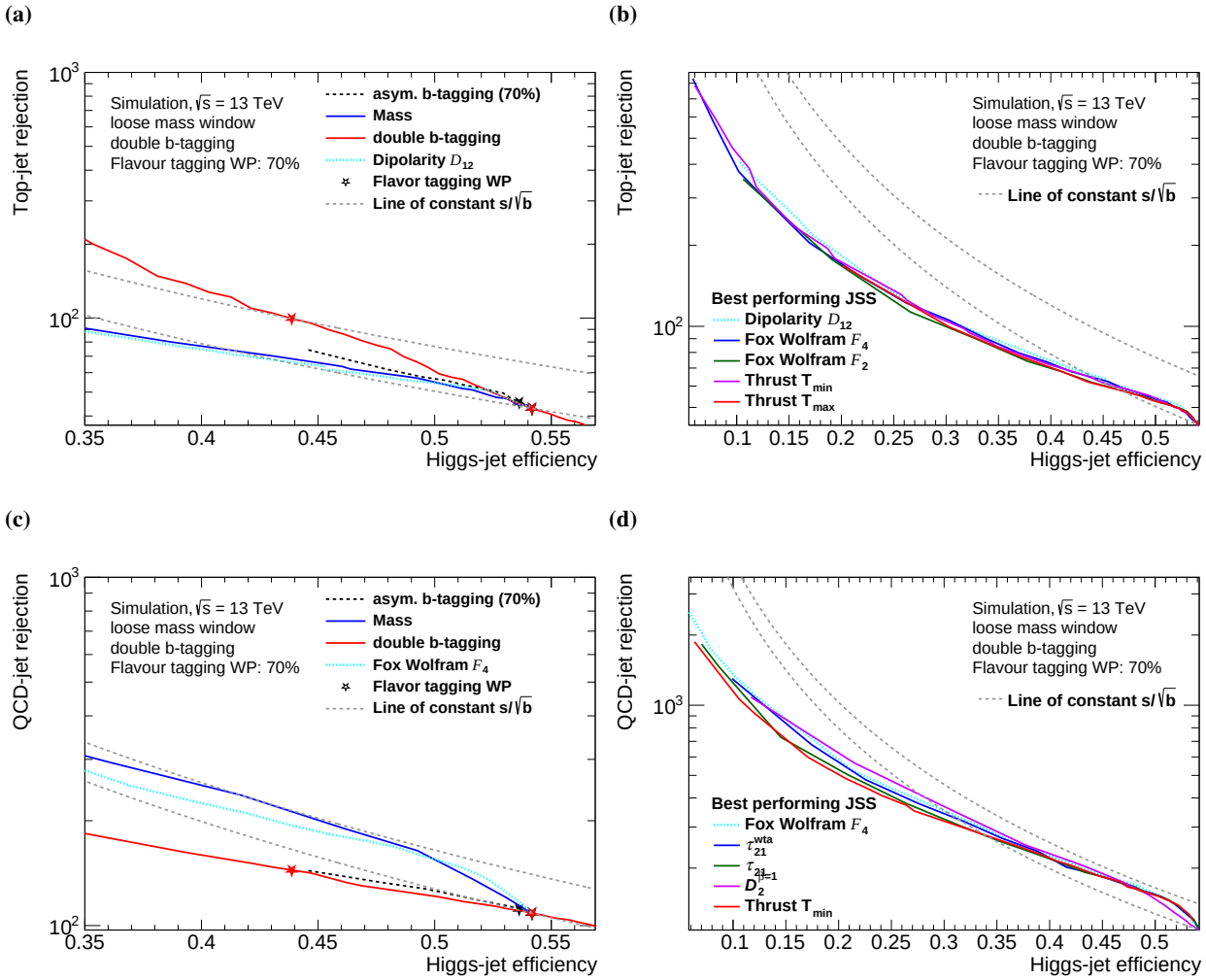

Figure 3.32: ROC curves comparing the performance of different Higgs taggers in which the jet substructure (JSS) variables (including the jet mass) are applied in addition to the double b-tagging selection requirement with the working point at 70% b-tagging efficiency and a variable loose mass window requirement as defined in Section 3.3; (top) against top jets; (bottom) against QCD jets.

A summary of the most discriminating substructure variables for different baseline Higgs tagging selections can be found in Table 3.3.

Table 3.3: Ranking of the best-performing discriminating variables. The requirements on the variables are optimized after applying a baseline selection with a loose mass window and one of the two b-tagging scenarios. The corresponding resulting optimal relative sensitivity $\Delta\sigma^{\max}$and the Higgs tagging scenarios are shown as well. (*) In case of an additional b-tagging, the corresponding improvements is obtained by choosing a tighter b-tagging working point.

single b-tagging (70%), loose mass cut					
top jet			QCD jet		
asymmetric b-tagging (*)	$\Delta\sigma = 2.44$	$\varepsilon_S = 0.56$	$D_2^{\beta=1}$	$\Delta\sigma = 4.50$	$\varepsilon_S = 0.59$
Fox Wolfram $\mathcal{F}_3$	$\Delta\sigma = 1.35$	$\varepsilon_S = 0.89$	τ_{21}^{wta}	$\Delta\sigma = 4.43$	$\varepsilon_S = 0.69$
Exclusive Dipolarity $\mathcal{D}_{12}^{excl}$	$\Delta\sigma = 1.35$	$\varepsilon_S = 0.86$	asymmetric b-tagging (*)	$\Delta\sigma = 4.41$	$\varepsilon_S = 0.70$
single b-tagging (*)	$\Delta\sigma = 1.35$	$\varepsilon_S = 0.88$	τ_{21}	$\Delta\sigma = 4.35$	$\varepsilon_S = 0.68$
$C_2^{\beta=1}$	$\Delta\sigma = 1.34$	$\varepsilon_S = 0.90$	single b-tagging (*)	$\Delta\sigma = 4.34$	$\varepsilon_S = 0.88$
Dipolarity $\mathcal{D}_{12}$	$\Delta\sigma = 1.34$	$\varepsilon_S = 0.84$	Fox Wolfram $\mathcal{F}_4$	$\Delta\sigma = 4.31$	$\varepsilon_S = 0.72$
Fox Wolfram $\mathcal{F}_2$	$\Delta\sigma = 1.34$	$\varepsilon_S = 0.89$	Thrust T_{min}	$\Delta\sigma = 4.27$	$\varepsilon_S = 0.71$
double b-tagging (*) (70%), loose mass cut					
top jet			QCD jet		
double b-tagging (*)	$\Delta\sigma = 4.78$	$\varepsilon_S = 0.42$	asymmetric b-tagging (*)	$\Delta\sigma = 13.88$	$\varepsilon_S = 0.47$
asymmetric b-tagging (*)	$\Delta\sigma = 4.23$	$\varepsilon_S = 0.47$	Fox Wolfram $\mathcal{F}_4$	$\Delta\sigma = 9.19$	$\varepsilon_S = 0.46$
Dipolarity $\mathcal{D}_{12}$	$\Delta\sigma = 4.07$	$\varepsilon_S = 0.50$	τ_{21}^{wta}	$\Delta\sigma = 9.11$	$\varepsilon_S = 0.48$
Fox Wolfram $\mathcal{F}_4$	$\Delta\sigma = 4.03$	$\varepsilon_S = 0.49$	τ_{21}	$\Delta\sigma = 9.09$	$\varepsilon_S = 0.46$
Fox Wolfram $\mathcal{F}_2$	$\Delta\sigma = 4.02$	$\varepsilon_S = 0.50$	$D_2^{\beta=1}$	$\Delta\sigma = 9.09$	$\varepsilon_S = 0.45$
Thrust T_{max}	$\Delta\sigma = 4.01$	$\varepsilon_S = 0.50$	Thrust T_{min}	$\Delta\sigma = 9.08$	$\varepsilon_S = 0.48$
Sphericity $\mathcal{S}$	$\Delta\sigma = 4.01$	$\varepsilon_S = 0.49$	Fox Wolfram $\mathcal{F}_2$	$\Delta\sigma = 9.08$	$\varepsilon_S = 0.45$

Substructure-based Higgs tagging in a 0 b-tag region: Higgs jets failing the b-tagging requirement might be recoverable by an orthogonal selection based on only substructure variables. There are about 7% of the Higgs jets in the reweighted Higgs jet signal sample with $p_{\mathrm{T}}^J > 250$ GeV. The background rejection of b-vetoed top jets and QCD jets is shown in Fig. 3.34 for the b-tagging working points of 70% and 85% b-tagging efficiency. For the large-R jets failing the tighter single b-tagging requirement of a 70% working point , the best discrimination against top jets and QCD jets can be achieved by a looser (single- or double-) b-tagging requirement than by any substructure observable. For the large-R jets failing the 85% b-tagging working point requirement, the signal is in general not distinguishable from the background contribution by means of substructure discriminants. The background rejection is only of order of $O(10)$. Thus, such a signal region would not contribute to a an overall sensitivity of a given physics analysis. For highly boosted large-R jets with $p_{\mathrm{T}} > 1200$ GeV where track jets with a fixed radius parameter R cannot be well separated, the substructure discriminants cannot improve the Higgs tagging performance either (see Fig. 3.34).

3.5 Conclusion and outlook

In this chapter, different Higgs tagging selections for the identification of boosted hadronic Higgs boson decays were presented. The studies are performed independent of the topology of a final state from a hard interaction, regarding the most frequent sources of background, i.e. hadronic top quark

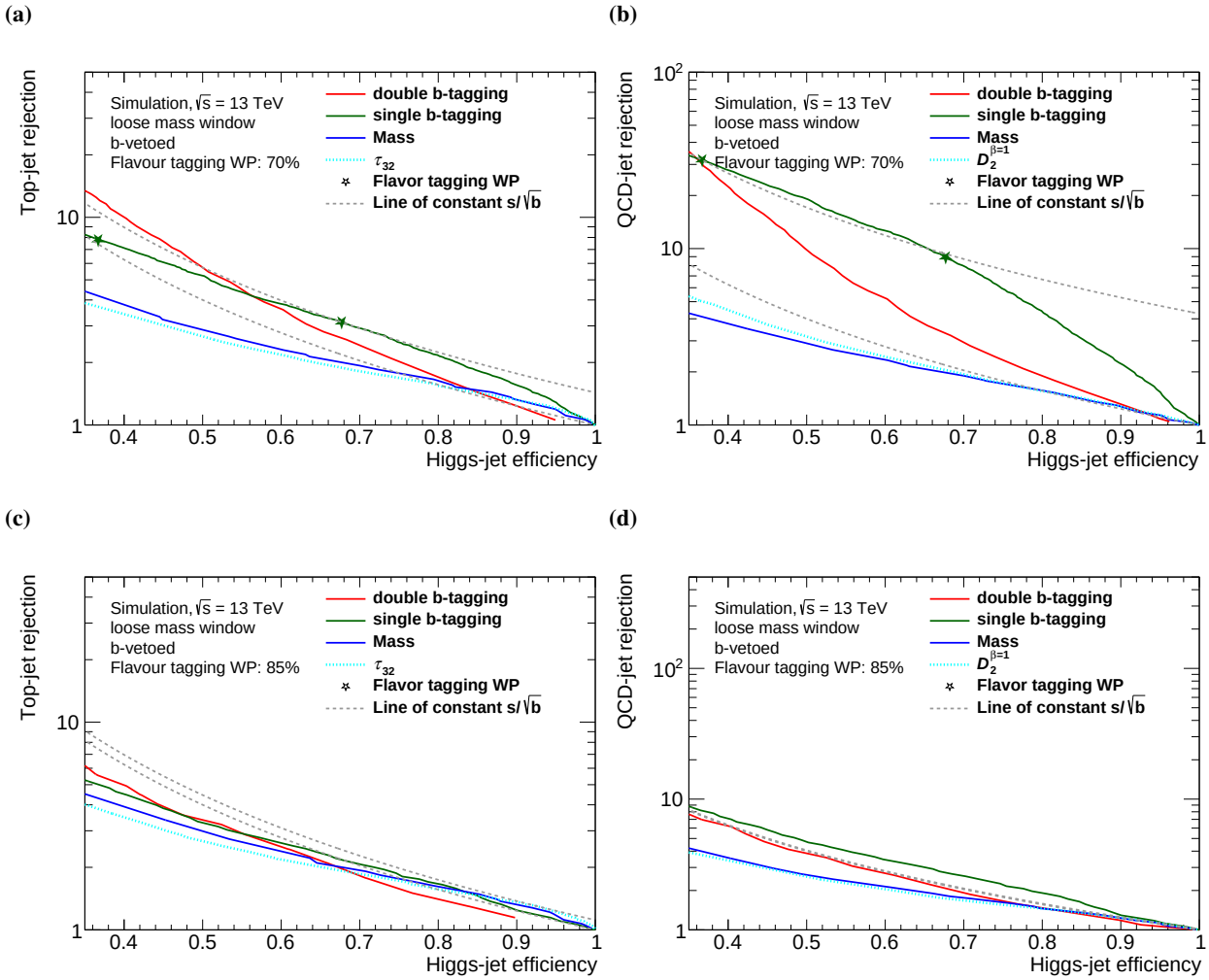

Figure 3.33: ROC curves comparing the performance of different Higgs taggers in which the jet substructure (JSS) variables (including the jet mass) are applied in addition to the b-vetoed track jet selection requirement with the working point at 70% b-tagging efficiency and a loose p_{T}^{J}-dependent mass window requirement as defined in Section 3.3; (top) against top jets; (bottom) against QCD jets.

decays and QCD radiation. As far as possible, the studies disregard the exact composition of the total background and the signal-to-background ratio, which may be different in different physics analyses.

The most powerful tool to reject the top jet and QCD jet backgrounds efficiently is via b-tagging of track jets within the candidate large-R jet. The best significance improvement of about a factor 8 against the quark or gluon irradiation compared to a Higgs-untagged p_{T}^{J}-inclusive region can be achieved by the symmetric double b-tagging at a b-tagging working point of 70% b-tagging efficiency. The single b-tagging, in contrast, preserves a high Higgs tagging signal efficiency and still improves the signal significance by a factor of 4.3 when using the optimal b-tagging selection at 60% working point. For analyses in which the the top jet background is dominant, the tightest possible double

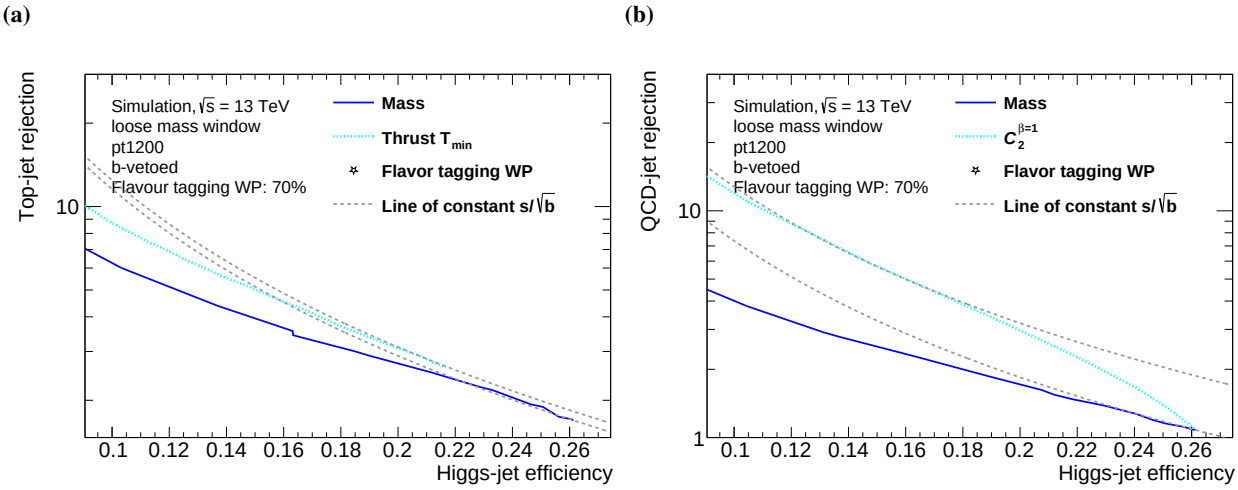

Figure 3.34: ROC curves comparing the performance of different Higgs taggers to large-R jets with $p_{\mathrm{T}}^{J} >$ 1200 GeV. The jet substructure (JSS) variables T_{min}, $C_2^{(\beta=1)}$ and the large-R jet mass are applied in addition to the b-vetoed track jet selection requirement with the working point at 70% b-tagging efficiency and a loose p_{T}^{J}-dependent mass window requirement as defined in Section 3.3; (left) against top jets; (right) against QCD jets.

b-tagged selection is recommendable. With a double b-tagging selection at the 60% working point the significance can be improved by a factor of 4.8. single b-tagging is not appropriate to reject the jets from top quark decays.

The b-tagging based Higgs jet identification significantly deteriorates at large-R jet transverse momenta larger than 1000 GeV, due to the merging track jets with a radius parameter of $R = 0.2$. This problem has been addressed in Ref. [103] by advanced track jet or sub-jet reconstruction techniques. The efficient reconstruction of two track jets, which are each matched to a particle-level b-quark, is shown in Fig. 3.35.

The efficiency to reconstruct two separate track jets using a fixed radius parameter of $R = 0.2$ drops to very low values at large-R jet $p_{\mathrm{T}}^{J} \approx 1$ TeV. New methods have therefore been developed to efficiently reconstruct distinct sub- or track jets from a highly boosted Higgs boson decay. The exclusive-k_t algorithm defines exactly two sub-jets (Exk_t sub-jets) within a large-R jet, whose tracks are then used for the $h \to b\bar{b}$ signal discrimination via similar multivariate techniques as for the fixed-radius track jets. Alternatively, center-of-mass sub-jets (COM sub-jets) are defined using the exclusive-k_t reclustering in the rest frame of the large-R jet. The third alternative, used also in subsequent chapters of this thesis, are track jets with a variable, p_{T}-dependent radius parameter (VR track jets). The track jets are reconstructed by the anti-k_t algorithm in which the radius parameter of the track jet, $\Omega(p_{\mathrm{T}}^{\mathrm{tj}})$, depends on the transverse momentum $p_{\mathrm{T}}^{\mathrm{tj}}$ and shrinks with increasing p_{T} of the studied proto jet [103],

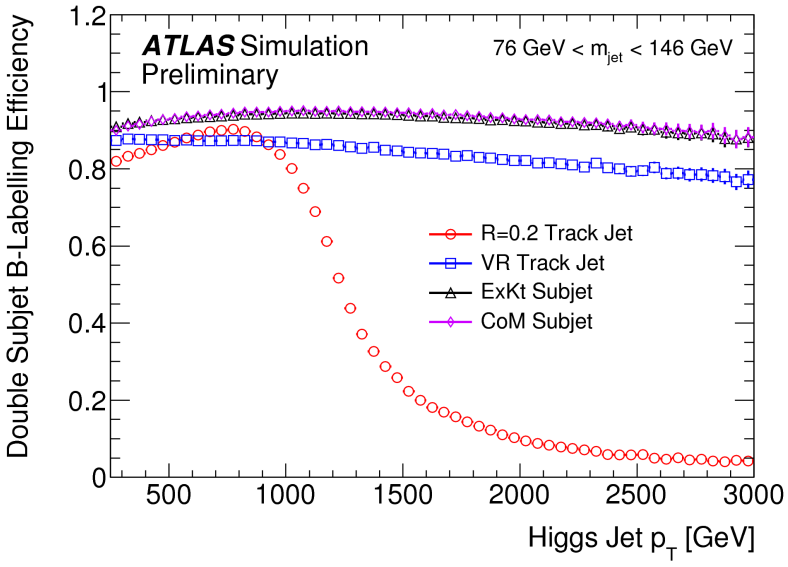

Figure 3.35: Efficiency of the reconstruction of two separate track or sub-jets from a $h \to b\bar{b}$ decay, shown for different definitions of track jets or sub-jets. Each track jet is spatially matched to a generator level b-hadron. Figure from Ref. [103], illustrating benefits of advanced track jet reconstruction.

$$\Omega(p_{\mathrm{T}}^{\mathrm{tj}}) = \max\left(0.02, \frac{1}{p_{\mathrm{T}}^{\mathrm{tj}}}\right). \tag{3.25}$$

The inverse proportionality with $p_{\mathrm{T}}^{\mathrm{tj}}$ reflects the stronger collimation of track jet with increasing track jet transverse momentum. All three new techniques well recover the efficiencies of large-R jets up to 3 TeV. While the reconstruction techniques involving sub-jets (Exk_t, COM) perform slightly better than VR track jets, the VR track jet design is closer to the well studied, established fixed-radius jets, easing the b-tagging calibration necessary for an physics analysis application.

Furthermore, the Higgs tagging based on the reconstructed large-R jet mass was studied. The Higgs jets are large-R jets from $h \to b\bar{b}$ decays are expected to have a mass within a window around 125 GeV with optimal upper and lower mass thresholds are parameterized as a function of large-R jet p_{T}^{J}. Because of the p_{T}^{J}-dependent jet mass resolution, the optimal mass window for a fixed Higgs tagging efficiency is about 60% larger at large-R jet transverse momenta of 2.5 TeV compared to 800 GeV. This p_{T}^{J}-dependent mass window requirement increases the signal significance against quark and gluon radiation by a factor of 1.9 and hadronic top quark decays by a factor of 1.3. The mass window optimization performed in this chapter minimized the size of the mass window for a given signal efficiency. An alternative optimization in terms of the signal significance would require the information about the background composition. It has , which depends on a given physics analysis. The large-R jet mass itself was shown to be the by far most powerful jet substructure observable. Other substructure observables show a reasonable discrimination power before applying the baseline

b-tagging and mass-based Higgs-identification, but their performance is significantly weaker than those baseline selection requirements. If used as an additional discriminant together with the baseline selections, no substructure variable shows an exceptional discrimination power any more.

The best-performing substructure variables are dipolarity or variables defined in the center-of-mass frame (Fox-Wolfram moments, thrust, and sphericity). Additional notable variables for the suppression of hard quark or gluon emission are the subjettiness ratio τ_{21} and the double-ratio of energy correlation functions D_2. The impact of leading substructure variables is summarized in Figs. 3.36 and 3.37 for the QCD jets and the top jets backgrounds, respectively. The color scale indicates the size of the correlation between a given substructure variable and the mass observable for the respective *b*-tagging pre-selected background sample.

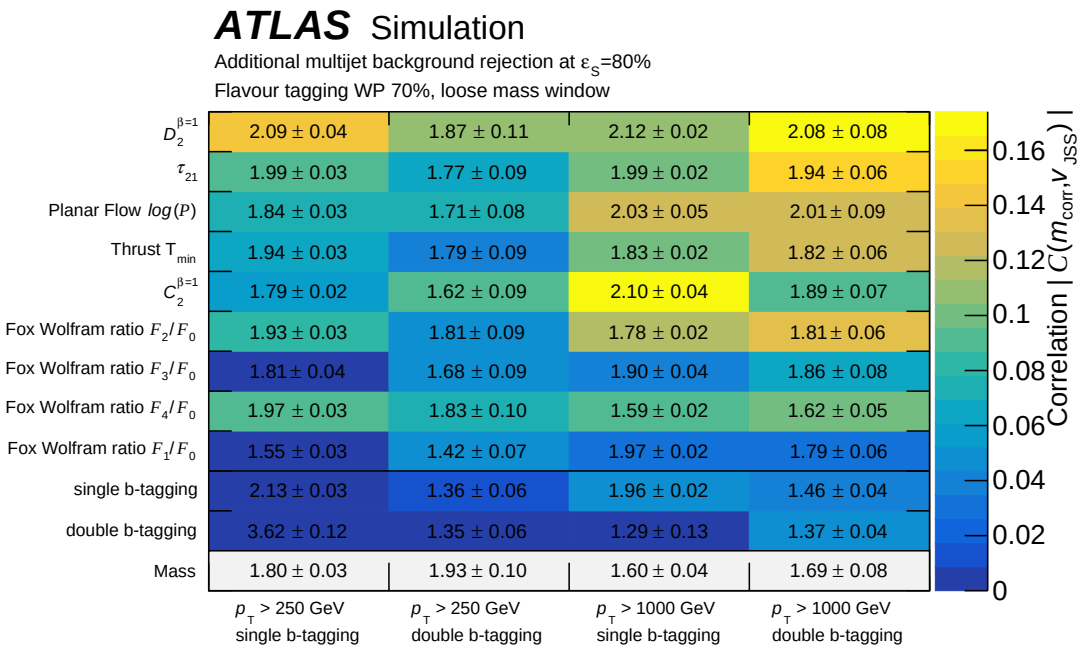

Figure 3.36: QCD jet (multijet) rejection factor at a Higgs jet signal efficiency of $\varepsilon_S = 80\%$ as obtained from selected substructure variables after applying the loose mass window and one of the two different baseline *b*-tagging selections, shown separately for the p_{T}^J ranges with $p_{\mathrm{T}}^J > 250$ GeV and $p_{\mathrm{T}}^J > 1000$ GeV. The color scale of the z-axis indicates the absolute value of the Pearson correlation coefficient between the jet mass and the jet substructure variable. The last row shows the background rejection from a loose mass window requirement applied on top of a given baseline *b*-tagging selection. Plot published in Ref. [110].

The scan over more than 40 different substructure variables serves for future developments. The employment of substructure variables have shown to only marginally improve the Higgs tagging efficiency. In these studies, the related systematic uncertainties have so far mostly been neglected. For this, additional modeling uncertainties of these substructure observables have to be estimated. However, in contrast to *b*-tagging, a validation of these estimates with data and is impossible, since there is no control data sample that is pure in hadronically decaying Higgs bosons. An attempt to

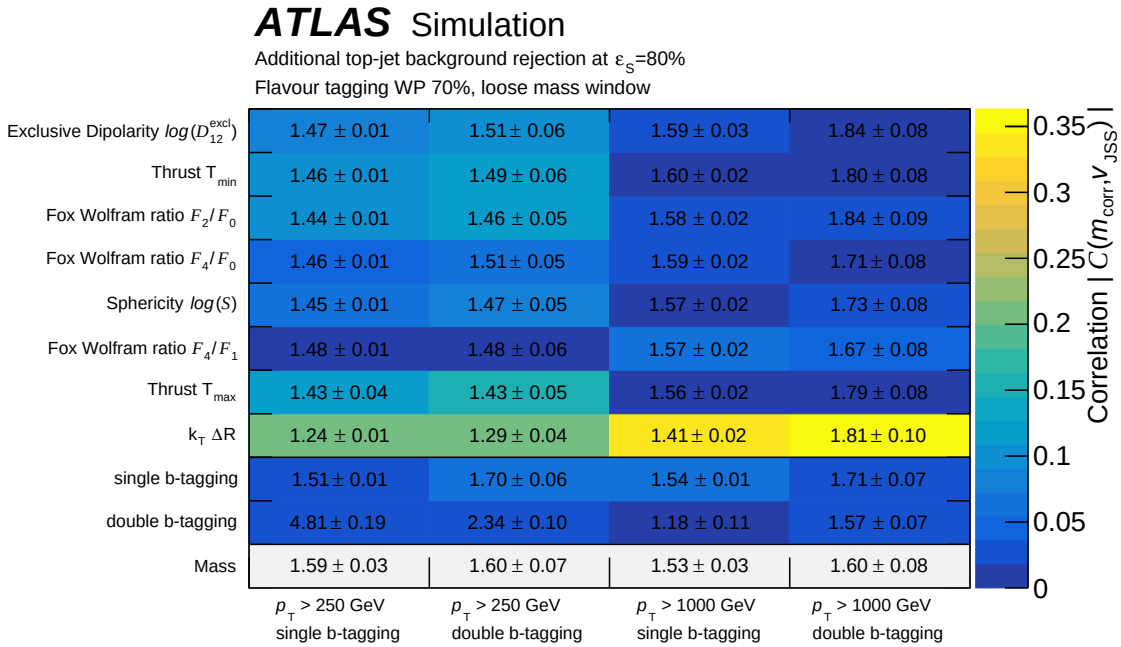

Figure 3.37: top jet rejection factor at a Higgs jet signal efficiency of $\varepsilon_S = 80\%$ as obtained from selected substructure variables after applying the loose mass window and one of the two different baseline b-tagging selections, shown separately for the p_T^J ranges with $p_T^J > 250$ GeV and $p_T^J > 1000$ GeV. The color scale of the z-axis indicates the absolute value of the Pearson correlation coefficient between the jet mass and the jet substructure variable. The last row shows the background rejection from a loose mass window requirement applied on top of a given baseline b-tagging selection. Plot published in Ref. [110].

use $g \to b\bar{b}$ as a close proxy to $h \to b\bar{b}$ decays has been developed [110]. However, the losses in signal sensitivity caused by the mentioned uncertainties are expected to be larger than the expected small sensitivity improvements from the substructure discriminants. This statement holds also for the combination of several substructure observables by means of multivariate techniques. Therefore, novel techniques utilizing multivariate methods for the Higgs tagging that have been developed in Ref. [145] use only the four-momenta of involved jets and the calibrated b-tagging information as an input.

CHAPTER FOUR

SEARCH FOR DIBOSON RESONANCES DECAYING TO A GAUGE AND A HIGGS BOSON

many theoretical models which answer open questions of the Standard Model (SM) by introducing new interactions at higher energy scales can be be probed with the ATLAS detector by searching for new heavy resonances in the invariant mass spectrum of their decay products. Theories beyond the SM (BSM) predicting such new particles are numerous and the examples explored in this analysis are described in detail in Chapter 1. The analysis performed in this chapter is a model independent search for new resonances decaying into a massive SM weak vector boson V ($V = W, Z$) and a Higgs boson h, as illustrated in Fig. 4.1. The search can also be interpreted in the framework of the two benchmark models described in Chapter 1 predicting resonances X with different spin and parity quantum numbers. The heavy vector triplet (HVT) models A or B (c.f. Section 1.3.2) with a heavy vector boson V' ($V' = W', Z'$) is used as benchmark for a spin-1 particle searches, while the two-Higgs doublet model (2HDM) (c.f. Section 1.3.1) including a pseudo-scalar A boson serves as a benchmark model for spin-0 particles searches.

The hypothetical new heavy particle is typically produced at rest, and thus decays into two bosons with a back-to-back topology in the transverse plane. The SM gauge boson V is reconstructed in the leptonic decay modes, $Z \to \nu\nu$, $Z \to \ell\ell$ and $W \to \ell\nu$, with $\ell = e, \mu$. τ-leptons are taken into account if they decay leptonically. The number of light charged leptons ℓ in the final state thus defines the event selection categorization into the three decay channels: 0-lepton, 1-lepton and 2-lepton. Missing transverse energy $E_{\mathrm{T}}^{\mathrm{miss}}$ indicates undetected neutrinos in the final state as in the 0- and 1-lepton channels. The different channels require different reconstruction techniques and are affected by different SM background contributions.

All three channels share the reconstruction technique for the Higgs boson candidate. The Higgs boson is reconstructed via its dominant decay mode, $h \to b\bar{b}$, by reconstructing either two well separated jets in the so-called *resolved* event topology or one large-size jet, containing the hadronization products of two b-quarks and referred to as events with the *merged* topology (c.f. Chapter 3). The latter is characteristic for highly boosted Higgs boson decays. The reconstruction techniques in both the *resolved* and the *merged* topology employ b-tagging to improve the identification of an $h \to b\bar{b}$ decay. A detailed description of the object[1] and event reconstruction is given in Section 4.2.2. Depending on the benchmark model considered, different production modes of the new resonance are of interest. Three production modes are considered here (see Fig. 4.2). The heavy vector bosons are in most cases

[1] i.e. particles, jets and $E_{\mathrm{T}}^{\mathrm{miss}}$

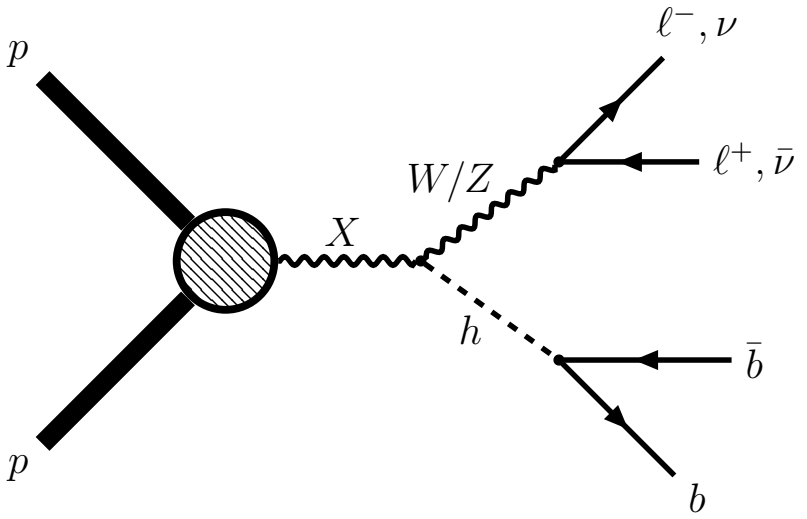

Figure 4.1: Tree-level Feynman diagram for the production of a heavy particle X and its subsequent decay into a weak gauge boson W/Z and a Higgs boson h, which subsequently decay into leptons and $b\bar{b}$ pairs, respectively. The blob in the production vertex contains the different X boson production mechanisms, such as those shown in Fig. 4.2.

produced by a Drell-Yan-like (DY) process of quark-antiquark annihilation (Fig. 4.2(a)). An additional production mode, the vector boson fusion (VBF)(Fig. 4.2(b)), relevant for some regions of HVT parameter space is studied in detail in Chapter 5. The pseudo-scalar A within the 2HDM can produced via gluon-gluon fusion (ggA mode) Fig. 4.2(c) and in association with b-quarks (bb$A$ mode) Fig. 4.2(d). The sensitivity to these different production modes i optimized by small modifications to the event selection, for example by requiring additional b-tagged jets in the final state.

The final discriminant between the SM background and the BSM signal processes is the reconstructed invariant mass of the Vh diboson system. While in the case of the 1- and 2-lepton channel, the invariant mass of the resonance candidate m_{Vh} can be fully reconstructed, the transverse mass,

$$m_{\mathrm{T}} = \sqrt{\left(E_{h,\mathrm{T}} + E_{\mathrm{T}}^{\mathrm{miss}}\right)^2 - \left(\vec{p}_{h,\mathrm{T}} + \vec{E}_{\mathrm{T}}^{\mathrm{miss}}\right)^2}, \tag{4.1}$$

is employed in case of the 0-lepton channel as the closest proxy to the invariant mass. Here $E_{h,\mathrm{T}}$ and $\vec{p}_{h,\mathrm{T}}$ are the energy and four-momentum of the Higgs boson candidate in the transverse plane and $E_{\mathrm{T}}^{\mathrm{miss}}$ and $\vec{E}_{\mathrm{T}}^{\mathrm{miss}}$ are the magnitude and the vector of the missing transverse momentum.

In case of the 0-lepton channel, the longitudinal component of the Z boson momentum is unknown, which is why m_{T} is introduced as a proxy for the invariant mass of the resonance. The missing degree of freedom lost by the longitudinal component of the escaped neutrino in the 1-lepton channel is constrained by imposing the requirement that the invariant mass of the ℓ-ν-system be equal to the W-boson mass, $m_W = 80.37$ GeV [6].

All considered signal and relevant SM background processes are modeled by modern Monte Carlo

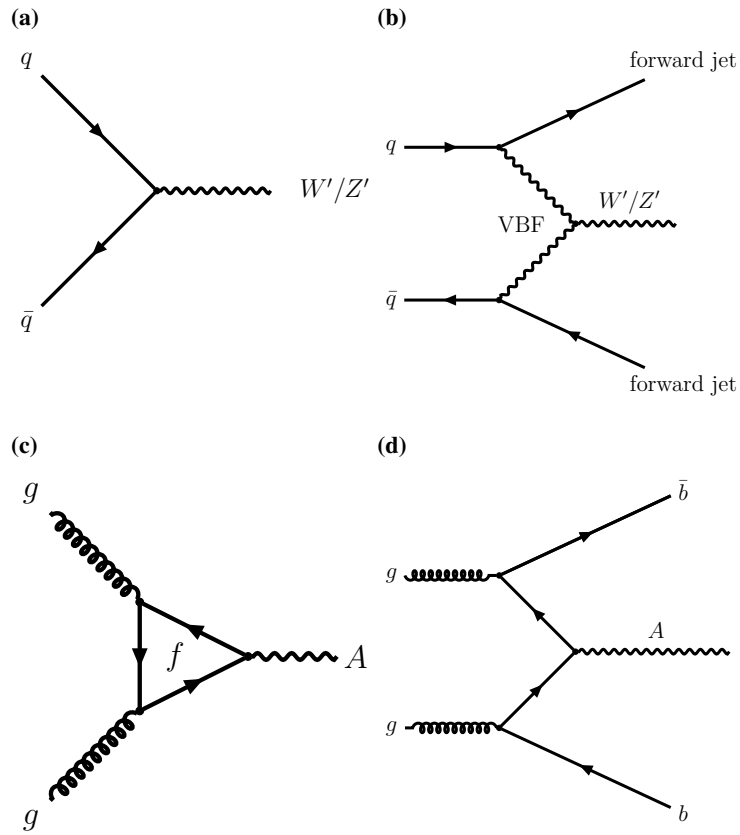

Figure 4.2: Tree-level Feynman diagrams for the different signal production modes, V' production via (a) Drell-Yan-like (DY) quark-antiquark annihilation and (b) vector boson fusion (VBF), relevant for the HVT models; pseudo-scalar A production in the 2HDM via (c) gluon-gluon fusion (ggA mode) and (d) production in association with b-quarks (bb$A$ mode).

(MC) generators. One exception is the modeling of the multi-jet background, for which a dedicated data-driven method is employed.

An analysis in this final state has already been performed with smaller |ATLAS datasets, corresponding to integrated luminosities of 3.2 fb^{-1} [146] and 36 fb^{-1} [41]. The results obtained with the full Run 2 dataset are published for the HVT Z' and ggA mode interpretation in Ref. [147] and for the HVT W' interpretation in Ref. [148], containing results presented in this chapter. The search for Vh resonances in a fully hadronic final state are presented in Ref. [149]. A semi-leptonic decay of a VV-resonance has been explored in Ref. [150] using similar reconstruction techniques and the same dataset as in the analysis presented in this chapter. Searches in similar phase space have been also perforemed by the CMS collaboration [151, 152].

This chapter is structured as follows: A detailed description of the employed ATLAS dataset and the simulation of signal and background process simulation is given in Section 4.1. The physics object and the event reconstruction is described in Section 4.2. A validation and correction of the MC

background prediction by means of data in signal-depleted control regions is presented in Section 4.3. The evaluation of systematic uncertainties on the measurement of the final discriminants is discussed in Section 4.4. The methods used for the statistical interpretation of data and the employed fit models are described in Sections 4.5 and 4.6, respectively. The results of the statistical interpretation of data are presented in Section 4.7.

4.1 Data and simulated signal and background processes

Data used for this analysis has been recorded at the ATLAS detector between 2015 and 2018 in proton-proton-collisions with a center of mass energy $\sqrt{s} = 13$ TeV. The accumulated total integrated luminosity is 139 fb^{-1} [153]. All recorded events are required to pass certain quality criteria ensuring that the detector is in a good operation condition during the data taking.

The large event rate from the ATLAS detector is reduced by a set of high-level triggers (c.f. Section 2.2.5) depending on the search channel. For the 0-lepton channel, different $E_{\mathrm{T}}^{\mathrm{miss}}$ triggers are applied with $E_{\mathrm{T}}^{\mathrm{miss}}$ thresholds in the range between 70 − 110 GeV. The thresholds are adapted to increasing luminosity in the different data taking periods during Run 2. To reduce the data rates, the lower online $E_{\mathrm{T}}^{\mathrm{miss}}$ threshold was raised from 70 GeV in 2015 to varying thresholds between 90 GeV and 110 GeV in 2016 and eventually to 110 GeV in 2017 and 2018. The selected triggers provide a selection efficiency of about 80% at $E_{\mathrm{T}}^{\mathrm{miss}} = 150$ GeV.

Events in the 2-lepton channel are triggered by a combination of single-electron and single-muon triggers with and without lepton isolation criteria. Muon triggers with moderate isolation criteria using a variable sized cone around the muon are applied requiring the transverse momentum of $p_{\mathrm{T}} > 26$ GeV. An exception is the data recorded in 2015, operated at lower event rates, in which muons with $p_{\mathrm{T}} > 20$ GeV and a loose isolation criterion were used for the event trigger. For all data taking periods, an additional muon trigger with no isolation requirement is used to recover efficiency for muons with a $p_{\mathrm{T}} > 50$ GeV. Electron triggers with various different p_{T} and isolation requirements are also used. Requirements ranging from strictly isolated electrons with $E_{\mathrm{T}}^{\mathrm{trig}} > 24$ GeV to electrons with $E_{\mathrm{T}}^{\mathrm{trig}} > 24$ GeV without requirement on the isolation. A reconstructed charged lepton is required to be matched to the the trigger object and satisfy a minimum p_{T} requirement of 27 GeV. The combined trigger efficiency for all selected signal candidates is larger than 90%.

In the 1-lepton channel, a combination of the described lepton triggers and $E_{\mathrm{T}}^{\mathrm{miss}}$ triggers is used. For low vector boson transverse momentum p_{T}^{V}, the lepton triggers are used, while for events with $p_{\mathrm{T}}^{V} > 150$ GeV the $E_{\mathrm{T}}^{\mathrm{miss}}$ trigger replaces the muon trigger due to a higher efficiency. The combined trigger efficiency for all selected 1-lepton signal events is above 90% and reaches values close to 1 for high gauge and Higgs boson momenta.

The detailed list of employed triggers is given in Appendix B.11. The recorded observed data are compared to the predictions from the MC simulation.

Benchmark signal scenarios and modeling

For the interpretation of the observed data different signals samples from the HVT model and the 2HDM are simulated. The heavy vector bosons Z'/W' are generated separately for three distinct analysis channels ($Z \to \nu\bar{\nu}$, $Z \to \ell^+\ell^-$ and $W \to \ell\nu$) via the DY production mode. In each case, the $c\bar{c}$ and $b\bar{b}$ decay modes of the Higgs boson are simulated. The MadGraph 2.3.3 event generator [154] at leading-order (LO) accuracy is used for the matrix element (ME) calculation. MadGraph is interfaced with Pythia 8.186 for the modeling of the parton shower (PS) using the NNPDF 2.3 LO set of PDFs and the A14 tune. A grid of signal samples is generated for hypothetical Z' and W' masses between 300 GeV and 5 TeV. An interpolation between the grid points is performed using a morphing technique [155, 156] to increase the discovery potential signals between the simulated grid points. All HVT signal samples are generated assuming a vanishing natural width of the of the Z'/W' resonance, as well as the HVT model A benchmark scenario with the coupling parameter value of $g_V = 1$.

For the interpretation of the observed data within the 2HDM, four different sets of samples with a pseudo-scalar A boson decaying to Zh are simulated. The four sets result from the combination of the two leptonic Z boson decay modes ($Z \to \ell^+\ell^-$, $Z \to \nu\bar{\nu}$) and the two relevant A boson production modes, the bb$A$ mode and the ggA mode. All samples are generated assuming the narrow-width approximation (NWA). The samples are are generated for pseudo-scalar A boson masses in the range between 220 GeV and 2 TeV. The ggA mode is simulated at leading order (LO) accuracy using the 2HDM FeynRules model [157] with MadGraph 2.3.3. MadGraph is interfaced with Pythia 8.186 using the A14 tune and the NNPDF 2.3 LO set of PDFs. The bb$A$ mode is simulated at next-to leading order (NLO) precision using MG5_aMC@NLO 2.2.3. The NNPDF 2.3 LO set of PDFs is used in the four-flavor scheme (4FS), i.e. containing only the four lightest quarks in the PDF description of the sea quarks, while the b-quark is treated as massive in the generator calculations. The PS is simulated by the interfaced Pythia 8.186 shower generator using the A14 set of tuned parameters. Since 2HDM parameters are sensitive to the natural width Γ_A of the resonance, the generated narrow width fo the resonance is smeared by a modified Breit-Wigner distribution [158],

$$f(x) = \frac{e^{\frac{-(ln(x-x_0)-ln(m)^2)}{2\times ln(s)^2}}}{\sqrt{2\pi}(x-x_0)ln(s)} \times \frac{1}{x^2 + 0.25w^2}, \tag{4.2}$$

for the interpretations of broader resonances. Here x_0, s and m are free parameters that are determined by fitting the smeared original distributions generated from NWA to the distributions simulated without the with finite width. These distributions are obtained at particle-level. The smearing has been validated to result in the same m_{Vh} distribution as the simulated sample including non-resonant and interference effects for widths $\Gamma_A/m_A < 10\%$.

The background processes are also simulated employing MC generators, except for the multi-jet background in the 1-lepton channel, which is determined from data. The most relevant backgrounds in the search for a Vh-resonance are top quark pair production ($t\bar{t}$) and vector boson production in association with jets (V+jets). Example Feynman diagrams for these background processes are shown in Fig. 4.3.

The $t\bar{t}$ background process is modeled using the PowhegBox v2 [55–58] MC generator at NLO accuracy using the NNPDF 3.0 NLO PDF set [159]. The ME event generator is interfaced with

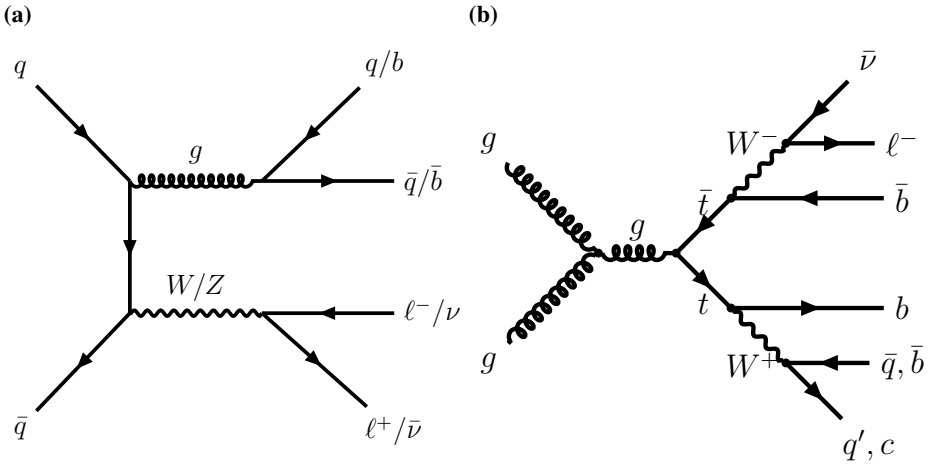

Figure 4.3: Tree-level Feynman diagrams for the two dominant Standard model background processes in the search for Vh resonances: (a) V+jets and (b) $t\bar{t}$ production.

Pythia 8.230 [115] which models the PS, hadronization and underlying event. Pythia is employed using the A14 set of tuned parameters [117]. The resummation damping factor h_{damp}, which regulates the kinematics of the leading gluon emission is set to 1.5 times the top quark mass (m_{top} = 172.76 [6]), which has shown to provide best agreement between simulation and observation in $t\bar{t}$ enriched event topologies [160]. The cross section is computed at next-to-next-to leading order (NNLO) accuracy. This computation includes the resummation of next-to-next-to-leading logarithmic (NNLL) soft gluon terms using the Top++2.0 package [161–167].

In case of the signal production in association with b-quarks (bb$A$ mode) bb$A$ mode, additional background contribution comes from the $t\bar{t}$ production in association with b- or c-quarks. These additional heavy-flavor (HF) quarks are simulated by the PS generator, leading to a modeling accuracy which is lower than for the hard interaction. To account for the mismodelings of the rate of the additionally irradiated HF quarks, the simulated $t\bar{t}$ sample is split into two sub-samples, with their normalization determined separately from data. If a HF particle-level quark that is not originating from a top quark decay can be matched to a reconstructed jet, the event is referred to as a $t\bar{t}$+HF event, otherwise it is classified as a $t\bar{t}$ +light flavor ($t\bar{t}$+LF) event.

The production of single top quarks in association with W bosons (Wt) and the single top quark production in the s- and t-channel (see Fig. 4.4) are also modeled with the PowhegBox v2 event generator at NLO accuracy. The five-flavor scheme has been applied in the NNPDF 3.0 NLO PDF set. A diagram removal scheme [168] is used to remove interference and double-counted terms appearing both in the $t\bar{t}$ and the Wt event generation. The parton shower in single top quark events has been simulated by Pythia 8.230 using the A14 tune and the NNPDF 2.3 LO set of PDFs.

The $t\bar{t}$ production in association with a vector boson ($t\bar{t}V$) or with a Higgs boson ($t\bar{t}h$) is simulated utilizing the MadGraph5_aMC@NLO v2.3.3 generator at NLO accuracy employing the NNPDF 2.3 LO PDF set. The events are interfaced to Pythia 8.230 for the PS modeling, using the A14 set of tuned parameters and the NNPDF 2.3 LO PDF set.

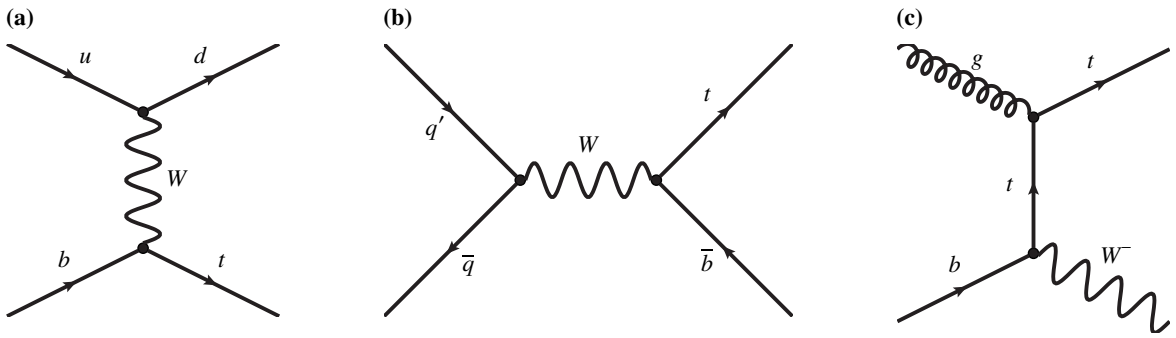

Figure 4.4: Tree-level Feynman diagrams for single top quark production in the (a) t-channel, (b) s-channel and (c) in association with a W boson [169].

The distribution of the final discriminating observable from the Single top quark, $t\bar{t}V$ and $t\bar{t}h$ events is similar to the ones from the $t\bar{t}$ process. Furthermore, their expected combined contribution to the total background is less than 6%, 15% and 1% for the 0, 1 and 2-lepton channel, respectively. Since there are no dedicated kinematic regions in data available to disentangle contributions from those background processes, the single top quark, $t\bar{t}V$ and $t\bar{t}h$ contributions are merged with the $t\bar{t}$ background contributions. The combined contribution is collectively referred to as top quark background. In the analysis dedicated to signals produced via bb$A$ mode, the single top quark, $t\bar{t}V$ and $t\bar{t}h$ contributions are merged with $t\bar{t}$+LF component only, keeping $t\bar{t}$+HF as a separate sample.

Production of single vector bosons in association with jets recoiling in the transverse plane is referred to as V+jets ($V = Z, W$). V+jets events are generated using Sherpa-v2.2.1 [170]. The calculation of the ME is performed at NLO accuracy for the boson production with up to two partons. Events with up to four partons are generated at LO matrix elements employing methods of the Comix [171] and OpenLoops [172–174] libraries. The ME are matched to the within sherpa to the PS within Sherpa using the MEPS@NLO prescription [175–178] and the NNPDF 3.0 NLO PDF set. The production cross section for V+jets samples is calculated at a NNLO precision [179]. The number of generated HF quarks in the ME and the PS has a strong impact on the shape of the kinematic variables, in particular on the final discriminant $m_{(\mathrm{T},)\mathrm{Vh}}$. Therefore, the generated V+jets events are classified according to the multiplicity of jets with HF content, into V+jets (l), V+jets (bl,cl) and V+jets (bb,bc,cc) components. A reconstructed small-R jet (c.f. Section 4.2.1) is considered ot have HF content, if a b- or c-quark at generator level can be ghost-associated [90] to a jet.

Diboson processes (WW, WZ and ZZ) are generated using Sherpa 2.2.1 including off-shell and Higgs contributions. The ME for events with up to one additional parton is calculated at NLO accuracy in QCD and at LO for up to three additional partons. The matching with the PS is done using the MEPS@NLO prescription. Loop induced diboson production via the gluon-gluon fusion (ggF) production mode are simulated separately at LO in QCD using OpenLoops in Sherpa 2.2.2.

Events from a non-resonant production of a SM-like Higgs boson in association with a vector boson (Zh, Wh) are generated using Powheg [57]. The ME prediction is accurate at NLO for the Vh bosons produced together with up to one additional parton. Powheg is interfaced with Pythia 8.212

Table 4.1: Summary of the Monte-Carlo generators used to produce the various background processes. The column *Prediction order* gives the precision in QCD of the inclusive production cross section σ_{prod} applied to the respective process. The order at which the corresponding matrix elements are calculated in the Monte Carlo is not necessarily the same as for the cross section [147, 148].

Process	Generator	Prediction order of σ_{prod}
	Vector boson + jets	
$W \to \ell\nu$, $Z \to \ell\bar{\ell}$, $Z \to \nu\bar{\nu}$	Sherpa 2.2.1	NNLO
	Top backgrounds	
$t\bar{t}$	Powheg + Pythia8	NNLO+NNLL
single top (s/t/Wt-channel)	Powheg + Pythia8	NLO
$t\bar{t} + h$	MG5_aMC@NLO + Pythia8	NLO (QCD) and NLO (EW)
$t\bar{t} + V$	MG5_aMC@NLO + Pythia8	NLO
	Diboson	
$qg/q\bar{q} \to VV \to \ell\ell/\ell\nu/\nu\nu + q\bar{q}$	Sherpa 2.2.1	NLO
$gg \to VV \to \ell\ell/\ell\nu/\nu\nu + q\bar{q}$	Sherpa 2.2.2	NLO
$qg/q\bar{q} \to \ell\ell\nu\nu$	Sherpa 2.2.2	NLO
	SM Higgs	
$qq \to Wh \to \ell\nu + b\bar{b}$	Powheg + Pythia8	NNLO (QCD) and NLO (EW)
$qq \to Zh \to \ell\ell/\nu\nu + b\bar{b}$	Powheg + Pythia8	NNLO (QCD) and NLO (EW)
$gg \to Zh \to \ell\ell/\nu\nu + b\bar{b}$	Powheg + Pythia8	NLO+NLL

for the PS using the AZNLO set of tuned parameters [180] and the PDF4LHC15 PDF set [181]. The production cross section is computed at NLO accuracy including respecting next-to-leading logarithmic (NLL) soft gluon resummation [182]. Events with loop-induced Vh production via the ggF mode are generated separately at LO.

An overview of the event generators used for the generation of the various processes and the accuracy on the prediction of the corresponding production cross sections is given in Table 4.1. All simulated MC events are reweighted to compensate discrepancies between data and simulation in subsidiary performance measurements [51, 75, 76, 81, 92, 97], accounting for the modeling of energy or momentum scale and resolution for jets and leptons and the corresponding reconstruction and identification efficiencies.

Multi-jet background

Events containing only quarks and gluons in the final state of the hard interaction process are collectively called multi-jet events. The vast majority of the collision data consists of multi-jet events. Such events do neither contain real $E_{\text{T}}^{\text{miss}}$ from neutrinos nor prompt charged leptons and are therefore almost fully discarded mostly by the signal selection criteria of the present analysis. However, due to the sheer amount of such events at the LHC and the imperfect particle reconstruction performance in the detector, a fraction of multi-jet events may still pass the event selection criteria.

The $E_{\mathrm{T}}^{\mathrm{miss}}$ in multi-jet event may be non-vanishing due to e.g. inefficiencies in the jet reconstruction or imperfect jet energy measurement. In that way, the so-called fake $E_{\mathrm{T}}^{\mathrm{miss}}$ is reconstructed. The impact of such events differs for the three analysis channels. In the 0-lepton channel, the multi-jet background is suppressed to a negligible level after the application of appropriate event selection requirements. This has been confirmed in dedicated regions of validation data.

Non-prompt leptons can emerge in secondary vertices from hadronic decay showers or by interaction of particles with the detector material. These contributions are subject to several sources of uncertainties and a modeling by MC is very difficult. Fortunately, contributions from such multi-jet processes with non-promt or fake leptons are negligible in the 2-leptons channel. This is verified in a validation region requiring two leptons with equal charge in the final state.

In the 1-lepton channel, the multi-jet contribution is significant and reaches up to 20% of the total background in some regions of the phase space. A data-driven estimation was therefore performed. The shape of the final discriminant m_{Vh} distribution from the multi-jet background is extracted from a dedicated control region of data, that closely follows the signal event selection criteria (c.f. Section 4.2) but employs inverted lepton isolation criteria [41]. Instead of isolated charged leptons only events with non-isolated leptons are selected. It is assumed, that the shape of the m_{Vh} distribution from multi-jet events with non-prompt leptons is similar for multi-jet events with isolated and non-isolated leptons. An extrapolation from the non-isolated control region to the signal region defined by the signal event selections criteria is then performed from the fit of the $E_{\mathrm{T}}^{\mathrm{miss}}$ distribution in control and signal data regions. Since the multi-jet events populate low $E_{\mathrm{T}}^{\mathrm{miss}}$ values, as opposed to the signal ant other background events, the fit can be used to measure the ratio of multi-jet events in the control and the signal regions. With this approach, the precise knowledge of the efficiency of the lepton isolation criteria is not critical.

4.2 Event reconstruction and selection

The reconstructed charged leptons, jets and missing transverse momentum are commonly referred to as physics objects. Their definition is given in the following section. The event selection criteria applied on these objects in order to discriminate the signal from the background for each of the three channels is given in Section 4.2.2.

4.2.1 Object definition

The primary vertex (PV) in the event is selected as the vertex with the highest sum of squared transverse momenta p_{T}^2 of the tracks associated to that vertex. Events are reconstructed following the common reconstruction algorithms described in Section 2.4. Since no perfect identification of particles is possible, a certain working point (WP) is chosen for a given identification algorithm, trading between particle identification efficiency and the corresponding misidentification rate. This choice of WP for each identification algorithm is strongly analysis dependent and will be described in this section for the present analysis.

Electrons are required to satisfy the *tight* identification WP with the lowest misidentification rate (c.f. Section 2.4.3). The electron-veto, on the other hand, employs the *loose* identification WP. Electrons must be isolated from other, presumably hadronic activities by *tight* isolation criterion, allowing for less than 6% of energy deposits and additionally recorded tracks in the electrons vicinity, as described in Section 2.4.3. The minimum required electron p_{T} is 7 GeV and the pseudo-rapidity must be smaller than 2.47, sparing in addition the uninstrumented detector region of $1.37 < |\eta| < 1.52$ between the barrel and the endcap parts of the detector.

Combined muons (c.f. Section 2.4.4), i.e. those reconstructed by combining trajectories in the Inner Detector (ID) and the muon spectrometer, are required to fulfill the *tight* identification requirements. For the muon veto, on the other hand, the *loose* selection requirements are chosen to increase the veto efficiency. The *high-p_T* requirements are applied for muon candidates with a transverse momentum above 100 GeV. To reject muons from secondary hadron decays the muon must satisfy the TightTrackOnly criterion on the $p_{\mathrm{T}}^{\mathrm{varcone},0.3}$ isolation disciminant, i.e. the sum of p_{T} of all tracks around the muon is required to be smaller than 6% relative to the muon p_{T}. The muon transverse momentum has to be above 7 GeV.

Hadronic τ-lepton decays are reconstructed to allow for a τ-veto in the event. They are reconstructed, as described in Section 2.4.5, from calorimeter jets associated with either one or three charged tracks. Leptonic τ-lepton decays cannot be distinguished from prompt electrons or muons.

The hadronically decaying Higgs boson candidates is are reconstructed by means of one or several of the three following jet definitions, all of them based on the anti-k_t algorithm (c.f. Section 2.4.5). The jets reconstructed with a radius parameter $R = 0.4$ from noise suppressed topological clusters in the calorimeter system are referred to as small-R jets. Small-R jets are reconstructed up to pseudo-rapidities of 4.5. Two different jet p_{T}-thresholds are used for different η regions. Small-R jets in the central region of the detector with $|\eta| < 2.5$ are required to have a transverse momentum above 20 GeV. Here, the jet vertex tagger (JVT) [89] is applied to suppress contributions from pile-up-induced jets. The JVT requirement is applied to jets with $p_{\mathrm{T}} < 60$ GeV and $|\eta| < 2.5$. The JVT WP with a nominal efficiency of 90% for jets from the PV is chosen. The p_{T} threshold for jets with $|\eta| > 2.5$ is increased to 30 GeV to compensate for the non-coverage of the JVT in the forward detector region. Identification of small-R jets stemming from b-quarks is performed by the multivariate MV2 algorithm, c.f. Section 2.4.5. The applied WP has a 70% identification efficiency for jets fro b-quarks in simulated $t\bar{t}$ events [183]. Jets passing the MV2 selection criteria are referred to as b-tagged jets.

The di-jet system representing the Higgs boson candidate is defined by the two b-tagged small-R jets with highest p_{T}. In events with only one b-tagged jet, the highest-p_{T} non-b-tagged jet is used instead. The highest-p_{T} jet (leading jet) must have a p_{T} of at least 45 GeV. The events in which the Higgs boson candidate is reconstructed from such a di-jet system are referred to as events with the *resolved* topology, since the Higgs boson decay products can be resolved into two reconstructed jets. Events with at least two small-R jets and none of them is b-tagged are discarded. In particular, those events are not reconstructed by any other techniques described below either.

With increasing momentum of the Higgs boson, the b-quarks become much more collimated such that the small-R-jets can no longer reproduce the partonic structure of the $h \to b\bar{b}$ decay. Jets with a radius parameter $R = 1.0$, similar to those discussed in Chapter 3, are defined with the intention to

enfold the full $h \to b\bar{b}$ decay. These jets are referred to as large-R jets. For the large-R jets, the anti-k_t algorithm uses track-calorimeter clusters (TCCs) as inputs [78]. TCCs are built using combined information from the calorimeter and the ID. The large jet surface is sensitive to background jets and noise. Therefore, a trimming procedure as described in Section 2.4.5 has been applied to suppress background contributions. Large-R jets are required to have a minimum transverse momentum of 250 GeV and $|\eta| < 2.0$.

Since the common b-tagging procedure cannot be easily applied on the large-R jets, a third jet type, the so-called track jets are employed to identify the $h \to b\bar{b}$ decay within a large-R jet. The track jets are build by clustering the ID tracks with a radius parameter of variable p_{T}-dependent size (c.f. Section 3.5). track jets are then ghost-associated to large-R jets and b-tagged using the MV2 identification algorithm. A large-R jet is discarded if there are less than two track jets associated with it. The track jets are also required to be well separated from each other by the condition,

$$\Delta R(tj_i, tj_j) > \min(R_i, R_j), \tag{4.3}$$

where R_i is the radius parameter of the corresponding track jet. Otherwise the event is rejected, since the b-tagging calibration for track jets is likely not applicable in this topology. The resulting loss in HVT signal acceptance for masses of 700 GeV, 2000 GeVand 5000 GeVis 4%, 9% and 11%, respectively.

A muon-in-jet correction as described in section Section 3.3.1 has been applied to correct the energy of large-R and small-R jets. The muons used for this correction are not required to pass the isolation criteria. The energy of small-R jets containing muons is additionally corrected by a p_{T}-dependent term computed from simulated SM $V(h \to b\bar{b})$ events, by determining the ratio of particle level jet p_{T} and the p_{T} of the reconstructed jet after the muon-in-jet correction. This p_{T}-dependent correction improves the di-jet mass resolution of the Higgs boson candidate.

Finally, the missing transverse momentum $E_{\mathrm{T}}^{\mathrm{miss}}$ is calculated from the calibrated calorimeter cells associated to reconstructed particles or jets, adding also a soft term, as described in Section 2.4.6. The soft term takes into account all tracks compatible with the primary vertex but not associated to any reconstructed particles or jets $E_{\mathrm{T}}^{\mathrm{miss}}$ calculation. In addition to $E_{\mathrm{T}}^{\mathrm{miss}}$, a further observable $p_{\mathrm{T}}^{\mathrm{miss}}$, quantifying the momentum imbalance, is calculated as the negative vectorial sum, $\sum \vec{p}_{\mathrm{T}}$, of transverse momenta of all tracks from the primary vertex. Since the inner detector only records charged particle tracks, the $p_{\mathrm{T}}^{\mathrm{miss}}$value is in general lower than the $E_{\mathrm{T}}^{\mathrm{miss}}$. To decrease contribution from fake $E_{\mathrm{T}}^{\mathrm{miss}}$ measurement, i.e. $E_{\mathrm{T}}^{\mathrm{miss}}$ not caused by undetectable particles but rather from mis-measured jet and lepton energies, a significance variable $\mathcal{S}$ has been developed [184], normalizing the measured $E_{\mathrm{T}}^{\mathrm{miss}}$ relative to the energy resolution of objects entering the $E_{\mathrm{T}}^{\mathrm{miss}}$ computation. This observable quantifies the probability that the $E_{\mathrm{T}}^{\mathrm{miss}}$ is induced by undetectable particles.

The above described objects are reconstructed by dedicated independent reconstruction algorithms. Ambiguities can arise by the reconstruction of the same physical particle by different algorithms. An overlap removal procedure [150, 185] discards sequentially all but one of the overlapping objects based on the following criteria. A hadronically decaying τ-lepton within a cone of $R < 0.2$ around an light lepton is discarded. The τ-lepton is not discarded, if its p_{T} is above 50 GeV and the lepton is a muon but not a combined muon. If an electron and a muon share the same track, the electron is discarded. A small-R jet with angular separation of $R < 0.2$ from an electron satisfying the isolation

criteria is removed. The small-R jet is also removed if it is separated by less than $R = 0.2$ from a muon if either the jet has only two or less associated tracks or the muon carries the 70% of the jet momentum. Potentially surviving jets are removed if they are located in a cone of variable size up to a maximum of $R = 0.4$ around a lepton. The cone size shrinks with increasing lepton momentum as $\Delta R = \min(0.4, 0.004 + 10\ \text{GeV}/p_{\text{T}}^{\ell})$.

The vector boson V is – dependent on the sub-channel – reconstructed from different combinations of leptons and $E_{\text{T}}^{\text{miss}}$, depending on the analysis channel. The Z boson in the 2-lepton channel is reconstructed from the four-momenta of same-flavor and oppositely charged leptons. The opposite-charge requirement is not applied for electrons to account for their high charge misidentication rate.

The four-momentum of the W boson in the 1-lepton channel is defined by the constraint on the invariant mass of the neutrino-lepton pair. The neutrino four-momentum is reconstructed from the $E_{\text{T}}^{\text{miss}}$ and the unknown longitudinal momentum component. This longitudinal component can be determined by imposing the requirement that the invariant mass of the neutrino-lepton system be equal to the W boson mass of $m_W = 80.4$ GeV. From the two solutions of the corresponding quadratic equation for $p_{\text{z},\nu}$, the smaller value is taken and in case of a complex solution, the real part is taken.

In the 0-lepton channel, the longitudinal component of the Z boson momentum cannot be reconstructed, since momenta of two neutrinos cannot be measured in the calorimeter. Instead, the $E_{\text{T}}^{\text{miss}}$ is considered as the transverse component of the Z boson momentum while the Z boson mass is imposed to be $m_Z = 91.2$ GeV [6].

4.2.2 Event selection

The Higgs boson candidate is reconstructed in the same way in all three analysis channels. First, a small-R di-jet pair is considered as a Higgs boson candidate. Events with such candidates are referred to as events with *resolved* topology. The invariant mass m_{jj} of the di-jet system must be compatible with the Higgs boson mass of 125 GeV, i.e. required to be within 110 GeV $< m_{jj} <$ 145 GeV. This requirement is loosened to 100 GeV $< m_{jj} <$ 145 GeV in the 2-lepton channel, taking advantage of the lower background contributions

If there are no candidates with the *resolved* topology or the event is rejected by further *resolved* topology criteria, as described below, the leading large-R jet is considered as the Higgs boson candidate. Such events are referred to as events with the *merged* event topology. The invariant mass of the large-R jet must be within 75 GeV $< m_J <$ 145 GeV to be compatible with the Higgs boson mass of 125 GeV. The b-tagging (c.f. Section 2.4.5) is applied to better identify the Higgs boson candidates and thus increase the signal sensitivity. The number of b-tagged jets in an event defines data region categories with 1, 2 and more than two (3+) b-tags. Latter is an inclusive selection of events with the *resolved* event topology and at least 3 b-tagged jets and is employed in the search for a pseudo-scalar A boson produced via the bb$A$ mode. Events with the *merged* event topology are also classified into similar data region categories based on the number of b-tagged track jets. In the analysis searching for a signal produced via the bb$A$ mode, additional signal region categories are introduced for events with the *merged* event topology containing additional track jets, that are not associated to the large-R jet. These regions are referred to as regions with additional b-tags (*add.* b-tag).

Table 4.2: Summary of event selection criteria for each analysis channel and event category as described in the text. $^{(*)}$ The requirement applies in the case of only two central jets in teh final state. $^{(**)}$ The τ-lepton veto is only applied for the Z' and A search. $^{(\dagger)}$ The tighter threshold (80 GeV) is used for the single electron channel. $^{(\dagger\dagger)}$ The requirement is only applied for $m_{Zh} > 320$ GeV. $^{(\ddagger\ddagger)}$ Only the two leading track jets which are ghost associated to the large-R jet are considered when classifying events into b-tag categories [147, 148].

Variable	Resolved	Merged
Common selection		
Number of jets	≥2 small-R jets (0, 2-lep.) 2 or 3 small-R jets (1-lep.)	≥1 large-R jet ≥ 2 VR track jets (matched to leading large-R jet)‡‡
Leading jet p_{T} [GeV]	> 45	> 250
m_H [GeV]	110–140 (0,1-lep.), 100–145 (2-lep.)	75–145
0-lepton selection		
$E_{\mathrm{T}}^{\mathrm{miss}}$ [GeV]	> 150	> 200
H_T [GeV]	> 150 (120^*)	–
$\Delta\phi_{bb}$	$< 7\pi/9$	–
$p_{\mathrm{T}}^{\mathrm{mis}}$ [GeV]	> 60	
$\Delta\phi(\vec{E}_{\mathrm{T}}^{\mathrm{mis}}, \vec{p}_{\mathrm{T}}^{\mathrm{mis}})$	$< \pi/2$	
$\Delta\phi(\vec{E}_{\mathrm{T}}^{\mathrm{mis}}, H)$	$> 2\pi/3$	
$\min\left[\Delta\phi(E_{\mathrm{T}}^{\mathrm{miss}}, R = 0.4\mathrm{jet})\right]$	$> \pi/9$ (2 or 3 jets), $> \pi/6$ (≥ 4 jets)	
$N_{\tau_{\mathrm{had}}}$	0^{**}	
MET significance S	$\begin{cases} > 9 & \text{if } m_{Vh} < 400, \\ > 6.6 + 0.01 \cdot m_{Vh} & \text{if } 400 < m_{Vh} < 700, \\ > 13.6 & \text{if } m_{Vh} > 700, \end{cases}$	
1-lepton selection		
Leading lepton p_{T} [GeV]	> 27	> 27
$E_{\mathrm{T}}^{\mathrm{miss}}$ [GeV]	> 40 ($80^{\dagger}$)	> 100
$p_{\mathrm{T},W}$ [GeV]	$> \max\left[150,\ 710 - (3.3 \times 10^5\ \mathrm{GeV})/m_{Vh}\right]$	$> \max\left[150,\ 394 \cdot \ln(m_{Vh}/(1\ \mathrm{GeV})) - 2350\right]$
$m_{\mathrm{T},W}$ [GeV]	< 300	
2-lepton selection		
Leading lepton p_{T} [GeV]	> 27	> 27
Sub-leading lepton p_{T} [GeV]	> 20	> 25
$E_{\mathrm{T}}^{\mathrm{miss}}/\sqrt{H_{\mathrm{T}}}$ [$\sqrt{\mathrm{GeV}}$]	$< 1.15\ + 8 \times 10^{-3} \cdot m_{Vh}/(1\ \mathrm{GeV})$	
$p_{\mathrm{T},\ell\ell}$ [GeV]	$> 20 + 9 \cdot \sqrt{m_{Vh}/(1\ \mathrm{GeV}) - 320}^{\dagger\dagger}$	
$m_{\ell\ell}$ [GeV]	$[\max[40\ \mathrm{GeV},\ 87 - 0.030 \cdot m_{Vh}/(1\ \mathrm{GeV})],\ 97 + 0.013 \cdot m_{Vh}/(1\ \mathrm{GeV})]$	

The three analysis channels are affected by different background processes, as shown in Fig. 4.8, calling for different strategies for background mitigation. The following subsections describe and motivate additional kinematic event selection requirements that are applied in the three channels to further reduce the background contribution. An overview of all applied event selection criteria in the different channels is given in Table 4.2.

Event selection in the 0-lepton channel

The characterizing selection criterion for the 0-lepton channel is the missing transverse momentum $E_{\mathrm{T}}^{\mathrm{miss}}$ induced by the escaping neutrino pair. Events are selected if they have an offline reconstructed $E_{\mathrm{T}}^{\mathrm{miss}}$ of at least 150. This cut is further tightened to 200 GeVin the merged regime. Events are selected if they have an p_T^{miss} larger than 60 GeVwith similar azimuthal orientation as the $E_{\mathrm{T}}^{\mathrm{miss}}$ by requiring $\varphi(E_{\mathrm{T}}^{\mathrm{miss}}, p_T^{miss}) < \pi/2$.

The $E_{\mathrm{T}}^{\mathrm{miss}}$ can be faked by inaccurately measured input objects. A selection requirement on $\sigma_{E_{\mathrm{T}}^{\mathrm{miss}}}$ is set to reduce contributions from fake-$E_{\mathrm{T}}^{\mathrm{miss}}$. The requirement is defined such that it optimizes search sensitivity. The threshold value is parameterized as a function of the transverse di-boson mass, $m_{\mathrm{T,Zh}}$.

The sum of the transverse momenta of all hard objects in the event, H_{T}, is used to discriminate signal and background processes. For events with two jets H_{T} has to be larger than 120 GeV, for jet multiplicities of at least 3 jets it has to be larger than 150 GeV.

Events with leptons are rejected. Events with hadronically decaying τ-leptons are discarded for the interpretation of the results by a Z' or a A signal hypothesis. The $W' \to \nu\ell$ analysis shows a significant fraction of events in which the lepton is not reconstructed and a large $E_{\mathrm{T}}^{\mathrm{miss}}$ shows instead. In this case, the τ-veto is repealed and events with up to 1 τ-lepton are included in the statistical interpretation of data. However, the fraction of events containing τ-leptons is about an order of magnitude smaller than those without. The background composition between events with and without τ-leptons are similar, except a slightly decreased contribution from the Z+jets background components. Differences between the τ-lepton inclusive and the τ-vetoed signal and control regions are small for background processes. For a combined interpretation of the 0- and 1-lepton channel data by a W' signal, the results shown in this thesis are derived specifically for the τ-lepton inclusive selection. For background processes, the intermediate results for the τ-lepton inclusive and the τ-vetoed signal and control regions are similar and not shown explicitly.

Motivated by the expected back-to-back topology of signal events in the transverse plane, the following requirements to azimuthal angles between objects are set. The selected jets from the Higgs decay must satisfy the condition $\Delta\varphi(j_1, j_2) < 7/9\pi$ to suppress the selection of back-to-back produced bottom or top quark pairs. An analogue requirement to track jets in the *merged* category is implicitly fulfilled by the large-R jet association. The back-to-back topology of the Higgs boson and the gauge boson is implemented by a requirement on the separation between large-R jet and $E_{\mathrm{T}}^{\mathrm{miss}}$ by $\Delta\varphi(J, E_{\mathrm{T}}^{\mathrm{miss}}) > 2\pi/3$. Additionally, events are discarded if any reconstructed small-R jet is close to the $E_{\mathrm{T}}^{\mathrm{miss}}$ by an azimuthal separation of $\varphi(j, E_{\mathrm{T}}^{\mathrm{miss}}) < \pi/9$ for a small-R jet multiplicity of up to three and $\varphi(j, E_{\mathrm{T}}^{\mathrm{miss}}) < \pi/6$ otherwise.

The signal acceptance and selection efficiency is strongly dependent on the resonance mass and moderately dependent on the spin of the resonance. The acceptance × efficiency for the four considered signal scenarios is shown in Fig. 4.5.

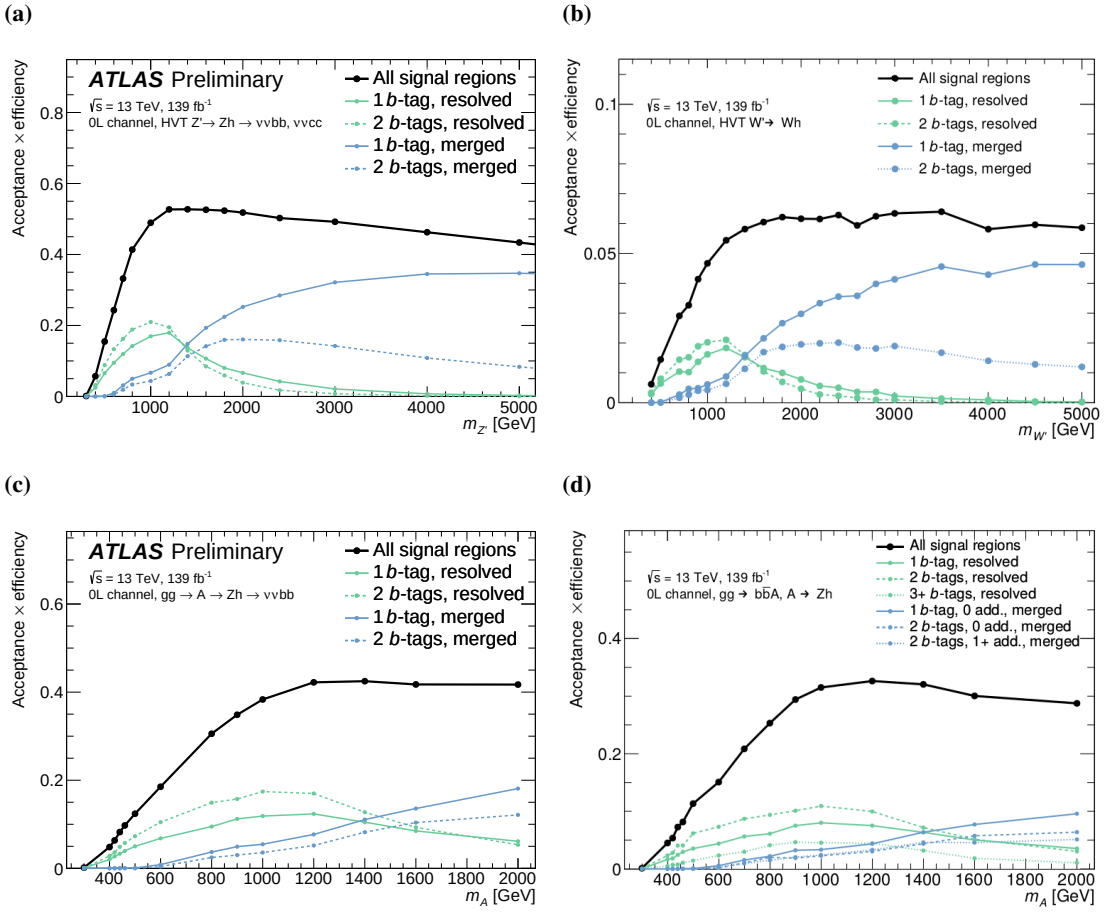

Figure 4.5: The expected signal event selection efficiency as function of the resonance mass in the 0-lepton channel, for the signal benchmark scenario of a (a) HVT Z' boson and (b) HVT W' boson as well as a pseudo-scalar A boson produced via the two production modes (c) ggA mode and (d) bb$A$ mode [147].

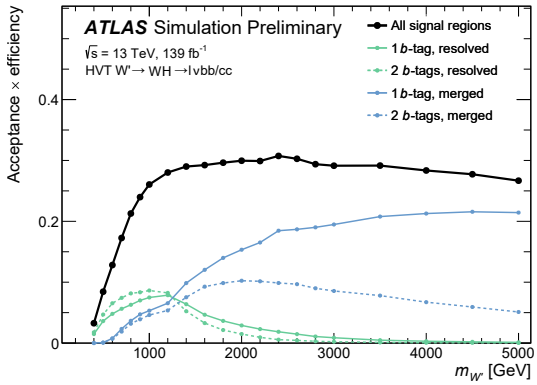

Figure 4.6: The expected signal event selection efficiency as function of the resonance mass in the 1-lepton channel, for the signal benchmark scenario of a HVT W' boson. [148]

Event selection in the 1-lepton channel

The 1-lepton channel is characterized by the selection of exactly one muon or electron. The lepton must satisfy the tight identification criteria and no other leptons with loose identification criteria are allowed. The p_{T} of the lepton has to be above 27 GeV. And must be spacially consistent with the object that triggered the event recording. In case of an electron (muon) event, a minimum $E_{\mathrm{T}}^{\mathrm{miss}}$ of 40(80) GeVis required. In the events with the *merged* event topology, the minimum $E_{\mathrm{T}}^{\mathrm{miss}}$ requirement is raised to 100 GeV to suppress contributions from multi-jet background. Furthermore, to suppress multi-jet and top quark background components, events are rejected if containing more than 3 small-R jets. The reconstructed W boson momentum must satisfy a minimum $p_{\mathrm{T},W}$, consistent with the back-to-back topology of signal events. The $p_{\mathrm{T},W}$ threshold is parameterized as a function of the reconstructed resonance, given in Table 4.2.

The transverse mass of the W boson is defined as

$$m_{T,W} = \sqrt{\left(p_{\mathrm{T},\ell} + E_{\mathrm{T}}^{\mathrm{miss}})\right)^2 - \left(\vec{p}_{\ell,\mathrm{T}} + \vec{E}_{\mathrm{T}}^{\mathrm{miss}}\right)^2}, \tag{4.4}$$

and is required to be below 300 GeV. Here, $\vec{p}_{\ell,\mathrm{T}}$ is the transverse component of the lepton momentum.

The signal acceptance and selection efficiency is strongly dependent on the resonance mass. The acceptance × efficiency for the W' signal is shown in Fig. 4.6.

Event selection in the 2-lepton channel

The 2-lepton channel is characterized by a lepton pair originating from a single Z decay. Therefore, signal leptons are required to have the same flavor. Muons are furthermore required to have opposite charge. Electrons are subject to high charge misidentication rates and no requirement to the charge is set. Events containing a third lepton satisfying the loose identification criteria are discarded. At least one of these leptons is required to match one of the objects that triggered the event recording. The

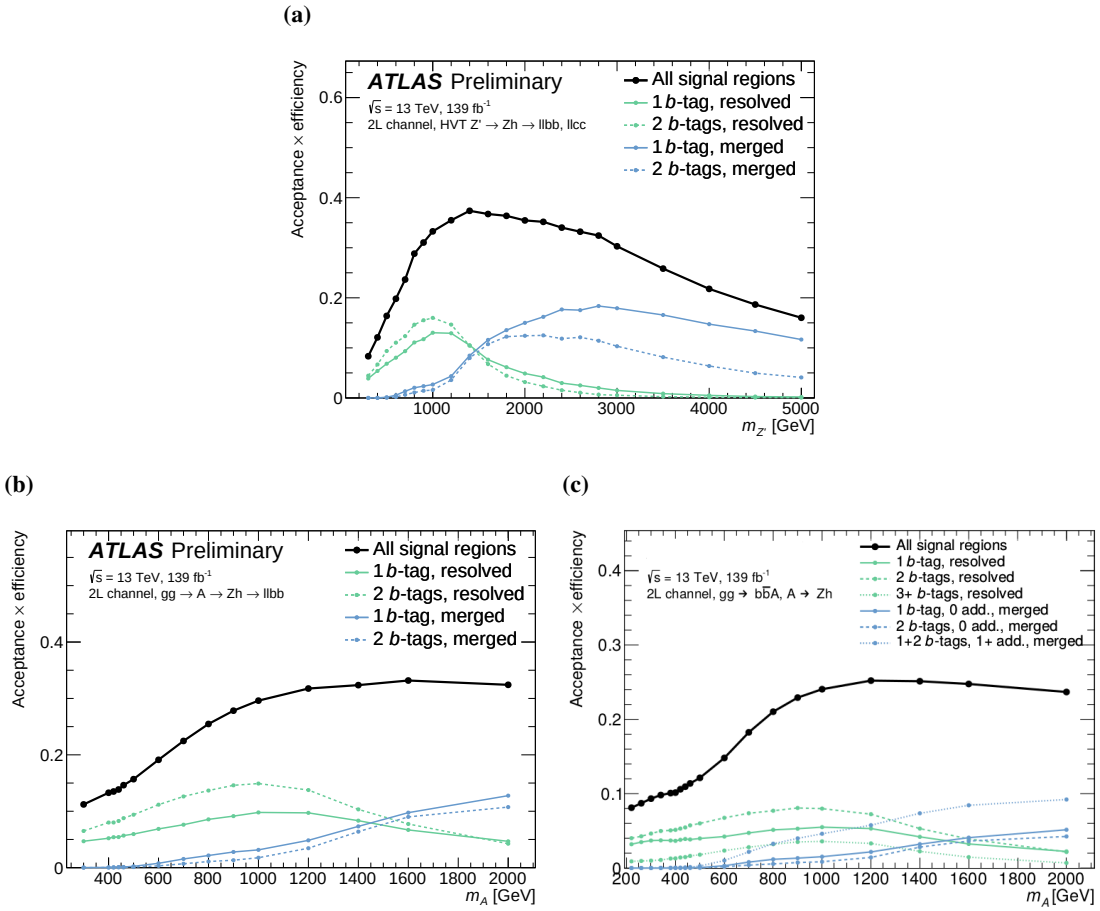

Figure 4.7: The expected signal event selection efficiency as function of the resonance mass in the 2-lepton channel, for the signal benchmark scenario of a (a) HVT Z' boson as well as a pseudo-scalar A boson produced via the two production modes (b) ggA mode and (c) bb$A$ mode. [147]

offline reconstructed p_{T} has to be at least 5% above the corresponding trigger threshold. Leptons have to pass a p_{T} requirement of at least 27(25) GeVfor the leading (sub-leading) lepton. The invariant mass of the di-lepton system must be compatible with the Z boson hypothesis, satisfying a m_{Vh} dependent condition. The condition suppresses contributions from backgrounds without real $Z \to \ell\ell$ decays, as $t\bar{t}$ and multijet backgrounds. The leptons within $t\bar{t}$ processes are produced in leptonic W boson decays and thus contain neutrinos. To reduce such background a veto on $E_{\mathrm{T}}^{\mathrm{miss}}$ is applied via the m_{Vh} dependent condition given in Table 4.2.

The Z boson p_{T}^{Z} has to satisfy a requirement increasing with higher resonance masses, reflecting higher expected momenta in high-mass resonances. The p_{T}^{Z} requirement is repealed for events with $m_{Vh} < 320$ GeV.

The signal acceptance and selection efficiency is strongly dependent on the resonance mass and moderately dependent on the spin of the resonance. The acceptance × efficiency for the Z' and the pseudo-scalar A (bb$A$ mode and ggA mode) is shown in Fig. 4.7.

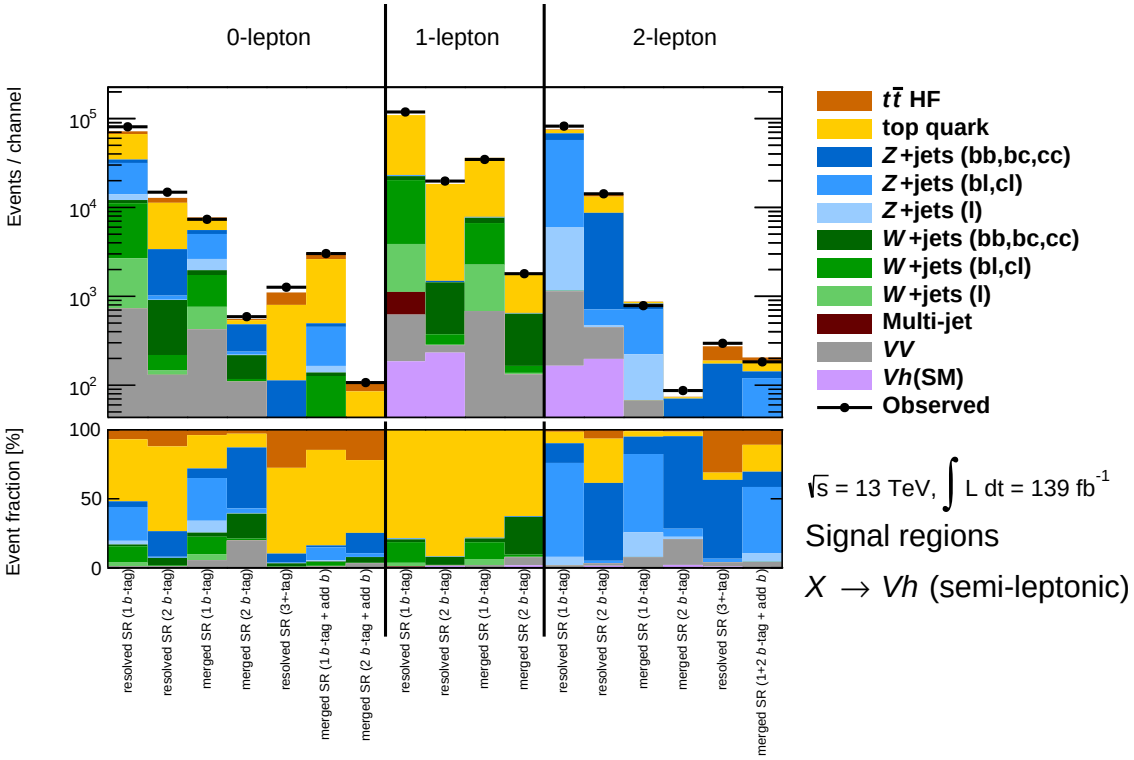

Figure 4.8: Overview of the expected background and observed total event yields in the various signal regions employed in the Vh resonance search. The top quark and $t\bar{t}$+HF background components are combined into a single sample for the statistical interpretation of data when searching for the HVT Z' and W' bosons as well as the ggA mode of the pseudo-scalar A boson production. The lower panel shows the relative contribution of the corresponding background component with respect to the total expected background.

4.3 Background estimation

The 1-lepton channel and the *resolved* regions in the 0-lepton channels are mainly occupied by top quark background components. The relative contribution of top quark background components decreases with increasing diboson mass m_{Vh}. For a high mass HVT resonance, i.e. not yet excluded Z' or W' masses, the most sensitive kinematic regime are predicted to be dominated by the Z+jets (bb,bc,cc) and W+jets (bb,bc,cc) background components. The 0- and 2-lepton channel is occupied by Z+jets background components, while the 0 and 1-lepton channels also yield significant contributions from W+jets.

On the other side, the top quark contribution increases with increasing b-tagging multiplicities and becomes the most relevant background component in the bb$A$ mode sensitive regions in the 0-lepton channel. Signal regions with at least 3 b-tagged jets (small-R jets or track jets) in the 0-lepton channel are dominated with a fraction of over 90% by top quark background components. As described

in Section 4.1, for the interpretation of data by a 2HDM signal produced via the bb$A$ mode, the $t\bar{t}$+HF is treated individually. While this $t\bar{t}$+HF component contributes less than 30% of all top quark background components in the 0-lepton channel, $t\bar{t}$+HF is the major top quark background component in the 2-lepton channel, with up to 80% of the top quark background processes.

Before studying data in the actual signal region (SR) comparisons between prediction and observation are required to ensure the validity of the background description. This is possible in signal depleted event selections using recorded data without risking an observation bias.

In addition to the 25 SRs, signal depleted CRs are defined to control the background modeling, i.e. to constrain open parameters in the background description. In particular, the normalization of the main background components, top quark background components and V+jets, is determined entirely in the final fit. The constraint on individual background components is driven by dedicated regions with negligible signal content and kinematically closely related to the signal regions. The total expected and observed event yields in the control regions is shown in Fig. 4.9.

Two types of CRs are defined: The inversion of the Higgs boson candidate mass requirement, referred to as $m_{jj/J}$-sideband CRs, is defined corresponding to each SR for the reconstructed mass, in the range of 50 GeV $\leq m_{bb} \leq$ 200 GeV, sparing the signal regions. The $m_{jj/J}$-sideband CRs in the 2-lepton channel are not incorporated in the final fit but is used to validate and correct the background description.

The second type of control region targets the top quark background components. It is defined in the 2-lepton channel by inverting the same-flavor condition of the two leptons, i.e. requiring an electron and a muon. The $t\bar{t}$ CR is almost pure in top quark background components, which can be seen in Fig. 4.9. It gives a good handle on the open parameters in the modeling of top quark background components, in particular the top quark normalization and relative composition of its sub-samples $t\bar{t}$+HF and $t\bar{t}$+LF in the interpretation of a signal produced via the bb$A$ mode. The $m_{jj/J}$-sideband CRs, the $t\bar{t}$ CR and the signal regions are simultaneously fitted in the final statistical interpretation in Section 4.7 and enable the constraining of free parameters in the background prediction. In the interpretation of data by a signal produced via the bb$A$ mode, the $m_{jj/J}$-sideband CRs are not included, since the additional signal regions with *add. b*-tag are sufficient to constrain the open parameters in the fit.

Additionally, a further group of signal depleted event selection is used, referred to as validation regions (VR). In contrast to the CRs, the VRs are not included in the fit but serve background validation and correction studies. For all sub-channels an event selection with an applied b-tag veto is used to validate the description of V+jets background components. The 0-tag VRs are defined as an $m_{jj/J}$ inclusive selection and have better statistical precision than the SRs. The inclusion of the 0-tag validation region (VR) in the fit would dominate the determination of many free parameters. A determination of parameters in this region is disfavored, since the most dominant process in this region is V+jets (l), which has an almost negligible contribution to the most signal-sensitive SRs, i.e. regions with 2 b-tagged jets. However, known mismodelings in the simulation of kinematic observables in similar phase space [150] in samples generated by SHERPA are studied in this region.

Lastly, to estimate the effect of non-prompt leptons by either multi-jet background components or semi-leptonic decays of $t\bar{t}$ or Wt processes in the 2-lepton channel, same-sign VRs are designed. Same-sign VRs are defined by the same selection criteria as the SR, but demand two muons of the

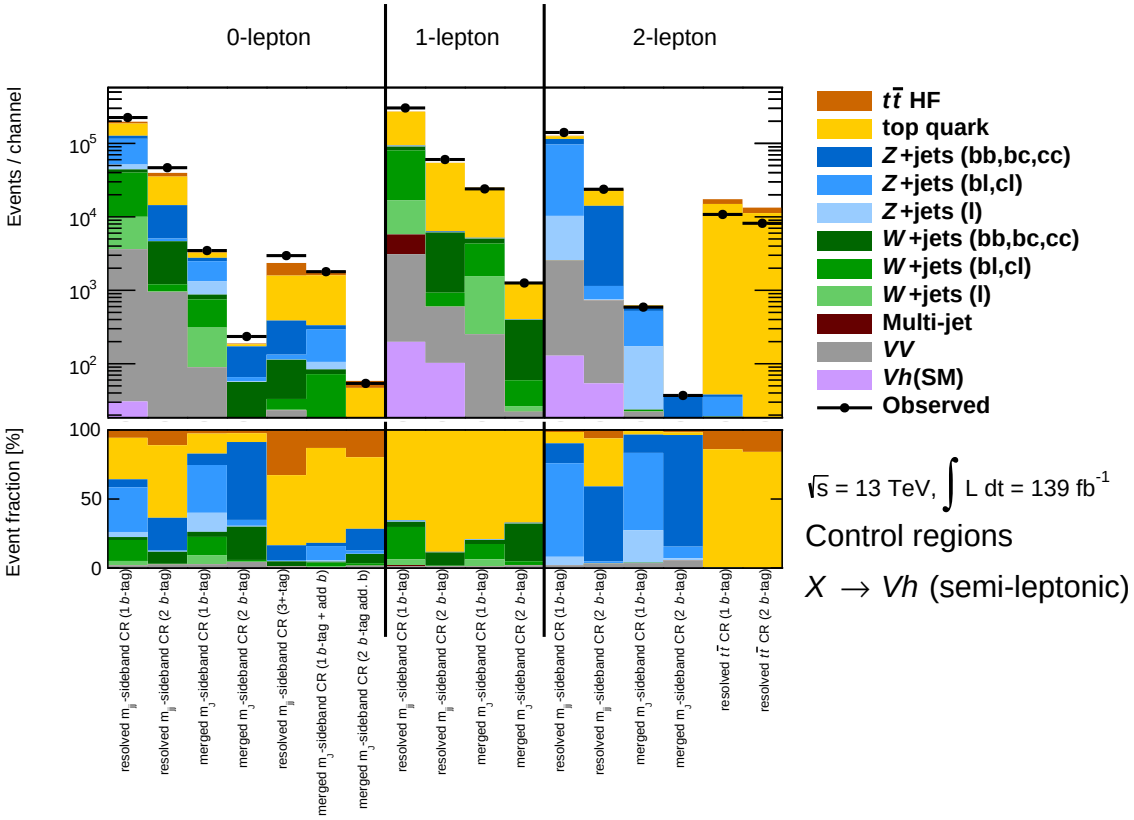

Figure 4.9: Overview of the expected and observed total background yields in the various control regions employed in the Vh resonance search. The background components top quark and $t\bar{t}$+HF are combined for the statistical interpretation of the Z', the W' and the ggA mode of the pseudo-scalar A production. The lower panel shows the relative contribution of the corresponding background components. The $m_{jj/J}$-sideband CRs in the 2-lepton channel are not incorporated in the final fit but is used to validate and correct the background description.

same sign. The same-sign VRs show that the impact of non-prompt lepton background contributions is negligible for the 2-lepton sub-channel.

Background modeling correction

All observables used for either the event selection or the reconstruction of the final discriminant, m_{Vh}, were studied *blinded* in the control region (CR) and VR. Some kinematic observables show significant and systematic discrepancies between prediction and observation. This expresses as a systematic slope in the ratio between observation and prediction as a function of the examined observables. Due to the close relationship between $m_{jj/J}$-sideband CRs and SRs, the observed slope is expected to be similar in the SRs. Observed mismodeled variables in this sense are the p_{T} distributions of the Higgs candidate and the p_{T} distribution of the reconstructed gauge boson.

The the p_{T} distribution of the Higgs candidate, p_{T}^{jj}, in the 0- and 2-lepton *resolved* categories are corrected by a scale factor applied to all V+jets events.The p_{T}^{jj} mismodeling in the 0- and 2-lepton channel is assumed to be caused by Z+jets background only, because the top quark background components do not show corresponding slopes in the dedicated $t\bar{t}$ CR. The scale factor is derived within CRs or VRs.

In the 0-lepton channel, the resolved 0-tag VR region is used to derive the scale factor for events with the *resolved* topology. For this purpose, the predicted p_{T}^{jj} distribution from non-Z+jets background components are subtracted from the observed p_{T}^{jj} distribution. Subsequently, the ratio between the p_{T}^{jj} distributions of the reduced observation and Z+jets background components is compensated by an adequate p_{T}^{jj} dependent scale factor. Similar scale factor functions are also computed in the $m_{jj/J}$-sideband CRs for different b-tagging multiplicities. The so-derived functions agreed within the statistical uncertainty with the 0-tag VR but suffered from poor statistic precision. The weight function for events in the 0-lepton channel, illustrated in Fig. 4.10, is applied to all events reconstructed by the *resolved* reconstruction technique.

Similar studies in the m_{jj}-sideband CRs of the 2-lepton channel show significant differences in the derived weight functions for different b-tagging multiplicities. Therefore, two different weight functions are used for all signal and control regions with the according b-tagging multiplicity, as shown in Fig. 4.10.

For both, the 0- and the 2-lepton channel, the unweighted distributions are treated as a 1σ uncertainty on the distribution of the final discriminant in the fit.

Other variables, i.e. $p_{\mathrm{T}}^{\mathrm{miss}}$, p_{T}^{V}, $E_{\mathrm{T}}^{\mathrm{miss}}$ and p_{T}^{J}, also show mismodelings. Due to their correlation to the p_{T}^{jj} distribution, some mismodelings can be partially fixed by the p_{T}^{jj} reweighting. In addition, these observables are also the base for a analogous reweighting procedure. However, subsequent *blinded* CR, background-only fitting studies show the corresponding unweighted distribution to be more consistent with the data than the reweighted distributions. Therefore, instead of using the reweighted function as nominal prediction in the final fit, the additionally reweighted distribution are used as 1σ variation of corresponding non-closure uncertainties.

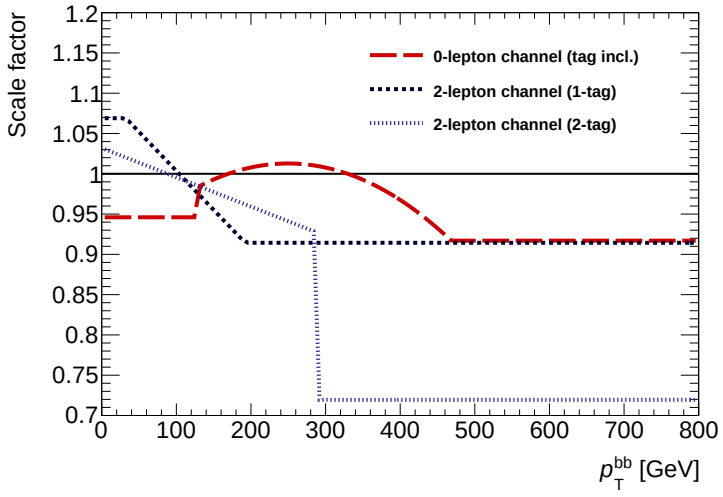

Figure 4.10: Event-wise scale factors as a function of the p_T^{jj} are applied to events reconstructed by the *resolved* reconstruction technique in the 0- and 2-lepton channels. The scale factor remains constant for values beyond the axis range.

Only in the case of the 0- and 2-lepton channels, the nominal distribution is the result of a p_T^{jj}-reweighting for the and without reweigting in the 1-lepton channel.

In the 0-lepton channel a non-closure uncertainty corresponding to the p_T^{miss}-reweighting is imposed to all $m_{T,Zh}$ distributions of all *resolved* sub-channels. Two distinct p_T^{miss}-reweighting functions are defined separately for the 1 and for the 2 *b*-tag data regions. In the 1-lepton a non-closure uncertainty that is derived by a reweighing on the *W* boson momentum, separately for 1-and 2-tag data regions with the *resolved* event topology.

In all three channels a $m_{(T,)Vh}$ distribution resulting from a Higgs boson candidate p_T^J-reweighting specifies a further non-closure uncertainty for the *merged* categories. The underlying function of p_T^J is derived separately for all regions with different tagging multiplicities in the 0- and 1-lepton channel, and (tag-)inclusively for the 2-lepton channel. Latter is treated inclusively due to the poorer statistical population in the merged categories of the 2-lepton channel.

4.4 Systematic uncertainties

Imperfect theory description of signal and background processes as well as imperfect simulation of the detector response lead to a number of systematic uncertainties, impacting the final statistical interpretation of data.

These systematic uncertainties can be classified into three groups: The experimental uncertainties from the imperfect description of particle reconstruction and identification efficiency, as well as their energy or momentum measurement; the theory uncertainty on the predicted cross section; and the modeling of kinematic properties of signal and background processes and uncertainties on the data-driven normalization and modeling corrections based on the dedicated CRs (c.f. Section 4.3).

A given source of a systematic uncertainty will modify the normalization or the shape of the final discriminant $m_{(\mathrm{T},)\mathrm{Vh}}$ in a given process. The resulting $m_{(\mathrm{T},)\mathrm{Vh}}$ distribution corresponding to the uncertainty of one standard deviation is referred to as *variation* with respect to the *nominal* distribution and is used in the final fit as a constraint on the parameterized description of the final discriminant.

Experimental uncertainties are induced by biases in the instrumentation setup, e.g. miscalibrated energy scale or reconstruction efficiency. Such sources simultaneously affect all signal and background processes. Thus, the impact of a given experimental source of uncertainty is correlated among all signal and control regions and physics processes. These uncertainties are discussed in Section 4.4.1.

Theoretical modeling uncertainties such as the uncertainties on the parton shower model or the choice of the renormalization and factorization scales, are related to the event generation. In addition, the uncertainties due to higher-order loop corrections may affect both, the normalization and to a smaller extent also the kinematic properties of a given process. Such theory uncertainties are a priori process-related and thus uncorrelated among all signal and background processes. These theory uncertainties are discussed in Sections 4.4.2 to 4.4.4.

Finally, systematic differences between prediction and data are observed in the dedicated CRs (c.f. Section 4.3). These mismodelings are not covered by the sources of uncertainties mentioned above and are taken into account via dedicated non-closure uncertainties.

4.4.1 Experimental uncertainties

Experimental uncertainties arise from the imperfect simulation of the detector instrumentation response to final state particles, affecting the luminosity measurement, trigger efficiencies, reconstruction and identification of leptons and jets, b-tagging efficiencies and estimation of non-suppressed pile-up contributions to jets. Impact of experimental uncertainties on the discriminant observables in this analysis is estimated by varying the corresponding parameters in the simulation of the detector response, separately for each simulated sample. Each of these experimental systematic uncertainties simultaneously affect the different signal and background processes in all data and control region regions.

Experimental uncertainties can be classified by the reconstructed object they are related to: Small-R and large-R jets, muons, electrons, the b-tagging, or to the event as a whole.

small-R jets The calibration of the jet energy scale (JES) and the measurement of the jet energy resolution (JER)[51] is subject to multiple sources of uncertainty. The JES is determined in-situ in three stages (c.f. Section 2.4.5) Each of these steps induces systematic uncertainties, e.g. due to simulation or determination of the momentum of the recoiling object. Embracing effects also from jet flavor dependence, background jet rejection efficiency, the calibration has been performed with a set of 125 parameters in total. In order to reduce the number of free parameter, an eigenvector decomposition has been performed for the 98 1-dimensional terms (i.e terms only depending on p_{T}) to 15 effective parameters. The effective parameters are grouped by the uncertainties' origins: Detector effects, fragmentation and hadronization model, statistical uncertainty in the calibration and a mixed term. Including two dimensional terms, e.g η-dependent, a total of 30 individual uncertainties from the JES calibration are considered. Each of these uncertainties are treated as individual parameter in the final statistical interpretation of data. Furthermore, the measured width of the JER is simulated in MC by a Gaussian smearing of the jet energy. The width of the smearing is determined *in-situ* [51]. The covariance matrix has been decomposed to the six leading effective terms, plus one term encapsulating the residual uncertainty. The impact of the uncertainties on the JER to the m_{Vh}-distribution is propagated by an additional smearing corresponding to each effective parameter of the JER measurement. The effect on the normalization induced by uncertainties resulting from the JES (JER) calibration, added in quadrature, sums up to 3.3% (0.2%) in the signal regions with the *resolved* event topology and 1.2% (0.5%) in signal regions with the *merged* event topology.

The JVT rejects jets that do not have their origin in the events primary vertex. The efficiency of the JVT has been estimated [89]. The impact of uncertainties on the JVT efficiency to the $m_{(\mathrm{T},)\mathrm{Vh}}$ distribution is evaluated. The normalization of the total background amounts to 0.6% (0.1%) in regions with the *resolved* (*merged*) event topology.

large-R jets The uncertainties induced by the large-R-jets are estimated by comparing calorimeter- and track-based energy measurements and mass measurements in observation and prediction [78, 81]. The covariance matrix describing the uncertainties in the subsidiary JES calibration measurement is decomposed in 5 orthogonal uncertainty components, describing a baseline term, the residual difference between observation and prediction, the fragmentation and hadronization model, the total statistical uncertainty of the calibration and uncertainties related to the tracking. The jet energy resolution (JER) for large-R jets are evaluated by an additional smearing of the jets' mass or energy. The smearing is performed by an additional component, a relative 2%, reflecting the uncertainty on the measured resolution [81].

The jet mass resolution (JMR) for large-R jets is simulated, similar to the JER, by smearing the reconstructed jet mass according to a Gaussian distributed random value with the width of the JMR as obtained from the calibration. The JMR is a p_{T} and η dependent property. The uncertainty on this JMR is estimated to be 20% of the nominal JMR [81, 186]. The impact of this uncertainty on the event reconstruction, the event selection and the distribution of the final discriminant $m_{(\mathrm{T},)\mathrm{Vh}}$ is evaluated by an additional smearing of all reconstructed large-R jets in the event. The smearing is performed by artificially modifying the jet four-momentum to match the large-R mass, which is obtained by employing Gaussian distributed random values with the width of 20% of the nominal JMR. The distribution obtained by the smearing represents a 20% worse JMR, reflecting the upper $+1\sigma$ JMR uncertainty. Eventually, the obtained $m_{(\mathrm{T},)\mathrm{Vh}}$ distribution is mirrored with respect to the nominal

$m_{(\mathrm{T},)\mathrm{Vh}}$ distribution, representing the -1σ JMR uncertainty. The $\pm 1\sigma$ variations are fully correlated between all sample, signal and control regions. Statistical fluctuations in the ratio between the smeared and the nominal distributions are smoothed by the methodology described in Section 4.4.2. Due to large statistical fluctuations in the regime above $m_{(\mathrm{T},)\mathrm{Vh}} \approx 2$ TeV for background processes, only one bin is used to cover the range between 2 and 5 TeV.

The smearing is applied to the jets before the object and event selection and is also affecting the jet transverse momentum to a small extent. The $m_{(\mathrm{T},)\mathrm{Vh}}$ value of an individual event is affected by the m_J smearing only to a minor degree, since the resonance mass mainly assembles from the momentum of the decay products and their separation angle. The main effect of smearing is the induced migration between the $m_{jj/J}$-sideband CRs and the corresponding signal regions. The smearing reduces the background content in the m_{jj}-sideband CRs by 0.5% above 700 GeV in all channels. The migration effects are differently pronounced, depending on the transverse momentum of the Higgs boson candidate, that is strongly correlated to the reconstructed diboson mass. Therefore, the shape of the $m_{(\mathrm{T},)\mathrm{Vh}}$ is affected by the uncertainty on the JMR.

The impact of the JMR uncertainty on the final discriminant $m_{(\mathrm{T},)\mathrm{Vh}}$ distribution depends whether the main part of the mass distribution m_J of the corresponding sample is distributed within, below or above the m_J selection window. The effect of the JMR uncertainty is therefore expected to be different between top quark, V+jets, SM diboson processes (Vh and VV) and signal processes and evaluated separately for each of these background components. To increase statistical precision, the relative uncertainty for all Z+jets and W+jets components is determined from an V+jets inclusive selection. The studied effect of the JMR uncertainty on the QCD induced jets is expected to behave similar for W+jets and Z+jets.

Fig. 4.11 shows m_J distribution of for top quark and V+jets background components and the relative change of the m_J and $m_{\mathrm{T,Zh}}$ distributions. The top quark component is shown for the 1-lepton 2 b-tag merged m_J-sideband CR and signal region and the V+jets in the 0-lepton 2 b-tag merged m_J-sideband CR and signal region. These both background components are each the leading background components in the respective regions. A more complete set of plots showing JMR uncertainties including the different background components in all three channels as well as 1 tag regions and the effect on the *resolved* m_{jj}-sideband CRs is given in Appendix C.2. No difference is seen between 1, 2 b-tag regions. The 1, 2 and 3+ b-tag $m_{jj/J}$-sideband CRs are evaluated inclusively. Furthermore, no distinction is made between events with and without additional b-tagged track jets, that are not associated to the Higgs boson candidate. Since the *resolved* m_{jj}-sideband CRs are prioritized over the *merged* m_J-sideband CRs, a step is visible between SR and the m_J-sideband CR in Figs. 4.11(a) and 4.11(b). The main migration occurs between the *merged* SR and the *resolved* m_{jj}-sideband CRs.

For a large range in $m_{(\mathrm{T},)\mathrm{Vh}}$ (above 1 TeV), the contributions from top quark in the signal region is increased by the additional smearing by about, while it is reduced in the $m_{jj/J}$-sideband CRs. In contrast, contributions from the V+jets component is increased by 2% for masses above ≈ 1.2 TeV and reduced by 2% for low masses (≈ 500 GeV), leading to a harder $m_{(\mathrm{T},)\mathrm{Vh}}$ spectrum. The impact of the JMR uncertainty on the signal region $m_{(\mathrm{T},)\mathrm{Vh}}$ distribution is lower than the statistical precision of the MC samples and less than 0.5%

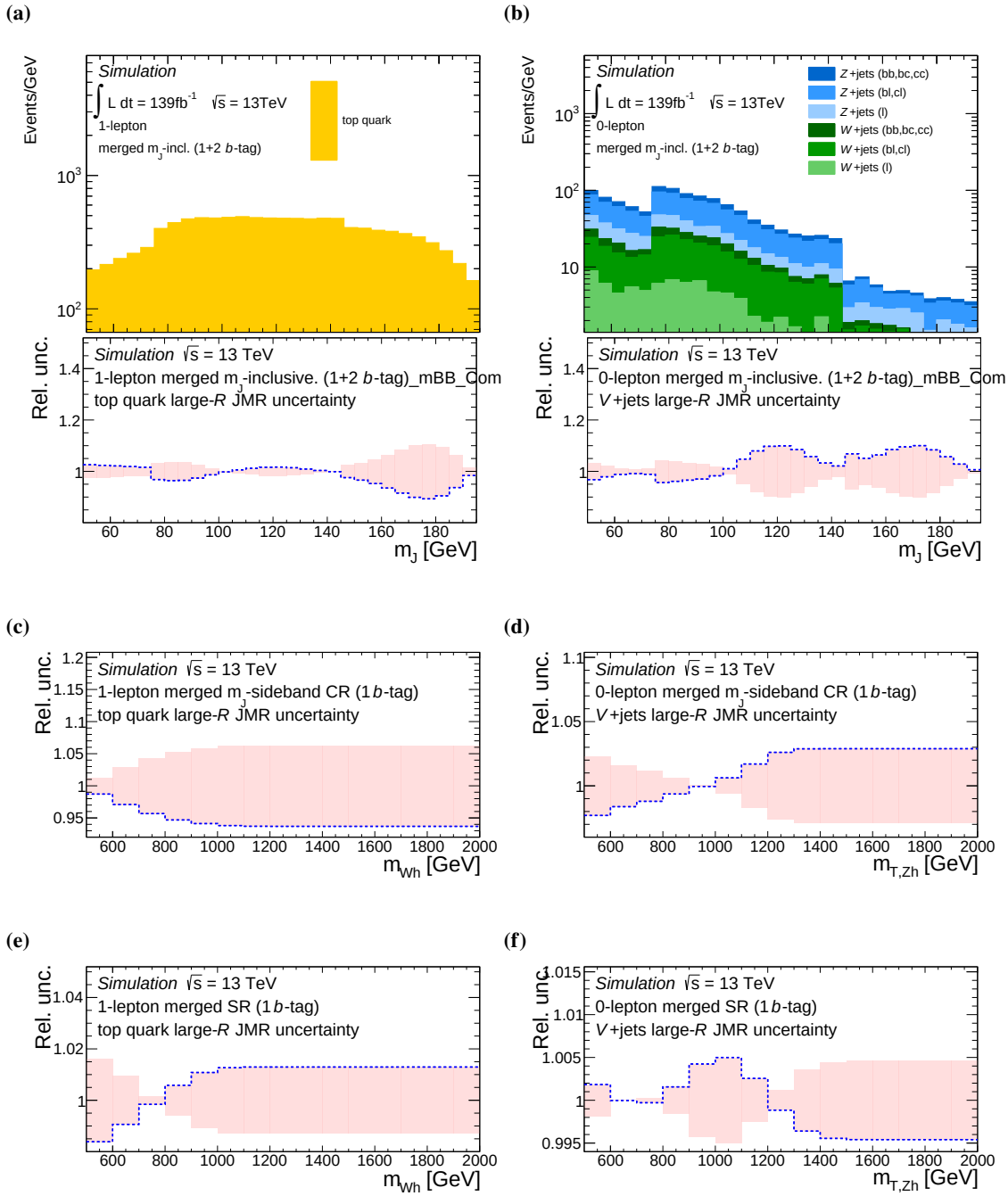

Figure 4.11: (a),(b) Expected m_J distribution of Higgs boson candidate jets in the m_J-inclusive combination of SR and m_J-sideband CR for (2 b-tag) for (left) top quark and (right) V+jets background components. The ratio panel shows the relative uncertainty effect of the JMR uncertainty. The relative change obtained by the described smearing is indicated as blue, dashed line ($+1\sigma$). The impact of the JMR uncertainty on the $m_{(\mathrm{T},)\mathrm{Vh}}$ distribution is shown in the 2 b-tag (c),(d) m_J-sideband CR and (e),(f) signal region for (left) the top quark and (right) the V+jets background components.

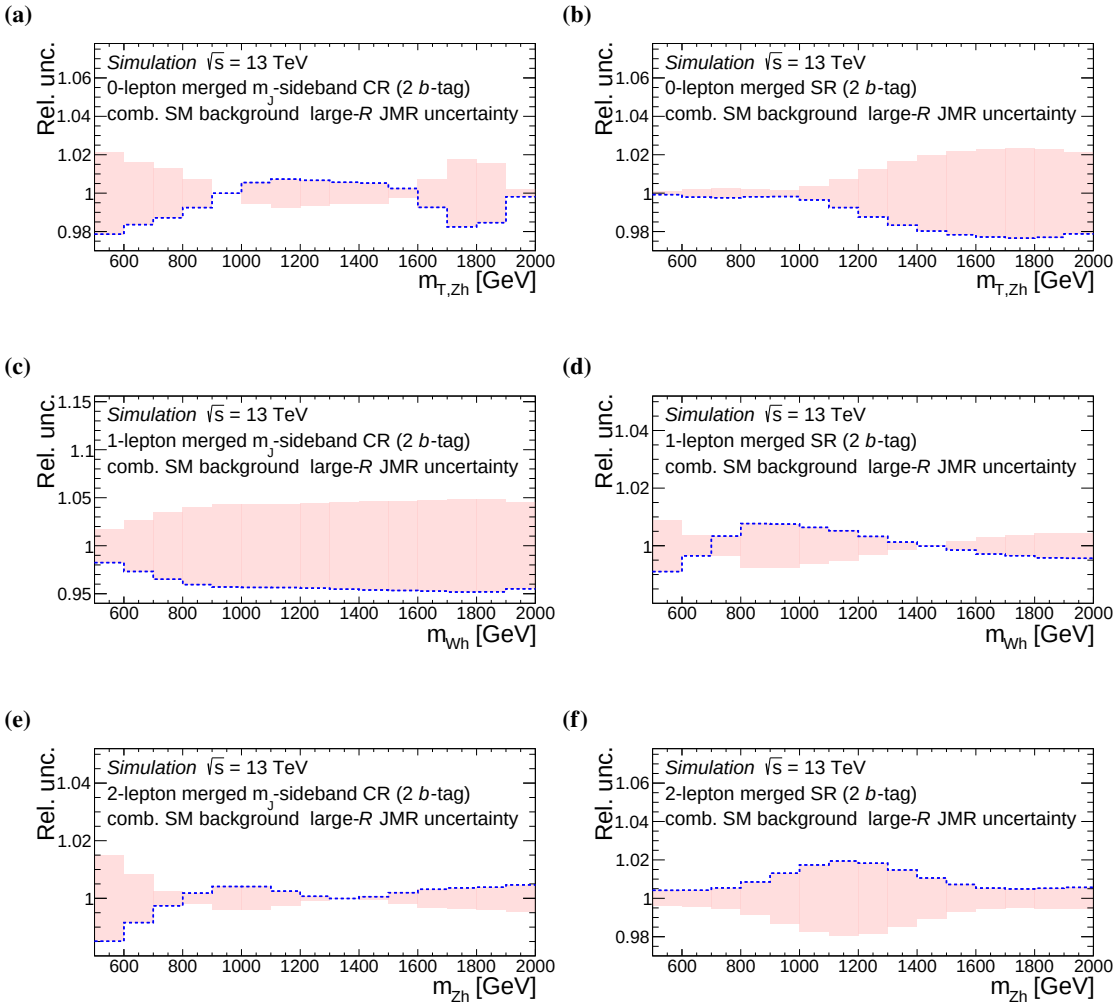

Figure 4.12: The impact of the JMR uncertainty on the combined expected background $m_{(\mathrm{T},)\mathrm{Vh}}$ distribution in the 2 b-tag (a),(c),(e) m_J-sideband CR and (b),(d),(f) signal region of the (a),(b) 0-, (c),(d) 1- and (e),(f) 2-lepton channel. The relative change obtained by the described smearing is indicated as blue, dashed line ($+1\sigma$).

The described relative change of the $m_{(\mathrm{T},)\mathrm{Vh}}$ distribution for top quark and V+jets background components agrees among the channels within statistical uncertainties. Since the background composition is different, the total background expectation varies differently for the three channels, which is shown in Fig. 4.12. The total uncertainty is largest for the m_J-sideband CRs of the 1-lepton channel with 5%, which is dominated by top quark background components. The uncertainty on the large-R JMR in other channels amounts to about 1-2%.

Signal processes are affected by the described smearing by a migration from the SRs into the *resolved* and *merged* $m_{jj/J}$-sideband CRs. No impact on the shape of the signal distribution is induced by the JMR uncertainties over the relevant range of the $m_{(\mathrm{T},)\mathrm{Vh}}$ distribution. The relevant range is

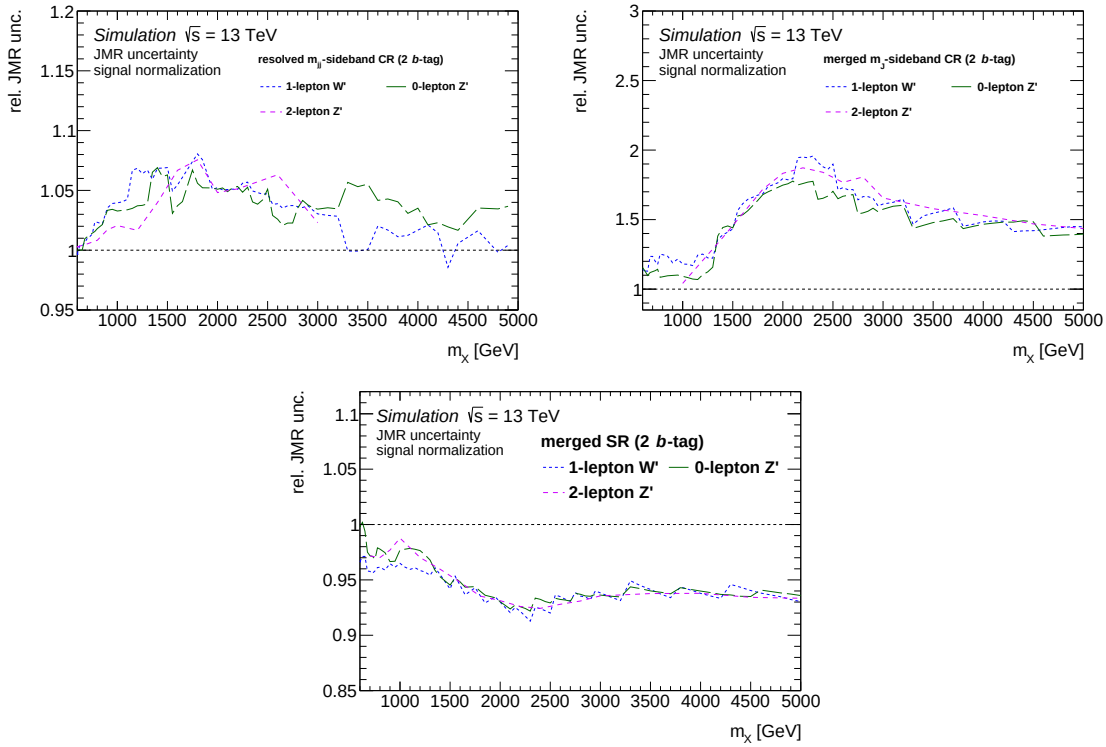

Figure 4.13: The global normalization uncertainty on the signal efficiency as a function of the resonance mass in the (a) *resolved* m_{jj}-sideband CR, (b) *merged* m_J-sideband CR and (c) the signal region with 2 b-tagged jets.

studied for each simulated signal process between 0.7 to 1.2 times the resonance mass. The total normalization uncertainty in the SR and the *resolved* and *merged* $m_{jj/J}$-sideband CRs is shown for HVT Z'/W'resonance masses between 500 GeV and 5 TeV in Fig. 4.13. The effect of the JMR uncertainty on the signal efficiencies is independent on the signal model but only on the signal mass. This also holds for the other considered signal scenarios (bb$A$ mode, ggA mode in the 0- and 2 lepton channel as well as the W' recorded in the 0-lepton channel). The mass smearing decreases the signal efficiency in the *merged* SRs by $\approx$ 3% for a resonance mass of 1 TeV and up to 8% for resonance masses of 3 TeV and above. The smeared large-R jet mass leads to an increased signal contribution in the m_J-sideband CRs by up to 100% in the *merged* m_J-sideband CRs for the 2.5 TeV and around 5% for masses above $\approx$ 1.2 TeV.

The smaller loss in signal sensitivity for lower resonance masses is explained by the generally better mass resolution at transverse momenta (c.f. Fig. 3.10). Additionally, low resonance mass signal events migrate primarily into the *resolved* m_{jj}-sideband CRs, which are prioritized over the *merged* m_J-sideband CRs.

***b*-tagging** Uncertainties on the determination of the b-tagging efficiency and misidentification rate impact the m_{Vh}-distribution. Data-to-simulation correction factors have been measured in samples of $t\bar{t} \rightarrow b\bar{q}W^+W^- \rightarrow \ell\nu q\bar{q}b\bar{b}$ events for both calorimeter and track jets [98, 100, 183]. Uncertainties on

these correction factors are decomposed into uncorrelated components pertaining the flavor content for b-jets, c-jets and light-flavor jets. An additional component is added by extrapolating high-p_{T} b- and c-jet that has been extracted from simulations.

Leptons Systematic uncertainties originating from the reconstruction, identification, isolation and trigger efficiencies of muons [187] and electrons [70] have a relative small effect on the result. The impact on the normalization by uncertainties resulting from muons is below 0.4% and from electrons around 1%. However, in the high resonance mass regime ($\gtrsim 1.2TeV$), the spacial resolution of of the muon trajectory due to detector alignment has the most dominating effect on the signal sensitivity, referred to as the *sagitta resolution bias*. In a muon trajectory fixed by three detector interactions, the sagitta is defined as the distance between the middle interaction point and the connection line between the both outer points. For a straight line of a highly boosted muon, the reconstructed momentum is highly sensitive on this source of uncertainty.

Pile-up and luminosity To account for differences in the predictions of the average number of events per bunch crossing between data and simulation, a correction factor has been applied. The average number of events quantifies the amount of pile-up activity. The effect of the uncertainty on this so-called *pile-up reweighting* has been evaluated. Finally, a global luminosity uncertainty of 1.7% is applied to the normalization of the simulations [188, 189].

Other uncertainties have been considered, but were found to have a negligible effect: The uncertainty from τ-lepton reconstruction and calibration have been considered using the recommendations in Ref. [190]. Effects on the $E_{\mathrm{T}}^{\mathrm{miss}}$ reconstruction from energy scale and resolution of the small-R jets, leptons and the soft-track [191, 192] have been studied.

Smoothing and symmetrization of experimental uncertainties.

The finite sample size of the MC generated background and signal samples induce statistical uncertainty leading to large fluctuations between the *nominal* distribution and the *variation*, that are unrelated to the described source of uncertainty. Such fluctuations can cause the fit in the final interpretation of data to spuriously constrain the describing parameters. The assumption is made, that systematic relative systematic uncertainties appear smoothly over the range in $m_{(\mathrm{T},)\mathrm{Vh}}$ and are by construction centered symmetric around the nominal value. To mitigate the statistical fluctuations, a smoothing algorithm is applied on the relative uncertainty, i.e. the ration between variation and *nominal* distribution. After choosing adequate bin sizes, with less than 5% statistical uncertainty, the algorithm identifies all local extrema of the relative uncertainty. Then the bin with the smallest extrema, i.e. most consistent with the neighboring bin, is merged with the neighboring bin. The merging is repeated until only 4 local extrema remain.

The resulting $+1\sigma$ and -1σ distributions are then symmetrized in each bin by,

$$\tilde{n}_{\pm\sigma} = n_{\mathrm{nominal}} \pm \frac{n_{+\sigma} - n_{-\sigma}}{n_{+\sigma} + n_{-\sigma}}. \tag{4.5}$$

4.4.2 Theory uncertainties from *surrogate* samples

The *nominal* predictions as well as the *variations* describing the experimental uncertainties are derived by the full simulation [193] of the ATLAS detector as described in section Section 2.3. This kind of samples is referred to as *standard* samples in this paragraph.

Those *standard* samples consume huge amounts of computing resources for the full simulation of the detector which is not necessary for the estimation of theoretical uncertainties. For some sources of modeling uncertainties, no or only a small subset of the *standard* samples has been simulated. Two less resource consuming methods are employed to produce corresponding samples. A faster detector simulation is performed using AtlFast [194], that is limited in accuracy. AtlFast still generates predictions at the level of reconstructed events. In the other method, the process of detector simulation and object reconstruction is entirely skipped and the physics objects are taken directly from the objects at particle level. Such samples, as well as samples corresponding to a small subset of the *standard* samples are collectively referred to as *surrogate* samples.in this paragraph. The context-related meaning of the term *surrogate* sample is summarized in Appendix B.12 and explicitly denoted in the corresponding subsections. This paragraph is describing generically the treatment of the transfer from *surrogate* samples to *standard* samples, for the use in the final statistical interpretation of data. In order to not describe effects by the variation that actually stem from differences between *standard* samples and *surrogate* sample, for each kind of *surrogate* sample a *nominal* sample has been to serve as reference. The choice of the bin sizes is optimized for each interpretation separately to optimize search sensitivity. Evaluating the systematic uncertainty is therefore required in a generic, fine binning, that can be rearranged to match the optimized bin choice of the various interpretations.

Problems arise while estimating relative uncertainties in *surrogate* samples and transfer them to *standard* samples by multiplication. The consecutive, bin-wise division and multiplication enhances statistical fluctuations and is undefined in regions of phase space with no occupation within the *surrogate* samples. The overestimation of the uncertainties in individual bins induced by statistical fluctuation would cause the final fit to spuriously constrain the describing parameters. Furthermore, an inter and extrapolation is needed for bins with no *surrogate* sample coverage.

An algorithm is developed that solves both problems and generates a quasi smooth function employing a Gaussian kernel smoothing (GKS). In a first step, the histograms are converted to coarser binned histograms. Too large bins would inflict unfair comparisons between events of different kinematics in a steeply falling spectrum, systematic effects could easily be hidden by a too coarse bin choice.

The histogram bin width is chosen such to have a statistical uncertainty on the considered bin content of both compared *surrogate* samples (*nominal* and *variation*) below a certain threshold. Starting at high $m_{\text{(T,)Vh}}$ mass values, each bin range is determined iteratively by lowering the lower boundary of each bin by 10 GeV until the above requirements are met. The employed threshold is adapted to each use case of studied physics process and data region to obtain a uniform statistical precision for 12 bins in each case.

The bin choice for signal samples is chosen relative to the resonance mass in steps of $0.1 \cdot m_X$ in the range of 0.5 to $1.2 \cdot m_X$ around the hypothesized signal mass.

The GKS has been applied to the relative variations derived employing the descibed binning. The kernels are defined via a Gauss distribution,

$$G(x, x_0) = \exp\left\{-\left(\frac{x - x_0}{2\sigma}\right)^2\right\},$$

with the bandwidth parameter σ. x and x_0 are values of the final discriminant, $m_{\text{(T,)Vh}}$. The smoothed relative uncertainty is sampled in a fine-granular, quasi-continuous histogram, C_{smooth}, equal the binning of the nominal distribution. Each C_{smooth} bin is computed as the Gaussian weighted sum of adjacent bins of the relative uncertainty, as

$$C_{\text{smooth}}(x) = \frac{1}{\sum_{x_0} G(x, x_0)} \sum_{x_0} G(x, x_0) \cdot C_0(x_0).$$

Bins of C_0 in which the relative deviation exceeds 70% and the statistical uncertainty of the variation is compatible with 1 are considered empty and are interpolated by the GKS.

The effect of using different bandwidth parameters in the GKS has been studied in detail and illustrating example results are shown in 4.14. The $m_{\text{T,Zh}}$ distribution for the nominal and an alternative MC setup of the $t\bar{t}$ background prescription. The curves resulting from the GKS are shown using $\sigma = 5$ GeV, $\sigma = 20$ GeV and $\sigma = 80$ GeV, respectively. For large σ values, the smoothed distribution tends to fail to describe characteristic features of the uncertainty curve, while for too small σ values the smoothed distribution tends to follow statistical fluctuations. The optimal choice of σ is dependent on the statistical power of the variation and has to be adapted to each process, and channel. As a starting point, $1/5$ of the root mean square (RMS) range of the corresponding background or signal $m_{\text{(T,)Vh}}$ distribution is used. If the resulting smoothed histogram C_{smooth} is in at least one bin not compatible within 1 standard deviation to the original histogram, C_0, then the bandwidth parameter is lowered by 20% and the smoothing repeated starting with C_0. The reduction of σ is repeated until C_{smooth} and C_0 is consistent within statistics. This procedure preserves statistically significant deviations but smooths statistical fluctuations. The bandwidth for the most m_{Vh} distributions turns out to be ≈ 35 GeV. The final result of the smoothing is not sensitive to the precise value of σ but rather on the order of magnitude.

After the smoothing, in case of two sided variations, the variations are symmetrized employing Eq. (4.5) or otherwise mirrored with respect to the nominal distribution. To prevent the smoothing to affect the corresponding global normalization, the smoothed variation is scaled to match the original normalization.

4.4.3 Theory uncertainties for background processes

The impact of the theory uncertainties on the expected background $m_{\text{(T,)Vh}}$ distributions is evaluated for the most relevant background sources, top quark, V+jets, which are studied separately for each signal and control region. The components of the V+jets (Z+jets (bb,bc,cc), Z+jets (bl,cl), Z+jets (l),

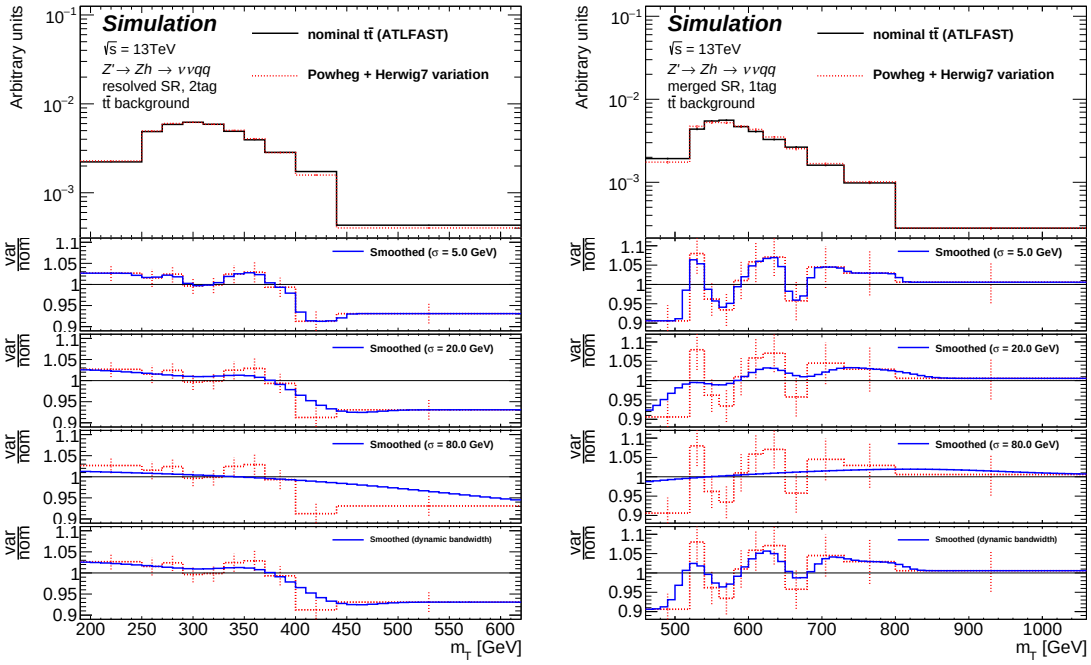

Figure 4.14: Demonstration of the evaluation of the m_{Vh} dependent relative uncertainty, in an example PYTHIA 8 – HERWIG 7 comparison. The prediction of m_{Vh} distributions using *surrogate* sample using nominal or varied generator setups have been compared. A Gaussian kernel smoothing has been applied to mitigate statistical fluctuations and interpolate empty areas. The optimal choice of bandwidth parameter is (sub-)channel dependent and, therefore, determined dynamically to return a smoothed curve being in statistical agreement with the original distribution.

W+jets (bb,bc,cc), W+jets (bl,cl), W+jets (l)) are evaluated individually. Theory uncertainties on the top quark background components are only estimated separately for the $t\bar{t}$+HF and the $t\bar{t}$+LF components for interpretation of data by the bb$A$ mode signal scenario, otherwise inclusively. The impact of all theory uncertainties are studied separately for each SR and CR.

Normalization differences implied by the different MC samples amount up to 40%. These large uncertainties are omitted by determining the normalization of those background processes entirely from data, directly from the simultaneous final fit of the $m_{(\mathrm{T},)\mathrm{Vh}}$ distribution in all signal and control regions (c.f. Section 4.6). Therefore, the theory uncertainties affect only the shape of the final discriminant $m_{(\mathrm{T},)\mathrm{Vh}}$ distribution (shape uncertainties) and the relative normalization between the various signal and control regions, as described below.

The impact of theory uncertainties on the shape of the $m_{(\mathrm{T},)\mathrm{Vh}}$ distribution from the minor background components, the VV and Vh diboson processes are considered to be negligible. The normalization of those background components is taken from the prediction of the MC generators and a conservative 50% uncertainty on the normalization is assumed.

The estimation of theory uncertainties for top quark background components follows the recommendations in Ref. [195].

ME generators and SMCs both generate final-state partons. The connection of ME final-state partons to those of the self-contained parton shower Monte Carlo (SMC) at NLO precision can be achieved by two different approaches [196]. POWHEG-BOX-v2, used for the *nominal* $t\bar{t}$ prediction, generates the hardest emission at NLO, independently of the PS algorithm. If interfaced with an SMC, like PYTHIA, final-state partons have to be matched to those jets generated by the SMC to avoid double-counting, inducing an uncertainty due to the choice of the matching scheme. An alternative way of generating events at NLO is implemented in MC@NLO. Individual terms describing final-state partons of in the ME and the SMC are divergent, but cancel each other when merged to the actual observable jet. The scheme used to merge these partons is as well a cause for an uncertainty, similar to the matching in the POWHEG-BOX approach. Both approaches are formally at same precision. Discrepancies between both methods are used to estimate the uncertainty arising from the ME matching method. Hence, the so-called *ME matching model* uncertainty to $t\bar{t}$ background estimated by a comparison of signal yields predicted by the *nominal* event generator to the prediction by an alternative event generator (MADGRAPH5_aMC@NLO [114]).

Two widely used approaches exist to model the PS. The *string* (or *Lund model* [59]) treats all lower-energetic gluons as fields lines. The *cluster model* describes the hadronization occurring via pre-confinement of color singlet clusters [60]. The uncertainty on the $t\bar{t}$ background event yields that originates from choice of the *PS model* is estimated by a comparison between two $t\bar{t}$ samples. The *nominal* sample is generated using PYTHIA 8, which describes the PS by the *string model*. An alternative sample is generated using HERWIG 7 [197] simulating the PS by the *cluster model*.

In the bb$A$ mode interpretation the background prediction the $t\bar{t}$ samples are split based on the presence of HF-labeled additional jets in the event. The *nominal* prediction of $t\bar{t}$ samples is made by generating the top-quark pair in the ME while additional b-quarks are generated by the SMC. An uncertainty on the b-quark generation by the SMC generator is additionally imposed, referred to as the $t\bar{t}b\bar{b}$ *4-flavor-scheme* uncertainty. The alternative MC generator setup describes the b-quarks as massive particles in the parton density function (PDF) and the ME generator produces an additional b-quark pair ($t\bar{t}$ $b\bar{b}$). For the estimation of the $t\bar{t}b\bar{b}$ *4-flavor-scheme* uncertainty, only events containing at least one b-labeled jet are included. The relative uncertainty is afterwards extrapolated to all events containing HF-labeled jet (i.e. b- or c-jets)[2].

The kinematic of the leading gluon emission is controlled in the PS algorithm by the cutoff scale, h_{damp}. The *nominal* value, found to well model the $t\bar{t}$ system, is chosen to 1.5 times the mass of the top-quark. To account for missing higher-order corrections in the ME calculation and the PS of the leading parton emission, h_{damp} is varied by a factor 2 to $h_{\text{damp}} = 3.0\ m_t$. The event samples used to estimate uncertainties due to PS, ME matching and a varied h_{damp} parameter were produced using ATLFAST [194] simplified detector simulation, and are transposed to fully simulated events as described in Section 4.4.2.

For top quark processes, also the A14 tune [198] and the factorization and renormalization scales, μ_{F} and μ_R, have impact on hadronically sensitive observables, referred to as *initial-state radiation (ISR) and final-state radiation (FSR)*. Those hadronic activities have been studied in Ref. [195] and the enveloping combination from μ_R, μ_F and A14 tune variations are identified as appropriate description for the variations on *ISR and FSR* activity, as given in Table 4.3. The impact of an increased or

[2] Note that corresponding b- (c-)quarks must not be a decay product of a top-quark (b-quark) to label the jet

decreased activity from *ISR and FSR* to the $m_{(\mathrm{T},)\mathrm{Vh}}$ distribution of top quark background contributions is studied. Event weights of the *nominal* $t\bar{t}$ sample are recalculated using the adjusted parameters for the renormalization and factorization scales and the eigenvector variations of the A14 tune.

Table 4.3: *Nominal* and *variation* values of parameters used to study the impacts of increased and decreased activity from initial-state radiation (ISR) and final-state radiation (FSR) in association with the $t\bar{t}$ system [195]. Parameters of the eigenvariations of the A14 tune are denoted only if larger than 1%.

Source of uncertainty	Varied parameter	Description		Up variation	Down variation
Initial state radiation	μ_R	Renormalization scale		0.5	2.0
	μ_F	Factorization scale		0.5	2.0
	`SpaceShower::alphaSvalue`	α_S for ISR	`VAR3c`	0.140	0.115
Final state radiation	μ_R	Renormalization scale		2.0	0.5
	`SpaceShower::pT0Ref`	ISR p_T cutoff	`VAR2`	1.60	1.50
	`SpaceShower::pTdampFudge`	ISR factorization/ renormalization scale damping	`VAR2`	1.04	1.08
	`TimeShower::alphaSvalue`	α_S for FSR	`VAR2`	0.139	0.111

The impact of the discussed relative uncertainties on the distribution of other minor top quark background components (i.e. single-top, $t\bar{t}V$ and $t\bar{t}h$) are assumed to be equal to the impact in $t\bar{t}$ samples. The derived relative uncertainties for the $t\bar{t}$ background component is therefore extrapolated to the other top quark background components.

The *ME matching model* and *PS model* uncertainties on V+jets background processes are both simulataneously accounted for by comparing the *nominal* predictions (Sherpa-v2.2.1) to those simulated by MG5_aMC@NLO-v2.2.2 interfaced with Pythia 8. The generator used for the *nominal* samples simulates the PS using the *cluster model*, while the alternative sample is simulated employing the *Lund model*. The *nominal* generator setup provides a prediction of up to two partons at NLO in the ME and up to two further at LO accuracy. Additional partons simulated by the PS generator are merged using the MEPS@NLO merging technique [199]. This technique is opposed to the MC@NLO matching technique employed in the alternative sample. Major differences in the algorithms result in a conservative estimation of a convoluted *matrix element matching and parton shower (ME+PS) modeling* uncertainty.

The renormalization and factorization scales are a source of uncertainties, These *QCD-scale* uncertainties for V+jets background components are estimated by varying the renormalization scale, μ_R, and the factorization scale, μ_F, individually by a factor 2, omitting counter-directed variations, resulting in six combinations[3]. A event reweighting of *nominal* events is done by utilizing the varied parameters. The final *QCD-scale* uncertainty is obtained from the envelope of of all 6 individual *variations*.

For Z+jets in the 2-lepton channel, the *QCD-scale* uncertainties as well as PDF uncertainties described below are computed from *surrogate* samples, that are produced employing a full detector simulation but contain only Z bosons decaying to e^+e^-. The resulting relative variation is extrapolated to events decaying via $Z \to \mu^+\mu^-$.

For all major backgrounds, i.e. $t\bar{t}$ and V+jets, the impact of uncertainty of the parton density function (PDF) is estimated by a common methodology. Two approaches are used. First, the $m_{(\mathrm{T},)\mathrm{Vh}}$

[3] $(\mu_R, \mu_F) = (0.5, 0.5), (0.5, 1.0), (1.0, 0.5), (1.0, 2.0), (2.0, 1.0), (2.0, 2.0)$

Table 4.4: Nominal and alternative PDF sets that are used to estimate the impact of PDF uncertainties on the $m_{(\mathrm{T},)\mathrm{Vh}}$ distribution.

		PDF set	Accuracy	Ref.
SM background	*nominal*	NNPDF 3.0	NLO	[10]
	100 replica	NNPDF 3.0	NLO	
	alternative set	CT14	NLO	[11]
	alternative set	MMHT2014	NLO	[12]
	alternative set	PDF4LHC	NLO	[200]
HVT and 2HDM signals	*nominal*	NNPDF 2.3	LO	[116]
	alternative set	MSTW2008	LO	[120]
	alternative set	CT10	LO	[201]

distributions using the (*nominal*) NNPDF 30 PDF description is compared to the distributions obtained by employing alternative sets of PDF, measured by further collaborations [11, 12, 200]. Second, the intrinsic uncertainty given by the NNPDF collaboration is provided by an ensemble of 100 replica PDF sets, all within the bounds of their post-fit uncertainties [10]. In addition to the PDF itself, the impact of the strong coupling constant, α_S, used in the nominal description of the PDF is varied, the resulting distributions are studied independently and treated separately in the final interpretation of data. The event weights are recalculated based on the kinematics of the initial-state partons involved in the hard process using the LHAPDF toolkit [13], to match the kinematics of the above described *variations*.

The recommended procedure for the estimation of the impact of the intrinsic NNPDF uncertainty follows two steps. First, each of the 100 PDF sets is applied to predict the corresponding $m_{(\mathrm{T},)\mathrm{Vh}}$ distribution. In each bin in $m_{(\mathrm{T},)\mathrm{Vh}}$, the standard variation of the 100 predictions is considered as the internal NNPDF uncertainties, calculated as,

$$\Delta x_{\mathrm{NNPDF}} = \sqrt{\frac{1}{N-1}\sum_i (x_i - \bar{x})^2}\,, \tag{4.6}$$

with N being the total number of PDF in the ensemble, x_i the event yield corresponding to the i-th PDF set and $\bar{x}$ the average value with the ensemble. The variations obtained by this approach result each in an uncertainty that is with about 3% almost constant over the full range of $m_{(\mathrm{T},)\mathrm{Vh}}$, i.e. the impact on the shape of the $m_{(\mathrm{T},)\mathrm{Vh}}$ distribution becomes negligible and is in particular smaller than any of the individual variations. A different approach is to remove the normalization component of the distributions obtained from each individual element of the PDF ensemble before the bin-wise calculation of . The resulting shape of the envelope-like *variation* receives back a normalization component, that has to be removed by an adequate scaling, since the normalization of the background is left floating in the fit. While the 100 PDFs are physically compatible with the PDF measurement performed by NNPDF, the obtained shape does no longer resemble any of the 100 PDFs and in particular does not parameterize PDF-induced correlations between the bins in the final fit. Is is however a proper conservative estimation of internal uncertainties from the NNPDF. The final PDF uncertainty is considered as the largest variation arising from the internal uncertainties or the

comparisons of different PDF models.

Shape uncertainties

The numerous variations for the 9 (sub-)samples in 46 different SRs and CRs have been independently evaluated. The following section shows representative signal regions for the most dominant sources of background components. Since the normalization of the main backgrounds is determined entirely from the fit, differences in the normalization of between *nominal* distribution and the various *variations* are disregarded here and the normalization proportions between the signal and control region handled separately by introducing uncertainties on the migration between these data regions later.

Fig. 4.15 shows the theory shape uncertainties on the top quark background components in the 1-lepton 2 b-tag SRs with the *resolved* and the *merged* event topology. Corresponding uncertainties to top quark background components in the 0- and 2-lepton channel agree within the statistical precision of the used MC samples. Also, the results for the 1 and 2 b-tag region is in general found to be similar. A more complete set of plots showing modeling uncertainties for other data regions can be found in Appendix C.3. The largest impact on the shape of the m_{WH} distribution is seen in the *PS model* with an increase (decrease) of up to 2% low-mass (high-mass) tail, as can be seen in the first ratio panel. While the $m_{(\mathrm{T},)\mathrm{Vh}}$ spectrum of events with the *resolved* topology is predicted to be relative softer spectrum, the spectrum of events in the *merged* category are predicted to be harder. The distribution describing the *ME matching model* uncertainties predicts less entries in both the low- and high-mass tails by about 1%. The impact of *ISR and FSR* uncertainties less than 0.5%, while the impact of ISR even decreases for events with 2 b-tagged jets. The lower impact is explained by the selection bias of two jets that most likely stem from the hard-interactions top quark decay. PDF uncertainties in general have a low impact on the $m_{(\mathrm{T},)\mathrm{Vh}}$ shape. The impact of the incorporated α_S is less than 0.05% and is neglected in the final statistical interpretation of data. The comparison from the predictions obtained by different PDF models is found to be smaller than 0.5%, with MMHT2014 giving the most conservative uncertainty. The last row in Fig. 4.15 shows 6 out of the 100 deviations obtained by employing the corresponding alternative PDFs. The gray shade indicates the above described standard deviation (Section 4.4.3) including all 100 PDFs. The obtained uncertainty is larger than 0.5% and thus used as the more conservative estimation of for the PDF uncertainties in the final statistical interpretation of data.

The additional $t\bar{t}b\bar{b}$ *4-flavor-scheme* uncertainty is shown in Fig. 4.16, as applied to $t\bar{t}$+HF events in the interpretation of data with a signal produced via the bb$A$ mode. Here, the bb$A$ mode sensitive regions are shown, i.e. the 3+ b-tag region with the *resolved* event topology and the 2 b-tag region with the *merged* event topology with additional b-tagged track jets. The generation of the $b\bar{b}$ by the ME predicts a significantly harder spectrum, i.e. more $t\bar{t}$+HF events in the high-mass tails compared to the *nominal* predictions, with up to 15% (30%) for the *merged* (*resolved*) regions.

The impact of theory uncertainties on the shape of V+jets is shown in Fig. 4.17 for the Z+jets (bb,bc,cc) background component in the 0-lepton 2 b-tag regions with *resolved* and *merged* event topology. Further corresponding V+jets components and data regions can be found in Appendix C.3. As for the top quark background components, the dominating uncertainty is induced by the uncertainty on the *ME+PS modeling*. The $m_{(\mathrm{T},)\mathrm{Vh}}$ shape obtained by employing the alternative event generators

is predicted to be softer for the *resolved* data regions while simultaneously harder for the events with the *merged* event topology. The *ME+PS modeling* induces an uncertainty of up to 35% for masses higher than $\approx$ 700 GeV in events with the *resolved* event topology and 10% for events with the *merged* topology. Among the six probed variations on the *QCD-scales*, those with a varied factorization scale μ_F are found to give the most conservative limits. The renormalization scale μ_R has a significantly smaller effect on the shape of the final discriminant. However, the variations obtained by simultaneously varying the both scales by a factor 2 is used in the final statistical interpretation of data. The impact is up to 2% in the *merged* data regions. The shape uncertainty due to the choice of the strong coupling constant within the NNPDF description is found to be below 0.1% for V+jets background components and is therefore not considered in the final statistical interpretation of data. The comparison from the predictions obtained by employing the MMHT2014 PDF set is found to be up to 1.5% in the high-mass tails. On the other hand side, the impact of the internal NNPDF uncertainty is less than 1% in the tails.

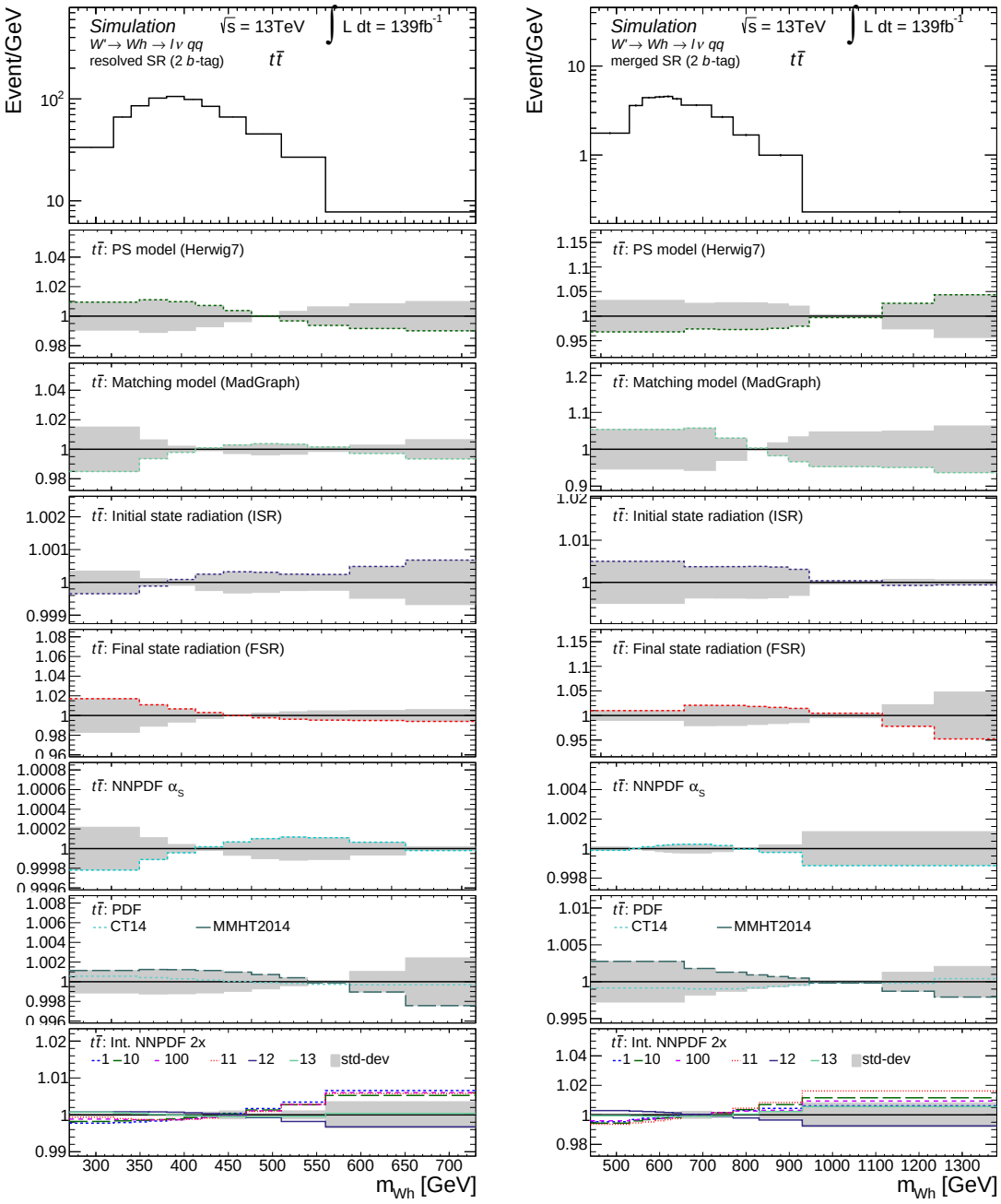

Figure 4.15: Expected m_{VH}-distributions of $t\bar{t}$ background components in the **1-lepton resolved signal regions** as predicted by POWHEG interfaced with PYTHIA 8 with an integrated luminosity of 139 fb^{-1}(nominal). The multiple ratio panels show the shape uncertainties without normalization component for uncertainties originating from theoretical uncertainties. The first row of the ratio panels show the *PS model* uncertainty; the second row shows *ME matching model* uncertainties; third and fourth row show *ISR and FSR* uncertainties; the three bottom rows show the uncertainty of the PDF uncertainties and the NNPDF-incorporated α_S. The gray shades in each ratio panel indicate the total uncertainty as used in the final statistical interpretation of data.

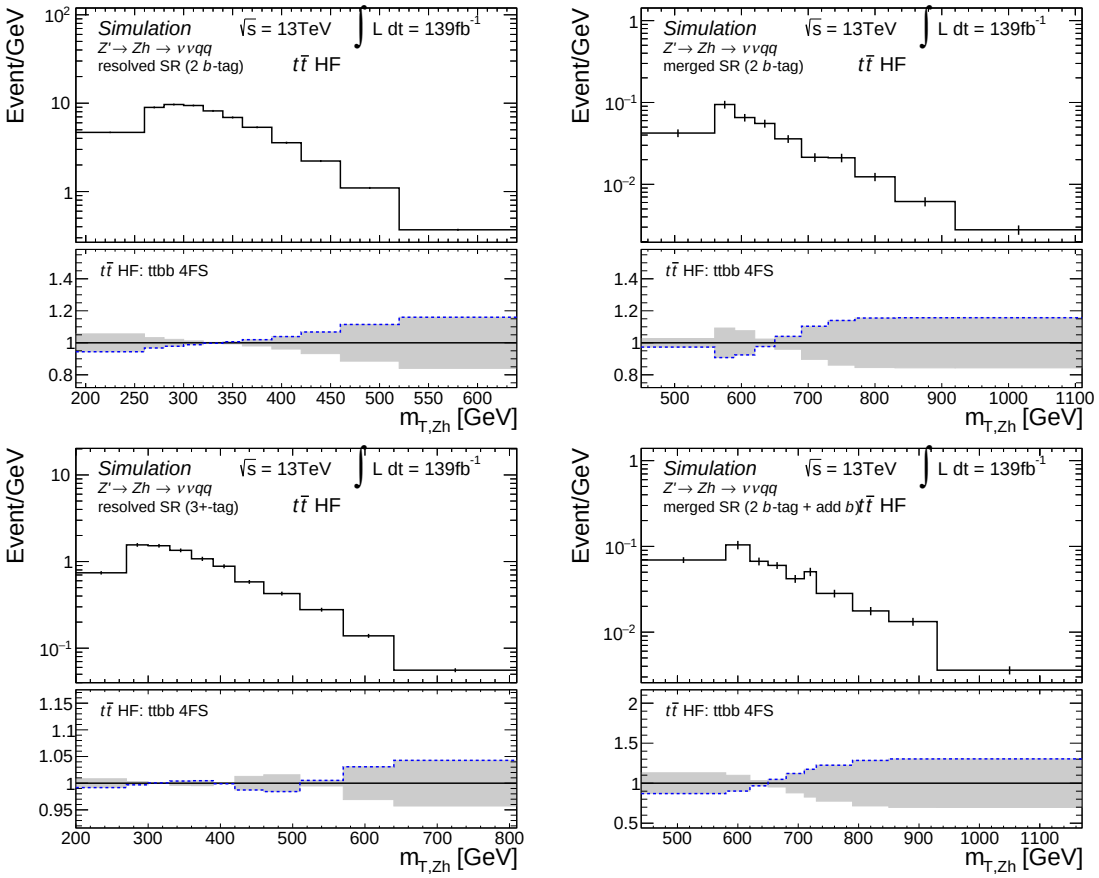

Figure 4.16: Expected $m_{\mathrm{T,Zh}}$-distributions of $t\bar{t}$ background components in the **0-lepton bb*A* mode sensitive signal regions** as predicted by POWHEG interfaced with PYTHIA 8 with an integrated luminosity of 139 fb^{-1}in the (left) *resolved* and (right) *merged* signal regions with (top row) two or (bottom row) three or more *b*-tags. The ratio panel shows the $t\bar{t}b\bar{b}$ *4-flavor-scheme* uncertainty. The gray shade in the ratio panel indicates the total uncertainty as used in the final statistical interpretation of data.

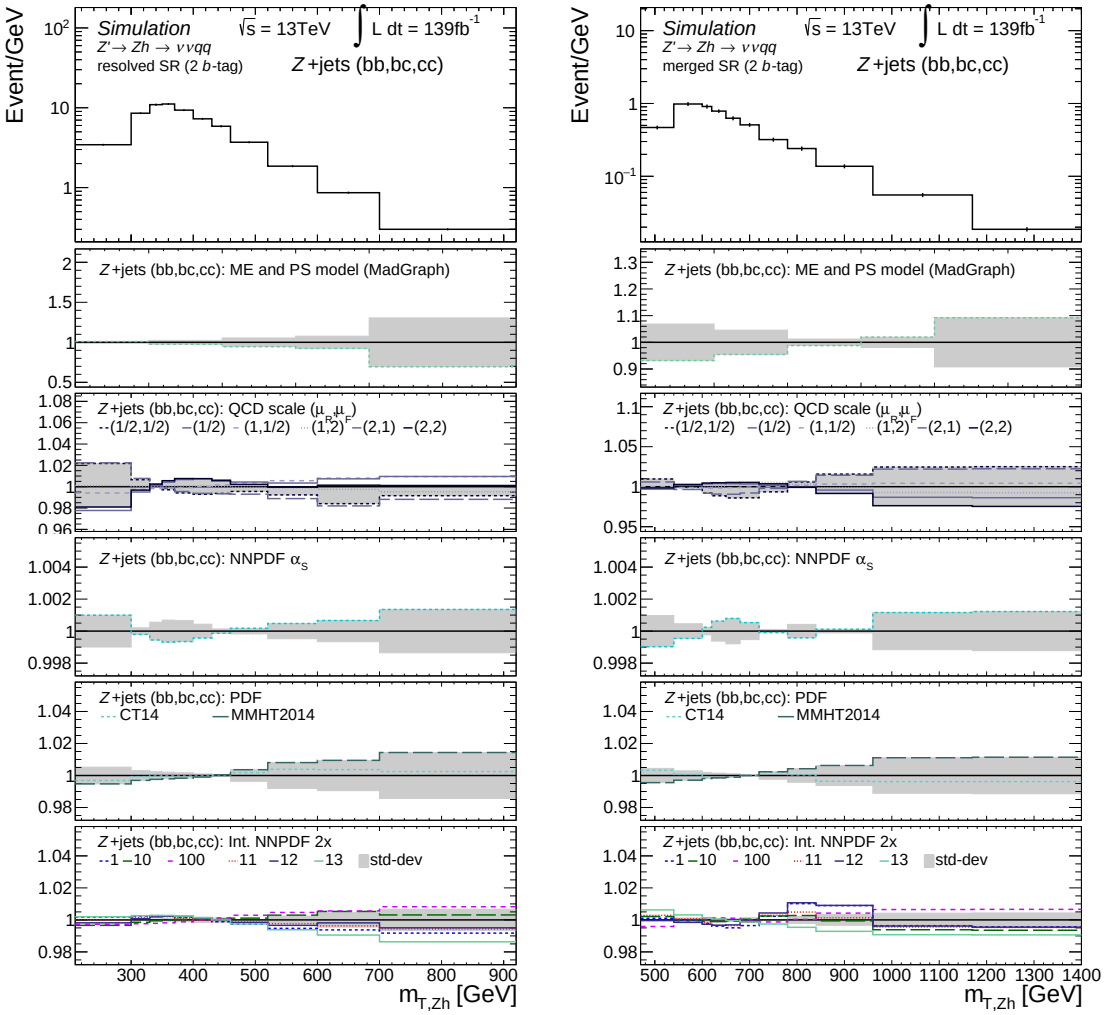

Figure 4.17: Expected $m_{\mathrm{T,Zh}}$-distributions of Z+jets (bb,bc,cc) background components in the **0-lepton signal regions** as predicted by SHERPA with an integrated luminosity of 139 fb^{-1}(nominal). Distribution of the nominal predictions of Z+jets (bb,bc,cc) background in the (left) *resolved* and (right) *merged* signal regions with 2 *b*-tags. The multiple ratio panels show the shape uncertainties without normalization component for uncertainties originating from theoretical uncertainties. The row of the ratio panels show the *PS model* uncertainty, the second *QCD-scale* uncertainties and the three bottom rows show the PDF connected uncertainties. The gray shades in each ratio panel indicate the total uncertainty as used in the final statistical interpretation of data.

Uncertainties due to migration between different signal and control regions

By leaving the normalization of the above background components as a free-floating parameter in the final fit, the normalization component within each single data region had to be removed from the relative uncertainties, to avoid too many degrees of freedom. The relative fractions of a given background contribution in each signal and control region are taken from the *nominal* simulation. To avoid, that the background yields in the various data regions are treated fully correlated in the final fit, an additional migration uncertainty is assigned, based on the alternative MC samples. Such migration uncertainty parameters are introduced for each process individually to describe the migration from the $m_{jj/J}$-sideband CRs to the corresponding SR, from the regions with *resolved* event topology to the *merged* regions and between the 0- and 2-lepton (1-lepton) channels of corresponding data regions. These uncertainties are calculated by comparing the nominal total event yields in a given SR or CR to the yield predicted by an alternative MC sample,

$$\sigma_w^{A\to B} = \sqrt{\sum_{\text{var}}^{N} \left(\frac{\left| \frac{n_A^{\text{var}}}{n_B^{\text{var}}} - \frac{n_A^{\text{nom}}}{n_B^{\text{nom}}} \right|}{\frac{n_A^{\text{nom}}}{n_B^{\text{nom}}}} \right)^2}. \tag{4.7}$$

Here $n_{A(B)}^{\text{nom(alt)}}$ is the number of expected events for a given process in region $A(B)$ as predicted by the nominal (alternative) MC sample. The alternative MC samples take into account the ME matching, PS modeling, ISR and FSR, renormalization and factorization scales as well as the uncertainties from the PDF measurement. For the interpretation of data a signal produced via the bb$A$ mode, the additional $t\bar{t}b\bar{b}$ *4-flavor-scheme* uncertainty is included as well.

The impact of all theoretical uncertainties is summed in quadrature. The corresponding uncertainty values are listed in Table 4.5 for the interpretation of data with the HVT model scenarios and in Table 4.6 for the interpretation by the 2HDM produced via bb$A$ mode.

Table 4.5: Migration uncertainties for the transition of events between data regions A and B, shown separately for the dominant background processes. The migration uncertainty between *resolved* and *merged* regions is calculated in an $m_{jj/J}$- and b-tag-inclusive event selection. (†) was derived by collaboration member [202], stated for completeness; (*) Not enough statistics in the corresponding regions for the evaluation, a migration uncertainty of 20% assumed. (**) The migration between the 0- and 1-lepton channels is needed for a combination of the both channels in the interpretation of data by a W' resonances.

channel $A \to B$	top quark	Z+jets			W+jets		
		bb, bc, cc	bl, cl	l	bb, bc, cc	bl, cl	l
0-lepton channel							
merged SR $\to m_J$-sideband CR (1 b-tag)	12%	12%	3%	10%	25%	14%	14%
merged SR $\to m_J$-sideband CR (2 b-tag)	11%	6%	(*)	(*)	28%	2%	18%
merged $\to$ *resolved* (1 b-tag)	20%	14%	15%	8%	30%	35%	24%
merged $\to$ *resolved* (2 b-tag)	9%	10%	(*)	(*)	46%	(*)	(*)
resolved SR $\to m_{jj}$-sideband CR (1 b-tag)	2%	6%	4%	5%	5%	10%	4%
resolved SR $\to m_{jj}$-sideband CR (2 b-tag)	2%	5%	(*)	(*)	—	—	—
1-lepton channel							
merged $\to$ *resolved* (1 b-tag)	20%	9%	13%	29%	15%	13%	20%
merged $\to$ *resolved* (2 b-tag)	18%	18%	12%	10%	22%	12%	21%
merged SR $\to m_J$-sideband CR (1 b-tag)	3%	20%	7%	99%	3%	2%	4%
merged SR $\to m_J$-sideband CR (2 b-tag)	3%	20%	7%	99%	3%	2%	4%
resolved SR $\to m_{jj}$-sideband CR (1 b-tag)	2%	6%	5%	29%	3%	1%	2%
resolved SR $\to m_{jj}$-sideband CR (2 b-tag)	2%	6%	5%	29%	3%	1%	2%
2-lepton channel (†)							
merged $\to$ *resolved*	18%	19%	28%	23%	14%	19%	17%
resolved SR $\to t\bar{t}$ CR	1.2%	—	—	—	—	—	—
Between 0- and 2-lepton channels							
merged	21%	8%	6%	5%	—	—	—
resolved (1 b-tag)	7%	5%	6%	4%	—	—	—
resolved (2 b-tag)	7%	5%	6%	4%	—	—	—
resolved (3+ b-tag)	18%	4%	7%	50%	—	—	—
Between 0- and 1-lepton channels**							
merged m_J-sideband CRs	12%	28%	27%	34%	4%	4%	3%
merged SR	7%	7%	25%	39%	5%	4%	4%
resolved m_{jj}-sideband CRs	11%	4%	8%	10%	6%	4%	2%
resolved SR	10%	4%	7%	8%	5%	4%	2%

Table 4.6: Migration uncertainties for the transition of events between data regions A and B, shown separately for the dominant background processes. The migration uncertainty between *resolved* and *merged* regions is calculated in an $m_{jj/J}$- and b-tag-inclusive event selection. (†) was derived by collaboration member [202], stated for completeness.

channel $A \rightarrow B$	top quark	$t\bar{t}$+HF	Z+jets (bb,bc,cc)	Z+jets (bl,cl)	Z+jets (l)
0-lepton channel					
merged → *resolved*	8%	46%	12%	21%	50%
2-lepton channel (†)					
merged → *resolved*	18%	18%	19%	28%	28%
resolved SR → $t\bar{t}$ CR	2.4%	—	—	—	—
Between 0- and 2-lepton channels					
resolved (1+2 b-tag)	7%	50%	5%	6%	4%
resolved (3+ b-tag)	18%	15%	4%	7%	50%
merged	21%	28%	8%	6%	5%

4.4.4 Signal modeling uncertainties

The aim of this analysis is the measurement of or an upper limit on the cross section of a hypothesizes signal process, $\sigma_s = \sigma(pp \rightarrow X \rightarrow Vh)$. Therefore, there is a fundamental difference in the interpretation and the derivation of theory uncertainties of signal processes with respect to those of background processes. In contrast to background processes, for which the prediction uncertainty is calculated for n_b, the signal uncertainty is given by the uncertainty on the signal selection efficiency, ε_s. The number of selected signal, n_s, events is by the product of the integrated luminosity, the cross section and the signal selection efficiency, ε_s. The signal event yield is described by the freely-floating, dimensionless signal strength parameter, μ, in the final statistical interpretation and is connected to the signal cross section via

$$n_s = \mu \cdot \int Ldt \cdot \sigma_s \cdot \varepsilon_s, \tag{4.8}$$

with σ_s normalized to 1 pb. The shape of the signal m_{Vh} distribution is calculated as the uncertainty on the differential, i.e. bin-by-bin, signal selection efficiency, $\varepsilon_s(b_i)$. Deviations in the differential cross section, $\sigma(b_i)$, induced by a theory uncertainty in a given bin b_i of the differential distribution, enter the signal efficiency twice, in the numerator and the denominator,

$$\Delta\varepsilon_s(b_i) = \varepsilon_s^{\text{nom}}(b_i) - \varepsilon_s^{\text{alt}}(b_i) = \frac{n_s^{\text{nom}}(b_i) - n_s^{\text{alt}}(b_i)}{n_{s,\text{total}}^{\text{nom}} - n_{s,\text{total}}^{\text{alt}}}, \tag{4.9}$$

where $n_{s,\text{total}} \propto \sigma_s$ and $n_s \propto \sigma_s$ As a consequence a small normalization uncertainty component fully correlated to the shape uncertainty remains and is not removed.

Normalization and shape uncertainties have been studied for the 8 signal processes[4] for each mass hypothesis separately. The uncertainties have been evaluated in the signal regions, while the uncertainty

[4] bb$A$ mode, ggA mode and HVT Z' in 0- and 2-lepton channel and HVT W' in the 1- and 0-lepton channel. The latter channel is not yet included in the final statistical interpretation of data presented in Section 4.7

Table 4.7: Eigentunes of the A14 set of tuned parameters [117] used to estimate uncertainties due to parton shower modeling

Description	**Pythia 8 tune parameter**		**up**	**down**
`Var1`				
MPI+CR (UE activity and incl jet shapes)	`BeamRemnants:reconnectRange`	merging probability	1.73	1.69
	`MultipartonInteractions:alphaSvalue`	MPI α_S	0.131	0.121
`Var2`				
ISR/FSR (jet shapes and substructure)	`TimeShower:alphaSvalue`	FSR α_S	0.139	0.111
	`SpaceShower:pT0Ref`	ISR p T cutoff	1.60	1.50
	`SpaceShower:pTdampFudge`	Factorisation/renorm scale damping	1.04	1.08
`Var3c`				
ISR (dijet decorrelation)	`SpaceShower:alphaSvalue`	ISR α_S	0.140	0.115

on the signal content in the CR has been neglected.

Three sources of uncertainties have been considered: *PS model*, *QCD-scale* and PDF uncertainties. To account for *PS model* uncertainties, the nominal prediction using Pythia 8, i.e. the *string* PS model [59], is compared to the prediction made by employing Herwig 7 [197] (i.e. the *cluster model* [60])[5]. Furthermore the effects of increased or decreased hadronic activities from initial- and final-state radiation (ISR/FSR), the underlying event (UE) and multiple-parton interactions (MPI) have been studied by varying the Pythia shower parameter according to the eigentunes [117]. The parameter values used in the eigentunes are listed in Table 4.7. The combined *PS model* uncertainty used for the final statistical interpretation of data is extracted by enveloping the PS model uncertainty and the quadratic sum of the individual eigentune terms.

Secondly, the used LO PDF set is compared to the predictions of two alternative equally LO PDF sets, as listed in Table 4.4. Events are reweighted analogously to SM background processes using the LhaPdf tool [13]. For each signal scenario, the PDF set with the greatest impact on the selection efficiency is considered the overall PDF uncertainty.

As for the background processes, μ_R and μ_F are individually varied by a factor of 2. The largest deviation in each bin is taken as the total *QCD-scale* uncertainty. The *QCD-scale* uncertainty has been evaluated for the 2HDM signal processes only and show a negligible contribution to the total signal selection uncertainty. The impact on the signal efficiency for HVT samples is expected to be lower, since no strong-interaction vertices exist at tree-level. Therefore, no *QCD-scale* uncertainty for the HVT signal scenarios is studied.

Replication of a SR-like selection at particle level

Dedicated *surrogate* samples are produced with both the nominal generator setup as well as adjusted settings describing the systematic variations from modeling uncertainties described above. For computing resource reasons, their detector interaction is not simulated but the kinematics are evaluated using stable particles at particle-level (PL) and transferred to reconstruction level as described

[5] The selection efficiency the the bb$A$ mode pseudo-scalar A has not tested separately against a PS variation using the Herwig generator. The Pythia tune variations are considered to describe the PS uncertainties sufficiently.

in Section 4.4.2. A replication of the signal region selection described in Section 4.2.1 is designed on particle-level (PL).

Jets are defined by clustering all stable particles except neutrinos and muons using the anti-k_t algorithm with radii $R = 1.0$ and $R = 0.4$ for large-R and small-R jets. In addition, in order to replicate track jets, the variable radius track jet algorithm is used to cluster charged particles. These track jet proxies are matched to large-R by a simple $\Delta R < 0.8$ criterion, regarding the two leading jets in each large-R jet only.

A b-label is assigned to track jets and small-R jet, if a PL b-quark could be ghost-associated [90] to the corresponding jet. b-tagging was imitated based on the p_{T}- and η-depending b-tagging efficiency for track jets [97] and small-R jets [92] at the 70% working point (c.f. Fig. 2.18). If a jet within $|\eta| < 2.5$ is b-labeled, a b-tag is assigned by a random generator reflecting the corresponding p_{T}- and η-depending b-tagging efficiency. For non-b-labeled jets, a global miss-tagging rate of $1/313$ for small-R jets and $1/171$ for track jets is employed.

The selection requirements for the events on PL are defined in close analogy to those defined in the SR at reconstruction level, if applicable. The applied cuts are listed in B.13.

To validate the PL selection, the signal selection efficiency as function of the resonance masses is compared to those at reconstruction level (e.g. Fig. 4.5(a)) The corresponding particle level signal efficiency is depicted in Fig. 4.18 which agrees well with the efficiencies at reconstruction level. Other signal selection efficiencies on PL can be found in Appendices C.22 and C.23.

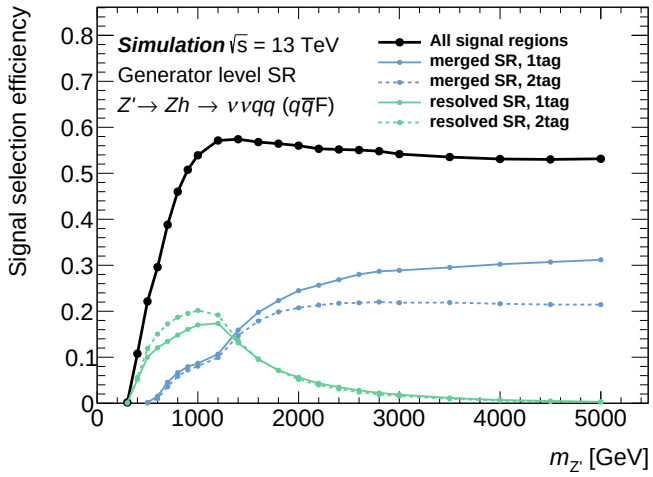

Figure 4.18: HVT model A,B signal selection efficiencies at particle-level (PL) in **0-lepton** SR as function of the Z' mass.

Fig. 4.19 shows the distribution of the m_{Vh} reconstructed from components at PL of an HVT signal Z' decay with a mass of $m_{Z'} = 500$ GeV. The shape of the signal $m_{\mathrm{T,Zh}}$ distribution is slightly different from the distribution built from reconstructed objects shown in Fig. 4.20. However, the here studied

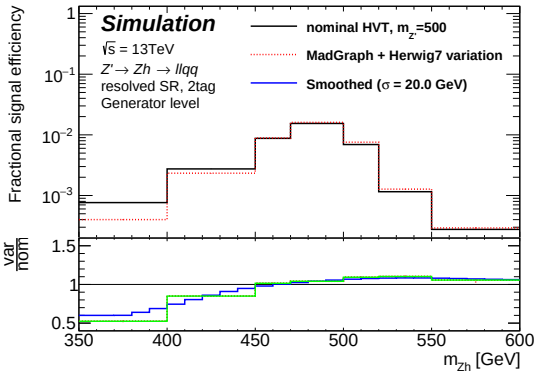

Figure 4.19: Comparison of a Z'-boson decay spectrum in PL-events in the 2-tag resolved SR. The discrepancy has been used to estimate the corresponding uncertainty on reconstruction level after the method decribed in Section 4.4.2, which is indicated in blue in the lower panel.

uncertainties are assumed to affect the kinematics already at PL. Uncertainties from sources causing the difference between PL and reconstruction level are described by the experimental uncertainties.

Signal modeling uncertainty results

The shapes of all eight signal scenarios for several different mass hypotheses is evaluated in all signal regions and the resulting shape *variations* are used in the final statistical interpretation of data. One set of such shape variations for the HVT $Z' \to \ell\ell b\bar{b}$ in the 2-tag resolved region with a mass of 500 GeV is shown in Fig. 4.20.

The total normalization component can be compactly represented as a function of the corresponding resonance mass. As for background processes, the dominating theory uncertainty for signal processes is induced by the *PS model*, shown in Fig. 4.21 for the HVT Z' signal scenario in the 0- and 2-lepton channels. The most conservative *PS model* uncertainty for the largest range of resonance masses is obtained by varying the Pythia tune parameter. This holds for all signal scenarios. In particular the signal selection efficiency in the *resolved* regions is impacted with up to 8% at $m_X \approx 500$ by uncertainties induced by the shower parameters. In this regime, The leading contribution is induced by the Var2 set of parameters describing increased and decreased activities from *ISR and FSR*. With increasing resonance masses, the Var3c set of parameters becomes leading contribution at resonance masses of $\approx$ 1 TeV. The Var3c set of parameters describes the decorrelation of two ISR jets and their distance in pseudo-rapidity. None of the 3 Eigentunes is negligible. In case the shower tunes provide the most conservative limits, the 3 variations are treated independently in the final statistical interpretation of data resulting in a total pre-fit uncertainty corresponding to the quadratic sum of the individual components.

The *PS model* uncertainty at higher mass, especially in energy regimes in which the *merged* event topology becomes more sensitive than the *resolved*, the more conservative estimation is obtained by the comparison between the *Lund* and *cluster* models, i.e. the comparison to the sample generated by Herwig. The uncertainty on the normalization amounts to 5% compared to 3% obtained by the

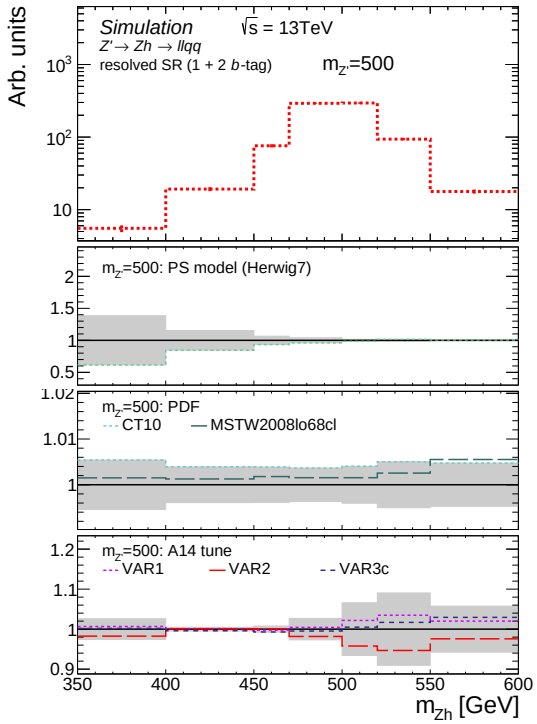

Figure 4.20: The expected m_{Vh}-distribution of a HVT $Z' \rightarrow Zh \rightarrow llbb$ in the 2-lepton *resolved* signal region. The three lower panels show the normalization and shape uncertainties due to sources of theory uncertainties. The gray shade is the uncertainty assumed for the final statistical interpretation of data, composed as described in the text from the (colored lines) individual uncertainty estimates.

Pythia tune variation. Since the bb$A$ mode signal scenario is most relevant in the mass region below 1 TeV, the estimation *PS model* uncertainties via the comparison with a Herwig generated sample is not done.

The impact of varied *QCD-scales* amounts to less than 0.1% for the ggA mode signal production and is shown in Fig. 4.22. For the bb$A$ mode, the relative uncertainty induced by the *QCD-scale* is shown in Fig. 4.23 and is found to be up to ≈ 3%. Since the signal MC samples are generated at LO accuracy, in which no QCD vertex exists, no *QCD-scale* uncertainty is calculated for the HVT signal scenarios.

The PDF uncertainty is smaller than 1% for all signal scenarios and shown in Fig. 4.24.

4.5 Statistical interpretation methods

The final statistical interpretation of the recorded data is done in two steps. First the each of the predictions from the competing hypotheses, i.e. the SM hypothesis and the various BSM hypotheses, is fitted to the data in histograms of the final discriminant, $m_{(\mathrm{T},)\mathrm{Vh}}$. The parameterized predictions encode all statistical and systematic uncertainties, introduced in the previous sections. In a second step

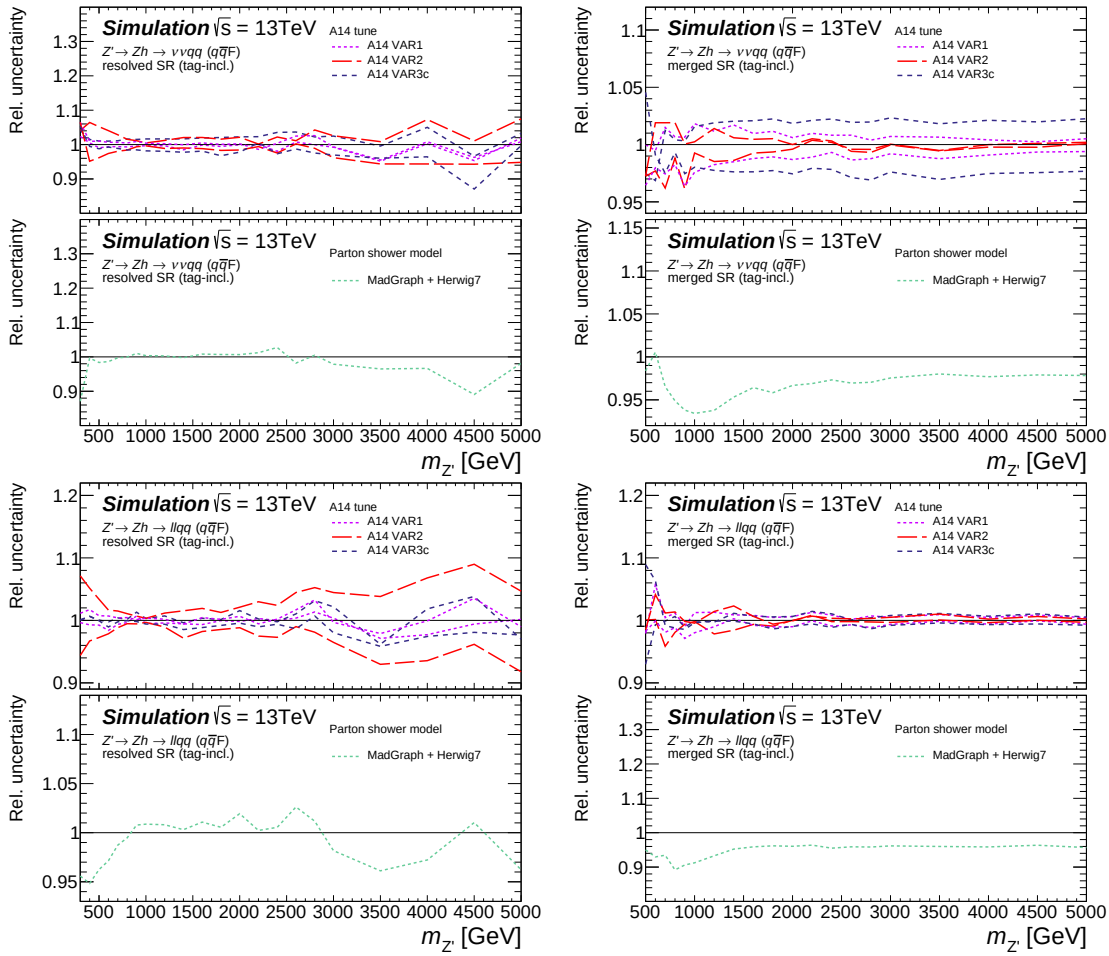

Figure 4.21: Relative *PS model* uncertainty on the HVT model A,B signal selection efficiency in (top row) the **0-lepton** and (bottom row) the **2-lepton** channel (left) *resolved* and (right) *merged* SRs as function of the Z' mass. The ratio panels show the normalization uncertainties on the total signal selection efficiency due to the parton shower, estimated by varying the shower tune parameter by the A14 eigenmodes (upper panels) or by comparing different generator (lower pannels). The 1- and 2-tag region show similar resulst and are collectively shown here in a 1+2-tag merged region;

these competing hypothesis are tested against each other for plausibility incorporating the impacts of these uncertainties and quantify the level of plausibility for all hypotheses.

4.5.1 The binned maximum likelihood fit

The final statistical interpretation of data is done by a binned maximum likelihood (ML) fit to data that is performed simultaneously in all signal and control regions, implemented by the RooFit package [203]. The ML fit bases on a likelihood function (LhF) that is a function of the signal strength, μ, and several so-called *nuissance parameter*s (NPs). The *parameter of interest* (POI) in this search is

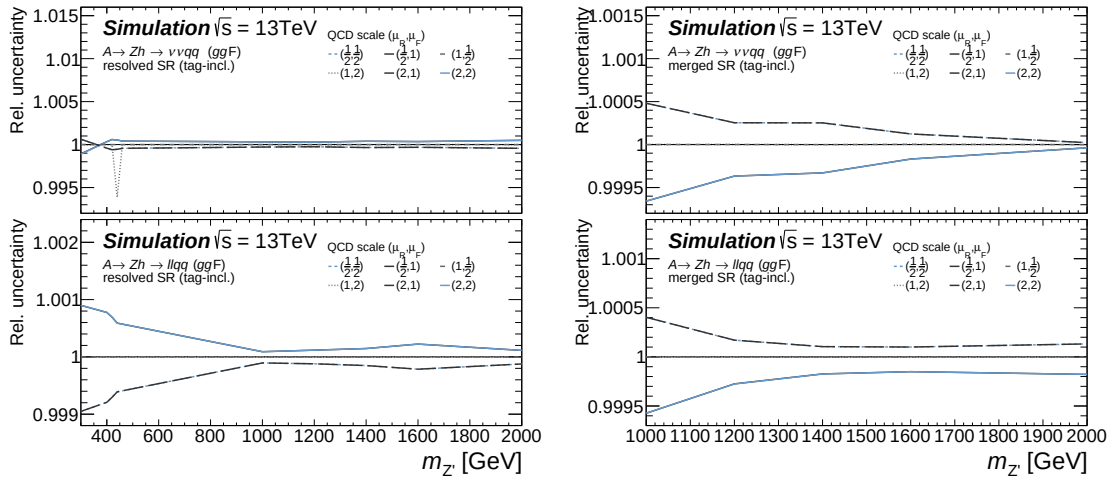

Figure 4.22: Relative *QCD-scale* uncertainty on the ggA mode produced 2HDM signal selection efficiency in SR as function of the A mass. The various ratio panels show the normalization uncertainties on the total signal selection efficiency due to individual sources. Resolved 3-tag region (left) and inclusive merged (1+2-tag) region in association with a additional b-tagged track jet not matched to the large-R jet (right); the 1- and 2-tag region look similar and are collectively shown here in a 1+2-tag merged region;

the production cross section $\sigma(pp \to X \to Vh)$ with for different signals with m_X ($X = Z', W', A$), that is related linearly to the signal strength parameter. On the other hand, the NPs account for the several discussed experimental and theory systematic uncertainties as well as normalization of the simulated backgrounds.

The m_{Vh} distributions of all signal and control regions are sub-divided in histogram bins of variable size, asserting a sufficient statistical precision in each bin. The binning is chosen such that the expected statistical uncertainty is less than 15%. Additionally, the bin width is required to be larger than the width of the resonance mass. The bin ranges are determined iteratively by lowering the lower boundary of each bin by 10 GeV until the above requirements are met.

The likelihood function is given by,

$$\mathcal{L}(\mu, \vec{\alpha}, \vec{\gamma}) = \prod_c \prod_b \mathcal{P}ois\left(n_{c,b}^{\text{obs}} \mid n_{c,b}^{\text{sig}}(\mu, \vec{\alpha}) + n_{cb}^{\text{bkg}}(\vec{\alpha})\right) \prod_k f_k(\tilde{\alpha} \mid \alpha_k). \prod_{i \in \text{bins}} \mathcal{P}ois\left(b_i(\vec{\alpha}_b) | \gamma_i \tau_i\right). \tag{4.10}$$

Here, the double product goes over all bins in all signal and control regions. $\mathcal{P}ois(n_{c,b}^{\text{obs}} | n_{c,b}^{\text{sig}} + n_{cb}^{\text{bkg}})$ is the Poisson probability of measuring $n_{c,b}^{\text{obs}}$ events in the bin. The number of predicted events in each bin is parameterized by the NPs, $\vec{\alpha}$ and the signal-strength, μ.

The NPs $\vec{\alpha}$ parameterize uncertainties, such as the normalization of the background predictions, migration between the different kinematic regions or uncertainties on the shape of a signal or background process. The uncertainties on the shape of a process is described in Section 4.4 by two variation corresponding to the $\pm 1\sigma$ uncertainty due to the particular source. For each source of

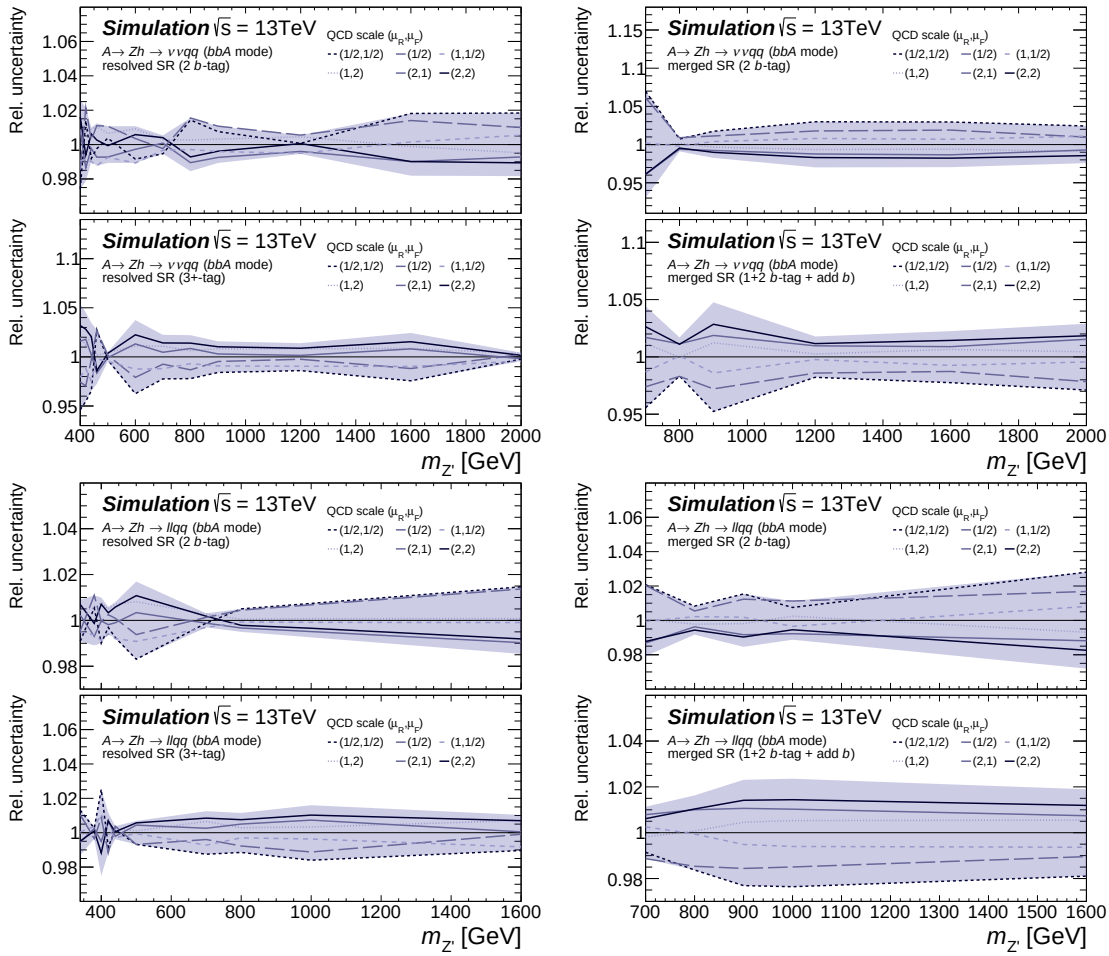

Figure 4.23: Relative *QCD-scale* uncertainty on the 2HDM signal selection efficiency, produced via the bb$A$ mode, in (top row) **0-lepton** and (bottom row) **2-lepton** SR as function of the A mass. The individual panels show the normalization uncertainties on the total signal selection efficiency due to the *QCD-scale* uncertainty in the bb$A$ mode sensitive signal regions. On the left hand side, the *resolved* regions with 2 or 3+ b-tags are shown and on the right hand side, *merged* regions with or without additional b-tagged track jets (*add.* b-tag) are shown.

uncertainty the associated *nuissance parameter* (NP) change the according prescription via,

$$h_k(x) = \begin{cases} h_k^0(x) + \alpha_k \left(h_k^+(x) - h_k^0(x) \right), & \alpha_k \geq 0, \\ h_k^0(x) - \alpha_k \left(h_k^-(x) - h_k^0(x) \right), & \alpha_k < 0, \end{cases} \tag{4.11}$$

Here $h_k^0(x)$ is the nominal distribution and $h_k^{\pm}(x)$ is the $\pm 1\sigma$ variation of the corresponding uncertainty. The parameters describing these sources of uncertainties are constrained in subsidiary measurements during the calibration in dedicated control regions or by or by comparing different MC generator setups.

The parameter $\tilde{\alpha}$ is referred to as *prior* uncertainty and corresponds to the uncertainty that is estimated

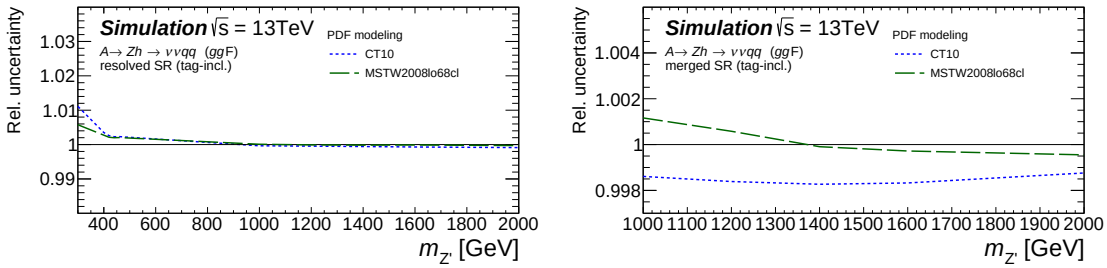

Figure 4.24: Relative uncertainty on the 2HDM signal selection efficiency in **0-lepton** SR as function of the A mass. The plots show the normalization uncertainties on the total signal selection efficiency due to PDF uncertainty. The 1- and 2-tag region look similar and are collectively shown in a 1+2-tag (left) *resolved* and (right) *merged* region.

in the subsidiary measurements. The most parameters in this analysis are log-normal constrained, assuming the logarithm of the NP is Gaussian distributed around the nominal value with a width equal to its prior uncertainty. This is achieved by a function $f_k(\tilde{\alpha} \mid \alpha_k)$[6] that is chosen appropriately and incorporates information about the NP from the subsidiary measurements. f_k is maximal for the nominal prediction. Thus, an acquired value $\tilde{\alpha} \neq \alpha_k$ would result in a penalty factor in the likelihood function.

In some cases, the nuisance parameter can be best constrained entirely from data in the dedicated CRs, which are described in Section 4.3. This is especially the case for the normalization of main backgrounds, if a signal or control region can be defined that is enriched in this particular background. These NPs are unconstrained by the likelihood function by setting $f_k = 1$ and are referred as freely floating NPs. In contrast, the normalization of minor backgrounds cannot be extracted from data and is also log-normal constrained, assuming a conservative prior uncertainty.

The last term in Eq. (4.10) accounts for the finite size of the MC samples[204], encoded by a Poisson distribution with the expectation value of $\gamma_i \tau_i$ for each bin. This term introduces the NPs γ_i and a constant τ_i that incorporates the statistical MC uncertainty. All NP are collectively represented by the parameter vector $\vec{\theta} = (\vec{\alpha}, \vec{\gamma})$.

Two types of fits are performed, conditional and unconditional fits. The values for μ and θ_i that maximize the likelihood in an unconditional fit are referred to as the maximum likelihood estimator (MLE), $\hat{\mu}$ and $\hat{\theta}_i$. The conditional fit fixes the signal strength to a given value μ. The NPs that maximize the likelihood in a conditional fit are referred to as $\hat{\hat{\theta}}_i$. a special type of conditional fit is the background-only fit, fixing $\mu = 0$.

4.5.2 Statistical tests

The final result is interpreted by comparing the plausibility of two alternative hypothesis. The null-hypothesis, is retrieved from a (conditional, $\mu = 0$) background-only fit. The signal-plus-background

[6] $f_k = ln(\beta_k - \alpha_k)^2/\delta_i$ where β_k and δ_i are chosen appropriately.

hypothesis, is retrieved for each signal hypothesis individually by an unconditional fit with a free floating signal strength parameter μ.

The significance of the results is determined via test statistics proposed in Ref. [205] implemented in the RooStat package, using the profile likelihood ratio,

$$\lambda(\mu) = \begin{cases} \frac{\mathcal{L}(\mu,\hat{\hat{\theta}})}{\mathcal{L}(\hat{\mu},\hat{\hat{\theta}})} & \text{if} \hat{\mu} \geq 0, \\ \frac{\mathcal{L}(\mu,\hat{\hat{\theta}})}{\mathcal{L}(0,\hat{\hat{\theta}})} & \text{if} \hat{\mu} < 0, \end{cases} \tag{4.12}$$

with the likelihood function as defined in Eq. (4.10) and $\lambda(\mu)$ adapting values between 0 and 1.

Test statistic for a discovery The test statistic for a positive signal is defined by

$$q_0 = \begin{cases} -2\ln\lambda(0) & \hat{\mu} \geq 0, \\ 0 & \hat{\mu} < 0. \end{cases} \tag{4.13}$$

Based on the test statistic, the p_0-value quantifies the level of disagreement between the data and the null-hypothesis. It is defined as

$$p_0 = \int_{q_0,obs}^{\text{inf}} f(q_0|0)dq_0, \tag{4.14}$$

with $f(q_0|0)$ the probability distribution function (p.d.f.), that can be approximated [206] by a Gaussian distribution. The cumulative distribution is given by,

$$F(q_0|0) = \Phi(\sqrt{q_0}), \tag{4.15}$$

with Φ the cumulative of the standard Gaussian. Using this approximation, the discovery significance is obtained by [205]

$$Z_0 = \Phi^{-1}(1 - p_0) = \sqrt{q_0}. \tag{4.16}$$

Test statistic for upper cross section limits In case the null-hypothesis cannot be excluded, the test statistic for positive signals is defined by[7]

$$q_\mu = \begin{cases} -2\ln\lambda(\mu) & \hat{\mu} \leq 0, \\ 0 & \hat{\mu} > 0. \end{cases} \tag{4.17}$$

[7] Note the inequality sign changed direction w.r.t. Eq. (4.13).

As for the discovery a p_μ value is defined as the cumulative distribution

$$p_\mu = \int_{q_\mu,obs}^{\inf} f(q_{\mu'}|\mu) dq_{\mu'} = 1 - \Phi(\sqrt{q_\mu}). \tag{4.18}$$

A value μ is said to be excluded a certain confidence level (C.L.) α if $(1 - p_\mu) > \alpha$. The Limits quoted in this thesis show the largest value μ excluded at 95% C.L. . The limit can be calculated as

$$\mu_{\text{limit}} = \hat{\mu} + \sigma\Phi^{-1}(\alpha), \tag{4.19}$$

with σ the uncertainty on the signal strength determined from a pseudo-data set [205]. The uncertainty on the expected limit is given as $N = 1, 2$ standard deviation, calculated using [205]

$$\text{band}_{\pm N\sigma} = \mu' + \sigma(\Phi^{-1}(\alpha) \pm N). \tag{4.20}$$

Limits obtained by the asymptotic approximation described above are validated by also been calculated using pseudo-experiments to in a phase space region that is strongly limited by the low amount of recorded data. It was found that both statistical methods agree within 20%.

In case a theory provides a one-to-one relationship between theory model parameter and the predicted cross sections, the resulting limit at 95% C.L. is mapped from the cross section limits to the parameter space of the corresponding model.

4.5.3 Nuisance parameter pulls and constraints

To assert the validity of the maximum likelihood fit post-fit prescription of the various signal and control regions are regarded. In addition to the m_{Vh} distributions, also the acquired MLE for all NPs, $\hat{\theta}_i$, are regarded. The pull $\mathcal{P}$ is defined as

$$\mathcal{P} = \frac{\hat{\theta_k} - \theta_{k,0}}{\Delta\theta_k}, \tag{4.21}$$

with $\theta_{k,0}$ the nominal (pre-fit) value of θ_k and $\Delta\theta_k$ the prior uncertainty on the corresponding NP.

A priori overestimated uncertainties can be constrained by data. The post-fit uncertainties are extracted from the diagonal elements of the covariance matrix, that can be estimated by the inverse Hessian matrix[205],

$$cov(i,j) \approx H^{-1}_{i,j} = \left(\frac{-\partial^2 \ln(\mathcal{L}(\hat{\hat{\theta}}, \hat{\hat{\theta}})}{\partial\theta_i \partial\theta_j} \right)^{-1} \tag{4.22}$$

The total post-fit uncertainty is also reduced with respect to the pre-fit uncertainty if multiple uncertainties cover the same deviations in the prediction. Their individual post-fit uncertainties cannot be constrained but the combined uncertainty is reduced with respect to the pre-fit uncertainty due to the non-diagonal elements in the covariance matrix.

4.5.4 Impact of nuisance parameters on the signal strength

The impact of an individual NP to μ is defined [207] as,

$$\Delta\hat{\mu}^{\pm} = \hat{\hat{\mu}}_{\theta_0 \pm \Delta\theta}, \tag{4.23}$$

and is estimated by fixing the NP and perform a N-1-dimensional likelihood scan Eq. (4.10) over all other NP, determine,

$$\mathcal{L}'(\theta_i) := \mathcal{L}(\hat{\hat{\mu}}, \hat{\hat{\theta}}_1, \ldots, \theta_i, \ldots, \hat{\hat{\theta}}_n), \tag{4.24}$$

with $\hat{\hat{\mu}}$, $\hat{\hat{\theta}}_k$ are the MLE for μ and θ_k under the condition of the fixed NP.

The difference in likelihoods is defined as,

$$\Delta\mathcal{L}(\theta_i) = -\ln\left(\frac{\mathcal{L}'(\theta_i)}{\mathcal{L}(\hat{\mu}, \hat{\theta}_1, \ldots, \hat{\theta}_i, \ldots, \hat{\theta}_n)}\right) = \quad -\left(\ln(\mathcal{L}'(\theta_i)) - \ln\mathcal{L}(\hat{\mu}, \hat{\theta}_1, \ldots, \hat{\theta}_i, \ldots, \hat{\theta}_n)\right). \tag{4.25}$$

$\Delta\mathcal{L}(\theta_i) = 0$ corresponds to the the global maximum likelihood. The scan is performed until $\Delta\mathcal{L}(\theta_i) = 1/2$, corresponding to the $\pm 1\sigma$-variation of the fixed parameter. The extreme values of $\hat{\hat{\mu}}$ is measured. The interval size in $\Delta\hat{\mu} = \hat{\hat{\mu}} - \hat{\mu}$ denote the corresponding uncertainty conveyed by the NP to the signal strength.

4.6 The Vh resonance fitting models

Three different BSM fit scenarios are considered. The HVT W' signal scenario is fitted to the data in the 1-lepton channel. Furthermore, the HVT Z' signal scenario as well as the 2HDM scenario with an A boson produced via the ggA mode is fitted to data the 0- and 2 lepton channels simulataneously. Accordingly, the production of the A boson via the bb$A$ mode is fitted in these two channels with two major modifications, the separate treatment of the $t\bar{t}$+HF background component and the addition of further signal regions with higher b-tagging multiplicity. The signal and control regions that are used in these three fits are summarized in Table 4.8.

The global normalization of the major background processes is treated as an freely floating parameter. The normalization of the minor backgrounds is taken from the MC simulations and a conservative, 50% log-normal constrained uncertainty is assumed. The assumed normalization uncertainty for each background process for the three different fit scenarios is given in Table 4.9.

Additionally, the relative normalization proportion between regions with shared traits, i.e. a *merged* signal region and the corresponding *merged* m_J-sideband CR, is considered by migration uncertainties, implemented by a further normalization scale acting only on one of the participating data regions. The pre-fit uncertainty for this migration is given in Tables 4.5 and 4.6 for the HVT fitting scenarios and for the bb$A$ mode scenario, respectively.

Table 4.8: The signal and control regions included in the statistical interpretation of data of the 2HDM and HVT model hypotheses. The term *add. b*-tag denotes regions with the *merged* event topology and additional *b*-tagged track jets that are not associated with the Higgs candidate jet.

Fit	Channel	Resolved signal regions	Merged signal regions	Resolved control regions	Merged control regions
ggA mode, HVT Z'	0-lepton	1, 2 tag	1, 2 tag	1, 2 tag m_{jj}-sideband CR	1, 2 tag m_J-sideband CR
	2-lepton	1, 2 tag	1, 2 tag	1+2 tag $t\bar{t}$ CR	–
bb$A$ mode	0-lepton	1, 2, 3+ tag	1, 2 tag, 1,2 add.	–	–
	2-lepton	1, 2, 3+ tag	1, 2 tag, 1+2 add.	1+2, 3+ tag $t\bar{t}$ CR	–
HVT W'	1-lepton	1, 2 tag	1, 2 tag	1, 2 tag m_{jj}-sideband CR	1, 2 tag m_J-sideband CR

The individual systematic uncertainties discussed in Section 4.4 are incorporated in the fit by a parametrization via Eq. (4.11) employing one NP for each uncertainty. The experimental uncertainties are treated fully correlated between the signal and background processes and among all fitted data regions, parameterized by 84 individual NP listed in Appendix B.2. NPs describing the theory uncertainties are treated fully uncorrelated between the different signal and background processes but fully correlated between the channels and the employed data regions.

All Non-closure uncertainties, that are introduced to capture systematic deviations between prediction and observation seen in the control regions (c.f. Section 4.3) are described each by an individual NP.

Table 4.9: Overview of the nuisance parameters (NP) employed in the maximum likelihood fits in the four signal scenarios

Fit scenario	**HVT Z' / ggA mode**	**HVT W'**	**bb$A$ mode**	
Parameter	**Prior uncertainty**			**Comment**
top quark normalization	*floating*	*floating*	*floating*	
$t\bar{t}$+HF normalization	–	–	*floating*	
Z+jets (bb,bc,cc) normalization	*floating*	*floating*	*floating*	↑
Z+jets (bl,cl) normalization	*floating*	*floating*	*floating*	Normalization
Z+jets (l) normalization	50%	50%	50%	determined in
W+jets (bb,bc,cc) normalization	*floating*	*floating*	*floating*	data control regions
W+jets (bl,cl) normalization	*floating*	*floating*	*floating*	↓
W+jets (l) normalization	50%	50%	50%	
VV normalization	50%	50%	50%	
Vh(SM) normalization	50%	50%	50%	
Migration uncertainties	c.f. Table 4.5		c.f. Table 4.6	MC-to-MC comparisons (c.f. Section 4.4.3)
Experimental uncertainties	84 NPs for shape + norm.; correlated among all regions and processes			Subsidiary measurements (c.f. Section 4.4.1)
Background theory uncertainties	NP for shape only	NP for shape only	NP for shape only	MC-to-MC comparisons (c.f. Section 4.4.3)
Signal theory uncertainties	NP for shape + norm.	NP for shape + norm.	NP for shape + norm.	MC-to-MC comparisons (c.f. Section 4.4.4)
Non-closure uncertainties	**0-lepton**	**1-lepton**	**2-lepton**	
Parameter	**Applied to**			**Comment**
Large-R jet p_{T}^{J}	All SM bkg	All SM bkg	All SM bkg	
Small-R di-jet p_{T}^{jj}	V+jets	n/a	V+jets	c.f. Fig. 4.10
$p_{\mathrm{T}}^{\mathrm{miss}}$	Bkg. in *resolved* topology	n/a	n/a	
Stat. NP, $\gamma_{r,i}$	MC statistical uncertainty			Bin-wise

4.7 Results

For the three described fit scenarios, post-fit distribution of the background-only fits (conditional $\mu = 0$), is shown in Figs. 4.25 to 4.28. The post-fit $m_{(\mathrm{T},)\mathrm{Vh}}$ distribution for the 0-lepton and 2-lepton signal regions used for the HVT Z' and the 2HDM ggA mode interpretation of data is shown in Figs. 4.25 and 4.26, respectively. The largest excess of events with respect to the SM expectation is seen in the 2-lepton channel at around 500 GeV, corresponding to a local significance of 2.24σ [147]. The post-fit m_{Wh} distributions in the signal regions employed for the interpretation of a W' boson in the 1-lepton channel is shown in Fig. 4.27. Here, the largest deviation from the prediction is observed at a resonance mass $m_{Wh} \approx 3$ TeV corresponding to a local significance of 1.1σ. The 2HDM bb$A$ mode interpretation is performed with additional signal regions compared to the ggA mode interpretation. The post-fit $m_{\mathrm{T,Zh}}/m_{Zh}$ distribution of those additional signal regions is shown in Fig. 4.26. The fit strategy for the bb$A$ mode interpretation of data in the 0- and 2-lepton channels is different from that of the HVT interpretation when it comes to the sub-division of top quark sample into $t\bar{t}$+HF and top quark. However, the post-fit $m_{(\mathrm{T},)\mathrm{Vh}}$ background-only fit results in the common signal regions are are similar and not shown explicitly. The largest deviation to the SM prediction is observed for a resonance mass of 500 GeV, driven by the signal regions that are also included in the ggA mode signal interpretation. The local significance amounts to 1.7σ.

Since no significant excess over the SM expectation is observed, upper limits at 95% C.L. to the production cross sections are set. The exclusion contour for a HVT $q\bar{q} \to W' \to Wh$ signal is shown in Fig. 4.29. Cross sections from 1.3pb for $m_{W'} = 400$GeV to 0.56fb for $m_{W'} = 5$TeV are excluded. The cross section predicted by the HVT model A (B) is indicated as purple (blue) line. A W' boson within the benchmark model A (B) is excluded up to a resonance mass of 3.15 TeV [148]. The upper cross section limit on a HVT Z' boson production is shown in Fig. 4.29. The limit ranges from 1.0pb for $m_{Z'} = 300$GeV to 0.4fb for $m_{Z'} = 5$TeV. The cross section of a $q\bar{q} \to Z' \to Zh$ resonance as it is predicted by the HVT model A (B) is indicated as red (blue) line. The Z' boson mass withing the benchmark model A (B) can thus be excluded up to a resonance mass of 2.9 TeV [147].

The resulting cross section limits on signal $gg \to A \to Zh$ signal, fitting the same signal and control regions, are slightly different due to the different spin properties of the pseudo-scalar A boson. The exclusion ranges from 0.7pb at $m_A = 300$GeV to 2fb for $m_{Z'} = 1.6$TeV. The exclusion contour is shown in Fig. 4.30. Adding of bb$A$ mode sensitive regions, limits are also set to the production cross section of the b-associated pseudo-scalar A production mode, which is shown in Fig. 4.30. The limit ranges from 3.5 pb at 300 GeV to 2 fb at 1.8 GeV.

The 2HDM predicts the A boson production via both production modes, the bb$A$ mode and the ggA mode, whose relative occurrence is dependent on the 2HDM model parameter. The both one-dimensional limits given in Fig. 4.30 are statistically dependent, since the employed signal regions are overlapping and the excess at ≈ 500 GeV is mainly induced by the same events. A simultaneous scan for signal cross sections of both production modes is performed. The scan is performed by fixing the cross section for both production modes to values within a 99×99-grid and minimizing the likelihood function. The difference of the negative-log-likelihood (NLL) between the global maximum and each grid point, Δ(NLL), is used to identify the limit at 95% (68%) C.L. by requiring $\Delta(\mathrm{NLL}) = 5.99$ (2.30). The scan is shown in Fig. 4.31 separately for a variety of mass points, with the best-fit cross sections indicated by a marker. For none of the scanned mass, the best fit value indicates

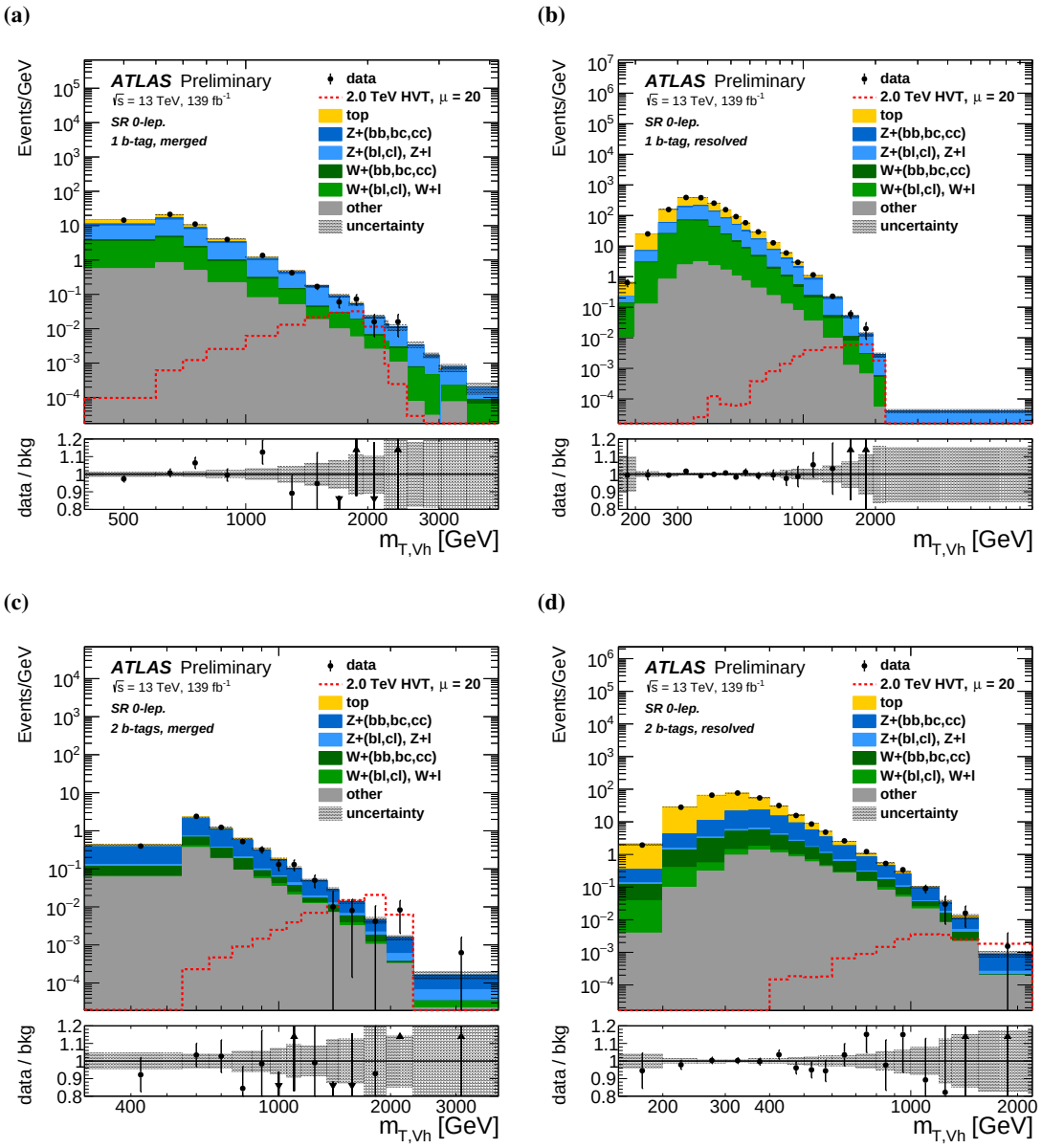

Figure 4.25: The expected and observed (post-fit) m_{Zh} distribution in the (a),(c) 1 and (b),(d) 2 b-tag signal regions with the (a),(b) *resolved* and (c),(d) *merged* event topology in the **0-lepton channel**. The quantity on the ordinate is the number of events divided by the width of the corresponding bin. The background is shown after a background-only ML fit to data. The entry "other" summarizes the VV and Vh background component. The lower panel shows the ratio of observed data to the predicted (post-fit) background. The benchmark model HVT model A is shown normalized to 20 times the theoretical cross section predicted by the HVT model A [147].

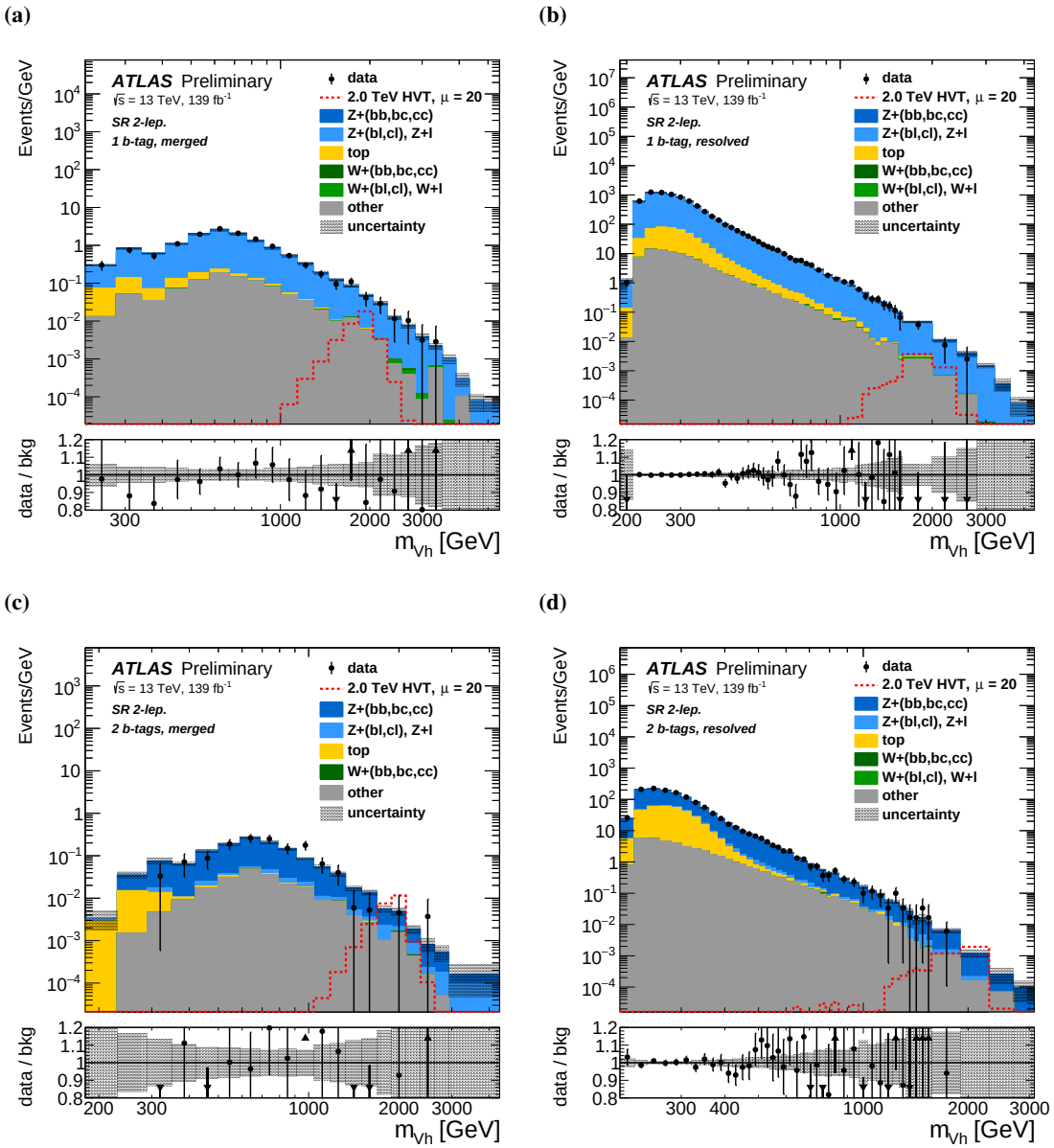

Figure 4.26: The expected and observed (post-fit) m_{Wh} distribution in the (a),(c) 1 and (b),(d) 2 b-tag signal regions with the (a),(b) *resolved* and (c),(d) *merged* event topology of the **2-lepton channel**. The background is shown after a background-only ML fit to data. The entry "other" summarizes the VV and Vh background component. The lower panel shows the ratio of observed data to the predicted (post-fit) background. The benchmark model HVT model A is shown scaled to 1 pb [147].

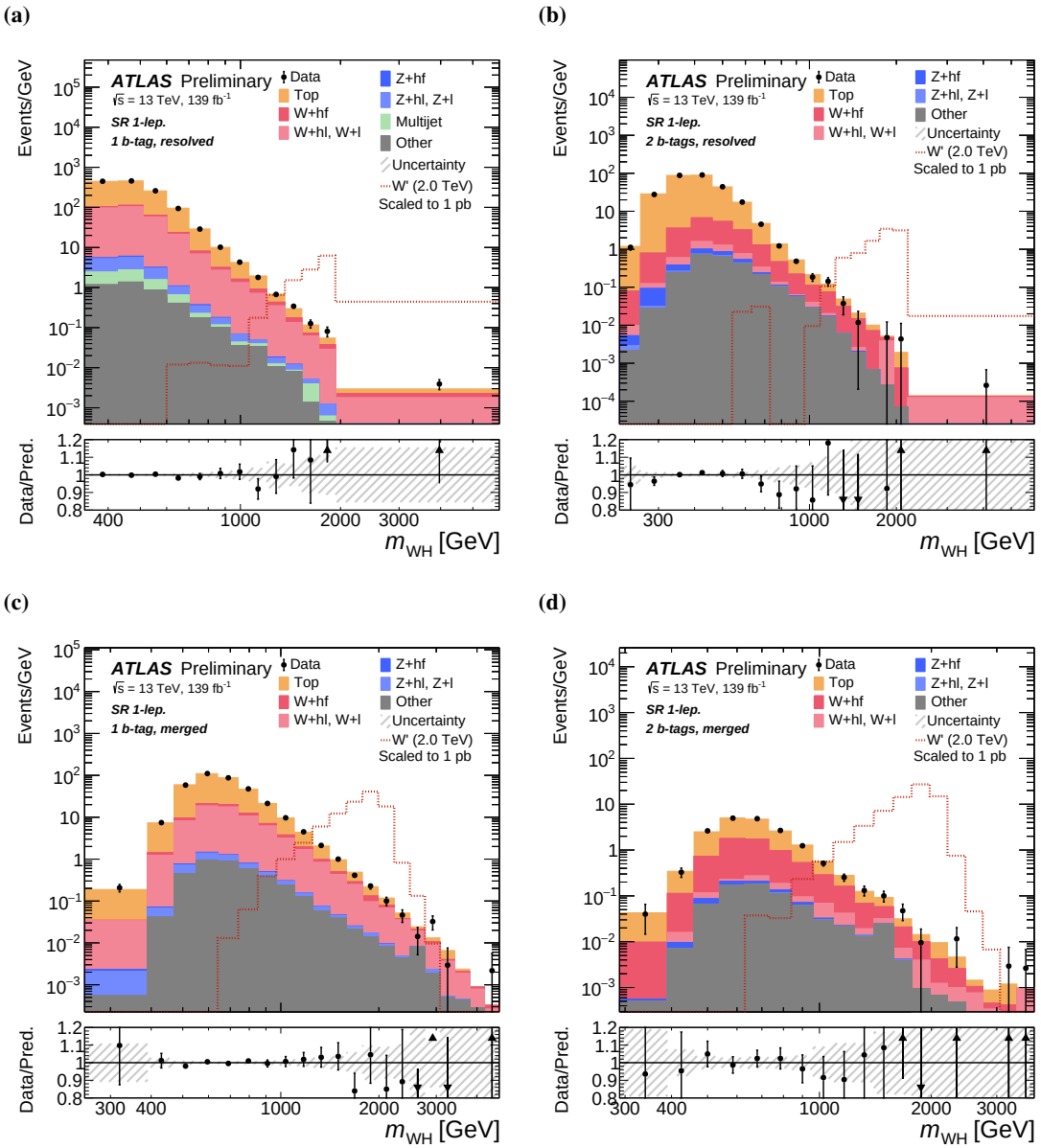

Figure 4.27: The expected and observed (post-fit) m_{Wh} distribution in the (a),(c) 1 and (b),(d) 2 b-tag signal regions with the (a),(b) *resolved* and (c),(d) *merged* event topology of the **1-lepton channel**. The background is shown after a background-only ML fit to data. The entry "other" summarizes the VV and Vh background component. The lower panel shows the ratio of observed data to the predicted (post-fit) background. The benchmark model HVT model A is shown scaled to 1 pb [148].

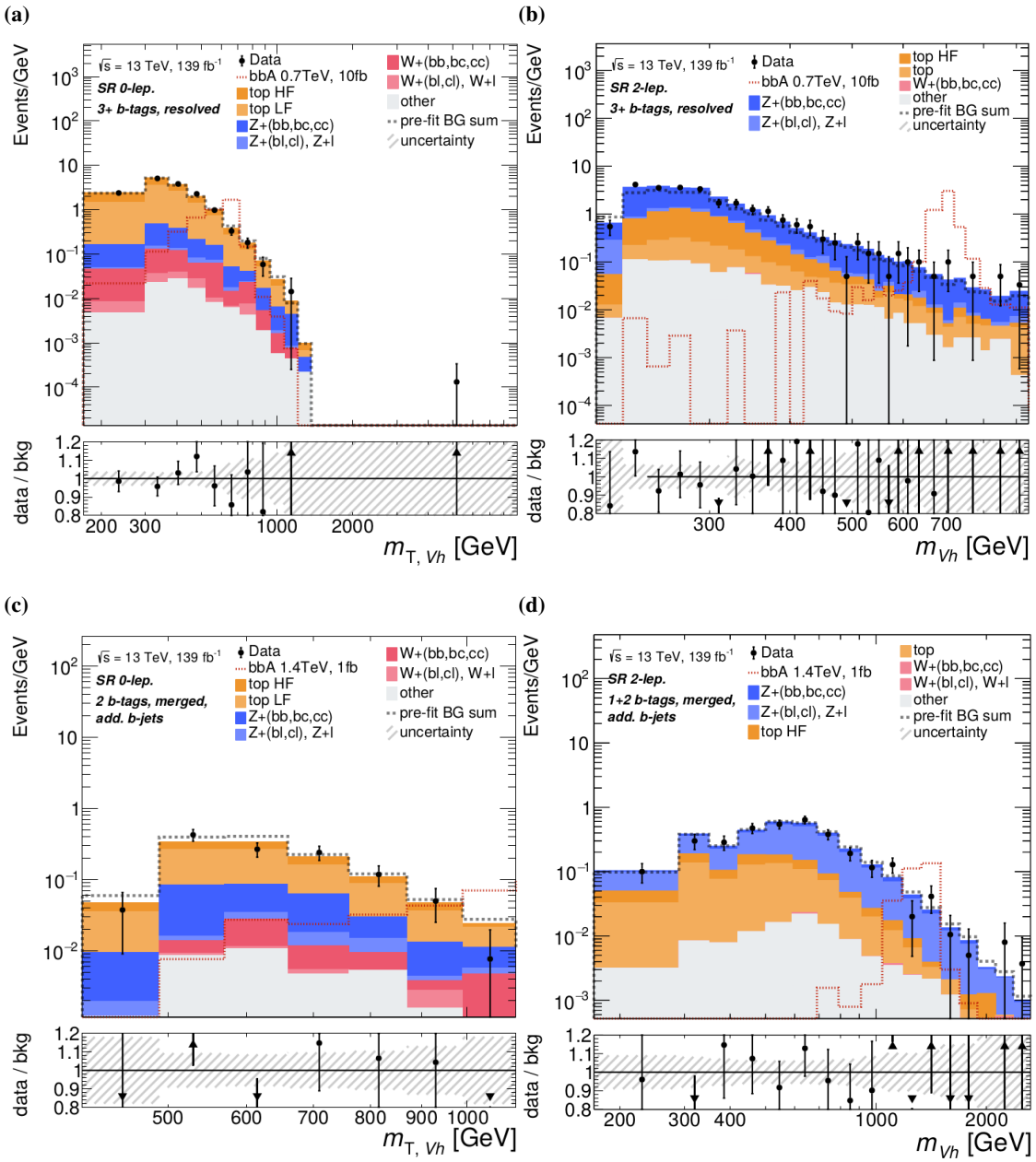

Figure 4.28: The expected and observed (post-fit) $m_{(\mathrm{T},)\mathrm{Vh}}$ distribution in the (a),(c) 0-lepton channel and (b),(d) 2-lepton channel signal regions with the (a),(b) *resolved* and (c),(d) *merged* event topology. Shown are the regions with high *b*-tagging multiplicities that are sensitive to the pseudo-scalar *A* boson produced via the bb*A* mode. The background is shown after a background-only ML fit to data. The entry "other" summarizes the *VV* and *Vh* background component. The lower panel shows the ratio of observed data to the predicted (post-fit) background. The signal $m_{(\mathrm{T},)\mathrm{Vh}}$-distribution of a hypothesized pseudo-scalar *A* boson (bb*A* mode), normalized to 10 fb^{-1}, is indicated by a red dashed line [208, 209].

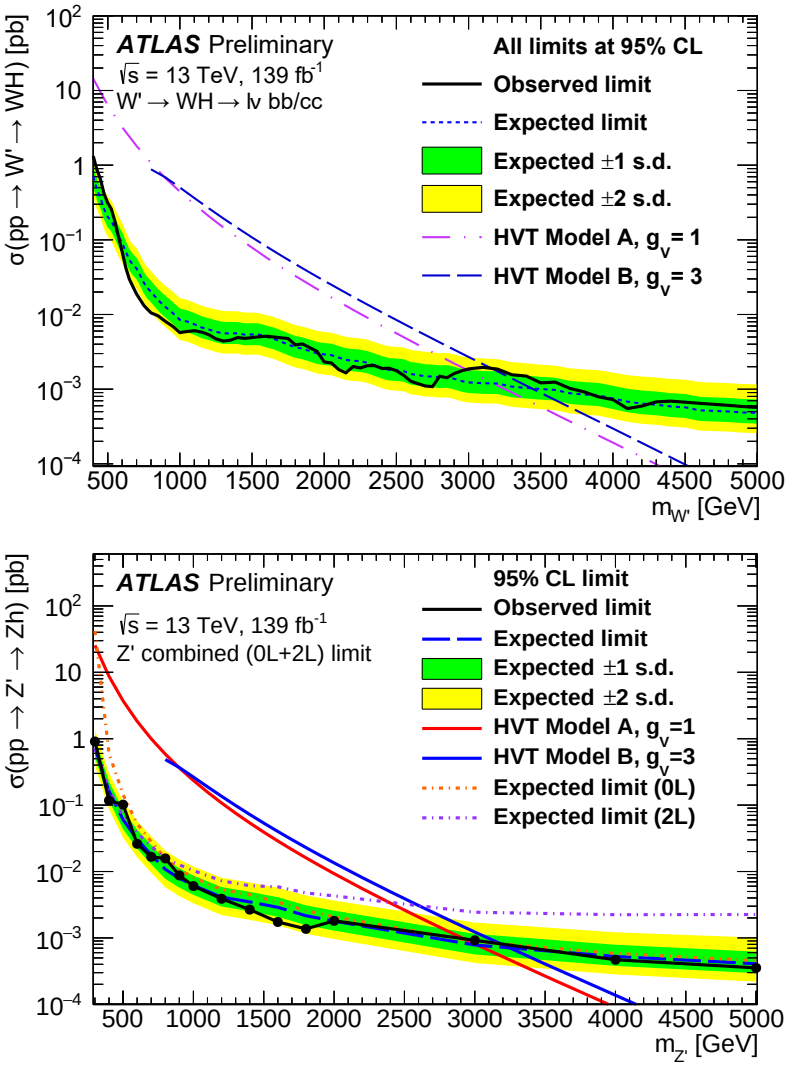

Figure 4.29: Upper limit at 95% C.L. on the $pp \to V' \to Vh$ production cross section times decay branching ratio as a function of the resonance mass for (top) $pp \to Z' \to Zh$ [147] and (bottom) $pp \to W' \to Wh$ [148] from the combination of the 0-lepton and 2-lepton channels (top) and from the 1-lepton channel (bottom). A branching fraction $h \to b\bar{b}/c\bar{c}$ of 0.598 [6] is assumed. The predicted dependence of the cross section on resonance mass is also shown for the two benchmark scenarios, HVT models A and B. The Z' boson mass in benchmark model A (B) can be excluded up to 2.9 TeV (3.2 TeV), while the W' boson mass can be excluded up to 3 TeV (3.2 TeV).

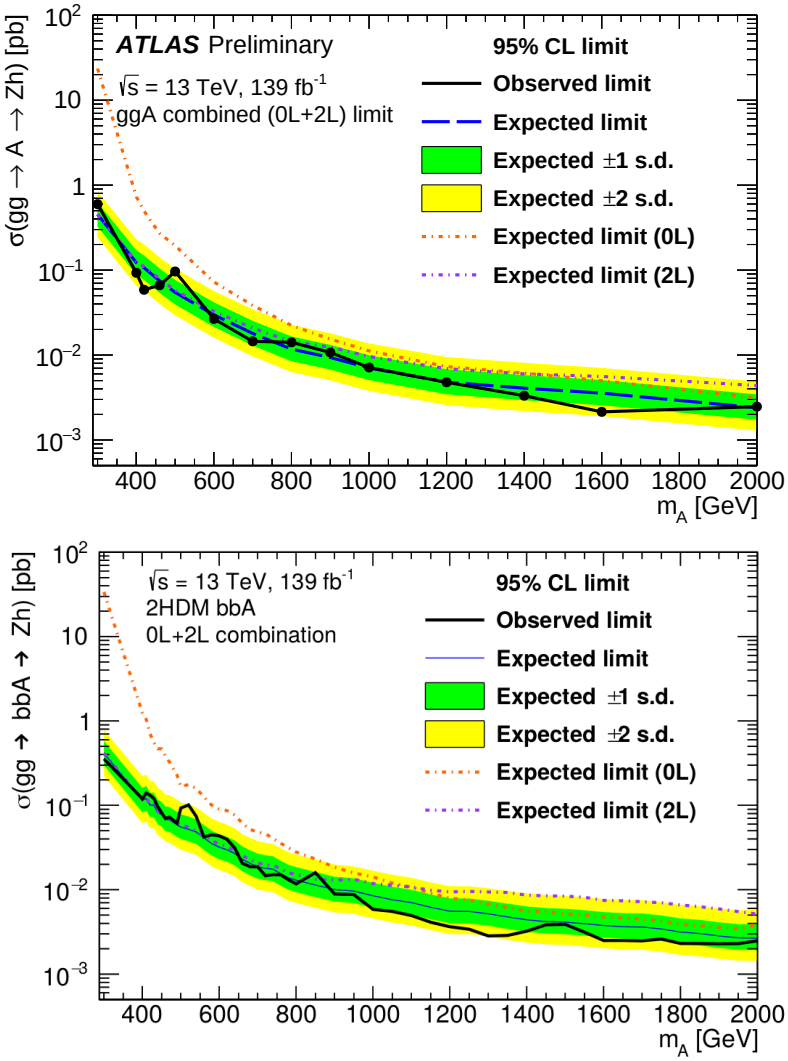

Figure 4.30: Upper limit at 95% C.L. on the $pp \to A \to Zh$ production cross section times decay branching ratio as a function of the resonance mass m_A for (top) gluon-gluon fusion production $gg \to A \to Zh$ [147] and (bottom) associated production with a b-jet pair $pp \to b\bar{b}A \to b\bar{b}Zh$ [208, 209] from combination of the 0-lepton and 2-lepton channels. The limits obtained from the 0- and 2-lepton channel are indicated separately. A branching fraction of 0.569 for $h \to b\bar{b}$ [6] is assumed.

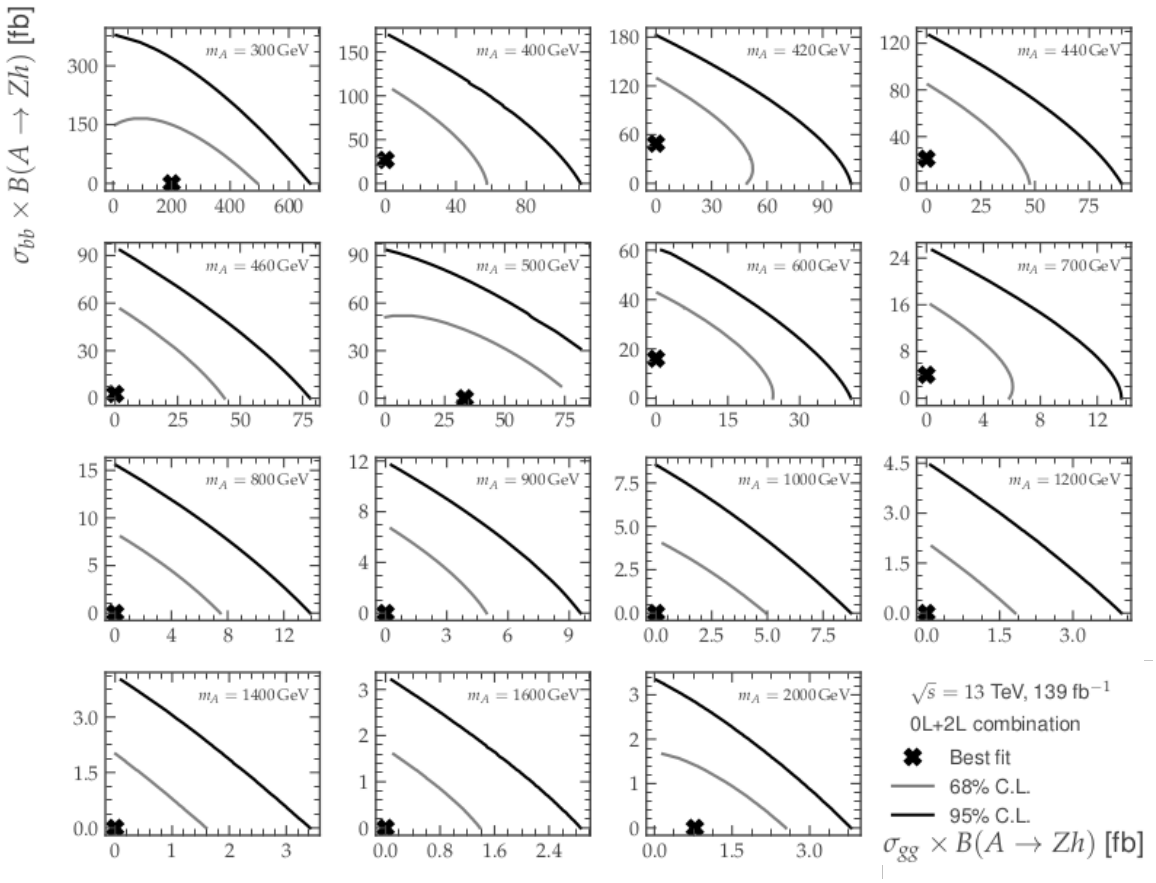

Figure 4.31: Observed two-dimensional likelihood 95% and 68% upper limits on the production cross section times branching ratio of the both for a 2HDM pseudo-scalar boson A in bbA vs ggA production mode and decaying into Zh for A masses in the range 300 to 2000 GeV [208, 209].

the simultaneous production via both modes, which would likely be the case for a large part of the parameter space in the 2HDM theory.

The cross sections and their underlying signal strengths depend to a large extent on the estimated uncertainties, in particular the theoretical uncertainties described in Section 4.4.3. The impact $\Delta\mu$ of the uncertainties is estimated as described in Section 4.5.4 and two examples for the interpretation of data in the HVT Z' interpretation is shown in Figs. 4.32 to 4.34 for a resonance mass of 500, 700 GeV and 2 TeV, respectively. Theory uncertainties are for the most resonance masses the most relevant uncertainties.

Since the pre-fit uncertainty for these theoretical sources is estimated by a comparison of the nominal prediction to that obtained by an alternative MC generator, the pre-fit uncertainty is a conservative estimation. By exploiting the information contained in the data within the signal and control region, these pre-fit uncertainties is significantly constrained and thus the impact on the signal strength is reduced. The impact is therefore given for each uncertainty with the pre-fit as well as the post-fit uncertainty.

The pull $\mathcal{P}$ (c.f. Eq. (4.21)) is overlaid on top of the impact in Figs. 4.32 to 4.34. The dominating impact on the signal strength with a resonance mass of 500 GeV is caused by *PS model* uncertainties of the top quark background. The indicated pull on the top quark's *PS model* NP shows that the data is best described by an intermediate background prediction between the nominal and the alternative MC setup. For higher masses the theory uncertainty on the top quark prediction becomes less important. This is in agreement with the fact that the top quark background is located at small $m_{(\mathrm{T},)\mathrm{Vh}}$ values. Instead, the *ME+PS modeling* uncertainties to the V+jets description become more important.

The production cross section limit of a W' and Z' is interpreted also in the more general 2-dimensional parameter space of the HVT, given by the coupling constants g_H and g_F (c.f. Eq. (1.39)), not restricted to the benchmark model A or B. The exclusion at 95% C.L. is given for the signal mass hypotheses of 2, 3 and 4 TeV for both the W' boson and the Z' boson in Fig. 4.35. The benchmark scenarios model A and B are indicated by a marker. The produced signal samples employ the narrow width approximation which is a good approximation for low couplings, g_H and g_F. For higher coupling strength this approximation increasingly becomes inadequate which is indicated by a gray shade at the edges of the parameter space. Simultaneously strong couplings to both the fermion fields and the boson fields are excluded also for masses beyond the above given mass limits. In contrast, HVT parameter configuration setting g_F to zero is not excluded for any mass point yet. Such a configuration is referred to as the HVT model C and is discussed in Chapter 5.

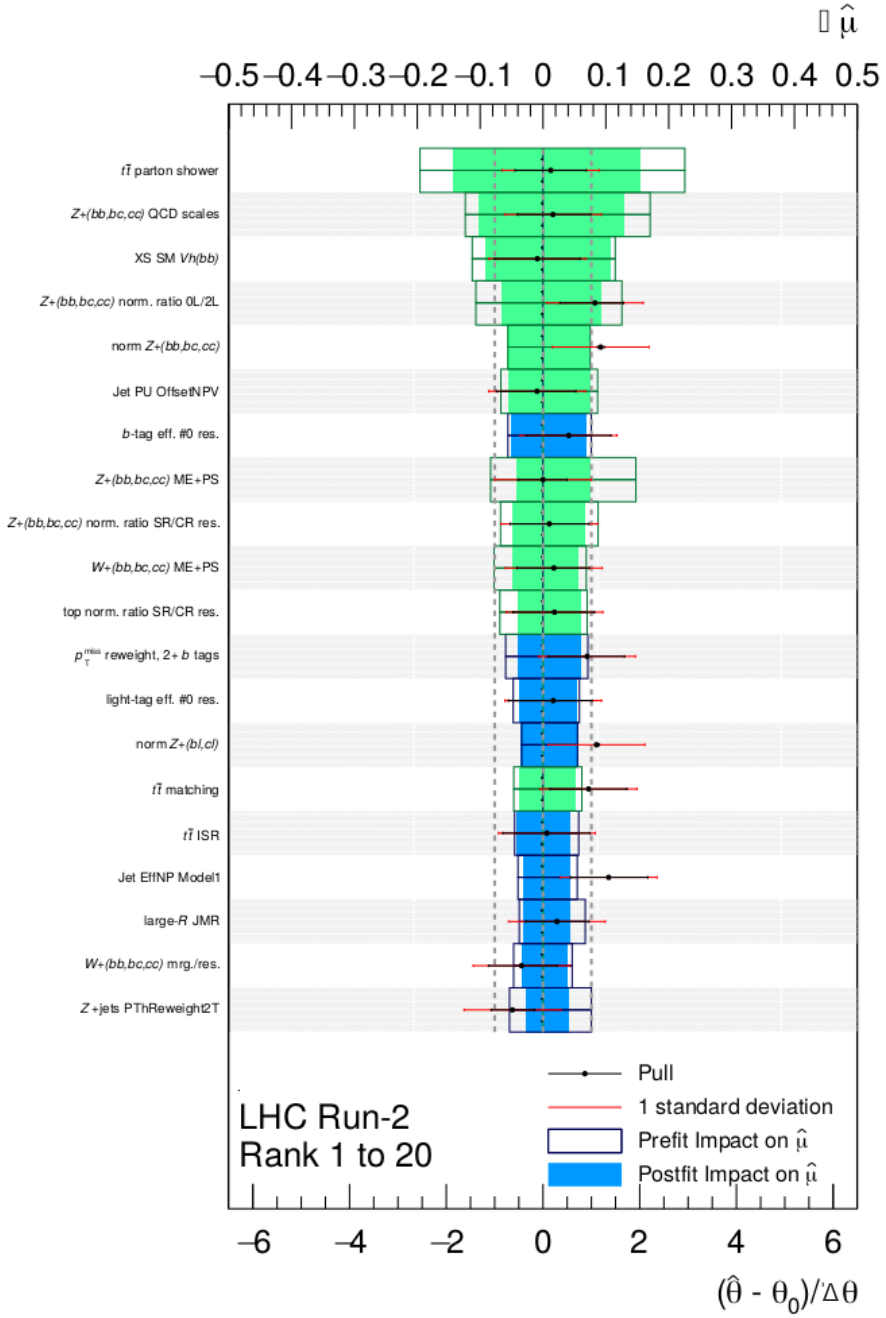

Figure 4.32: Impact of the 20 most relevant nuisance parameters on the best-fit signal strength, $\hat{\mu}$, for a Z' signal with $m_{Z'} = 500$ GeV. The box contours (colored boxes) show the impact for a NP value set to one pre-fit (post-fit) standard deviation from the nominal NP value. The black dots with error bars indicate the pulls on the NPs $(\hat{\theta} - \theta_0)/\Delta\theta$ (lower abscissa). The green box color indicates a negative correlation between the pulls and the corresponding impact $\Delta\mu$.

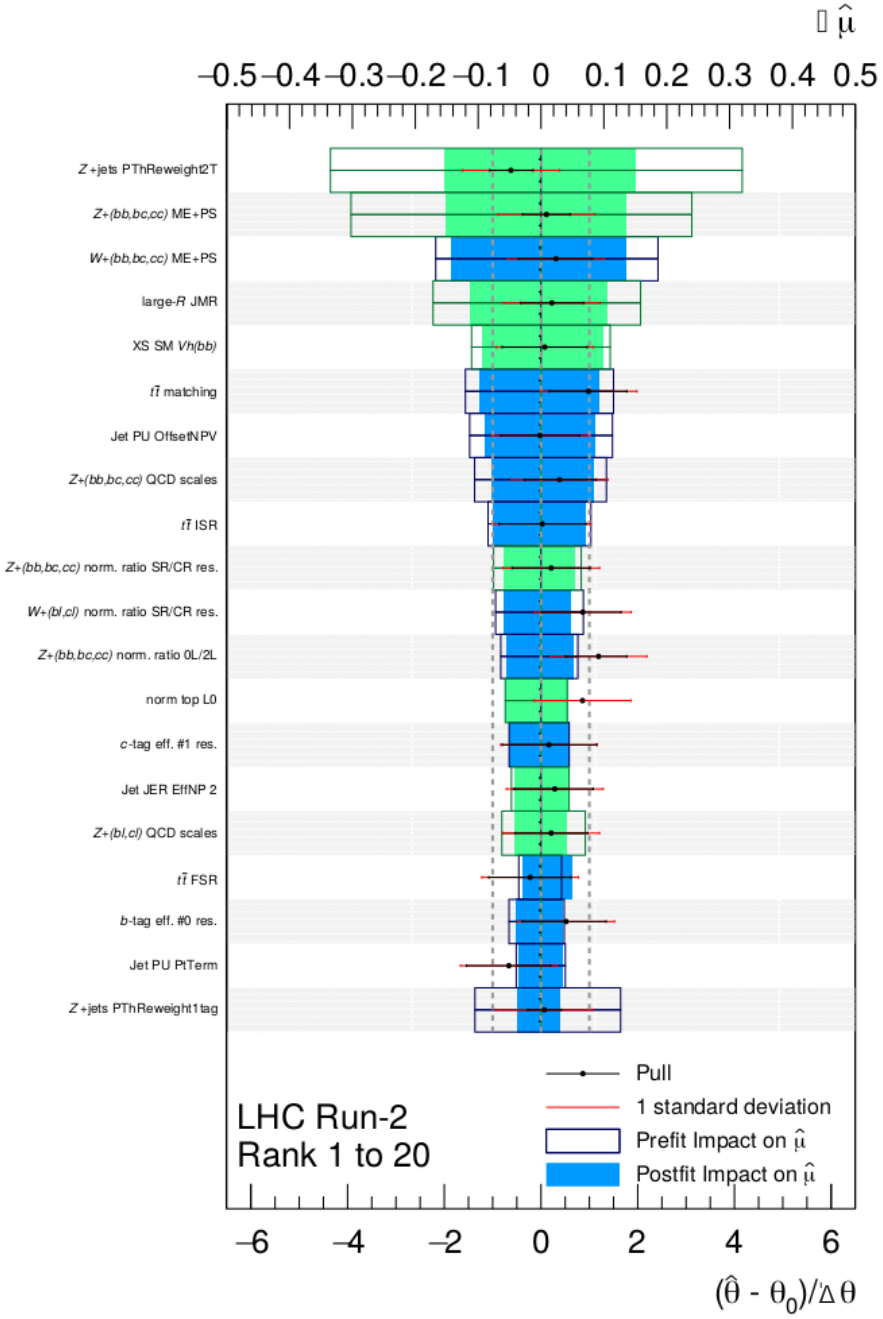

Figure 4.33: Impact of the 20 most relevant nuisance parameters on the best-fit signal strength, $\hat{\mu}$, for a Z' signal with $m_{Z'} = 700$ GeV. The box contours (colored boxes) show the impact for a NP value set to one pre-fit (post-fit) standard deviation from the nominal NP value. The black dots with error bars indicate the pulls on the NPs $(\hat{\theta} - \theta_0)/\Delta\theta$ (lower abscissa). The green box color indicates a negative correlation between the pulls and the corresponding impact $\Delta\mu$.

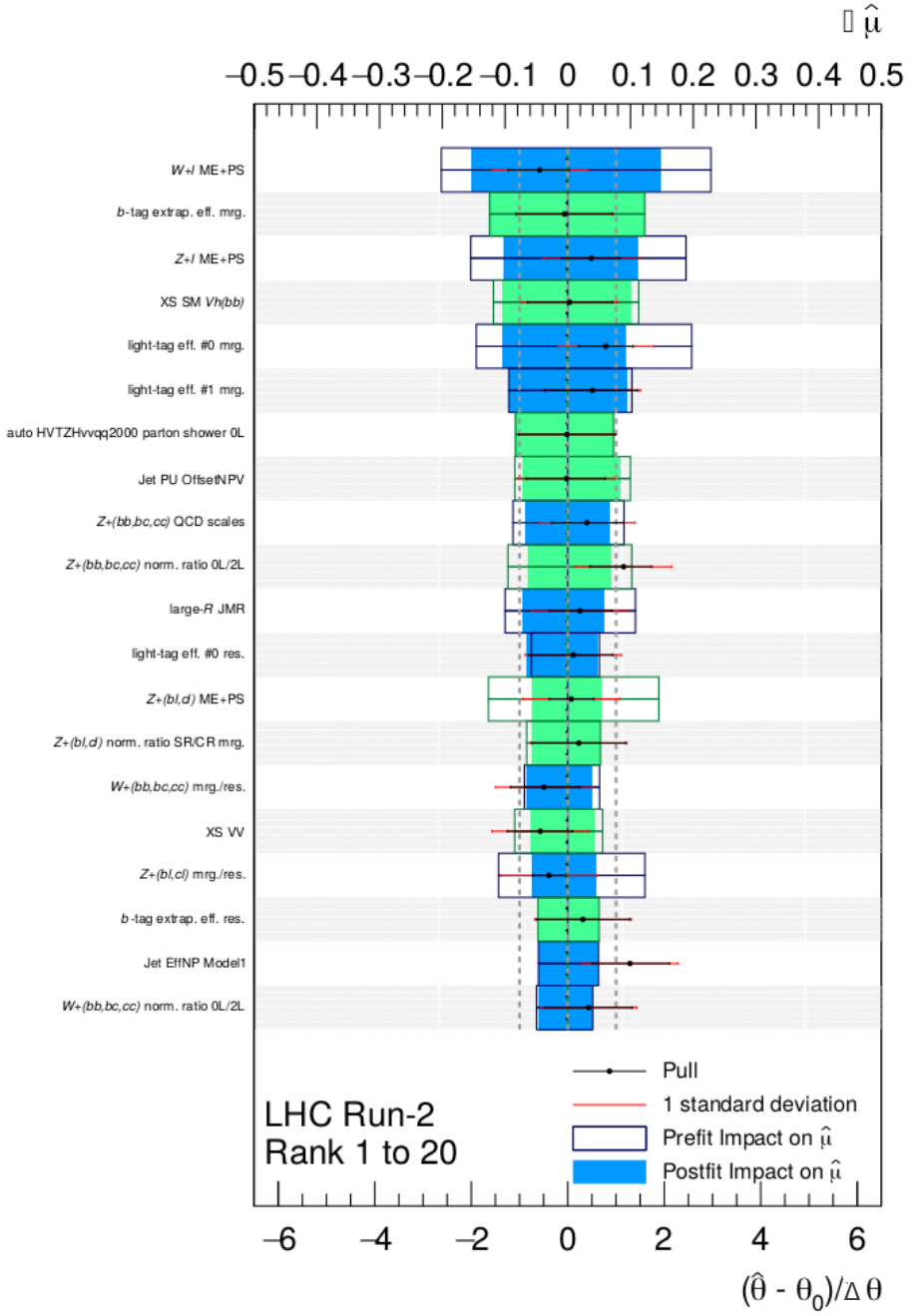

Figure 4.34: Impact of the 20 most relevant nuisance parameters on the best-fit signal strength, $\hat{\mu}$, for a Z' signal with $m_{Z'} = 2000$ GeV. The box contours (colored boxes) show the impact for a NP value set to one pre-fit (post-fit) standard deviation from the nominal NP value. The black dots with error bars indicate the pulls on the NPs $(\hat{\theta} - \theta_0)/\Delta\theta$ (lower abscissa). The green box color indicates a negative correlation between the pulls and the corresponding impact $\Delta\mu$.

(a)

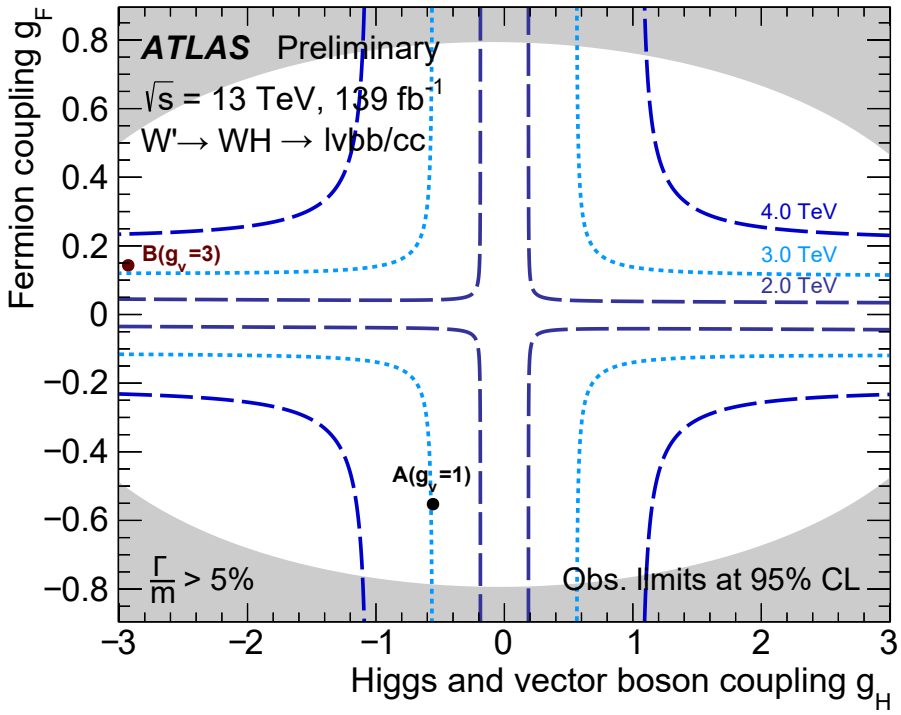

Figure 4.35: Observed limits at 95% C.L. in the 2-dimensional parameter space of the coupling coefficients to the Higgs boson g_H and the fermions g_F of the HVT model. The dashed lines indicate the W' masses of 2 TeV, 3 TeV and 4 TeV. The black markers indicate coupling constants defining the benchmark models HVT Models A and B. The gray area with high coupling indicates the area of phase-space in which the decay width of the resonance is expected to dominate the signal m_{Wh} shape [148].

CHAPTER FIVE

SEARCH FOR ZH RESONANCE PRODUCTION VIA VECTOR BOSON FUSION

In this chapter, the feasibility to probe phenomena beyond the Standard Model (SM) via a generic search for heavy new particles, decaying into a Z boson and a SM-like Higgs boson (h) is studied. The invariant mass, m_{Zh}, of the diboson system is used as final discriminant between signal and background processes. The Higgs boson is reconstructed from the jets originating from the dominant $h \to b\bar{b}$ decay mode, while the Z boson is reconstructed from two oppositely charged leptons of same flavor ($Z \to \ell^+\ell^-$ with $\ell^\pm = e^\pm$ or $\mu^\pm$). Signal candidate events are selected based on the transverse back-to-back production of the Z and the Higgs boson. from the two-body decay of a new heavy resonance produced approximately at rest in the transverse plane. A potential signal would manifest itself as excess of events in the invariant mass distribution, m_{Zh}, on top of a smooth SM background distribution.

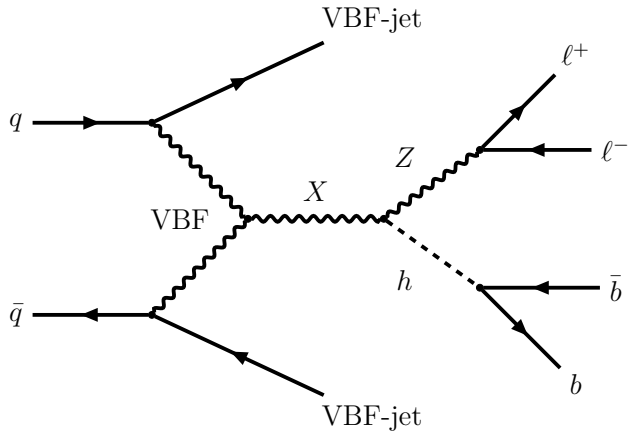

Figure 5.1: Tree-level Feynman diagram for the production of a heavy particle X via the vector boson fusion production mode, with the subsequent diboson decay $X \to Zh$.

The search in this chapter is closely related to the analysis presented in Chapter 4, inheriting the basic event selection criteria and background predictions. While this *parent analysis* is searching for Drell-Yan-like (DY) production of resonances via quark-antiquark annihilation ($q\bar{q}$), gluon-gluon fusion (ggF) and in association with b-quarks (bb$A$ mode), the search in this chapter focuses on the diboson

resonance production via vector boson fusion (VBF) alone. This process has a characteristic signature of two additional jets measured in the forward regions of the detector in opposite η-hemispheres.

The tree-level Feynman diagram for the VBF production of a Zh diboson resonance is depicted in Fig. 5.1. The two partons from two colliding protons emit vector bosons which fuse into a new resonance. The partons themselves continue on the path close to the collision axis and are reconstructed as jets in the forward region of the detector. The requirement of two forward jets reduces the contribution of SM background processes by a factor of about 100. For the interpretation of the data, a benchmark heavy vector triplet (HVT) signal hypothesis (c.f.Section 1.3.2) with an electrically neutral, massive spin-1 vector boson resonance, Z', is used.

Resonances from HVT Models A and B discussed in the context of the *parent analysis* could also be produced via the VBF production mechanism. However, for large regions of the parameter space in these models, the production cross section via VBF is very small compared to the $q\bar{q}$ production, as shown in Fig. 5.2. However, there are certain parts of the HVT parameter space where the coupling between the hypothetical spin-1 particles and fermions is strongly suppressed and the VBF production mode dominates over the $q\bar{q}$.

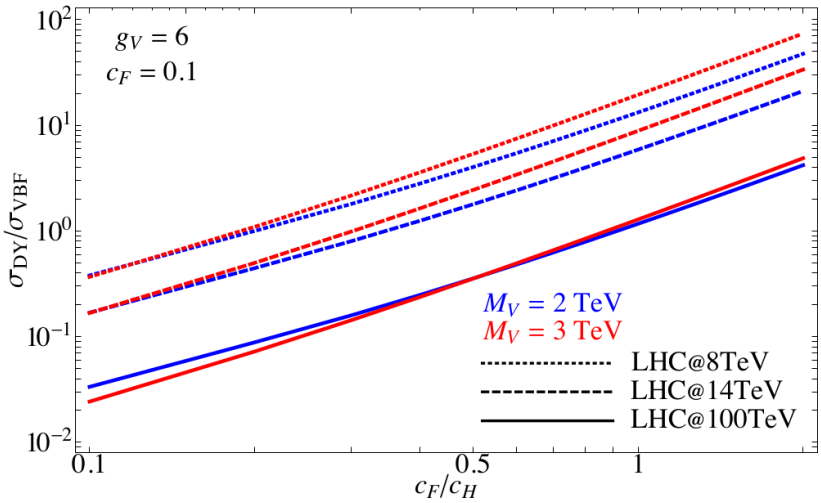

Figure 5.2: Ratio of cross sections for the production of a heavy vector triplet particle via $q\bar{q}$ (aka Drell-Yan, DY) and VBF production mode [40]. The VBF production becomes dominant for very low ratio of coupling parameters, c_F/c_H. Resonances in model A and B, which are defined with $c_F/c_H \gtrapprox 1$, are produced predominantly via $q\bar{q}$. In the limit case of model C ($c_F \to 0$), such resonances are produced in VBF production mode only.

In this specific, so-called HVT model C benchmark signal scenario studied in this chapter, the coupling, c_F, of the spin-1 resonance to fermions is set to zero. Spin-1 particles decaying into a Z boson and a Higgs boson as predicted by the HVT model C have been simulated at leading order (LO) QCD accuracy using MadGraph 5 [53], employing the NNPDF2.3 LO parton density function (PDF) set [116]. MadGraph 5 is interfaced to Pythia 8 [210] for the simulation of the parton shower using the A14 set of tuned parameters [198]. The event generator was interfaced to EvtGen v1.2.0 [118] for the simulation of bottom and charm hadron decays. Several Monte Carlo (MC) samples are generated

for Z' masses in the range from 300 GeV up to 3 TeV, with a subsequent detailed simulation of the detector response using GEANT 4 [61].

The predicted cross sections for signals from a HVT model C are significantly smaller than those of model A and B. Therefore, a model C signal would contribute to negligible extent to the signal regions of the *parent analysis*. On the other hand, by applying additional VBF selection criteria, the background contributions are further reduced, providing the sensitivity for the HVT model C signal, while signals produced via $q\bar{q}$ in model A and B become negligible after the VBF selection.

In this chapter, the feasibility of the search for $X \to Zh$ resonances produced via VBF in the 2-lepton (i.e. $Z \to \ell^+\ell^-$) decay channel is explored. Similar searches for the Vh resonances could also be performed in the 0- and 1-lepton channels. However, the sensitivity for the signal at low resonance masses is expected to be the highest in the 2-lepton channel due to a better invariant mass resolution. The 0- and 1-lepton channels, on the other hand, rely on the $E_{\mathrm{T}}^{\mathrm{miss}}$ reconstruction, which is prone to larger background contributions at lower $E_{\mathrm{T}}^{\mathrm{miss}}$ values. The background contribution decreases at large $E_{\mathrm{T}}^{\mathrm{miss}}$ values, i.e. for larger resonance masses, but the signal sensitivity with the current dataset is expected to be small at these large masses due to an already low expected HVT model C signal cross section. A similar search for $V' \to VV$ resonance decays via VBF V' production that has been performed in Ref. [150] sets upper limits on the cross section, $\sigma(X \to VV)$ between 0.1 pb at resonance mass $m_X = 500$ and 10^{-4} pb at resonance masses between 3 and 5 TeV.

The studies in this chapter build on the studies performed in the *parent analysis* (c.f. Chapter 4). The set of MC samples described in Section 4.1 is used to describe the major background contributions from the $t\bar{t}$ production and Z boson production in association with jets (Z+jets). These Z bosons are produced via quark-antiquark annihilation and recoil against a gluon or quark emmision (c.f. Fig. 4.3(a)). In addition to those background processes, further processes, relevant for the selection of VBF signal candidates, are considered. Electroweak production of a Z boson in association with two jets (VBF-Z) is simulated by SHERPA 2.2.1 [211]. This is found to be a minor background component with less than 1% contribution.

Furthermore, single top-quark production in association with a Z boson (tZq) is modeled by MADGRAPH 5 interfaced with PYTHIA 8.230 for the parton shower using the A14 set of tuned parameters. Single top-quark production in association with a W boson (Wt), as well as top-quark pairs produced in association with a Higgs boson ($t\bar{t}h$) or in association with a vector boson ($t\bar{t}V$) are also considered, simulated by MC as described in detail in the *parent analysis*. These top-quark related processes ($t\bar{t}h$, $t\bar{t}V$, tZq, Wt and single-top produced via the t-channel) are found to have minor impact on the total background with less than 1% relative contribution each. Furthermore, the shape of the distributions of the final discriminant is similar to the $t\bar{t}$ background component and the two can therefore not be disentangled in the final fit. Therefore these backgrounds are collectively treated and referred to as top quark backgrounds.

5.1 Event selection

The baseline event selection in the presented VBF signal search is fully adopted from the *parent analysis*, c.f. Section 4.2.2, including the object definitions given in Section 4.2.1. Main features of

the selection requirements are outlined here, while for exact numerical values used for the selection the reader is referred to Section 4.2.2. Events are recorded if they pass the single-lepton trigger requirements given in Appendix B.11. Events are required to have two reconstructed oppositely charged leptons with the same flavor (e^+e^- or $\mu^+\mu^-$), where one lepton has to be matched to the corresponding triggering object and pass the offline p_{T} threshold to ensure the full trigger efficiency. The invariant mass of the dilepton system has to be compatible with the measured Z boson mass [6]. The p_{T} of the Z boson is required to be above a certain threshold value that is parameterized as a function of the reconstructed candidate diboson mass, m_{Zh}. Events with significant missing transverse momentum are vetoed.

The Higgs boson candidate in each event is preferably reconstructed using two highest-p_{T} b-tagged small-R jets. These events are referred to as having the *resolved* event topology. The Higgs boson candidate is reconstructed as the four-vector sum of the corresponding two jets. In case only one b-tagged jet is present in the event, the highest-p_{T} non-b-tagged jet is used instead. The two jets selected in such a way are referred to as the *signal jets*. Highly boosted and therefore collimated Higgs boson decay products often cannot be reconstructed as two small-R jets. If the reconstruction of the resolved event topology fails, the Higgs boson candidate is attempted to be reconstructed as a large-R jet containing both Higgs boson decay products. Such events are referred to as events with *merged* event topology. The track jets that are ghost-associated [90] with the large-R jet are used for the b-tagging within the boosted $h \to b\bar{b}$ decays. Events with b-tagged track jets that are not associated to the large-R jet are discarded to mitigate background contributions from $t\bar{t}$ production. The reconstructed dijet or large-R jet mass, $m_{jj/J}$, is required to be compatible with the mass of the SM-like Higgs boson of $m_h = 125$ GeV. A summary of all baseline selection criteria, in particular numerical threshold values can be found in Table 4.2.

Each of the above event selection criteria has been optimized in the context of $q\bar{q}$ signal production. While similar criteria are also expected to be suitable for the VBF signal, it remains to be studied in future, how these criteria may be optimized for the properties of the VBF topology. In contrast to the $q\bar{q}$ signal production, the resonance produced via VBF is, in general, not produced at rest, but has an finite amount of transverse momentum, $p_{\mathrm{T}}^{Z'}$. For the standard signal processes, the $p_{\mathrm{T}}^{Z'}$ peaks around 100 GeV, as can be seen in Fig. 5.3. The larger values of Z' boson p_{T} smears out also the p_{T}-distribution of the Higgs and the Z boson and leads to their softer p_{T} spectra. The p_{T}^{Z} and $p_{\mathrm{T}}^{jj/J}$ requirements on the are optimized for the harder boson p_{T} spectra in signals produced via $q\bar{q}$ and might be further optimized for the VBF topology to increase the signal sensitivity.

As in the case of the *parent analysis*, the multiplicity of b-tags in an event is employed to subdivide the signal region with resolved event topology into regions with 1 and with 2 b-tags. The expected number of background events in the 2 b-tag regions with *merged* event topology is expected to be in the order of 5 events. In order to avoid large statistical uncertainties, no subdivision based on b-tag multiplicity is therefore applied in the *merged* signal region. Instead, the *merged* regions with 1 and 2 b-tags are combined into a single one.

Signal events produced via VBF are characterized by the presence of two additional jets in the forward region of opposite η-hemispheres, as illustrated in Fig. 5.4. Further event selection criteria are introduced to select these so-called *VBF jets*. The *VBF jet* candidates are reconstructed as small-R jets with looser η-selection requirement compared to the *signal jets*, i.e. $|\eta| < 4.5$. Candidate *VBF jets* in this additional η-region with $2.5 < |\eta| < 4.5$ are required to have $p_{\mathrm{T}} > 30$ GeV, to allow for the

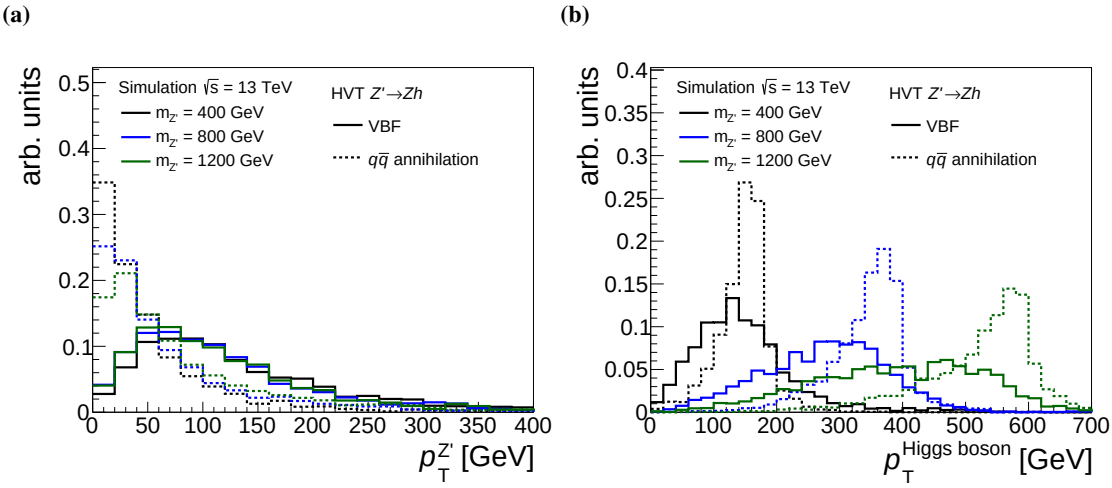

Figure 5.3: The expected p_{T} distribution of (a) the hypothetical spin-1 particle Z' in HVT models and of (b) the Higgs boson. The distributions are shown separately for the Z' boson production via VBF (solid lines) and $q\bar{q}$ (dashed lines).

sufficient pile-up suppression by the jet vertex tagger (JVT) [89]. VBF signal candidate events with the *resolved* event topology are therefore required to have at least four distinct small-R jets in the final state. In case of the selection with the *merged* event topology, the *VBF jet* candidates are required to have an angular distance of at least $\Delta R > 1.4$ from the large-R signal jet, to avoid the double counting of jet constituents. The highest-p_{T} non-signal jet is considered to be the leading *VBF jet* (j_1). The sub-leading *VBF jet* (j_2) is the highest-p_{T} jet falling in the opposite η-hemisphere, resulting in $\eta_{\mathrm{j}_1} \cdot \eta_{\mathrm{j}_2} < 0$. The *VBF jets* are characterized by a large gap in pseudo-rapidity, $\Delta\eta_{\mathrm{jj}}^{\mathrm{VBF}}$.

It has been found that a large pseudo-rapidity gap $\Delta\eta_{\mathrm{jj}}^{\mathrm{VBF}}$ between the *VBF jets* and hence a large invariant dijet mass, $m_{\mathrm{jj}}^{\mathrm{VBF}}$, are well suited discriminants to suppress the non-VBF background contributions, as can be seen in Fig. 5.5(a). The $\Delta\eta_{\mathrm{jj}}^{\mathrm{VBF}}$ distribution for signal events has its maximum, depending on the resonance mass, between 6 and 9. The background distribution, on the other hand, has two distinct peaks around 4 and 6. A kink in the background distribution is visible at $\eta = 5$. This can be explained as a selection bias from the requirement of the *VBF jets* being in opposite hemispheres, and due to the increased number of jets that become available above $|\eta| > 2.5$, in contrast to the *signal jets*. The $m_{\mathrm{jj}}^{\mathrm{VBF}}$ observable is strongly correlated to $\Delta\eta_{\mathrm{jj}}^{\mathrm{VBF}}$ but also depends on the jet momenta. It can, therefore, discriminate better between the signal and the background with low-p_{T} jets compared to the $\Delta\eta_{\mathrm{jj}}^{\mathrm{VBF}}$ observable. The $m_{\mathrm{jj}}^{\mathrm{VBF}}$ values in signal events are widely spread, reaching values of up to 2 TeV for most resonance masses. In contrast, for the background processes the $m_{\mathrm{jj}}^{\mathrm{VBF}}$ distribution peaks at 0. Additional observable, the centrality, ζ, is introduced to quantify to what extent the reconstructed Zh-diboson system is produced centered between the two *VBF jets*,

$$\zeta = \frac{|\eta_{Zh} - (\eta_{\mathrm{j}_1} + \eta_{\mathrm{j}_2})/2|}{|\eta_{\mathrm{j}_1} + \eta_{\mathrm{j}_2}|}. \tag{5.1}$$

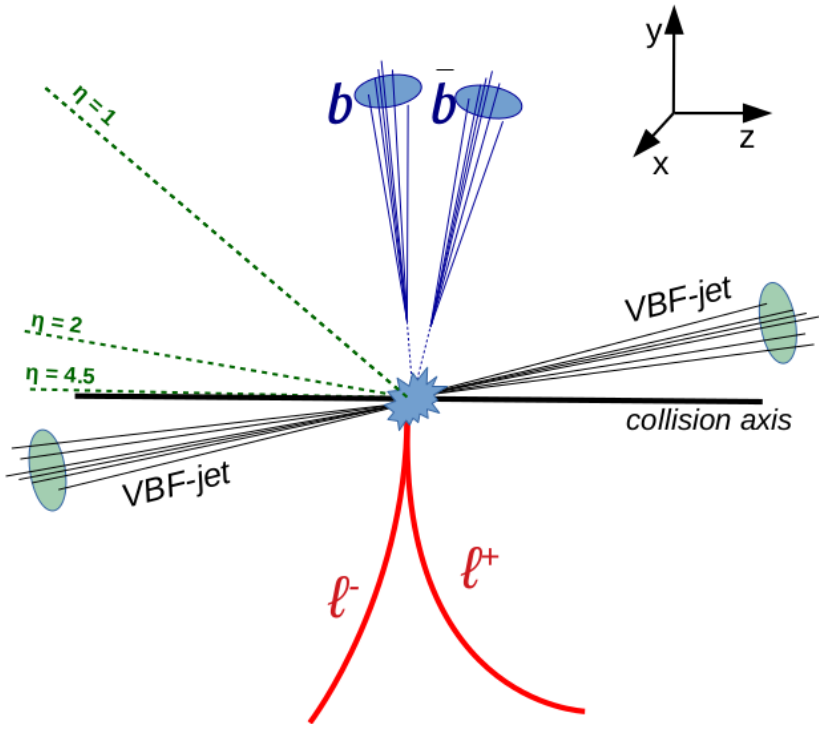

Figure 5.4: Event topology for a VBF production of a HVT Z' resonance decaying into $Zh \to \ell^+\ell^- b\bar{b}$. The two quarks emmiting the vector bosons continue their path in the forward detector region and manifest themselves as additional jets (*VBF jets*) with large separation in pseudo-rapidity, $\Delta\eta_{jj}^{VBF}$. The green dashed lines indicate the η values of 1,2 and 4.5. Latter is the η-threshold for *VBF jet* reconstruction.

The centrality, ζ, (c.f. Ref. [212]) can be used to distinguish between the QCD and EW processes. As seen from Fig. 5.5(c) for signal events this observable is peaking at low values around 0.3. However, the discrimination power of this observable is limited, because the described *signal jet* and *VBF jet* selection criteria bias the event selection towards a signal-like ζ distribution.

Based on the discriminant observables introduced above, the signal selection requirements are optimized to achieve the maximum signal significance. The signal significance is approximated by $s/\sqrt{b}$, with s being the number of expected signal and b the number of expected background events. Several configurations of $\Delta\eta_{jj}^{VBF}$, m_{jj}^{VBF} and ζ requirements are tested. Fig. 5.6 shows two-dimensional distributions of the observable pair (m_{jj}^{VBF}, $\Delta\eta_{jj}^{VBF}$), separately for the total SM background contribution and for an example signal mass point of 500 GeV, normalized to an integrated luminosity of 1 pb^{-1}. A similar figure for the two other observable pairs, (m_{jj}^{VBF}, ζ) and (ζ, $\Delta\eta_{jj}^{VBF}$), can be found in Appendix D.1. The signal significance is calculated at each point of the given two-dimensional parameter space by applying corresponding lower thresholds on the variables m_{jj}^{VBF}, $\Delta\eta_{jj}^{VBF}$ and ζ in an event. The results are shown in Fig. 5.6(c). The maximum signal significance for the signal with mass $m_{Z'} = 500$ GeV is obtained for the requirement of $m_{jj}^{VBF} > 770$ GeV and $\Delta\eta_{jj}^{VBF} > 1$. This significance stays relatively stable also for lower thresholds in the range of $m_{jj}^{VBF} \in [600, 1200]$ GeV and $\Delta\eta_{jj}^{VBF} \in [0, 4]$ or for an upper threshold of $\zeta < 0.5$. The optimal event selection requirement is

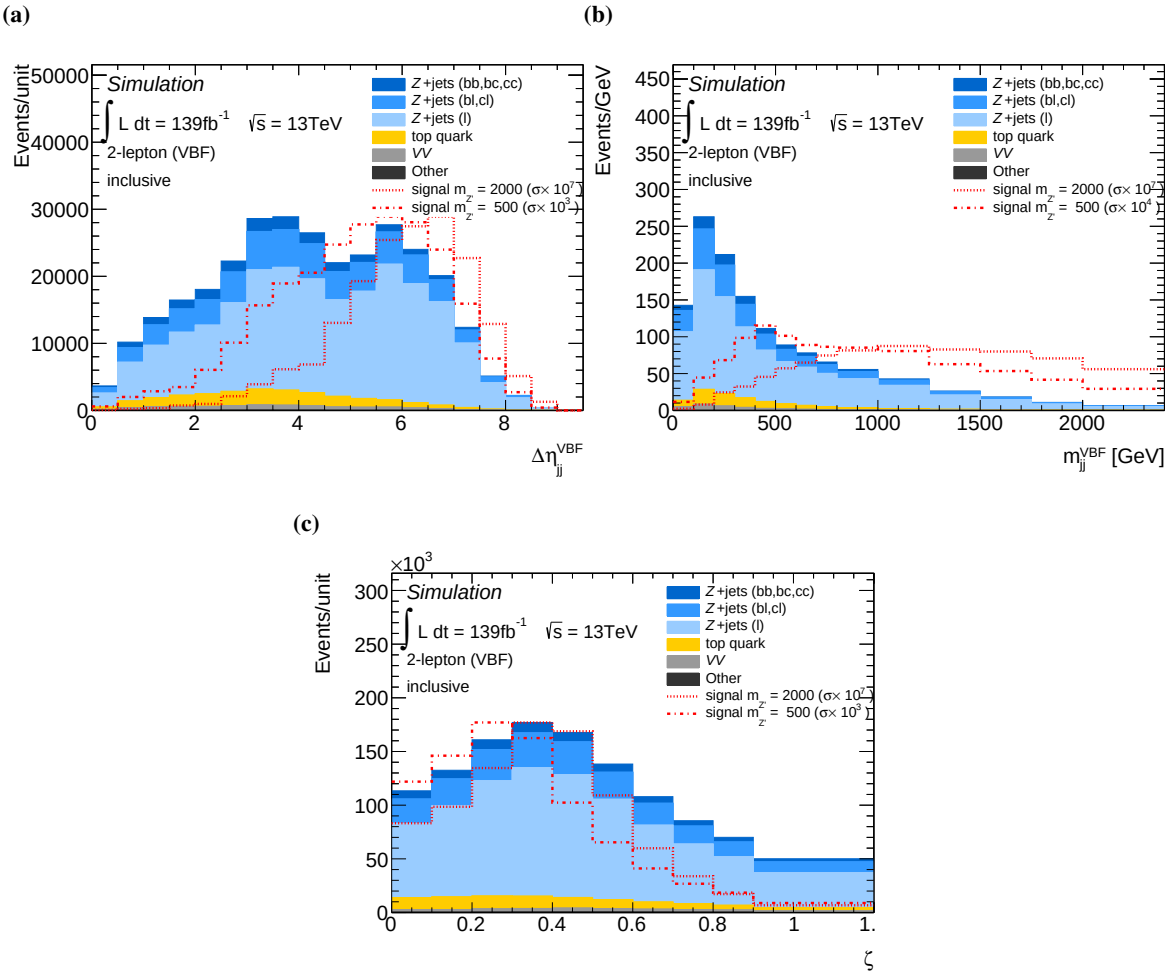

Figure 5.5: The expected (a) pseudo-rapidity gap, $\Delta\eta_{jj}^{VBF}$, (b) invariant dijet mass, m_{jj}^{VBF}, and (c) centrality,ζ, distributions from the signal and SM background processes after the selection criteria from Table 4.2 plus the requirement of two *VBF jet* candidates. The signal predictions are shown for the VBF Z' production within the HVT model C for two different Z' mass points.

slightly dependent on the resonance mass (see Appendix D.1). The optimum m_{jj}^{VBF} threshold increases for signals with higher resonance mass, up to an optimal m_{jj}^{VBF} requirement of 1.5 TeV for a resonance mass of 2 TeV. However, as for the shown example, the resulting significance stays stable for a large region of the 2-dimensional parameter space even at lower event selection thresholds. Furthermore, the optimization of the significance defined by $s/\sqrt{b}$ breaks down for the low background contribution, expected after a large threshold value of e.g. 1.5 TeV. The more conservative event selection with $m_{jj}^{VBF} > 600$ GeV and $\Delta\eta_{jj}^{VBF} > 4$ is chosen for the present analysis, since it also provides a larger number of events in control data regions and, therefore, facilitates the validation of the background modeling. This choice also ensures consistency and combination with future searches in the 0- and 1-lepton channels.

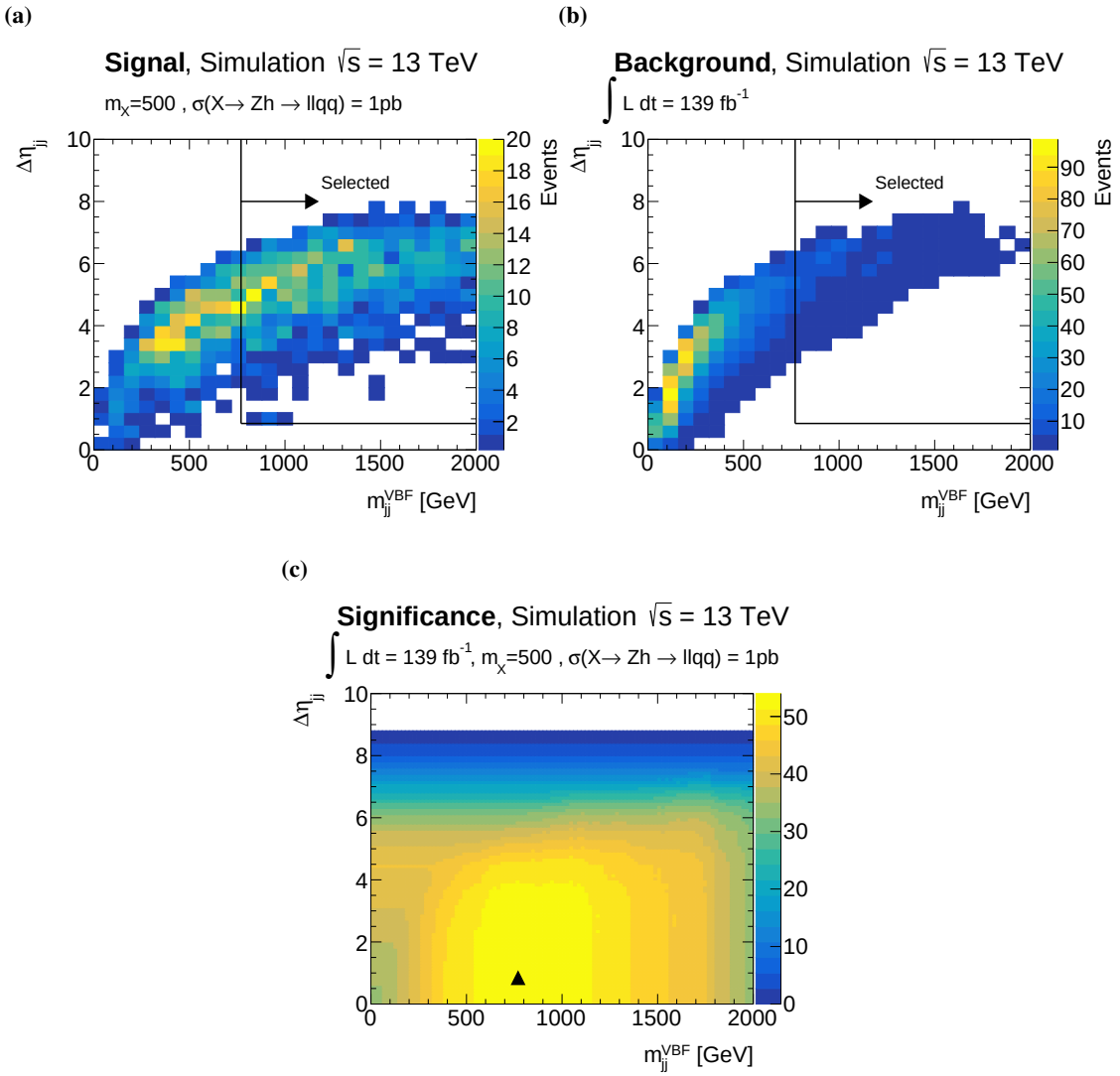

Figure 5.6: Two-dimensional distribution (m_{jj}^{VBF},$\Delta\eta_{jj}^{VBF}$) for a signal sample with (a) m_X = 500 GeV and for (b) the sum of all SM background processes. The corresponding signal significance is shown in (c).

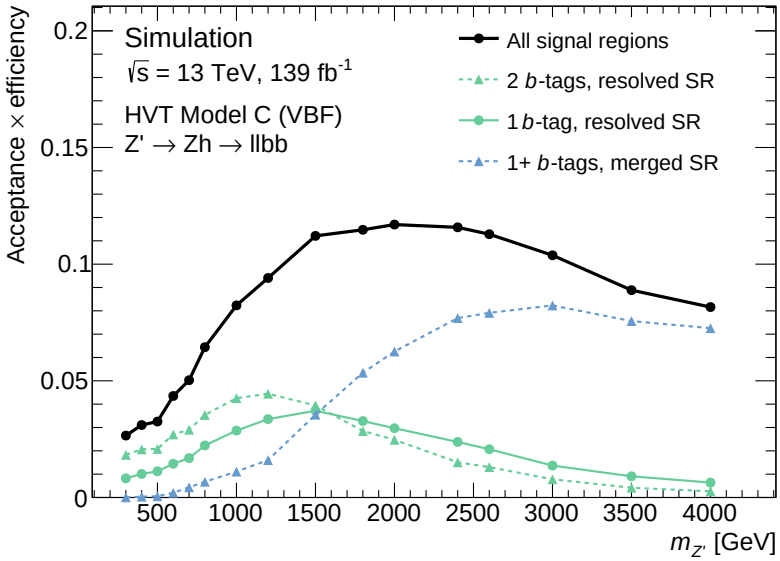

Figure 5.7: The reconstruction efficiency as a function of the resonance mass in an HVT model C $Z' \to Zh \to \ell^+\ell^- b\bar{b}$ signal events, selected by the 2-lepton selection requirements given in Table 4.2 with the additional requirement of two *VBF jets* with an invariant mass, $m_{\mathrm{jj}} > 600$GeV and a pseudo-rapidity gap, $\Delta\eta > 4.0$.

The signal selection efficiency after requiring the $m_{\mathrm{jj}}^{\mathrm{VBF}} > 600$ GeV and $\Delta\eta_{\mathrm{jj}}^{\mathrm{VBF}} > 4$ selection criteria in addition to the *parent analysis* selection is between 3% and 8% for the events with *resolved* topology and around 8% for events with the *merged* topology. Fig. 5.48 shows the signal efficiency as a function of the resonance mass. The efficiency for events with the *resolved* event topology increases with the resonance mass to a maximum of 8% at 1000 GeV and decreases for higher resonance masses. At low $m_{Z'}$ masses relevant hadronic decay products do not always pass the small-R jet p_{T} threshold of 30 GeV, resulting in a lower signal selection efficiency. Furthermore, ambiguities in the correct association of *signal* and *VBF jets* to the four selected jets results in a deteriorated signal efficiency for low resonance masses. On the other hand, at high resonance masses the Higgs boson decay products become collimated and the small-R jets from the Higgs boson decay start to merge. Comparing to the corresponding signal efficiency in the *parent analysis* (c.f. Fig. 4.7) a shift of the efficiency curve towards higher resonance mass values can be observed, as shown in Fig. 5.48. This shift is a direct consequence of the softer p_{T} spectra of the Z and Higgs bosons seen in Fig. 5.3. The transition region in which the *merged* event topology becomes more important compared to the *resolved* one hence also shifts to higher resonance masses.

5.2 Background modeling

Background processes for the VBF $Z' \to Zh$ search in the 2-lepton decay channel are modeled using MC simulation. The shape of the distribution of the final discriminant m_{Zh} from the main background sources, i.e. top quark production and Z boson production in association with jets, is obtained from the MC simulation, while the normalization of each of these distributions is determined via free floating normalization parameters in the simultaneous fit of all control and signal regions.

As in the case of the *parent analysis*, the main background process in this search is a Z boson production in association with jets (Z+jets). The Z+jets samples are subdivided according to the flavor content, i.e. to the number of jets that can be ghost-matched to generator level b- or c-quarks: Z+jets (bb,bc,cc) with at least two matched b- or c-quarks, Z+jets (bl,cl) with exactly one b- or c-quark and Z+jets (l) without any matched b- or c-quarks.

The Z bosons produced via electroweak (EW) production (i.e. VBF production) are included in the Z+jets (l) component of the QCD Z+jets production. EW produced Z bosons are naturally accompanied by two VBF-like jets. This process has been simulated by Sherpa 2.2.1 and shown to contribute less than 1% of the total background expectation.

Fig. 5.8 shows the expected composition of SM backgrounds in the three signal regions. The *resolved* SR with 1 b-tag is dominated by the Z+jets (bl,cl) component, contributing with 65% to the total background. The Z+jets (bb,bc,cc) component contributes with around 19% while the misidentified b-jets from the Z+jets (l) component only comprise less than about 8% of the total background.

The expected contribution from top quark events is smaller than 8%. About 6.3% of these 8% arise from semi-leptonic $t\bar{t}$ decays with one prompt charged lepton and the second non-prompt lepton mainly originating from the leptonic decay of a b-hadron. The non-prompt lepton passes the isolation criteria, if the accompanying hadronic activity from the b-decay is not distinct enough to veto the lepton. Such events are likely to be mismodeled by MC, and their contribution is therefore estimated from dedicated control data. The validity of the simulation of non-prompt leptons in semi-leptonic $t\bar{t}$ decays can be checked in a validation data region with same-charge leptons (same-charge validation region). This region is enriched with semi-leptonic $t\bar{t}$ events and provides similar event yields expected from semi-leptonic $t\bar{t}$ process in the SR. The comparison of observed and simulated m_{Zh} distributions in the same-sign VR is shown in Fig. 5.9.

The predictions agree with observation withing large statistical uncertainties in data. This validation data region confirms that events with non-prompt leptons[1] are only a minor background component. Therefore, the semi-leptonic $t\bar{t}$ component is taken from the MC predictions and combined with events from fully-leptonic $t\bar{t}$ decays and other top quark processes. However, the shape of the m_{Zh} distributions from semi-leptonic $t\bar{t}$ decays has a significantly harder spectrum from the one from fully-leptonic $t\bar{t}$ processes, as can be seen in Fig. 5.10. Furthermore, the contribution of the semi-leptonic component in the 2 b-tag region is negligible. A variation in the relative composition between the semi-leptonic and fully-leptonic components therefore implies a different normalization of

[1] This includes other top quark background components (e.g. from semi-leptonic Wt) and from multi-jet background (c.f. Ref. Section 4.1).

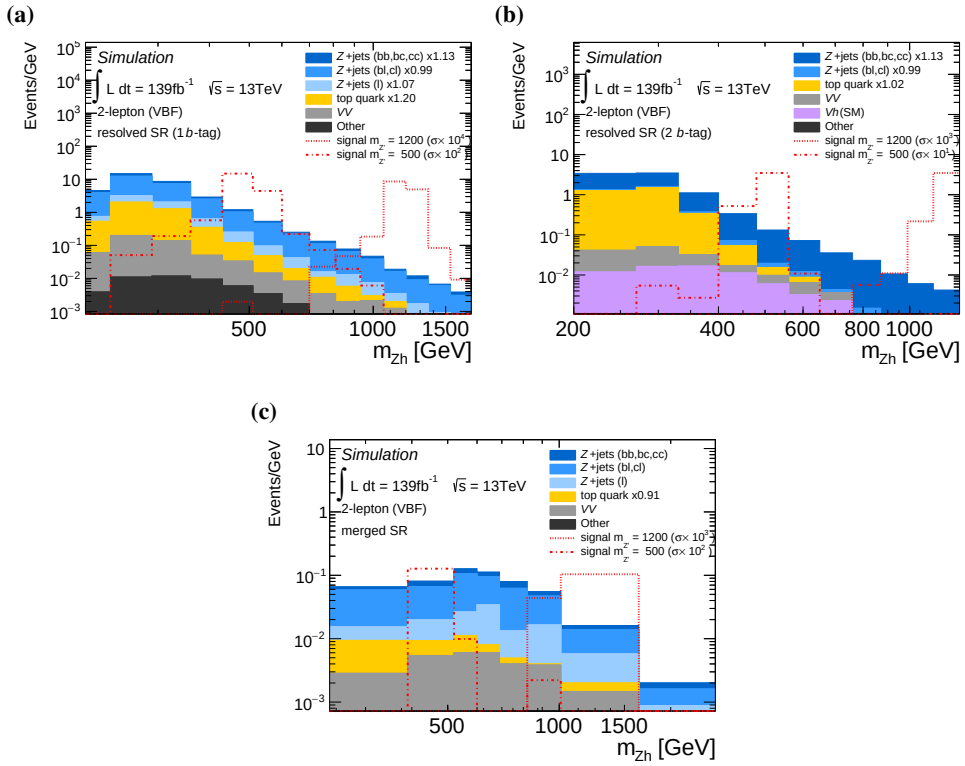

Figure 5.8: The expected diboson invariant mass distribution in the *resolved* 1 and 2 b-tag signal regions with (a) 1 and (b) 2 b-tags and (c) in the merged signal region. A signal with $m_{Z'} = 500$ GeV and a cross section 100 times larger than predicted by the HVT model C is indicated by a dashed red line for comparison.

the total top quark background in the two signal regions. A larger admixture of semi-leptonic $t\bar{t}$ events in each SR cannot be ruled out and is taken into account by a conservative uncertainty of 100%.

Other background contributions from diboson processes (VV, where $V = W, Z$), non-resonant Higgs boson production in association with a vector boson (Vh) or the $t\bar{t}$ production in association with bosons ($t\bar{t}V$, $t\bar{t}h$) sum up to less than 1% of the total background in the 1 b-tag region and are taken from simulation alone.

The signal region with the *resolved* event topology and 2 b-tags is dominated by Z+jets (bb,bc,cc) events, contributing with 58%. Other Z+jets components are minor in this signal region ($\approx$ 3%). Other processes, on the other hand, become more relevant: top quark events contribute up to 37% of the total background at lower resonance masses below $m_{Zh} \approx 500$ GeV. The requirement of the second b-jet in the 2 b-tag regions reduces the fraction of semi-leptonic $t\bar{t}$ decays to about 1% of the total $t\bar{t}$ contribution. Contributions from non-resonant diboson events (Vh, VV) is small in the bulk of the distribution ($\approx$ 1%) but contribute each up to 5% to the total background in the high mass tail (above 500 GeV) of the *resolved* SR with 2 b-tags.

The merged signal region is dominated by the Z+jets (bl,cl) component contributing more than 55% to the total background. Z+jets (bb,bc,cc) and Z+jets (l) components are each contributing with 16%.

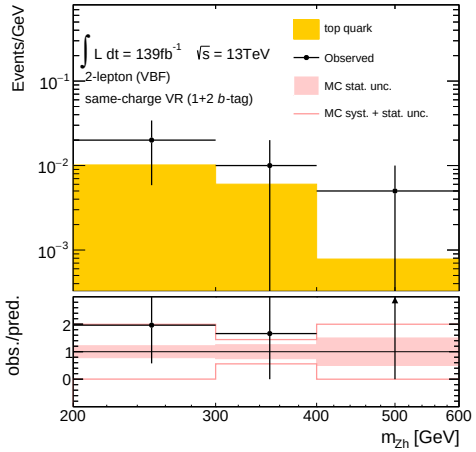

Figure 5.9: The observed and expected m_{Zh}-distribution in the same-charge validation region (b-tag inclusive selection). The region is enriched in semi-leptonic $t\bar{t}$ decays. The lower panels show the ratio of the observed and expected event yields. Statistical uncertainties in data and simulation are shown separately. The data error bars represent the statistical uncertainties of observed events evaluated using a 1σ range of a Poisson distribution. The shaded area represent the statistical uncertainty of the finite-sized MC samples. The red contour represents the total pre-fit uncertainty, corresponding to the quadratic sum of all individual systematic uncertainty and the statistical uncertainty of the MC samples.

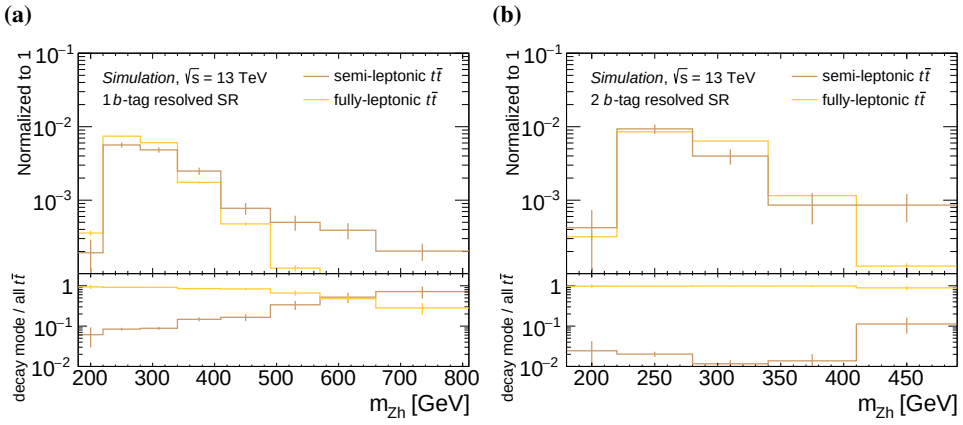

Figure 5.10: The expected shape of the m_{Zh} distributions of top quark background sub-components (fully-leptonic and semi-leptonic $t\bar{t}$ decays) in the (a) 1- b-tag and (b) 2 b-tag signal regions, normalized to the same area. The lower panels show the predicted fraction of the two $t\bar{t}$ decay modes of all $t\bar{t}$ decays.

Top quark backgrounds ($t\bar{t}$, $t\bar{t}h$, $t\bar{t}V$, and single-top) only contribute in total with 6%, while diboson processes, VV, also contribute with 6%. A summary of the expected numbers of background events in each signal region is given in Table 5.1.

Table 5.1: The expected and observed number of events in all VBF signal regions (SRs) and control regions (CRs) at an integrated luminosity of 139fb^{-1}. The uncertainties given in the table include statistical uncertainties only.

Process	***merged* SR**	**1 b-tag *resolved* SR**	**2 b-tag *resolved* SR**
Z+jets (bb,bc,cc)	12.31 ± 0.64	277.82 ± 11.87	316.03 ± 9.41
Z+jets (bl,cl)	42.45 ± 1.41	1304.86 ± 29.85	12.15 ± 1.47
Z+jets (l)	12.77 ± 1.17	159.13 ± 18.75	0.14 ± 0.19
top quark	4.80 ± 0.30	207.40 ± 1.95	200.34 ± 1.77
VV	4.24 ± 0.41	29.60 ± 1.07	6.59 ± 0.40
Vh (SM)	0.09 ± 0.01	1.50 ± 0.16	2.37 ± 0.17
Total expected background	76.65 ± 2.01	1980.31 ± 37.26	537.62 ± 9.70
	merged **m_J-sideband CR**	**1 b-tag *resolved*** **m_{jj}-sideband CR**	**2 b-tag *resolved*** **m_{jj}-sideband CR**
Z+jets (bb,bc,cc)	10.00 ± 0.55	469.58 ± 15.96	547.56 ± 9.86
Z+jets (bl,cl)	34.63 ± 1.29	2409.79 ± 43.49	23.32 ± 2.47
Z+jets (l)	15.42 ± 1.19	247.45 ± 27.52	0.11 ± 0.93
top quark	3.25 ± 0.25	355.08 ± 2.51	363.02 ± 2.38
VV	1.72 ± 0.25	63.87 ± 1.54	15.24 ± 0.52
Vh (SM)	0.04 ± 0.02	1.10 ± 0.12	0.66 ± 0.07
Total expected background	65.06 ± 1.87	3546.87 ± 53.96	949.91 ± 10.49
Observed	42.00 ± 6.48	3958.00 ± 62.91	1092.00 ± 33.05
	merged **$t\bar{t}$ CR**	**1 b-tag *resolved*** **$t\bar{t}$ CR**	**2 b-tag *resolved*** **$t\bar{t}$ CR**
Z+jets (bb,bc,cc)	—	0.07 ± 0.04	0.04 ± 0.03
Z+jets (bl,cl)	0.10 ± 0.06	0.36 ± 0.12	—
Z+jets (l)	—	—	—
top quark	4.72 ± 0.34	415.40 ± 2.71	429.15 ± 2.59
VV	0.07 ± 0.06	0.05 ± 0.03	—
Vh (SM)	—	—	—
Total expected background	4.89 ± 0.35	415.88 ± 2.71	429.19 ± 2.59
Observed	2.00 ± 1.41	498.00 ± 22.32	450.00 ± 21.21

5.2.1 Signal-depleted control regions in data

Similarly as in the *parent analysis*, the background processes are constrained by additional measurements in signal-depleted control regions (CRs). Normalization of the dominant background contribution from $t\bar{t}$, Z+jets (bb,bc,cc) and Z+jets (bl,cl) are determined from the fit of the final discriminant simultaneously in the signal and control regions. Each control region (CR) will be described in more detail in the following. Expected and observed event yields in all CRs are summarized in Table 5.1.

***$t\bar{t}$* CR** By inverting the same-flavor requirement of the two charged leptons the signal and Z+jets background contributions are strongly suppressed. The corresponding $t\bar{t}$ CR is almost pure in $t\bar{t}$ events that comprise more than 99.9% of all events in that CR. This allows for a reliable constraint of the $t\bar{t}$ contribution in the signal region (SR). It is predicted that only about 0.1% of all generated events of

a hypothesized $Z' \to Zh$ signal within the tested mass range of $m_{Z'} \in [300, 3000]$ GeV satisfy the $t\bar{t}$ CR selection requirements.

For the *merged* event topology, the MC background simulations predict a total of 4.89 ± 0.35 background events within the $t\bar{t}$ CR. The observed 2 events agree well with this prediction. This is regarded as a cross check, but due to the limited statistical power the merged $t\bar{t}$ CR is not used in the final statistical interpretation of data.

The modeling of top quark backgrounds in the signal regions with *resolved* event topology has been studied in detail in the corresponding *resolved* $t\bar{t}$ CR. The predicted fraction of semi-leptonic and fully-leptonic $t\bar{t}$ decays, shown in Fig. 5.10, agrees between the SR and the $t\bar{t}$ CR within the statistical uncertainty. The comparison of the shapes of m_{Zh} distributions for the semi-leptonic and fully-leptonic $t\bar{t}$ decays in the $t\bar{t}$ CR is shown in Fig. 5.11.

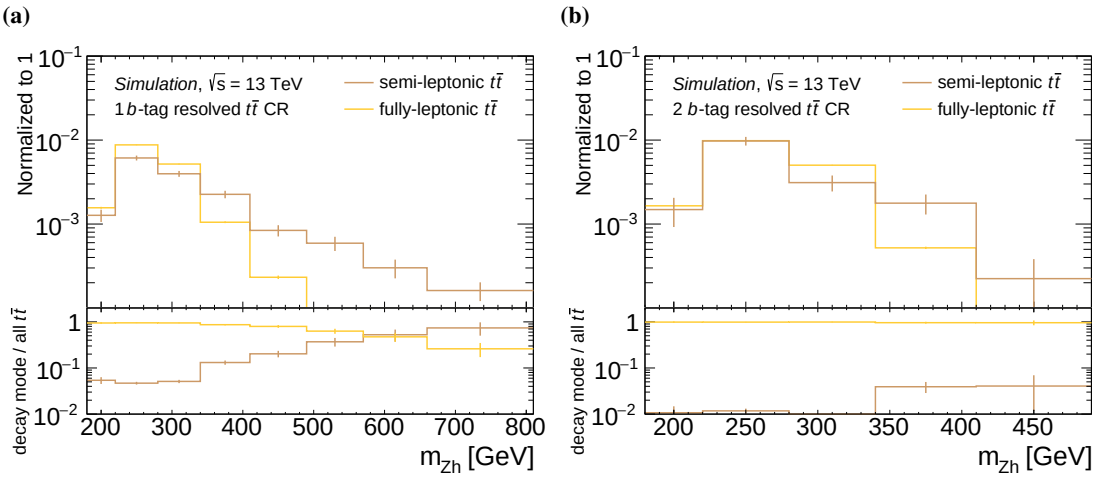

Figure 5.11: The expected shape of the m_{Zh} distributions of top quark background sub-components (fully-leptonic and semi-leptonic $t\bar{t}$ decays) in the (a) 1- b-tag and (b) 2 b-tag $t\bar{t}$ CRs, normalized to the same area. The lower panels show the predicted fraction of the two $t\bar{t}$ decay modes of all $t\bar{t}$ decays.

The differences between the observed and predicted normalization and in the shape of m_{Zh} distributions in the high mass tails are both seen in the $t\bar{t}$ CR data, as shown in Figs. 5.12(a) and 5.12(b). An uncertainty is introduced on the fraction of semi-leptonic $t\bar{t}$ decays in the combined total top quark contribution corresponding to a two times higher than nominal number of semi-leptonic $t\bar{t}$ events. This covers the m_{Zh} shape variations between the two signal regions presented in Fig. 5.10. This uncertainty is constrained in the final fit driven by the observation in the $t\bar{t}$ CR. The uncertainty from the semi-leptonic $t\bar{t}$ processes also covers the statistically insignificant deviations seen in Fig. 5.9.

The observed and expected distributions of observables related to the reconstruction of Z' and Higgs boson candidates are shown in Figs. 5.12 and 5.13. Distributions of observables that are employed for the baseline event selection are shown in Figs. 5.14 and 5.15. The number of jets in the $t\bar{t}$ CRs is underrepresented in the simulated samples, but covered by the uncertainty of additional admixed semi-leptonic $t\bar{t}$ decays described above. No other significant deviation between data and MC is

observed for the shape of any of the distributions. The $t\bar{t}$ background normalization is slightly underestimated by the MC prediction. A normalization factor of 1.02 retrieved from the fit in the CRs is applied to align data and MC. The normalization factor coincides with the one that are obtained in the *parent analysis*. To account for the differences between 1 and 2 b-tag regions, an additional parameter is introduced in the final fit to handle the uncertainty on the migration of $t\bar{t}$ events from one region to another. The pre-fit migration uncertainty is estimated to be 20% using the approach described in Section 4.4.3, which agrees with the observations from the $t\bar{t}$ CR. The final overall normalization of the $t\bar{t}$ background contributions is determined from the simultaneous fit from all SRs and CRs, where the top quark contribution is mainly constrained from the $t\bar{t}$ CR.

Resolved m_{jj}-sideband CR The inversion of the mass window requirement in events with the *resolved* event topology defines the *resolved* m_{jj}-sideband CRs. The background composition in a m_{jj}-sideband CR is similar to the one in the corresponding signal region except for the suppressed contributions from non-resonant diboson production. In the 1 b-tag m_{jj}-sideband CR with *resolved* event topology, the fraction of all signal events from the HVT $Z' \to Zh$ signal processes is quite significant with up to 47% for a Z' resonance mass of 300 GeV. The signal leakage has also been observed in the *parent analysis* analysis, but the additional ambiguity in the jet pairing (c.f. Fig. 5.48) further enhances the leakage for the VBF final states. The signal leakage decreases with higher resonance mass, reaching 13% at resonance masses of 3 TeV. The identification of the second b-tagged jet in the 2 b-tag region reduces the fraction of wrong jet pairings, reducing the signal leakage to 20% for signal with $m_{Z'} = 300$ GeV. In general, the m_{Zh} signal distribution in the m_{jj}-sideband CRs does not have a resonant character, since the pairing of *signal jets* does not resemble the true Higgs boson decay. The width of the signal m_{Zh} distribution in the m_{jj}-sideband CRs with *resolved* event topology amounts to more than 30% of the resonance mass. Therefore, a potential signal would not be visible in the *resolved* m_{jj}-sideband CRs. In general, the *resolved* m_{jj}-sideband CRs are well suited to constrain the normalization and shape of the Z+jets (bl,cl) and Z+jets (bb,bc,cc) components in the 1 and 2 b-tag signal regions with *resolved* event topology.

The observed and expected distributions of m_{Zh} and m_{jj} observables in the *resolved* m_{jj}-sideband CRs are shown in Fig. 5.16. The corresponding distributions for the p_{T}^{jj} and p_{T}^{Z} observables are shown in Fig. 5.17. In contrast to the *parent analysis*, the difference in the shape of the observed and expected p_{T}^{jj} and p_{T}^{Z} distributions of the reconstructed Higgs and Z boson candidates, respectively, is less pronounced. Therefore no corresponding systematic uncertainty is assigned.

Other observables that are used for the event selection are studied in the m_{jj}-sideband CRs and shown in Figs. 5.18 and 5.19. The transverse momentum distributions of the leading ($p_{\mathrm{T}}^{lep,1}$) and sub-leading lepton ($p_{\mathrm{T}}^{lep,2}$) as well as the reconstructed di-lepton mass, $m_{\ell\ell}$, is shown in Fig. 5.18. The simulated background prediction agrees well with the observed data. Unlike in the $t\bar{t}$ CRs, the number of small-R jets in the m_{jj}-sideband CRs is modeled well, as shown in Fig. 5.19.

Merged m_J-sideband CR The SRs and CRs with *merged* event topology are significantly less populated than the regions with *resolved* event topology.

In the *merged* m_J-sideband CR 42 events are recorded, with a pre-fit prediction of 65.0 ± 1.9 events. Low statistical precision does not allow for an as detailed modeling validation as in regions with *resolved* event topology. Distributions of observables used for event selection and reconstruction of the Z' resonance are shown in Figs. 5.20 and 5.21.

There is a significant mismodeling of m_{Zh}, p_{T}^{Z} and p_{T}^{J} distributions in low-energy tails in the *merged* m_J-sideband CR as shown in Fig. 5.21. The mismodeling is observed for events in a p_{T}^{J} range that is in most cases reconstructed with a*resolved* topology. A mismodeling in this regime can be explained by event migration between regions with the *merged* and*resolved* topology. Such a migration would barely influence the shape of distribution in regions with *resolved* event topology due to the large number of events compared to the region with *merged* topology.

To account for this mismodeling, an additional empirical non-closure uncertainty of 50% is imposed on the normalization of all Z+jets events with a large-R jet p_{T} of less than 400 GeV. The correction is not applied to top quark since the contribution from top quark in the regime of $p_{\mathrm{T}}^{J} > 400$ GeV is small. Discrepancies below 400 GeV are accounted by the region migration uncertainty described in Section 5.3.2. The reweighting by the p_{T}^{J} observable is consistent with the methodology done in the *parent analysis*. The impact of the p_{T}^{J} reweighting on the final discriminant can be seen in Fig. 5.22.

The 1σ deviation of this non-closure uncertainty corresponds to the event-wise reweighting that would remove the mismodeling observed in Fig. 5.21(c). A similar uncertainty has also been evaluated using the reconstructed gauge boson p_{T}, indicating a 50% uncertainty on the normalization of all Z+jets events with a reconstructed di-lepton p_{T} of less than 300 GeV, to account for mismodeling seen in Fig. 5.21(b). Both reweighting approaches show a comparable agreement between observation and prediction for the m_{Zh} distribution.

The uncertainties described above are strongly correlated. Therefore, only one of the two can be used to describe the observed non-closure. For consistency with the *parent analysis*, the Higgs boson candidate p_{T}^{J} is chosen as a baseline reweighting variable. The p_{T}^{J}-reweighted distribution of the final discriminant m_{Zh} is shown in Fig. 5.22.

Untagged validation region Finally, a further region is defined with a veto on all events with b-jets in order to validate the Z+jets predictions. This validation region is not used for the statistical interpretation of data in Section 5.4, since it is dominated by Z+jets (l) events, which are not the dominant Z+jets component in the SRs. However, this validation region is more stable against statistical fluctuations and serves as an additional cross check of the background modeling. In particular, the VBF-related observables are expected to be less affected by the multiplicity of b-jets in the event, since the b-tagging is only done in the central detector region. Fig. 5.23 shows the corresponding comparisons of observed and simulated distributions in the introduced validation regions. The observed relative differences between observed and expected distributions are similar to those in the *resolved* 1 b-tag m_{jj}-sideband CRs. A significant systematic mismodeling is observed in the description of the kinematic properties of the *VBF jets*, most pronounced in the $p_{\mathrm{T}}^{\mathrm{VBF,}}$ distribution of *VBF jets*, as shown in Figs. 5.23(e) and 5.23(f).

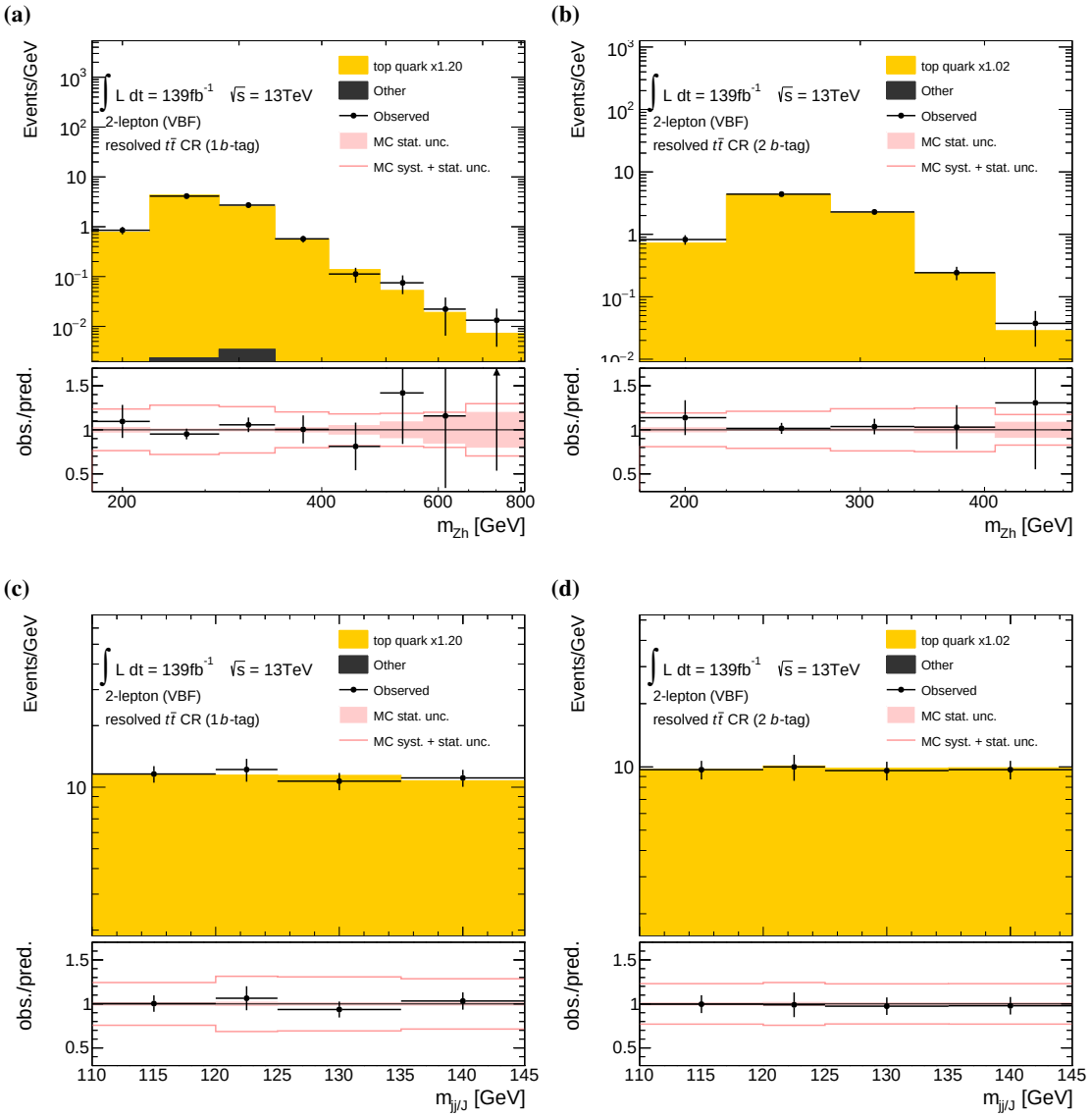

Figure 5.12: The observed and expected distributions for (a) and (b) invariant diboson mass m_{Zh}, (c) and (d) invariant mass of the Higgs candidate. The left-hand side shows distributions in the 1 b-tag and the right-hand side in the 2 b-tag $t\bar{t}$ CR. The lower panels show the ratio of the observed and expected event yields. Statistical uncertainties in data and simulation are shown separately. The data error bars represent the statistical uncertainties of observed events evaluated using a 1σ range of a Poisson distribution. The shaded area represent the statistical uncertainty of the finite-sized MC samples. The red contour represents the total pre-fit uncertainty, corresponding to the quadratic sum of all individual systematic uncertainty and the statistical uncertainty of the MC samples.

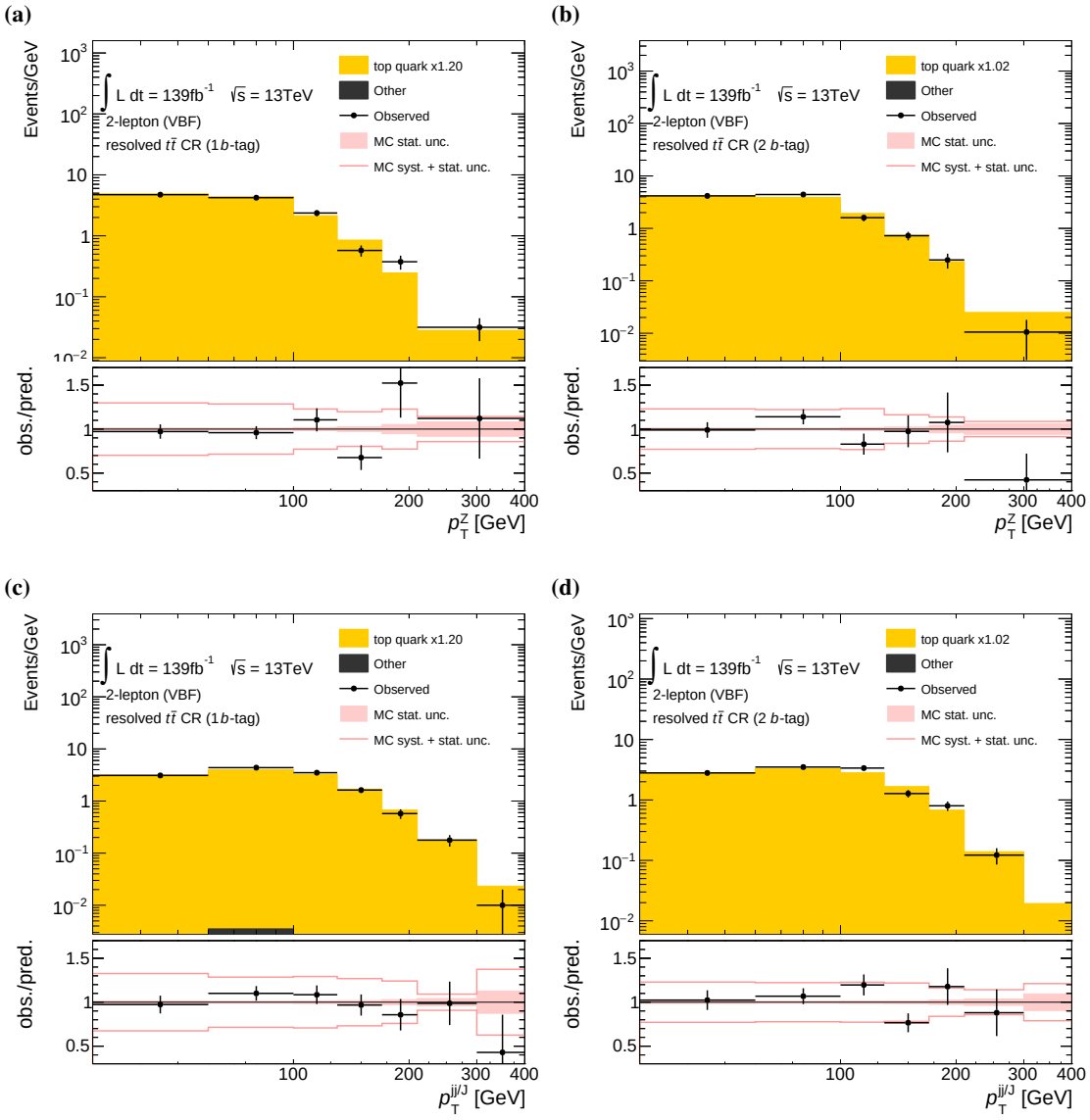

Figure 5.13: The observed and expected distributions for the transverse momentum of (a) and (b) the Z boson candidate, (c) and (d) the Higgs boson candidate. The left-hand side shows distributions in the 1 b-tag and the right-hand side in the 2 b-tag $t\bar{t}$ CR. The lower panels show the ratio of the observed and expected event yields. Statistical uncertainties in data and simulation are shown separately. The data error bars represent the statistical uncertainties of observed events evaluated using a 1σ range of a Poisson distribution. The shaded area represent the statistical uncertainty of the finite-sized MC samples. The red contour represents the total pre-fit uncertainty, corresponding to the quadratic sum of all individual systematic uncertainty and the statistical uncertainty of the MC samples.

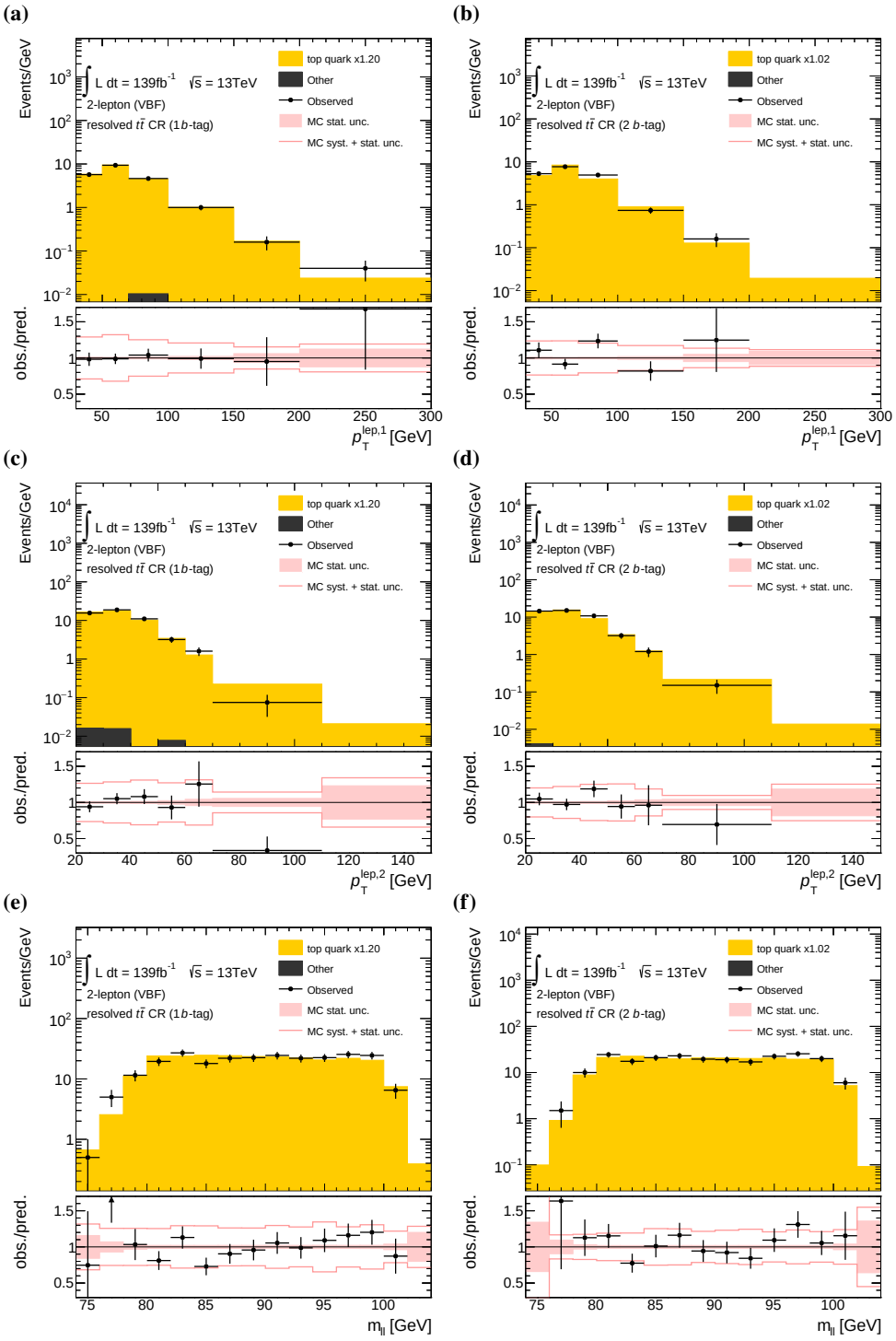

Figure 5.14: The observed and expected distributions for the transverse momentum of (a) and (b) the highest-p_T lepton, $p_T^{\ell,1}$, (c) and (d) of the second lepton, $p_T^{\ell,2}$ and (e) and (f) the invariant mass of the Z boson candidate. The left-hand side shows distributions in the 1 b-tag and the right-hand side in the 2 b-tag $t\bar{t}$ CR. The lower panels show the ratio of the observed and expected event yields. Statistical uncertainties in data and simulation are shown separately. The data error bars represent the statistical uncertainties of observed events evaluated using a 1σ range of a Poisson distribution. The shaded area represent the statistical uncertainty of the finite-sized MC samples. The red contour represents the total pre-fit uncertainty, corresponding to the quadratic sum of all individual systematic uncertainty and the statistical uncertainty of the MC samples.

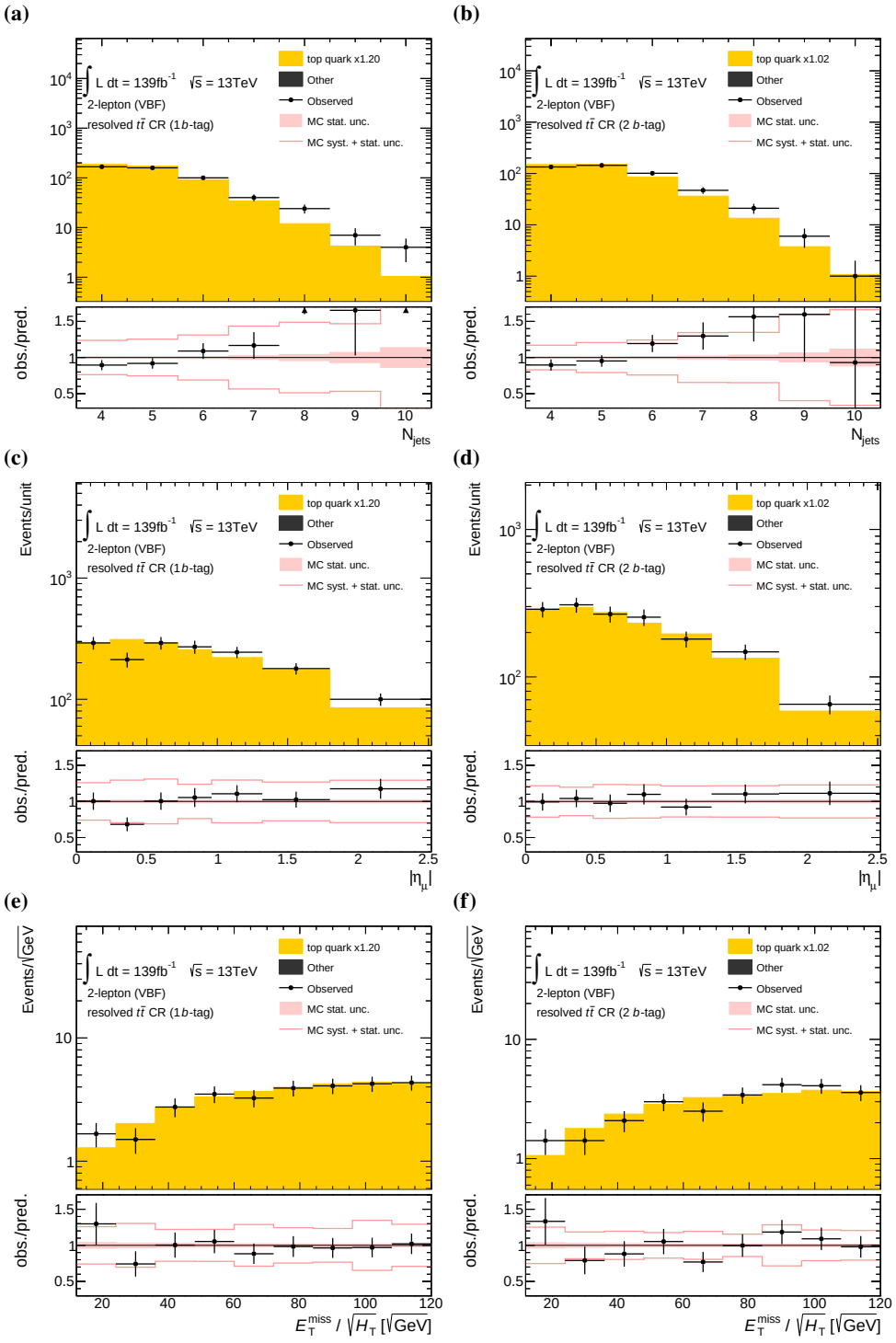

Figure 5.15: The observed and expected distributions for the transverse momentum of (a) and (b) the number of small-R jets, N_{jets}, (c) and (d) the pseudo-rapidity of the leading muon and (e) and (f) the ratio $E_{\text{T}}^{\text{miss}}/H_{\text{T}}$. The left-hand side shows distributions in the 1 b-tag and the right-hand side in the 2 b-tag $t\bar{t}$ CR. The lower panels show the ratio of the observed and expected event yields. Statistical uncertainties in data and simulation are shown separately. The data error bars represent the statistical uncertainties of observed events evaluated using a 1σ range of a Poisson distribution. The shaded area represent the statistical uncertainty of the finite-sized MC samples. The red contour represents the total pre-fit uncertainty, corresponding to the quadratic sum of all individual systematic uncertainty and the statistical uncertainty of the MC samples.

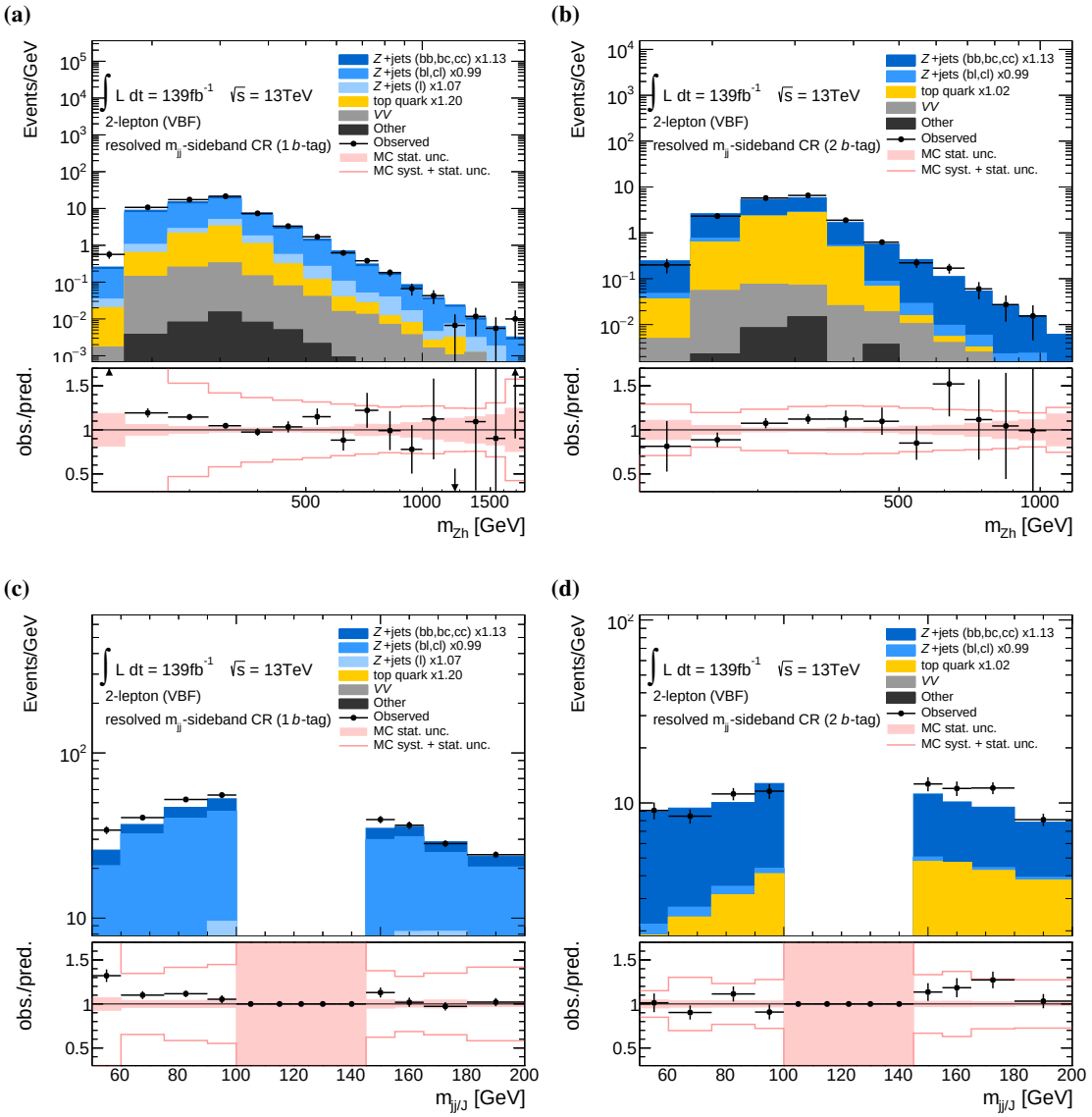

Figure 5.16: The observed and expected distributions for (a) and (b) invariant diboson mass m_{Zh}, (c) and (d) invariant mass of the Higgs candidate. The left-hand side shows distributions in the 1 b-tag and the right-hand side in the 2 b-tag m_{jj}-sideband CRs with *resolved* event topology. The main backgrounds are scaled by the normalization factor obtained in the final fit. The lower panels show the ratio of the observed and expected event yields. Statistical uncertainties in data and simulation are shown separately. The data error bars represent the statistical uncertainties of observed events evaluated using a 1σ range of a Poisson distribution. The shaded area represent the statistical uncertainty of the finite-sized MC samples. The red contour represents the total pre-fit uncertainty, corresponding to the quadratic sum of all individual systematic uncertainty and the statistical uncertainty of the MC samples.

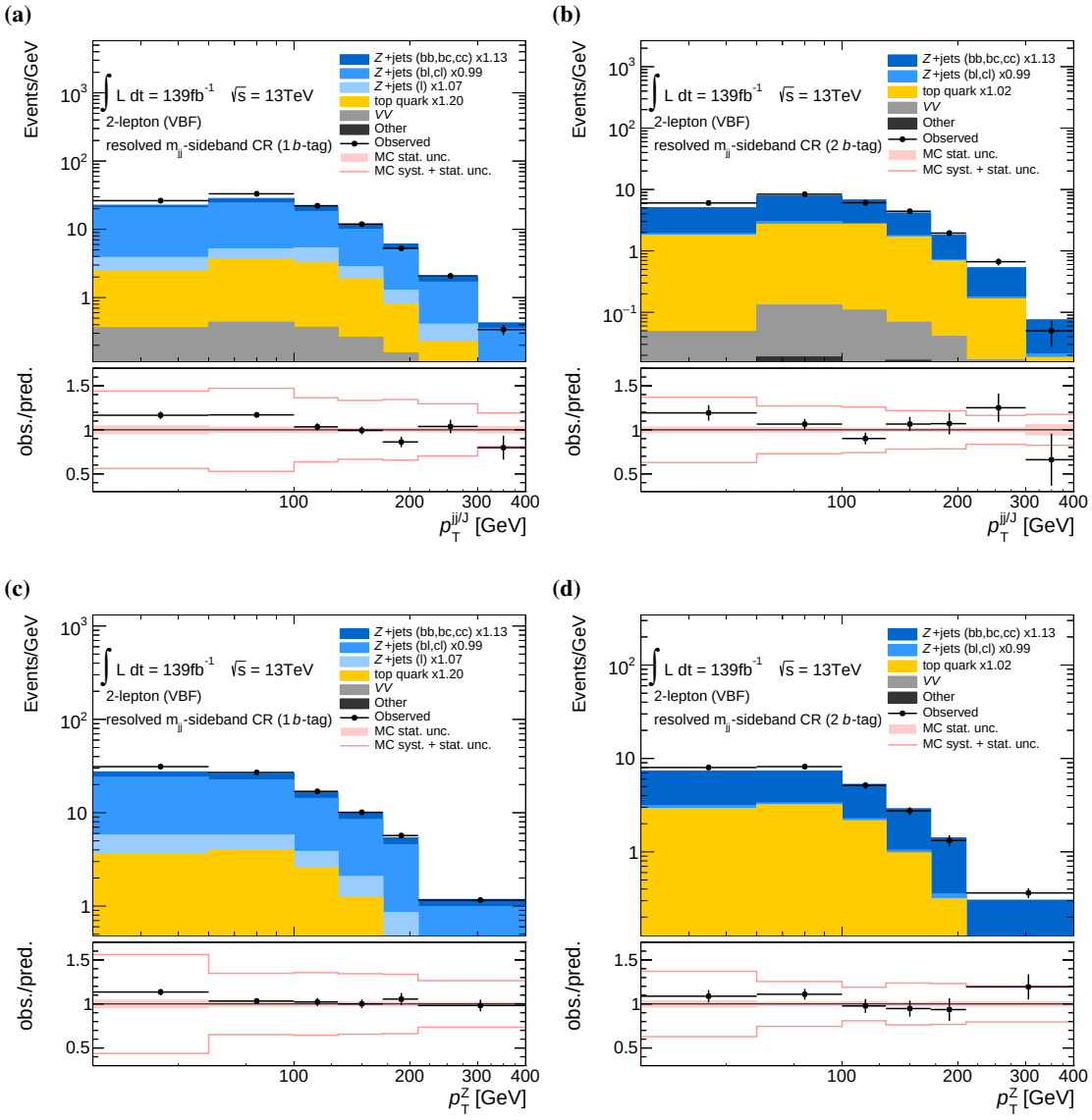

Figure 5.17: The observed and expected distributions for the transverse momentum of (a) and (b) the Z boson candidate, (c) and (d) the Higgs boson candidate. The left-hand side shows distributions in the 1 b-tag and the right-hand side in the 2 b-tag m_{jj}-sideband CRs with *resolved* event topology. The lower panels show the ratio of the observed and expected event yields. Statistical uncertainties in data and simulation are shown separately. The data error bars represent the statistical uncertainties of observed events evaluated using a 1σ range of a Poisson distribution. The shaded area represent the statistical uncertainty of the finite-sized MC samples. The red contour represents the total pre-fit uncertainty, corresponding to the quadratic sum of all individual systematic uncertainty and the statistical uncertainty of the MC samples.

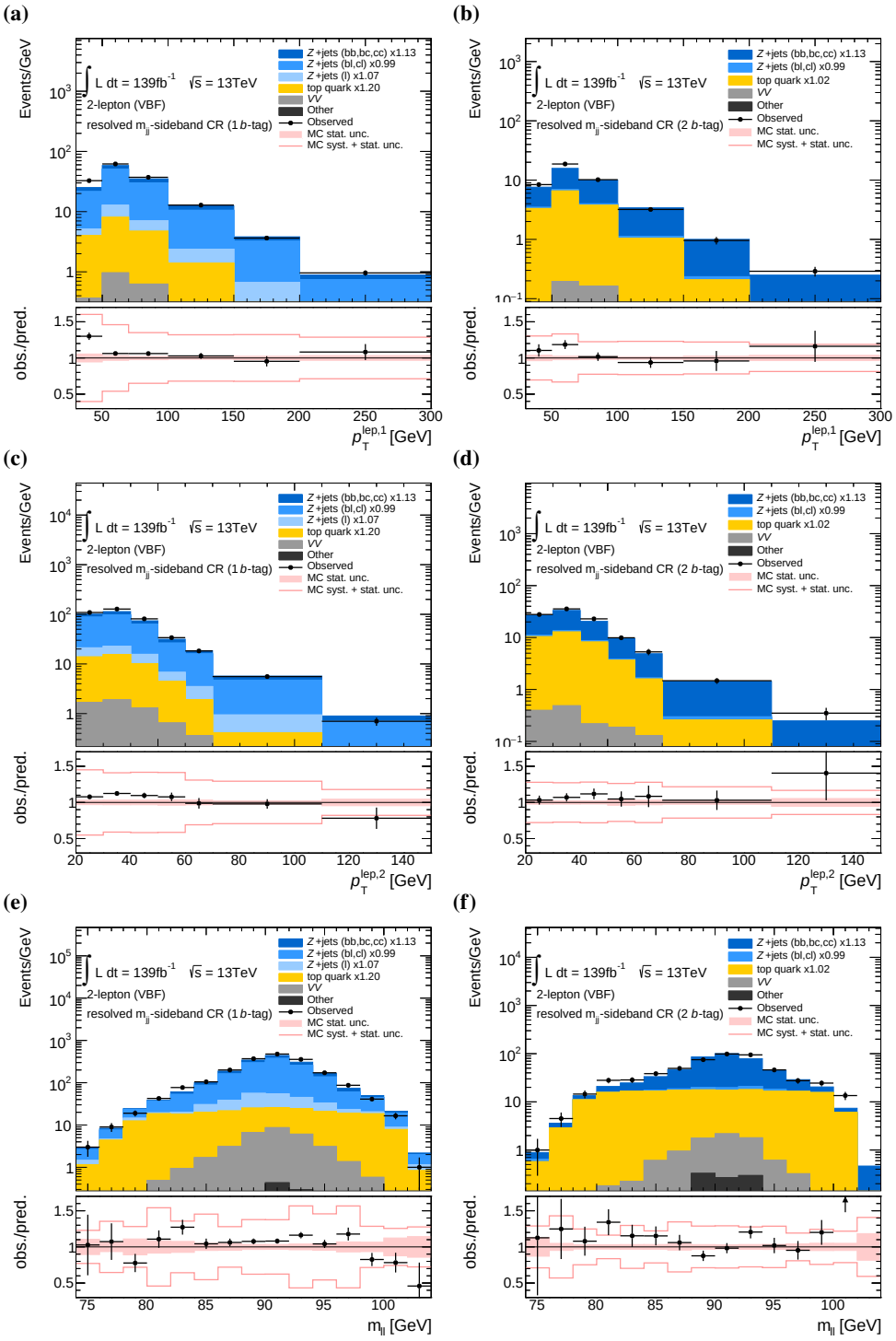

Figure 5.18: The observed and expected distributions for the transverse momentum of (a) and (b) the highest-p_T lepton, $p_T^{\ell,1}$, (c) and (d) of the second lepton, $p_T^{\ell,2}$ and (e) and (f) the invariant mass of the Z boson candidate. The left-hand side shows distributions in the 1 b-tag and the right-hand side in the 2 b-tag m_{jj}-sideband CRs with the *resolved* event topology. The lower panels show the ratio of the observed and expected event yields. Statistical uncertainties in data and simulation are shown separately. The data error bars represent the statistical uncertainties of observed events evaluated using a 1σ range of a Poisson distribution. The shaded area represent the statistical uncertainty of the finite-sized MC samples. The red contour represents the total pre-fit uncertainty, corresponding to the quadratic sum of all individual systematic uncertainty and the statistical uncertainty of the MC samples.

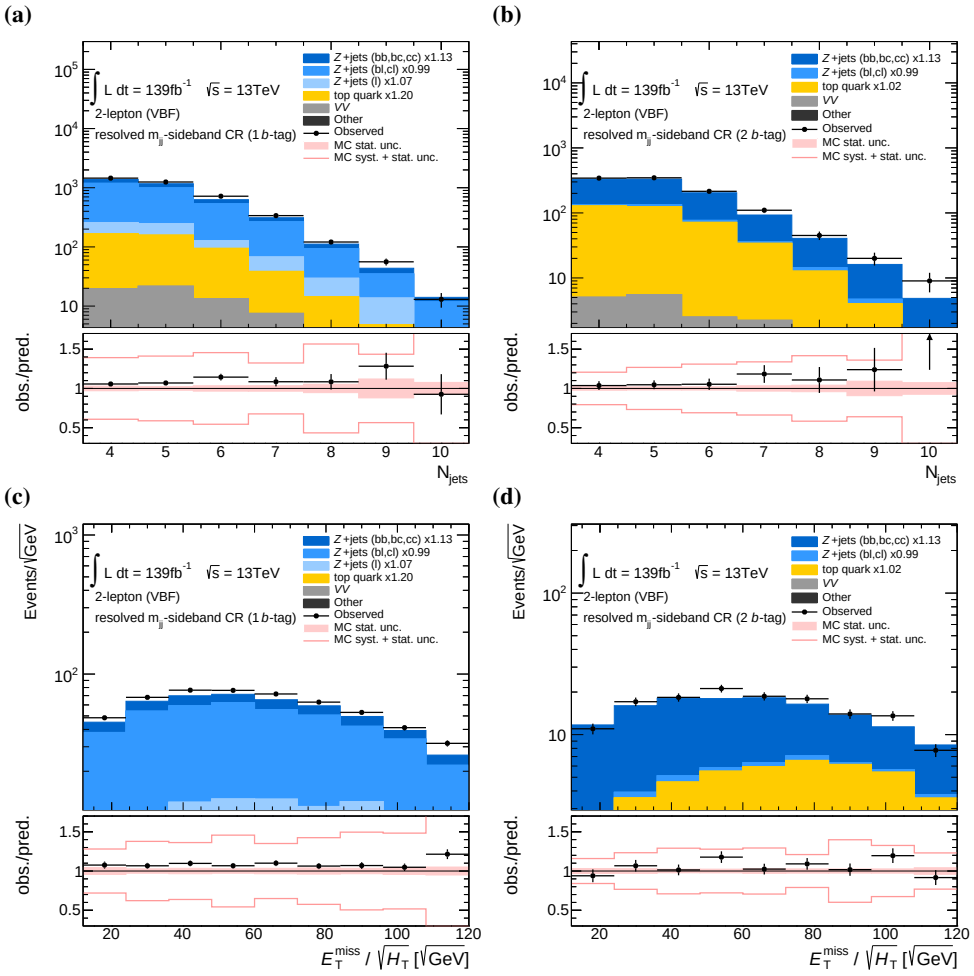

Figure 5.19: The observed and expected distributions for the transverse momentum of (a) and (b) the number of small-R jets, N_{jets}, (c) and (d) the pseudo-rapidity of the leading muon and (e) and (f) the ratio $E_{\text{T}}^{\text{miss}}/H_{\text{T}}$. The left-hand side shows distributions in the 1 b-tag and the right-hand side in the 2 b-tag *resolved* m_{jj}-sideband CRs. The lower panels show the ratio of the observed and expected event yields. Statistical uncertainties in data and simulation are shown separately. The data error bars represent the statistical uncertainties of observed events evaluated using a 1σ range of a Poisson distribution. The shaded area represent the statistical uncertainty of the finite-sized MC samples. The red contour represents the total pre-fit uncertainty, corresponding to the quadratic sum of all individual systematic uncertainty and the statistical uncertainty of the MC samples.

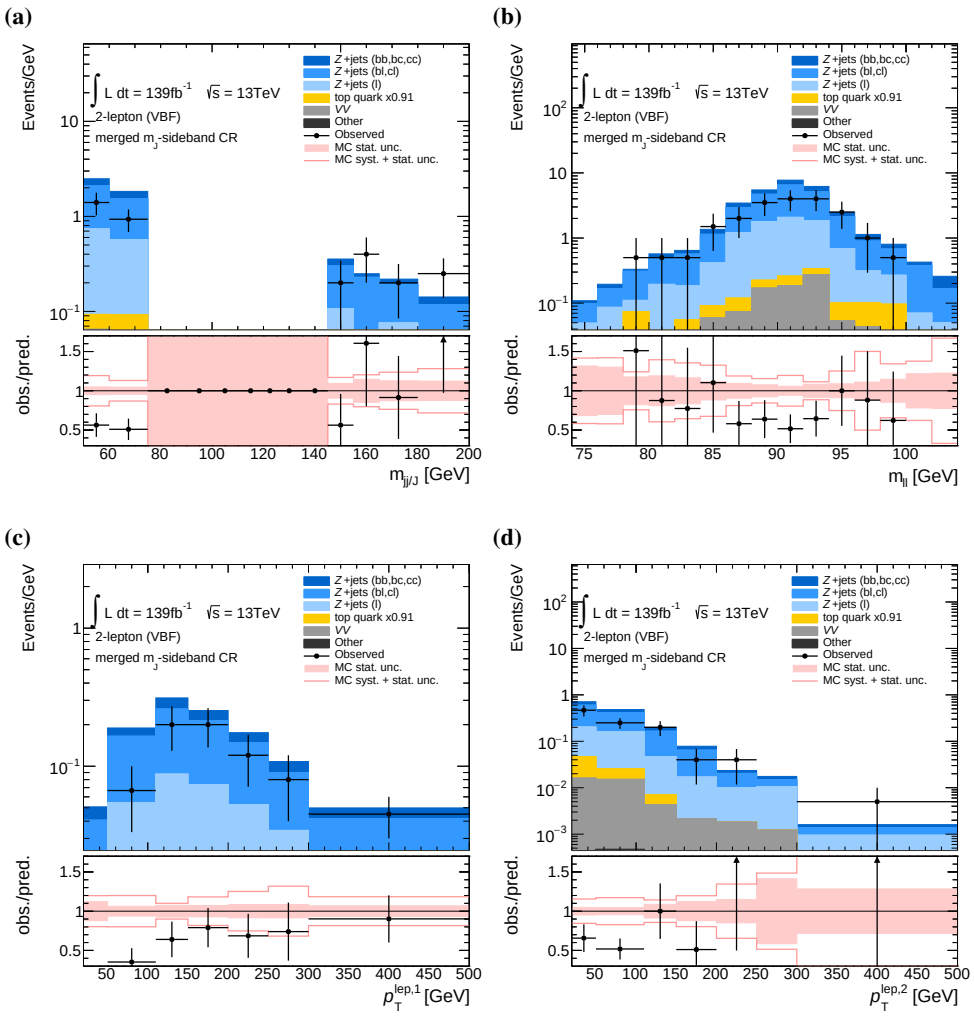

Figure 5.20: The observed and expected distributions for the invariant masses (a) of the Higgs boson candidate and (b) Z boson candidate and the transverse momenta of the (c) leading and (d) the sub-leading lepton. The left-hand side shows distributions in the 1 b-tag and the right-hand side in the *resolved* m_{jj}-sideband CR. The lower panels show the ratio of the observed and expected event yields. Statistical uncertainties in data and simulation are shown separately. The data error bars represent the statistical uncertainties of observed events evaluated using a 1σ range of a Poisson distribution. The shaded area represent the statistical uncertainty of the finite-sized MC samples. The red contour represents the total pre-fit uncertainty, corresponding to the quadratic sum of all individual systematic uncertainty and the statistical uncertainty of the MC samples.

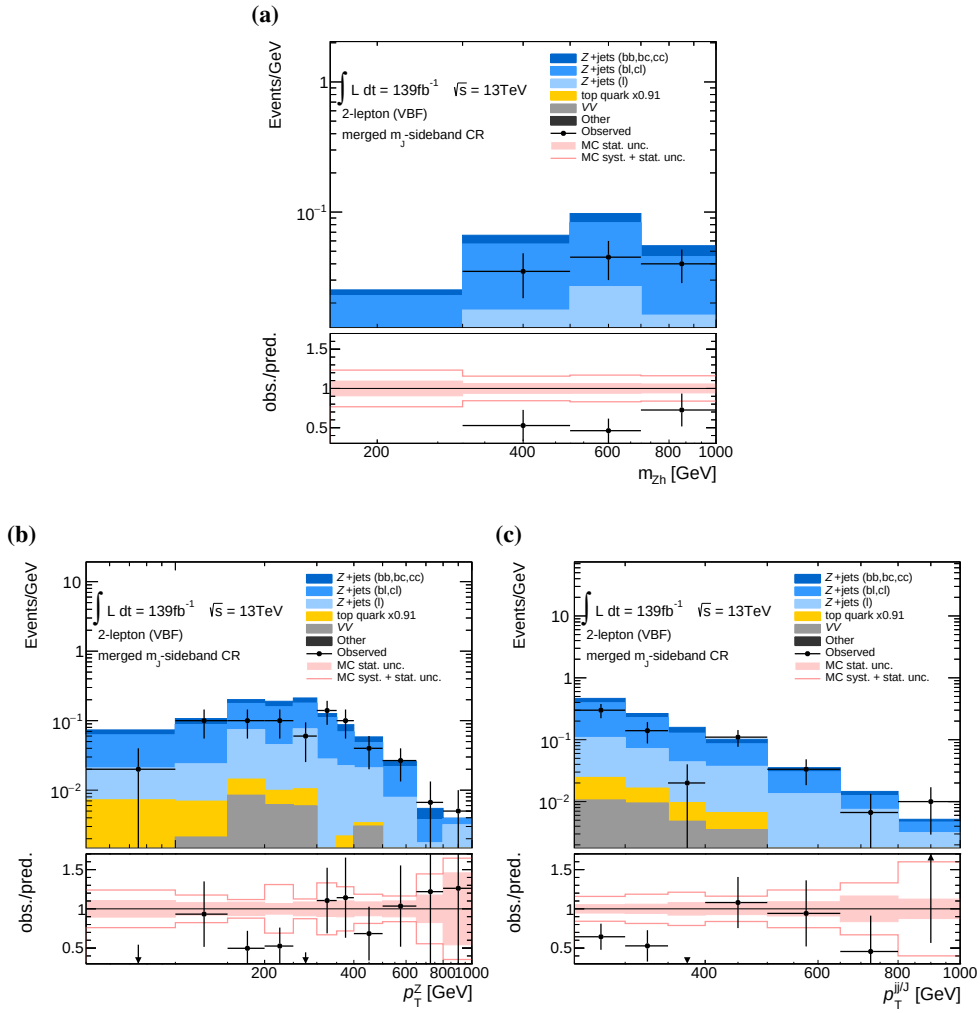

Figure 5.21: The observed and expected distributions for the (a) invariant diboson mass m_{Zh}, and the transverse momentum of (b) the Z boson candidate and (c) the Higgs boson candidate in the *merged* m_J-sideband CR. The lower panels show the ratio of the observed and expected event yields. Statistical uncertainties in data and simulation are shown separately. The data error bars represent the statistical uncertainties of observed events evaluated using a 1σ range of a Poisson distribution. The shaded area represent the statistical uncertainty of the finite-sized MC samples. The red contour represents the total pre-fit uncertainty, corresponding to the quadratic sum of all individual systematic uncertainty and the statistical uncertainty of the MC samples.

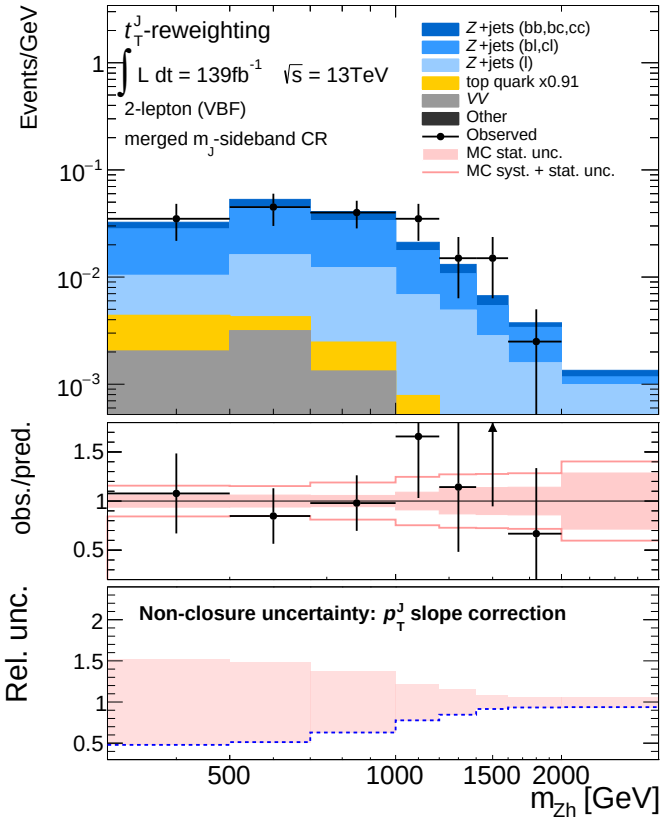

Figure 5.22: The expected and observed distribution of the final discriminant, m_{Zh}, after a event-wise p_T^J-reweighting of the Z+jets events in the m_J-sideband CR with *merged* topology p_T. The center panel in shows the residual ratio between observation and prediction after the p_T^J-reweighting. The corresponding deviation of the m_{Zh} distribution relative to the nominal one is shown in the bottom panel. This is applied as an additional non-closure uncertainty in the final statistical interpretation of data.

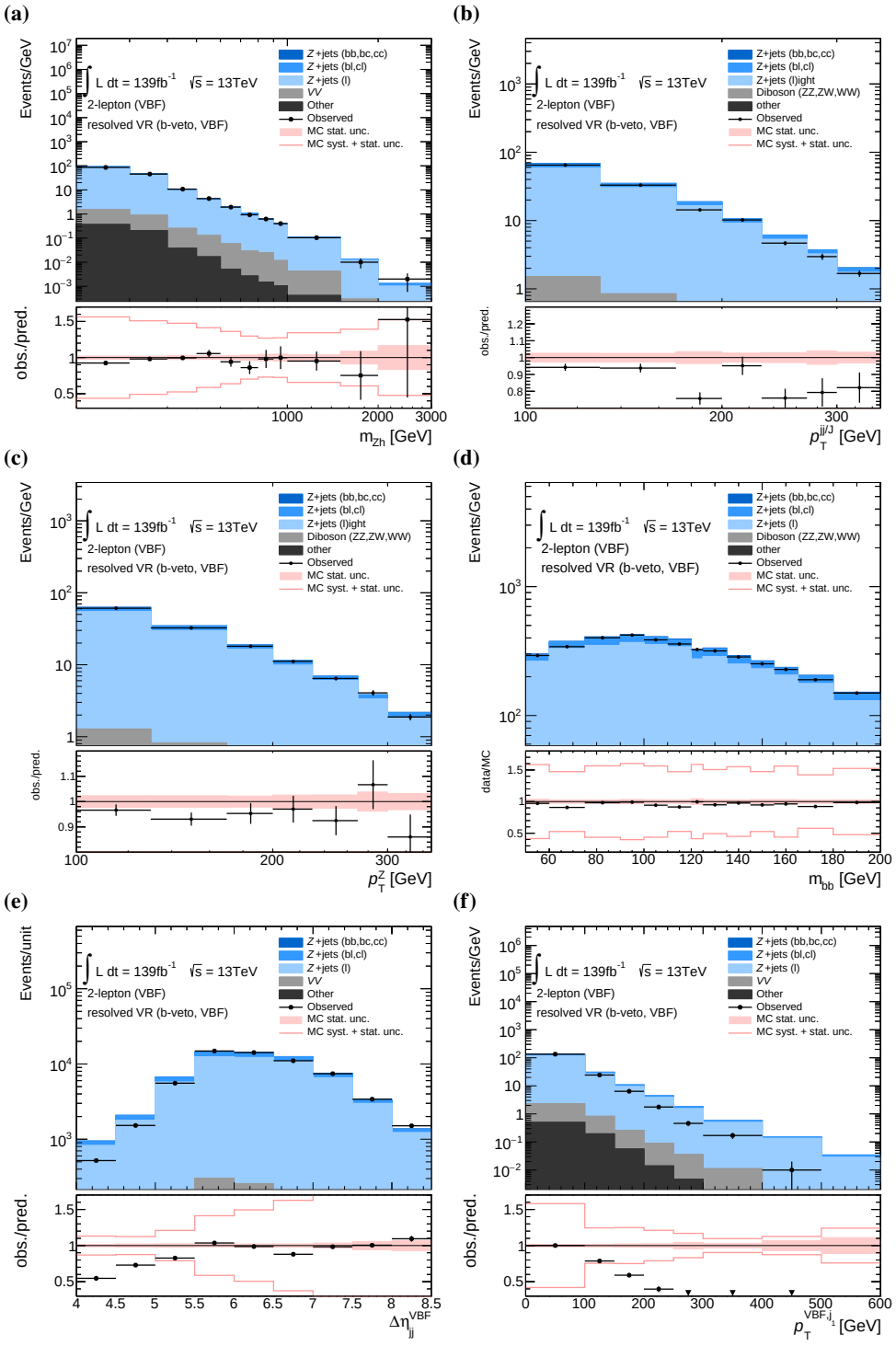

Figure 5.23: The observed and expected distributions of (a) the diboson mass, the reconstructed transverse momenta of (b) the Higgs boson and (c) the Z boson, the pseudo-rapidity gap and (f) the transverse momentum of the leading *VBF jet* in the untagged validation region. (d) The observed and expected distribution of the reconstructed Higgs boson candidate mass, while the m_{jj} is shown in the untagged validation region with relaxed m_{jj} requirement. The lower panels show the ratio of the observed and expected event yields. Statistical uncertainties in data and simulation are shown separately. The data error bars represent the statistical uncertainties of observed events evaluated using a 1σ range of a Poisson distribution. The shaded area represent the statistical uncertainty of the finite-sized MC samples. The red contour represents the total pre-fit uncertainty, corresponding to the quadratic sum of all individual systematic uncertainty and the statistical uncertainty of the MC samples.

5.2.2 Corrections of the *VBF jet* mismodeling

Related analyses of VBF event topologies [150] have shown mismodelings of the kinematic properties of the *VBF jets*. Figs. 5.24 and 5.25 show the pseudo-rapidity distribution of the leading and sub-leading *VBF jet*, η_{j_1} and η_{j_1}, respectively in the same control regions. No significant shape differences are observed between simulation and observation. Figs. 5.26 and 5.27 show the observed and expected distributions of the typical VBF discriminant observables, m_{jj}^{VBF} and $\Delta\eta_{jj}^{\mathrm{VBF}}$, in the $t\bar{t}$ CR and in the m_{jj}-sideband CRs with *resolved* event topology.The observed and expected m_{jj}^{VBF} distributions agree within statistical uncertainties. Events in the 1 b-tag m_{jj}-sideband CR with $\Delta\eta_{jj}^{\mathrm{VBF}} \lessapprox 5$ are over-represented in MC, especially in the m_{jj}-sideband CRs that is dominated by the Z+jets process, while the high $\Delta\eta_{jj}^{\mathrm{VBF}}$-tails ($\Delta\eta_{jj}^{\mathrm{VBF}} \gtrapprox 8$), a small excess of data is observed within the m_{jj}-sideband CR. Latter is covered by the large systematic uncertainties in the forward detector regions. A significant systematic slope in the ratio between observation and prediction is visible. The $\Delta\eta_{jj}^{\mathrm{VBF}}$ observable is correlated to the $p_{\mathrm{T}}^{\mathrm{VBF},j_1}$ and $p_{\mathrm{T}}^{\mathrm{VBF},j_2}$ observables and its distribution is corrected with the $p_{\mathrm{T}}^{\mathrm{VBF},}$-reweighting correction as described below (c.f. Fig. 5.34(a)).

The p_{T} distributions of the *VBF jets* are significantly mismodeled as can be seen in Figs. 5.28 and 5.29, for the $t\bar{t}$ CRs and the m_{jj}-sideband CRs, respectively. The contribution of high-p_{T} *VBF jets* are overestimated for both the leading and the sub-leading *VBF jet* in the m_{jj}-sideband CRs. In contrast, the top quark component, that can be studied separately in the $t\bar{t}$ CRs, shows a mismodeling only for the sub-leading *VBF jet*. The systematic deviations from the observed distributions are not covered by the experimental and theoy uncertainties. A corresponding non-closure uncertainty is therefore imposed to both $t\bar{t}$ and Z+jets contributions to account for the impact on the reconstructed diboson mass, m_{Zh}.

The impact of the $p_{\mathrm{T}}^{\mathrm{VBF,j}}$ mismodeling on the final discriminant, m_{Zh}, is estimated as follows: In a first step, a $p_{\mathrm{T}}^{\mathrm{VBF},j_1}$-dependent correction factor is applied to all simulated $t\bar{t}$ events. The correction is parameterized as a linear function of $p_{\mathrm{T}}^{\mathrm{VBF},j_1}$, obtained from a fit to the ratio between observation and simulation in the $t\bar{t}$ CR. Fits are performed separately for the 1 b-tag and the 2 b-tag CRs. In the second step, remaining differences in the m_{jj}-sideband regions are assumed to originate from the Z+jets modeling. After subtracting the predicted $t\bar{t}$ contributions from the observed data, an analogous $p_{\mathrm{T}}^{\mathrm{VBF},j_1}$-based correction factor is derived for the simulated Z+jets events [2]. The resulting parametrizations are summarized in Table 5.2.

The $p_{\mathrm{T}}^{\mathrm{VBF},j_2}$ transverse momentum distributions from the sub-leading *VBF jet*, obtained after the $p_{\mathrm{T}}^{\mathrm{VBF},j_1}$-based reweighting are shown in Fig. 5.30. The $p_{\mathrm{T}}^{\mathrm{VBF},j_1}$-dependent reweighting does not automatically correct for the slope in the ratio between observation and simulation of $p_{\mathrm{T}}^{\mathrm{VBF},j_2}$ distributions. Therefore, a second independent reweighting correction is derived as a function of $p_{\mathrm{T}}^{\mathrm{VBF},j_2}$, following the same reweighting procedure as for $p_{\mathrm{T}}^{\mathrm{VBF},j_1}$.

The difference between the nominal and the resulting reweighted m_{Zh} distribution is treated as 1σ systematic uncertainty on the shape of the m_{Zh} background description due to the *VBF jet* mismodeling. The uncertainties are introduced separately for six different background components, i.e. for each

[2] The Z+jets correction can also be derived in the untagged validation region. The resulting parametrization of the event weights coincides within a precision of 1% with those derived in the 1 b-tag m_{jj}-sideband CR.

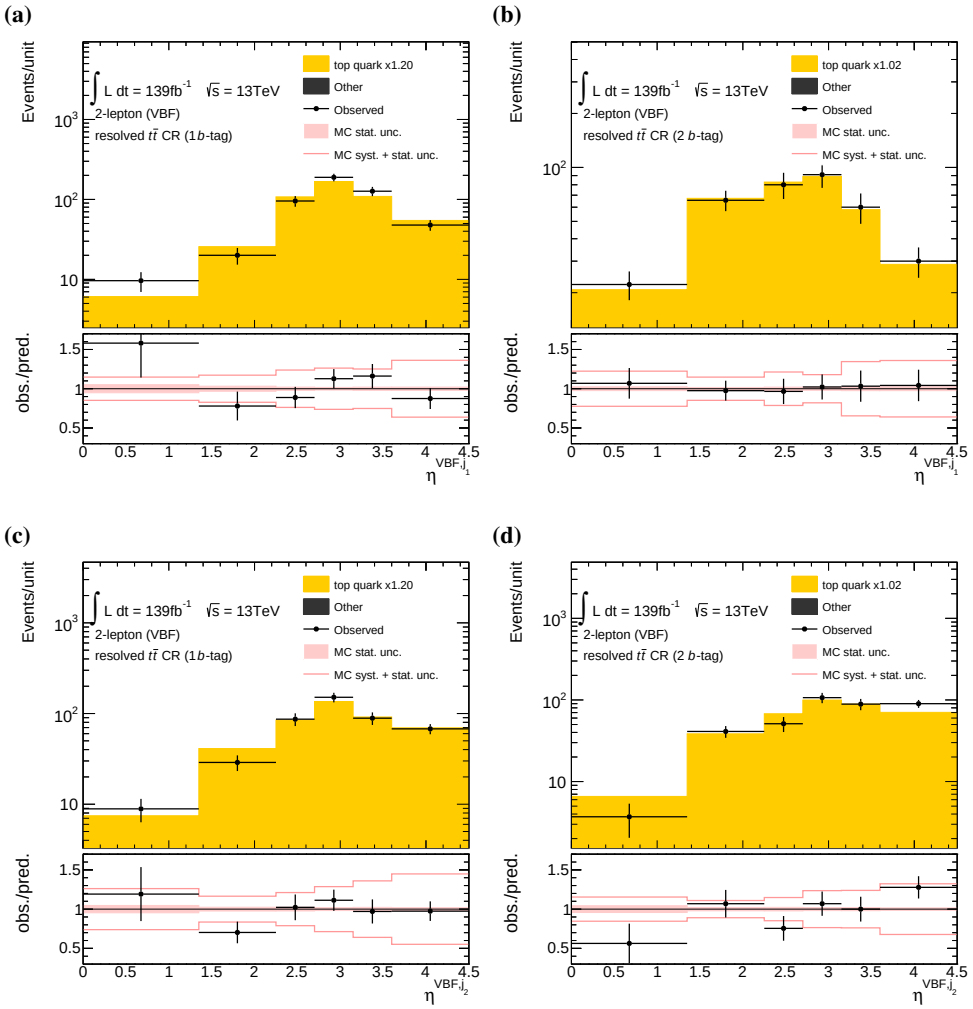

Figure 5.24: The observed and expected pseudo-rapidity distributions of the two *VBF jets*, (a) and (b) leading and (c) and (d) sub-leading *VBF jet*, in the (a) and (c) 1 *b*-tag and (b) and (d) 2 *b*-tag $t\bar{t}$ CRs with resolved event topology. The lower panels show the ratio of the observed and expected event yields. Statistical uncertainties in data and simulation are shown separately. The data error bars represent the statistical uncertainties of observed events evaluated using a 1σ range of a Poisson distribution. The shaded area represent the statistical uncertainty of the finite-sized MC samples. The red contour represents the total pre-fit uncertainty, corresponding to the quadratic sum of all individual systematic uncertainty and the statistical uncertainty of the MC samples.

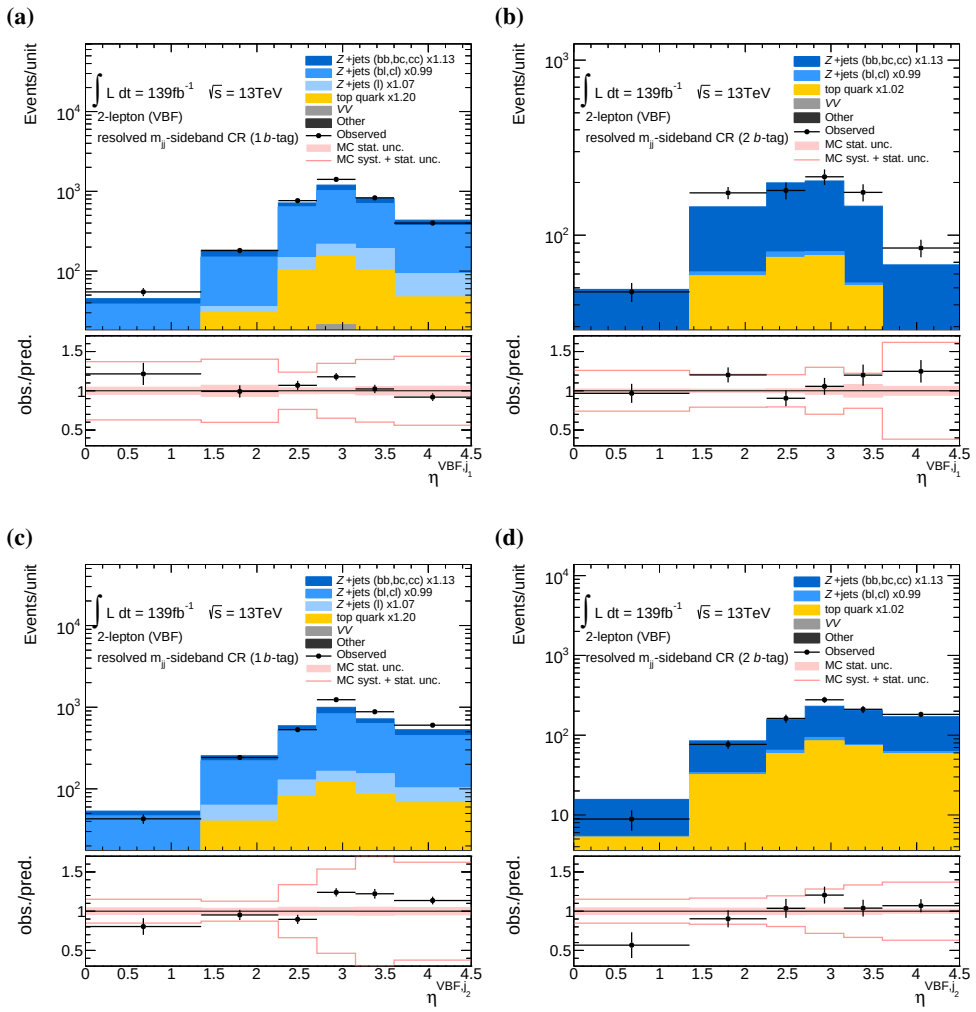

Figure 5.25: The observed and expected pseudo-rapidity distributions of the two *VBF jets*, (a) and (b) the leading and (c) and (d) the sub-leading *VBF jet*, in the (a) and (c) 1 b-tag and (b) and (d) 2 b-tag m_{jj}-sideband CRs with resolved event topology. The lower panels show the ratio of the observed and expected event yields. Statistical uncertainties in data and simulation are shown separately. The data error bars represent the statistical uncertainties of observed events evaluated using a 1σ range of a Poisson distribution. The shaded area represent the statistical uncertainty of the finite-sized MC samples. The red contour represents the total pre-fit uncertainty, corresponding to the quadratic sum of all individual systematic uncertainty and the statistical uncertainty of the MC samples.

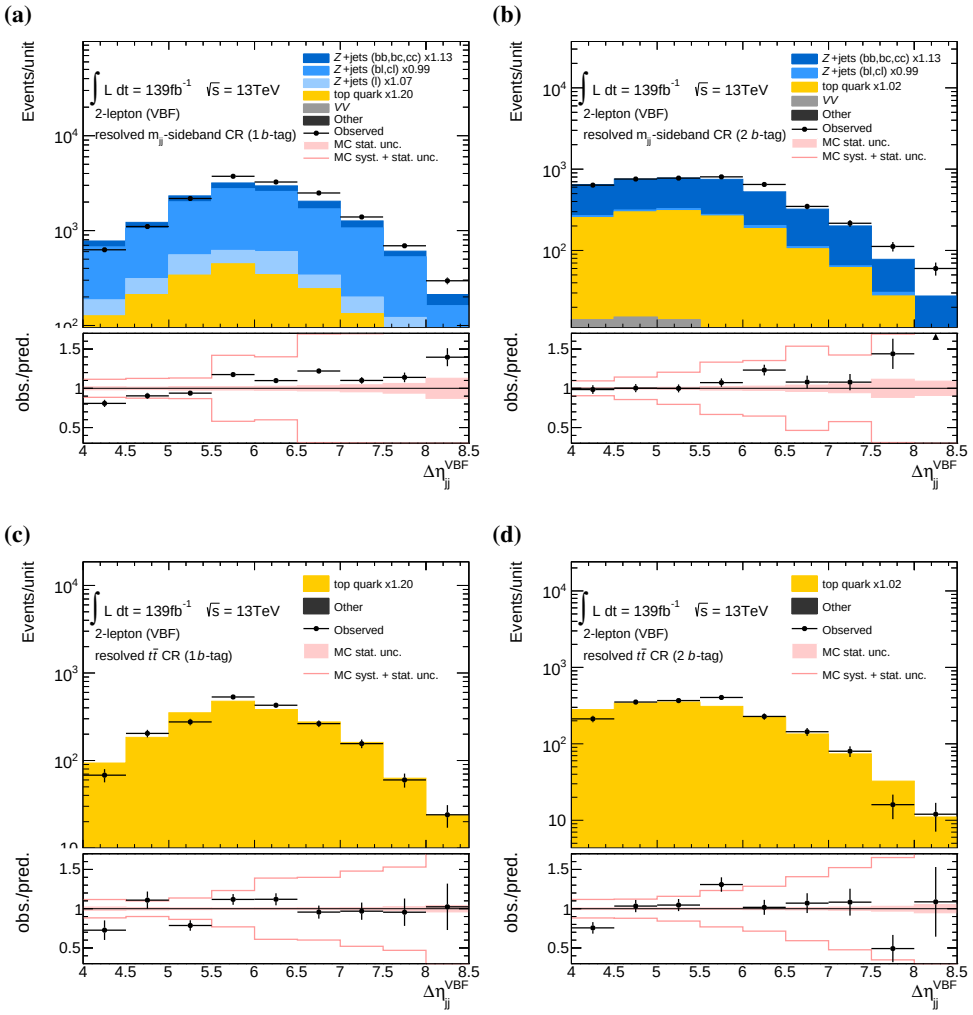

Figure 5.26: The observed and expected distributions of the pseudo-rapidity gap, $\Delta\eta_{jj}^{VBF}$ of the two *VBF jets* in the different CRs with the *resolved* event topology. (a) and (b) show the m_{jj}-sideband CRs and (c) and (d) show the $t\bar{t}$ CR. On the left-hand side, the 1 b-tag regions and on the right-hand side the 2 b-tag region is shown.

Table 5.2: Event weights applied to $t\bar{t}$ and Z+jets for the evaluation of the corresponding m_{Zh} uncertainty, following the procedure described in the text.

Process	Applied regions	$w(p_T^{VBF,j_1})$	$w(p_T^{VBF,j_2})$
top quark	1 b-tag *resolved* regions	$1.11 - 1.9310^{-3} \cdot p_T^{VBF,j_1}$[GeV]	$1.22 - 5.3110^{-3} \cdot p_T^{VBF,j_2}$[GeV]
	2 b-tag *resolved* regions	$1.20 - 2.2310^{-3} \cdot p_T^{VBF,j_1}$[GeV]	$1.27 - 5.3610^{-3} \cdot p_T^{VBF,j_2}$[GeV]
Z+jets	1 b-tag *resolved* regions	$1.23 - 3.2010^{-3} \cdot p_T^{VBF,j_1}$[GeV]	$1.31 - 7.1110^{-3} \cdot p_T^{VBF,j_2}$[GeV]
	2 b-tag *resolved* regions	$1.13 - 1.6410^{-3} \cdot p_T^{VBF,j_1}$[GeV]	$1.18 - 3.6910^{-3} \cdot p_T^{VBF,j_2}$[GeV]

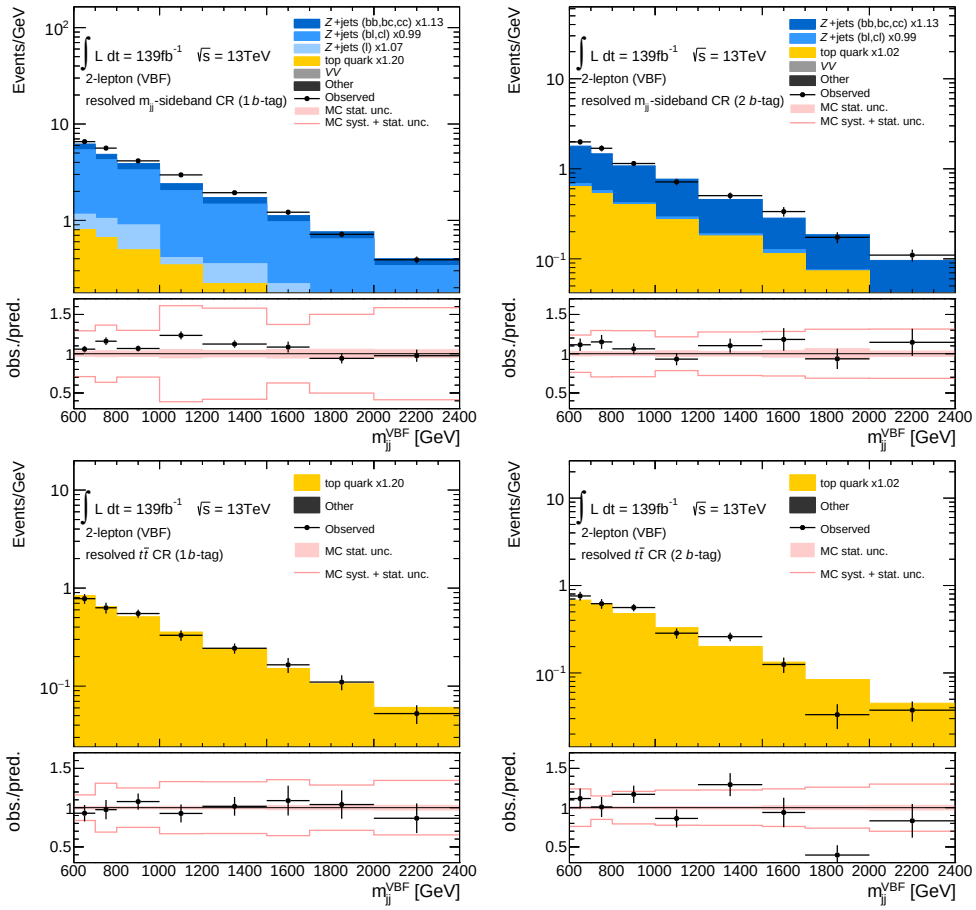

Figure 5.27: The observed and expected distributions of the invariant mass, m_{jj}^{VBF} of the two *VBF jets* in the different CRs with the *resolved* event topology. (a) and (b) show the m_{jj}-sideband CRs and (c) and (d) show the $t\bar{t}$ CR. On the left-hand side, the 1 b-tag regions and on the right-hand side the 2 b-tag region is shown.

of the two *VBF jets* and for each of the three dominant background sources: $t\bar{t}$, Z+jets (bl,cl) and Z+jets (bb,bc,cc).

Figs. 5.31 and 5.32 show the expected m_{Zh} distributions after the reweighting for the $t\bar{t}$ and Z+jets production, respectively, in the signal regions. The deviations from the nominal distribution amount to about 1% in the bulk of the distributions. The uncertainty in the 1 b-tag signal region is more pronounced, with a relative deviation of up to 15% in the tails. Uncertainties related to the $p_{\mathrm{T}}^{\mathrm{VBF,j_1}}$ and $p_{\mathrm{T}}^{\mathrm{VBF,j_2}}$ mismodeling are of similar size, but with different impact on the m_{Zh} shape. Statistical fluctuations in the evaluation of the described uncertainty are mitigated using the same procedure as for the theoretical uncertainties, described in Section 4.4.2.

The impact of *VBF jet* p_{T}-reweighting on the p_{T} of both reconstructed bosons can be seen in Fig. 5.34. The insignificant slope in the ratio between observation and simulation that was seen for the unweighted distribution of the boson p_{T} (c.f. Figs. 5.17(a) and 5.17(c)) is reduced by the $p_{\mathrm{T}}^{\mathrm{VBF,j_1}}$-reweighting, indicating that the introduced *VBF jet* mismodeling uncertainties cover also the mismodeling of p_{T}^{Z}

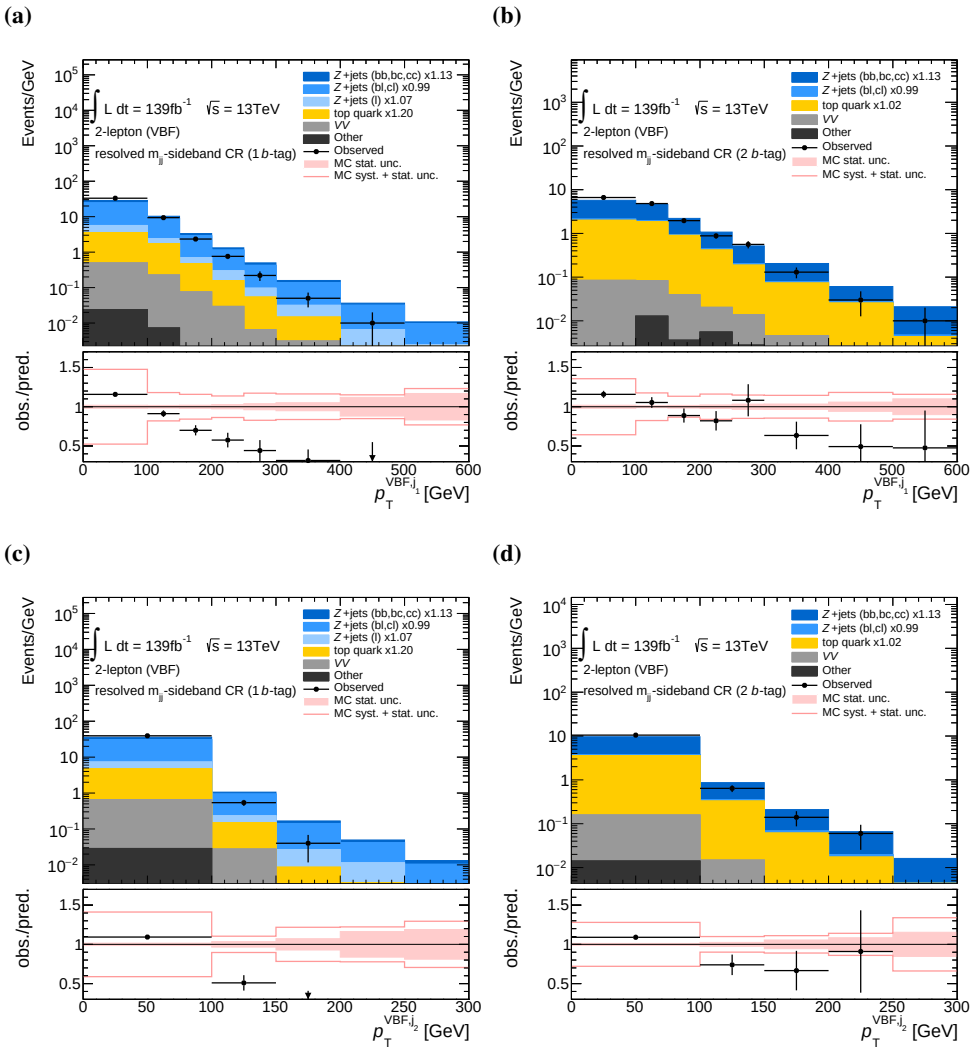

Figure 5.28: The observed and expected distributions of the transverse momenta of (a) and (b) the leading *VBF jet*, and (c) and (d) the sub-leading *VBF jet* in the m_{jj}-sideband CRs with resolved event topology. The lower panels show the ratio of the observed and expected event yields. Statistical uncertainties in data and simulation are shown separately. The data error bars represent the statistical uncertainties of observed events evaluated using a 1σ range of a Poisson distribution. The shaded area represent the statistical uncertainty of the finite-sized MC samples. The red contour represents the total pre-fit uncertainty, corresponding to the quadratic sum of all individual systematic uncertainty and the statistical uncertainty of the MC samples.

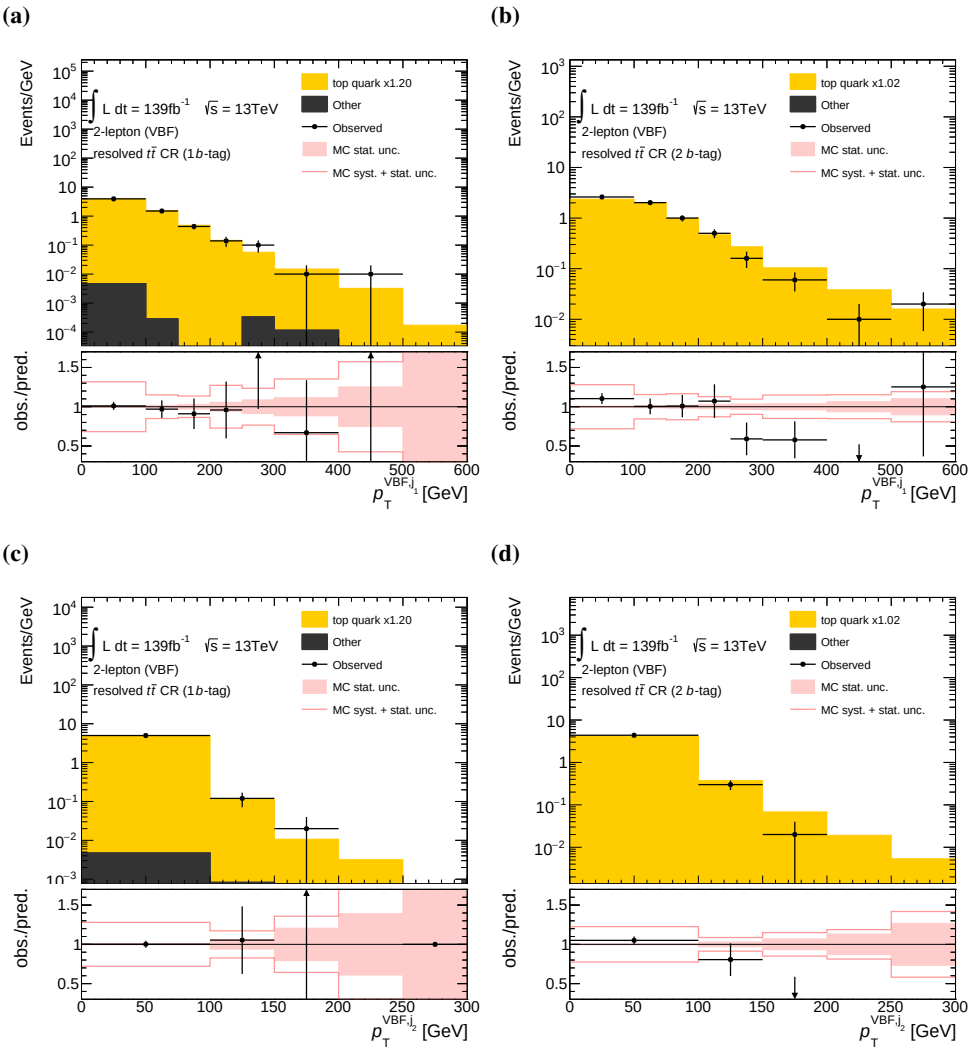

Figure 5.29: The observed and expected distributions of the transverse momenta of (a) and (b) the leading *VBF jet*, and (c) and (d) the sub-leading *VBF jet* in the $t\bar{t}$ CR. The lower panels show the ratio of the observed and expected event yields. Statistical uncertainties in data and simulation are shown separately. The data error bars represent the statistical uncertainties of observed events evaluated using a 1σ range of a Poisson distribution. The shaded area represent the statistical uncertainty of the finite-sized MC samples. The red contour represents the total pre-fit uncertainty, corresponding to the quadratic sum of all individual systematic uncertainty and the statistical uncertainty of the MC samples.

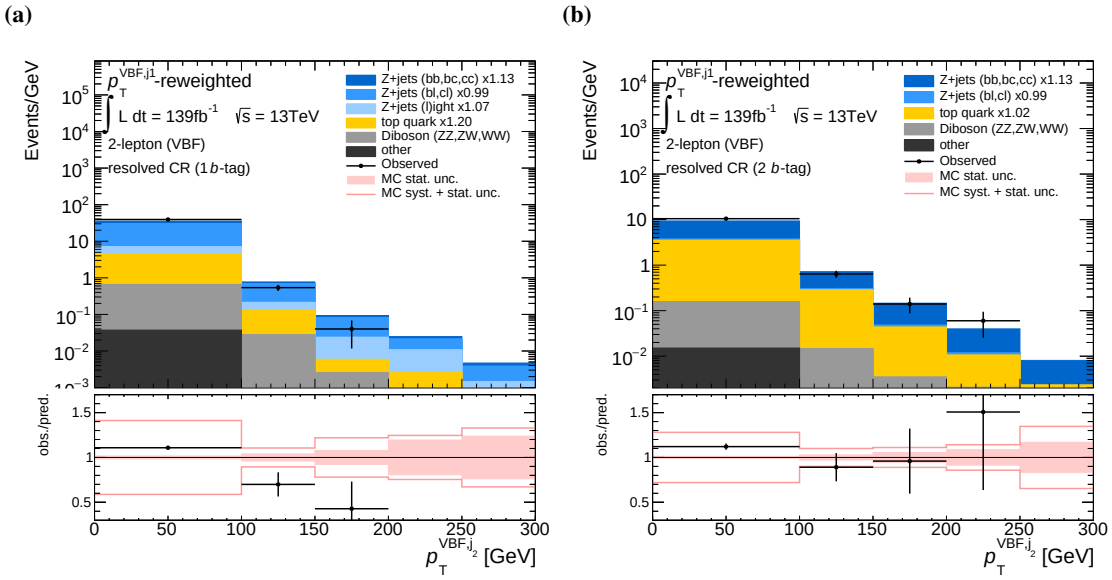

Figure 5.30: The expected and observed transverse momentum distributions of the sub-leading *VBF jet*, after the $p_{\mathrm{T}}^{\mathrm{VBF,j_1}}$-dependent event reweighting procedure (see text), in the (a) 1 and (b) 2 b-tag m_{jj}-sideband CRs with the *resolved* event topology.

and p_{T}^{jj} distributions. The mismodeling of the $\Delta\eta_{\mathrm{jj}}^{\mathrm{VBF}}$ variable seen in Fig. 5.26(a) is corrected by the $p_{\mathrm{T}}^{\mathrm{VBF,j_1}}$ reweighting, as can be seen in Fig. 5.34(a). The over-estimate of the number of events with sub-leading *VBF jet* in the center detector region ($\eta^{VBF,\mathrm{j_1}} < 1.35$) is covered by the $p_{\mathrm{T}}^{\mathrm{VBF,j_2}}$-dependent reweighting, as can be seen in Figs. 5.34(b) and 5.34(c).

An analogue uncertainty in events with the *merged* topology is not considered due to the limited statistical precision of data in the *merged* CR.

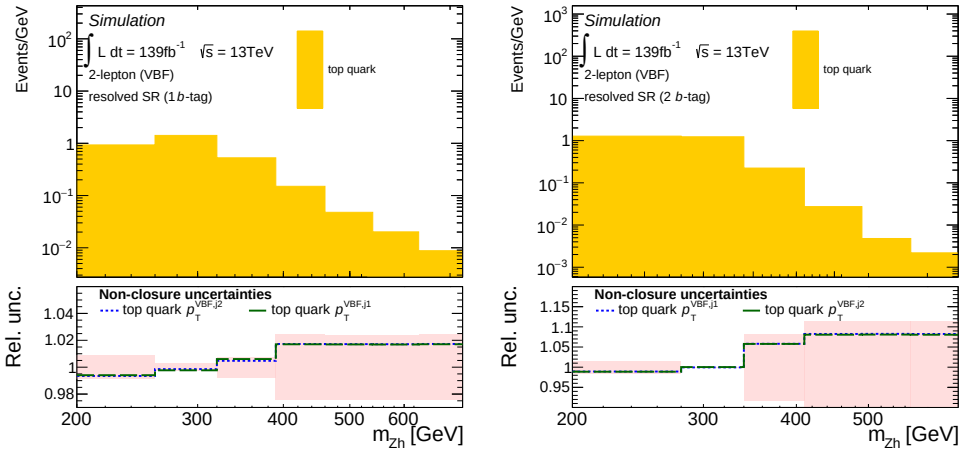

Figure 5.31: The expected $t\bar{t}$ m_{VH}-distributions in the *resolved* VBF signal regions with 1 b-tag (left) and 2 b-tags (right). The blue line (green line) in the ratio panel shows the relative deviation from the nominal distribution after applying the $p_T^{VBF,j1}$-based ($p_T^{VBF,j2}$-based) event reweighting. The deviation is shown without the normalization component, i.e. shape only.

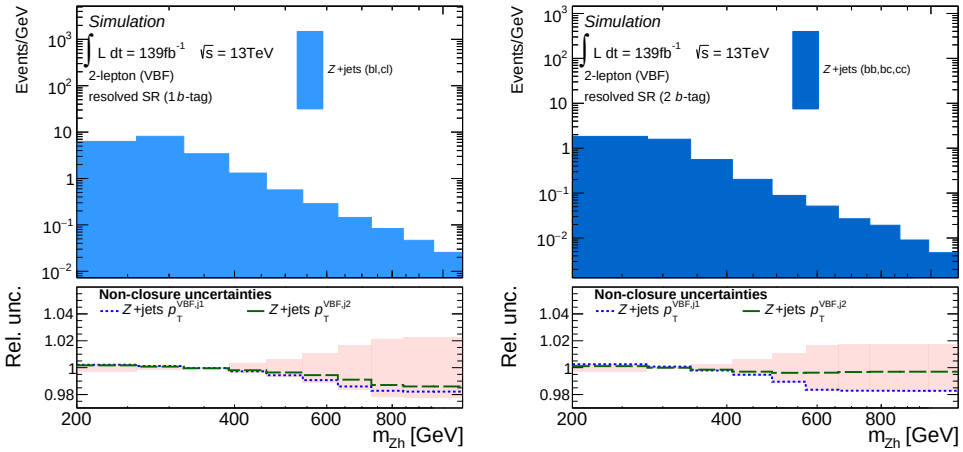

Figure 5.32: The expected Z+jets m_{VH}-distributions in the *resolved* VBF signal regions with 1 b-tag (left) and 2 b-tags (right). The blue line (green line) in the ratio panel shows the relative deviation from the nominal distribution after applying the $p_T^{VBF,j1}$-based ($p_T^{VBF,j2}$-based) event reweighting. The deviation is shown without the normalization component, i.e. shape only.

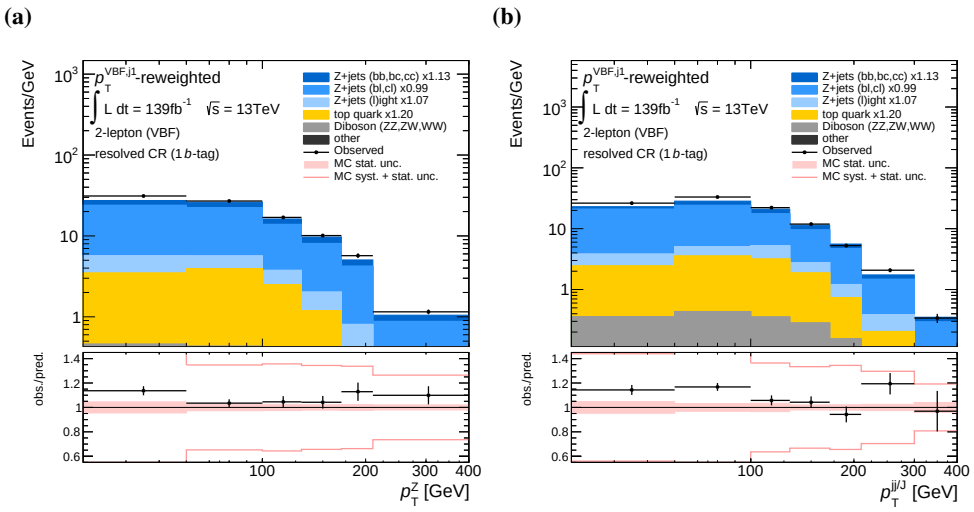

Figure 5.33: The observed and expected distributions of transverse momentum of the reconstructed bosons, p_{T}^{Z} (a) and p_{T}^{jj} (b) in the *resolved* 1 b-tag m_{jj}-sideband CRs, after the $p_{\mathrm{T}}^{\mathrm{VBF,j_1}}$-dependent event reweighting procedure is applied (see text).

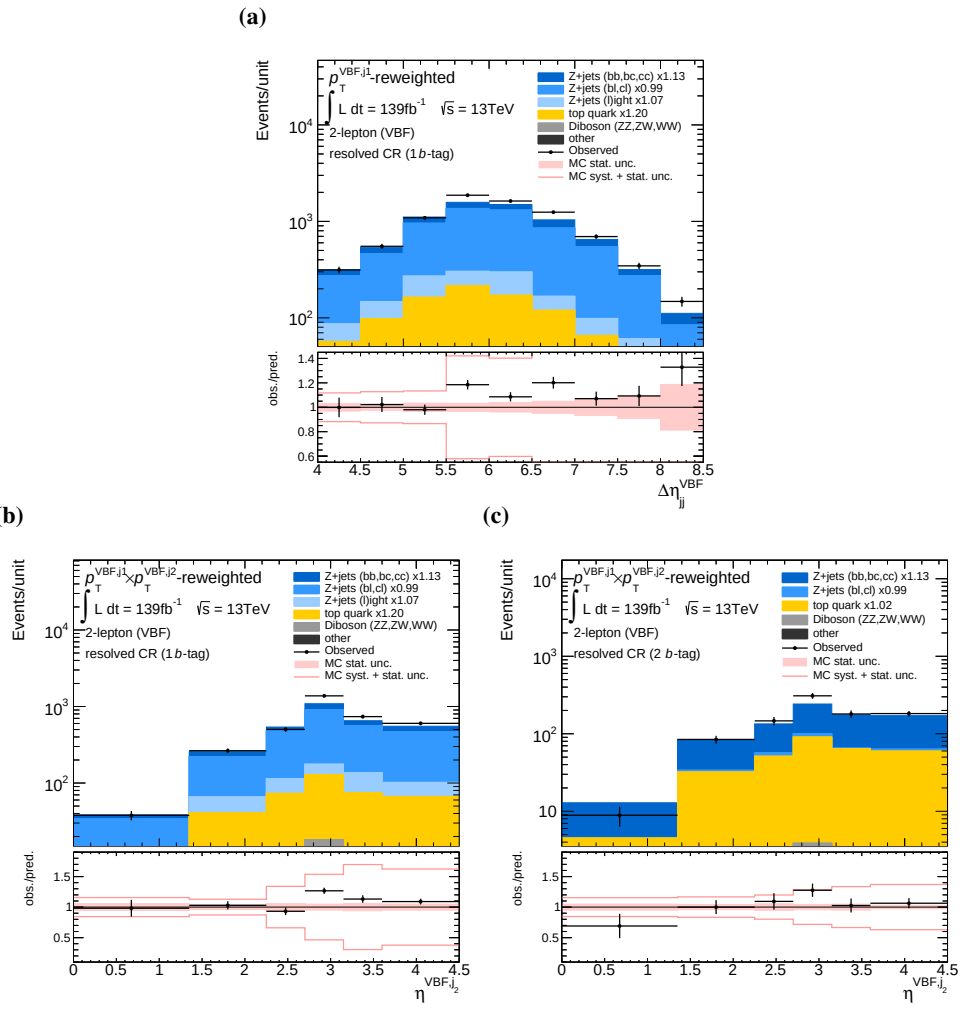

Figure 5.34: The observed and expected distributions of the sub-leading *VBF jet* η distribution in *resolved* m_{jj}-sideband CRs with (a,c) 1 b-tag and (b) 2 b-tag, after the (a,b) $p_T^{VBF,j_2} \times p_T^{VBF,j_2}$-dependent or (c) p_T^{VBF,j_1}-dependent event reweighting procedure is applied. These variables were formerly not covered by the uncertainties (c.f. Figs. 5.25(c), 5.25(d) and 5.26(a)

5.3 Systematic uncertainties

Imperfect theory description of signal and background processes as well as imperfect simulation of the detector response lead to a number of systematic uncertainties, impacting the final statistical interpretation of data.

These systematic uncertainties can be classified into three groups: The experimental uncertainties from the imperfect description of particle reconstruction and identification efficiency, as well as their energy or momentum measurement; the theory uncertainty on the predicted cross section; and the modeling of kinematic properties of signal and background processes and uncertainties on the data-driven normalization and modeling corrections based on the dedicated CRs (c.f. Section 5.2).

A given source of a systematic uncertainty will modify the normalization or the shape of the final discriminant m_{Zh} in a given process. The resulting m_{Zh} distribution corresponding to the uncertainty of one standard deviation is referred to as *variation* with respect to the *nominal* distribution and is used in the final fit as a constraint on the parameterized description of the final discriminant.

Experimental uncertainties are induced by biases in the instrumentation setup, e.g. miscalibrated energy scale or reconstruction efficiency. Such sources simultaneously affect all signal and background processes. Thus, the impact of a given experimental source of uncertainty is correlated among all signal and control regions and physics processes. These uncertainties are discussed in Section 5.3.1.

Theoretical modeling uncertainties such as the uncertainties on the parton shower model or the choice of the renormalization and factorization scales, are related to the event generation. In addition, the uncertainties due to higher-order loop corrections may affect both, the normalization and to a smaller extent also the kinematic properties of a given process. Such theory uncertainties are a priori process-related and thus uncorrelated among all signal and background processes. The modeling uncertainties are discussed in Section 5.3.2.

Finally, systematic differences between prediction and data are observed in the dedicated CRs (c.f. Section 5.2). These mismodelings are not covered by the sources of uncertainties mentioned above and are taken into account via dedicated non-closure uncertainties.

5.3.1 Experimental uncertainties

Experimental uncertainties arise from the imperfect simulation of the detector instrumentation response to final state particles, affecting the luminosity measurement, trigger efficiencies, reconstruction and identification of leptons and jets, b-tagging efficiencies and estimation of non-suppressed pile-up contributions to jets. Impact of experimental uncertainties on the discriminant observables in this analysis is estimated by varying the corresponding parameters in the simulation of the detector response, separately for each simulated sample.

Each source of experimental uncertainty discussed in this section is described in more detail in the *parent analysis* in Section 4.4.1. The impact of these uncertainties is evaluated here for the case of the VBF-sensitive event selection. The VBF topology is particularly affected by the jet-related uncertainties, with the dominant effects summarized in Table 5.3 and discussed in the following.

Table 5.3: Pre-fit impact of experimental uncertainties on the normalization of the m_{Zh} total background distribution in the different signal regions VBF 2-lepton analysis.

Uncertainty	*merged* SR	*resolved* SR, 1 *b*-tag	*resolved* SR, 2 *b*-tag
Electrons	±1.6%	±1.1%	±1.0%
Muon	±1.2%	±0.5%	±0.4%
Tau	±0.35%	±0.0%	±0.0%
E_T^{miss}	±0.4%	±1.1%	±0.8%
Jet vertex tagging	±0.5%	±0.9%	±1.0%
large-R jet energy scale (JES)	±5.4%	—	—
large-R jet energy resolution (JER)	±0.8%	—	—
large-R jet mass resolution (JMR)	±1.2%	—	—
track jet b-tagging efficiency	±1.0%	—	—
track jet c-tagging efficiency	±2.4%	—	—
track jet light quark misidentification rate	±6.7%	—	—
small-R JER	±13.6%	±33.8%	±20.0%
small-R JES (η-intercal.)	±6.0%	±11.0%	±7.0%
small-R JES (p_{T}-terms)	±3.34%	±8.2%	±5.3%
small-R JES: Flavor terms	±8.3%	±20.6%	±12.2%
small-R JES: Pile-up terms	±5.0%	±17.3%	±10.6%
small-R jet b-tagging efficiency	—	±0.67%	±4.0%
small-R jet c-tagging efficiency	—	±1.7%	±0.9%
small-R jet light quark misidentification rate	—	±2.8%	±0.7%
Total experimental uncertainty	±20.3%	±45.4%	±27.5%

Small-R jets The explicit requirement of four distinct small-R jets in the final state makes this analysis susceptible to the uncertainties in the reconstruction of these jets. Even in events with the *merged* topology, the uncertainties from small-R jet reconstruction have the most dominant pre-fit impact due to two *VBF jets* in the final state (see Table 5.3). The energy (or p_{T}) distribution of *VBF jets* tends to low values for all background processes (see Figs. 5.28 and 5.29). The $p_{\mathrm{T}}^{\mathrm{VBF,j}}$-distributions are delimited by the event selection requirement of $p_{\mathrm{T}}^{\mathrm{VBF,j}} > 30$ GeV. The large fraction of background events close to the event selection threshold causes the event selection efficiency to be very sensitive to small uncertainties in the jet energy calibration. The calibration of the jet energy scale (JES) and the measurement of the jet energy resolution (JER) [51] is subject to multiple sources of uncertainty. The JES is determined in-situ in three stages. Each step takes advantage of a well calibrated additional object in the event, recoiling against the jet (c.f. Section 2.4.5), and provides uncertainties covering effects from the jet flavor content, pile-up jet rejection efficiency as well as theory modeling and statistical limitations in the calibration. The calibration introduces a set of 125 uncorrelated uncertainty parameters, whose impact on the stribution is individually studied. In particular, forward jets are calibrated by the *η-intercalibration* procedure [51]. A di-jet system, that is balanced in the transverse plane, is used to calibrate jets in different η regions with respect to each other. This di-jet based calibration step enables an extrapolation of the energy scale to jets in the forward detector region beyond $|\eta| > 0.8$. The described calibration procedure typically yields large uncertainties on JES for the *VBF jets* compared to those for the central jets. The impact of the JER uncertainties on the m_{Zh} distribution is evaluated by an additional smearing of the jet energy according to the uncertainty of the

JER measurement. The JER uncertainty is the dominant contribution to the background normalization uncertainty in the 2-lepton VBF channel, resulting in an uncertainty of up to 33.8% on the total expected number of background events in the 1 b-tag region.

Jet vertex tagger (JVT) The JVT algorithm [89] rejects jets which do not originate from the primary vertex. The efficiency of the JVT selection has been estimated and the uncertainty on this efficiency measurement increases for jets in the forward region (*VBF jets*), due to the lack of the inner detector coverage above $|\eta| > 2.5$.

Large-R jets The uncertainties induced by the large-R jet energy scale calibration are estimated by comparing the observed and simulated large-R jet mass measurements as well as the corresponding calorimeter- and track-based energy measurements [78, 81]. The covariance matrix describing the uncertainties in the subsidiary JES calibration measurement is decomposed in 5 orthogonal uncertainty components, describing a baseline term, the residual difference between observation and prediction, the fragmentation and hadronization model, the total statistical uncertainty of the calibration and uncertainties related to the tracking. The impact of the large-R jet mass resolution (JMR) and jet energy resolution (JER) uncertainties on the event selection in the present search are evaluated by an additional smearing of the jet mass and energy, respectively. The jet mass (energy) is modified artificially by a random value corresponding to a gaussian distribution with a standard deviation of 20% (2%) relative to the *nominal* JMR (JER) The smearing is applied to the jet before the event selection. Thus, it is accounted for the effect on the m_{Zh} distribution as well as JMR-related migration effects between the m_{jj}-sideband CRs and the corresponding signal regions. The corresponding normalization uncertainty induced by the large-R jet reconstruction is summarized in Table 5.3.

***b*-tagging** The impact of the b-tagging efficiency and misidentification rate uncertainties on the m_{Zh} distribution is also studied, both for the small-R jets in the *resolved* and the VR track jets in the *merged* event topology region. The b-tagging calibration is performed in data, enriched with $t\bar{t} \to b\bar{q}W^+W^- \to \ell\nu q\bar{q}b\bar{b}$ events [98, 100, 183]. The average impact of the obtained b-tagging uncertainties on the normalization of the m_{Zh} distribution in the signal and control regions with *resolved* event topology is below 1%, but may reach values of up to 5% in the tails. Uncertainties on the misidentification rate of jets from the light quarks affect the m_{Zh} distribution by about 9% on average with values of up to 20% in the high mass tails of the resonance mass distribution.

The relative impact of all considered sources of uncertainties on the total m_{Zh} background distribution is presented in Figs. 5.35 and 5.36 for the *resolved* and the *merged* signal regions, respectively.

The changes in the shape of the m_{Zh} distribution due to the described experimental uncertainties undergo the smoothing and averaging procedure described in Section 4.4.1 before being included in the final fit to data.

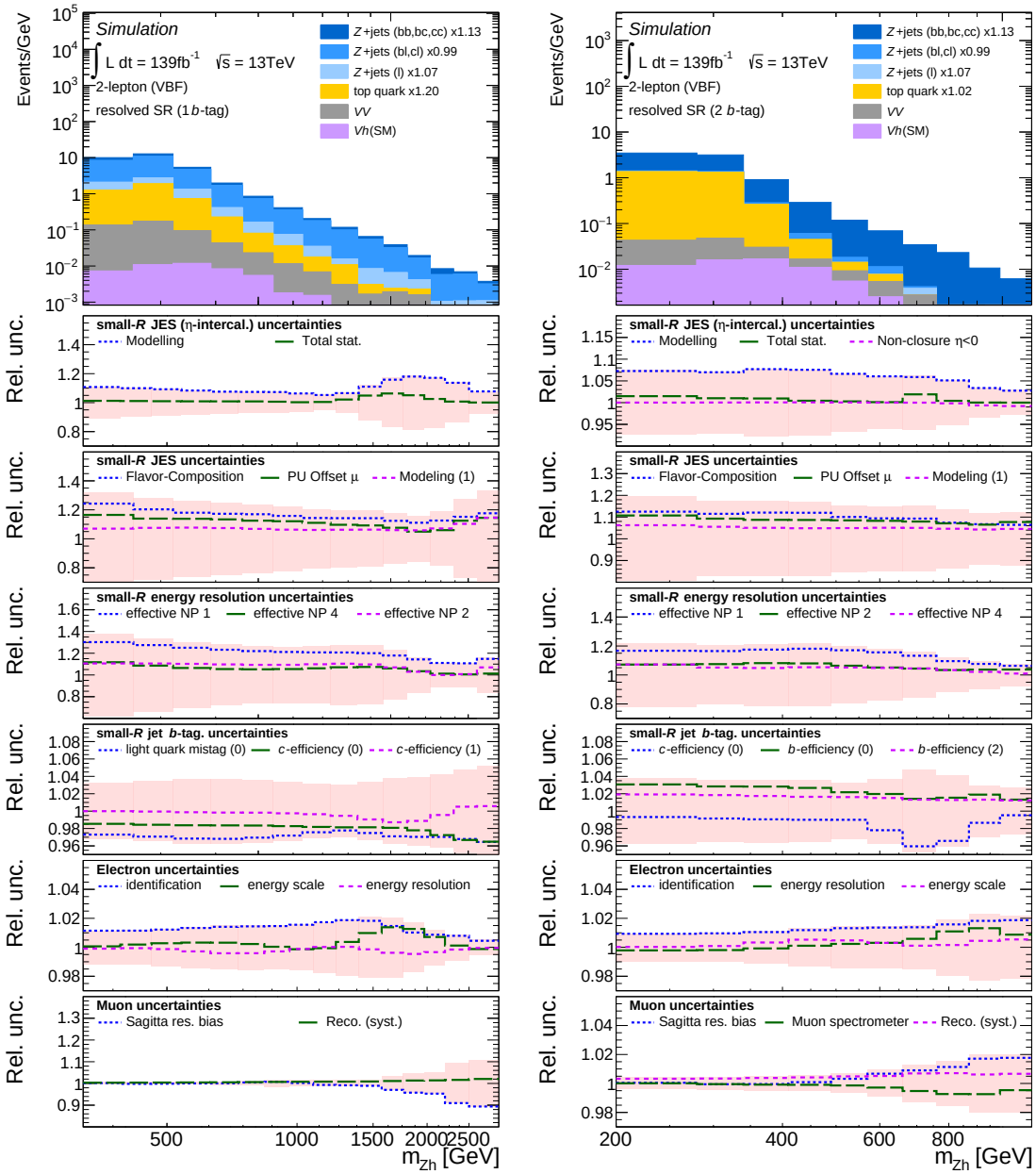

Figure 5.35: The expected m_{Zh} background distributions in the (left) 1 and (right) 2 b-tag signal regions with the *resolved* event topology (upper panels) and the relative change of the total background distributions with respect to the nominal distribution after introducing a given source of experimental uncertainty. For a given source of uncertainty the impact of each disjunct sub-component is added in quadrature. Only up to 3 leading sub-components are shown explicitly.

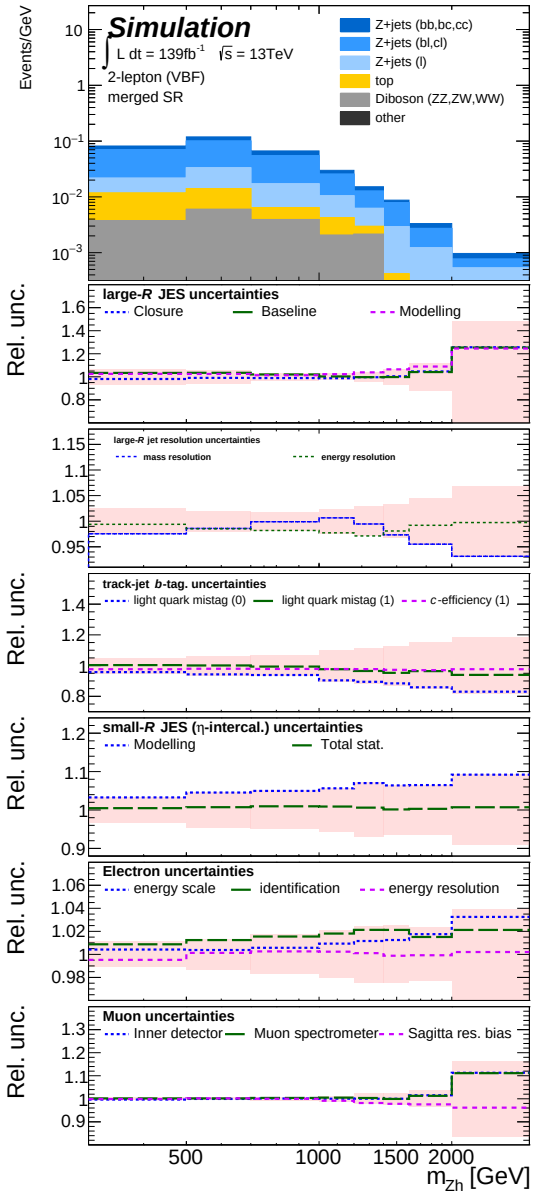

Figure 5.36: The expected m_{Zh} background distribution in the signal region with the *merged* event topology (upper panel) and the relative change of the total background distributions with respect to the nominal distribution after introducing a given source of experimental uncertainty. For a given source of uncertainty the impact of each disjunct sub-component is added in quadrature. Only up to 3 leading sub-components are shown explicitly.

5.3.2 Theory uncertainties

Theory uncertainties are related to biases in the MC event generation and higher-order cross section calculations before the simulation of the detector response. They can lead to uncertainties on the normalization and the shape of the m_{Zh} distributions that are used for the final statistical interpretation of the data. In contrast to experimental uncertainties, the impact of these uncertainties is process-dependent and they are considered to be fully uncorrelated among the different simulated signal and background processes in the fit.

The theory uncertainties discussed here are related to the matching of the matrix element (ME) to the parton shower, the PDF measurement, the parton shower (PS) model, hadronization and underlying event and the choice of the QCD renormalization and factorization scale. The techniques used to evaluate the impact of these uncertainties are described in more detail in Sections 4.4.3 and 4.4.4.

The theory uncertainties for the VBF channel are evaluated in a similar manner as for the *parent analysis*. They have to be extrapolated from *surrogate* samples, as described in Section 4.4.2.

Theory uncertainties for background processes

The impact of theory uncertainties on the expected background distributions is evaluated for the most relevant background processes, i.e. top quark, Z+jets (bb,bc,cc) and Z+jets (bl,cl) processes, which are studied separately for each signal and control region. The employed methodology is the same as in the *parent analysis* and is described in Section 4.4.3.

Normalization differences implied by the different MC samples amount up to 40% in case of the variations of the renormalization and factorization scales (QCD scale), μ_R and μ_F. These large uncertainties are omitted by determining the normalization of those background processes entirely from data, directly from the simultaneous final fit of the m_{Zh} distribution in all signal and control regions (c.f. Section 5.4). Therefore, the theory uncertainties affect only the shape of the final discriminant m_{Zh} distribution (shape uncertainties) and the relative normalization between the various signal and control regions, as described below.

The impact of theory uncertainties on the shape of the m_{Zh} distribution from the minor backgrounds, the VV and Vh diboson and Z+jets (l) processes are considered to be negligible. The normalization of those background components is taken from the prediction of the MC generators and a conservative 50% uncertainty on the normalization is assumed. The impact of theory uncertainties on the shape of the main background m_{Zh} distributions in the signal regions is shown in Figs. 5.37 and 5.38.

top quark background Fig. 5.37 shows the m_{Zh} shape modeling uncertainty for the top quark pair production in the signal regions with the *resolved* event topology. The largest impact on the shape of the top quark distribution is caused by the uncertainty of the ME matching model. The m_{Zh} shape prediction made by the alternative event generator, aMC@NLO, is up to 8% larger than the nominal prediction for reconstructed m_{Zh} masses in the high-mass tail above 400GeV in the 2 b-tag signal region with the *resolved* event topology. In contrast, in the corresponding 1 b-tag region the alternative prediction is up to 15% lower than the nominal one. A similar behavior, but less pronounced, is also

observed for the parton shower (PS) uncertainty and the uncertainty for the leading gluon emission. The MC generator setups corresponding to an increased initial-state radiation (ISR) and final-state radiation (FSR) activities predict about 2% more events in the high-mass tails compared to the nominal prediction. ISR has a significantly smaller impact on the 2 b-tag event selection, since the accidental selection of an ISR jet by the Higgs boson reconstruction algorithm is less likely in events with 2 b-tagged jets. The uncertainties on the PDFs have a minor impact at the percent level. The relative changes obtained with an alternative MC generator are compatible with the discrepancy between data and prediction that is observed in the $t\bar{t}$ CR (c.f. Figs. 5.12(a) and 5.12(b)).

In addition to PDF uncertainties from alternative samples, also the intrinsic uncertainties from the nominal PDF set are considered. An ensemble of 100 PDF sets is provided by the NNPDF group to describe the intrinsic NNPDF uncertainties [10]. The bottom panel in Fig. 5.37 shows a subset of the individually predicted m_{Zh} distributions as colored lines showing individually deviations about 3%. The methodology used to combine those 100 variations to the intrinsic NNPDF uncertainty by a bin-by-bin standard deviation (std-dev) is described by Section 4.4.3. This method results in an almost flat distribution with 1%. The comparison to an alternative MMHT2014 PDF set yields a uncertainty of $< 1\%$. Therefore, the intrinsic NNPDF is conservatively used for the final statistical interpretation of data. The uncertainty on the strong coupling constant, α_S, as incorporated in the description of the NNPDF set (NNPDF α_S) is employed in addition and has only a minor impact on the m_{Zh} shape.

In the signal and control regions with the *merged* event topology the alternative MC distributions predict a smaller number of events in the low-mass tail compared to the nominal prediction, which is also compatible with the observations in data. However, the evaluated modeling uncertainties in the signal and control regions with the *merged* event topology suffer from a large statistical uncertainty due to a small number of simulated events in those regions. Furthermore, the predictions in the *merged* regions are dominated by statistical uncertainties, such that a superposition of statistically imprecisely measured modeling uncertainty would lead to a double counting of statistical uncertainties.

For other minor top quark background components, the theory uncertainties are evaluated in simulated $t\bar{t}$ processes and are then extrapolated by assuming the same relative shape difference from the nominal prediction as for the $t\bar{t}$ process.

Z+jets backgrounds Fig. 5.38 shows the m_{Zh} shape modeling uncertainties for the Z+jets backgrounds in the signal regions with the *resolved* event topology. In each of those regions, only the variation for the dominant component of the Z+jets is shown, Z+jets (bl,cl) for the 1 b-tag region and Z+jets (bb,bc,cc) for the 2 b-tag region. No significant systematic shape uncertainty is seen for the subdominant Z+jets components in each of these regions.

The largest impact on the shape of the Z+jets m_{Zh}-distributions is seen for the uncertainties from the matrix element (ME) matching and PS model. The tails of the m_{Zh} distribution are strongly affected (up to 40% relative change). A large impact is seen also for the QCD scale uncertainties, in particular from the renormalization and factorization scales, $(\mu_R, \mu_F) = (0.5, 0.5)$ and $(2.0, 2.0)$, with up to 5% relative change.

As for the top quark background, the intrinsic uncertainties of the NNPDF PDF set gives provides a more conservative uncertainty compared to the alternative PDF sets. The intrinsic NNPDF uncertainty

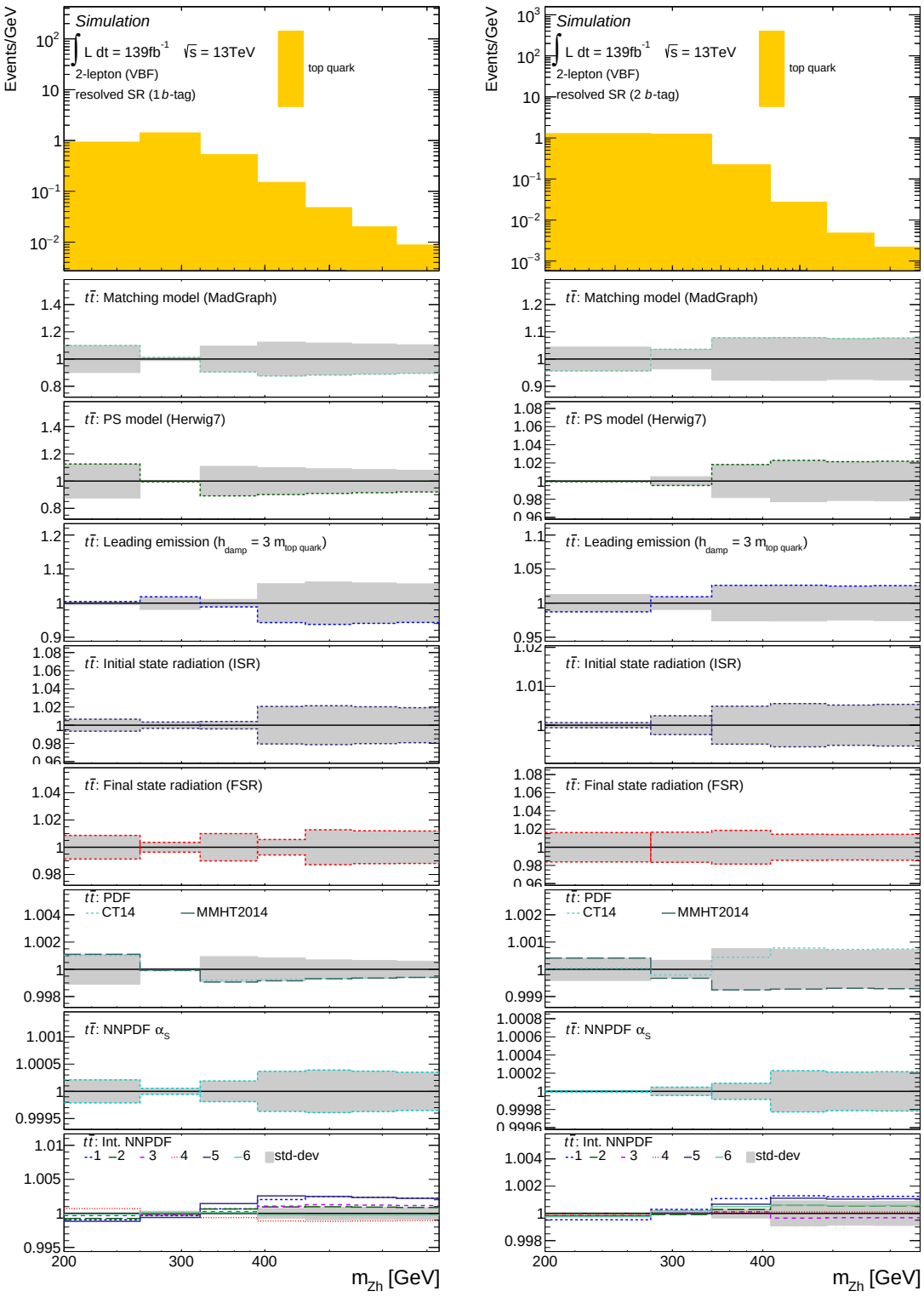

Figure 5.37: The expected nominal m_{Zh} distribution (upper panel) for the for the $t\bar{t}$ background process in the 1 b-tag (left) and 2 b-tag (right) VBF signal regions with resolved topology, as well as the relative changes of the m_{Zh} shape (lower panels) induced by different sources of theory uncertainties. The relative changes are determined assuming the same number of events in each distribution (i.e. the same normalization).

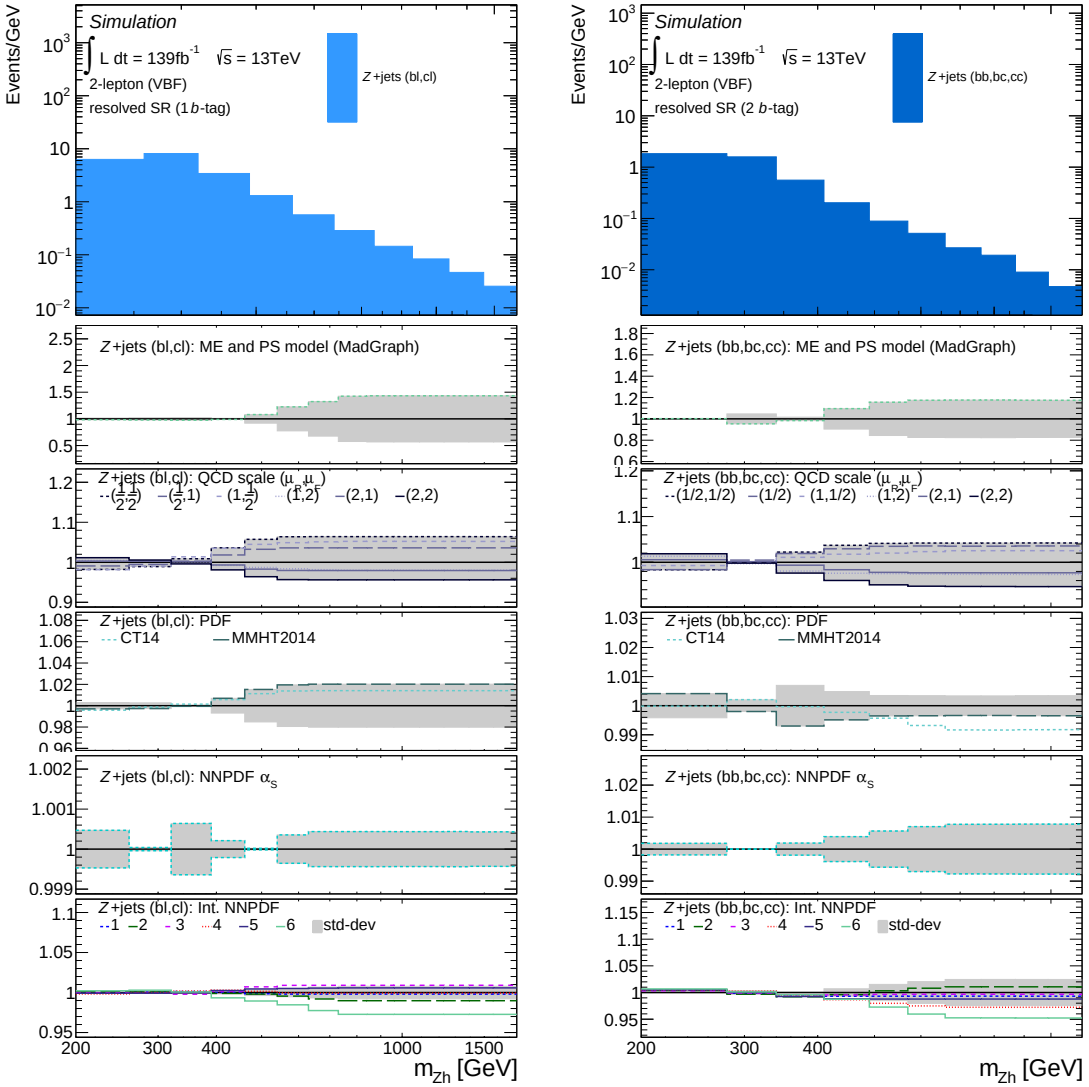

Figure 5.38: The expected nominal m_{Zh} distribution (upper panel) for the for the Z+jets (bl,cl) (left) and Z+jets (bb,bc,cc) (right) background process in the 1 b-tag (left) and 2 b-tag (right) VBF signal regions with resolved topology, as well as the relative changes of the m_{Zh} shape (lower panels) induced by different sources of theory uncertainties. The relative changes are determined assuming the same number of events in each distribution (i.e. the same normalization).

is employed in the final statistical evaluation of the data. In addition the variation of the strong coupling constant α_S incorporated in the NNPDF modeling is additionally employed. PDF uncertainties amount to less than 3% for the Z+jets background components.

Although the discussed uncertainties have a significant impact on the top quark and Z+jets normalization in the signal and control regions with the *merged* topology, no significant impact on the shape of the m_{Zh} distributions is seen. A systematic shape variation can be seen as negligible in the signal (control)

region with *merged* event topology, since the precision of the measurement in the signal (control) region is dominated by statistical uncertainties due to the low number of expected (observed) events.

Uncertainties due to migration between different signal and control regions

By leaving the normalization of the above background components as a free-floating parameter in the final fit, every correlation between the various signal and control regions is removed as well. In order to avoid these too many degrees of freedom, the relative fractions of a given background contribution in each signal and control region are taken from simulation and assigned an additional migration uncertainties based on the alternative MC samples. Such migration uncertainty parameters are introduced for each process individually to describe the migration from the CR to the SR and from the *resolved* to the *merged* regions. These uncertainties are calculated by comparing the nominal total event yields in a given SR or CR to the yield predicted by an alternative MC sample,

$$\sigma_w^{A\to B} = \sqrt{\sum_{\text{alt}} \left(\frac{\left| \frac{n_A^{\text{alt}}}{n_B^{\text{alt}}} - \frac{n_A^{\text{nom}}}{n_B^{\text{nom}}} \right|}{\frac{n_A^{\text{nom}}}{n_B^{\text{nom}}}} \right)^2}. \tag{5.2}$$

Here $n_{A(B)}^{\text{nom(alt)}}$ is the number of expected events for a given process in region $A(B)$ as predicted by the nominal (alternative) MC sample. The alternative MC samples take into account the ME matching, PS modeling, ISR and FSR, renormalization and factorization scales as well as the uncertainties from the PDF measurement. The impact of all theoretical uncertainties is summed in quadrature. The corresponding uncertainty values are listed in Table 5.4.

The large uncertainties for the migration of top quark events between the 1 and 2 b-tag regions are compatible with the difference between the observed and predicted top quark normalization in the $t\bar{t}$ CR (c.f. Fig. 5.12). Large top quark uncertainties are also obtained for the transition between corresponding regions with the *merged* and *resolved* event topology, as well as the transition between merged SRs and CRs. However, top quark background contribution in the *merged* regions is small, such that the evaluated uncertainties will only have a moderate impact on the final result.

It has to be noted that the top quark migration uncertainty between the 1 and 2 b-tag regions is not covered by the b-tagging uncertainties alone, as one would naively expect. The two *signal jets* in the 1 b-tag region with the *resolved* event topology are not always originating from the two b-hadrons, but might also originate from e.g. ISR/FSR, if the jet momentum is high enough. Therefore, the 1 b-tag event topology is more affected by the modeling uncertainties in addition to the b-tagging uncertainties or the uncertainty from the additional admixture of semi-leptonic $t\bar{t}$ events. Introducing a migration uncertainty on the ratio of events in the 1 b-tag and 2 b-tag region has therefore shown to significantly improve the fit result.

Table 5.4: Migration uncertainties for the transition of events between data regions A and B, shown separately for the dominant background processes. The migration uncertainty between regions with 1 and 2-b tag is calculated in an m_{jj}-inclusive event selection. Other migration uncertainties are calculated in a 1+2 b-tag inclusive event selection.

$A \rightarrow B$	top quark	Z+jets (bb,bc,cc)	Z+jets (bl,cl)	Z+jets (l)
1 b-tag $\rightarrow$ 2 b-tag	20.48%	6.63%	4.56%	15.63%
resolved SRs $\rightarrow$ m_{jj}-sideband CRs	6.56%	0.84%	0.91%	00.91%
resolved SRs $\rightarrow$ $t\bar{t}$ CRs	6.05%	–	–	–
resolved $\rightarrow$ merged	43%	7.60%	11.39%	18.22%
$\mathrm{SR}^{\mathrm{merg}} \rightarrow \mathrm{CR}^{merged}_{m_J}$	20%	2.51%	1.74%	10.26%

Theory uncertainties for signal processes

In contrast to background processes, for which the prediction uncertainty is calculated for n_s, the signal uncertainty is given by the uncertainty on the signal selection efficiency, ε_s, for reasons explained in Section 4.4.4. The shape of the signal m_{Zh} distribution is calculated as the uncertainty on the differential, i.e. bin-by-bin, signal selection efficiency, $\varepsilon_s(b_i)$. As a consequence a small normalization uncertainty component fully correlated to the shape uncertainty remains and is not removed.

The residual normalization and the shape uncertainties are studied for the HVT signal process produced via VBF, separately for each mass hypothesis. The uncertainties are evaluated in the signal regions, while the uncertainty on the signal contribution in the CR has been neglected, since the signal is expected to be small there.

Following the approach described in Section 4.4.4, three sources of uncertainties are considered: PS modeling uncertainties, uncertainties from the QCD renormalization and factorization scales and the PDF measurement uncertainty.

The uncertainties on the signal selection efficiency as a function of the signal mass are shown in Fig. 5.39. The uncertainties are evaluated at the particle level, and transposed to the event selection efficiency at detector level using the method described in Section 4.4.2. The average uncertainty on the signal selection efficiency is in the order of 5%. The largest uncertainty of up to 12% is caused by the PS modeling uncertainties in the *merged* signal region and in the *resolved* signal region for low resonance masses ($\lesssim$ 500GeV). The impact of the three intrinsic eigenvector variations for the A14 Pythia shower tune (Var1,Var2 and Var3c, c.f. Table 4.7) is studied as recommended in Ref .[117]. All three of these uncorrelated components of the variation components have a significant impact on the normalization and the shape of the differential signal selection efficiency. The leading contribution to the intrinsic PS uncertainties is induced by the Var2 component, describing the shape of ISR and FSR jets. Since the 3 components are designed fully uncorrelated, they need to be treated as three individual components in the statistical interpretation of data.

However, the comparison to alternative PS models[3] provides a more conservative uncertainty than the

[3] The nominal PS is described by the *Lund* (or *string*) *model*, which is compared to the *cluster model* used in the alternative Herwig PS generator.

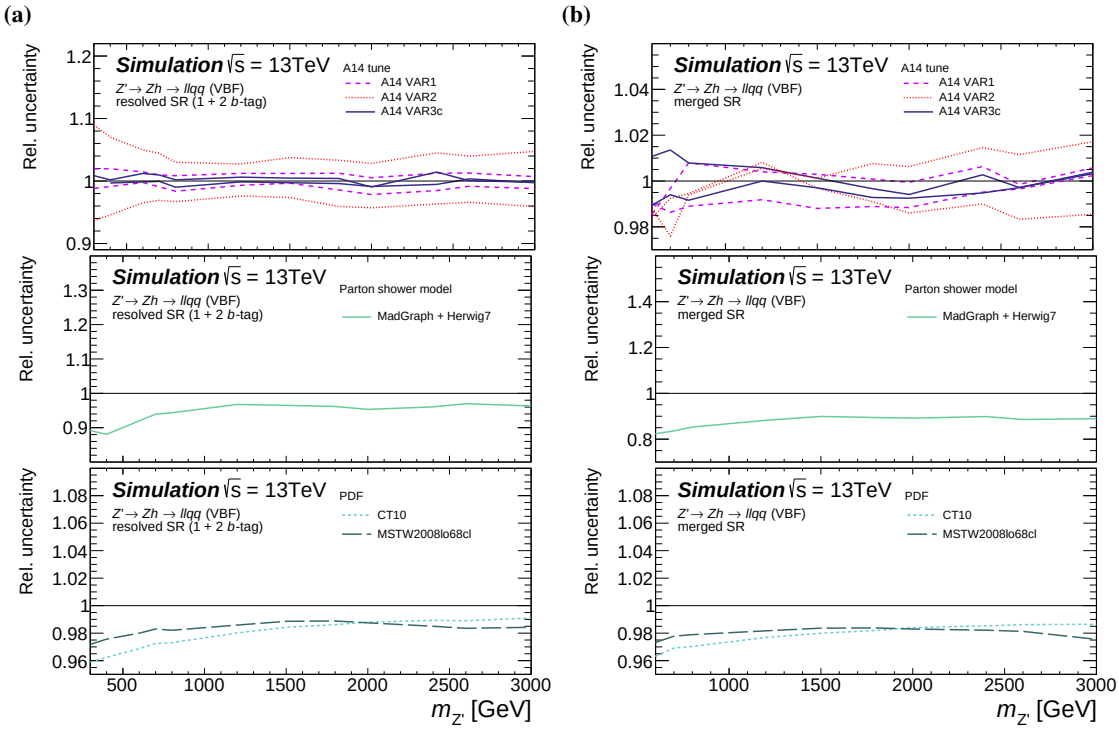

Figure 5.39: The relative uncertainty on the signal selection efficiency with respect to the nominal prediction (at particle generator level) as function of the Z' mass is shown for (a) the *resolved* and (b) the *merged* SRs. The 1 b-tag and 2 b-tag *resolved* SRs are combined together. The various ratio panels show the impact of the different uncertainty sources.

intrinsic Pythia PS variations and is therefore employed instead for the final statistical interpretation of the data, presented in Section 5.5.

The impact of the above sources of uncertainties on the shape of the m_{Zh} signal distribution is estimated for each resonance mass hypotheses separately in each of the three signal regions. As an example, the impact of the theory uncertainties on the VBF HVT $Z' \to \ell^+\ell^- b\bar{b}$ signals with a Z' mass of 500 GeV and 1 TeV in the *resolved* signal region is shown in Fig. 5.40. The 1 b-tag and 2 b-tag signal regions are combined together. The corresponding distributions for the separate 1 b-tag and the 2 b-tag signal regions are shown in Appendix D.2. Similarly, Fig. 5.41 shows the impact on the signal m_{Zh} distribution with a Z' mass of 1 TeV and 1.6 TeV in the region with the *merged* event topology.

PDF uncertainties, estimated by comparing the nominal to alternative sets of PDFs, do not affect the shape of the signal distribution. In contrast, the width of the signal m_{Zh} distribution is modified when using the alternative PS models. The resonance width modeled by the Herwig generator is 20 – 40% narrower (depending on the signal mass) than the nominal one from Pythia. However, the ratio plot also shows that there is almost no deviation at the resonance peak. Differences in the m_{Zh} tails are expected to have a negligible impact on the final result, since the signal contribution is expected to be small compared to the background. Similar behavior is also observed for other resonance masses.

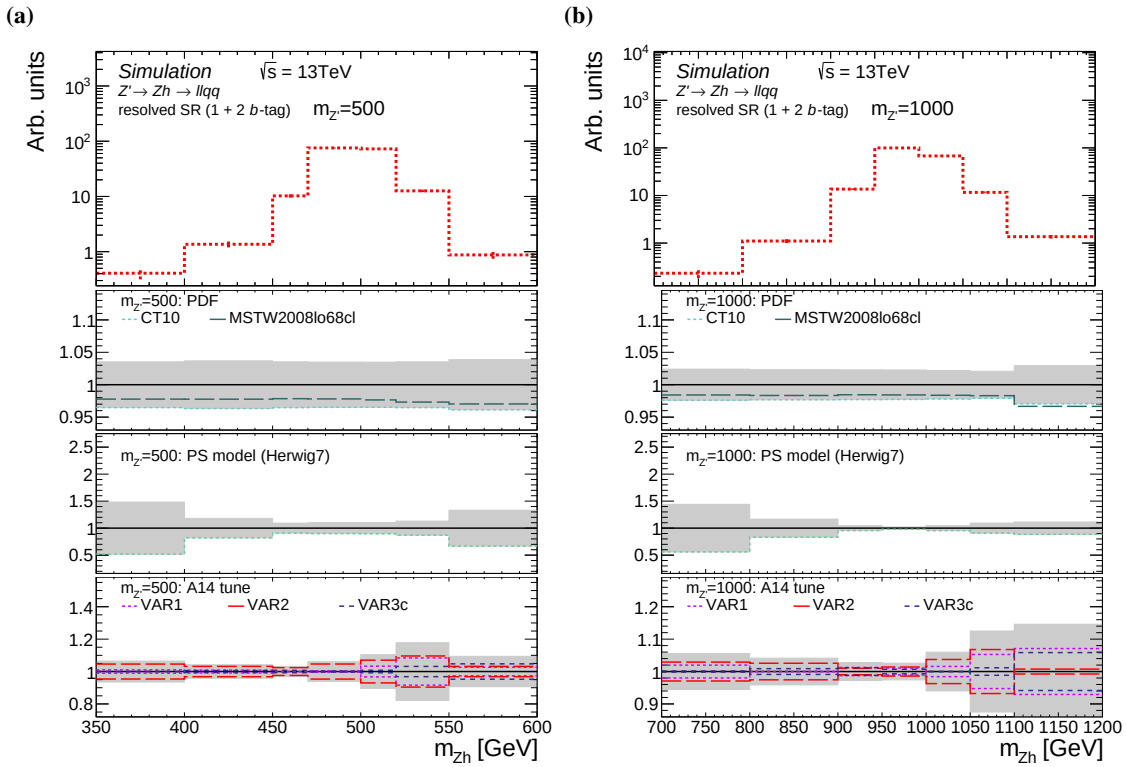

Figure 5.40: The expected nominal signal m_{Zh} distribution (differential efficiency, upper panels) in the *resolved* VBF signal regions for the HVT model C signal with a mass of (a) 500 GeV and (b) 1 TeV. The lower ratio panels show the relative changes in the differential efficiency, $\Delta\varepsilon_s(b_i)$, due to a given source of modeling uncertainty.

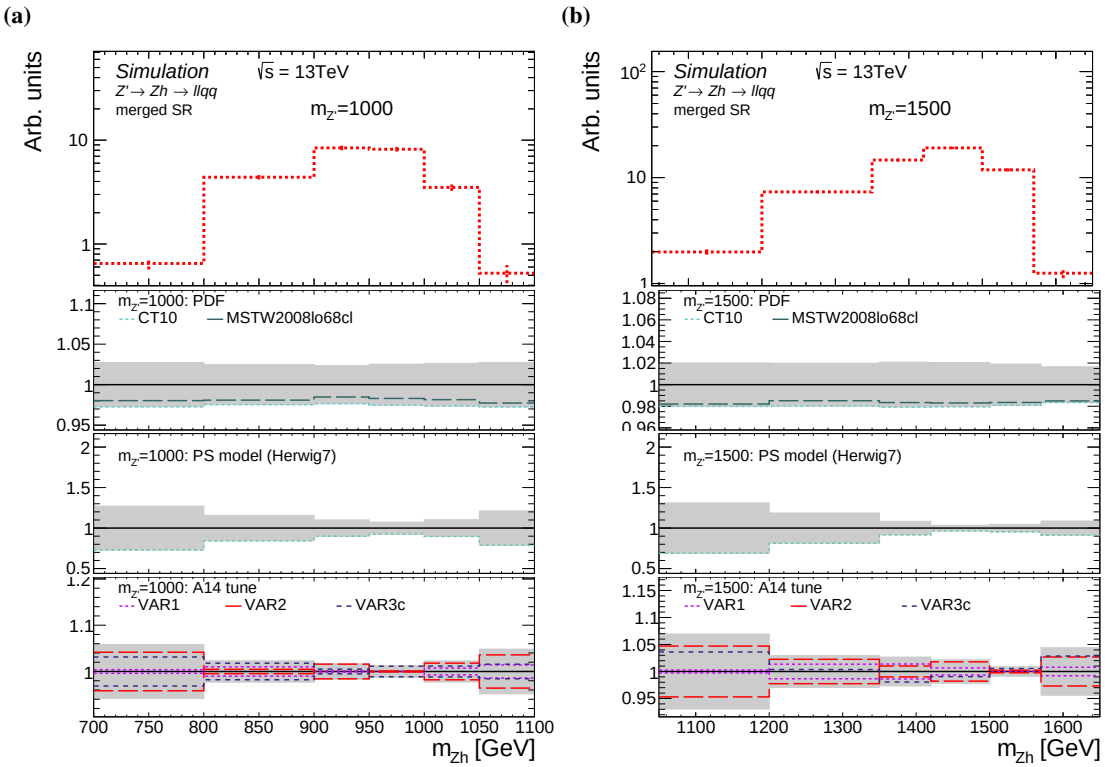

Figure 5.41: The expected nominal signal m_{Zh} distribution (differential efficiency, upper panels) in the *merged* VBF signal regions for the HVT model C signal with a mass of (a) 1 TeV and (b) 1.5 TeV. The lower ratio panels show the relative changes in the differential efficiency, $\Delta\varepsilon_s(b_i)$, due to a given source of modeling uncertainty.

5.4 Fit model for the statistical interpretation of data

In this section, the fit model for the statistical interpretation of the observed and the predicted data is described, relying on the statistical methods introduced in Section 4.5.

The reconstructed diboson mass, m_{Zh}, is used as the final discriminant in the fit. The statistical interpretation is performed via a binned maximum likelihood fit of the expected to the observed data, simultaneously in the three signal regions (*resolved* 1 b-tag and 2 b-tag regions and the *merged* region) as well as in the control regions (1 b-tag and 2 b-tag *resolved* m_{jj}-sideband CRs, 1 b-tag and 2 b-tag *resolved* $t\bar{t}$ CRs and *merged* m_J-sideband CR). The m_{Zh} distribution is stored in histograms with a variable bin width chosen such to have a statistical uncertainty on the total background below 25% and a minimum of 0.5 predicted events in each bin. Furthermore, the bin width is required to be larger than the width of the resonance mass, which is approximated by $\Delta m = 30\ \text{GeV} + m_{Zh}[\text{GeV}]/10$. Starting at high m_{Zh} mass values, each bin range is determined iteratively by lowering the lower boundary of each bin by 10 GeV until the above requirements are met. The resulting bin boundaries are given in Table 5.5.

The statistical model for the search for a Zh resonance produced via VBF is based on the likelihood function in Eq. (4.10). Apart from the signal strength parameter, μ (*parameter of interest* (POI)), there is also a large number of so-called NPs, θ_i, accounting for statistical and systematic uncertainties.

One set of NPs covers the statistical uncertainty of the MC prediction in each histogram bin. These NPs are assumed to follow a Poisson distribution around the true value, with the standard deviation, σ, equal to the statistical uncertainty of MC in the bin.

Additionally, for each background process there is one *nuissance parameter* (NP) introduced for the corresponding background normalization. These NPs can be regarded as additional scale factors multiplying the pre-fit prediction. For the main backgrounds (top quark, Z+jets (bb,bc,cc) and Z+jets (bl,cl)), the properties of the fitted CRs allow to constrain the normalization directly from data. The corresponding NPs are therefore left unconstrained (free-floating) in the fit. The normalization of the top quark background is primarily driven by the $t\bar{t}$ CR while the Z+jets (bl,cl) and Z+jets (bb,bc,cc) components are predominantly constrained by the fit in the 1 and 2 b-tag m_{jj}-sideband CRs, respectively. The normalization of minor background processes, i.e. VV and Vh diboson processes as well as the

Table 5.5: Bin boundaries of the signal and control regions used in the final statistical interpretation of the data.

Region	Histogram bin borders [GeV]
resolved 1 b-tag SR	200,260,320,390,460,540,630,730,840,960,1090,1230,1390,1570,1760,1970,2200,2500,2930,6000
resolved 2 b-tag SR	200,280,340,410,490,570,660,760,870,990,1130,1280,1440,1620,1820,6000
merged SR	190,300,500,700,1000,1200,1400,1600,2000,3000,6000
resolved 1 b-tag $t\bar{t}$ CR	180,260,320,390,470,550,640,740,850,970,6000
resolved 1 b-tag m_{jj}-sideband CR	140,290,350,420,500,590,690,800,920,1050,1190,1340,1510,1700,1910,2140,6000
resolved 2 b-tag $t\bar{t}$ CR	180,290,350,420,500,590,680,800,6000
resolved 2 b-tag m_{jj}-sideband CR	140,280,340,410,490,570,660,760,870,990,1130,1280,1440,2030,6000
merged m_J-sideband CR	160,300,500,700,1000,1200,1400,1600,2000,3000,6000

Table 5.6: Overview of the nuisance parameters (NP) employed in the maximum likelihood fit

Parameter	**Prior uncertainty**	**Comment**
Global top quark normalization	unconstrained	
Global Z+jets (bb,bc,cc) normalization	unconstrained	
Global Z+jets (bl,cl) normalization	unconstrained	
Global Z+jets (l) normalization	50%	
Global VV normalization	50%	
Global Vh(SM) normalization	50%	
Migration uncertainties	c.f. Table 5.4	applied to individual CR
Experimental uncertainties	75 NPs for shape + normalization	from subsidiary measurements (c.f. Section 5.3.1)
Background modeling uncertainties	18 NP for shape-only	from MC-to-MC comparisons (c.f. Section 5.3.2)
Signal modeling uncertainties	2 NP for shape + normalization	from MC-to-MC comparisons (c.f. Section 5.3.2)
CR motivated empirical uncertainties		
large-R jet p_{T}^{J} correction	0.5 if $p_T^J < 400$GeV	Z+jets all *merged* regions c.f. Section 5.2
VBF jet $p_{\mathrm{T}}^{\mathrm{VBF,j}}$ correction	c.f. Table 5.2	Z+jets (bb,bc,cc), Z+jets (bl,cl), top quark all *resolved* regions c.f. Section 5.2
Stat. NP, $\gamma_{r,i}$	MC statistical uncertainty	bin-wise

Z+jets (l) component, is constrained by the theory prediction and is assigned a log-normal constrained NP centered around the nominal MC prediction. Conservative uncertainty of 50% is assigned to each of the NPs describing the normalization of one of those minor backgrounds.

One NP is also introduced for each systematic shape uncertainty described in Section 5.3, as parameterized via Eq. (4.11). Shape uncertainties smaller than 0.5% in all m_{Zh} bins within a particular signal or control region are neglected in this region and the corresponding NP is removed from the parametrization of this region (the so-called pruning of the NPs).

Modeling uncertainties discussed in Section 5.3.2 are related to individual background processes. While the normalization of each signal and background process is treated separately, the modeling uncertainties affect the shape of the m_{Zh} distributions and the migration of events from one region to another. The latter uncertainty is implemented by introducing an additional NP acting only on one of the both involved regions. Such NP is log-normal constrained with an uncertainty determined from comparisons of nominal and alternative MC samples using Eq. (5.2).

The non-closure uncertainties introduced in Section 5.2 are accounting for the differences between predicted and observed in the $p_{\mathrm{T}}^{\mathrm{VBF,j}}$ and p_{T}^{J} distributions in the control regions. An overview of all NPs used in the fits is given in Table 5.6.

The fits are performed in two different setups: In the first setup, only the signal-depleted control regions are fitted, i.e. the $m_{jj/J}$-sideband CRs and the $t\bar{t}$ CRs. The impact of the signal contribution is assumed to be negligible in these regions. Therefore, the SM background-only MC prediction is fitted to the recorded data. This background-only CR fit is a conditional fit with the signal strength set to $\mu = 0$. This *CR-only fit* has been used to validate the background description as elaborated in Section 5.5.1.

In the second setup, several fits are performed employing both, the signal and the control regions.

One of these fit scenarios includes only the merged data regions, the second one the regions with the *resolved* topology only and the third involves both the resolved and the merged regions simultaneously. In all three cases, the SRs and CRs are fitted simultaneously. In each of the three scenarios, three different fits are performed. First an unconditional maximum likelihood (ML) fit is performed providing the maximum likelihood estimator (MLE) for NPs ($\hat{\theta}$) and the signal strength ($\hat{\mu}$). Second, the background-only fit with $\mu = 0$ represents the null-hypothesis, H_0 for the statistical test of a discovery (Eq. (4.13)), with the alternative hypothesis, H_1, given by the first (unconditional) fit. Third, in the context of exclusion limits, the signal-plus-background fit is performed with varying values of μ. This signal-plus-background hypothesis, H_{SB} is compared to the H_1 hypothesis of the unconditional fit to extract the upper limits on the signal strength, μ, using the test statistic given in Eq. (4.17)

The final results are obtained from the third fit scenario of the second setup, i.e. from a simultaneous fit of all resolved and merged SRs and CRs. The results are presented in Section 5.5.2. In case of the signal-plus-background hypothesis, the signal contribution is normalized to the prediction of the HVT model C. Since the described analysis is still blinded within the ATLAS collaboration, i.e. no recorded data are yet revealed in the SRs, only the expected search sensitivity will be presented in the following. For this purpose, the recorded data are replaced by the so-called pseudo-data given by the simulated MC samples.

5.5 Results

In this section, the results of the fits in the two introduced setups are presented. The background-only fit to the recorded data in the CRs alone is presented in Section 5.5.1 and is used to validate the background modeling. The results of the background-only, signal-plus-background and unconditional fits in the second setup involving both the SRs and the CRs are presented in Section 5.5.2. These fits are performed with pseudo-data and are used to evaluate the sensitivity of the search for Zh resonances produced via VBF in the framework of the HVT model C.

5.5.1 Background validation in control regions

Before looking into the signal regions, a background-only fit (conditional fit with $\mu = 0$) is performed simultaneously to the data in all CRs in order to validate the background modeling. Since the SRs are not included in the fit, there is no bias introduced on the signal sensitivity. In this *CR-only fit*, the following five CRs are fitted simultaneously: 1 and 2 b-tag *resolved* m_{jj}-sideband CRs, 1 and 2 b-tag *resolved* $t\bar{t}$ CRs and the *merged* m_J-sideband CR. The merged region suffers from low statistical power and the mismodeling uncertainties at resonance masses below 800 GeV, as elaborated in Section 5.2.1. However, since the *merged* signal regions will be driving the signal sensitivity beyond resonance masses of 1.2 TeV in the second fit setup the *merged* m_J-sideband CR is included in the final and in the *CR-only fit*. The *merged* $t\bar{t}$ CR is not included in the fit due to the low statistical power.

All nuisance parameters and their a priori uncertainty used in the *CR-only fit* are equivalent to those used in the inclusive fit of all SRs and CRs, as listed in Table 5.6, except for the NP controlling the migration between SR and CR, which are not included since no SRs are fitted. Another NP is introduced here instead to decorrelate the m_{jj}-sideband CR from the $t\bar{t}$ CR using a region specific normalization scale factor (SF) in the $t\bar{t}$ CR. The prior uncertainty on this scale factor is assumed to be the same as the migration uncertainty from the SR to the $t\bar{t}$ CR.

The normalizations of each background component obtained from the *CR-only fit* are summarized in Table 5.7, relative to the nominal MC prediction. The largest deviation from unity of about 13% is obtained for the normalization of the Z+jets (bb,bc,cc) component. The normalization of the Z+jets (l) background is 2%, which is compatible with the independent observations made in the 0 b-tag validation region (see Fig. 5.23). The down-scaled contribution of top quark backgrounds in the *merged* compared to the *resolved* regions (migration SF of 0.89) is compatible with the independent observations in the *merged* $t\bar{t}$ CR, which is not included in the fit. Here, 6 events have been predicted while only 2 are observed. The large post-fit uncertainty of 50% on this top quark background migration SF is tolerable since top quark backgrounds only have a minor contribution of less than 5% to the total number of events in the regions with the *merged* topology. In general, all normalization scale factors are compatible within uncertainties with the pre-fit MC predictions.

The pulls, $\mathcal{P}$, described by Eq. (4.21), are evaluated for each constrained NP in the *CR-only fit* to assert the validity of the fit. Fig. 5.42 shows the pulls for a selection of NPs whose best-fit value differs by more than 25% from the pre-fit value, relative to the corresponding pre-fit uncertainty. A complete summary of all of pulls can be found in Appendix D.3.

Table 5.7: Summary of background normalization and migration SFs and resulting from a CR-only maximum likelihood fit. Unconstrained NP are distributed around 1 and are directly interpreted as the normalization SF. For the log-normally constrained NPs, the pulls $\mathcal{P}$ (c.f. Eq. (4.21)) with respect to the a priori uncertainty are given as well.

Sample	**Normalization** SF	**Pull** $\mathcal{P}$	
top quark	$+1.02 \pm 0.11$	*(floating)*	
Z+jets (bb,bc,cc)	$+1.13 \pm 0.16$	*(floating)*	
Z+jets (bl,cl)	$+0.99 \pm 0.19$	*(floating)*	
$Vh(SM)$	1.00 ± 0.50	$+0.00 \pm 0.99$	
VV	1.02 ± 0.49	$+0.04 \pm 0.98$	
Z+jets (l)	1.02 ± 0.48	$+0.03 \pm 0.96$	
Migration SF			
top quark migration (1 b-tag $\rightarrow$ 2 b-tag)	1.18 ± 0.08	$+0.54 \pm 0.39$	(1 b-tag regions)
top quark migration ($CR^{m_{jj}}_{res} \rightarrow CR_{e-\mu}$)	0.95 ± 0.06	-0.07 ± 0.95	(*resolved* m_{jj}-CRs)
top quark migration (res $\rightarrow$ merg)	0.89 ± 0.40	-0.25 ± 0.93	(*merged* regions)
Z+jets (bb,bc,cc) migration (res $\rightarrow$ merg)	1.00 ± 0.08	-0.03 ± 0.99	(*merged* regions)
Z+jets (bl,cl) migration (res $\rightarrow$ merg)	1.00 ± 0.11	$+0.01 \pm 0.98$	(*merged* regions)
Z+jets (l) migration (res $\rightarrow$ merg)	0.99 ± 0.07	-0.04 ± 0.99	(*merged* regions)

The largest observed pull of 0.87 ± 0.33 is related to the p_{T}^{J}-dependent reweighting in the *merged* control region, described in Section 5.2.1 The reweighting correction is based on the observed differences in prediction and observation in the m_{jj}-sideband CRs. Since the described fit only includes the CRs, the corresponding NPs is pulled by about 1σ *by design*. The reweighting correction prevents the non-physical pulls of other NPs, while fitting the *merged* region. Similarly, the uncertainty on the fraction of semi-leptonic $t\bar{t}$ decays ("$t\bar{t}$ semi-lep. admixture") is motivated by observations made in several observables in the control regions and the same-sign validation region (c.f. Section 5.2). The NP describing the uncertainty on the admixture of semi-leptonic $t\bar{t}$ events is strongly pulled to a value of 0.63 ± 0.68. The pull value is interpreted as a 63% increase in the predicted contribution of semi-leptonically decaying $t\bar{t}$ events. This is consistent with independent observations seen in the same-sign validation region (c.f. Fig. 5.9). Other pull values which are larger than 25% are obtained for NPs of experimental nature, mainly the JES and JER of the small-R jets.

The uncertainties described in Section 5.3 are conservative estimates for the uncertainties on various NPs, totaling to up to a 50% uncertainty relative to the nominal total background prediction. The individual pre-fit uncertainties can be *constrained* by the fit to the data in the control regions. The constrained post-fit NP uncertainties are extracted from the diagonal elements of the NP covariance matrix of the fit, as described in Section 4.5.3. A NP can be constrained if the a priori uncertainty in a certain region of phase space is large compared to the statistical precision in data. For the validity of the fit, it is crucial that the NP constraints are not induced by statistical fluctuations. Therefore, every large constraint is investigated. The post-fit uncertainty of the most constrained NPs (Fig. 5.42) agree with the corresponding pre-fit uncertainty estimate within 20%. An exception is the uncertainty in the CR-based p_{T}^{J}-reweighting which is expected to be constrained by design.

The post-fit correlation between the different NPs is shown in Fig. 5.43 for all NPs with at least one

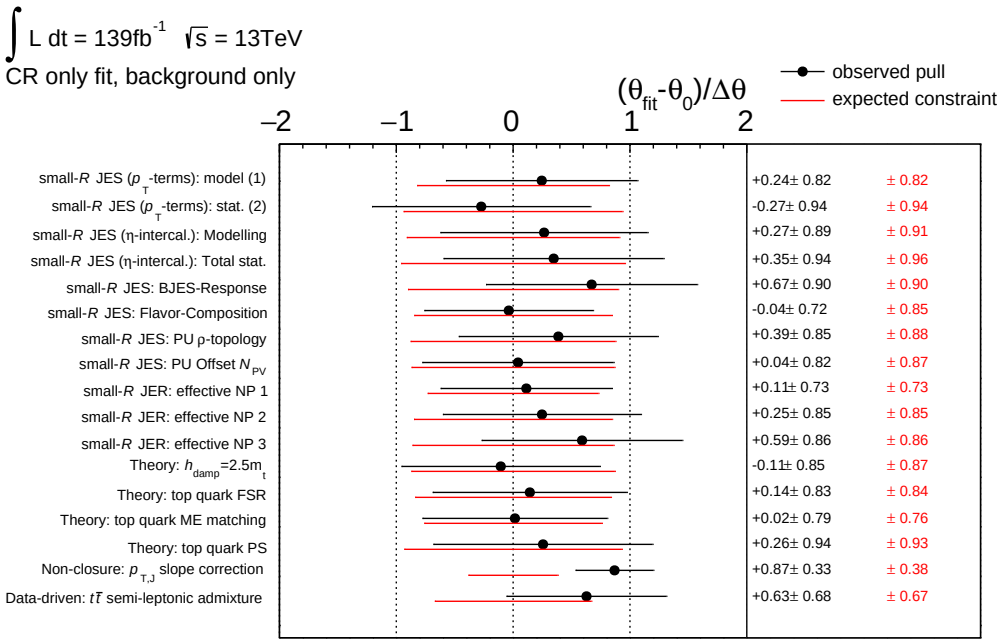

Figure 5.42: The observed (black) pulls for a selected set of NPs as obtained from a *CR-only fit* using the background-only hypothesis. The expected pulls (red) are by definition equal the nominal value. The expected constraint can be derived by using pseudo-data. All NPs with a pull larger than 0.25 or a post-fit uncertainty deviating by more than 20% from the pre-fit uncertainty are shown.

Table 5.8: Observed and expected post-fit event yields obtained from the *CR-only fit* for an integrated luminosity of 139 fb^{-1}. The reported uncertainties include both the statistical and systematic post-fit uncertainties.

Process	**merged m_J-sideband CR**	**1 b-tag *resolved* m_{jj}-sideband CR**	**1 b-tag *resolved* $t\bar{t}$ CR**	**2 b-tag *resolved* m_{jj}-sideband CR**	**2 b-tag *resolved* $t\bar{t}$ CR**
Z+jets (bb,bc,cc)	8.66 ± 0.83	594.64 ± 31.28	0.09 ± 0.01	676.54 ± 24.04	0.05 ± 0.01
Z+jets (bl,cl)	24.80 ± 2.29	2621.79 ± 78.90	0.41 ± 0.03	25.49 ± 2.75	—
Z+jets (l)	9.60 ± 1.91	263.04 ± 74.32	—	0.06 ± 0.06	—
top quark	1.32 ± 0.48	403.03 ± 20.96	500.46 ± 16.43	371.12 ± 17.69	456.37 ± 15.10
VV	1.77 ± 0.35	70.42 ± 15.29	0.04 ± 0.02	16.80 ± 3.70	—
Vh (SM)	0.07 ± 0.02	3.29 ± 0.80	—	1.56 ± 0.40	—
Expected SM background	46.22 ± 3.16	3956.21 ± 115.76	501.00 ± 16.43	1091.57 ± 30.20	456.42 ± 15.10
Observed	42	3958	498	1092	450

correlation coefficient larger than 0.4. These correlations lead to a total uncertainty that is smaller than the quadratic sum of all individual components. However, the relatively strong correlation between the normalization parameters prevents the fit from constraining the normalization nuisance parameters of the background components individually. The total number of expected (post-fit) and observed background events in each control region is given in Table 5.8.

The comparison of the observed and expected (post-fit) m_{Zh} distributions is shown in Fig. 5.44. The prediction matches the observation within the given post-fit uncertainties and thus validates the

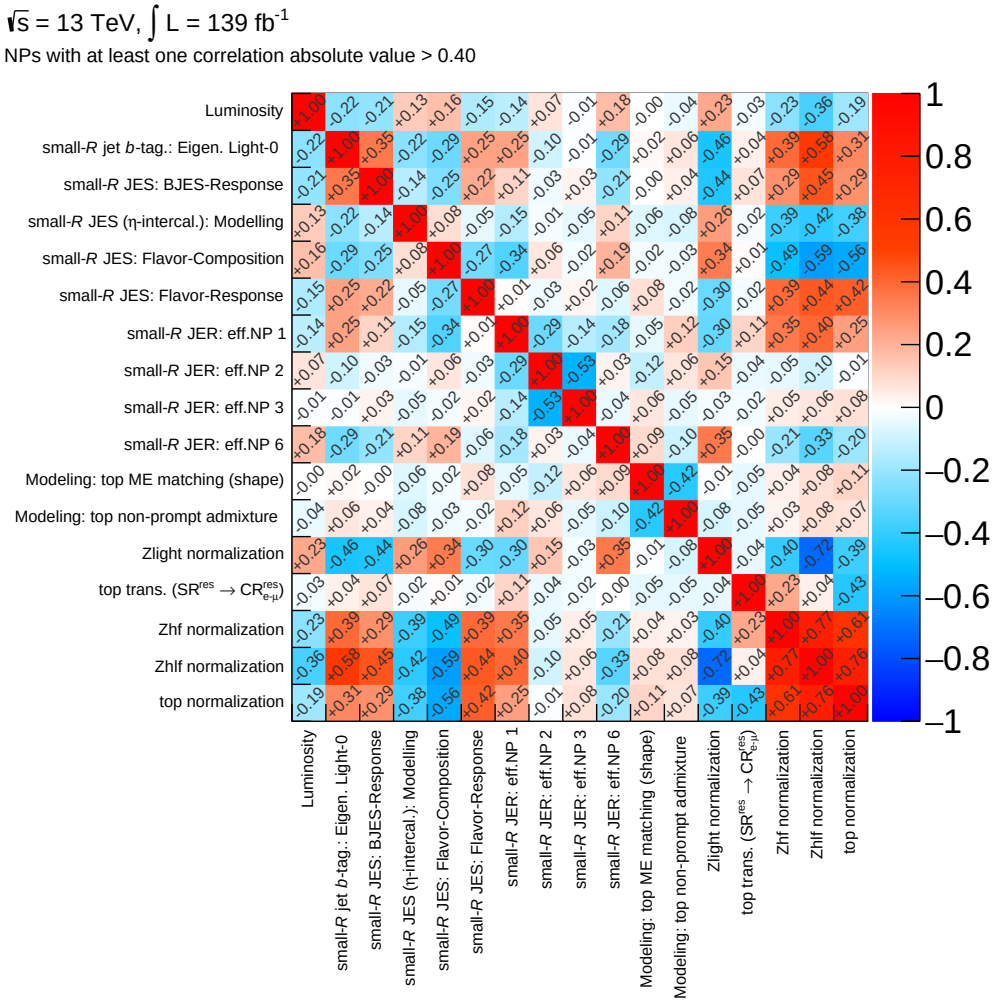

Figure 5.43: The correlation matrix for the NPs in a *CR-only fit*. Only the NPs with at least one correlation coefficient with an absolute value above 0.4 are shown.

Table 5.9: The expected post-fit event yields in the signal regions of the VBF Zh resonance search for an integrates luminosity of 139 fb^{-1}. All signal and control regions are fitted simultaneously. The quoted uncertainties indicate both the statistical and the post-fit systematic uncertainties. The uncertainties for the individual background predictions are larger than the total background uncertainty due to correlations between the normalization nuisance parameters in the fit.

Process	*merged* SR	1 *b*-tag *resolved* SR	2 *b*-tag *resolved* SR
Z+jets (bb,bc,cc)	12.31 ± 1.01	277.82 ± 13.44	316.03 ± 12.06
Z+jets (bl,cl)	42.45 ± 2.69	1304.86 ± 38.84	12.15 ± 1.69
Z+jets (l)	12.77 ± 1.34	159.13 ± 32.55	0.14 ± 0.08
top quark	4.80 ± 4.44	207.40 ± 12.85	200.34 ± 7.24
VV	4.24 ± 0.69	29.60 ± 4.88	6.59 ± 1.12
Vh (SM)	0.09 ± 0.05	1.50 ± 0.64	2.37 ± 0.97
Total expected background	76.65 ± 5.50	1980.31 ± 54.20	537.62 ± 14.25

background modeling.

5.5.2 Sensitivity of the VBF Zh resonance search

The data in the signal regions are still blinded, i.e. no recorded data in these regions can be studied. Before the unblinding, the search sensitivity, i.e. the expected upper limit on the signal production cross section and the discovery potential, can be evaluated using the pseudo-data represented by the simulated signal and background MC samples.

For this purpose, a fit is performed to pseudo-data in all signal and control regions. To evaluate the discovery potential, a conditional background-only fit ($\mu = 0$) is performed. The expected post-fit number of background events and the corresponding uncertainties for each SR are shown in Table 5.9.

Following the approach described in Section 4.5.4, the impact of the various NPs on the signal strength parameter μ is studied using the pseudo-data.

The 20 NPs with the largest impact on $\hat{\mu}$, ranked in descending order, are shown for the two signal mass hypotheses, $m_{Z'} = 300$ and $m_{Z'} = 1800$, in Figs. 5.45 and 5.46, respectively. The former (latter) mass hypothesis is typical for the signal events with the *resolved* (*merged*) event topology. In each plot, the (trivial) pulls and their corresponding 1σ post-fit constraints are overlayed on top of the impact on the signal strength $\Delta\hat{\mu}$ (c.f. Eq. (4.23)). The pull values are zero by definition for the fit to the expected pseudo-data. The exception are the pulls for the free-floating normalization parameters which are by design set to 1. The post-fit 1σ constraints on the pulls are below 1, i.e. lower than the pre-fit value, indicating that the SR and CR information sets further constraints on the NPs. As a consequence the impact due to such NPs is expected decrease w.r.t. the pre-fit impact by the SR and CR information. Additional NP ranking plots for other signal mass hypotheses can be found in Appendix D.4.

The largest impact on a signal with a mass $m_{Z'} = 300$ GeV, shown in Fig. 5.45, is caused by the uncertainty on the normalization of the Z+jets (bb,bc,cc) background. This is the dominant background

Table 5.10: The expected p_0-values and the corresponding expected signal discovery significance for an HVT $Z' \to Zh \to \ell^+\ell^- b\bar{b}$ signal produced via VBF with Z' masses of 300, 400, 500 and 600 GeVassuming production cross sections as predicted by the HVT model C. The results are obtained for an integrated luminosity of 139 fb^{-1}.

$m_{Z'}$	Expected p_0-value	Expected signal significance
300 GeV	0.022	2.01σ
400 GeV	0.093	1.32σ
500 GeV	0.178	0.92σ
600 GeV	0.246	0.68σ

component in the most sensitive 2 *b*-tag *resolved* signal region. The impact of Z+jets (bb,bc,cc) and top quark background modeling uncertainties estimated in Section 5.3.2 is highly ranked. The relevance of top quark related uncertainties reduces with the increasing signal mass, consistent with the decreasing fraction of this background at high m_{Zh} values.

At high signal masses ($\gtrsim$ 1.2 TeV) the *merged* signal region is the most sensitive one. The signal strength for a signal mass above 1.2 TeV is affected on the one hand by the uncertainty of the muon momentum resolution, since the muons from highly boosted Z decays traverse the muon spectrometer with low deflection, i.e. with a small *sagitta* value. On the other hand, uncertainties on the energy scale of large-R jets also become a very limiting systematic uncertainty. Furthermore, the p_{T}^{J}-reweighting uncertainty due to the mismodeling of low-p_{T} Higgs boson candidates (see Section 5.2.1) has also a large impact on the signal strength. In contrast to the low-mass signal hypotheses, the uncertainties on the normalization of the Z+jets (l) background component and on the misidentification rate of light-quark induced track jets become more important than the uncertainty of the Z+jets (bb,bc,cc) background normalization.

The expected signal significances for different signal mass hypotheses within the HVT model C are summarized in Table 5.10, together with the corresponding local p_0-values. The assumed signal cross sections correspond to the HVT model C predictions. With the currently collected 139 fb^{-1} of Run 2 data, a hypothetical fermiophobic Z' boson with a mass below 500 GeV would cause an excess of events above a SM prediction with a signal significance of more than 1σ. The sensitivity to Z' bosons with higher masses decreases below the 1σ level within the HVT model C. However, independently of the theory model this analysis can be used to set upper limits on the cross section for the VBF $X \to Zh$ resonance production.

Following the methodology described in Section 4.5.2, maximum likelihood fits of the signal-plus-background hypothesis to the background-only pseudo-data yield an expected upper limit on the production cross section at a given confidence level . The corresponding exclusion limits at 95% CL are shown in Fig. 5.47(a) in dependence on the Z' resonance mass. For comparison, the exclusion obtained from the fit of the *resolved* regions only is also shown. Although the *merged* region is statistically limited, the inclusion of this region in the fit significantly improves the upper limit on the cross section for resonance masses above 1 TeV by up to a factor of 3.1 at $m_{Z'}$ = 3 TeV.

The described final state is probed for the first time by ATLAS in this thesis. The same final state has been also probed by CMS [152], in search for resonance masses above 800 GeV. The CMS search is

performed in the *merged* event topology regime only. The CMS results are indicated by a dotted line in Fig. 5.47(b) and compared to the results of this thesis' work. At high masses ($m_{Z'} > 1$ TeV) the CMS exclusion limits are significantly better, because CMS includes the 0-lepton ($Z \rightarrow \nu\bar{\nu}$) decay channel in the search, in addition to the 2-lepton channel. Similarly as in the case of the *parent analysis* in Chapter 4, the 0-lepton channel provides a higher sensitivity for large resonance masses which leads to highly boosted Z and Higgs bosons. No Z' boson mass value within the HVT model C is expected to be excluded by this analysis. However, with additional data from Run 3, it may become possible to exclude the lower Z' mass range.

The sensitivity of the analysis in the 2-lepton channel decreases for boosted and therefore collimated lepton pairs. For resonance masses below 1 TeV, the presented ATLAS analysis in the 2-lepton channel is able to set the yet strongest limits on the VBF production of Zh resonances. The red line indicates the corresponding predicted cross section by the HVT model C $Z' \rightarrow Zh$ signal as a function of the Z' mass.

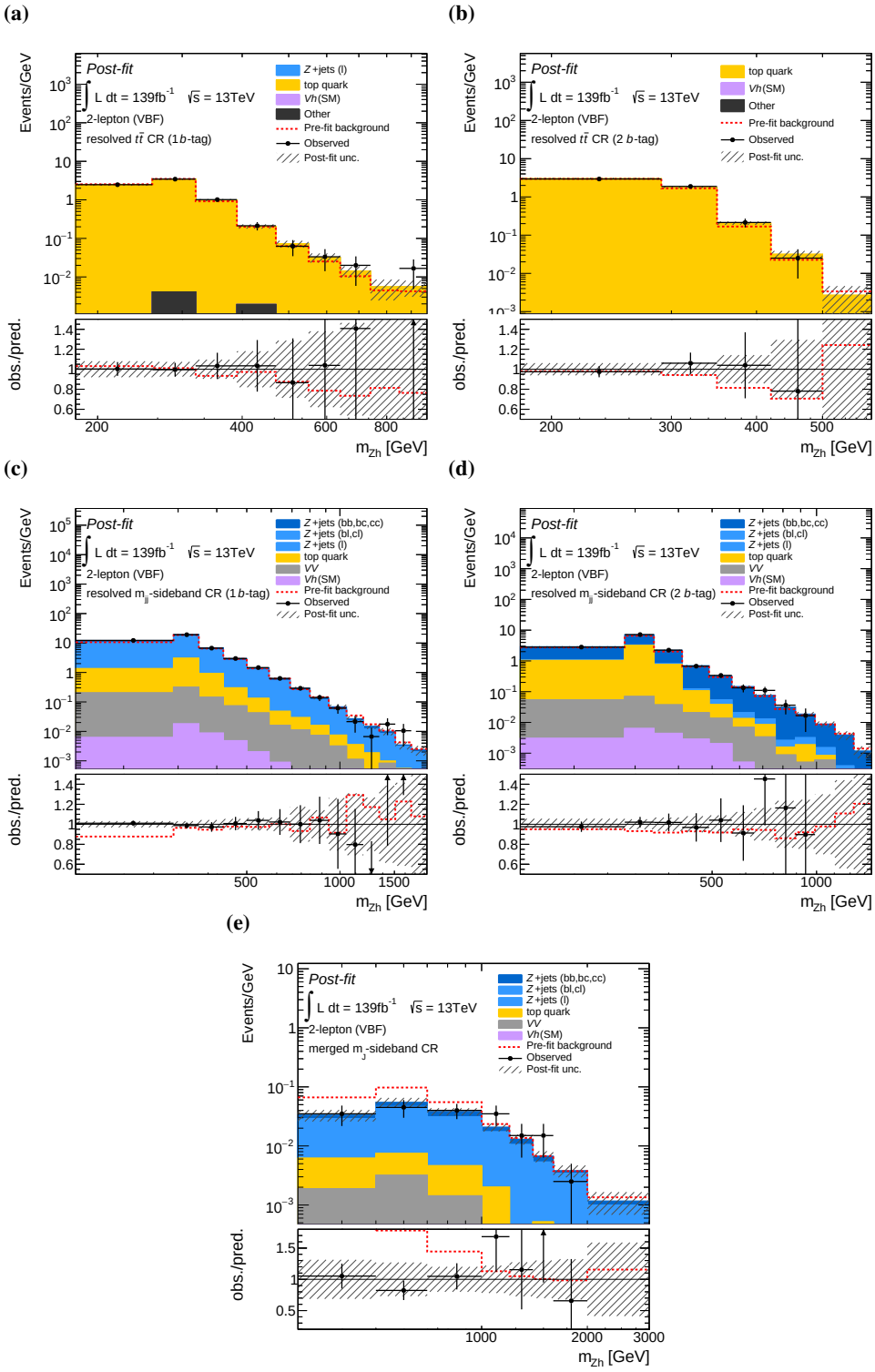

Figure 5.44: The observed and the expected post-fit m_{Zh} distributions in each of the fitted CRs in the *CR-only fit* for the Zh resonance search produced via the VBF. The lower panels show the ratio of the observed data and the total expected background, with the uncertainty bands corresponding to the total post-fit uncertainty. The red line indicates the distribution of the pre-fit background sum.

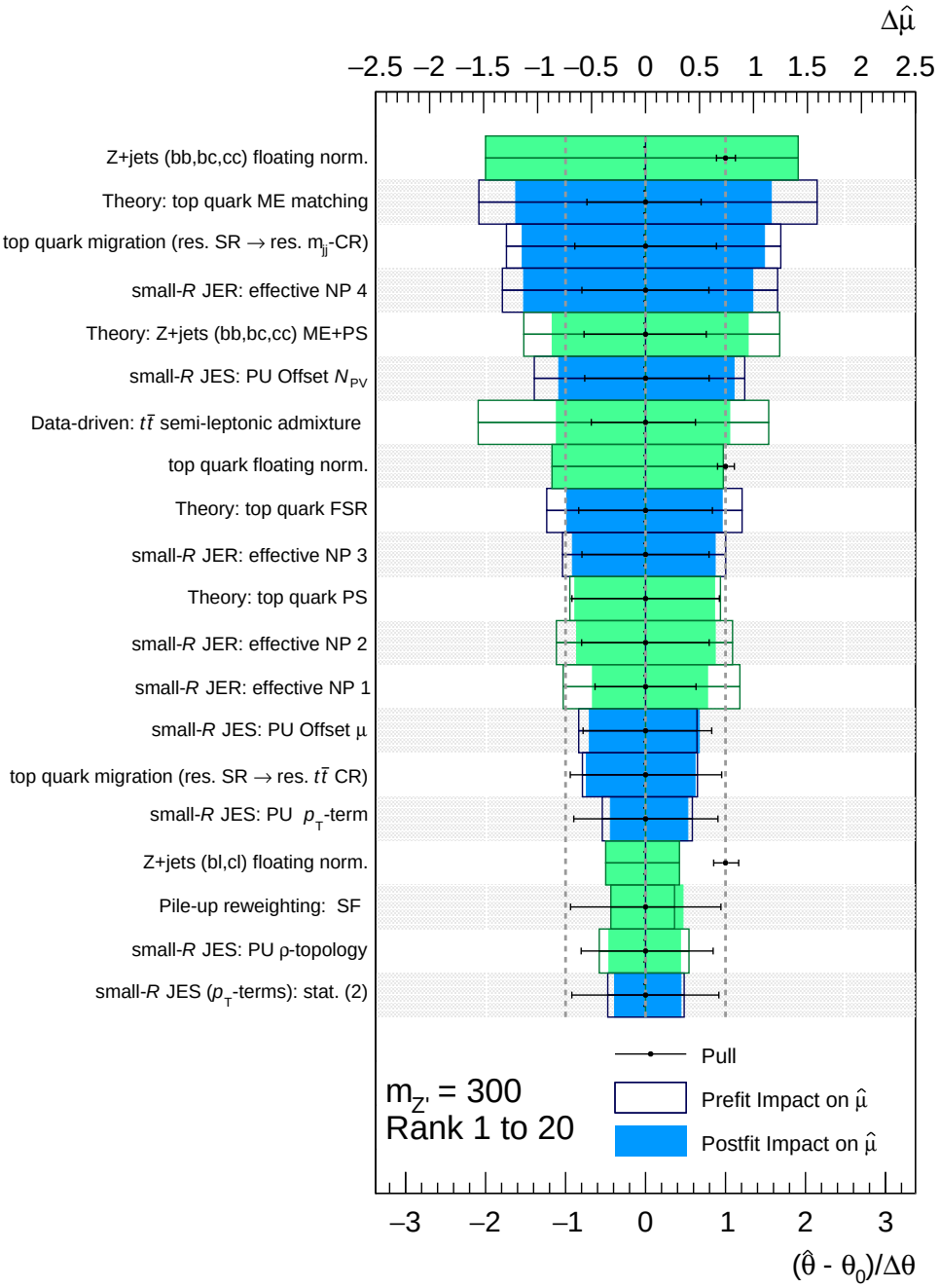

Figure 5.45: Impact of the 20 most relevant nuisance parameters on the best-fit signal strength, $\hat{\mu}$, for VBF Z' signal with $m_{Z'} = 300$ GeV. The box contours (colored boxes) show the impact for a NP value set to one pre-fit (post-fit) standard deviation from the nominal NP value. The black dots indicate the pulls of the NPs $(\hat{\theta} - \theta_0)/\Delta\theta$ (lower abscissa). The green box color indicates a negative correlation between the pulls and the corresponding impact $\Delta\mu$.

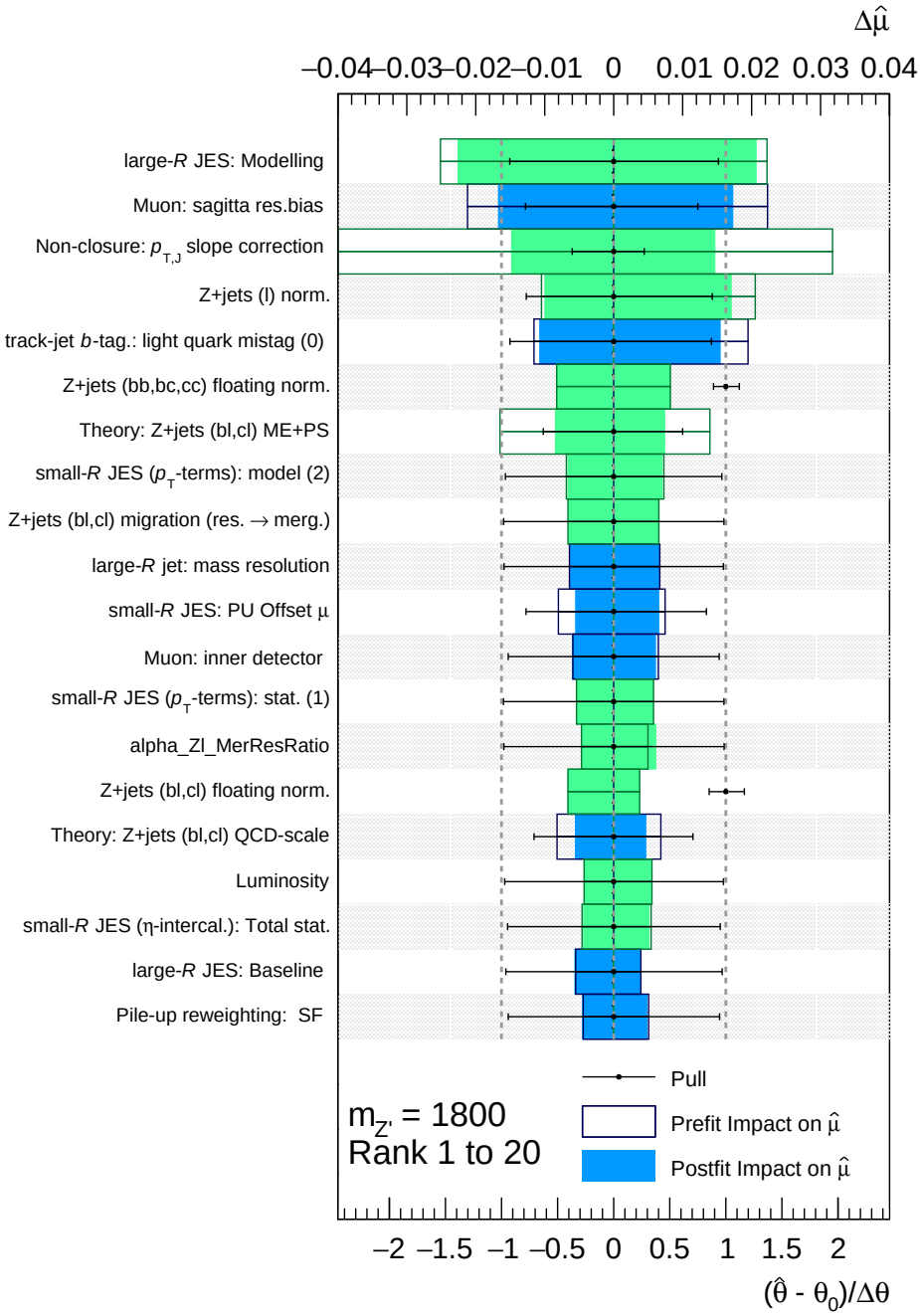

Figure 5.46: Impact of the 20 most relevant nuisance parameters on the best-fit signal strength, $\hat{\mu}$, for VBF Z' signal with $m_{Z'} = 1800$ GeV. The box contours (colored boxes) show the impact for a NP value set to one pre-fit (post-fit) standard deviation from the nominal NP value. The black dots indicate the pulls of the NPs $(\hat{\theta} - \theta_0)/\Delta\theta$ (lower abscissa). The green box color indicates a negative correlation between the pulls and the corresponding impact $\Delta\mu$.

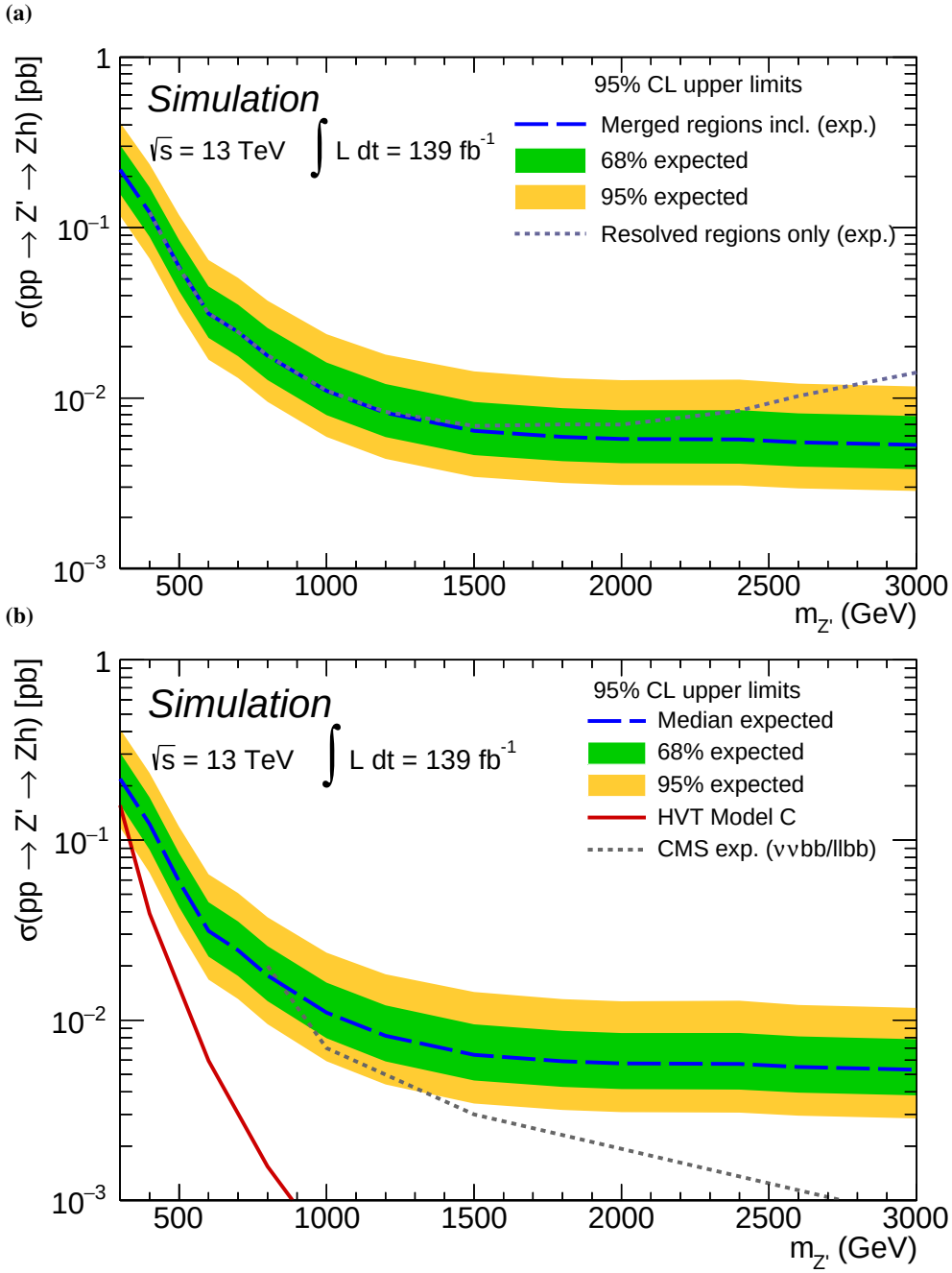

Figure 5.47: The expected upper 95% CL limits on VBF $Z' \rightarrow Zh$ resonance production as a function of the resonance mass, $m_{Z'}$ from combination of *resolved* and *merged* regions. The green and the yellow bands indicate the 1σ and 2σ uncertainty on the expected limit. For comparison (a) demonstrates the improvement by combining *merged* and *resolved* channels; the dotted curve indicates the expected limit from the *resolved* regions alone. The comparison to the prediction by the HVT model C and to the CMS exclusion limits is shown in (b). The solid red curve indicates the cross section predicted by HVT model C. The dotted gray curve represents the result of the search by the CMS experiment [152] which includes both the 2-lepton and the 0-lepton channel.

5.5.3 Future prospects

In this chapter, the feasibility of a search for a Zh-resonance in the VBF production mode has been studied. The next step will be to unblind data in the signal regions and, in case no significant excess of events is observed above the SM background, set the observed exclusion limits on the production cross section in this phase space for the first time in ATLAS.

For future analysis of this final state, there are still several optimizations of the event selection possible. The current selection requirements are fully inherited from the *parent analysis* and have not been optimized for the signal events with VBF topology. An optimization of each selection requirement could potentially improve the expected exclusion limits and the discovery potential.

One crucial weakness of the current event reconstruction is the trivial selection of the Higgs boson *signal jets*. The *signal jet* selection is optimized for signal events in which these are mostly the only jets in the final state. The two *signal jets* are chosen to be the two highest-p_{T} jets (leading and sub-leading jet), or in case of an additional b-tagged sub-sub-leading jet, this b-tagged jet is selected instead of the sub-leading untagged jet. This is a reasonable choice in the case of the *parent analysis*. However, in the case of the VBF signal, there are typically four signal jets expected in a signal event. Each signal event has the probability of 51%[4] to have at least one of the two b-hadron jets missed by the b-tagging algorithm. The efficiency of the selection of the correct *signal jet* pair (i.e. the two jets from the Higgs boson decay) out of the 4 jets in the event depends on the signal resonance mass and the kinematic properties of signal events.

In order to study the efficiency of the correct *signal jet* pair selection, at first a reference set of signal events is defined which have a jet multiplicity of at least 4, where at least 2 of these jets are central jets and are matched to a b-quark at generator level. Additionally, two of the remaining jets are required to lie in opposite η-hemispheres of the detector. These are the minimal requirements on a reconstructed VBF signal event with the two jets from the Higgs boson decay. The fraction of all signal events entering the reference sample is in the order of 30% and is shown in dependence on the resonance mass as a black line in Fig. 5.48. For very low resonance masses, the jet clustering algorithms fail to reconstruct both jets from the Higgs boson decay because of the low transverse momentum of the sub-leading jet. At higher resonance masses, the jets from the Higgs boson decay are strongly collimated and may be reconstructed as the *merged* event topology. The efficiency of the reference selection represents the maximal possible signal selection efficiency for the *resolved* event topology, assuming that the selection requires the presence of both VBF jets in the final state. Studies that considered also events with only one *VBF jet* in the final state, selected via simple p_{T} and η requirements showed a much smaller signal-to-background ratios for such events, implying their negligible contribution to the search sensitivity. The selection of signal candidates with only three jets in the final state may still be improved by using the multivariate techniques to distinguish between the different production modes [150].

The actual signal selection efficiency in terms of the correct jet pairing is even lower than the efficiency of the reference selection. In an environment with at least four jets in the final state the event reconstruction often selects the wrong jet permutation, i.e. one of the *VBF jets* can be mistaken for a *signal jet*. The green line in Fig. 5.48 shows the fraction of all signal events in which the current *signal*

[4] Assuming the b-tagging working point with 70% efficiency.

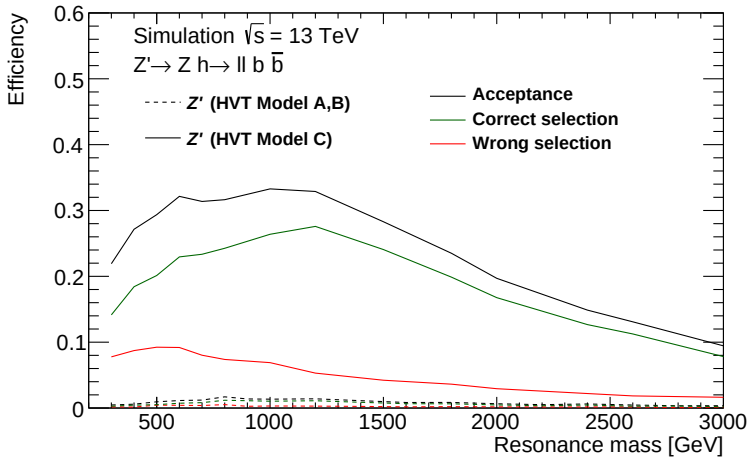

Figure 5.48: The expected event reconstruction and selection efficiency of reference VBF $Z' \to Zh \to \ell^+\ell^- b\bar{b}$ signal events (black line) using the generator level information to identify the two b-jets (maximum possible selection efficiency). The efficiencies of the default procedure of selecting the correct jet pair, i.e. two b-jets (green line), or a wrong jet combination (red line), i.e. at least one non-b-jet are also shown.

jet selection procedure selects the jets from the Higgs boson decay (i.e. the jets that are matched to b-quarks). In contrast, the red line indicates the fraction of events in which jets are wrongly paired. For low resonance masses, the selection of a wrong Higgs decay candidate is selected in almost 40% of all reference events, because the *signal jets* are more likely to have a low p_{T} and thus to be overtaken by a *VBF jet*. The wrong jet pairing has the consequence that the reconstructed kinematic observables (i.e. $\phi(V, h)$, $m_{jj/J}$, m_{Zh}, ...) do not resemble the event topology and thus have a reduced discrimination power between signal and background. Such events may fail the selection criteria more often, or if they do not, the m_{Zh} distribution does not show a resonant behavior. For example, the m_{Zh} signal distribution is significantly broader in the 1 b-tag region (see Fig. 5.8).

A potential improvement of the efficiency of the correct Higgs boson decay candidate selection may be achieved by means of multivariate techniques. It remains to future work to improve the selection of the correct *signal jet* pairs for example by using a multivariate technique.

CONCLUSIONS AND OUTLOOK

In this thesis, a search for resonances decaying into a Standard Model (SM) Higgs boson h and a weak gauge boson W or Z was performed. Two theoretical models extending the SM were explored and serve as benchmarks for interpreting the data. The two-Higgs doublet model (2HDM) is part of a large class of theories beyond the SM (BSM) and predicts the existence of a massive CP-odd scalar field A. The signal process $A \to Zh$ serves as benchmark for a spin-0 diboson resonance. Another large class of BSM theories describes new interactions at an energy scale above the electroweak scale and predicts an additional triplet of massive vector bosons (heavy vector triplet (HVT)). The two signal processes $Z' \to Zh$ and $W' \to Wh$ are used as a benchmark for the production of a spin-1 diboson resonance. Using the leptonic decay channels of the final state gauge bosons leads to a clear signature in the detector. As decay channel of the Higgs boson, on the other hand, $h \to b\bar{b}$ is chosen due to its large branching fraction of around 58%.

Especially for high resonance masses, the challenge is to efficiently reconstruct the strongly collimated hadronic Higgs decays. For this purpose, detailed generic Higgs tagging studies have been performed to improve the identification of the boosted $h \to b\bar{b}$ decays. The background jets mimicking the Higgs boson decays are mainly jets from fully hadronic top quark decays $t \to bq\bar{q}$ (top quark jets) or from final state gluon or quark radiation (QCD jets). The identification is based on jet mass reconstruction and on machine learning algorithms for b-jet identification (b-tagging). Jets with a large radius containing the entire boosted $h \to b\bar{b}$ decay are defined (large-R jet), and two small jets reconstructed from Inner Detector (ID) tracks (i.e. track jets) are associated with the large-R jet. The standard b-tagging algorithms are applied to these track jets. In this thesis, different combinations of selection criteria for this twofold application of the b-tagging algorithm have been investigated. The background suppression was optimized for all analyses involving boosted $h \to b\bar{b}$ decays. For high signal selection efficiency above 90%, the tagging of only one b-jet has to be used, which provides only moderate top quark jet rejection by about a factor of two. The QCD jet rejection reaches a factor of 10. Accepting lower signal efficiencies, the most successful strategy for suppressing top quark jets is based on applying the same b-tagging criteria to both track jets, increasing the top quark jet rejection exponentially with decreasing signal efficiency up to a factor of 100 for 40% signal efficiency. For the suppression of QCD jets, on the other hand, the asymmetric b-tagging requirement for the two track jets is optimal with a rejection factor of order 100 corresponding to signal efficiencies between 70% and 90%. Symmetric b-tagging criteria achieve even higher QCD jet rejection rates of up to a factor of 500.

Furthermore, the invariant mass of the large-R jet can be used as a discriminant, which provides additional background rejection by about one order of magnitude, depending on the b-tagging criteria. Furthermore, many jet substructure observables were investigated for $h \to b\bar{b}$ identification, both stand-alone and in combination with b-tagging and jet mass-based identification technique. Used alone, the k_t-splitting scale, i.e., the distance of the last two proto-jets of the k_t-jet finding algorithm, proved to be most effective for discrimination against QCD jets. The most effective variables for top quark jet rejection are the energy correlation functions of the calorimeter clusters, which capture the 2-prong character of the $h \to b\bar{b}$ decay. Combined with the b-tagging and mass criteria, however, the improvement in sensitivity is relatively small. This Higgs tagging procedure has been applied to the search for Wh and Zh resonances in this thesis and several other searches based on ATLAS data.

The largest background contributions in the Wh and Zh resonance searches arise from Z+jets, W+jets, and top quark pair production. The global normalization of these background components is determined from a fit of the final state invariant mass distributions of the different background processes in signal-depleted control regions to the data. Systematic uncertainties in the shape of the mass spectra in simulated events have been computed by comparing the predictions of different MC generator setups. The studied theoretical uncertainties are due to parton shower (PS) modeling (Lund model vs. cluster model), the matching scheme of the matrix element to the PS, and the choice of renormalization and factorization scales. The different fragmentation models vary the shape of the mass distribution by up to 5%, while the renormalization and factorization scales affect the shape by about 2%. Uncertainties in the PDFs are negligible with $\lesssim 0.1\%$. Similar theoretical uncertainties also affect the modeling of signal efficiencies. This signal efficiency has a systematic theory uncertainty of 3% comparing different hadronization models.

In the absence of significant excesses of events in the search channels, maximum likelihood fits of the signal and background invariant mass distributions to the data were used to determine 95% C.L. upper limits on the cross sections for the gluon-gluon fusion (ggF) and b-quark associated production (bbA) of spin-0 Vh resonances in the mass range from 280 to 2000 GeV, and for the Drell-Yan production of spin-1 Vh resonances in the mass range of 500 – 5000 GeV.

Model independent limits on the production cross section of a heavy charged vector boson W' were found to be around 5×10^{-3} pb for $m_{W'} = 1$ TeV and 6×10^{-4} pb for $m_{W'} = 5$ TeV. The limits for a neutral vector boson are around 6×10^{-3} pb for $m_{Z'} = 1$ TeV and 3.5×10^{-4} pb for $m_{Z'} = 5$ TeV. Z' boson masses can thus be excluded up to 2.9 TeV (3.2 TeV) in HVT benchmark model A (B), while W' boson masses can be excluded up to 3 TeV (3.2 TeV). Limits on the gluon-gluon fusion and the the b-associated production cross section of a pseudo-scalar A boson were found to be around 2.5×10^{-3} pb for $m_A = 2$ TeV and around 1.0×10^{-1} pb for $m_A = 400$ GeV. The largest excess was observed with a local significance of 1.8 σ at $m_A \approx 500$ GeV. Two-dimensional limits on both A boson production cross sections have been set constraining the 2HDM parameter space. The results have been presented at conferences. A journal publication of these studies is currently in preparation.

The search for heavy diboson resonances has been extended for the first time in ATLAS to vector boson fusion (VBF) production of Z' bosons. Sensitivity studies yield expected upper limits on the production cross section times branching ratio of around 5.5×10^{-3} pb for masses above 1TeV and down to 2×10^{-2} pb for masses below 800 GeV, while the VBF production cross section for a Z' boson in the HVT benchmark model C is still lower than the expected experimental sensitivity. A hypothetical Z' boson signal in this model would lead to an excess of events with an expected local

significance of up to 1.8 σ for masses below 500 GeV. It has been shown that, in contrast to the DY production channel, the resonance is not produced at rest but with an average p_{T} of 100 GeV. This initial momentum alters the back-to-back event topology of the decay products for resonances with masses $\lesssim$ 500 GeV making the event selection less optimal compared to the DY production mode. Therefore, further optimization of the selection criteria has the potential to improve the sensitivity to search for resonances produced via VBF. Based on these feasibility studies, a new analysis targeting the VBF production mode of Vh resonances is being developed in the ATLAS collaboration.

APPENDIX

A Supplementary results for the boosted $h \to b\bar{b}$ tagging

This appendix contains plots whose key message is essentially no different from those shown in the main body, Chapter 3, but which show slightly different parameter values, resulting in slightly different results.

A.1 Tight mass window tagging

In Appendices A.1 and A.2 the performance of the Higgs-tagger is shown using a tight mass window with a signal selection efficiency of 68% instead, for the top jet and for the QCD jet rejection, respectively.

A.2 JSS variable correlations

The correlation between different substructure observables in a Higgs-jet sample is given in Appendix A.3 and for the studied background jet sample in Appendix A.4.

A.3 Additionally tested substructure observables

Further substructure were tested but not shown in the main body to avoid redundency due to either poor separation power or closely similar defined as the ones shown in the main chapter. shows the splitting scale in the the second and third to last iteration step. shows the distribution of the τ_N^{wta} distribution, with slightly different definition of the seed-subjet with respect to the τ_N, given in the main chapter.

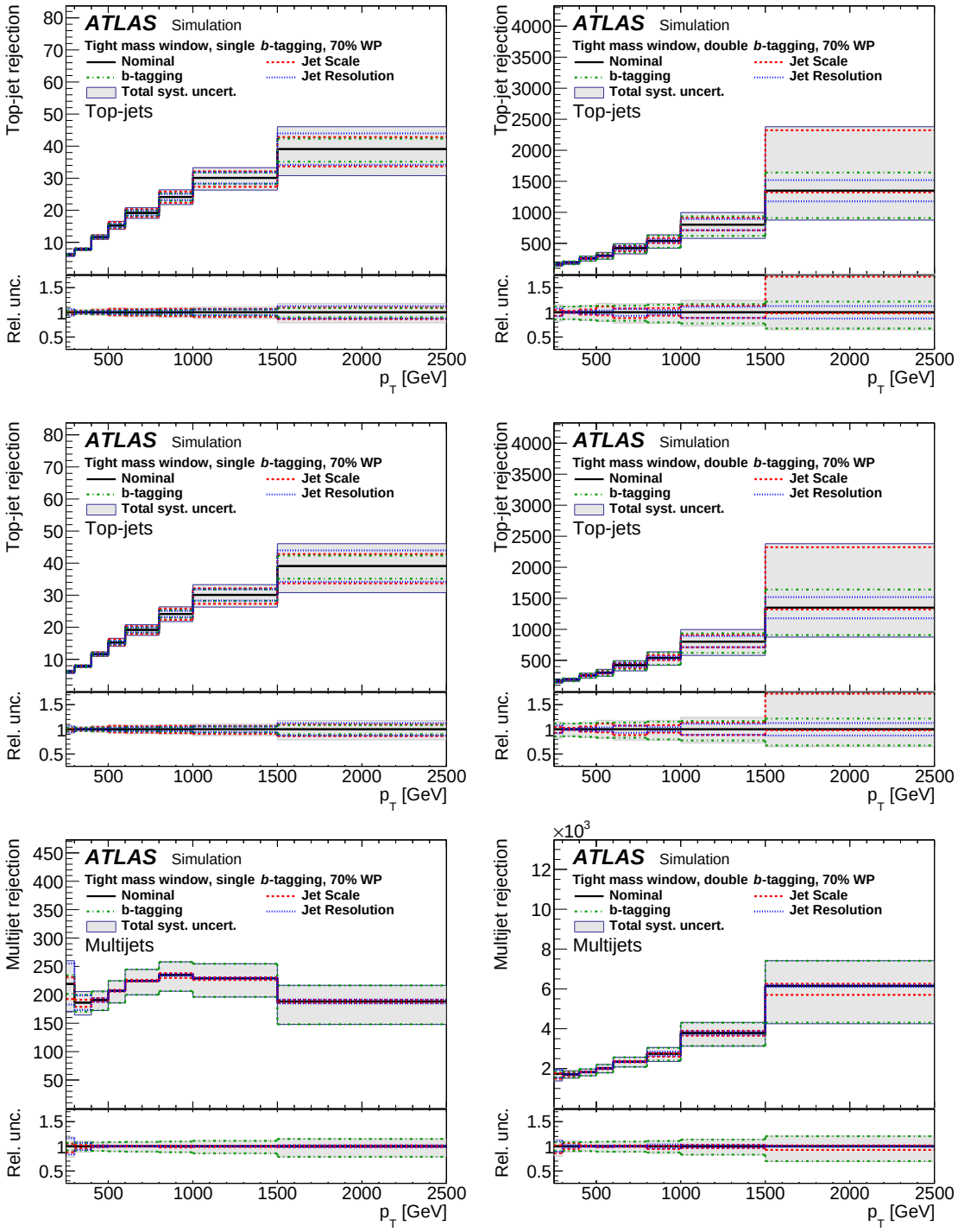

Figure A.1: Background rejection factor for single (left) and double b-tagging (right) in combination with a loose mass window as function of large-R p_{T}.

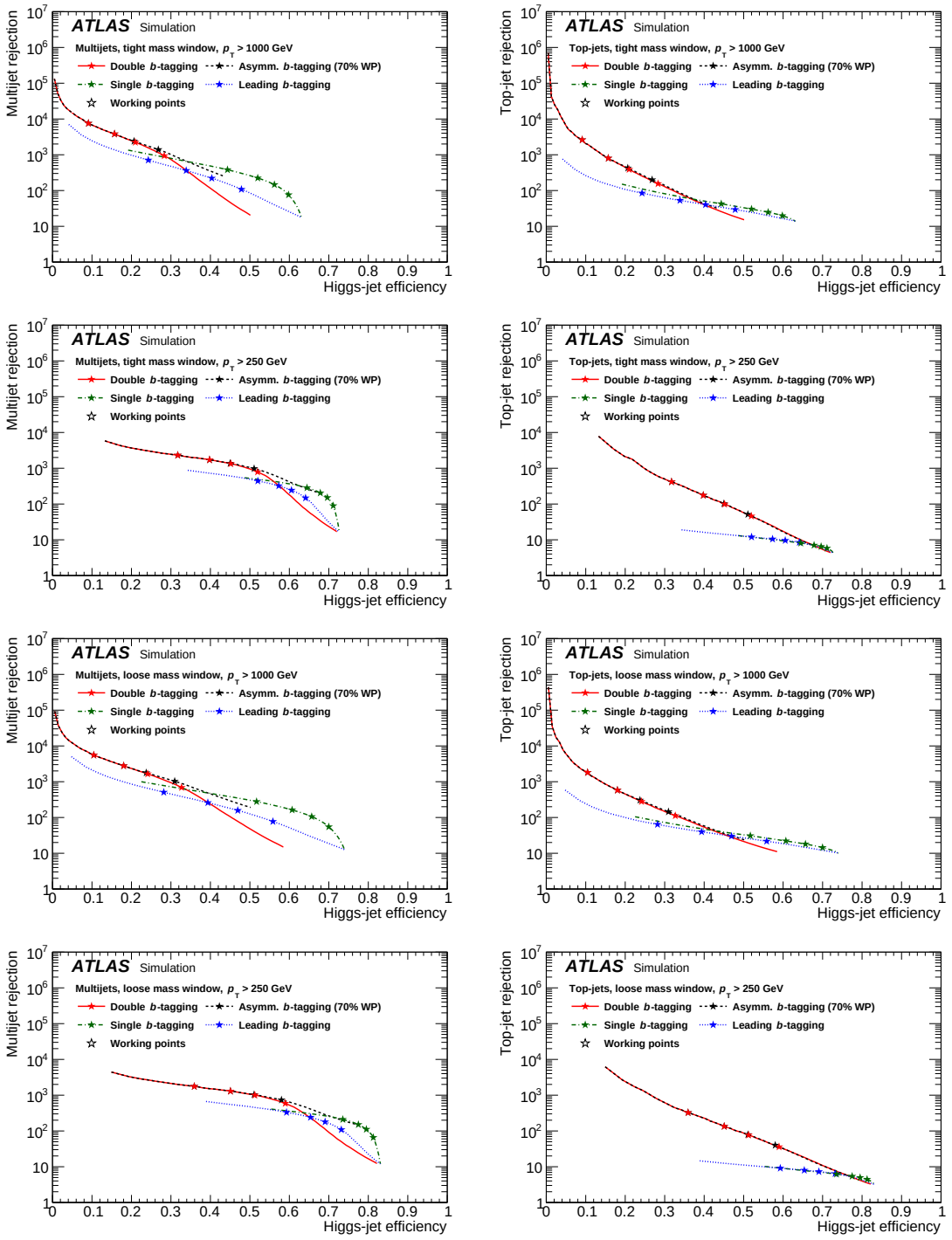

Figure A.2: (left) QCD jet background rejection and (right) top jet background rejection by varying b-tagging requirements with a tight mass window (upper two rows) or a loose mass window (lower two rows) applied.

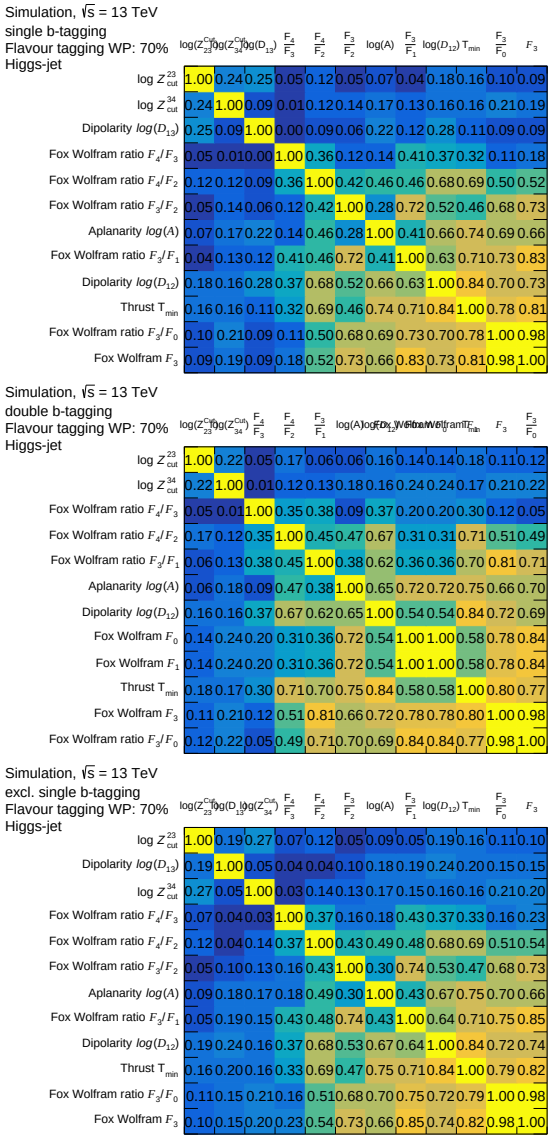

Figure A.3: Linear correlation coefficient between JSS variables in Higgs-jets. The subsample used to probe for correlations satisfy the (top) single b-tagging, (center) double b-tagging and (bottom) exclustive single b-tagging (aka. 1 b-tag) criterion.

Rejection curves with alternative baseline b-tagging

The performance of different JSS variables on top of a loose b-tagging (85%) requirments are shown in Appendices A.7 and A.8 for single and double b-tagging, respectively. An additional loose mass window (80%) is applied for the plot shown in Appendices A.9 and A.10.

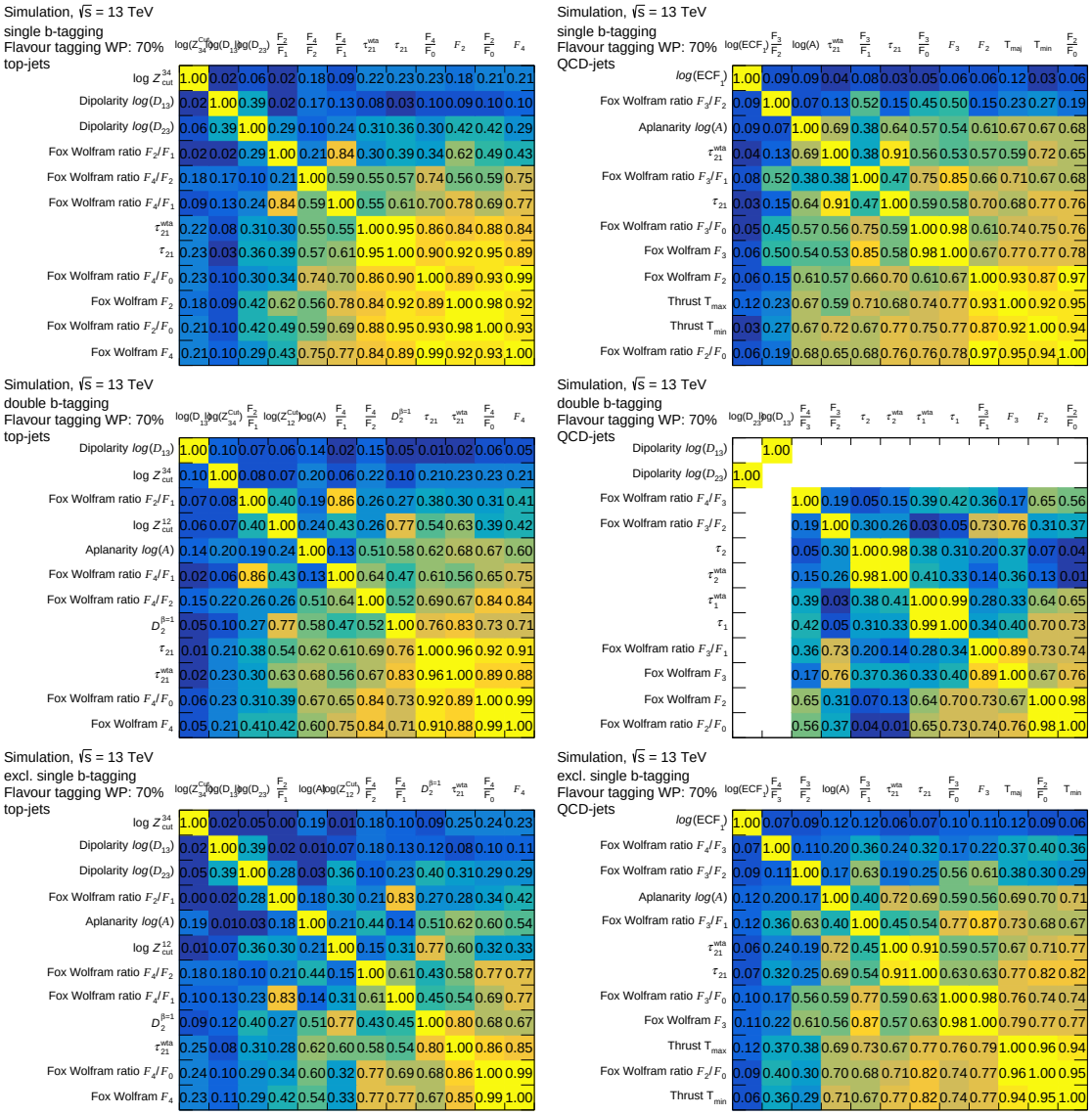

Figure A.4: Linear correlation coefficient between JSS variables in (left) top jets and (right) QCD jets. The subsample used to probe for correlations satisfy the (top) single b-tagging, (center) double b-tagging and (bottom) exclusive single b-tagging (aka. 1 b-tag) criterion.

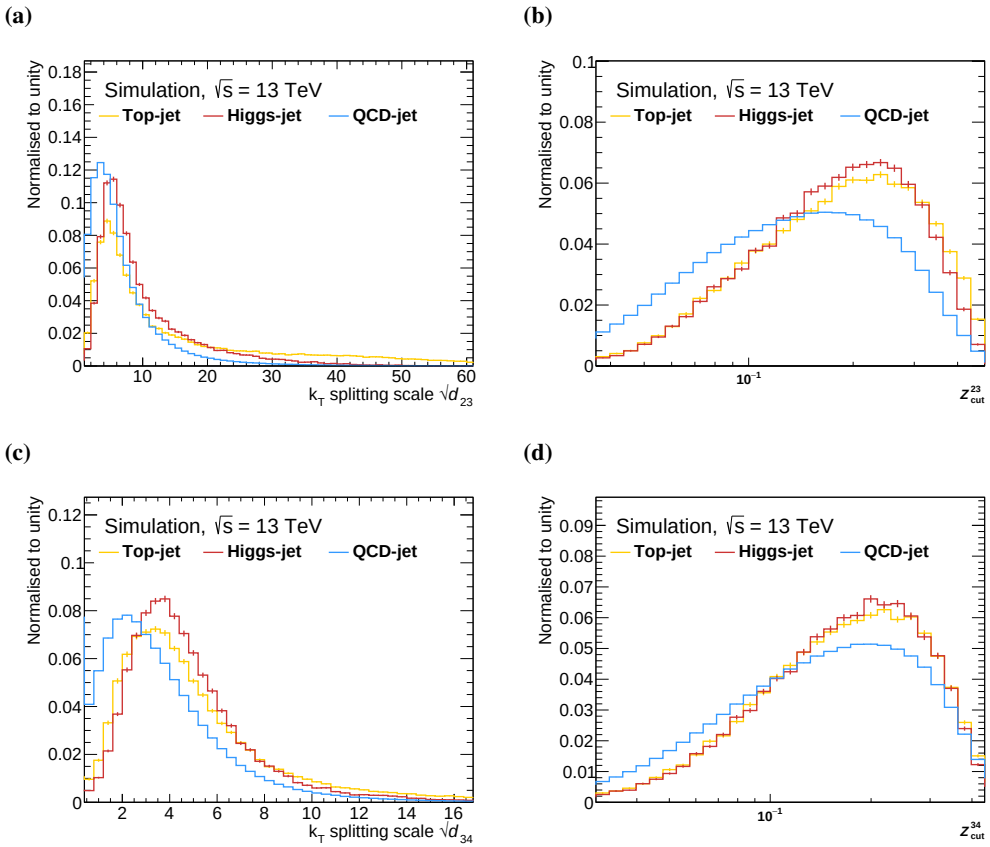

Figure A.5: Distribution of the splitting scales (a) $\sqrt{d_{23}}$, (c)$\sqrt{d_{34}}$ and the asymmetry variables (b) Z^{23}_{cut} and (d) Z^{34}_{cut} variables for the Higgs jet signal and top jet and QCD jet backgrounds.

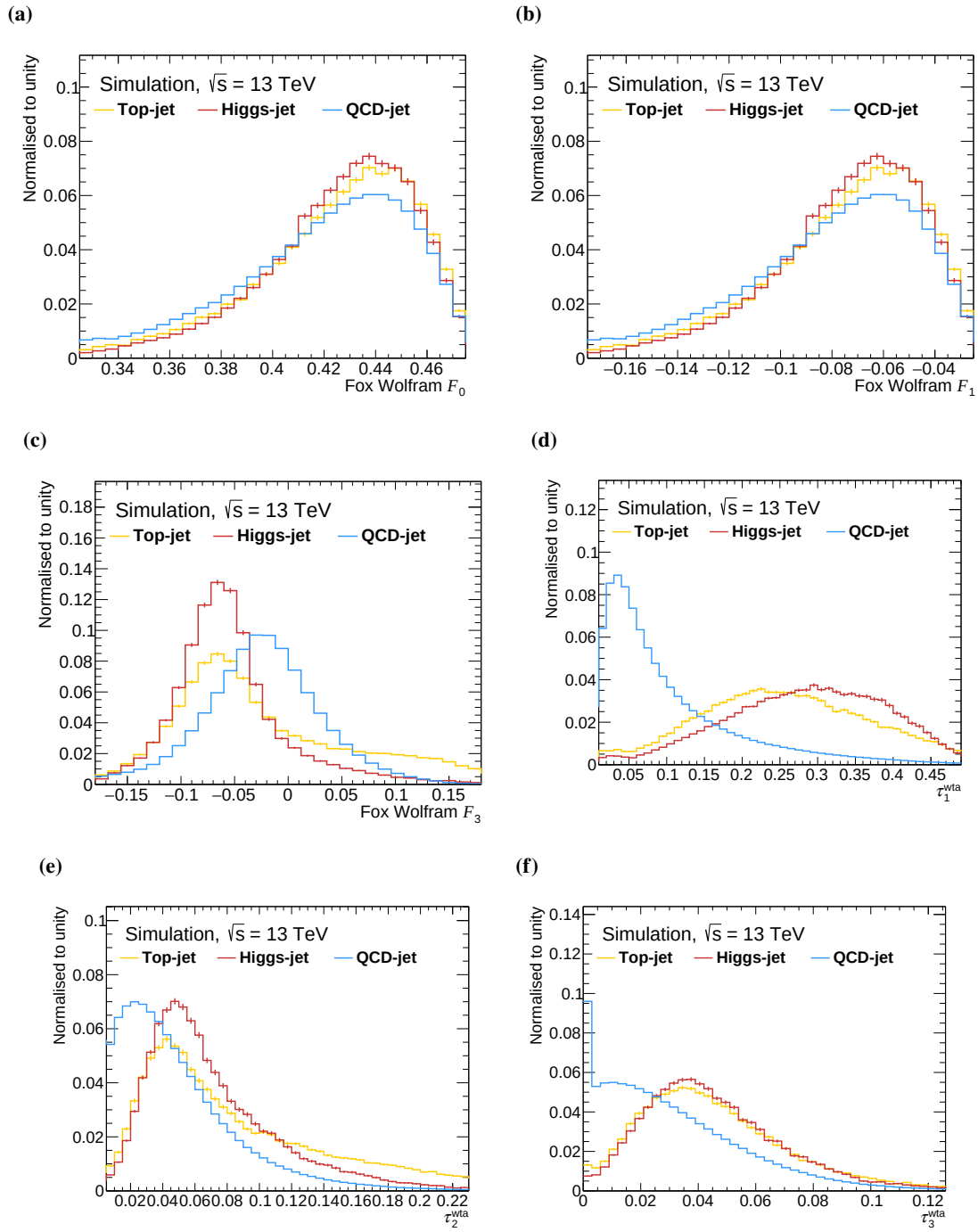

Figure A.6: Distribution of the Fox-Wolfram moments (a) $\mathcal{F}_0$, (b) $\mathcal{F}_1$, (c) $\mathcal{F}_3$ and for the (winner takes all (wta)) subjettiness variables (d) τ_1^{wta}, (e) τ_2^{wta} and (f) τ_3^{wta} for the Higgs jet signal and top jet and QCD jet backgrounds.

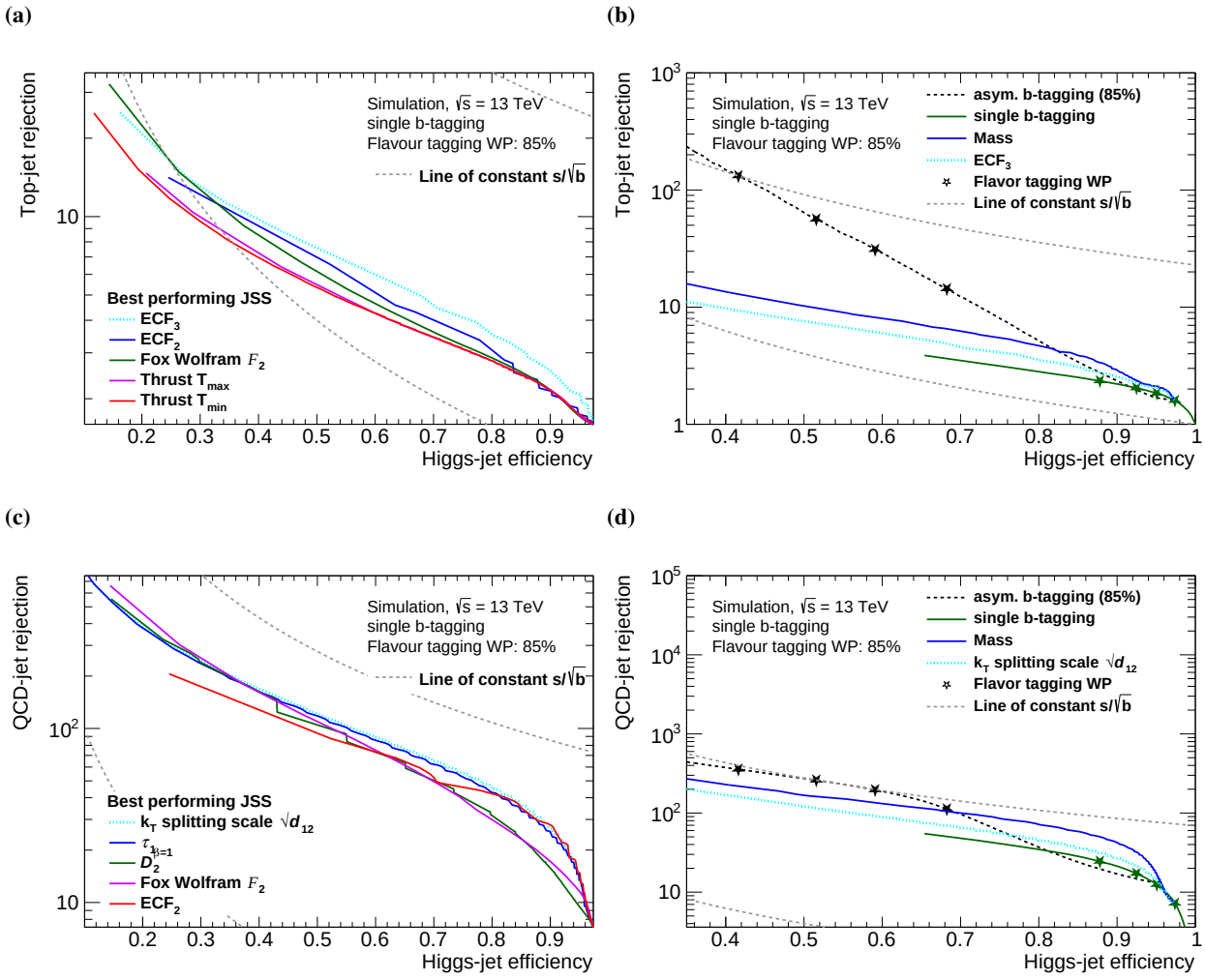

Figure A.7: receiver operating characteristic (ROC) curves comparing the performance of different Higgs taggers in which the jet substructure (JSS) variables (including the jet mass) are applied in addition to the single b-tagging requirement with the working point at 85% b-tagging efficiency; (top) against top jets; (bottom) against QCD jets.

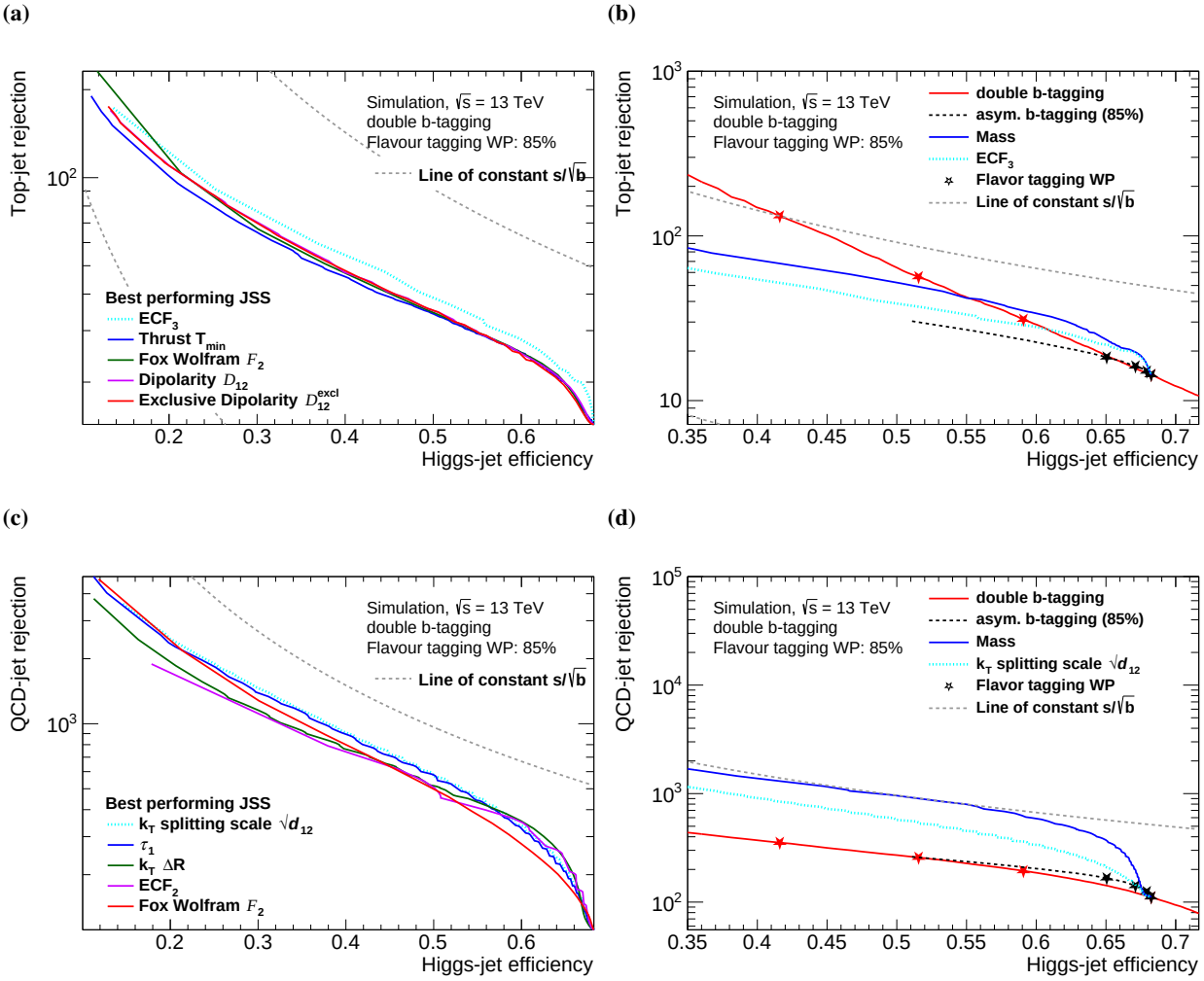

Figure A.8: ROC curves comparing the performance of different Higgs taggers in which the jet substructure (JSS) variables (including the jet mass) are applied in addition to the single b-tagging requirement with the working point at 85% b-tagging efficiency; (top) against top jets; (bottom) against QCD jets.

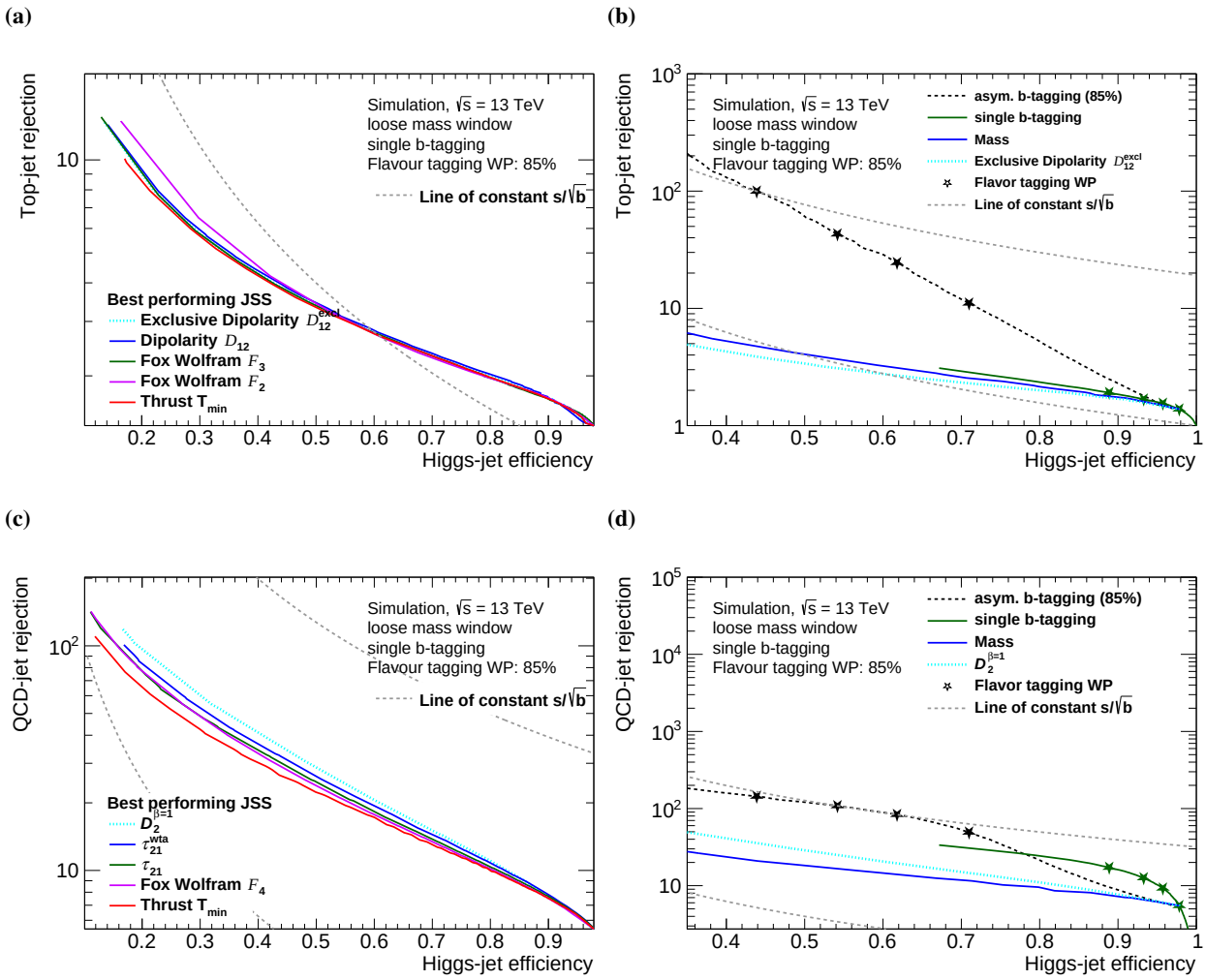

Figure A.9: ROC curves comparing the performance of different Higgs taggers in which the jet substructure (JSS) variables (including the jet mass) are applied in addition to the single b-tagging requirement with the working point at 85% b-tagging efficiency; (top) against top jets; (bottom) against QCD jets.

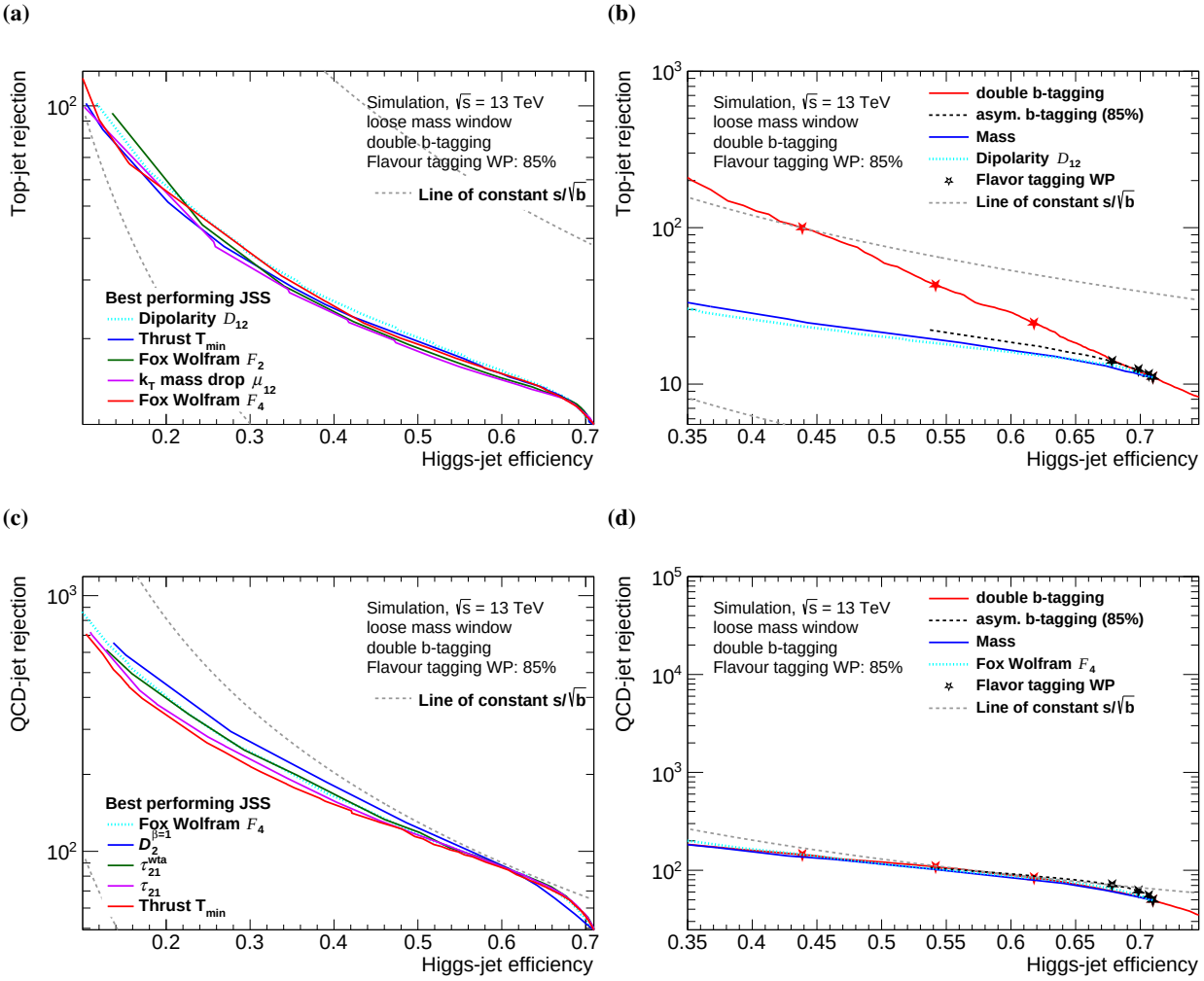

Figure A.10: ROC curves comparing the performance of different Higgs taggers in which the jet substructure (JSS) variables (including the jet mass) are applied in addition to the single b-tagging requirement with the working point at 85% b-tagging efficiency; (top) against top jets; (bottom) against QCD jets.

B Additional material for the Vh-resonance searches

This section is intended to help later attempts to reproduce the analyses given in Chapters 4 and 5 by providing detailed, technical information on triggers, NP, or the derivation of uncertainties.

B.1 Trigger menu

The trigger that are applied throughout both physics analyses in Chapters 4 and 5 is given in Appendix B.11

Table B.11: The requirements on the high level trigger objects (trigger menu) imposed to all events used for the analysis in Chapters 4 and 5. Summary of the lowest unprescaled $E_{\mathrm{T}}^{\mathrm{miss}}$, single electron and single muon trigger menu entries used for the Run 2 data taking periods.

MET Trigger	Electron trigger	Muon Trigger
	2015 Run	
HLT_xe70	HLT_e24_lhmedium_L1EM20VH HLT_e60_lhmedium HLT_e120_lhloose	HLT_mu20_iloose_L1MU15 HLT_mu50
	2016 Run	
HLT_xe90_mht_L1XE50 HLT_xe110_mht_L1XE50	HLT_e26_lhtight_nod0_ivarloose HLT_e60_lhmedium_nod0 HLT_e140_lhloose_nod0 HLT_e300_etcut	HLT_mu26_ivarmedium HLT_mu50
	2017 Run	
HLT_xe110_pufit_L1XE55	HLT_e26_lhtight_nod0_ivarloose HLT_e60_lhmedium_nod0 HLT_e140_lhloose_nod0 HLT_e300_etcut	HLT_mu26_ivarmedium HLT_mu50
	2018 Run	
HLT_xe110_pufit_xe70_L1XE50	HLT_e26_lhtight_nod0_ivarloose HLT_e60_lhmedium_nod0 HLT_e140_lhloose_nod0 HLT_e300_etcut	HLT_mu26_ivarmedium HLT_mu50

B.2 Information on the evaluation of theoretical uncertainties.

The relative uncertainties due to theoretical uncertainties are evaluated using *surrogate* sample. Appendix B.12 gives an overview how the *surrogate* sample is simulated.

Table B.12: Context related definition of *surrogate* sample.

Process	Uncertainty	Variation	*surrogate* sample
$t\bar{t}$	ME matching	MadGraph5_aMC@NLO + Pythia 8	AtlFast [194]
	Parton shower	Powheg-Box + Herwig 7	AtlFast [194]
	PDF	Alternative event weights using LhaPdf [13]	No pre-filtering at generator level.
	ISR/FSR	Alternative event weights with A14 tune variations [117]	Decreased statistical power in extreme phase spaces (e.g. high-$E_{\mathrm{T}}^{\mathrm{miss}}$)
V+jets	ME matching + PS	MadGraph5_aMC@NLO + Pythia 8	MC corresponding to data taking period 2015-2016
	PDF	Alternative event weights using LhaPdf [13]	representative subset of samples with intact alternative weights
	QCD scale	Alternative event weights	
HVT (quark-antiquark annihilation ($q\bar{q}$), VBF)	PS	MadGraph5 + + Herwig 7	generator level events, c.f. Section 4.4.4
	PDF	Alternative event weights using LhaPdf [13]	
	A14 shower tuneTable 4.3	Alternative event weights	
2HDM (gluon-gluon fusion (ggA mode))	PS	MadGraph5 + + Herwig 7	
	PDF	Alternative event weights using LhaPdf [13]	
	A14 shower tuneTable 4.3	Alternative event weights	
	QCD scale	Alternative event weights	
2HDM (in association with b-quarks (bb$A$ mode))	PS	MadGraph5 + + Herwig 7	
	PDF	Alternative event weights using LhaPdf [13]	
	A14 shower tuneTable 4.3	Alternative event weights	
	QCD scale	Alternative event weights	

Table B.13: Requirements to the event selection on generator level.

Common requirements		
variable	resolved	merged
N_{jets}	$\geq$ 2 small-R jets	$\geq$ 1 large-R jet
$p_{\text{T},jet}$	$\geq$ 45 GeV	$\geq$ 250 GeV
$\lvert\eta_{jet}\rvert$	4.5	$\leq$ 2.0
m_J		75 GeV $\leq m_J \leq$ 145 GeV
0-lepton channel		
m_{jj}	110 GeV $\leq m_{jj/J} \leq$ 140 GeV	
$E_{\text{T}}^{\text{miss}}$	$\geq$ 150 GeV	
H_T	$\geq$ 120 GeV for 2 signal jets $\geq$ 150 GeV for $\geq$ 3 signal jets	
$\Delta\phi(j,j)$	$> (7\pi/9.)$	
$\Delta\phi(h, E_{\text{T}}^{\text{miss}})$	$< \frac{2\pi}{3}$	
$\min_{j\in\text{jets}} \Delta\phi(E_{\text{T}}^{\text{miss}}, j)$	$\geq \pi/9$ (for up to 3 jets) $> (\pi/6)$(for at least 4 jets)	
1-lepton channel		
m_{jj}	110 GeV $\leq m_{jj/J} \leq$ 140 GeV	
p_{T}^{lepton}	$\geq$ 27 GeV	
$E_{\text{T}}^{\text{miss}}$	$\geq$ 40 GeV	$\geq$ 100 GeV
N_{jets}	$\leq$ 3	
$p_{\text{T},W}$	$> \max(710 - (3.3\times10^5/\frac{m_{Zh}}{\text{GeV}}), 150)$ GeV	$\max(394\cdot\log(\frac{m_{Zh}}{\text{GeV}}) - 2350, 150)$ GeV
m_W	$\leq$ 300 GeV	
$E_{\text{T}}^{\text{miss}}/\sqrt{H_T}$	$\leq (1.15 + (8\times10^{-3} m_{Zh}()/\text{ GeV})$	
2-lepton channel		
m_{jj}	100 GeV $\leq m_{jj/J} \leq$ 145 GeV	
$p_{\text{T}}^{\text{lepton 1}}$	$\geq$ 27 GeV	
$p_{\text{T}}^{\text{lepton 2}}$	$\geq$ 20 GeV	$\geq$ 25 GeV
$E_{\text{T}}^{\text{miss}}/\sqrt{H_T}$	$\leq (1.15 + (8\times10^{-3}\frac{m_{Zh}}{\text{GeV}}))$	
$p_{\text{T}\cdot Z}$	$\geq (20 + 9\cdot\sqrt{\frac{m_{Zh}}{\text{GeV}}} - 320\cdot\text{GeV}$	
m_Z	$\max(40, 87 - (0.03\frac{m_{Zh}}{\text{GeV}}), 97. + (0.013\cdot\frac{m_{Zh}}{\text{GeV}}))$	

Selection requirements on generator level

Appendix B.13 gives the event selection criteria as they are defined for generator level samples. These generator level samples are not simulated through the detector but the content in simulation of stable particles is directly used, neglecting experimental uncertainties such as on the reconstruction efficiency. The code using the TRUTH3 dataset is given in https://gitlab.cern.ch:8443/smaschek/vhreso_theosignal.

C Additional material for the Vh-resonance searches in the DY, ggF and bb$A$ mode production mode

C.1 Pre-fit control region plots

The nominal distribution of the reconstructed di-boson mass $m_{\text{T,Zh}}$ in the 0-lepton channel before the fit to the data. The uncertainties cover only statistical uncertainties. The descrepancies are covered

by the pull of the variables shown in Figs. 4.32 to 4.34 leading to the post-fit distributions given in Figs. 4.25 to 4.28.

C.2 jet mass resolution (JMR) uncertainties

The detailed representation of the imposed uncertainties on the JMR for the various channels and for the individual background processes is given in Appendices C.2 to C.7. In Appendices C.2 and C.3 shows the impact of the JMR uncertainty individiually on the top quark background for 1 b-tag and 2 b-tag, respectively. The impact of the tagging multiplicity on this uncertainty is not negligible, since the large-R jets in the 2 b-tag regions have a bias on the origin of the jet seed particles (stemming from two b-quarks) while the 1 b-tag region has not. Appendices C.4 and C.5 show the impact of JMR uncertainties on the V+jets and on the minor backgrounds (VV, Vh), respectively. The individual background processes are impacted by the JMR uncertainties to different extent. Appendices C.6 and C.7 show the effect of the JMR uncertainty to the combined SM background. The small but visible migration in the m_{jj}-sideband CR distributions of the *resolved* regions (note that this uncertainty affects the large-R jet) is shown in Appendix C.7.

C.3 Theory uncertainties on background $m_{\mathrm{(T,)Vh}}$ distributions for additional data regions

The different sources of theoretical uncertainties on the shape of the kinematic distributions are computed individually for each signal region and control region and for the 7 (8) main background components for the HVT and ggA mode analysis (for the acrshortbbA analysis). The expected nominal $m_{\mathrm{T,Zh}}$ distribution in the 0-lepton channel, together with the relative uncertainties due to the various sources of uncertainties, is shown in Appendices C.8 and C.10 to C.16. The corresponding expected nominal m_{Wh} distribution in the 1-lepton lepton channel with the corresponding relative uncertainties is shown in Appendices C.17 to C.21.

C.4 Theory uncertainties on signal $m_{\mathrm{(T,)Vh}}$ distributions for additional data regions

The heavy vector triplet (HVT) signal selection efficiency in the different signal regions for the generator level events and the correspondingly adapted event selection is shown in Appendix C.22. The two-Higgs doublet model (2HDM) signal selection efficiency is shown in Appendix C.23. The selection efficiency is close to what is computed on reconstruction level and shown in Figs. 4.5 to 4.7 which allows for the assumption that no significant reconstruction related bias impacts on the evaluation of the signal theory uncertainties.

Appendices C.24 to C.30 shows the impact on the reconstruction efficiency due to the studied sources of theoretical uncertainties as a function of the resonance mass. Since the signal distribution is generally localized in a relative small region of $m_{\mathrm{(T,)Vh}}$, the normalization component is shown here. Furthermore, Appendices C.31 to C.35 shows the impact on the signal $m_{\mathrm{(T,)Vh}}$ distributions due to the theoretical uncertainties.

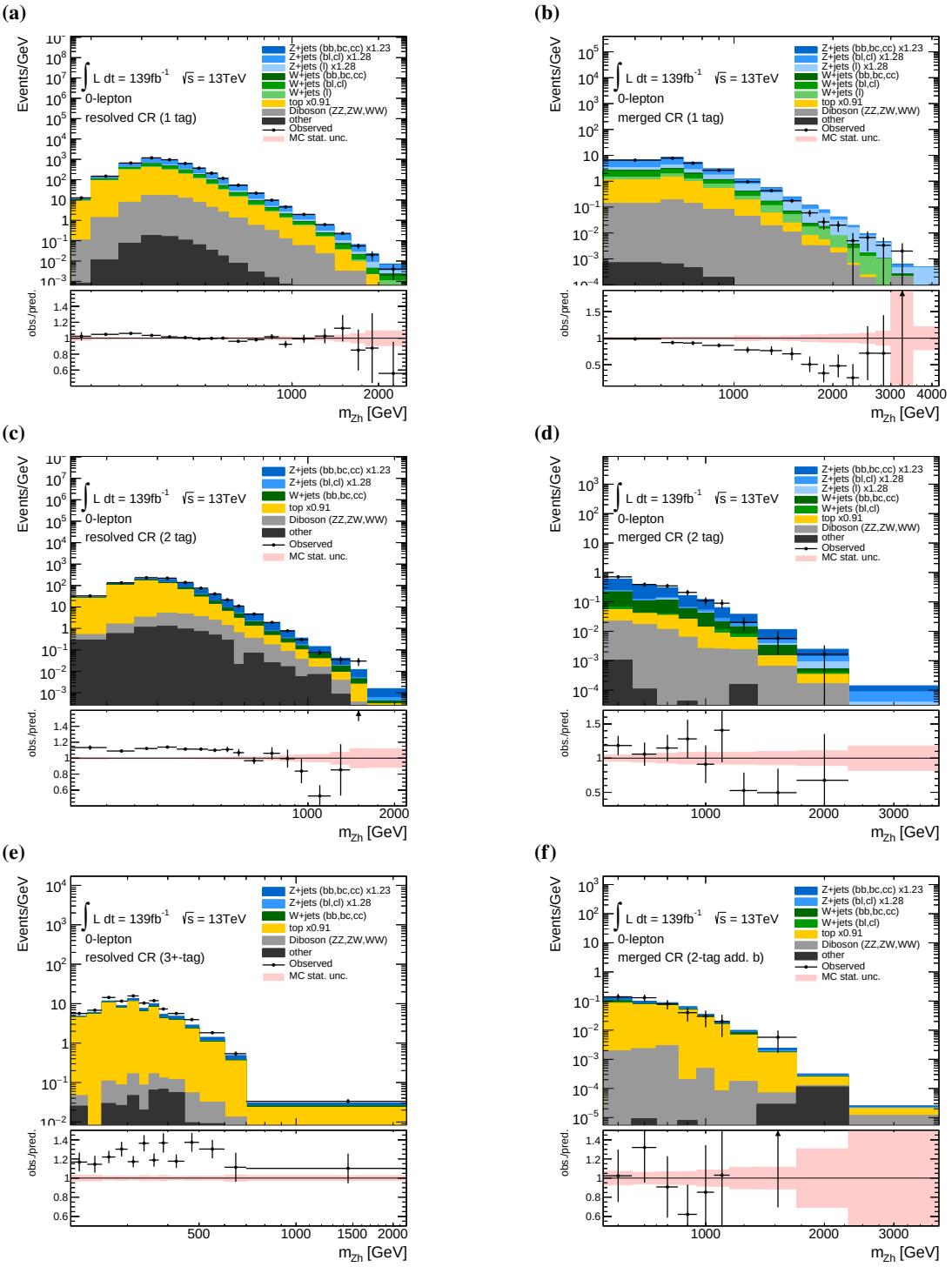

Figure C.1: Expected (pre-fit) and observed distributions m_{Zh}-distribution in the **0-lepton channel $m_{jj/J}$-sideband CRs** for (left) the *resolved* regions and (right) the *merged* regions. The plots in the three rows show different b-tagging multiplicities in increasing order with 1 b-tag, 2 b-tag and 3+ b-tag (2 b-tag with additional b-tag) for the *resolved* (*merged*) regions. The uncertainties cover only statistical uncertainties of data (black error bars) and of MC samples (red shade).

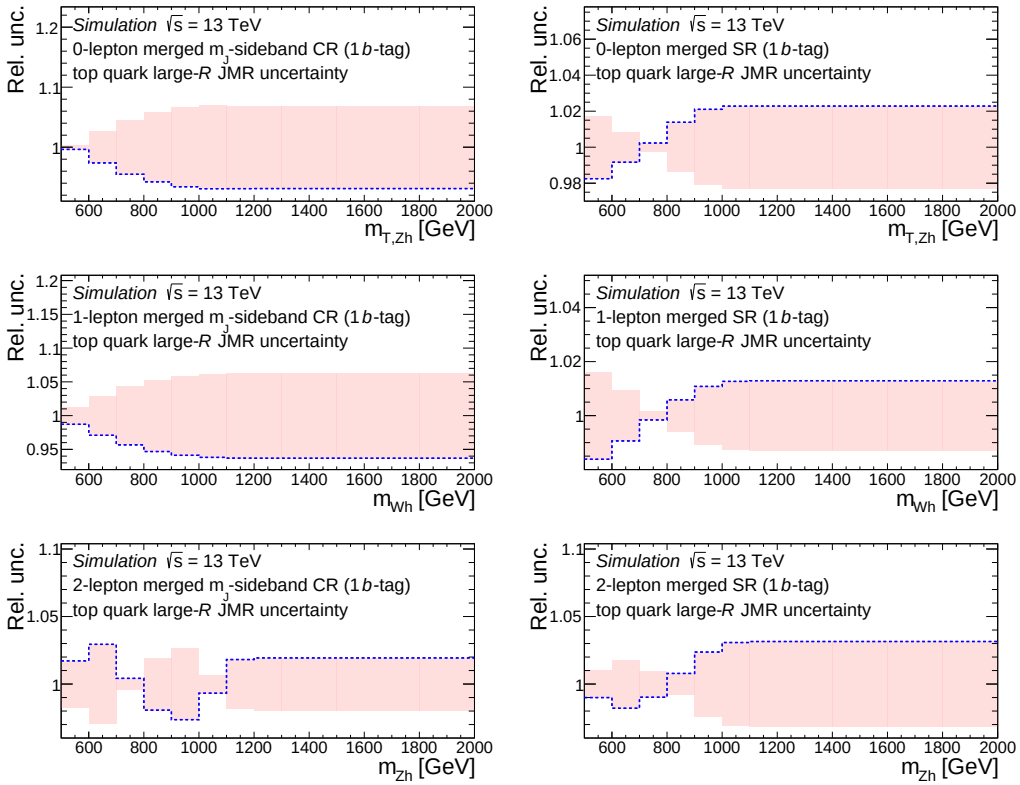

Figure C.2: The relative uncertainty on the $m_{(\mathrm{T},)\mathrm{Vh}}$ distribution of (left) the m_J-sideband CRs and (right) the signal regions of the top quark backgrounds due to the uncertainty on the large-R jet mass resolution (JMR).

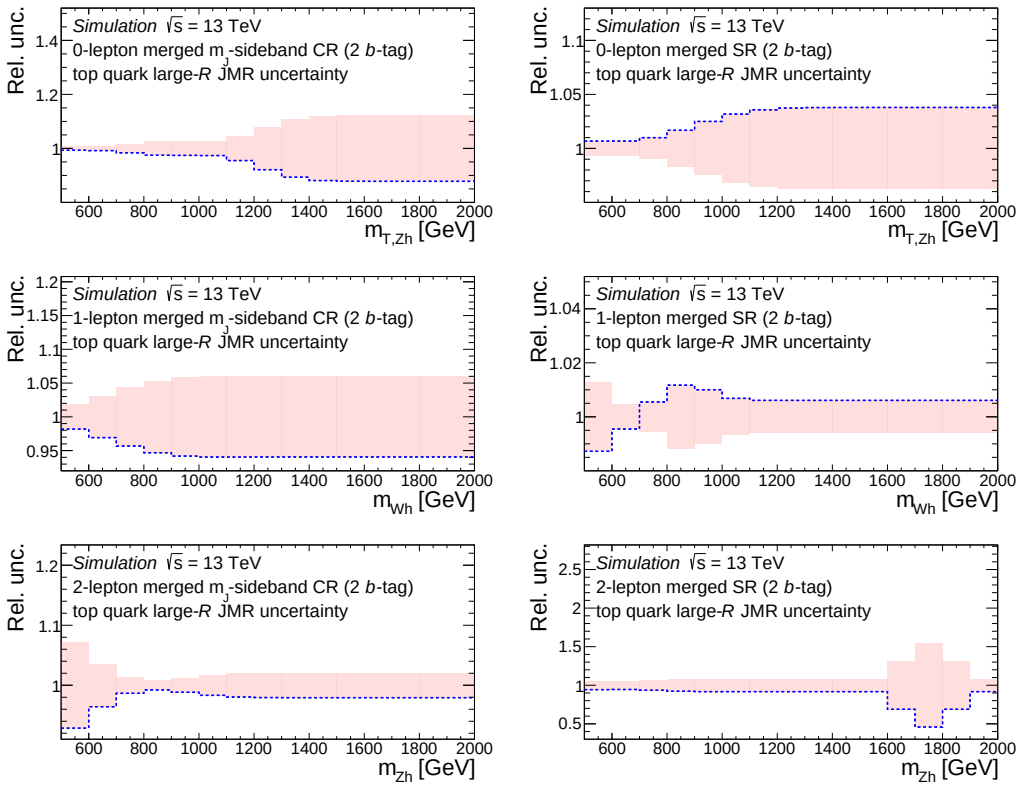

Figure C.3: The relative uncertainty on the $m_{(\mathrm{T},)\mathrm{Vh}}$ distribution of (left) the m_J-sideband CRs and (right) the signal regions of the top quark backgrounds due to the uncertainty on the large-R jet mass resolution (JMR).

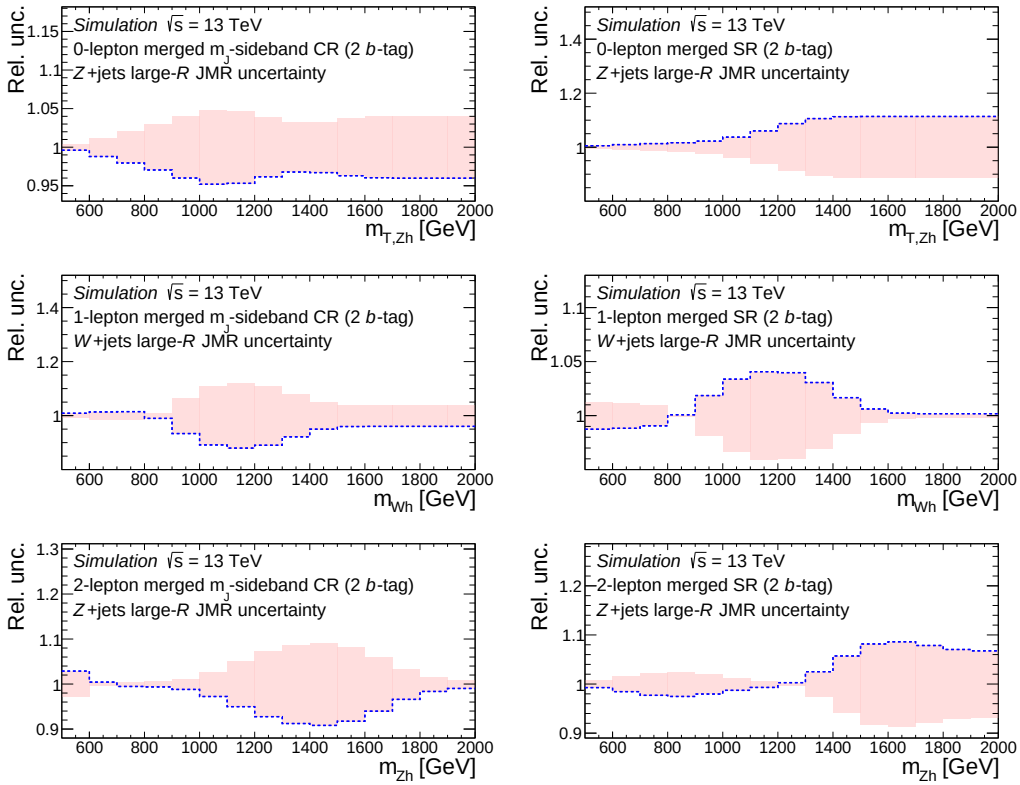

Figure C.4: The relative uncertainty on the $m_{(\mathrm{T},)\mathrm{Vh}}$ distribution of (left) the m_J-sideband CRs and (right) the signal regions of the V+jets backgrounds due to the uncertainty on the large-R jet mass resolution (JMR).

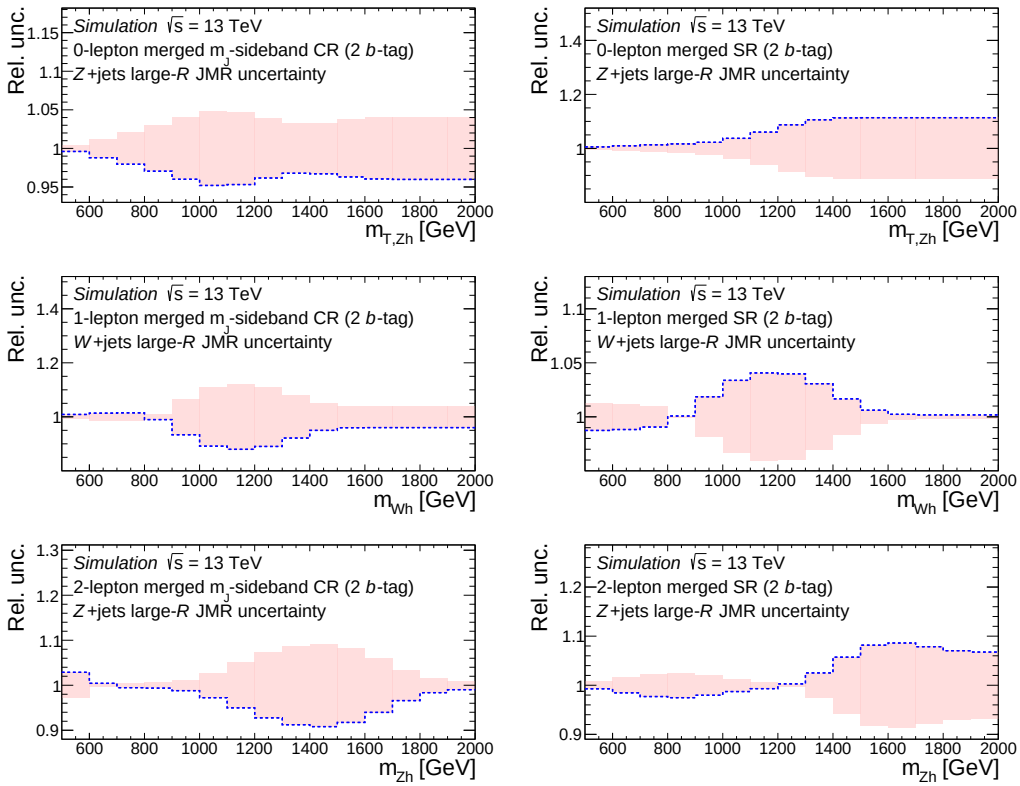

Figure C.5: The relative uncertainty on the $m_{(\mathrm{T},)\mathrm{Vh}}$ distribution of (left) the m_J-sideband CRs and (right) the signal regions of other minor backgrounds (VV, Vh) backgrounds due to the uncertainty on the large-R jet mass resolution (JMR).

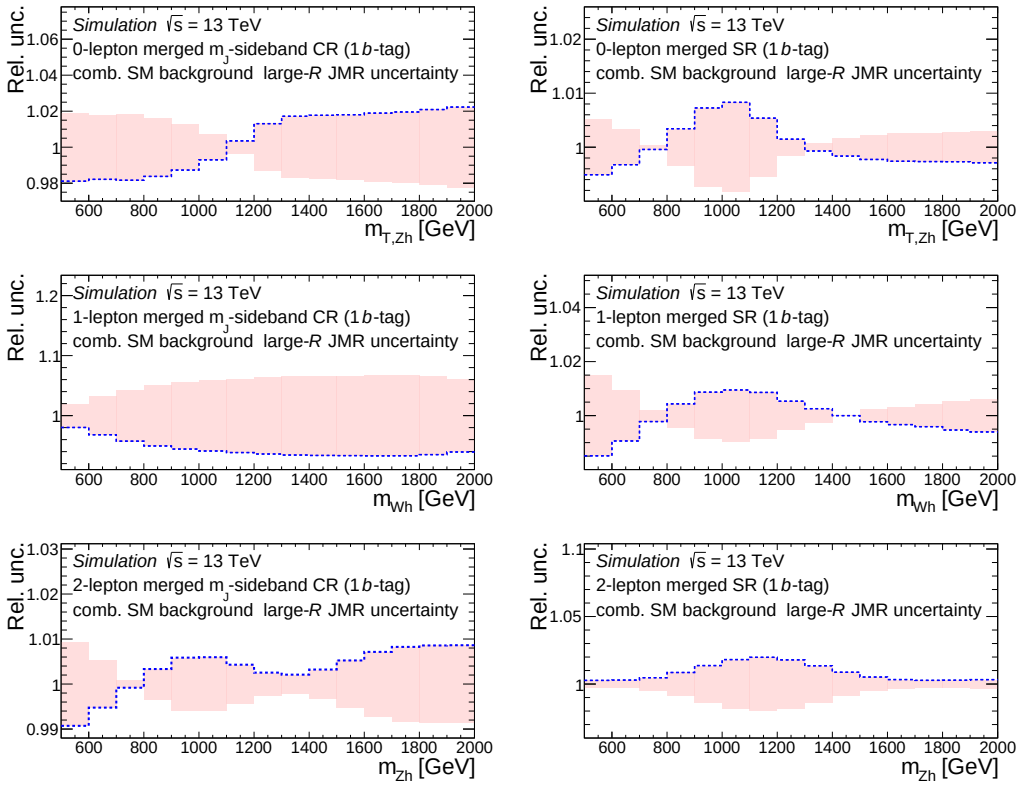

Figure C.6: The relative uncertainty on the $m_{(\mathrm{T},)\mathrm{Vh}}$ distribution of (left) the m_J-sideband CRs and (right) the signal regions of combined SM background due to the uncertainty on the large-R jet mass resolution (JMR). 1 b tag region

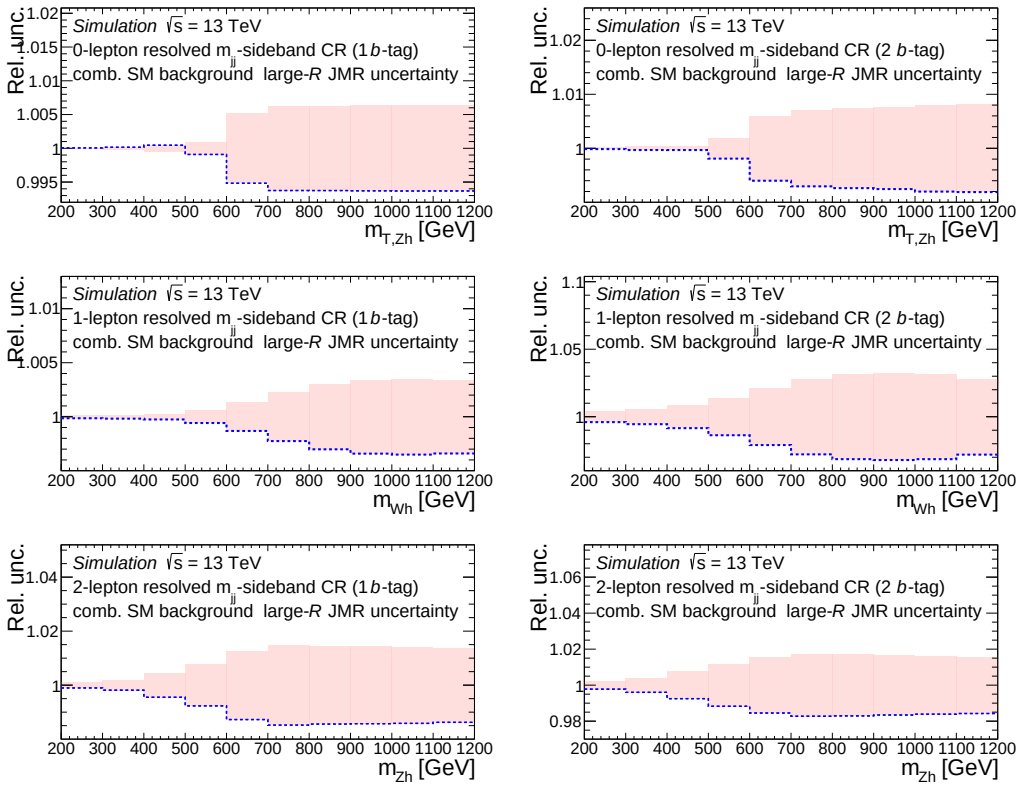

Figure C.7: The relative uncertainty on the $m_{(\mathrm{T},)\mathrm{Vh}}$ distribution of the (resolved) m_{jj}-sideband CRs with (left) 1 b-tag and (right) 2 b-tag of the combined SM backgrounds due to the uncertainty on the large-R jet mass resolution (JMR). resolved $m_{jj/J}$-sideband CRs

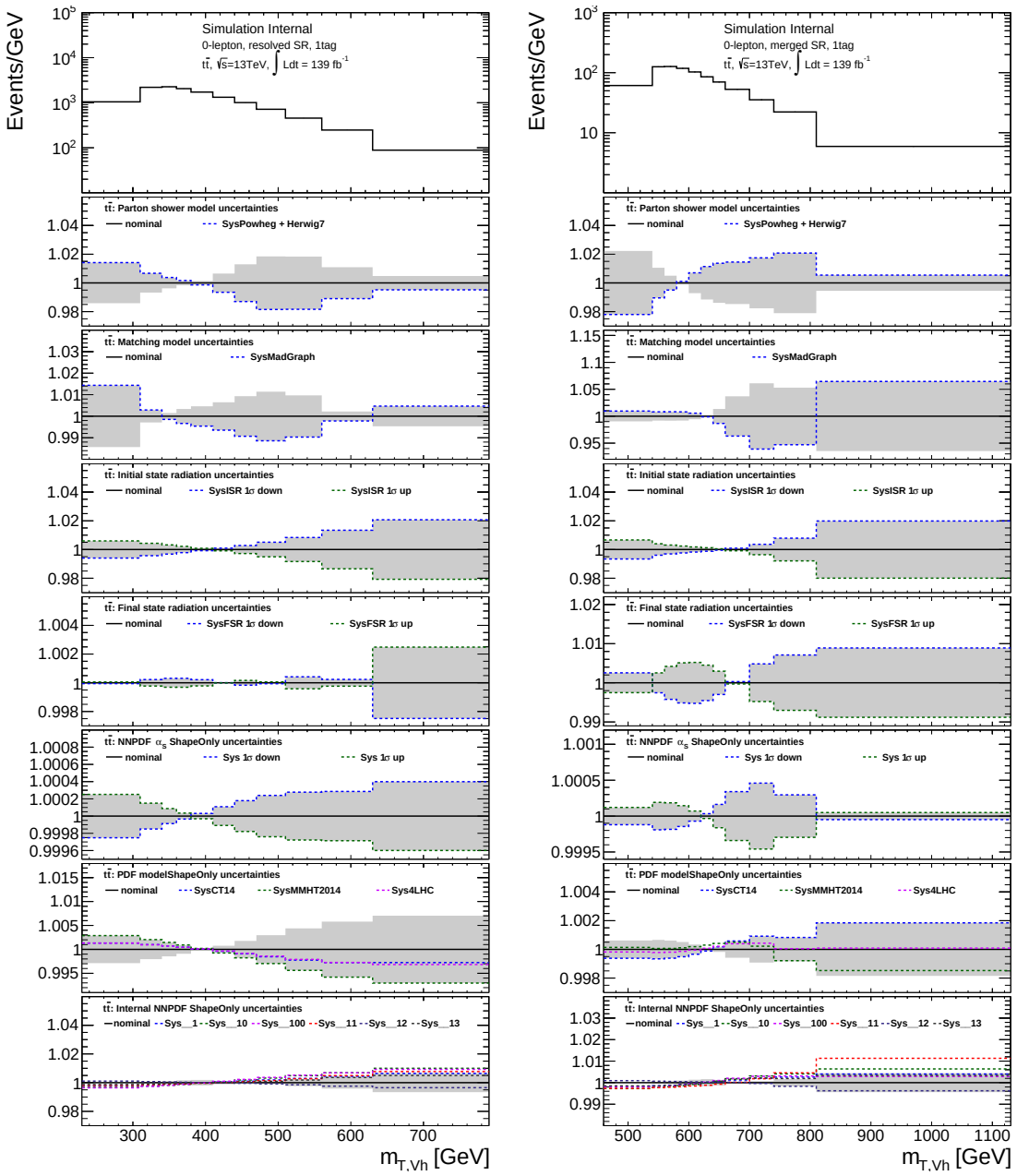

Figure C.8: Expected m_{VH}-distributions of $t\bar{t}$ background components in the **0-lepton 1 *b*-tag (left) *resolved* and (right) *merged* signal regions** as predicted by Powheg interfaced with Pythia 8 with an integrated luminosity of 139 fb^{-1}(nominal). The multiple ratio panels show the shape uncertainties without normalization component for uncertainties originating from theoretical uncertainties. The first row of the ratio panels show the *parton shower (PS) model* uncertainty; the second row shows *matrix element (ME) matching model* uncertainties; third and fourth row show *initial-state radiation (ISR) and final-state radiation (FSR)* uncertainties; the three bottom rows show the uncertainty of the parton density function (PDF) uncertainties and the NNPDF-incorporated α_S. The gray shades in each ratio panel indicate the total uncertainty as used in the final statistical interpretation of data.

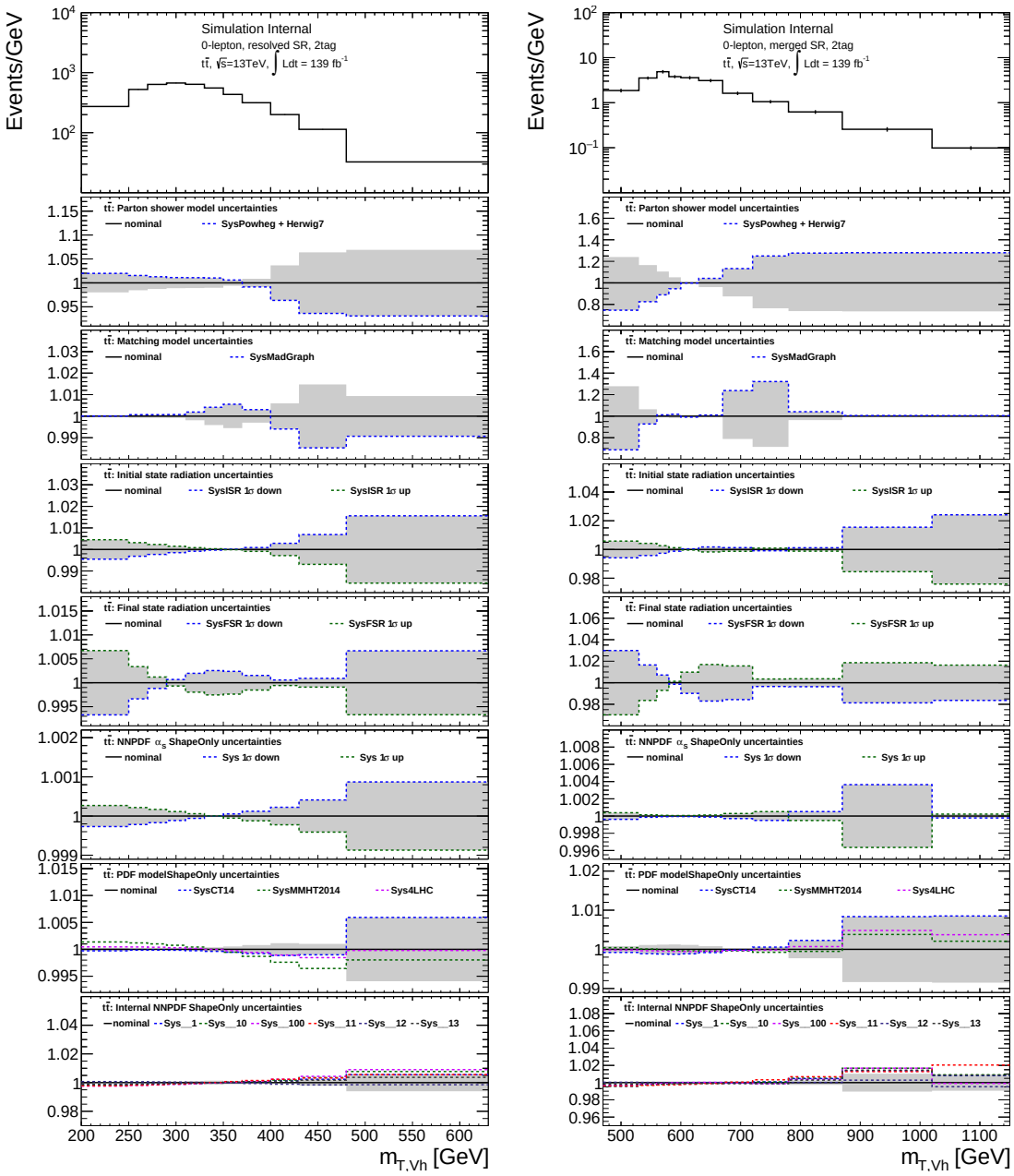

Figure C.9: Expected m_{VH}-distributions of $t\bar{t}$ background components in the **0-lepton 2 *b*-tag (left) *resolved* and (right) *merged* signal regions** as predicted by POWHEG interfaced with PYTHIA 8 with an integrated luminosity of 139 fb^{-1}(nominal). The multiple ratio panels show the shape uncertainties without normalization component for uncertainties originating from theoretical uncertainties. The first row of the ratio panels show the *PS model* uncertainty; the second row shows *ME matching model* uncertainties; third and fourth row show *ISR and FSR* uncertainties; the three bottom rows show the uncertainty of the PDF uncertainties and the NNPDF-incorporated α_S. The gray shades in each ratio panel indicate the total uncertainty as used in the final statistical interpretation of data.

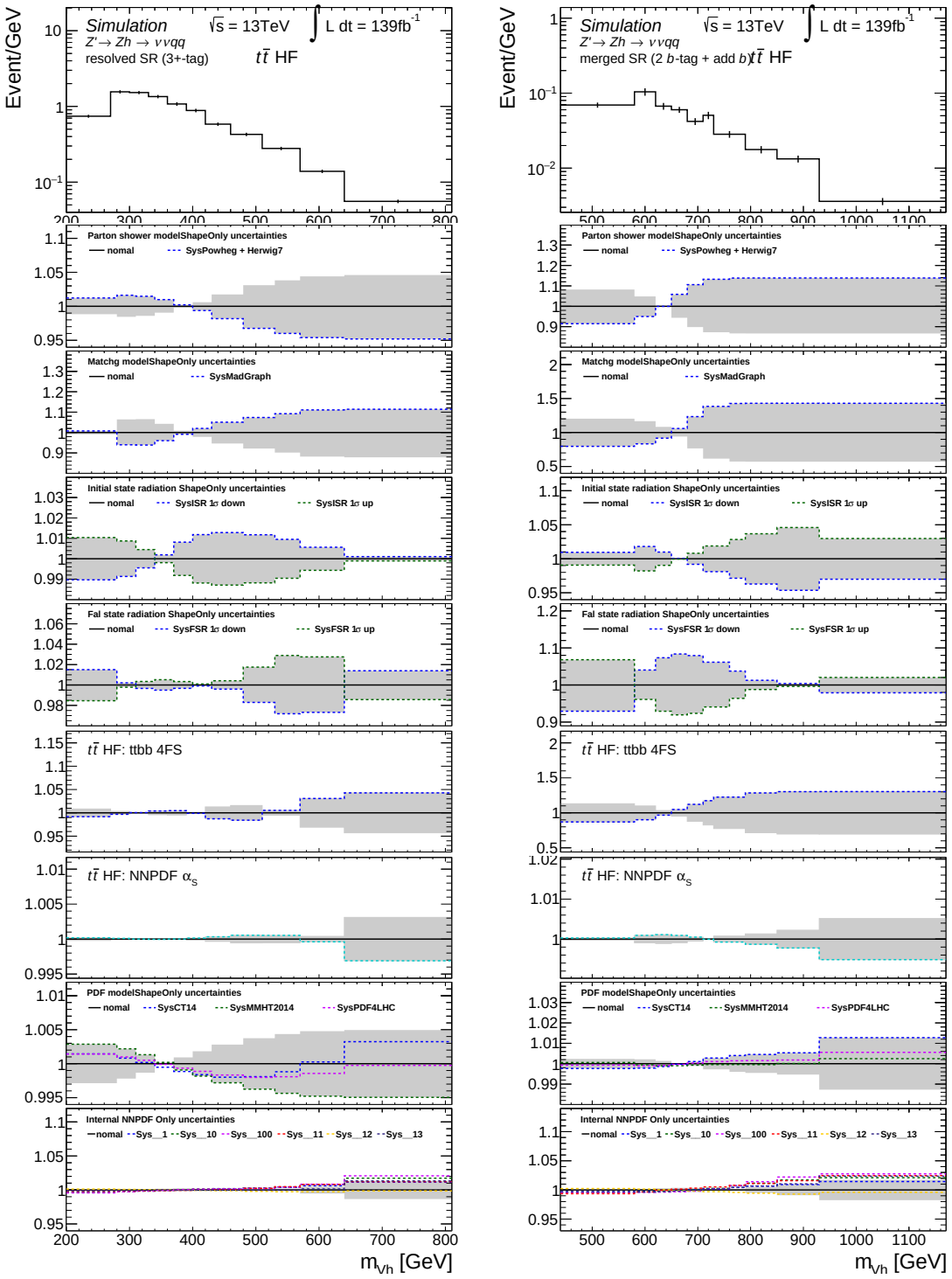

Figure C.10: Expected m_{VH}-distributions of $t\bar{t}$+HF background components in the **0-lepton bbA mode sensitive (left) *resolved* and (right) *merged* signal regions** as predicted by POWHEG interfaced with PYTHIA 8 with an integrated luminosity of 139 fb^{-1}(nominal). The multiple ratio panels show the shape uncertainties without normalization component for uncertainties originating from theoretical uncertainties. The first row of the ratio panels show the *PS model* uncertainty; the second row shows *ME matching model* uncertainties; third and fourth row show *ISR and FSR* uncertainties; The fifth row shows uncertainties due to the $t\bar{t}b\bar{b}$ *4-flavor-scheme* uncertainty. the three bottom rows show the uncertainty of the PDF uncertainties and the NNPDF-incorporated α_S. The gray shades in each ratio panel indicate the total uncertainty as used in the final statistical interpretation of data. T

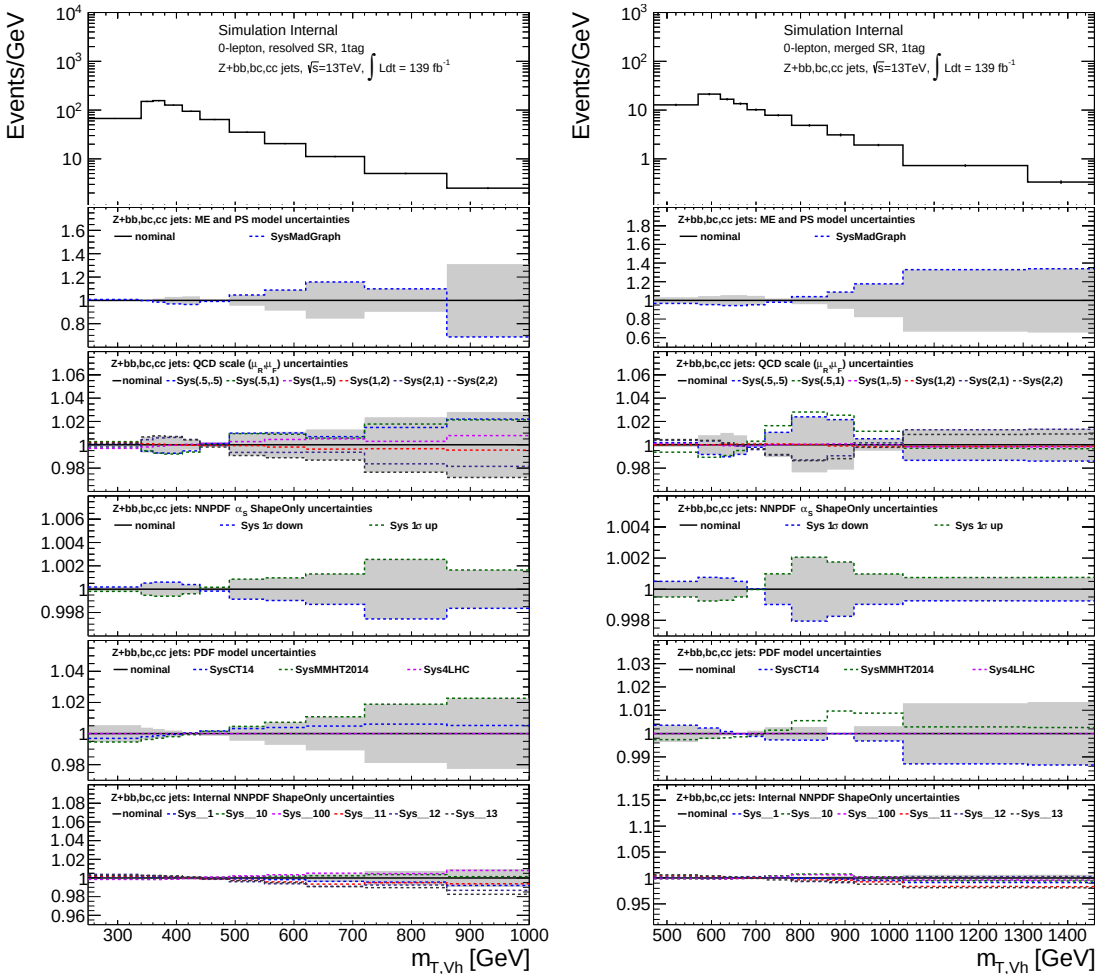

Figure C.11: Expected $m_{\mathrm{T,Zh}}$-distributions of Z+jets (bb,bc,cc) background components in the **0-lepton 1 *b*-tag (left) *resolved* and (right) *merged* signal regions** as predicted by SHERPA with an integrated luminosity of 139 fb^{-1}(nominal). Distribution of the nominal predictions of Z+jets (bb,bc,cc) background in the (left) *resolved* and (right) *merged* signal regions with 2 *b*-tags. The multiple ratio panels show the shape uncertainties without normalization component for uncertainties originating from theoretical uncertainties. The row of the ratio panels show the *PS model* uncertainty, the second *QCD-scale* uncertainties and the three bottom rows show the PDF connected uncertainties. The gray shades in each ratio panel indicate the total uncertainty as used in the final statistical interpretation of data.

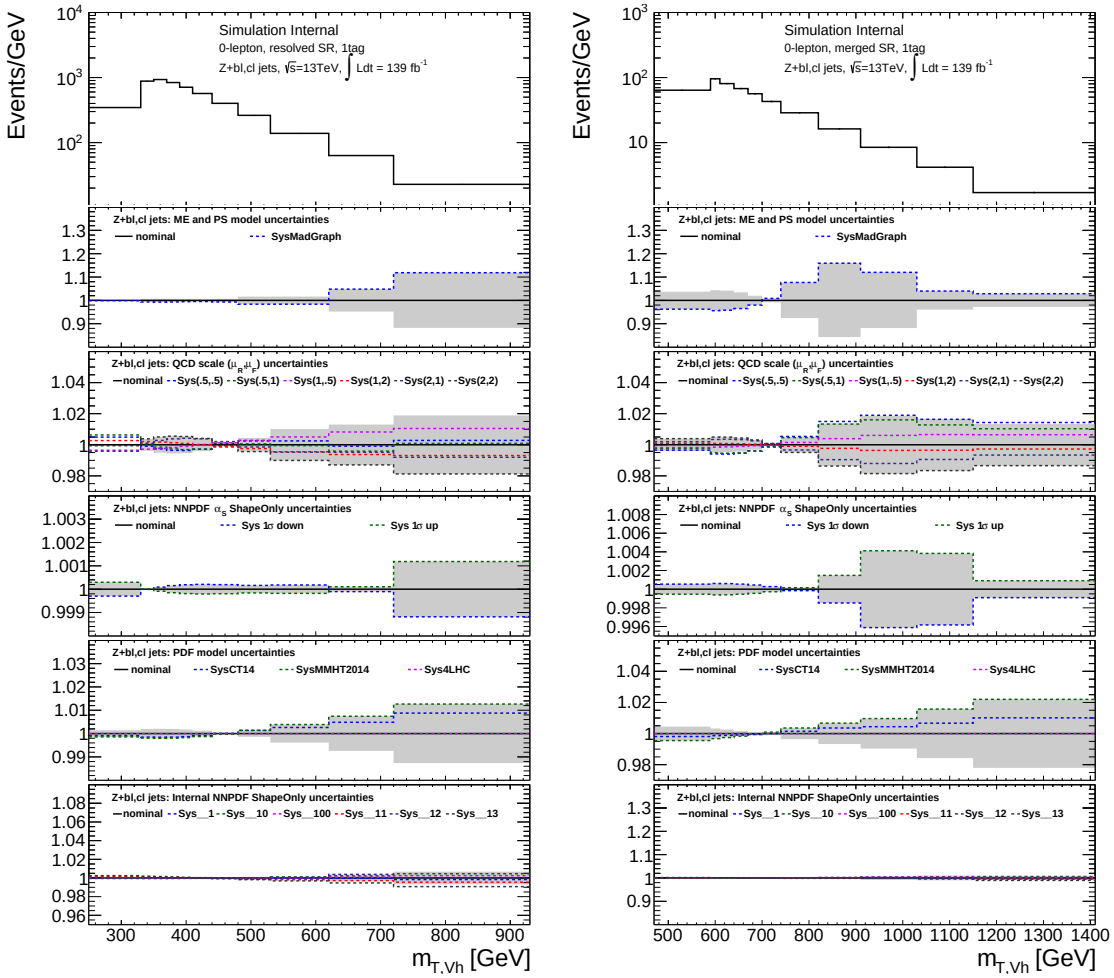

Figure C.12: Expected $m_{\mathrm{T,Zh}}$-distributions of Z+jets (bl,cl) background components in the **0-lepton 1 *b*-tag (left) *resolved* and (right) *merged* signal regions** as predicted by SHERPA with an integrated luminosity of 139 fb^{-1}(nominal). Distribution of the nominal predictions of Z+jets (bl,cl) background in the (left) *resolved* and (right) *merged* signal regions with 2 *b*-tags. The multiple ratio panels show the shape uncertainties without normalization component for uncertainties originating from theoretical uncertainties. The row of the ratio panels show the *PS model* uncertainty, the second *QCD-scale* uncertainties and the three bottom rows show the PDF connected uncertainties. The gray shades in each ratio panel indicate the total uncertainty as used in the final statistical interpretation of data.

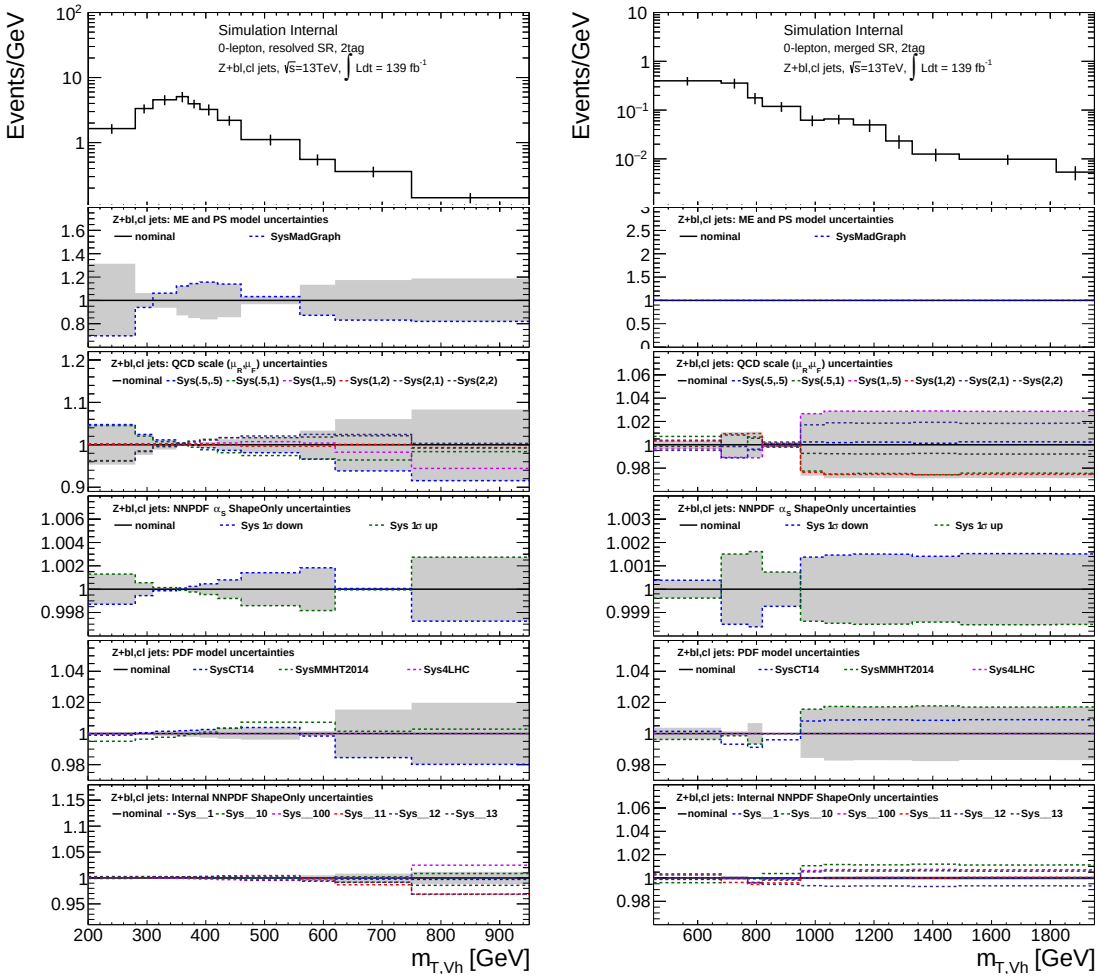

Figure C.13: Expected $m_{\mathrm{T,Zh}}$-distributions of Z+jets (bl,cl) background components in the **0-lepton 2 *b*-tag (left) *resolved* and (right) *merged* signal regions** as predicted by SHERPA with an integrated luminosity of 139 fb^{-1}(nominal). Distribution of the nominal predictions of Z+jets (bl,cl) background in the (left) *resolved* and (right) *merged* signal regions with 2 *b*-tags. The multiple ratio panels show the shape uncertainties without normalization component for uncertainties originating from theoretical uncertainties. The row of the ratio panels show the *PS model* uncertainty, the second *QCD-scale* uncertainties and the three bottom rows show the PDF connected uncertainties. The gray shades in each ratio panel indicate the total uncertainty as used in the final statistical interpretation of data.

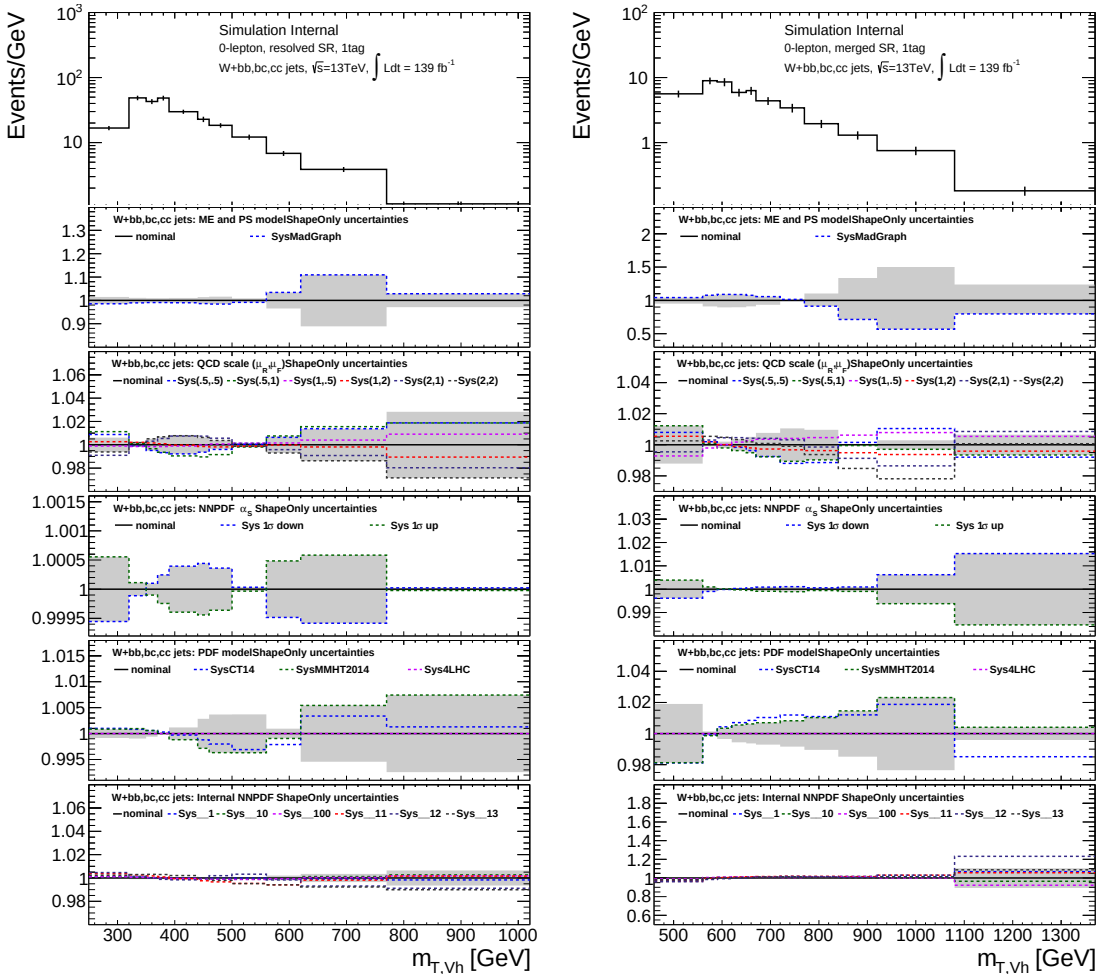

Figure C.14: Expected $m_{\mathrm{T,Zh}}$-distributions of W+jets (bb,bc,cc) background components in the **0-lepton 1 *b*-tag (left) *resolved* and (right) *merged* signal regions** as predicted by SHERPA with an integrated luminosity of 139 fb^{-1}(nominal). Distribution of the nominal predictions of W+jets (bb,bc,cc) background in the (left) *resolved* and (right) *merged* signal regions with 2 *b*-tags. The multiple ratio panels show the shape uncertainties without normalization component for uncertainties originating from theoretical uncertainties. The row of the ratio panels show the *PS model* uncertainty, the second *QCD-scale* uncertainties and the three bottom rows show the PDF connected uncertainties. The gray shades in each ratio panel indicate the total uncertainty as used in the final statistical interpretation of data.

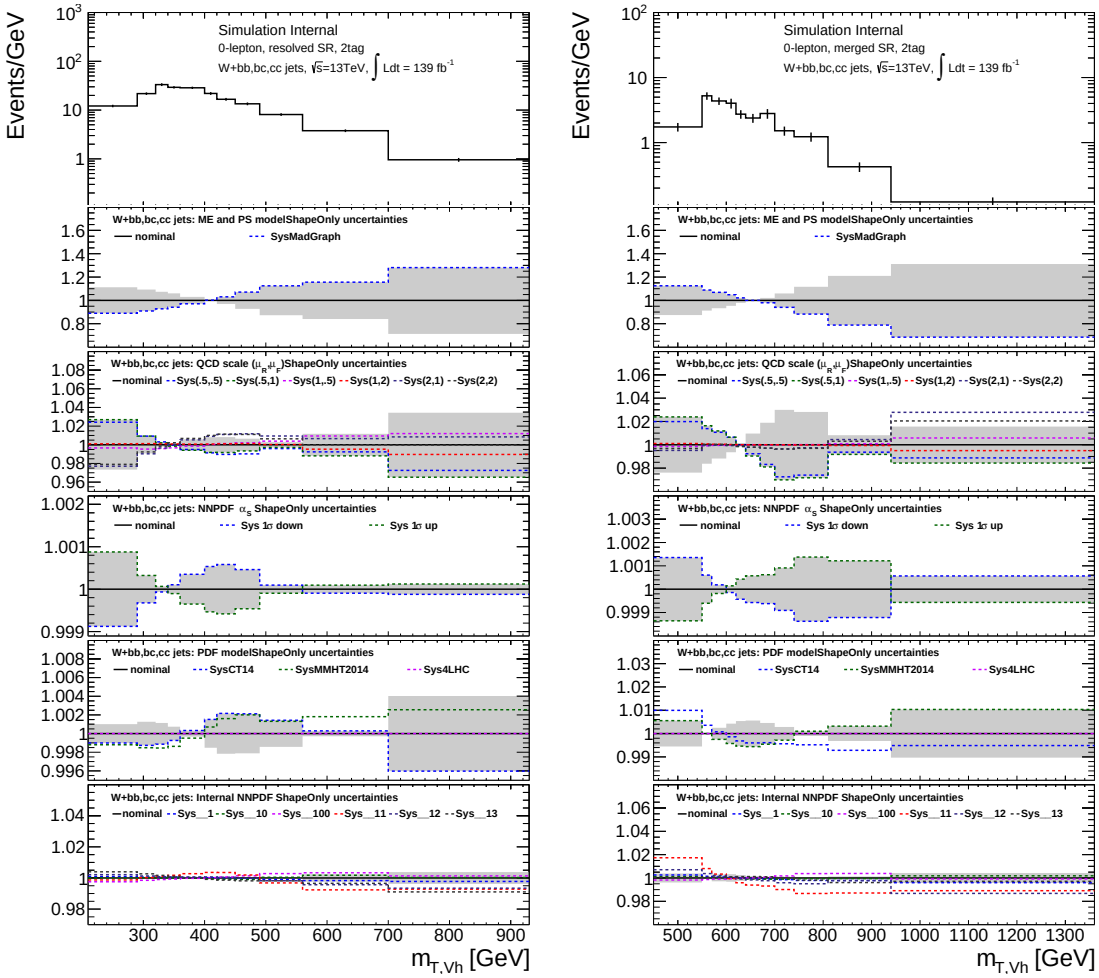

Figure C.15: Expected $m_{\mathrm{T,Zh}}$-distributions of W+jets (bb,bc,cc) background components in the **0-lepton 2 *b*-tag (left) *resolved* and (right) *merged* signal regions** as predicted by SHERPA with an integrated luminosity of 139 fb^{-1}(nominal). Distribution of the nominal predictions of W+jets (bb,bc,cc) background in the (left) *resolved* and (right) *merged* signal regions with 2 *b*-tags. The multiple ratio panels show the shape uncertainties without normalization component for uncertainties originating from theoretical uncertainties. The row of the ratio panels show the *PS model* uncertainty, the second *QCD-scale* uncertainties and the three bottom rows show the PDF connected uncertainties. The gray shades in each ratio panel indicate the total uncertainty as used in the final statistical interpretation of data.

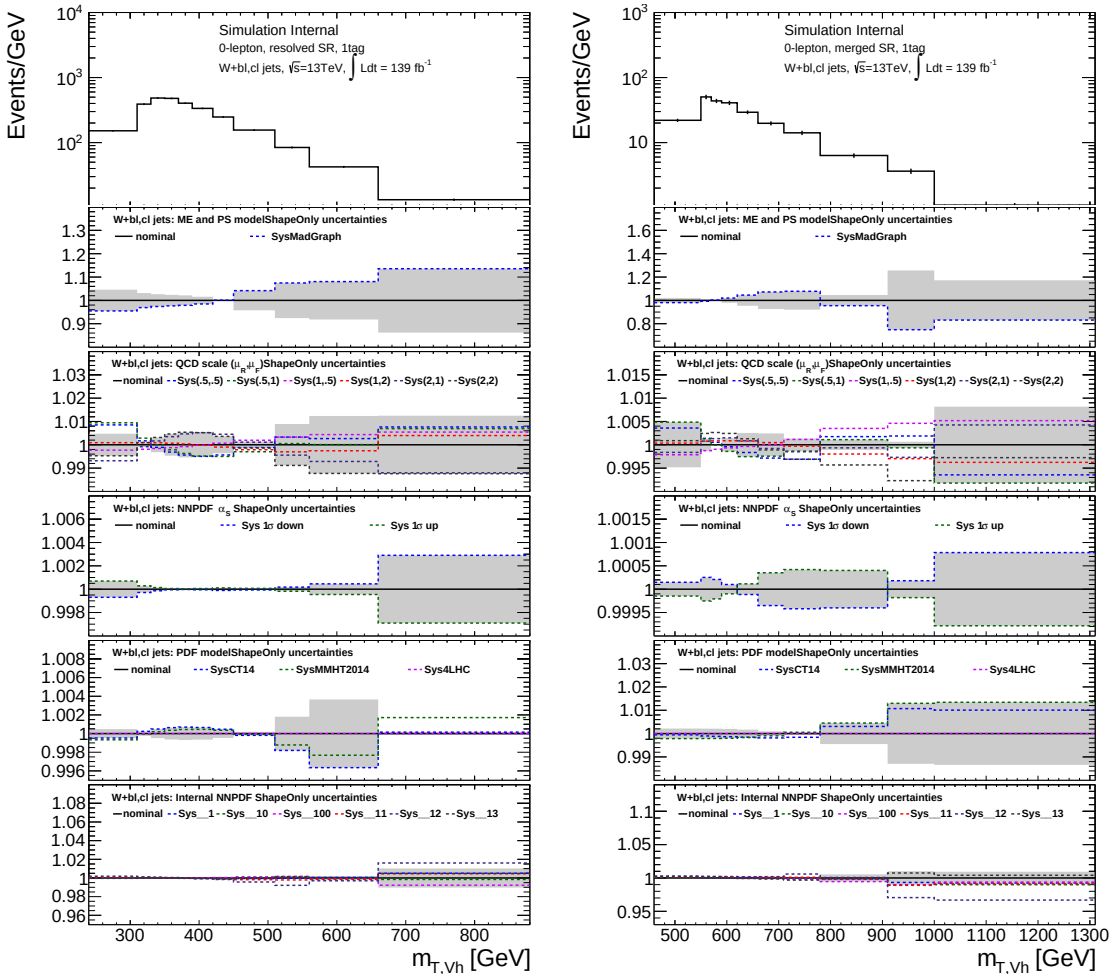

Figure C.16: Expected $m_{\mathrm{T,Zh}}$-distributions of W+jets (bl,cl) background components in the **0-lepton 1 *b*-tag (left) *resolved* and (right) *merged* signal regions** as predicted by SHERPA with an integrated luminosity of 139 fb^{-1}(nominal). Distribution of the nominal predictions of W+jets (bl,cl) background in the (left) *resolved* and (right) *merged* signal regions with 2 *b*-tags. The multiple ratio panels show the shape uncertainties without normalization component for uncertainties originating from theoretical uncertainties. The row of the ratio panels show the *PS model* uncertainty, the second *QCD-scale* uncertainties and the three bottom rows show the PDF connected uncertainties. The gray shades in each ratio panel indicate the total uncertainty as used in the final statistical interpretation of data.

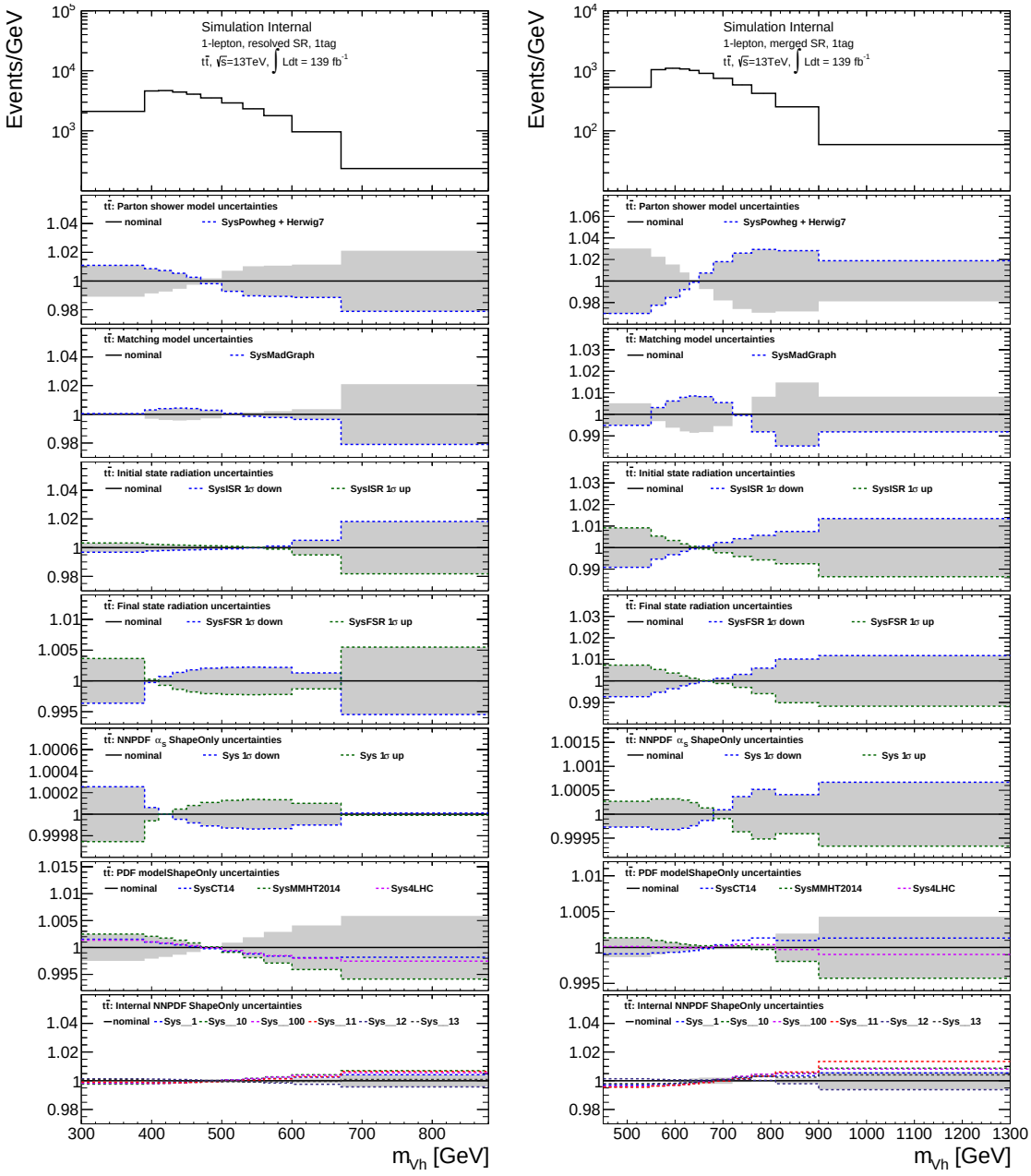

Figure C.17: Expected m_{VH}-distributions of $t\bar{t}$ background components in the **1-lepton 1 *b*-tag (left) *resolved* and (right) *merged* signal regions** as predicted by POWHEG interfaced with PYTHIA 8 with an integrated luminosity of 139 fb^{-1}(nominal). The multiple ratio panels show the shape uncertainties without normalization component for uncertainties originating from theoretical uncertainties. The first row of the ratio panels show the *PS model* uncertainty; the second row shows *ME matching model* uncertainties; third and fourth row show *ISR and FSR* uncertainties; the three bottom rows show the uncertainty of the PDF uncertainties and the NNPDF-incorporated α_S. The gray shades in each ratio panel indicate the total uncertainty as used in the final statistical interpretation of data.

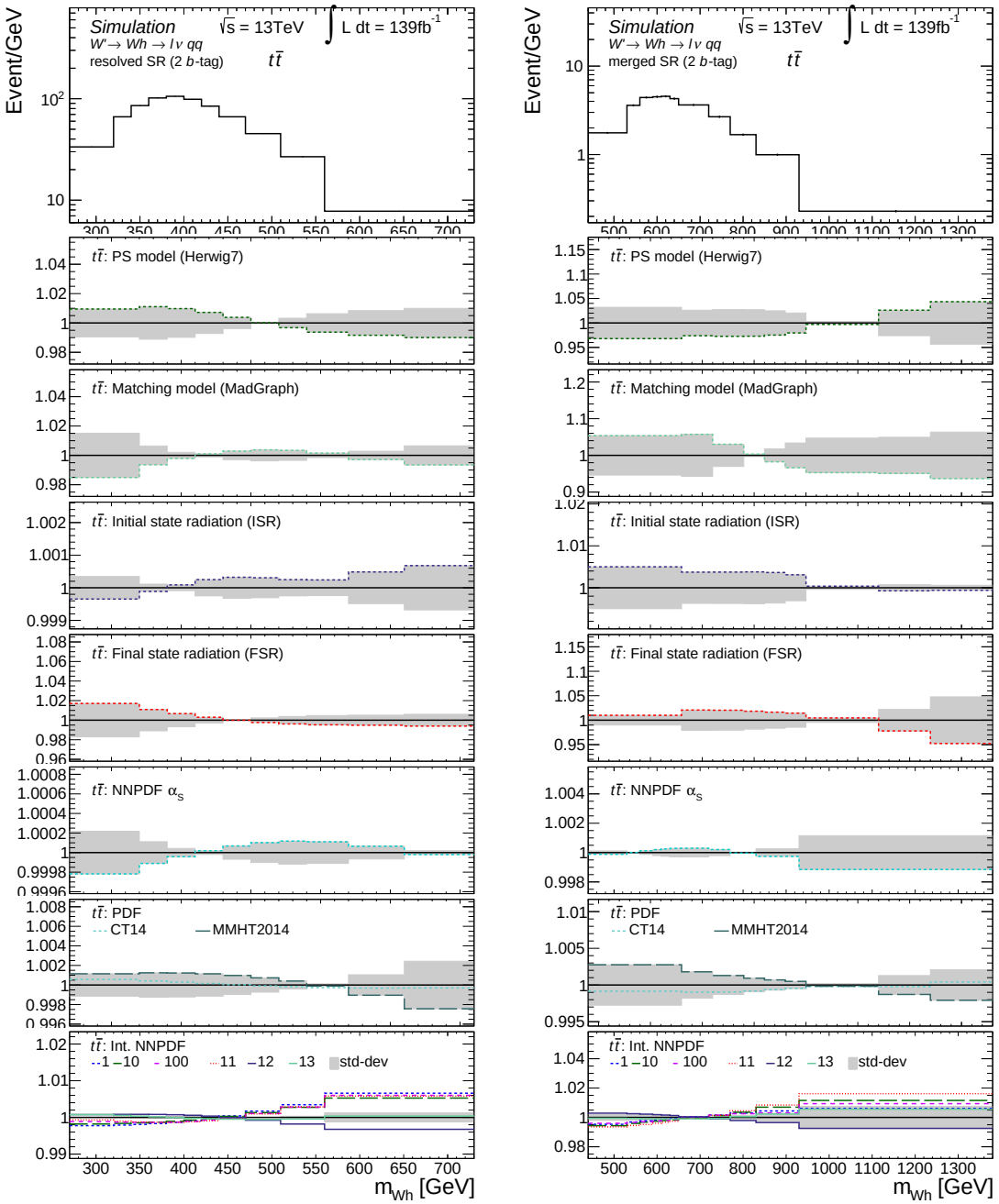

Figure C.18: Expected m_{VH}-distributions of $t\bar{t}$ background components in the **1-lepton 2 b-tag (left)** ***resolved*** **and (right)** ***merged*** **signal regions** as predicted by Powheg interfaced with Pythia 8 with an integrated luminosity of 139 fb^{-1}(nominal). The multiple ratio panels show the shape uncertainties without normalization component for uncertainties originating from theoretical uncertainties. The first row of the ratio panels show the *PS model* uncertainty; the second row shows *ME matching model* uncertainties; third and fourth row show *ISR and FSR* uncertainties; the three bottom rows show the uncertainty of the PDF uncertainties and the NNPDF-incorporated α_S. The gray shades in each ratio panel indicate the total uncertainty as used in the final statistical interpretation of data.

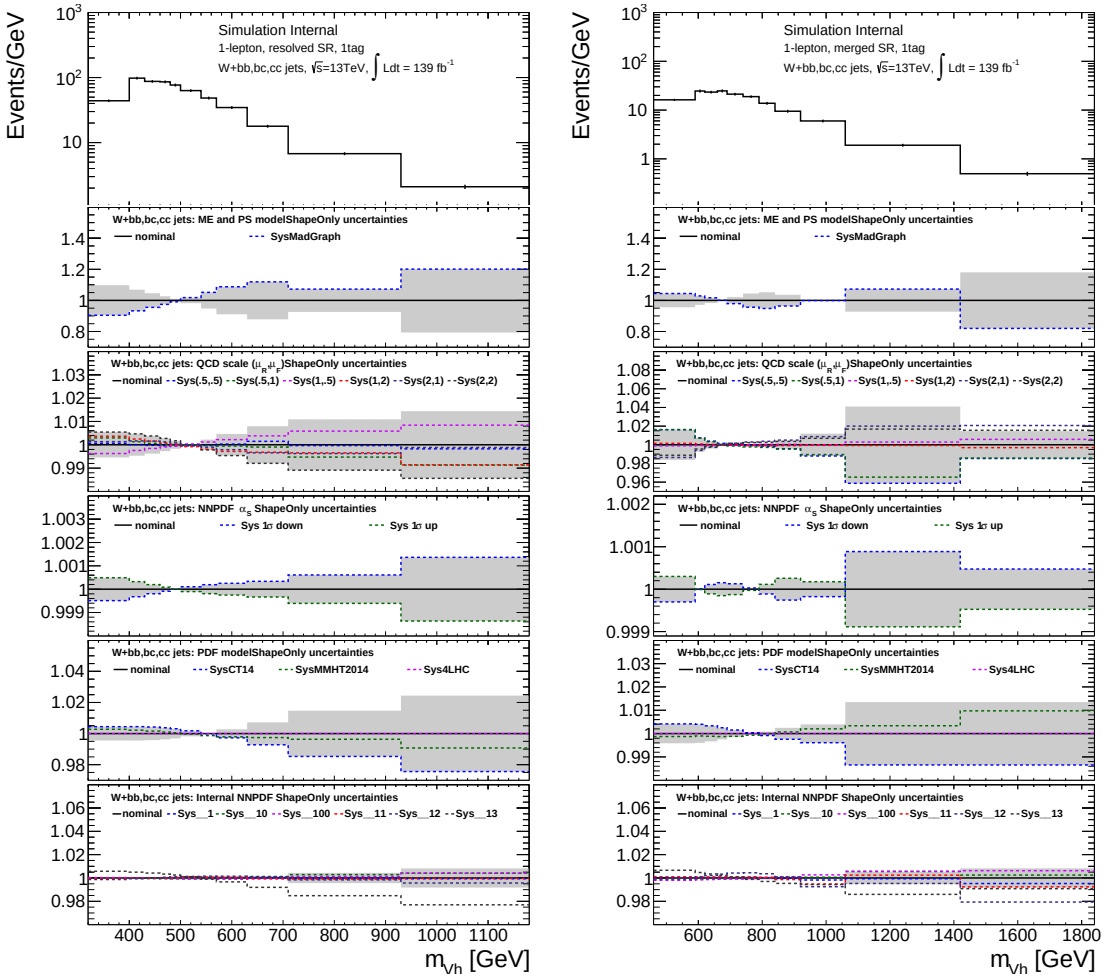

Figure C.19: Expected $m_{\mathrm{T,Zh}}$-distributions of W+jets (bb,bc,cc) background components in the **1-lepton 1 *b*-tag (left) *resolved* and (right) *merged* signal regions** as predicted by SHERPA with an integrated luminosity of 139 fb^{-1}(nominal). Distribution of the nominal predictions of W+jets (bb,bc,cc) background in the (left) *resolved* and (right) *merged* signal regions with 2 *b*-tags. The multiple ratio panels show the shape uncertainties without normalization component for uncertainties originating from theoretical uncertainties. The row of the ratio panels show the *PS model* uncertainty, the second *QCD-scale* uncertainties and the three bottom rows show the PDF connected uncertainties. The gray shades in each ratio panel indicate the total uncertainty as used in the final statistical interpretation of data.

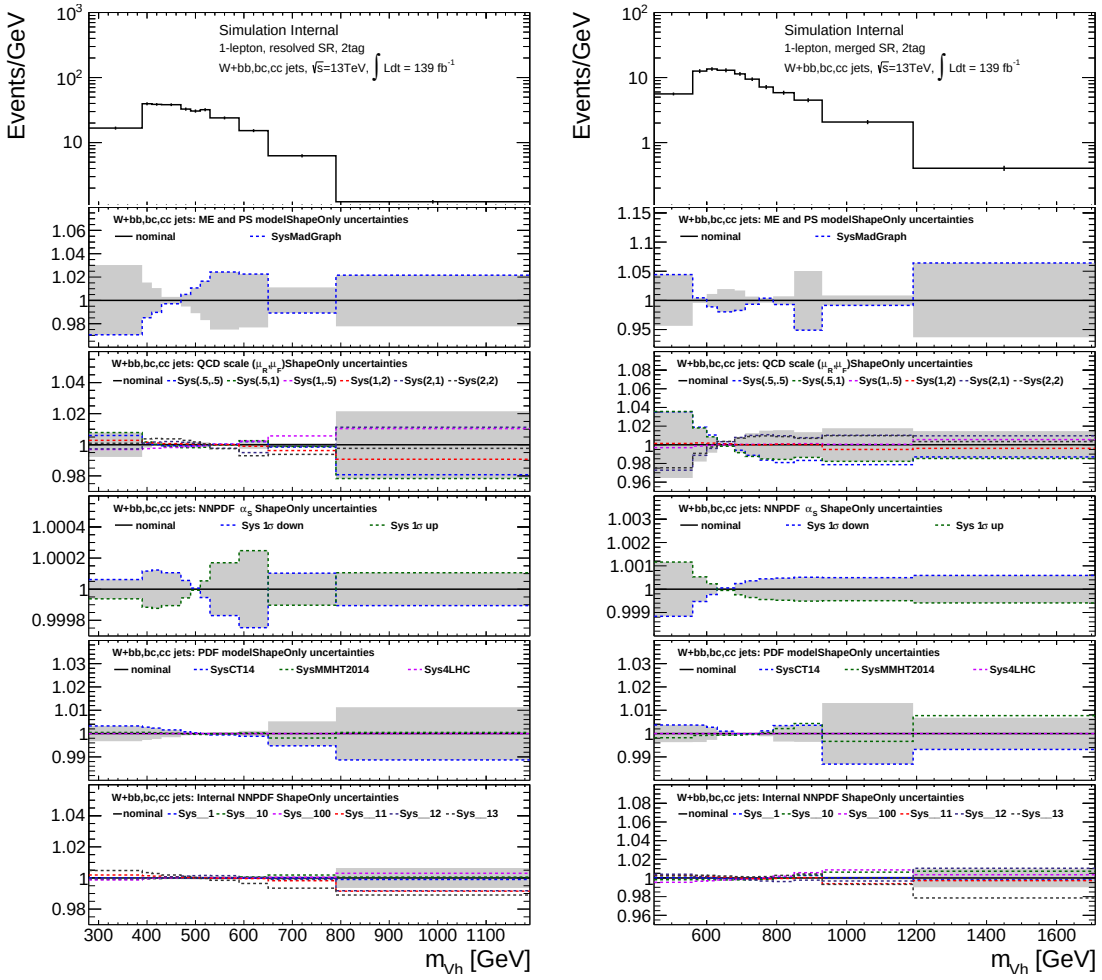

Figure C.20: Expected $m_{\mathrm{T,Zh}}$-distributions of W+jets (bb,bc,cc) background components in the **1-lepton 2 *b*-tag (left) *resolved* and (right) *merged* signal regions** as predicted by SHERPA with an integrated luminosity of 139 fb^{-1}(nominal). Distribution of the nominal predictions of W+jets (bb,bc,cc) background in the (left) *resolved* and (right) *merged* signal regions with 2 *b*-tags. The multiple ratio panels show the shape uncertainties without normalization component for uncertainties originating from theoretical uncertainties. The row of the ratio panels show the *PS model* uncertainty, the second *QCD-scale* uncertainties and the three bottom rows show the PDF connected uncertainties. The gray shades in each ratio panel indicate the total uncertainty as used in the final statistical interpretation of data.

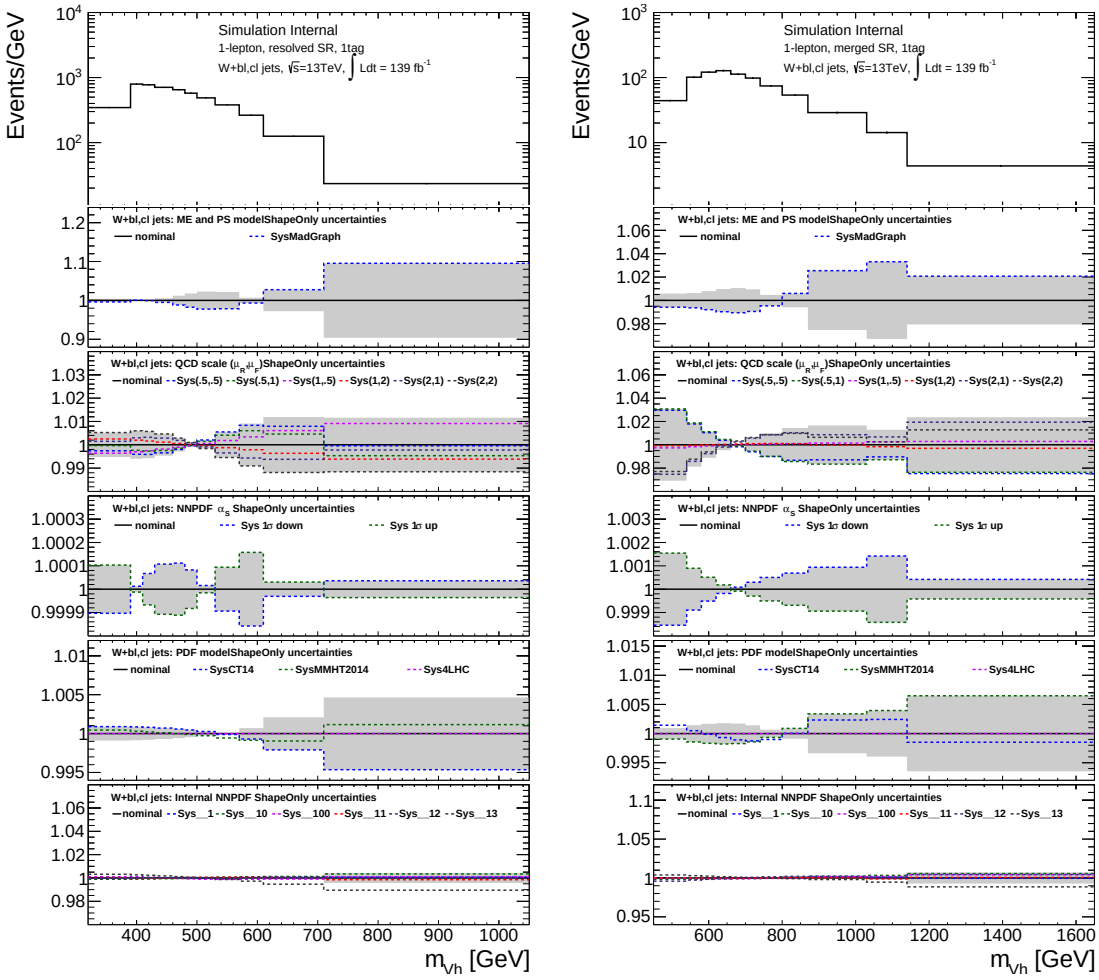

Figure C.21: Expected $m_{\mathrm{T,Zh}}$-distributions of W+jets (bl,cl) background components in the **1-lepton 1 *b*-tag (left) *resolved* and (right) *merged* signal regions** as predicted by SHERPA with an integrated luminosity of 139 fb^{-1}(nominal). Distribution of the nominal predictions of W+jets (bl,cl) background in the (left) *resolved* and (right) *merged* signal regions with 2 *b*-tags. The multiple ratio panels show the shape uncertainties without normalization component for uncertainties originating from theoretical uncertainties. The row of the ratio panels show the *PS model* uncertainty, the second *QCD-scale* uncertainties and the three bottom rows show the PDF connected uncertainties. The gray shades in each ratio panel indicate the total uncertainty as used in the final statistical interpretation of data.

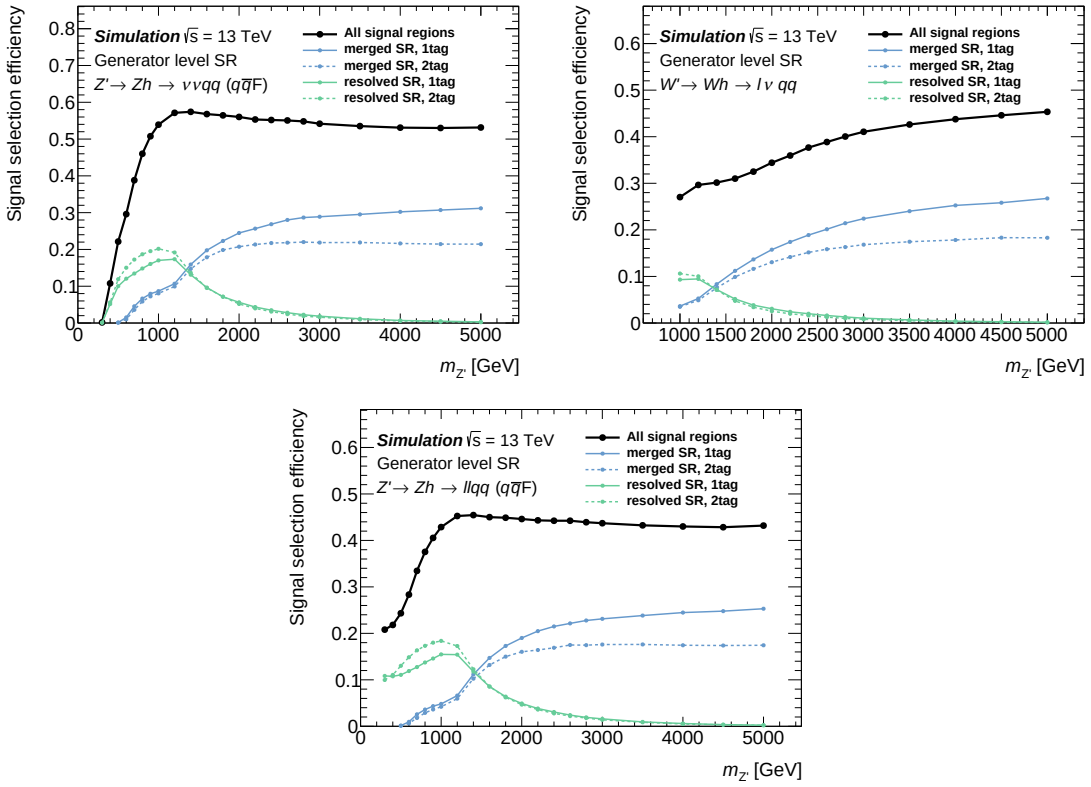

Figure C.22: HVT model A,B signal selection efficiencies at particle-level (PL) in **0-lepton**, **1-lepton** and **2-lepton** signal region (SR) as function of the Z'/W' mass.

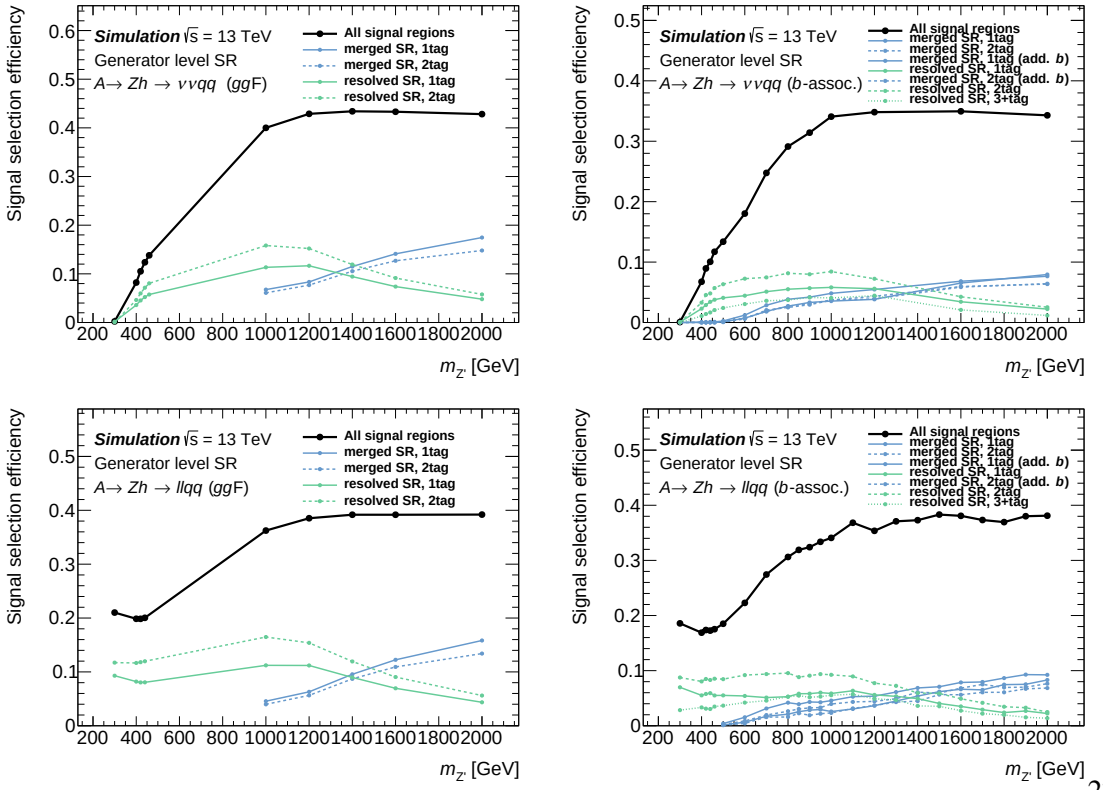

Figure C.23: 2HDM signal selection efficiencies at PL in **0-lepton** (top) and **2-lepton** (bottom) SR as function of the A mass. The plots on the left show the signal efficiencies for ggA mode production, the plots on the right the b-associated production.

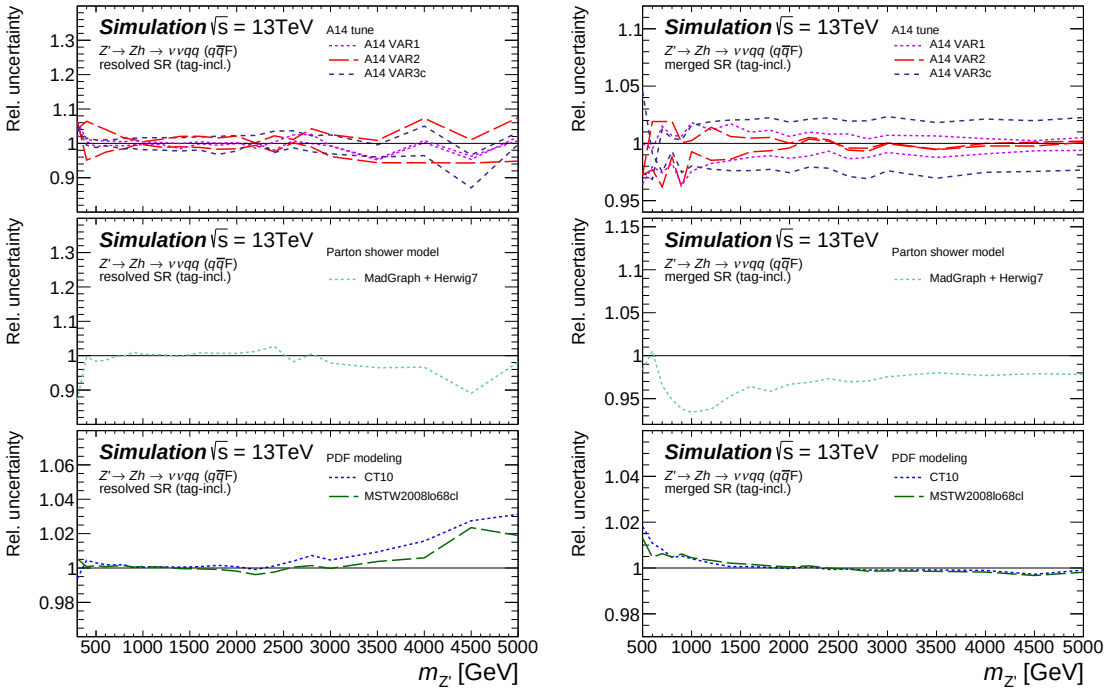

Figure C.24: Relative variation on the HVT model A,B signal selection efficiency (at generator level) in **0-lepton** SR as function of the A mass. The various ratio panels show the normalization uncertainties on the total signal selection efficiency due to individual sources. Resolved 3-tag region (left) and inclusive merged (1+2-tag) region in association with a additional b-tagged track jet not matched to the large-R jet (right); the 1- and 2-tag region look similar and are collectively shown here in a 1+2-tag merged region;

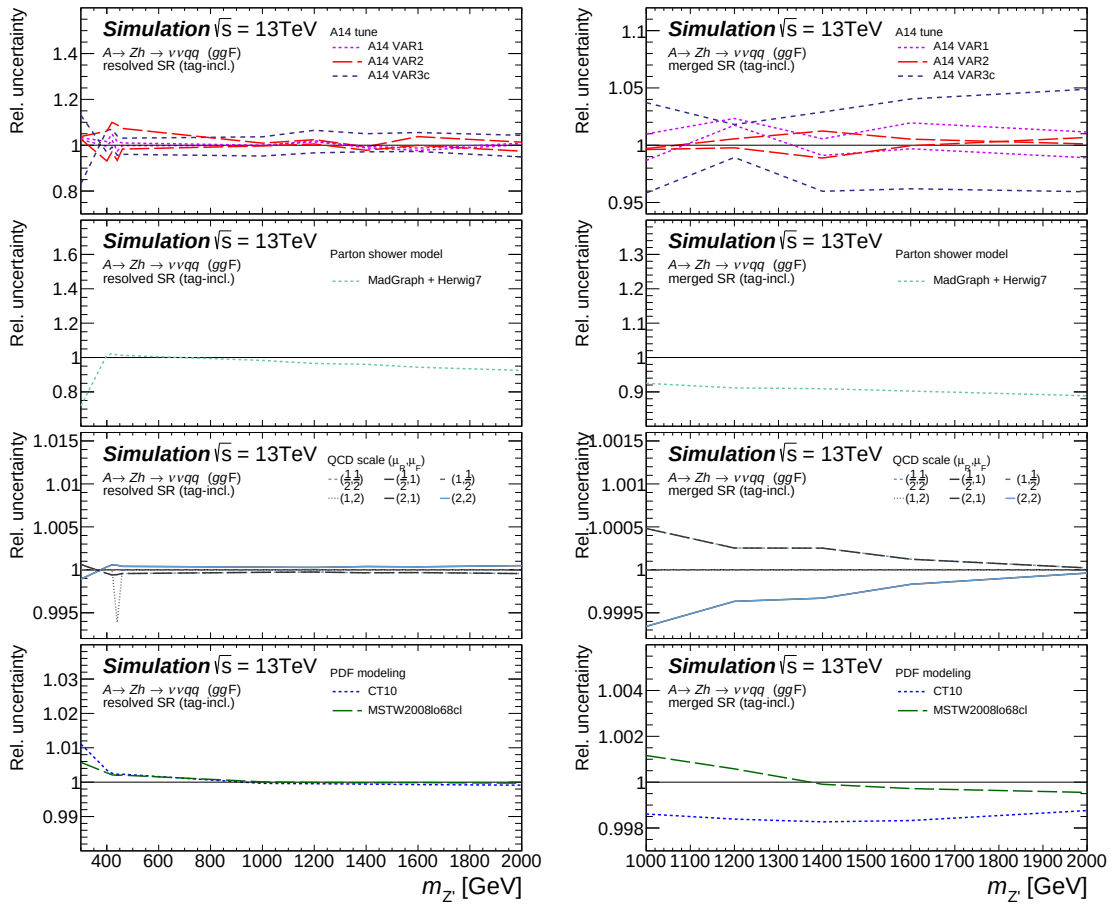

Figure C.25: Relative variation on the 2HDM signal selection efficiency (at generator level) in **0-lepton** SR as function of the A mass. The various ratio panels show the normalization uncertainties on the total signal selection efficiency due to individual sources. Resolved 3-tag region (left) and inclusive merged (1+2-tag) region in association with a additional b-tagged track jet not matched to the large-R jet (right); the 1- and 2-tag region look similar and are collectively shown here in a 1+2-tag merged region;

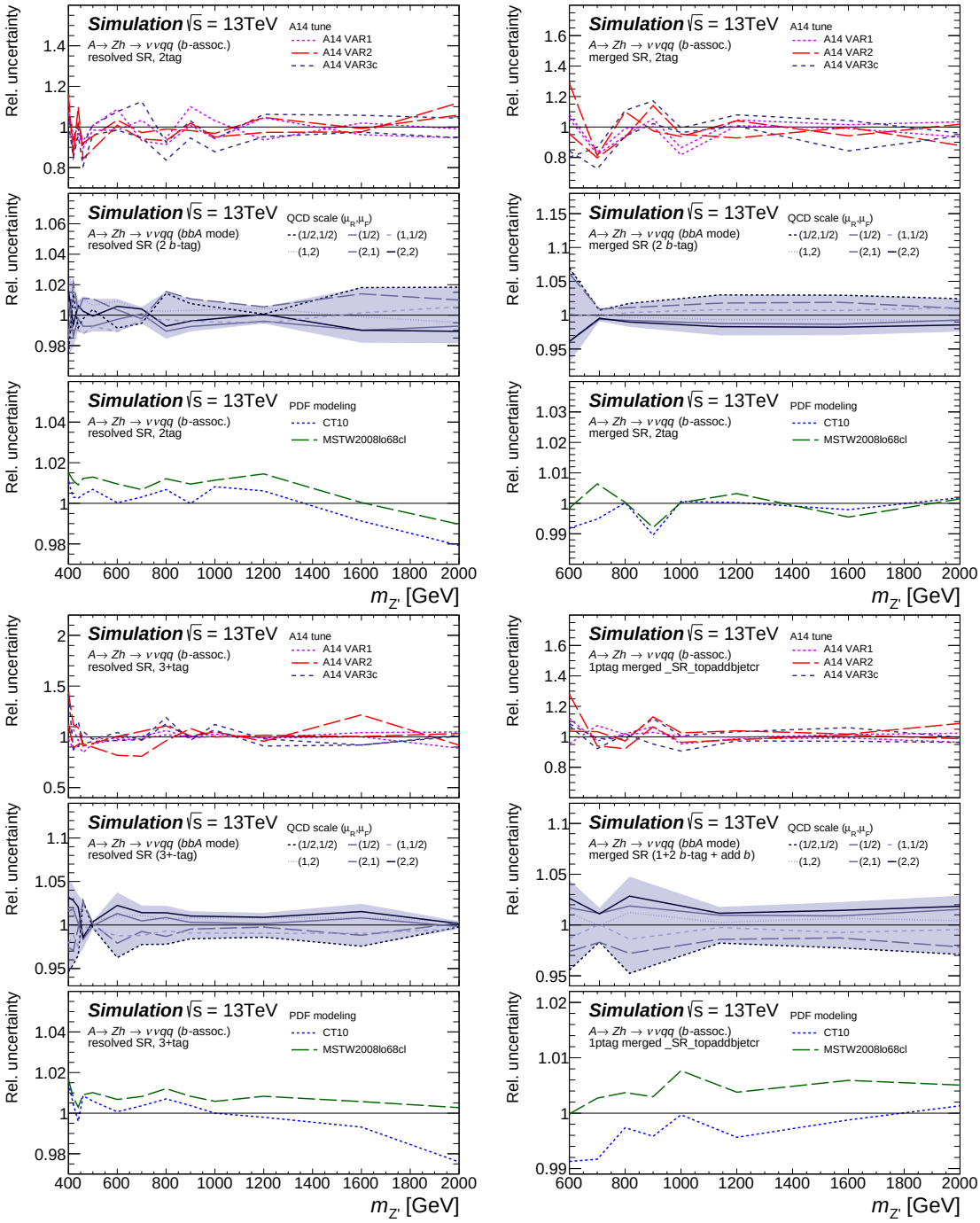

Figure C.26: Relative variation on the 2HDM signal selection efficiency (at generator level) in **0-lepton *b*-associated** SR as function of the A mass. The various ratio panels show the normalization uncertainties on the total signal selection efficiency due to individual sources. Resolved 3-tag region (left) and inclusive merged (1+2-tag) region in association with a additional b-tagged track jet not matched to the large-R jet (right); the 1- and 2-tag region look similar and are collectively shown here in a 1+2-tag merged region;

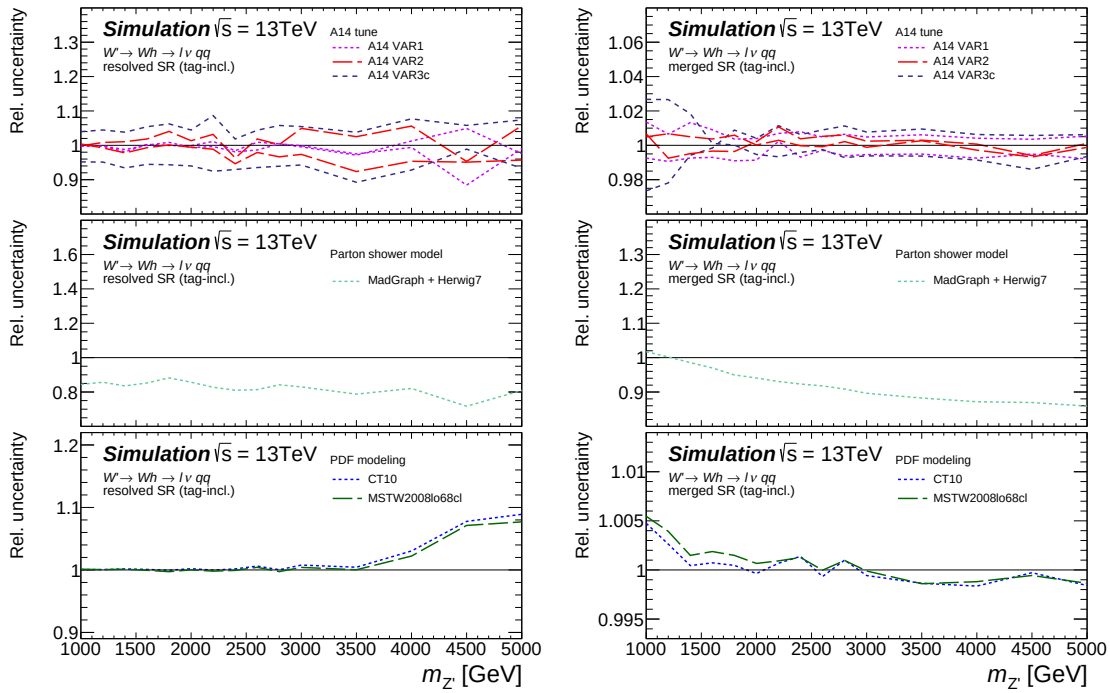

Figure C.27: Relative variation on the HVT model A,B signal selection efficiency (at generator level) in **1-lepton** SR as function of the W' mass. The various ratio panels show the normalization uncertainties on the total signal selection efficiency due to individual sources. Inclusive resolved region (left) and inclusive merged region (right); the 1- and 2-tag region look similar and are collectively shown here in a 1+2-tag region;

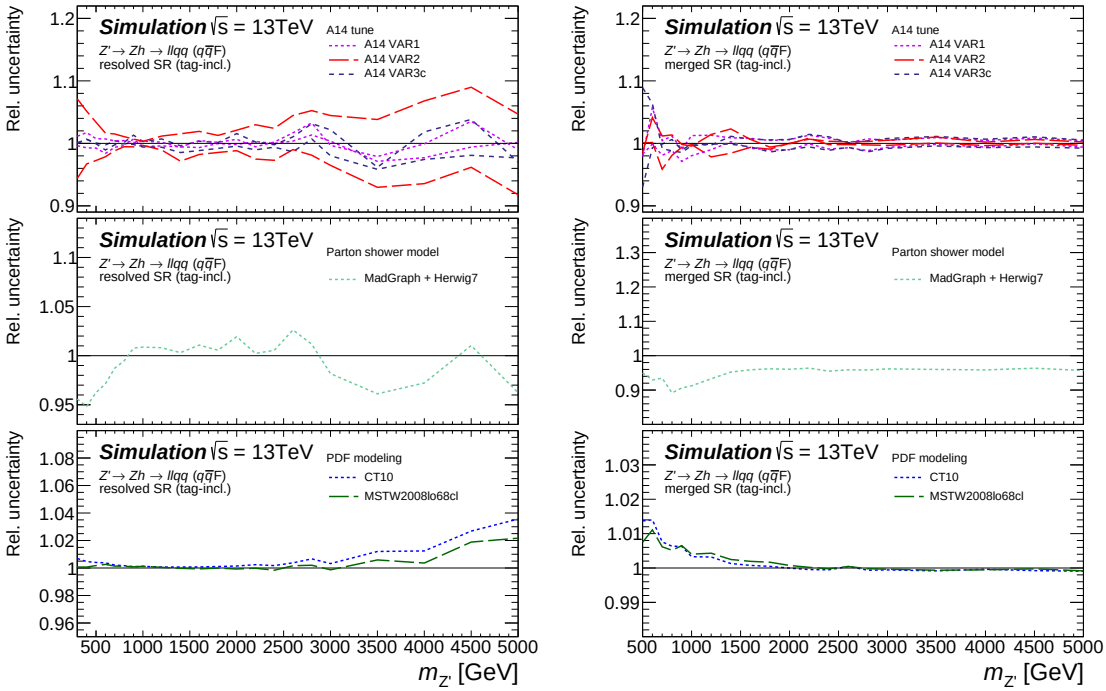

Figure C.28: Relative variation on the HVT model A,B signal selection efficiency (at generator level) in **2-lepton** SR as function of the A mass. The various ratio panels show the normalization uncertainties on the total signal selection efficiency due to individual sources. Resolved 3-tag region (left) and inclusive merged (1+2-tag) region in association with a additional b-tagged track jet not matched to the large-R jet (right); the 1- and 2-tag region look similar and are collectively shown here in a 1+2-tag merged region;

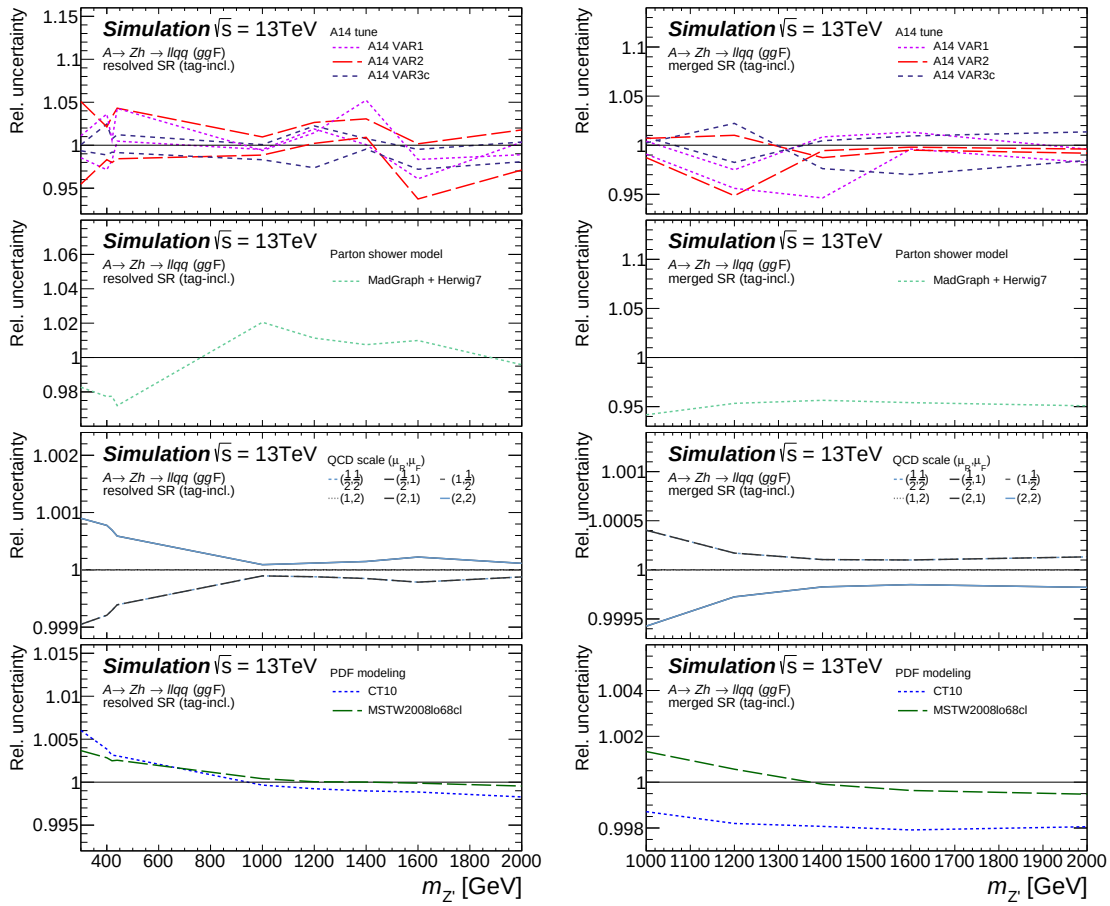

Figure C.29: Relative variation on the 2HDM signal selection efficiency (at generator level) in **2-lepton** SR as function of the A mass. The various ratio panels show the normalization uncertainties on the total signal selection efficiency due to individual sources. Resolved 3-tag region (left) and inclusive merged (1+2-tag) region in association with a additional b-tagged track jet not matched to the large-R jet (right); the 1- and 2-tag region look similar and are collectively shown here in a 1+2-tag merged region;

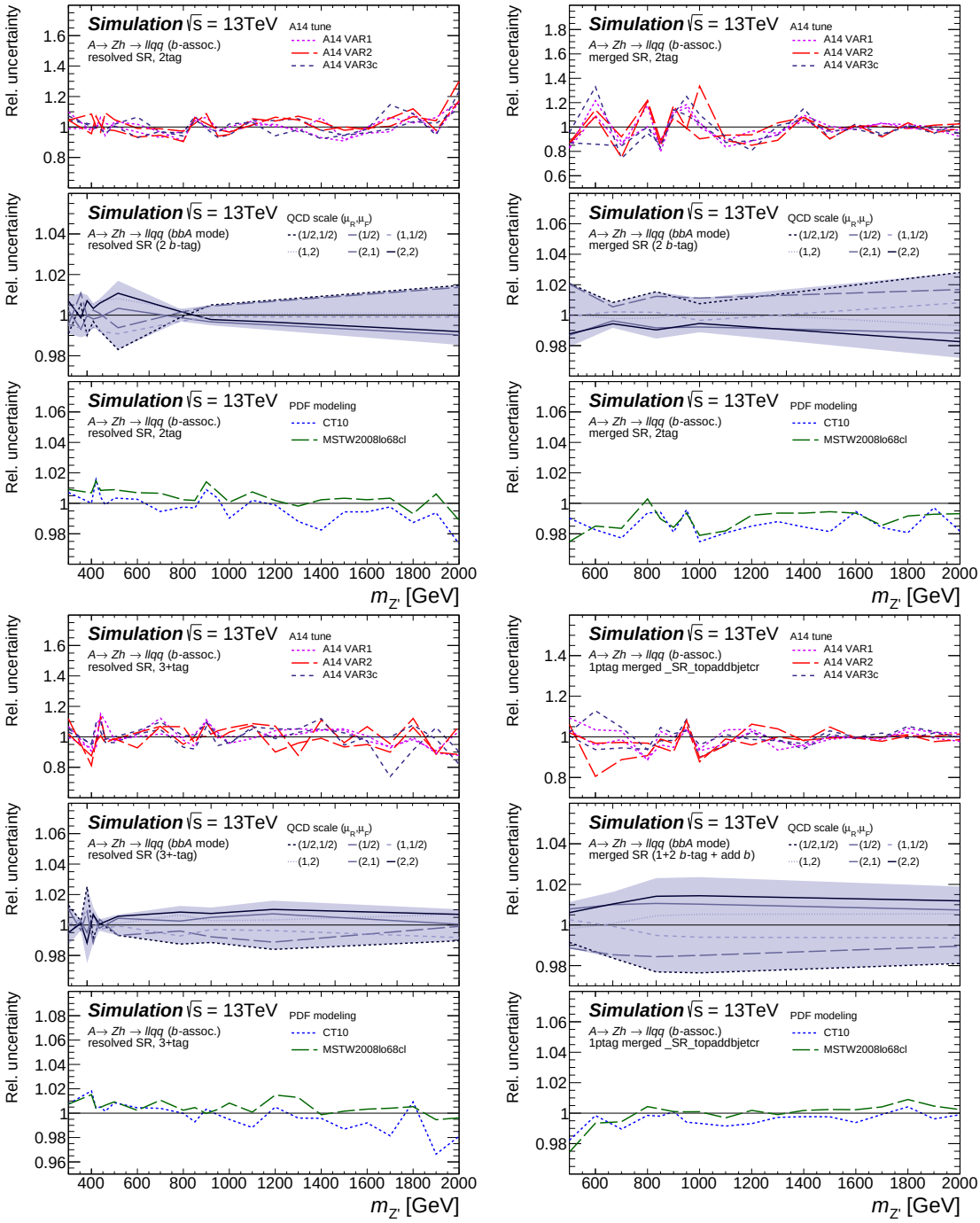

Figure C.30: Relative variation on the 2HDM signal selection efficiency (at generator level) in **2-lepton *b*-associated** SR as function of the A mass. The various ratio panels show the normalization uncertainties on the total signal selection efficiency due to individual sources. Resolved 3-tag region (left) and inclusive merged (1+2-tag) region in association with a additional b-tagged track jet not matched to the large-R jet (right); the 1- and 2-tag region look similar and are collectively shown here in a 1+2-tag merged region;

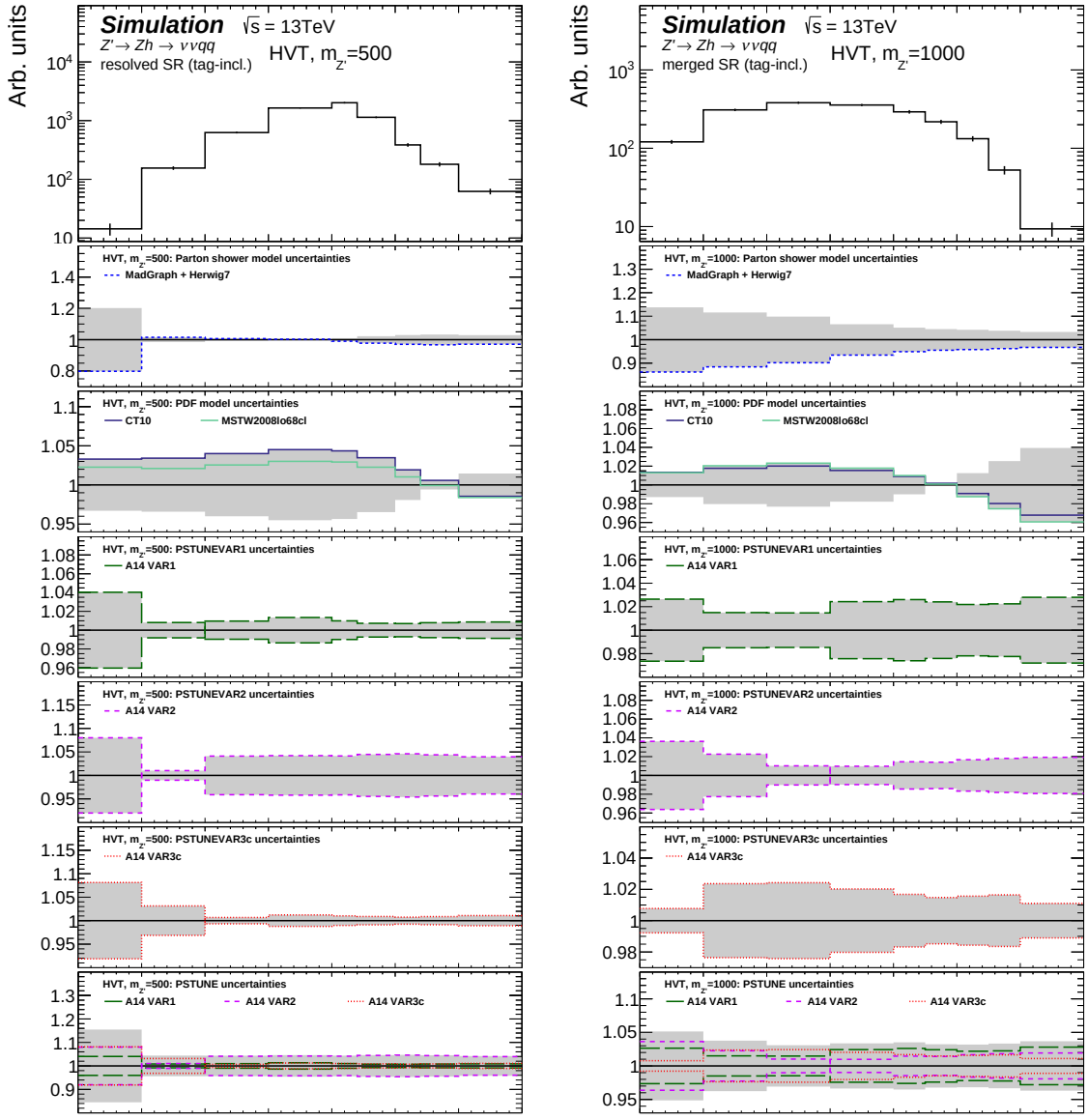

Figure C.31: The expected nominal signal m_{Zh} distribution (differential efficiency, upper panels) in the 1+2 b-tag (left) *resolved* and (right) *merged* signal regions of the 0-lepton channel for the HVT model A signal with a mass of (left) 500 GeV and (right) 1 TeV. The lower ratio panels show the relative changes in the differential efficiency, $\Delta\varepsilon_s(b_i)$, due to a given source of modeling uncertainty.

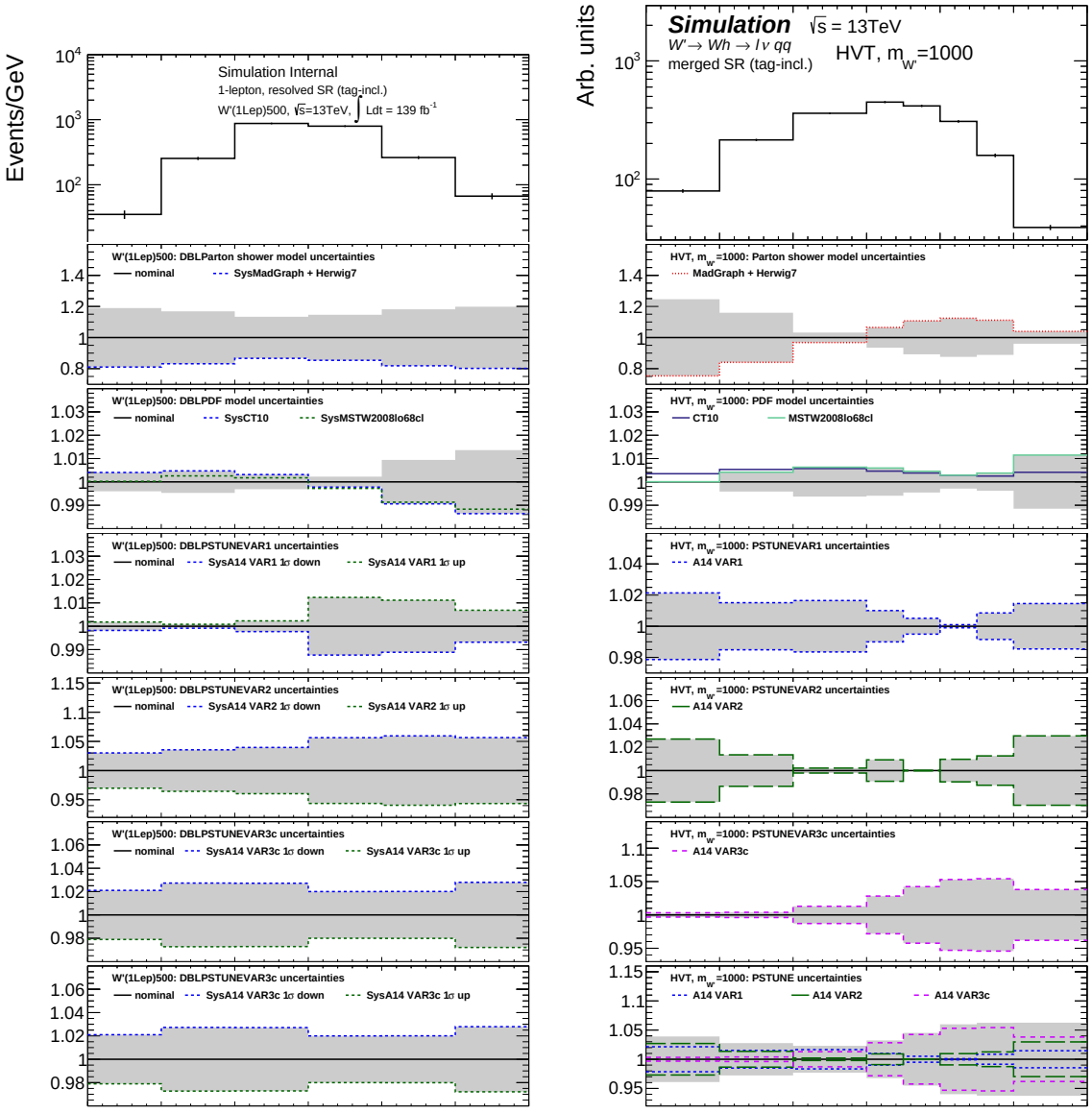

Figure C.32: The expected nominal signal m_{Zh} distribution (differential efficiency, upper panels) in the 1+2 b-tag (left) *resolved* and (right) *merged* signal regions of the 1-lepton channel for the HVT model A signal with a mass of (left) 500 GeV and (right) 1 TeV. The lower ratio panels show the relative changes in the differential efficiency, $\Delta\varepsilon_s(b_i)$, due to a given source of modeling uncertainty.

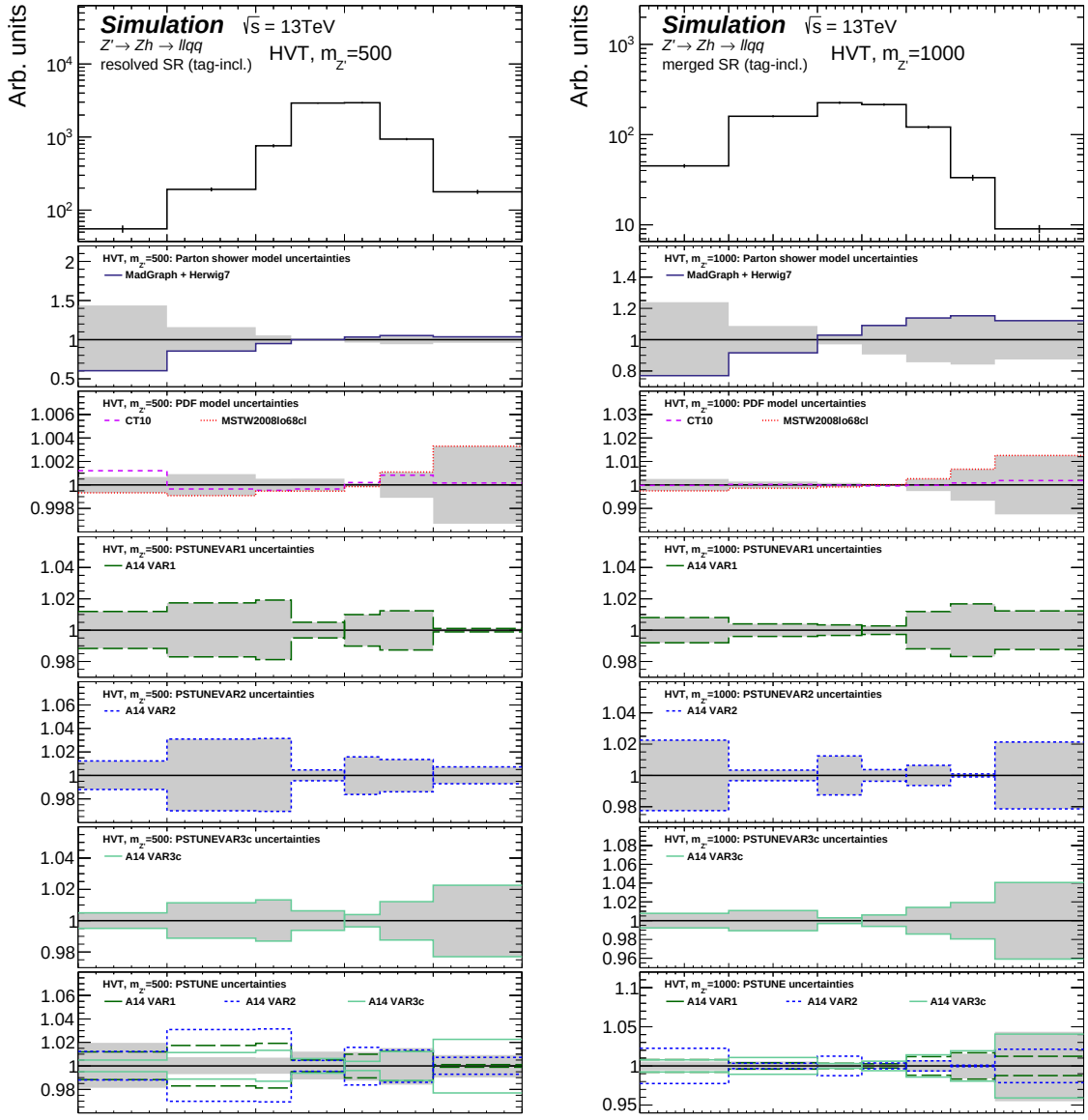

Figure C.33: The expected nominal signal m_{Zh} distribution (differential efficiency, upper panels) in the 1+2 b-tag (left) *resolved* and (right) *merged* signal regions of the 2-lepton channel for the HVT model A signal with a mass of (left) 500 GeV and (right) 1 TeV. The lower ratio panels show the relative changes in the differential efficiency, $\Delta\varepsilon_s(b_i)$, due to a given source of modeling uncertainty.

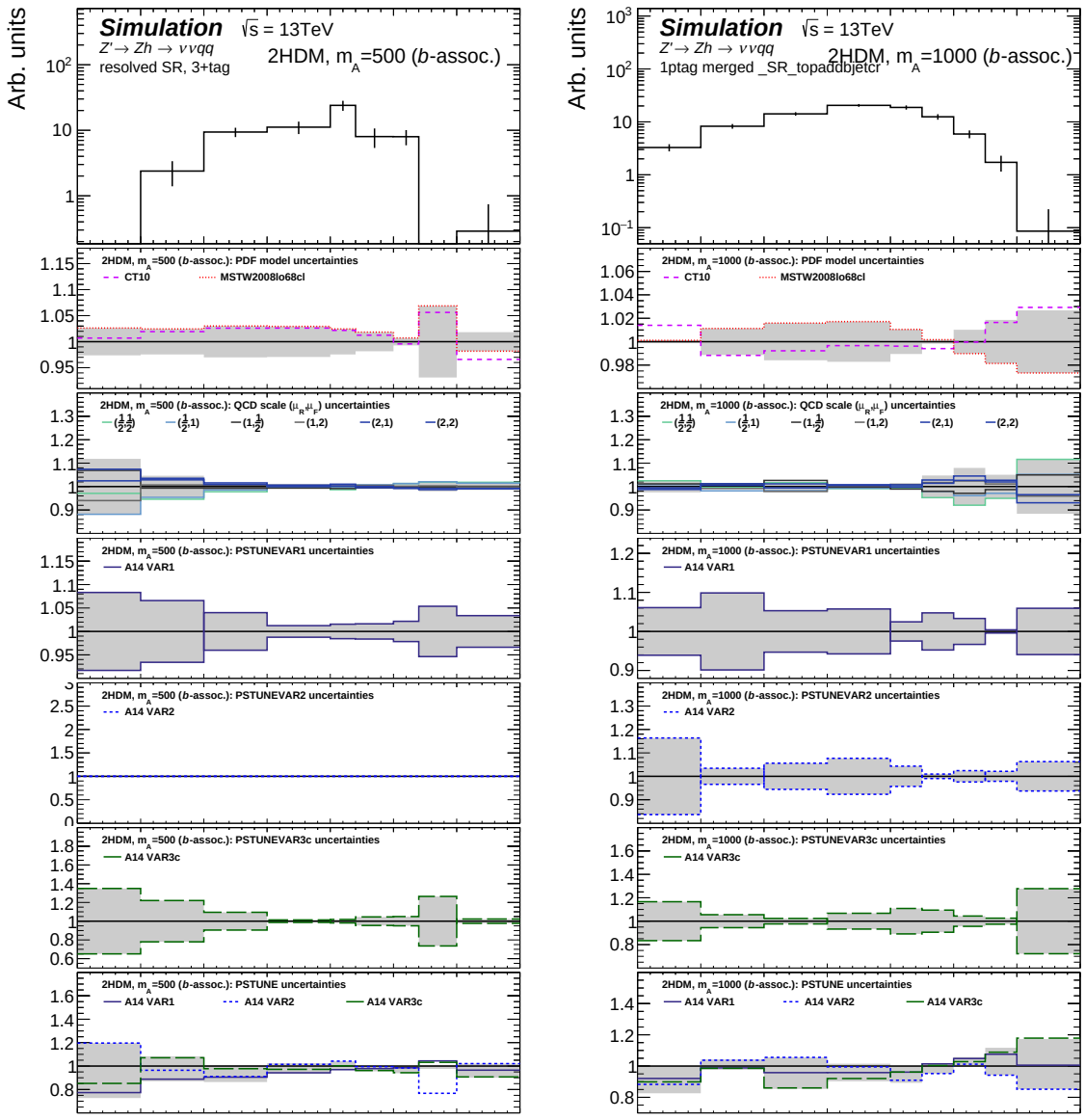

Figure C.34: The expected nominal signal m_{Zh} distribution (differential efficiency, upper panels) in the 1+2 b-tag (left) *resolved* and (right) *merged* signal regions of the 0-lepton channel for the 2HDM pseudo scalar produced via gluon-gluon fusion signal with a mass of (left) 500 GeV and (right) 1 TeV. The lower ratio panels show the relative changes in the differential efficiency, $\Delta\varepsilon_s(b_i)$, due to a given source of modeling uncertainty.

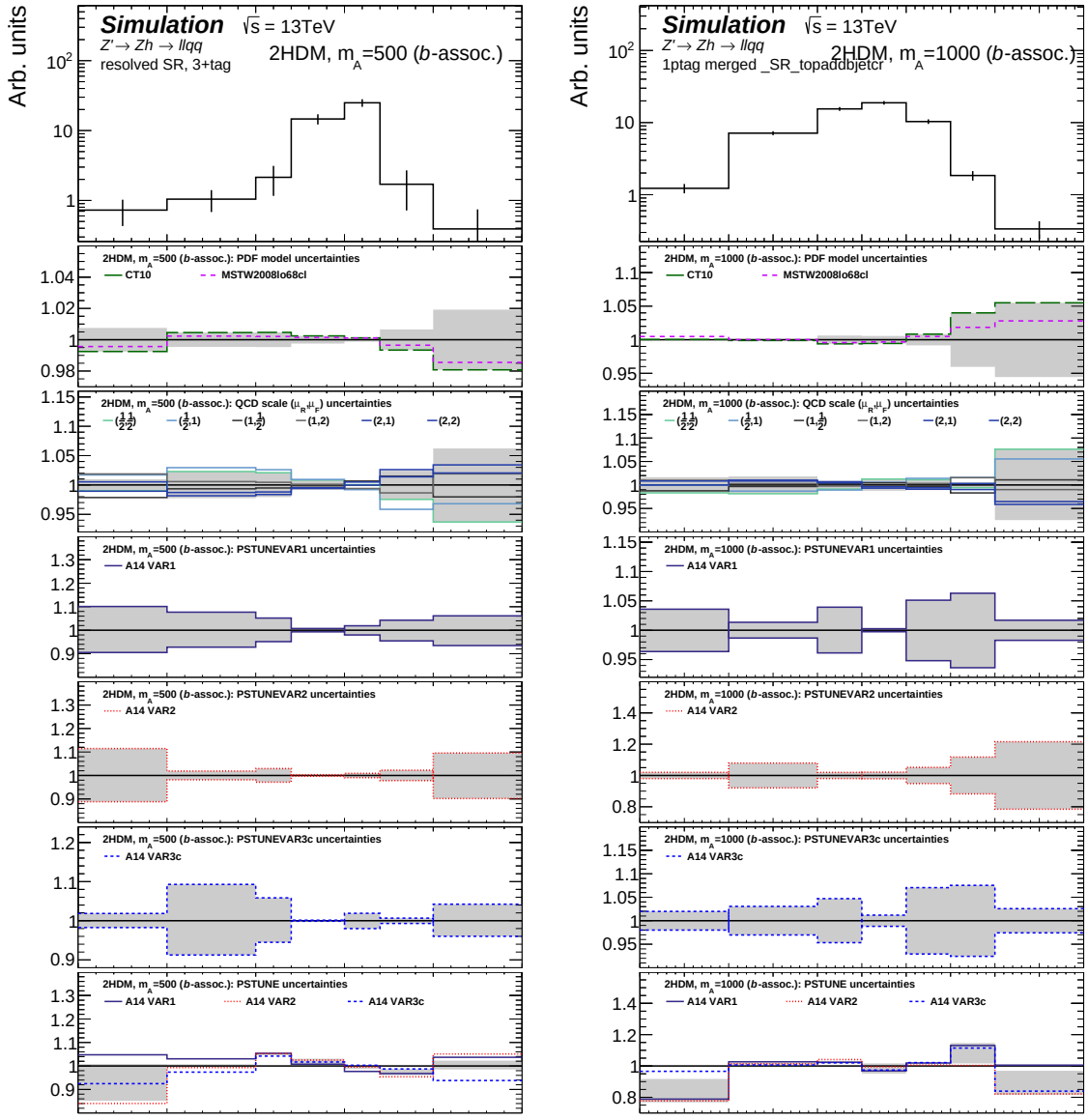

Figure C.35: The expected nominal signal m_{Zh} distribution (differential efficiency, upper panels) in the 3+ b-tag (left) *resolved* and (right) *merged* signal regions of the 2-lepton channel for the 2HDM pseudo scalar signal produced via the b-associated production mode with a mass of (left) 500 GeV and (right) 1 TeV. The lower ratio panels show the relative changes in the differential efficiency, $\Delta\varepsilon_s(b_i)$, due to a given source of modeling uncertainty.

D Additional material for the Zh-resonance search via the VBF production

Additional information to the results presented in Chapter 5 is given in this section.

D.1 Rectangular cut based VBF event selection

Several different configurations for a 2-dimensional rectangular event selection requirement on $\Delta\eta_{jj}^{VBF}$, m_{jj}^{VBF} and ζ was tested. Appendix D.1 shows two-dimensional distributions of the observable pairs (m_{jj}^{VBF}, ζ) and $(\zeta, \Delta\eta_{jj}^{VBF})$ separately for the total SM background contribution and for an example signal mass point of 500 GeV, normalized to an integrated luminosity of 1 pb^{-1}. The optimal event selection requirement is slightly dependent on the resonance mass, which can be seen in Appendix D.2.

D.2 Signal modeling uncertainties

The signal theory uncertainties shown in the main body are presented in a b-tag inclusive selection. The split-up selections of a signal with $m_{Z'} = 500$ GeV are shown in Appendices D.3 and D.4

D.3 More detailed information in the VBF feasibility tests

The post-fit correlation between the different NPs is shown in Fig. 5.43 for all NPs with at least one correlation coefficient larger than 25%. Pulls for the complete set of unpruned NPs is given in Appendices D.6 and D.7. Other uncertainties that the ones given in this table are negligible ($< 0.1\%$ in all bins).

D.4 Supplementary plots for the Asimov signal region fit studies

Impact of the systematical uncertainties to the singal strength parameter for further signal with masses $m_{Z'} \in [600, 800, 1000, 2600]$ GeV is shown in Appendices D.8 to D.11.

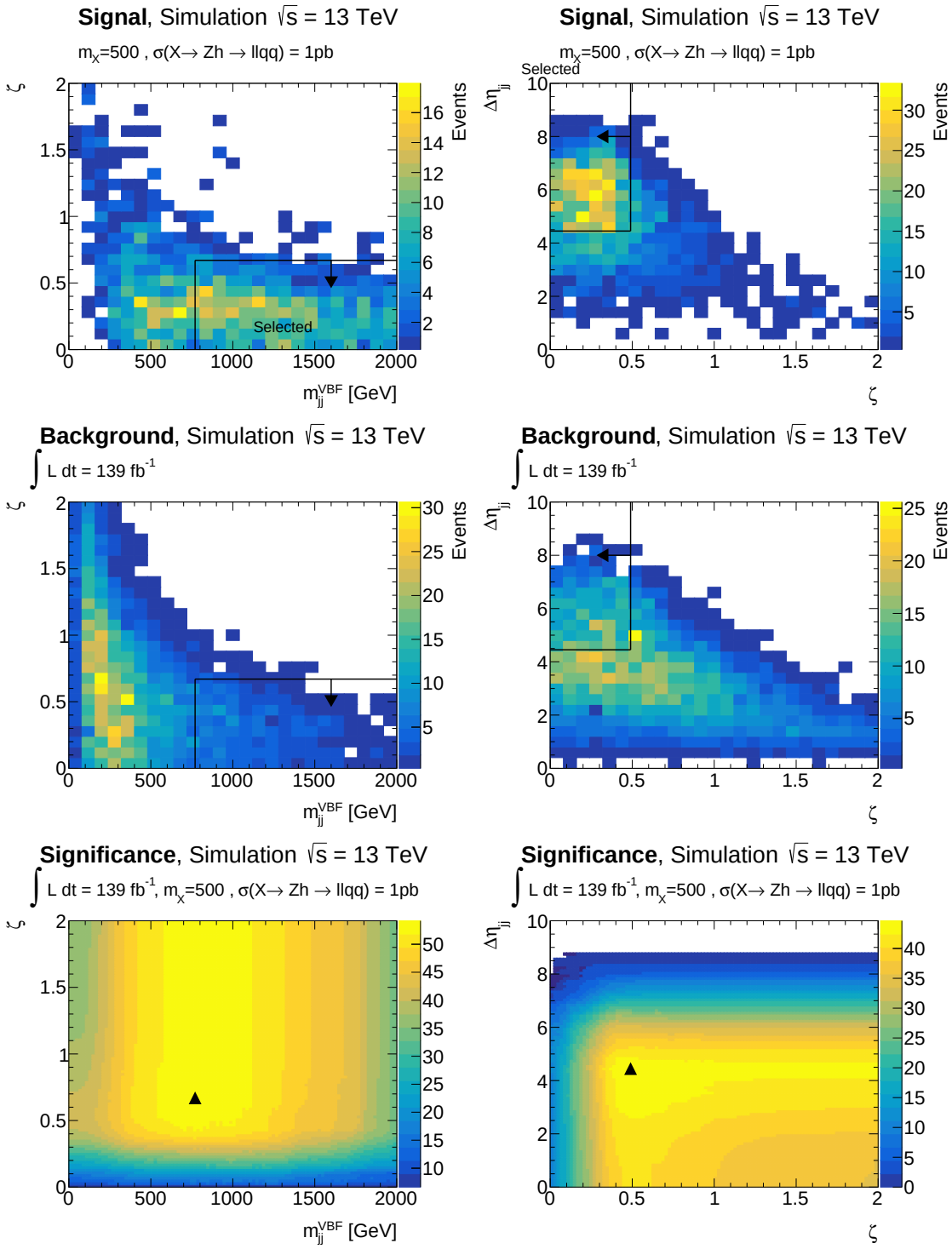

Figure D.1: Two-dimensional distribution (left) ($m_{\mathrm{jj}}^{\mathrm{VBF}}$, ζ) and (right) (ζ, $\Delta\eta_{\mathrm{jj}}^{\mathrm{VBF}}$) for the a signal sample with resonance mass $m_{Z'} = 500$ GeV (top row) and for the background processes (middle row). The corresponding signal significance in each of the 2-D distributions is shown in the bottom row.

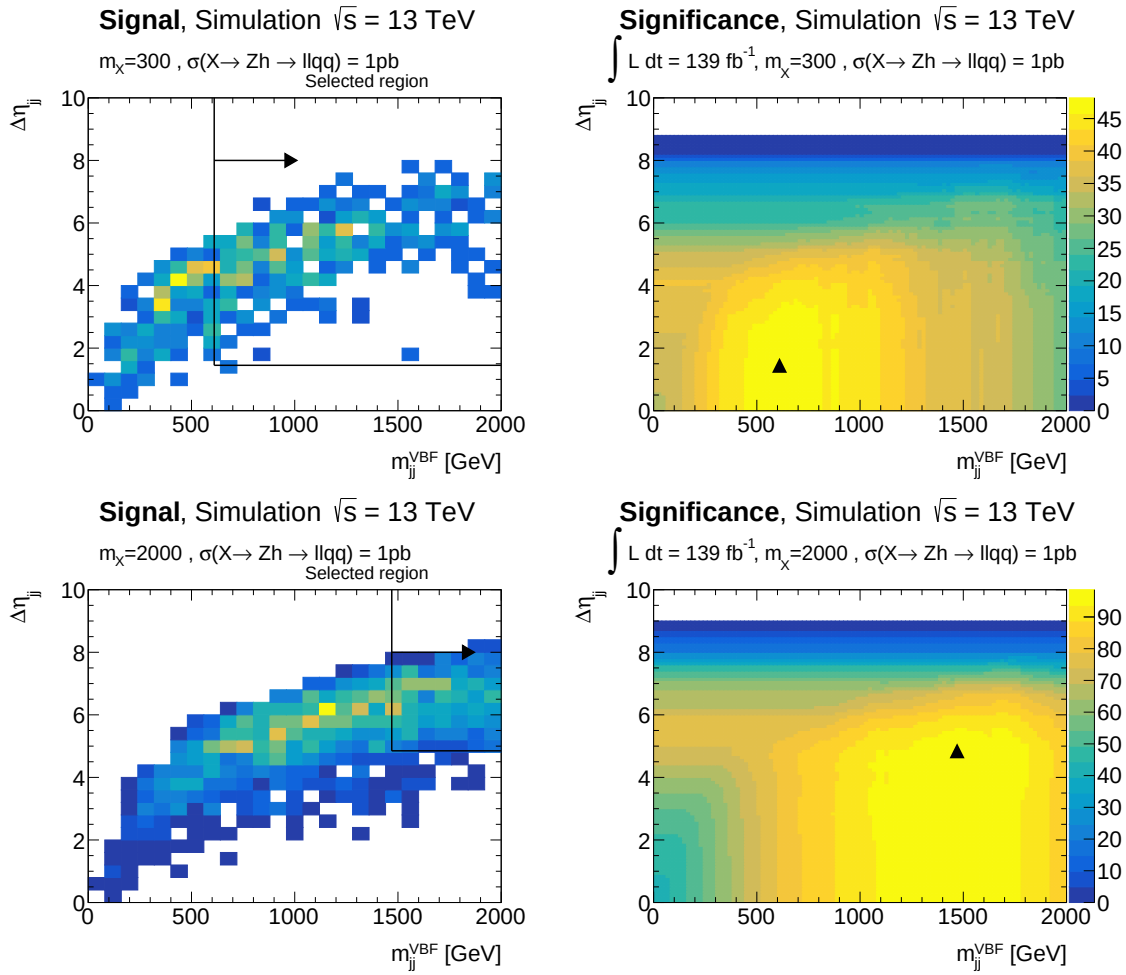

Figure D.2: Two-dimensional distribution ($m_{\mathrm{jj}}^{\mathrm{VBF}}$,$\Delta\eta_{\mathrm{jj}}^{\mathrm{VBF}}$) (top row) for the a signal sample with resonance mass (left) $m_{Z'} = 300$ GeV and (right) $m_{Z'} = 2000$ GeV. The corresponding signal significance in each of the 2-D distributions ($m_{\mathrm{jj}}^{\mathrm{VBF}}$,$\Delta\eta_{\mathrm{jj}}^{\mathrm{VBF}}$) is shown in the bottom row.

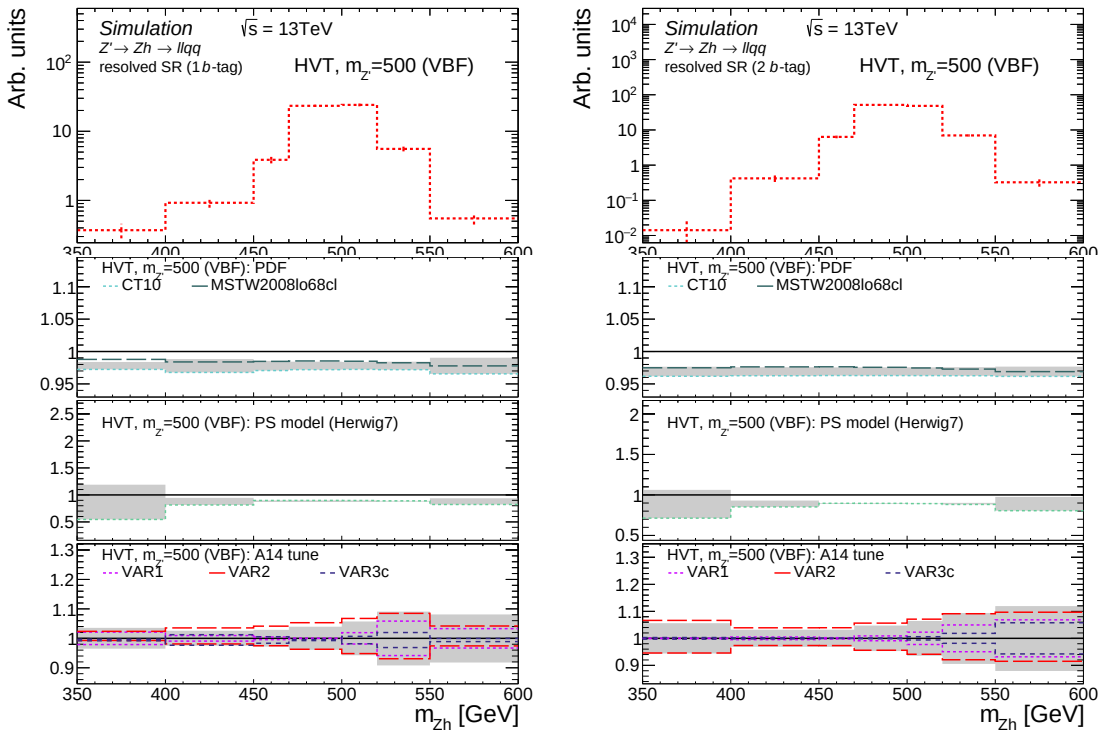

Figure D.3: Distribution of the nominal predictions of VBF model C signal in the resolved signal regions with 1- (left) or 2 b-tagged jets (right) for a mass hypothesis of 500 GeV. The various ratio panels are showing the shape uncertainties without normalization component for uncertainties originating from theoretical sources. The curve describing the relative uncertainties behave similar for different signal mass hypotheses but shifted with respect to the resonance mass. Differences in the course of the relative uncertainty are small between 1- and 2-tag region, due to the random generation of b-tagging.

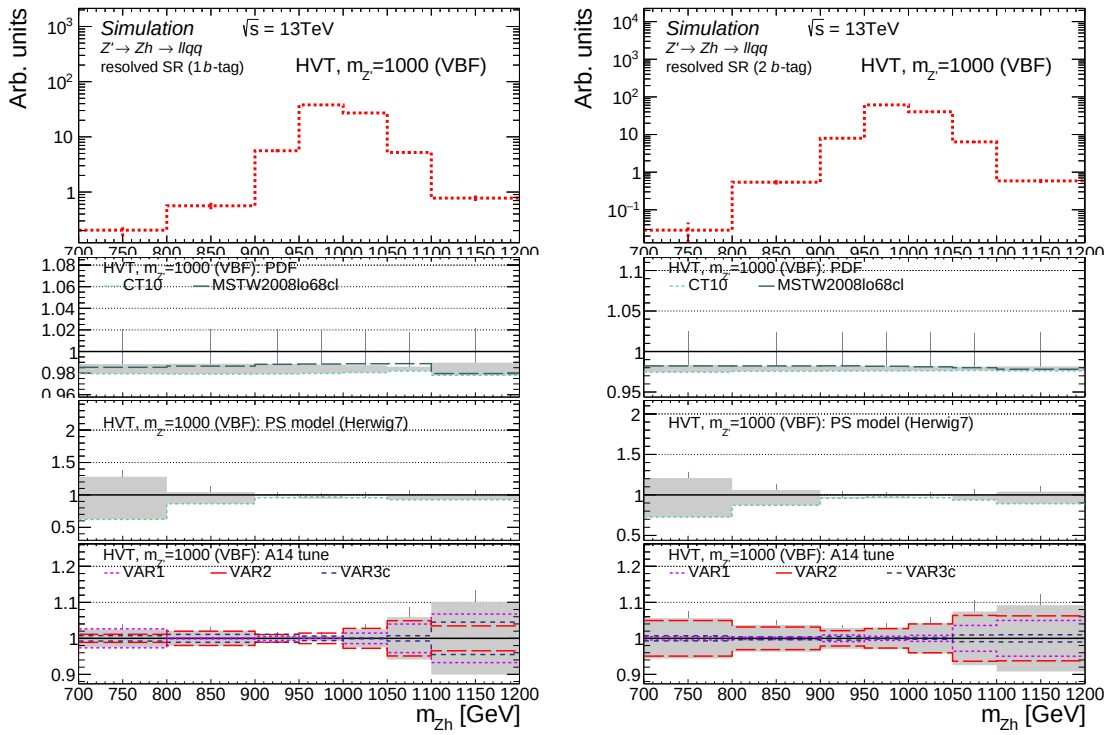

Figure D.4: Distribution of the nominal predictions of VBF model C signal in the resolved signal regions with 1- (left) or 2 b-tagged jets (right) for a mass hypothesis of 1000 GeV. The various ratio panels are showing the shape uncertainties without normalization component for uncertainties originating from theoretical sources. The curve describing the relative uncertainties behave similar for different signal mass hypotheses but shifted with respect to the resonance mass. Differences in the course of the relative uncertainty are small between 1- and 2-tag region, due to the random generation of b-tagging.

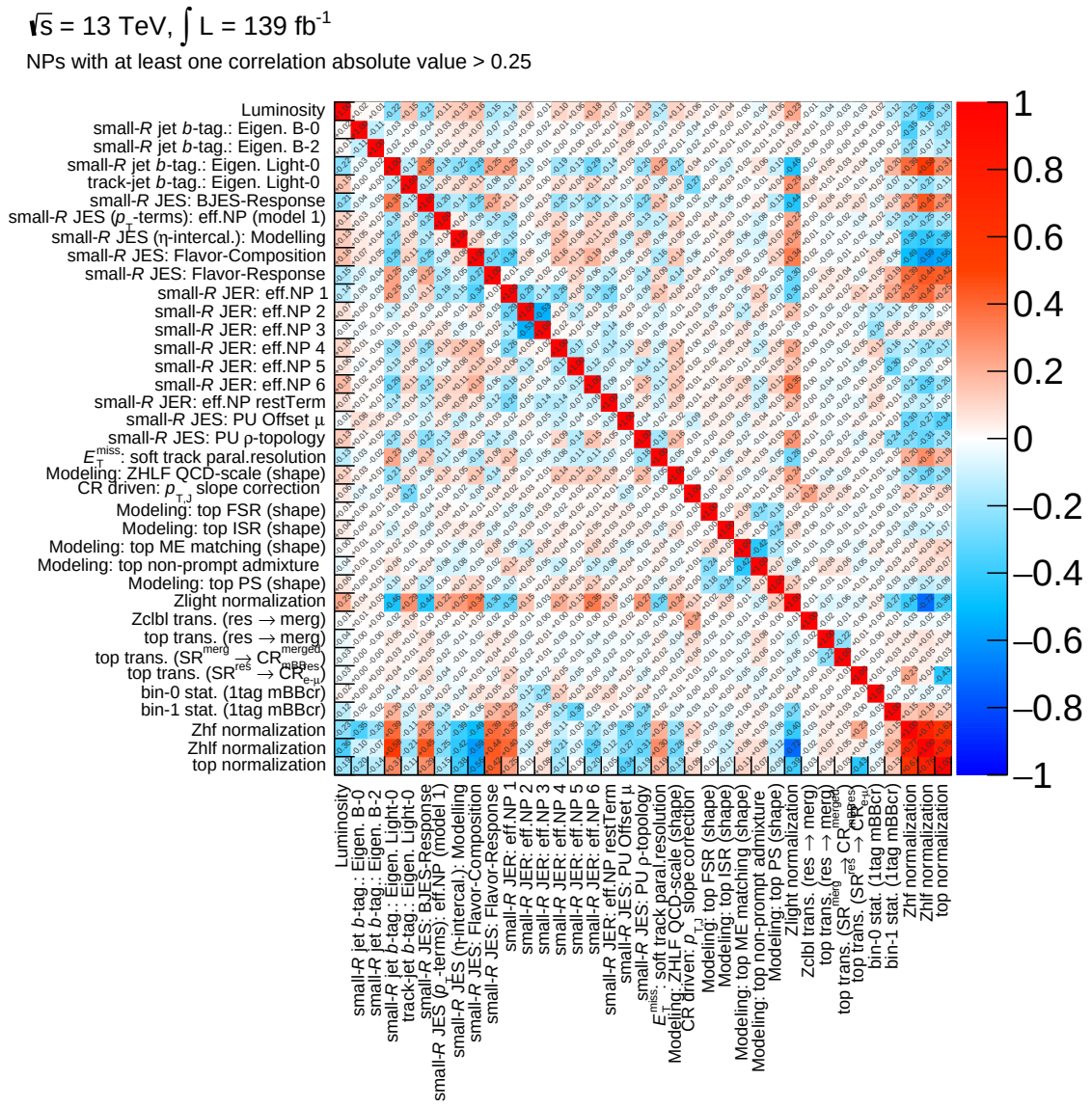

Figure D.5: The largest correlations among the nuisance parameters in a CR-only fit; displayed are NP with a correlation to at least one other NP above an absolute value of 0.25.

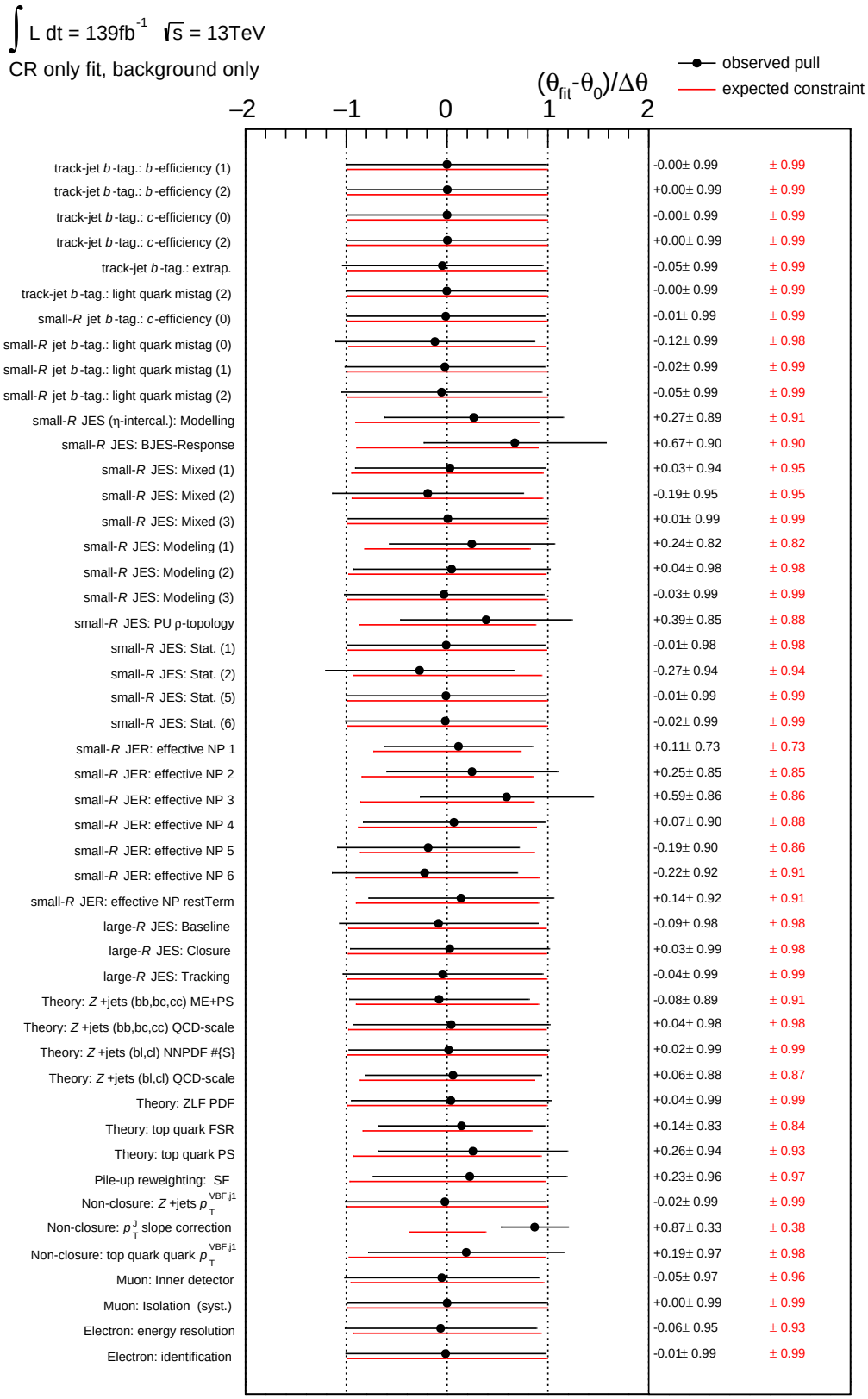

Figure D.6: Pulls in the CR-only fit. Page 1/2.

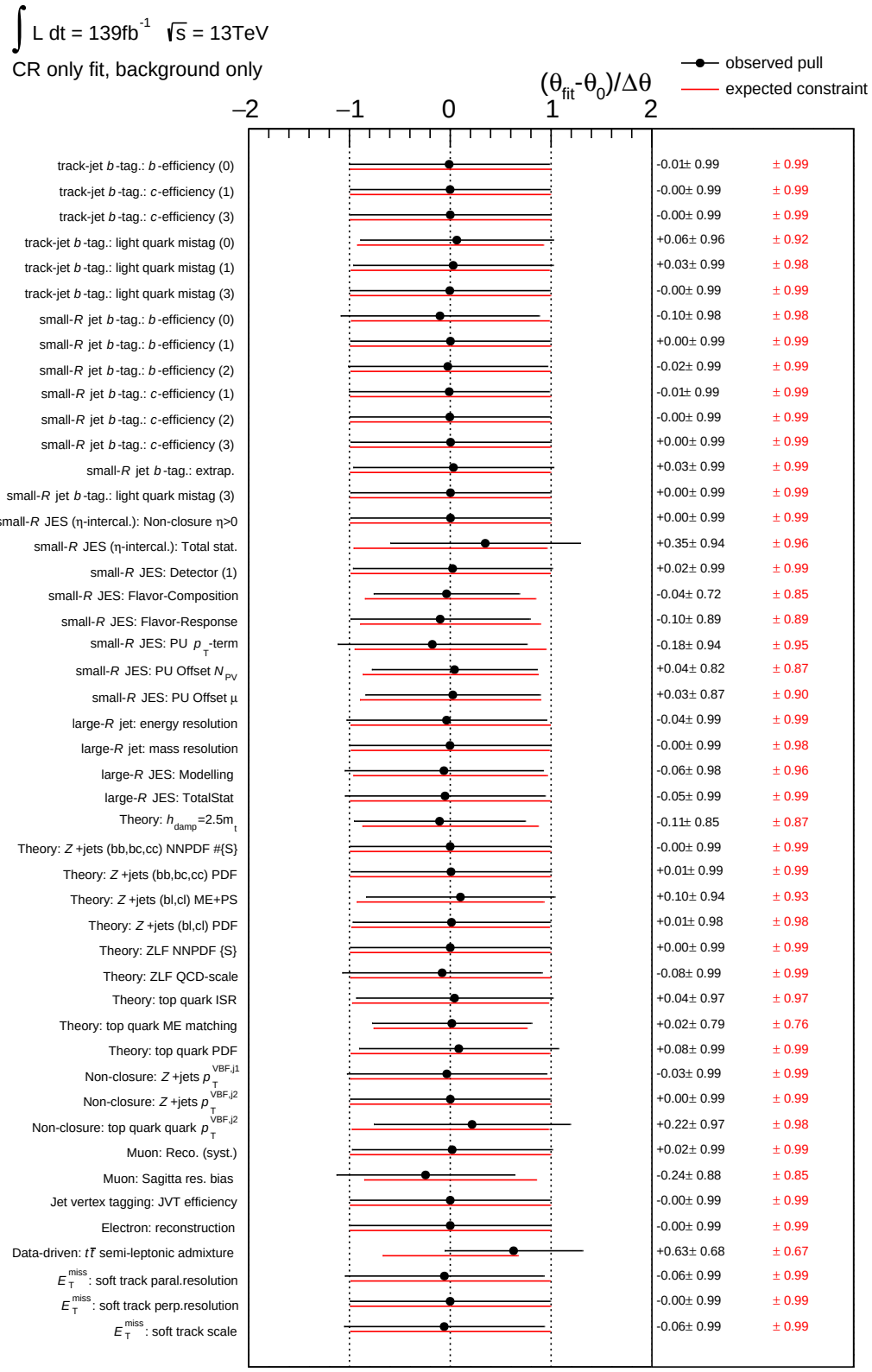

Figure D.7: Pulls in the CR-only fit. Page 2/2.

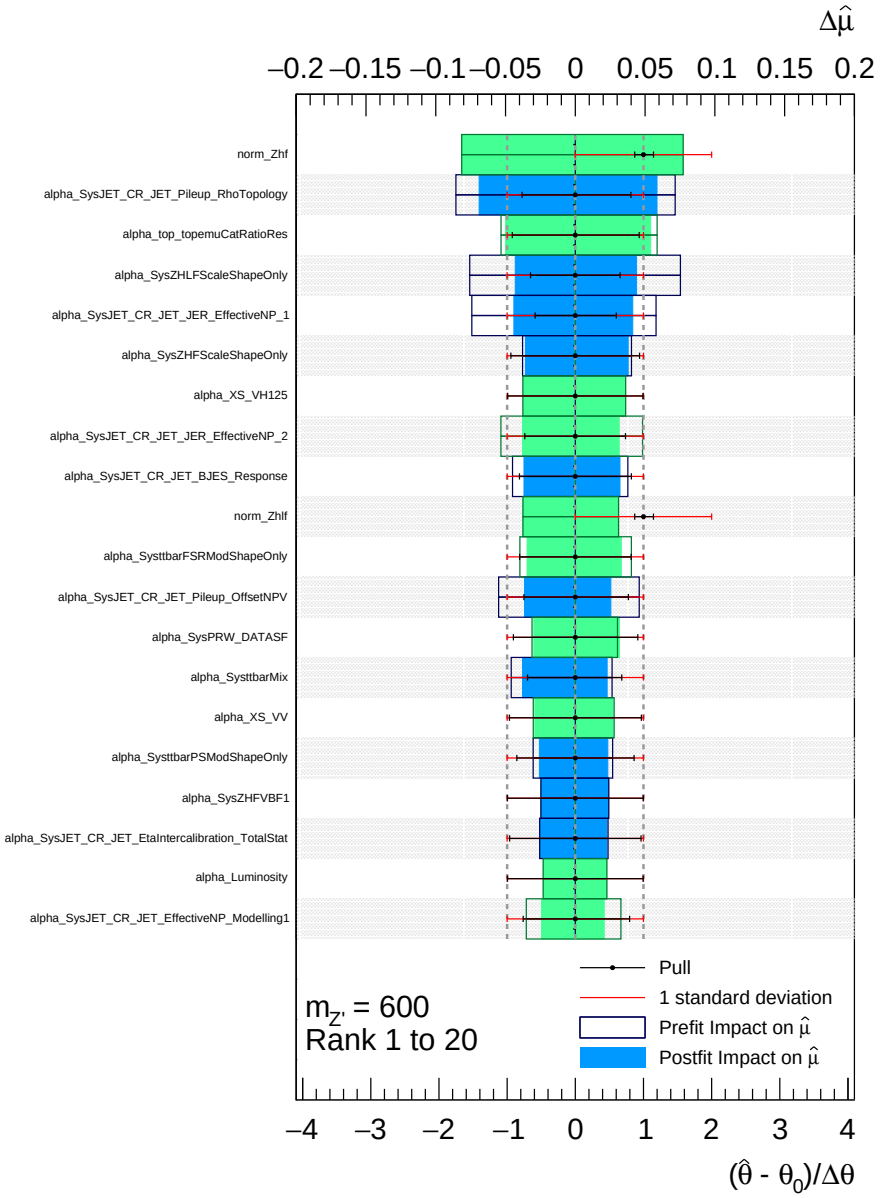

Figure D.8: Impact of the 20 most relevant parameter to the signal strength for a signal with mass $m_{Z'} = 600$ GeV. The box contours (colored boxes) show the impact of a parameter value fixed at one pre-fit (post-fit) standard deviation to the signal strength, μ. Green color indicates an negative correlation between $\Delta\theta$ and $\Delta\mu$. The overlayed markers show the post-fit values of the considered parameters θ after fitted to pseudo-data, constraining the uncertainty.

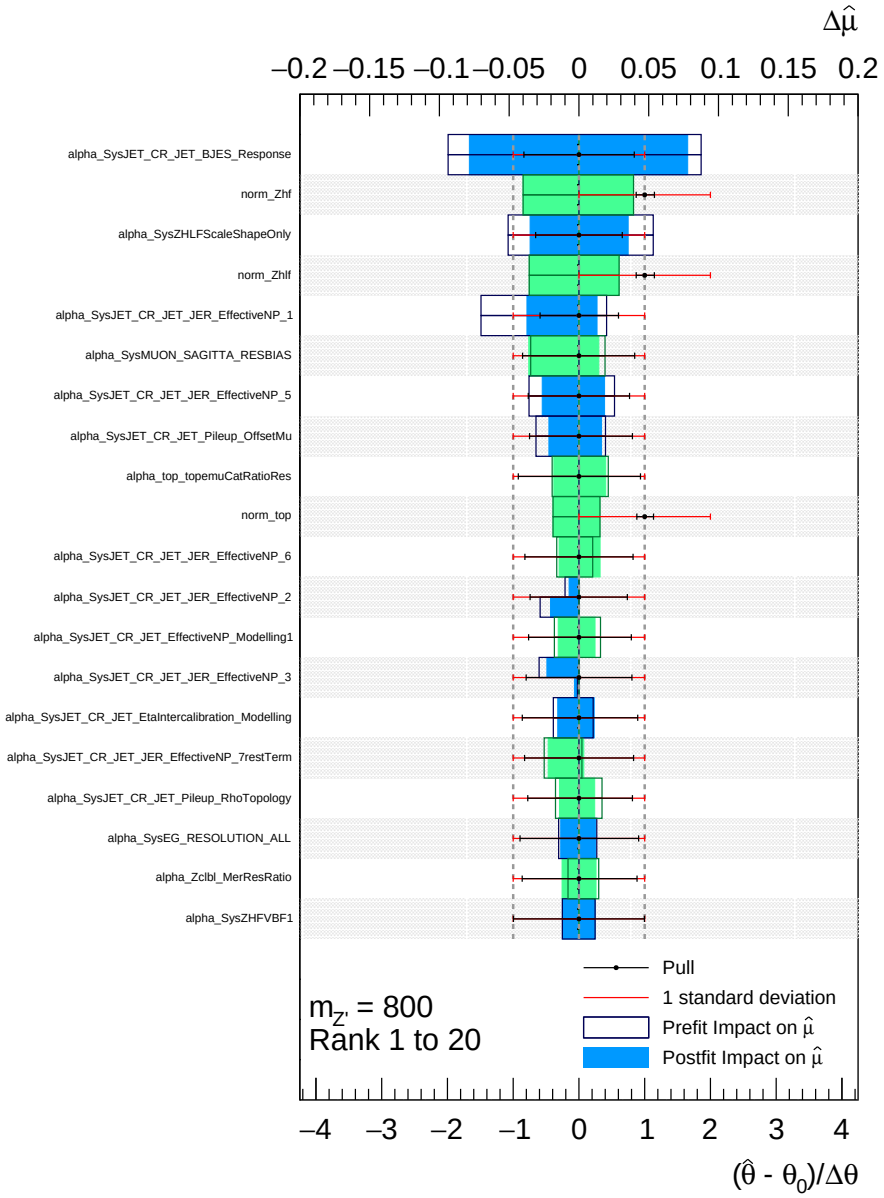

Figure D.9: Impact of the 20 most relevant parameter to the signal strength for a signal with mass $m_{Z'} = 800$ GeV. The box contours (colored boxes) show the impact of a parameter value fixed at one pre-fit (post-fit) standard deviation to the signal strength, μ. Green color indicates an negative correlation between $\Delta\theta$ and $\Delta\mu$. The overlayed markers show the post-fit values of the considered parameters θ after fitted to pseudo-data, constraining the uncertainty.

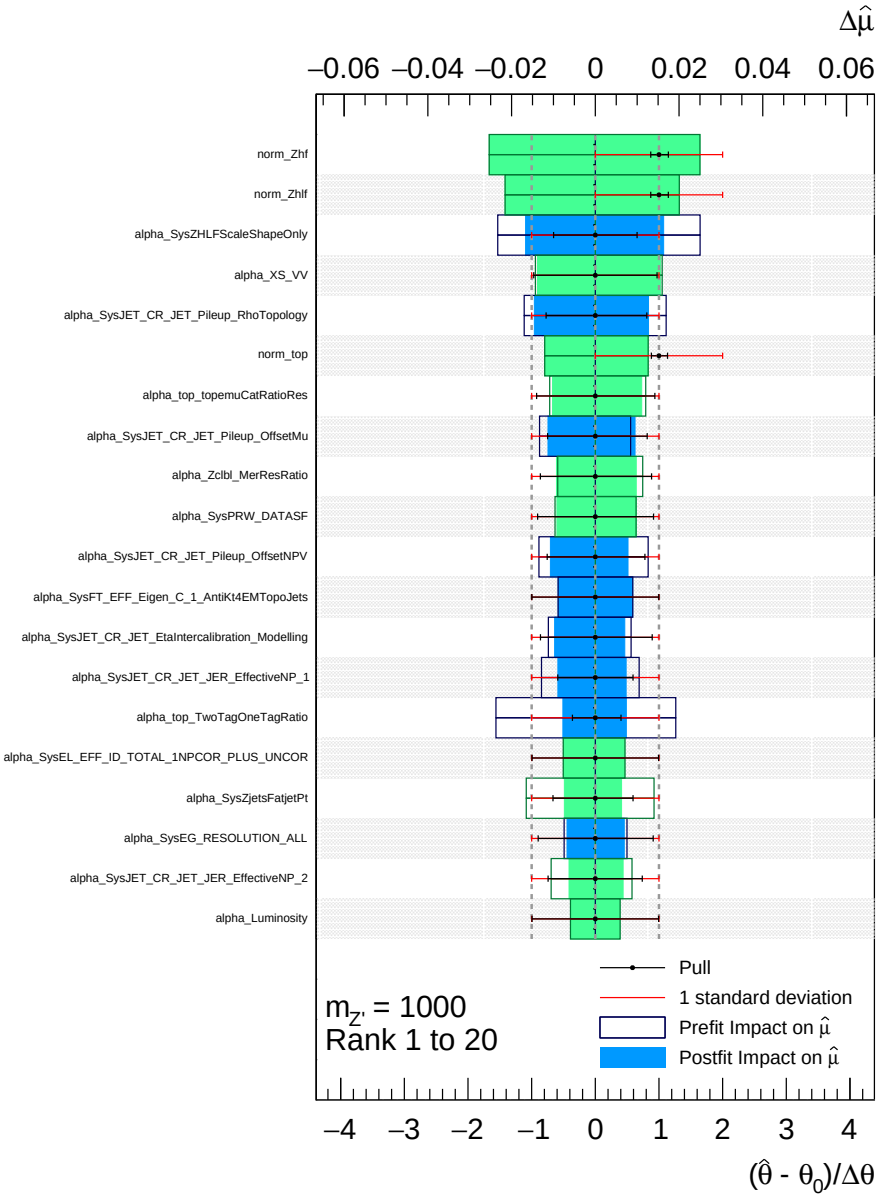

Figure D.10: Impact of the 20 most relevant parameter to the signal strength for a signal with mass $m_{Z'}$ = 1000 GeV. The box contours (colored boxes) show the impact of a parameter value fixed at one pre-fit (post-fit) standard deviation to the signal strength, μ. Green color indicates an negative correlation between $\Delta\theta$ and $\Delta\mu$. The overlayed markers show the post-fit values of the considered parameters θ after fitted to pseudo-data, constraining the uncertainty.

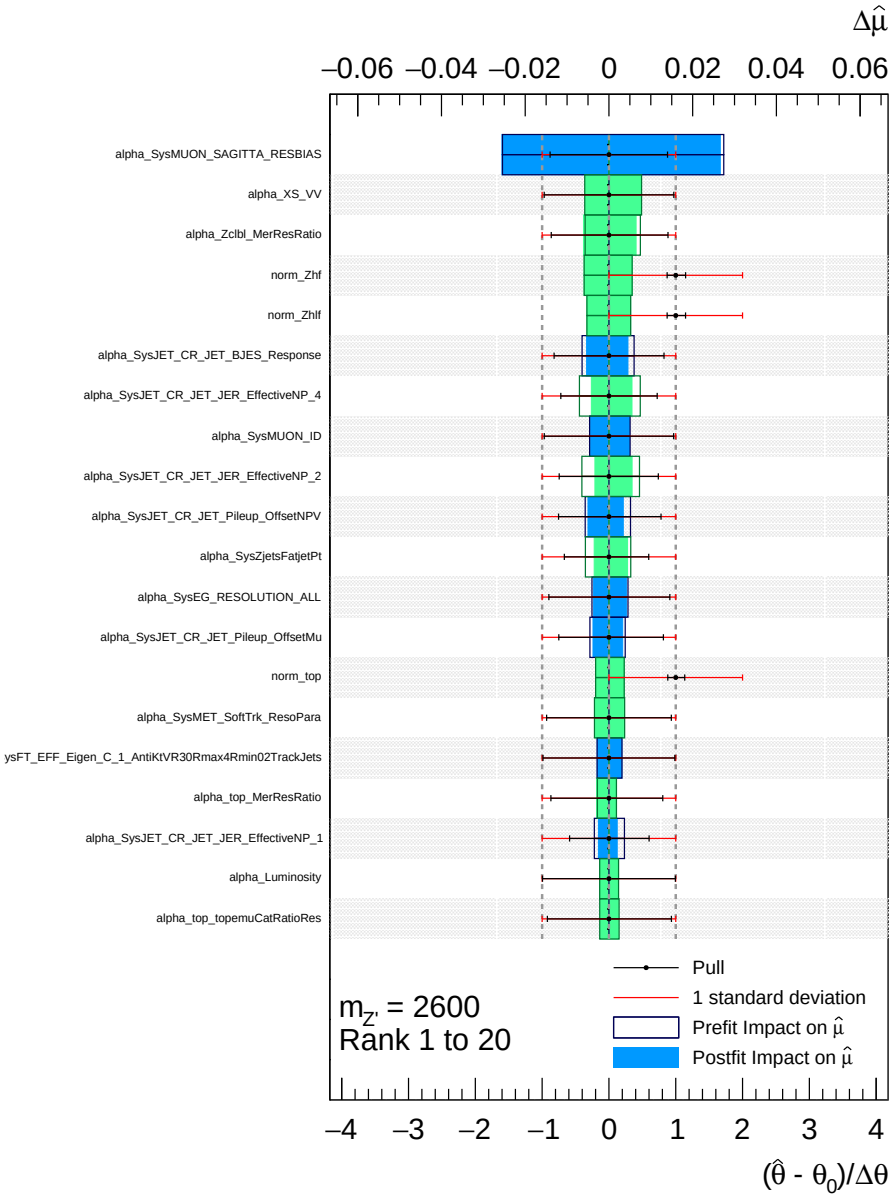

Figure D.11: Impact of the 20 most relevant parameter to the signal strength for a signal with mass $m_{Z'}$ = 2600 GeV. The box contours (colored boxes) show the impact of a parameter value fixed at one pre-fit (post-fit) standard deviation to the signal strength, μ. Green color indicates an negative correlation between $\Delta\theta$ and $\Delta\mu$. The overlayed markers show the post-fit values of the considered parameters θ after fitted to pseudo-data, constraining the uncertainty.

BIBLIOGRAPHY

[1] ATLAS Collaboration, G. Aad et al., *Observation of a new particle in the search for the Standard Model Higgs boson with the ATLAS detector at the LHC*, Phys. Lett. **B716** (2012) 1.

[2] CMS Collaboration, Chatrchyan S et al., *Observation of a new boson at a mass of 125 GeV with the CMS experiment at the LHC*, Phys. Lett. **B716** (2012) 30.

[3] C. N. Yang and R. L. Mills, *Conservation of Isotopic Spin and Isotopic Gauge Invariance*, Phys. Rev. **96** (1 1954) 191.

[4] Wikipedia, *The Standard Model particle content*, external Figure, 2019, URL: `https://en.wikipedia.org/wiki/Particle_physics`.

[5] F. Reines and C. L. Cowan, *Detection of the free neutrino*, Phys. Rev. **92** (1953) 830.

[6] Particle Data Group, M. Tanabashi et al., *Review of Particle Physics*, Phys. Rev. D **98** (3 2018) 030001.

[7] S. Abachi et al., *Observation of the top quark*, Phys. Rev. Lett. **74** (1995) 2632, arXiv: `hep-ex/9503003`.

[8] E. Radermacher, *The Experimental Discovery of the Intermediate Vector Bosons W^+, W^- and Z^0 at the CERN $p\bar{p}$ Collider*, Prog. Part. Nucl. Phys. **14** (1985) 231.

[9] J. Campbell, J. Huston and F. Krauss, *The black book of quantum chromodynamics: A primer for the LHC Era*, 2018 1.

[10] R. D. Ball et al., *Parton distributions for the LHC run II*, J. High Energy Phys. **2015** (2015).

[11] T.-J. Hou et al., *Reconstruction of Monte Carlo replicas from Hessian parton distributions*, JHEP **03** (2017) 099.

[12] L. A. Harland-Lang, A. D. Martin, P. Motylinski and R. S. Thorne, *Parton distributions in the LHC era: MMHT 2014 PDFs*, Eur. Phys. J.C **75** (2015).

[13] A. Buckley et al., *LHAPDF6: parton density access in the LHC precision era*, Eur. Phys. J.C **75** (2015).

[14] J. E. Huth et al., 'Toward a standardization of jet definitions, 1990 DPF Summer Study on High-energy Physics: Research Directions for the Decade (Snowmass 1990)' 0134.

[15] G. P. Salam and G. Soyez, *A Practical Seedless Infrared-Safe Cone jet algorithm*, JHEP **05** (2007) 086.

[16] S. D. Ellis and D. E. Soper, *Successive combination jet algorithm for hadron collisions*, Phys. Rev. D **48** (1993) 3160.

[17] S. Catani, Y. L. Dokshitzer, M. H. Seymour and B. R. Webber, *Longitudinally-invariant $k_\perp$-clustering algorithms for hadron-hadron collisions*, Nucl. Phys. B **406** (1993) 187.

[18] Y. L. Dokshitzer, G. D. Leder, S. Moretti and B. R. Webber, *Better jet clustering algorithms*, JHEP **08** (1997) 001.

[19] M. Cacciari, G. P. Salam and G. Soyez, *The anti-k_t jet clustering algorithm*, JHEP **04** (2008) 063.

[20] M. Joyce, T. Prokopec and N. Turok, *Nonlocal electroweak baryogenesis. Part 2: The Classical regime*, Phys. Rev. D **53** (1996) 2958.

[21] S. Weinberg, *Gauge hierarchies*, Phys. Lett. B **82** (1979) 387.

[22] M. J. G. Veltman, *The infrared - ultraviolet connection*, Acta Phys. Polon. B **12** (1981) 437.

[23] C. H. Llewellyn Smith and G. G. Ross, *The real gauge hierarchy problem*, Phys. Lett. B **105** (1981) 38.

[24] P. Fayet, *Supersymmetry and Weak, Electromagnetic and Strong Interactions*, Phys. Lett. **64B** (1976) 159.

[25] G. C. Branco et al., *Theory and phenomenology of two-Higgs-doublet models*, Phys. Rept. **516** (2012) 1.

[26] P. Fayet, *Spontaneously Broken Supersymmetric Theories of Weak, Electromagnetic and Strong Interactions*, Phys. Lett. **69B** (1977) 489.

[27] G. R. Farrar and P. Fayet, *Phenomenology of the Production, Decay, and Detection of New Hadronic States Associated with Supersymmetry*, Phys. Lett. **76B** (1978) 575.

[28] P. Fayet, *Relations Between the Masses of the Superpartners of Leptons and Quarks, the Goldstino Couplings and the Neutral Currents*, Phys. Lett. **84B** (1979) 416.

[29] S. Dimopoulos, and H. Georgi, *Softly Broken Supersymmetry and SU(5)*, Nucl. Phys. **B193** (1981) 150.

[30] R. Peccei and H. Quinn, *CP Conservation in the Presence of Pseudoparticles*, Phys. Rev. Lett. **38** (1977) 1440.

[31] J. E. Kim, *Light pseudoscalars, Particle Physics and Cosmology*, Phys. Rept. **150** (1987) 1.

[32] D. Kominis, *The Phenomenology of the CP odd scalar in two doublet models*, Nucl. Phys. B **427** (1994) 575.

[33] V. Barger, W. Y. Keung and E. Ma, *Gauge model with light W and Z bosons*, Phys. Rev. D **22** (3 1980) 727.

[34] M. Schmaltz and D. Tucker-Smith, *Little Higgs review*, Ann. Rev. Nucl. Part. Sci. **55** (2005) 229.

[35] M. J. Dugan, H. Georgi and D. B. Kaplan, *Anatomy of a composite Higgs model*, Nucl. Phys. B **254** (1985) 299.

[36] K. Agashe, R. Contino and A. Pomarol, *The minimal composite Higgs model*, Nucl. Phys. B **719** (2005) 165.

[37] F. Sannino and K. Tuominen, *Orientifold theory dynamics and symmetry breaking*, Phys. Rev. D **71** (2005) 051901.

[38] R. Foadi, M. T. Frandsen, T. A. Ryttov and F. Sannino, *Minimal walking technicolor: set up for collider physics*, Phys. Rev. D **76** (2007) 055005.

[39] A. Belyaev et al., *Technicolor walks at the LHC*, Phys. Rev. D **79** (2009) 035006.

[40] D. Pappadopulo, A. Thamm, R. Torre and A. Wulzer, *Heavy Vector Triplets: Bridging Theory and Data*, JHEP **09** (2014) 060.

[41] ATLAS Collaboration, M. Aaboud et al., *Search for heavy resonances decaying into a W or Z boson and a Higgs boson in final states with leptons and b-jets in 36 $fb^{-1}$of $\sqrt{s}$ = 13 TeV pp collisions with the ATLAS detector*, J. High Energy Phys. **2018** (2018).

[42] R. Contino, D. Marzocca, D. Pappadopulo and R. Rattazzi, *On the effect of resonances in composite Higgs phenomenology*, JHEP **10** (2011) 081.

[43] L. Evans and P. Bryant, *LHC Machine*, JINST **3** (2008) S08001.

[44] ATLAS Collaboration, G. Aad et al., *The ATLAS Experiment at the CERN Large Hadron Collider*, JINST **3** (2008) S08003.

[45] E. Mobs, *The CERN accelerator complex - 2019. Complexe des accélérateurs du CERN - 2019*, (2019), General Photo, URL: https://cds.cern.ch/record/2684277.

[46] Alice Collaboration, Aamodt, K et al., *The ALICE experiment at the CERN LHC*, JINST **3** (2008) S08002.

[47] LHCb Collaboration, Augusto Alvesn, A et al., *The LHCb Detector at the LHC*, JINST **3** (2008) S08005.

[48] CMS Collaboration, Chatrchyan S et al., *The CMS Experiment at the CERN LHC*, JINST **3** (2008) S08004.

[49] ATLAS Collaboration, M. Aaboud et al., *ATLAS public luminosity results Run 2*, 2021, URL: https://twiki.cern.ch/twiki/bin/view/AtlasPublic/LuminosityPublicResultsRun2 (visited on 30/09/2010).

[50] ATLAS Collaboration, G. Aad et al., *The upgraded Pixel detector and the commissioning of the Inner Detector tracking of the ATLAS experiment for Run-2 at the Large Hadron Collider*, PoS **EPS-HEP2015** (2015) 261, arXiv: 1608.07850 [physics.ins-det].

[51] ATLAS Collaboration, M. Aaboud et al., *Jet energy scale and resolution measured in proton–proton collisions at $\sqrt{s}$ = 13 TeV with the ATLAS detector*, Eur. Phys. J.C **81** (2021) 689.

[52] ATLAS Collaboration, G. Aad et al., *The Run-2 ATLAS Trigger System*, J. Phys. Conf. Ser. **762** (2016) 012003, ed. by L. Salinas and C. Torres.

[53] J. Alwall et al., *The automated computation of tree-level and next-to-leading order differential cross sections, and their matching to parton shower simulations*, J. High Energy Phys. **2014** (2014).

[54] E. Bothmann et al., *Event Generation with Sherpa 2.2*, SciPost Phys. **7** (3 2019) 34.

[55] S. Frixione, P. Nason and G. Ridolfi, *A positive-weight next-to-leading-order Monte Carlo for heavy flavour hadroproduction*, JHEP **09** (2007) 126.

[56] P. Nason, *A new method for combining NLO QCD with shower Monte Carlo algorithms*, JHEP **11** (2004) 040.

[57] S. Frixione, P. Nason and C. Oleari, *Matching NLO QCD computations with Parton Shower simulations: the POWHEG method*, JHEP **11** (2007) 070.

[58] S. Alioli, P. Nason, C. Oleari and E. Re, *A general framework for implementing NLO calculations in shower Monte Carlo programs: the POWHEG BOX*, JHEP **06** (2010) 043.

[59] B. Andersson, G. Gustafson, G. Ingelman and T. Sjostrand, *Parton Fragmentation and String Dynamics*, Phys. Rept. **97** (1983) 31.

[60] B. Webber, *A QCD model for jet fragmentation including soft gluon interference*, Nucl. Phys. B **238** (1984) 492.

[61] S. Agostinelli et al., *GEANT4: A simulation toolkit*, Nucl. Instrum. Meth. A **506** (2003) 250.

[62] ATLAS Collaboration, G. Aad et al., 'How ATLAS detects particles: diagram of particle paths in the detector', 2013, URL: https://cds.cern.ch/record/1505342.

[63] ATLAS Collaboration, G. Aad et al., *Concepts, Design and Implementation of the ATLAS New Tracking (NEWT)*, tech. rep., CERN, 2007, URL: http://cds.cern.ch/record/1020106.

[64] R. Fruehwirth, *Application of Kalman Filtering to Track Fitting in the DELPHI Detector*, (1987).

[65] ATLAS Collaboration, G. Aad et al., *Performance of primary vertex reconstruction in proton–proton collisions at $\sqrt{s}$ = 7 TeV in the ATLAS experiment*, ATLAS-CONF-2010-069, 2010, URL: https://cds.cern.ch/record/1281344.

[66] R. Fruhwirth, W. Waltenberger and P. Vanlaer, *Adaptive vertex fitting*, J. Phys. G **34** (2007) N343.

[67] ATLAS Collaboration, G. Aad et al., *Topological cell clustering in the ATLAS calorimeters and its performance in LHC Run 1*, Eur. Phys. J.C **77** (2017) 490.

[68] ATLAS Collaboration, M. Aaboud et al., *Determination of jet calibration and energy resolution in proton–proton collisions at $\sqrt{s}$ = 8 TeV using the ATLAS detector*, (2019), arXiv: 1910.04482 [hep-ex].

[69] ATLAS Collaboration, G. Aad et al., *Jet energy measurement with the ATLAS detector in proton-proton collisions at $\sqrt{s}$ = 7 TeV*, Eur. Phys. J.C **73** (2013) 2304.

[70] ATLAS Collaboration, M. Aaboud et al., *Electron reconstruction and identification in the ATLAS experiment using the 2015 and 2016 LHC proton-proton collision data at $\sqrt{s}$ = 13 TeV*, Eur. Phys. J.C **79** (2019) 639.

[71] ATLAS Collaboration, M. Aaboud et al., *Measurement of the photon identification efficiencies with the ATLAS detector using LHC Run 2 data collected in 2015 and 2016*, Eur. Phys. J.C **79** (2019) 205.

[72] ATLAS Collaboration, G. Aad et al., *Electron and photon reconstruction and performance in ATLAS using a dynamical, topological cell clustering-based approach*, (2017), URL: https://cds.cern.ch/record/2298955.

[73] ATLAS Collaboration, M. Aaboud et al., *Electron and photon performance measurements with the ATLAS detector using the 2015–2017 LHC proton–proton collision data*, JINST **14** (2019) P12006.

[74] ATLAS Collaboration, M. Aaboud et al., *Electron reconstruction and identification in the ATLAS experiment using the 2015 and 2016 LHC proton–proton collision data at* $\sqrt{s} = 13$ *TeV*, Eur. Phys. J.C **79** (2019) 639.

[75] ATLAS Collaboration, M. Aaboud et al., *Muon reconstruction and identification efficiency in ATLAS using the full Run 2 pp collision data set at* $\sqrt{s} = 13$ *TeV*, Eur. Phys. J. C **81** (2021) 578.

[76] ATLAS Collaboration, G. Aad et al., *Muon reconstruction performance of the ATLAS detector in proton-proton collision data at* $\sqrt{s}$ *=13 TeV*, Eur. Phys. J.C **76** (2016) 292.

[77] G. P. Salam et al., *FastJet User Manual*, Eur. Phys. J.C **C72** (2012) 1896.

[78] ATLAS Collaboration, M. Aaboud et al., *Improving jet substructure performance in ATLAS using Track-CaloClusters*, tech. rep. ATL-PHYS-PUB-2017-015, CERN, 2017, URL: https://cds.cern.ch/record/2275636.

[79] ATLAS Collaboration, M. Aaboud et al., *Jet energy scale measurements and their systematic uncertainties in proton–proton collisions at* $\sqrt{s} = 13$ *TeV with the ATLAS detector*, Phys. Rev. D **96** (2017) 072002.

[80] ATLAS Collaboration, G. Aad et al., *Jet energy scale measurements and their systematic uncertainties in proton-proton collisions at s=13 TeV with the ATLAS detector*, Physical Review D **96** (2017).

[81] ATLAS Collaboration, M. Aaboud et al., *In situ calibration of large-radius jet energy and mass in 13 TeV proton–proton collisions with the ATLAS detector*, Eur. Phys. J.C **79** (2019) 135.

[82] ATLAS Collaboration, G. Aad et al., *Performance of jet substructure techniques for large-R jets in proton-proton collisions at* $\sqrt{s} = 7$ *TeV using the ATLAS detector*, JHEP **09** (2013) 076.

[83] A. J. Larkoski, S. Marzani, G. Soyez and J. Thaler, *Soft Drop*, JHEP **05** (2014) 146.

[84] F. A. Dreyer, L. Necib, G. Soyez and J. Thaler, *Recursive Soft Drop*, JHEP **06** (2018) 093.

[85] S. D. Ellis, C. K. Vermilion and J. R. Walsh, *Recombination Algorithms and Jet Substructure: Pruning as a Tool for Heavy Particle Searches*, Phys. Rev. D **81** (2010) 094023.

[86] J. M. Butterworth, A. R. Davison, M. Rubin and G. P. Salam, *Jet substructure as a new Higgs search channel at the LHC*, Phys. Rev. Lett. **100** (2008) 242001.

[87] D. Krohn, J. Thaler and L.-T. Wang, *Jet Trimming*, JHEP **02** (2010) 084.

[88] ATLAS Collaboration, G. Aad et al., *Measurement of large radius jet mass reconstruction performance at* $\sqrt{s} = 8$ *TeV using the ATLAS detector*, ATLAS-CONF-2016-008, 2016, URL: https://cds.cern.ch/record/2139642.

[89] ATLAS Collaboration, G. Aad et al., *Performance of pile-up mitigation techniques for jets in pp collisions at* $\sqrt{s} = 8$ *TeV using the ATLAS detector*, Eur. Phys. J.C **76** (2016) 581.

[90] M. Cacciari, G. P. Salam and G. Soyez, *The Catchment Area of Jets*, JHEP **04** (2008) 005.

[91] ATLAS Collaboration, G. Aad et al., *Optimisation and performance studies of the ATLAS b-tagging algorithms for the 2017-18 LHC run*, ATL-PHYS-PUB-2017-013, 2017, URL: https://cds.cern.ch/record/2273281.

[92] ATLAS Collaboration, M. Aaboud et al., *ATLAS b-jet identification performance and efficiency measurement with $t\bar{t}$ events in pp collisions at $\sqrt{s}$ = 13 TeV*, Eur. Phys. J.C **79** (2019) 970.

[93] S. Heer, *The secondary vertex finding algorithm with the ATLAS detector*, PoS **EPS-HEP2017** (2017) 762, ed. by P. Checchia et al.

[94] ATLAS Collaboration, G. Aad et al., *A new inclusive secondary vertex algorithm for b-jet tagging in ATLAS*, J. Phys. Conf. Ser. **119** (2008) 032032.

[95] ATLAS Collaboration, G. Aad et al., *Performance of b-jet identification in the ATLAS experiment*, J. Instrum. **11** (2016) P04008.

[96] ATLAS Collaboration, G. Aad et al., *Optimisation of the ATLAS b-tagging performance for the 2016 LHC Run*, tech. rep. ATL-PHYS-PUB-2016-012, CERN, 2016, URL: https://cds.cern.ch/record/2160731.

[97] ATLAS Collaboration, M. Aaboud et al., *Public plots FTAG-2019-003*, 2019, URL: http://web.archive.org/web/20080207010024/http://www.808multimedia.com/winnt/kernel.htm (visited on 30/09/2010).

[98] ATLAS Collaboration, M. Aaboud et al., *Measurement of b-tagging efficiency of c-jets in $t\bar{t}$ events using a likelihood approach with the ATLAS detector*, ATLAS-CONF-2018-001, 2018, URL: https://cds.cern.ch/record/2306649.

[99] ATLAS Collaboration, M. Aaboud et al., *Measurements of b-jet tagging efficiency with the ATLAS detector using $t\bar{t}$ events at $\sqrt{s}$ = 13 TeV*, JHEP **08** (2018) 089.

[100] ATLAS Collaboration, M. Aaboud et al., *Calibration of light-flavour b-jet mistagging rates using ATLAS proton–proton collision data at $\sqrt{s}$ = 13 TeV*, ATLAS-CONF-2018-006, 2018, URL: https://cds.cern.ch/record/2314418.

[101] ATLAS Collaboration, G. Aad et al., *Flavor Tagging with Track Jets in Boosted Topologies with the ATLAS Detector*, (2014).

[102] D. Krohn, J. Thaler and L.-T. Wang, *Jets with variable R*, J. High Energy Phys. **2009** (2009) 059.

[103] ATLAS Collaboration, M. Aaboud et al., *Variable Radius, Exclusive-k_T, and Center-of-Mass Subjet Reconstruction for Higgs($\rightarrow b\bar{b}$) Tagging in ATLAS*, tech. rep. ATL-PHYS-PUB-2017-010, CERN, 2017, URL: https://cds.cern.ch/record/2268678.

[104] ATLAS Collaboration, M. Aaboud et al., *Identification of boosted Higgs bosons decaying into b-quark pairs with the ATLAS detector at 13 TeV*, Eur. Phys. J.C **79** (2019) 836.

[105] ATLAS Collaboration, G. Aad et al., *Performance of b-jet identification in the ATLAS experiment*, JINST **11** (2016) P04008.

[106] ATLAS Collaboration, M. Aaboud et al., *Measurements of b-jet tagging efficiency with the ATLAS detector using $t\bar{t}$ events at $\sqrt{s}$ = 13 TeV*, JHEP **08** (2018) 089.

[107] ATLAS Collaboration, M. Aaboud et al., *Performance of missing transverse momentum reconstruction with the ATLAS detector using proton-proton collisions at $\sqrt{s}$ = 13 TeV*, Eur. Phys. J.C **78** (2018) 903.

[108] ATLAS Collaboration, M. Aaboud et al., *E_T^{miss} performance in the ATLAS detector using 2015-2016 LHC p-p collisions*, (2018).

[109] ATLAS Collaboration, G. Aad et al., *Flavor Tagging with Track-Jets in Boosted Topologies with the ATLAS Detector*, ATL-PHYS-PUB-2014-013, 2014, URL: https://cds.cern.ch/record/1750681.

[110] ATLAS Collaboration, M. Aaboud et al., *Identification of boosted Higgs bosons decaying into b-quark pairs with the ATLAS detector at 13 TeV*, Eur. Phys. J.C **79** (2019) 836.

[111] M. Cacciari and G. P. Salam, *Pileup subtraction using jet areas*, Phys. Lett. B **659** (2008) 119.

[112] ATLAS Collaboration, G. Aad et al., *Performance of jet substructure techniques for large-R jets in proton–proton collisions at $\sqrt{s}$ = 7 TeV using the ATLAS detector*, JHEP **09** (2013) 076.

[113] L. Randall and R. Sundrum, *Large Mass Hierarchy from a Small Extra Dimension*, Phys. Rev. Lett. **83** (1999) 3370.

[114] J. Alwall et al., *The automated computation of tree-level and next-to-leading order differential cross sections, and their matching to parton shower simulations*, JHEP **07** (2014) 079.

[115] T. Sjöstrand et al., *An introduction to PYTHIA 8.2*, Comput. Phys. Commun. **191** (2015) 159.

[116] R. D. Ball et al., *Parton distributions with LHC data*, Nucl. Phys. B **867** (2013) 244.

[117] ATLAS Collaboration, G. Aad et al., *ATLAS Pythia 8 tunes to 7 TeV data*, tech. rep. ATL-PHYS-PUB-2014-021, CERN, 2014, URL: https://cds.cern.ch/record/1966419.

[118] D.J. Lange, *The EvtGen particle decay simulation package*, Nucl. Instr. Meth. A **462** (2001) 152.

[119] ATLAS Collaboration, G. Aad et al., *Summary of ATLAS Pythia 8 tunes*, ATL-PHYS-PUB-2012-003, 2012, URL: https://cds.cern.ch/record/1474107.

[120] A. D. Martin, W. J. Stirling, R. S. Thorne and G. Watt, *Heavy-quark mass dependence in global PDF analyses and 3- and 4-flavour parton distributions*, Eur. Phys. J.C **70** (2010) 51.

[121] ATLAS Collaboration, M. Aaboud et al., *B-tagging working points*, URL: %7Bhttps://twiki.cern.ch/twiki/bin/view/AtlasProtected/BTaggingBenchmarks%7D.

[122] ATLAS Collaboration, G. Aad et al., *ATLAS calorimeter performance Technical Design Report*, (1996).

[123] ATLAS Collaboration, M. Aaboud et al., *In situ calibration of large-radius jet energy and mass in 13 TeV proton–proton collisions with the ATLAS detector*, Eur. Phys. J.C **79** (2019) 135.

[124] ATLAS Collaboration, G. Aad et al., *Boosted Higgs ($\rightarrow b\bar{b}$) Boson Identification with the ATLAS Detector at $\sqrt{s}$ = 13 TeV*, ATLAS-CONF-2016-039, 2016, URL: https://cds.cern.ch/record/2206038.

[125] L. G. Almeida et al., *Substructure of high-p_T jets at the LHC*, Phys. Rev. D **79** (7 2009) 074017.

[126] ATLAS Collaboration, G. Aad et al., *ATLAS measurements of the properties of jets for boosted particle searches*, Phys. Rev. D **86** (7 2012) 072006.

[127] J. M. Butterworth, A. R. Davison, M. Rubin and G. P. Salam, *Jet Substructure as a New Higgs-Search Channel at the Large Hadron Collider*, Phys. Rev. Lett. **100** (2008) 242001.

[128] J. M. Butterworth, B. E. Cox and J. R. Forshaw, *WW scattering at the CERN LHC*, Phys. Rev. D **65** (2002) 096014.

[129] S. Catani, Y. L. Dokshitzer, M. H. Seymour and B. R. Webber, *Longitudinally invariant $k_\perp$ clustering algorithms for hadron hadron collisions*, Nucl. Phys. B **406** (1993) 187.

[130] CMS Collaboration, Chatrchyan S et al., *Identifying Hadronically Decaying Vector Bosons Merged into a Single Jet*, tech. rep. CMS-PAS-JME-13-006, CERN, 2013, URL: `https://cds.cern.ch/record/1577417`.

[131] A. J. Larkoski, I. Moult and D. Neill, *Power Counting to Better Jet Observables*, JHEP **12** (2014) 009.

[132] A. Hook, M. Jankowiak and J. G. Wacker, *Jet dipolarity: top tagging with color flow*, JHEP **04** (2012) 007.

[133] A. J. Larkoski, G. P. Salam and J. Thaler, *Energy Correlation Functions for Jet Substructure*, JHEP **06** (2013) 108.

[134] G. C. Fox and S. Wolfram, *Observables for the Analysis of Event Shapes in e^+e^- Annihilation and Other Processes*, Phys. Rev. Lett. **41** (1978) 1581.

[135] ATLAS Collaboration, G. Aad et al., *Identification of high transverse momentum top quarks in pp collisions at$\sqrt{s}$ = 8 TeV with the ATLAS detector*, J. High Energy Phys. **2016** (2016).

[136] ATLAS Collaboration, G. Aad et al., *Identification of boosted, hadronically decaying W bosons and comparisons with ATLAS data taken at $\sqrt{s}$ = 8 TeV*, Eur. Phys. J.C **76** (2016) 154.

[137] ATLAS Collaboration, G. Aad et al., *Identification of high transverse momentum top quarks in pp collisions at $\sqrt{s}$ = 8 TeV with the ATLAS detector*, JHEP **06** (2016) 093.

[138] L. G. Almeida et al., *Top quark jets at the LHC*, Phys. Rev. D **79** (2009) 074012.

[139] C. Chen, *New approach to identifying boosted hadronically-decaying particle using jet substructure in its center-of-mass frame*, Phys. Rev. D **85** (2012) 034007.

[140] ATLAS Collaboration, G. Aad et al., *ATLAS measurements of the properties of jets for boosted particle searches*, Phys. Rev. D **86** (2012) 072006.

[141] ATLAS Collaboration, G. Aad et al., *Measurement of k_T splitting scales in $W \to \ell\nu$ events at $\sqrt{s}$ = 7 TeV with the ATLAS detector*, Eur. Phys. J.C **73** (2013) 2432.

[142] J. Thaler and K. Van Tilburg, *Maximizing boosted top identification by minimizing N-subjettiness*, JHEP **02** (2012) 093.

[143] J. Thaler and K. Van Tilburg, *Identifying boosted objects with N-subjettiness*, JHEP **03** (2011) 015.

[144] S. Brandt, C. Peyrou, R. Sosnowski and A. Wroblewski, *The Principal axis of jets. An Attempt to analyze high-energy collisions as two-body processes*, Phys. Lett. **12** (1964) 57.

[145] ATLAS Collaboration, M. Aaboud et al., *Identification of Boosted Higgs Bosons Decaying Into $b\bar{b}$ With Neural Networks and Variable Radius Subjets in ATLAS*, tech. rep. ATL-PHYS-PUB-2020-019, CERN, 2020, URL: `https://cds.cern.ch/record/2724739`.

[146] ATLAS Collaboration, M. Aaboud et al., *Search for new resonances decaying to a W or Z boson and a Higgs boson in the $\ell^+\ell^- b\bar{b}$, $\ell\nu b\bar{b}$, and $\nu\bar{\nu}b\bar{b}$ channels with pp collisions at s=13 TeV with the ATLAS detector*, Phys. Lett. B **765** (2017) 32.

[147] ATLAS Collaboration, M. Aaboud et al., *Search for heavy resonances decaying into a Z boson and a Higgs boson in final states with leptons and b-jets in* 139 fb^{-1} *of pp collisions at* $\sqrt{s}$ = 13TeV *with the ATLAS detector*, tech. rep., CERN, 2020, URL: https://cds.cern.ch/record/2723658.

[148] ATLAS Collaboration, M. Aaboud et al., *Search for heavy resonances decaying into a W boson and a Higgs boson in final states with leptons and b-jets in* 139 fb^{-1} *of pp collisions at* $\sqrt{s}$ = 13TeV *with the ATLAS detector*, tech. rep., CERN, 2020, URL: https://cds.cern.ch/record/2728053.

[149] ATLAS Collaboration, M. Aaboud et al., *Search for resonances decaying into a weak vector boson and a Higgs boson in the fully hadronic final state produced in proton-proton collisions at s=13 TeV with the ATLAS detector*, Physical Review D **102** (2020).

[150] ATLAS Collaboration, M. Aaboud et al., *Search for heavy diboson resonances in semileptonic final states in pp collisions at* $\sqrt{s}$ = 13 *TeV with the ATLAS detector*, Eur. Phys. J.C **80** (2020) 1165.

[151] CMS Collaboration, Chatrchyan S et al., *Search for heavy resonances decaying into a vector boson and a Higgs boson in final states with charged leptons, neutrinos and b quarks at* $\sqrt{s}$ = 13 *TeV*, J. High Energy Phys. **2018** (2018).

[152] CMS Collaboration, Chatrchyan S et al., *Search for a heavy vector resonance decaying to a Z boson and a Higgs boson in proton-proton collisions at* $\sqrt{s}$ = 13 *TeV*, Eur. Phys. J. C **81** (2021) 688.

[153] ATLAS Collaboration, G. Aad et al., *Luminosity determination in pp collisions at* $\sqrt{s}$ = *8 TeV using the ATLAS detector at the LHC*, Eur. Phys. J.C **76** (2016) 653.

[154] J. Alwall et al., *The automated computation of tree-level and next-to-leading order differential cross sections, and their matching to parton shower simulations*, JHEP **07** (2014) 079.

[155] M. Baak, S. Gadatsch, R. Harrington and W. Verkerke, *Interpolation between multi-dimensional histograms using a new non-linear moment morphing method*, Nucl. Instrum. Meth. A **771** (2015) 39.

[156] L. Moneta et al., *The RooStats Project*, 2011, arXiv: 1009.1003 [physics.data-an].

[157] A. Alloul, N. D. Christensen, C. Degrande, C. Duhr and B. Fuks, *FeynRules 2.0 — A complete toolbox for tree-level phenomenology*, Comput. Phys. Commun. **185** (2014) 2250.

[158] ATLAS Collaboration, G. Aad et al., *Search for a heavy CP-odd Higgs Boson decaying to a Z boson and a heavy CP-even Higgs boson H with $A \to ZH \to llbb$ produced in 13 TeV Collisions with the ATLAS Detector*, tech. rep., CERN, 2016, URL: https://cds.cern.ch/record/2235744.

[159] R. D. Ball et al., *Parton distributions for the LHC run 2*, JHEP **04** (2015) 040.

[160] ATLAS Collaboration, G. Aad et al., *Studies on top-quark Monte Carlo modelling for Top2016*, ATL-PHYS-PUB-2016-020, 2016, URL: https://cds.cern.ch/record/2216168.

[161] M. Beneke, P. Falgari, S. Klein and C. Schwinn, *Hadronic top-quark pair production with NNLL threshold resummation*, Nucl. Phys. B **855** (2012) 695.

[162] M. Cacciari, M. Czakon, M. Mangano, A. Mitov and P. Nason, *Top-pair production at hadron colliders with next-to-next-to-leading logarithmic soft-gluon resummation*, Phys. Lett. B **710** (2012) 612.

[163] P. Bernreuther, M. Czakon and A. Mitov, *Percent level precision physics at the Tevatron: First genuine NNLO QCD corrections to $q\bar{q} \to t\bar{t} + X$*, Phys. Rev. Lett. **109** (2012) 132001.

[164] M. Czakon and A. Mitov, *NNLO corrections to top-pair production at hadron colliders: the all-fermionic scattering channels*, JHEP **12** (2012) 054.

[165] M. Czakon and A. Mitov, *NNLO corrections to top pair production at hadron colliders: the quark-gluon reaction*, JHEP **01** (2013) 080.

[166] M. Czakon, P. Fiedler and A. Mitov, *Total top-quark-pair-production cross section at hadron colliders through $O(\alpha_S^4)$*, Phys. Rev. Lett. **110** (2013) 252004.

[167] M. Czakon and A. Mitov, *Top++: A Program for the Calculation of the Top-Pair Cross-Section at Hadron Colliders*, Comput. Phys. Commun. **185** (2014) 2930.

[168] S. Frixione, E. Laenen, P. Motylinski, B. R. Webber and C. D. White, *Single-top hadroproduction in association with a W boson*, JHEP **07** (2008) 029.

[169] ATLAS Collaboration, M. Aaboud et al., *Measurement of single top-quark production in association with a W boson in the single-lepton channel at $\sqrt{s} = 8$ TeV with the ATLAS detector*, (2020), arXiv: `2007.01554 [hep-ex]`.

[170] E. Bothmann et al., *Event Generation with Sherpa 2.2*, SciPost Phys. **7** (2019) 034.

[171] T. Gleisberg and S. Höche, *Comix, a new matrix element generator*, JHEP **12** (2008) 039.

[172] F. Buccioni et al., *OpenLoops 2*, Eur. Phys. J.C **79** (2019) 866.

[173] Cascioli, Fabio and Maierhofer, Philipp and Pozzorini, Stefano, *Scattering Amplitudes with Open Loops*, Phys. Rev. Lett. **108** (2012) 111601.

[174] A. Denner, S. Dittmaier and L. Hofer, *Collier: A fortran-based complex one-loop library in extended regularizations*, Comput. Phys. Commun. **212** (2017) 220.

[175] S. Höche, F. Krauss, M. Schönherr and F. Siegert, *A critical appraisal of NLO+PS matching methods*, JHEP **09** (2012) 049.

[176] F Siegert et al., *QCD matrix elements + parton showers: The NLO case*, JHEP **04** (2013) 027.

[177] S. Catani, F. Krauss, R. Kuhn and B. R. Webber, *QCD Matrix Elements + Parton Showers*, JHEP **11** (2001) 063.

[178] S. Höche, F. Krauss, S. Schumann and F. Siegert, *QCD matrix elements and truncated showers*, JHEP **05** (2009) 053.

[179] C. Anastasiou, L. J. Dixon, K. Melnikov and F. Petriello, *High precision QCD at hadron colliders: Electroweak gauge boson rapidity distributions at NNLO*, Phys. Rev. D **69** (2004) 094008.

[180] ATLAS Collaboration, G. Aad et al., *Measurement of the Z/γ^* boson transverse momentum distribution in pp collisions at $\sqrt{s} = 7$ TeV with the ATLAS detector*, JHEP **09** (2014) 145.

[181] J. Butterworth et al., *PDF4LHC recommendations for LHC run 2*, J. Phys. G **43** (2016) 023001.

[182] R. V. Harlander, A. Kulesza, V. Theeuwes and T. Zirke, *Soft gluon resummation for gluon-induced Higgs Strahlung*, JHEP **11** (2014) 082.

[183] ATLAS Collaboration, M. Aaboud et al., *ATLAS b-jet identification performance and efficiency measurement with $t\bar{t}$ events in pp collisions at $\sqrt{s}$ = 13 TeV*, Eur. Phys. J.C **79** (2019) 970.

[184] ATLAS Collaboration, M. Aaboud et al., *Object-based missing transverse momentum significance in the ATLAS detector*, tech. rep. ATLAS-CONF-2018-038, CERN, 2018, URL: https://cds.cern.ch/record/2630948.

[185] ATLAS Collaboration, M. Aaboud et al., *Observation of $H \to b\bar{b}$ decays and VH production with the ATLAS detector*, Phys. Lett. B **786** (2018) 59.

[186] ATLAS Collaboration, M. Aaboud et al., *Jet pT and mass scale uncertainties for TCC trimmed jets*, tech. rep., unpublished: JetEtmiss group, 2019.

[187] ATLAS Collaboration, G. Aad et al., *Muon reconstruction performance of the ATLAS detector in proton–proton collision data at $\sqrt{s}$ = 13 TeV*, Eur. Phys. J.C **76** (2016) 292.

[188] ATLAS Collaboration, M. Aaboud et al., *Luminosity determination in pp collisions at $\sqrt{s}$ = 13 TeV using the ATLAS detector at the LHC*, tech. rep. ATLAS-CONF-2019-021, CERN, 2019, URL: https://cds.cern.ch/record/2677054.

[189] G. Avoni et al., *The new LUCID-2 detector for luminosity measurement and monitoring in ATLAS*, JINST **13** (2018) P07017.

[190] ATLAS Collaboration, G. Aad et al., *Identification and energy calibration of hadronically decaying tau leptons with the ATLAS experiment in pp collisions at $\sqrt{s}$=8 TeV*, Eur. Phys. J.C **75** (2015) 303.

[191] ATLAS Collaboration, M. Aaboud et al., *Performance of missing transverse momentum reconstruction with the ATLAS detector using proton–proton collisions at $\sqrt{s}$ = 13 TeV*, Eur. Phys. J.C **78** (2018) 903.

[192] ATLAS Collaboration, M. Aaboud et al., *E_T^{miss} performance in the ATLAS detector using 2015–2016 LHC pp collisions*, ATLAS-CONF-2018-023, 2018, URL: https://cds.cern.ch/record/2625233.

[193] ATLAS Collaboration, G. Aad et al., *The ATLAS Simulation Infrastructure*, Eur. Phys. J.C **70** (2010) 823.

[194] ATLAS Collaboration, G. Aad et al., *Fast Simulation for ATLAS: Atlfast-II and ISF*, tech. rep. ATL-SOFT-PROC-2012-065, CERN, 2012.

[195] ATLAS Collaboration, M. Aaboud et al., *Study of top-quark pair modelling and uncertainties using ATLAS measurements at $\sqrt{s}$=13 TeV*, tech. rep. ATL-PHYS-PUB-2020-023, CERN, 2020, URL: http://cds.cern.ch/record/2730443.

[196] P. Nason and B. Webber, *Next-to-Leading-Order Event Generators*, Annu. Rev. Nucl. Part. Sci. **62** (2012) 187.

[197] J. Bellm et al., *Herwig 7.0/Herwig++ 3.0 release note*, Eur. Phys. J.C **76** (2016) 196.

[198] ATLAS Collaboration, G. Aad et al., *ATLAS Pythia 8 tunes to 7 TeV data*, ATL-PHYS-PUB-2014-021, 2014, URL: https://cds.cern.ch/record/1966419.

[199] S. Höche, F. Krauss, M. Schönherr and F. Siegert, *QCD matrix elements + parton showers. The NLO case*, J. High Energy Phys. **2013** (2013).

[200] J. Rojo, *PDF4LHC recommendations for Run II*, 2016, arXiv: 1606.08243 [hep-ph].

[201] M. Guzzi et al., *CT10 parton distributions and other developments in the global QCD analysis*, 2011, arXiv: 1101.0561 [hep-ph].

[202] T. Qiu, *Collaborative analysis group member work, soon to be published*, Dissertation, 2021.

[203] W. Verkerke and D. P. Kirkby, *The RooFit toolkit for data modeling*, eConf **C0303241** (2003) MOLT007, ed. by L. Lyons and M. Karagoz, arXiv: physics/0306116.

[204] R. Barlow and C. Beeston, *Fitting using finite Monte Carlo samples*, Comput. Phys. Commun. **77** (1993) 219.

[205] G. Cowan, K. Cranmer, E. Gross and O. Vitells, *Asymptotic formulae for likelihood-based tests of new physics*, Eur. Phys. J.C **71** (2011).

[206] A. Wald, *Tests of Statistical Hypotheses Concerning Several Parameters When the Number of Observations is Large*, Transactions of the American Mathematical Society **54** (1943) 426, URL: http://www.jstor.org/stable/1990256.

[207] E. Gross, *Practical Statistics for High Energy Physics*, (2017), URL: https://doi.org/10.23730/CYRSP-2017-004.165.

[208] ATLAS Collaboration, M. Aaboud et al., *Search for heavy resonances decaying into a Z or a W boson and a Higgs boson in final states with leptons and b-jets in* $139\,\text{fb}^{-1}$ *of pp collisions at* $\sqrt{s} = 13$ *TeV with the ATLAS detector*, (), to be published.

[209] A. Hönle, 'Searches for new resonances decaying to a Higgs and a vector boson with the ATLAS detector at the LHC', CERN Thesis, Dissertation: Technische Universität München, 2021, URL: http://cds.cern.ch/record/2779497.

[210] T. Sjöstrand, S. Mrenna and P. Z. Skands, *A Brief Introduction to PYTHIA 8.1*, Comput. Phys. Commun. **178** (2008) 852.

[211] T. G. et al., *Event generation with SHERPA 1.1*, JHEP **02** (2009) 007.

[212] ATLAS Collaboration, M. Aaboud et al., *Evidence for electroweak production of two jets in association with a* $Z\gamma$ *pair in pp collisions at* $\sqrt{s} = 13$ *TeV with the ATLAS detector*, Phys. Lett. B **803** (2020) 135341.